

**AGARD-R-792**

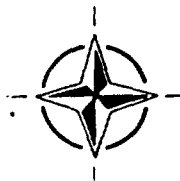
## ADVISORY GROUP FOR AEROSPACE RESEARCH & DEVELOPMENT

7 RUE ANCELLE 92200 NEUILLY SUR SEINE FRANCE

# (Interactions entre Ondes de Choc et Couches Limites dans les Ecoulements Supersoniques et Hypersoniques)

Accession For	
NTIS GRA&I	
DTIC TAB	
Unannounced	
Justification	
By	
Date	
DTIC	
A-1	

The material assembled in this report was prepared under the combined sponsorship of the AGARD Fluid Dynamics Panel and the von Kármán Institute (VKI) for Fluid Dynamics. It was presented in an AGARD-FDP-VKI Special Course at the VKI, Rhode-Saint-Genèse, Belgium, 24th—28th May 1993..



**North Atlantic Treaty Organization**  
***Organisation du Traité de l'Atlantique Nord***



**Best  
Available  
Copy**



# The Mission of AGARD

According to its Charter, the mission of AGARD is to bring together the leading personalities of the NATO nations in the fields of science and technology relating to aerospace for the following purposes:

- Recommending effective ways for the member nations to use their research and development capabilities for the common benefit of the NATO community;
- Providing scientific and technical advice and assistance to the Military Committee in the field of aerospace research and development (with particular regard to its military application);
- Continuously stimulating advances in the aerospace sciences relevant to strengthening the common defence posture;
- Improving the co-operation among member nations in aerospace research and development;
- Exchange of scientific and technical information;
- Providing assistance to member nations for the purpose of increasing their scientific and technical potential;
- Rendering scientific and technical assistance, as requested, to other NATO bodies and to member nations in connection with research and development problems in the aerospace field.

The highest authority within AGARD is the National Delegates Board consisting of officially appointed senior representatives from each member nation. The mission of AGARD is carried out through the Panels which are composed of experts appointed by the National Delegates, the Consultant and Exchange Programme and the Aerospace Applications Studies Programme. The results of AGARD work are reported to the member nations and the NATO Authorities through the AGARD series of publications of which this is one.

Participation in AGARD activities is by invitation only and is normally limited to citizens of the NATO nations.

The content of this publication has been reproduced  
directly from material supplied by AGARD or the authors.

Published August 1993

Copyright © AGARD 1993  
All Rights Reserved

ISBN 92-835-0718-5



*Printed by Specialised Printing Services Limited  
40 Chigwell Lane, Loughton, Essex IG10 3TZ*



# **Recent Publications of the Fluid Dynamics Panel**

## **AGARDOGRAPHS (AG)**

**Design and Testing of High-Performance Parachutes**  
AGARD AG-319, November 1991

**Experimental Techniques in the Field of Low Density Aerodynamics**  
AGARD AG-318 (E), April 1991

**Techniques Expérimentales Liées à l'Aérodynamique à Basse Densité**  
AGARD AG-318 (FR), April 1990

**A Survey of Measurements and Measuring Techniques in Rapidly Distorted Compressible Turbulent Boundary Layers**  
AGARD AG-315, May 1989

**Reynolds Number Effects in Transonic Flows**  
AGARD AG-303, December 1988

## **REPORTS (R)**

**Unstructured Grid Methods for Advection Dominated Flows**  
AGARD R-787, Special Course Notes, May 1992

**Skin Friction Drag Reduction**  
AGARD R-786, Special Course Notes, March 1992

**Engineering Methods in Aerodynamic Analysis and Design of Aircraft**  
AGARD R-783, Special Course Notes, January 1992

**Aircraft Dynamics at High Angles of Attack: Experiments and Modelling**  
AGARD R-776, Special Course Notes, March 1991

**Inverse Methods in Airfoil Design for Aeronautical and Turbomachinery Applications**  
AGARD R-780, Special Course Notes, November 1990

## **ADVISORY REPORTS (AR)**

**Air Intakes for High Speed Vehicles**  
AGARD AR-270, Report of WG 13, September 1991

**Appraisal of the Suitability of Turbulence Models in Flow Calculations**  
AGARD AR-291, Technical Status Review, July 1991

**Rotary-Balance Testing for Aircraft Dynamics**  
AGARD AR-265, Report of WG 11, December 1990

**Calculation of 3D Separated Turbulent Flows in Boundary Layer Limit**  
AGARD AR-255, Report of WG10, May 1990

**Adaptive Wind Tunnel Walls: Technology and Applications**  
AGARD AR-269, Report of WG12, April 1990

## **CONFERENCE PROCEEDINGS (CP)**

**Theoretical and Experimental Methods in Hypersonic Flows**  
AGARD CP-514, April 1993

**Aerodynamic Engine/Airframe Integration for High Performance Aircraft and Missiles**  
AGARD CP-498, September 1992

**Effects of Adverse Weather on Aerodynamics**  
AGARD CP-496, December 1991



**Manoeuvring Aerodynamics**  
AGARD CP-497, November 1991

**Vortex Flow Aerodynamics**  
AGARD CP-494, July 1991

**Missile Aerodynamics**  
AGARD CP-493, October 1990

**Aerodynamics of Combat Aircraft Controls and of Ground Effects**  
AGARD CP-465, April 1990

**Computational Methods for Aerodynamic Design (Inverse) and Optimization**  
AGARD-CP-463, March 1990

**Applications of Mesh Generation to Complex 3-D Configurations**  
AGARD CP-464, March 1990

**Fluid Dynamics of Three-Dimensional Turbulent Shear Flows and Transition**  
AGARD CP-438, April 1989

**Validation of Computational Fluid Dynamics**  
AGARD CP-437, December 1988

**Aerodynamic Data Accuracy and Quality: Requirements and Capabilities in Wind Tunnel Testing**  
AGARD CP-429, July 1988

**Aerodynamics of Hypersonic Lifting Vehicles**  
AGARD CP-428, November 1987

**Aerodynamic and Related Hydrodynamic Studies Using Water Facilities**  
AGARD CP-413, June 1987

**Applications of Computational Fluid Dynamics in Aeronautics**  
AGARD CP-412, November 1986

**Store Airframe Aerodynamics**  
AGARD CP-389, August 1986

**Unsteady Aerodynamics — Fundamentals and Applications to Aircraft Dynamics**  
AGARD CP-386, November 1985

**Aerodynamics and Acoustics of Propellers**  
AGARD CP-366, February 1985

**Improvement of Aerodynamic Performance through Boundary Layer Control and High Lift Systems**  
AGARD CP-365, August 1984

**Wind Tunnels and Testing Techniques**  
AGARD CP-348, February 1984

**Aerodynamics of Vortical Type Flows in Three Dimensions**  
AGARD CP-342, July 1983

**Missile Aerodynamics**  
AGARD CP-336, February 1983

**Prediction of Aerodynamic Loads on Rotorcraft**  
AGARD CP-334, September 1982

**Wall Interference in Wind Tunnels**  
AGARD CP-335, September 1982

**Fluid Dynamics of Jets with Applications to V/STOL**  
AGARD CP-308, January 1982

**Aerodynamics of Power Plant Installation**  
AGARD CP-301, September 1981

**Computation of Viscous-Inviscid Interactions**  
AGARD CP-291, February 1981

**Subsonic/Transonic Configuration Aerodynamics**  
AGARD CP-285, September 1980



# Foreword

Shock-wave/boundary-layer interactions continue to be ubiquitous phenomena in supersonic and hypersonic aerodynamics, and their importance is often crucial as, for example, for hypersonic controls and for air intakes in general. This is the reason for the continuous research efforts in this field, aiming at developing reliable methodologies for future vehicle design. Results from these programmes have been reported in Détery and Marvin's 1986 AGARDograph (AG-280) and in the 1989 AGARD FDP VKI Special Course on "Three-dimensional supersonic/hypersonic flows including separation".

The present course reviews the recent progress in this field. In particular, a large part of the course is devoted to swept interactions, both laminar and turbulent, including a discussion of the following topics:

- the flowfield structure,
- the scaling and similarity laws,
- the effect of shock strength on flow features,
- the effect of shock generator geometry for a given shock strength,
- experimental techniques, in particular optical techniques, for the investigation of swept interactions,
- contributions of numerical simulations to the understanding of swept interactions.

A limiting factor in the understanding and ability to predict shock wave/boundary-layer interactions is a good knowledge of turbulence behaviour. In particular, it is well known that classical turbulence models produce rather poor predictions in strongly interacting flowfields. Turbulence behaviour in shock-wave/boundary-layer interactions therefore constitutes the second major subject of this course, including a discussion of

- global flowfield unsteadiness due to turbulence and its impact on turbulence quantities,
- contribution of LDV to the physical description of typical shock-wave/boundary-layer interactions with incidence on turbulence modelling,
- specific issues in turbulence modelling for shock-wave/boundary-layer interactions with examples of applications.

Finally, a lecture is devoted specifically to hypersonic interactions. Special emphases are given to the following questions:

- heat transfer in hypersonic interactions,
- effect of transition on hypersonic interactions, including the striation phenomenon,
- computation of hypersonic laminar interactions and code validation.



# Avant-Propos

Les interactions onde de choc/couche limite demeurent des phénomènes omniprésents en aérodynamique supersonique et hypersonique, et leur importance est souvent cruciale, par exemple pour les surfaces de contrôle hypersoniques, de même que pour les entrées d'air en général. C'est pourquoi des programmes de recherche continuent à être consacrés à ce sujet, en vue de développer des méthodes fiables pour la conception de futurs véhicules. Les résultats de certains de ces programmes ont été exposés dans l'AGARDograph AG-280 de Détery et Marvin publié en 1986, ainsi que dans les notes du Cours AGARD FDP VKI de 1989 consacré aux "Écoulements supersoniques et hypersoniques tridimensionnels, y compris le décollement".

Ce cours-ci passe en revue les progrès récents dans le domaine. En particulier, une large part du cours est consacrée aux interactions dérapées, laminares et turbulentes et comprend une discussion des points suivants:

- la structure de l'écoulement,
- les paramètres d'échelle et les lois de similitude,
- l'effet de l'intensité du choc sur les caractéristiques de l'écoulement,
- l'effet de la géométrie du générateur de choc pour une intensité donnée,
- les techniques expérimentales, en particulier optiques pour l'étude des interactions dérapées,
- la contribution des simulations numériques à la compréhension des interactions dérapées.

Un facteur limitant la compréhension et la capacité de prédire les interactions onde de choc couche limite est la (mé)connaissance du comportement de la turbulence dans ces écoulements. En particulier, il est bien connu que les modèles classiques de turbulence fournissent des résultats assez médiocres pour les interactions fortes. C'est pourquoi le comportement de la turbulence dans les interactions onde de choc/couche limite constitue le second sujet principal du cours. On aborde

- l'instationnarité globale de l'écoulement déclenchée par la turbulence et son impact sur les grandeurs turbulentes,
- la contribution de la vélocimétrie laser (LDV) à la description physique d'interactions onde de choc couche limite typiques et l'impact sur la modélisation de la turbulence,
- les problèmes spécifiques de modélisation de la turbulence pour les interactions onde de choc couche limite avec exemples d'applications.

Enfin, un exposé est consacré plus particulièrement aux interactions hypersoniques. L'accent est mis sur les questions suivantes

- le transfert de chaleur dans les interactions hypersoniques,
- l'effet de la transition sur les interactions hypersoniques, y compris le phénomène de stries longitudinales,
- la simulation numérique d'interactions hypersoniques laminares, et la validation de codes.



# Special Course Staff

**Special Course Director:** Professor G. Degrez  
von Kármán Institute for Fluid Dynamics  
Chaussée de Waterloo, 72  
1640 Rhode-Saint-Genèse  
Belgium

## LECTURERS

Dr G. Simeonides  
ESA/ESTEC (YPA)  
Aerothermodynamic Section  
Postbus 299  
2200 AG Noordwijk  
The Netherlands

Mr J.M. Détery  
Head, Fundamental Aerodynamics Div.  
ONERA — BP 72  
92322 Châtillon Cedex  
France

Professor D. Vandromme  
Laboratoire de Mécanique des  
*Fluides Numériques*  
INSA de Rouen  
Place Emile Blondel, B.P. No. 8  
76131 Mont Saint Aignan  
France

Professor D.S. Dolling  
Center for Aeromechanics Research  
University of Texas at Austin  
Austin, TX 78712-1085  
United States

Professor D.D. Knight  
Mechanical and Aerospace Engineering Dept  
Rutgers University — P.O. Box 909  
Piscataway, NJ 08855-0909  
United States

Professor G.S. Settles  
Mechanical Engineering Department  
303 Reber Building  
Pennsylvania State University  
University Park, PA 16802  
United States

## SPECIAL COURSE COORDINATOR

Professor G. Degrez  
von Kármán Institute for Fluid Dynamics  
Chaussée de Waterloo, 72  
1640 Rhode-Saint-Genèse  
Belgium

## PANEL EXECUTIVE

Dr W. Goodrich

**Mail from Europe:**  
AGARD—OTAN  
Attn: FDP Executive  
7, rue Ancelle  
92200 Neuilly-sur-Seine  
France

**Mail from US and Canada:**  
AGARD—NATO  
Attn: FDP Executive  
Unit 21551  
APO AE 09777

Tel: 33(1)47 38 57 75  
Telex: 610176 (France)  
Telefax: 33(1) 47 38 57 99



# Contents

	Page
<b>Recent Publications of the Fluid Dynamics Panel</b>	iii
<b>Foreword</b>	v
<b>Avant-Propos</b>	vi
<b>Special Course Staff</b>	vii
	Reference
<b>Swept Shock/Boundary-Layer Interactions – Scaling Laws, Flowfield Structure, and Experimental Methods</b> by G.S. Settles	1
<b>Swept Shock Wave/Laminar Boundary Layer Interactions, Experimental and Numerical Results</b> by G. Degrez	2
<b>Numerical Simulation of 3-D Shock Wave Turbulent Boundary-Layer Interactions</b> by D.D. Knight	3
<b>Unsteady Phenomena in Shock-Wave/Boundary Layer Interaction</b> by D.S. Dolling	4
<b>Contribution of Laser Doppler Velocimetry to the Physical Description of Shock-Wave/Turbulent Boundary Layer Interactions with Incidence on Turbulence Modelling</b> by J.M. Détery	5
<b>Turbulence Modelling for Shock Wave/Boundary-Layer Interactions (Specific Issues and Examples of Applications)</b> by D. Vandromme	6
<b>Hypersonic Shock Wave Boundary Layer Interactions over Simplified Deflected Control Surface Configurations</b> by G. Simeonides	7



VCO	virtual conical origin
x,y,z	Cartesian coordinate system
x	coordinate normal to plate in heat transfer analysis
$\alpha$	angle made by fin with respect to the incoming freestream direction, deg.
$\beta$	angle made by surface-flow features with freestream direction in spherical polar coordinates, deg.
$\beta_0$	angle made by inviscid shock-wave trace on test surface with freestream direction, deg.
$\Delta\beta_0$	$= (\beta_0 - \mu_\infty)$ , reduced inviscid shock angle parameter
$\Delta\beta_1$	angular measure of $\lambda$ -foot defined in Fig. 28
$\Delta\beta_2$	angular measure of $\lambda$ -foot defined in Fig. 28
$\Delta\beta_L$	$= (\beta_L - \mu_\infty)$ , reduced upstream influence angle parameter
$\gamma$	ratio of specific heats
$\delta$	incoming undisturbed boundary-layer thickness, mm
$\Delta s$	oil-film leading-edge distance, m
$\theta$	incoming, undisturbed boundary-layer momentum thickness, mm
$\lambda$	shock generator leading-edge sweep-back angle, also laser wavelength
$\mu_\infty$	$= \sin^{-1}(1/M_\infty)$ , Mach angle of incoming freestream
$\nu$	oil viscosity, centistokes
$\xi_i$	$= (p_2/p_1)_i$ , incipient separation pressure ratio
$\rho$	density, kg/m <sup>3</sup>
$\tau_w$	wall shear stress, N/m <sup>2</sup>
$\phi$	azimuthal angle in spherical polar coordinates, deg.
$\Omega$	Ohms

## 2.2 Subscripts

aw	adiabatic wall conditions
i	incipient separation
is	incident shock
m	maximum
n	normal
p	plateau
pa	primary attachment
pk	peak value
ps	primary separation
r, ref	reference value
s	shock
s, S1	separation
U, ui	upstream influence
TP	triple-point
w	wall conditions
$\infty$	incoming freestream conditions
0	value at beginning of interaction
*	denotes incipient separation condition

## 3. INTRODUCTION

The interactions of shock waves and boundary-layers have long been a fundamental and critical problem area of fluid dynamics. They represent the imposition of the strongest adverse pressure gradients on viscous

layers which are susceptible to disruption by such gradients. Unfortunately, the nature of high-speed flow over practical missiles, aircraft, re-entry vehicles, and turbomachinery components makes such interactions unavoidable, with consequences ranging from tolerable to (occasionally) disastrous. Furthermore, the scale and performance constraints of such practical applications almost always dictate that the interactions in question will be both turbulent and three-dimensional. This three-dimensionality usually implies that the interactions are (or have components which are) moderately to highly swept.

The past 20 years have seen intensive research on the subject of swept shock wave/turbulent boundary-layer interactions. This research was conducted and supported because it was recognized that such flows are important, fundamental viscous/inviscid interactions, are key building-blocks in high-speed internal and external aerodynamic problems, and are primary test cases for numerical simulations. From the efforts of a number of investigators worldwide, a limited understanding of such interactions is now available whereas, only a few years ago, almost nothing was known.

Several recent publications have attempted an overview of this newfound understanding, including those in 1986 and 1990 by the present author and D. S. Dolling (Refs. 1,2). The present paper relies heavily upon Ref. 2 for the interaction scaling laws and part of the flowfield structure sections, while assembling material not previously reviewed for the section on experimental methods.

## 3.1 Present Scope

Refs. 1 and 2 are each on the order of 25,000 words long. Ref. 1 is a general review of swept interactions, while Ref. 2 concentrates specifically upon turbulent interactions produced by sharp fins and interaction unsteadiness. The present paper may be thought of as an update and supplement rather than as a replacement for these documents. Moreover, insofar as unsteady phenomena, numerical simulations, and laminar/transitional interactions are covered by other authors in this report, they are omitted from consideration here. Likewise, the present consideration of experimental methods forgoes any discussion of Laser Doppler Velocimetry in favor of the paper by J. Delery given elsewhere in this report.

This discussion is thus restricted to supersonic interactions with turbulent boundary layers, whence the main body of available data derives. Even so, a wide variety of swept interaction types exists. An effort was made to classify and describe several of these in Ref. 1, to which the reader is referred. Ref. 2, on the other hand, concentrated on the large body of available information concerning the sharp-fin-generated interaction with a turbulent boundary layer.



# Swept Shock/Boundary-Layer Interactions - Scaling Laws, Flowfield Structure, and Experimental Methods

Gary S. Settles  
Gas Dynamics Laboratory  
Mechanical Engineering Department  
303 Reber Building  
Penn State University  
University Park, PA 16802 USA

## 1. SUMMARY

A general review is given of several decades of research on the scaling laws and flowfield structures of swept shock wave/turbulent boundary layer interactions. Attention is further restricted to the experimental study and physical understanding of the steady-state aspects of these flows. The interaction produced by a sharp, upright fin mounted on a flat plate is taken as an archetype. An overall framework of quasiconical symmetry describing such interactions is first developed. Boundary-layer separation, the interaction footprint, Mach number scaling and Reynolds number scaling are then considered, followed by a discussion of the quasiconical similarity of interactions produced by geometrically-dissimilar shock generators. The detailed structure of these interaction flowfields is next reviewed, and is illustrated by both qualitative visualizations and quantitative flow images in the quasiconical framework. Finally, the experimental techniques used to investigate such flows are reviewed, with emphasis on modern non-intrusive optical flow diagnostics.

## 2. LIST OF SYMBOLS

### 2.1 Main Symbols

A amperes  
 $c_f$  incoming boundary-layer skin friction coefficient  
 $c_h$  incoming boundary-layer heat transfer coefficient  
 $c_p$  specific heat at constant pressure  
 $D, d$  shock generator leading-edge diameter, mm  
 $D$  thermal diffusivity  
 $\dot{q}$  heat generation rate,  $W/m^3$   
 $H, h$  step height, mm  
 $K$  constant  
 $k$  thermal conductivity  
 $l, l_n$  orthonormal coordinates based on inviscid shock wave trace on test surface  
 $L_i$  inception length from VCO to conical flow, mm

$L_n$   $= (l_n/\delta)Re_\delta^{-1/4}$ , non-dimensional distance measured normal to inviscid shock trace on test surface  
 $L_s$   $= (l_s/\delta)Re_\delta^{-1/4}$ , non-dimensional distance measured along inviscid shock trace on test surface  
 $Mn, M_n$   $= M_\infty \sin \beta_0$ , Mach number normal to inviscid shock wave trace on test surface  
 $M_n$  Mach number normal to separation line  
 $M_\infty$  incoming freestream Mach number  
 $n$  oil refractive index  
 $N'$  effective fringe number  
 $PA, A_1$  primary flow attachment line  
 $PS, S_1$  primary flow separation line  
 $p$  static pressure, MPa  
 $p_\infty$  incoming freestream static pressure, MPa  
 $p_1$  freestream static pressure before shock, MPa  
 $p_2$  freestream static pressure after shock, MPa  
 $q''_{conv}$  heat convected to flow,  $W/m^2$   
 $q''_{heat}$  heat efflux from heater,  $W/m^2$   
 $q''_{loss}$  heat conducted through insulator board,  $W/m^2$   
 $R, r$  distance measured from the virtual origin in spherical polar coordinate frame, mm  
 $r$  oil refraction angle  
 $R$  resistance,  $\Omega$   
 $Re$  freestream unit Reynolds number,  $m^{-1}$   
 $Re_\delta$  Reynolds number based on the incoming, undisturbed boundary-layer thickness  
 $Re_\theta$  Reynolds number based on the incoming, undisturbed boundary-layer momentum thickness  
 $S$  separation line  
 $S_{1,1}$  optical phase shift  
 $SA$  secondary flow attachment line  
 $SS, S_2$  secondary flow separation line  
 $t$  time  
 $t'$  effective flow time  
 $T$  temperature,  $^\circ K$   
 $T_0$  stagnation temperature,  $^\circ K$   
 $U, UI$  upstream influence line  
 $V$  velocity, m/s, also volts



As in Ref. 2, the present paper will also concentrate its attention on the simplest of all swept interactions, *ie* that generated by an equilibrium, adiabatic flat-plate turbulent boundary layer interacting with the swept, planar oblique shock wave generated by an upright, sharp-leading-edged fin at angle-of-attack  $\alpha$  (see Fig. 1). Known as a "sharp fin interaction" for brevity, this flow is a classical case, an archetype, of swept interactions in general. (The reader should note that various authors have also referred to this case as a "glancing-shock" or "swept-normal-shock" interaction.) Emphasis will be placed on experimental results which shed light on the physical behavior and phenomenology of these interactions rather than on prediction methods or aerothermodynamic applications *per se*.

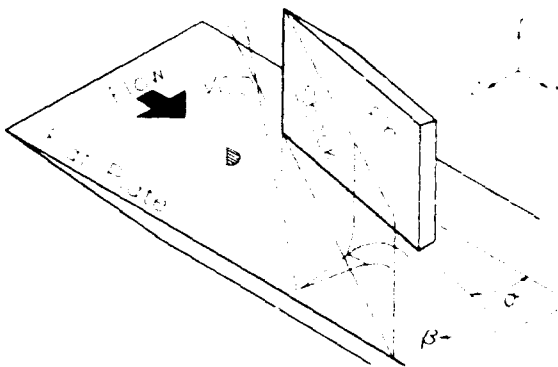


Fig. 1 - Sharp Fin Interaction Test Geometry.

This concentration on sharp fin interactions neglects several other swept interaction types--the blunt fin, swept compression corner, etc.--which are certainly not of negligible importance. However, relatively little new work has appeared on these topics since they were reviewed in Ref. 1 and other reviews mentioned below. The only other interaction type seeing significant recent activity is the important new area of crossing-shock interactions. While this area is not covered due to necessary limitations on the present scope, it is expected that crossing-shock interactions will be the subject of a separate review in due time.

### 3.2 Historical Sketch

The interaction of a shock wave with a boundary-layer was apparently first observed by Ferri (Ref. 3) in 1939. Following World War II, research on the subject concentrated on 2-D interactions, which were thought to be more amenable to study than swept interactions. The work of Stalker (Ref. 4) in 1960 was the first detailed attempt to study interaction sweepback. There followed a 25-year period of steady increase in the number of papers published annually on swept interactions, indicating that this subtopic of fluid dynamics was still a maturing research area during that time. The publication record reveals spurts of activity in the late 1960s and mid-70s,

presumably due to the cold-war "space race" and the SST and Space Shuttle development efforts. The most recent spurt of activity may be ascribed in part to the need for experimental benchmarks for CFD predictions, and to the NASP program.

It may be that the field of swept interactions is nearing maturity at the time of this writing. If so, it is principally the result of several research groups having concentrated on the problem, especially those at the NASA-Ames Research Center, Penn State, Princeton, and Rutgers Universities, and the Institute for Theoretical and Applied Mechanics in Novosibirsk.

Additional material pertinent to the present topic may be found in several existing survey papers, notably the one by Green (Ref. 5). The early work on swept interactions was surveyed, along with other shock interference flows, by Korkegi (Ref. 6) and more recently by Peake and Tobak (Ref. 7). Other pertinent reviews include those of Delery and Marvin (Ref. 8) and Stollery (Ref. 9).

### 3.3 Initial Assumptions

It should be helpful at the outset to identify some underlying characteristics, assumptions, and hypotheses concerning swept interactions. For example, it is traditionally assumed that these interactions depend primarily upon the freestream Mach number, the characteristics of the incoming boundary layer, and the shock generator geometry (Ref. 5). However, these dependencies cannot be determined by any closed-form solution of the governing equations of motion on account of the flow complexity. Experiments, similarity and dimensional reasoning, and (within the last 10 years) computational simulations have thus played a key role in the study of swept interactions. The computations, dealt with elsewhere in this report by D. D. Knight, have recently reached the level at which they can contribute to the fundamental understanding of swept interactions in ways not readily amenable to experiments. The experiments also now serve the role of providing benchmarks for the validation of the computations. To this end a shock/boundary-layer interaction database (Refs. 10 & 11) is available.

In the interaction structure there is a hierarchy of information that is also present in the existing experimental data: Swept interactions are rich in patterns, and the most easily obtained and most prevalent data are those of interaction "footprint" patterns on solid surfaces obtained by way of surface flow visualization methods. Mean surface pressure distributions were also taken in most of the past experiments, and a few experiments also included wall shear stress and heat transfer data. Dolling *et al* have specialized in unsteady surface pressure measurements in these flows. Off the surface, flowfield visualization



techniques and probe surveys of mean pitot pressures and flow angles have helped to map flowfield structures and to provide a connection with the footprint data. The highest level of the measurement hierarchy includes dynamic data via hot-wire, LDV, and other quantitative methods. Very few of such measurements have been made in 3-D shock boundary-layer interactions.

Much of the content of this paper derives from a parametric exploratory approach to the swept interaction problem. Since the problem is complex, it is a necessary first step to explore the range of possible flows by parametric studies. Only then can detailed investigations of particular interactions be interrelated in an overall framework of understanding. However, insofar as these interactions are only partially deterministic due to their dependence upon turbulent transport phenomena, the parametric exploratory approach is not expected to lead to complete understanding. Indeed, most of the knowledge gained thus far is directly related to the extent to which swept interactions depend upon inviscid phenomena.

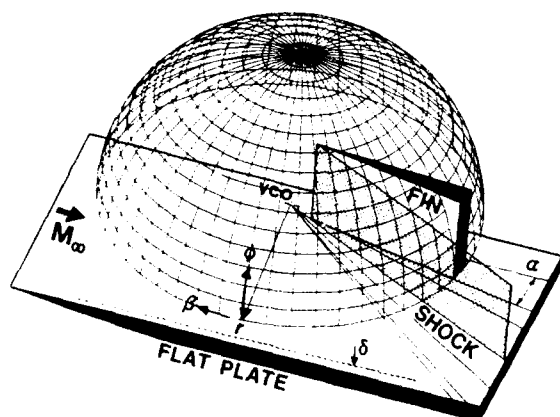


Fig. 2 - Spherical Polar Coordinate System.

An essential first step in understanding swept interactions is the choice of a proper coordinate system. Experience dictates that it is easy to go astray with this problem if a poor choice is made. Many of the past swept interaction studies have revealed some degree of either quasiconical or quasicylindrical flow symmetry. In principle, spherical polar coordinates are required for the former (see Fig. 2) and normal-tangential coordinates for the latter, although experimental data are sometimes available only in a streamwise-spanwise coordinate frame. In practice it is often reasonable to make the approximation of an orthogonal normal-tangential frame attached to the interaction sweep line, which is usually the "footprint trace" or projection of the outer ("inviscid") shock wave upon the interaction test surface. Following the tradition of both swept and unswept interaction studies, this footprint trace of the inviscid shock is taken as the proper reference line from which to

measure the interaction extent. Due to the limited scope of the present paper, discussed above, the spherical polar coordinate frame of Fig. 2 turns out to be the only one presently required. Its application to sharp fin interactions will be discussed in detail below.

Next, a firm connection is assumed between the swept interaction footprint topography and the features of the flowfield above the surface. This hypothesis is supported by recent experimental results to be described in the section on flowfield structure, and by the application of topology to the surface flow patterns (Ref. 12). Moreover, the topological rules (Ref. 12) governing these flow patterns are recognized as important aids to the understanding of swept interactions.

Finally, this paper considers only the mean-flow behavior of swept interactions. It appears that all interactions of shock waves with turbulent boundary-layers involve some degree of unsteadiness, typically manifested as a "trembling" motion observed in flowfield visualizations. However, there is no indication that such unsteadiness is the controlling phenomenon in any overall sense. A definite, identifiable mean-flow structure is found in all interaction cases considered here. It is thus assumed that the preponderance of mean-flow data on swept interactions is useful and pertinent despite the presence of unsteadiness.

### 3.4 Interaction Classifications

A brief overview of the different types of swept interactions is called for at the outset. Swept interactions will be discussed in terms of the classifications shown in Fig. 3 (from Ref. 1), which result from elementary dimensional analysis. In all cases the incoming flow provides a single length scale associated with the boundary-layer (here taken as the incoming thickness  $\delta_0$  for simplicity). When the overall dimensions of the shock generator are large enough that further increases in these dimensions do not change the interaction properties, the resulting interactions are classified as "semi-infinite." Further, cases within this classification in which the shock generator imposes no length dimension on the interaction are termed "dimensionless." In such "dimensionless" interactions it may be expected from elementary dimensional analysis that the flow will respond to the imposed incoming boundary-layer length scale with a single balancing length scale of its own (later to be identified as the interaction inception length).

However, if a semi-infinite shock generator does impose upon the interaction a length dimension comparable to  $\delta_0$  (such as a fin leading-edge thickness  $D$  or a step height  $H$ ), the resulting interaction is then termed "dimensional." Here,  $D/\delta_0$  or  $H/\delta_0$  is expected to characterize the flow in the immediate



vicinity of the imposed length dimension. Such interactions are discussed in Ref. 1 but are beyond the scope of the present paper.

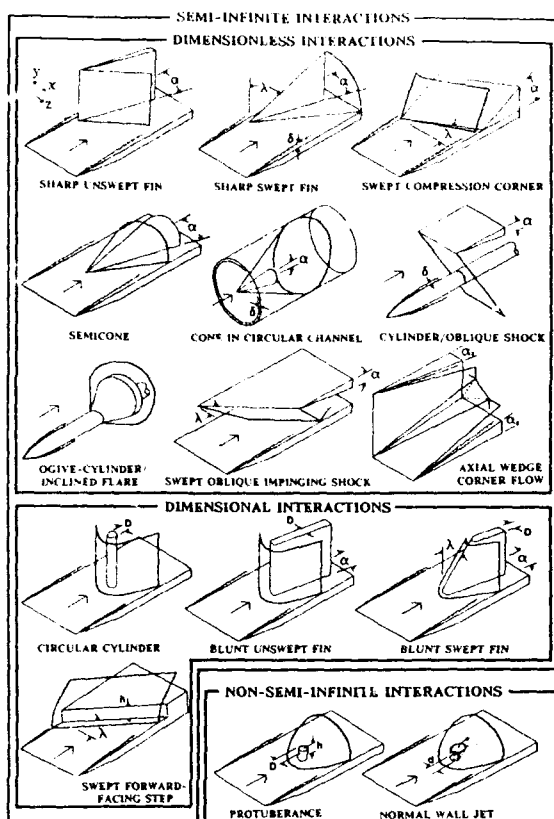


Fig. 3 - Interaction Classifications.

Finally, cases in which the shock generator fails to produce a semi-infinite interaction as defined above are termed non-semi-infinite or "protuberance" interactions. These cases typically involve shock generators whose overall dimensions are comparable to  $\delta_0$ . Protuberance interactions are also discussed in Ref. 1 and are also beyond the scope of the present paper.

### 3.5 Goals

Taking the sharp fin interaction as an archetype of swept interactions in general, the present paper has three goals:

- 1) Survey the current knowledge of the scaling laws which govern the shape, size, and behavior of the "footprint" of a swept interactions in terms of  $M_\infty$ ,  $Re$ ,  $\alpha$ , and  $\delta_0$ ,
- 2) Examine in detail the interaction flow-field structure which is responsible for the observed footprint behavior, and
- 3) Describe the experimental methods, both modern and time-honored, which have been applied to learn much of what is now known about swept interactions.

## 4. SCALING LAWS

The unswept sharp fin interaction of Figs. 1-3 is, at least in the inviscid sense, the simplest of all swept interactions. This simplicity derives from the fact that the properties of the shock wave prior to its interaction with the boundary-layer (the "inviscid shock") are known immediately from classical oblique-shock theory. As we will see, the swept interaction necessarily leads to fundamental changes of structure in both the shock wave and the boundary-layer, whereupon the flow may no longer be regarded as "simple."

As in all flows where direct solutions of the governing equations are not possible, dimensional and similarity methods are powerful tools in understanding swept interactions. For dimensionless sharp-fin interactions only a single parameter,  $\alpha$ , is required to describe the shock generator. The other parameters of the problem are entirely concerned with the incoming flow, and include  $M_\infty$ ,  $Re$ , and  $\delta_0$ . All are dimensionless parameters except  $\delta_0$ , which is the only length dimension in the boundary conditions of the problem. Thus, as mentioned earlier, the interaction is expected to respond to  $\delta_0$  by way of some characteristic length, but otherwise to be entirely dimensionless.

Thus, despite the nonlinearity of the governing equations and a host of related complications, there is nonetheless hope from the outset of achieving some overall similarity framework for the behavior of swept interactions. That framework is the subject this section of the paper, where the mean-flow symmetry and footprint structure of the interaction are explored and the influence of  $M_\infty$ ,  $Re$ ,  $\alpha$ , and  $\delta_0$  are examined.

### 4.1 Quasiconical Symmetry

All previous investigators of sharp fin interactions have found that the extent of the interaction grows with distance away from the fin leading edge. Many of these investigators (eg Refs. 13-23) further observed that this growth appeared to be conical, or nearly so, except for an initial region in the immediate vicinity of the juncture of the fin leading-edge and the flat plate. This observation is confirmed by recent parametric studies (Refs. 24-28) of sharp fin interactions over broad ranges of both Mach number and fin angle. It is now clear that the salient characteristic of this interaction is its *quasiconical* nature.

The dimensional description given earlier describes this class of swept interactions as having no length dimension except for one characteristic length which arises in response to the initial condition imposed by  $\delta_0$ . Let this length be called  $L_i$ , the *inception length* measured outward from the fin leading-edge along the shock wave direction, which encompasses the observed initial nonconical region of the interaction (see Fig. 4). Thus  $L_i/\delta_0$  is a natural nondimensional parameter describing the class of interactions under study.



The supersonic or hypersonic potential flow outside the interaction is well-known to exhibit conical behavior (Ref. 29), wherein the velocity vector is constant along rays emanating from a common origin, the conical vertex. Further, after Lighthill (Ref. 30) such a conical field will occur "in any flow where the boundary conditions define naturally no linear dimension." The present flow, outside the inception zone, is very close to satisfying this condition except for the issue of the non-conical growth of the incoming boundary-layer with spanwise distance along the interaction sweep line.

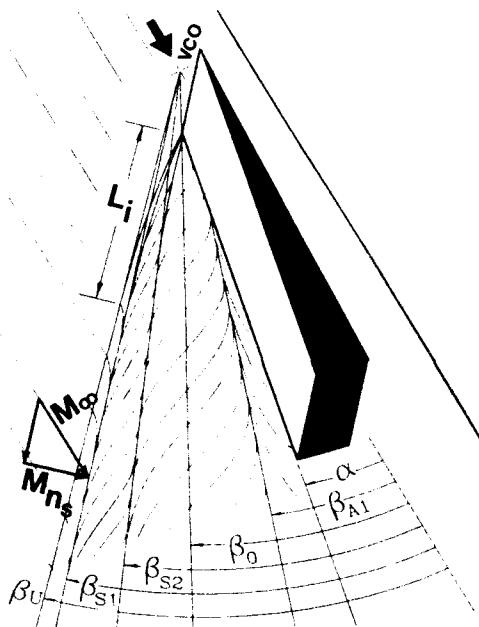


Fig. 4 - Sketch of Sharp Fin Interaction Footprint with Nomenclature Definitions.

An important contribution by Inger (Ref. 31) largely resolved this problem through an order-of-magnitude analysis of the governing equations. Inger found that a swept interaction can approach a quasiconical state at a large distance from the fin leading-edge. This distance, in fact, turns out to be the inception length,  $L_i$ , and how large it is depends upon  $\delta_0$ . Inger also found that  $L_i/\delta_0 \approx \cot \beta_0$ , in agreement with experimental data for sharp fin interactions. While some effect of the spanwise boundary-layer growth is probably present, it is a second-order effect compared to the overall quasiconical nature of the flow (Ref. 32).

The quasiconical symmetry of this class of swept interactions is now regarded as the most powerful simplification available in a problem of otherwise daunting complexity. As we will see, it allows a 3-D flow to be treated, in many respects, as if it were two-

dimensional. Much is already known about the behavior of conical 2-D flows, which are thoroughly reviewed, for example, in Ref. 33. Briefly, the proper coordinate frame for a conical flow is the spherical polar coordinate system in  $r$ ,  $\beta$ , and  $\phi$ , sketched in Fig. 2. Since  $r$  is degenerate in true conical flow, the interaction outside the inception zone is described entirely in angular measure by  $\beta$  and  $\phi$ . Streamlines and other features of the flow may be seen in two dimensions by projection from the vertex of the conical flow onto the surface of the sphere. Since experience has shown that such projections of swept interactions normally subtend small solid angles, the replacement of the appropriate spherical segment with a plane tangent to the sphere and normal to the inviscid shock wave is a frequent simplification. The pertinent Mach number describing the interaction is the component of  $M_{\infty}$  in this plane, namely  $M_n$ , rather than  $M_{\infty}$  itself.

This coordinate frame is adopted uniformly in the following discussion. Other than  $L_i$  and  $\delta_0$ , all "dimensions" of swept interactions are discussed only in angular measure. While it may be tempting to define length dimensions associated with, say, the upstream influence of the interaction, experience shows this to be highly misleading. For example, early investigators of this flow remarked upon the streamwise length of the interaction compared to that of a 2-D planar interaction of similar shock strength. However, in the present context of quasiconical flow this comparison is meaningless, since the streamwise length of the interaction can be as large or small as one wishes, depending upon the distance,  $r$ , which one takes from the conical vertex.

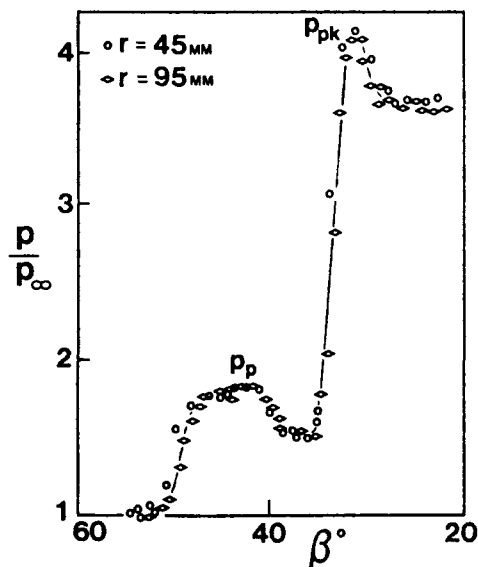


Fig. 5 - Surface Pressure Distributions (per Ref. 16).



As a demonstration of the conical nature of sharp-fin interactions, surface-pressure data from a Mach 3 interaction by Zubin and Ostapenko (Ref. 16) are shown in Fig. 5. These data were measured on two concentric circular arcs on a flat plate at different radii,  $r$ , from the vertex of the flow. Both measurement arcs were outside the inception zone. The data show excellent agreement when the pressure ratio is plotted in terms of the conical angle  $\beta$ . Such agreement cannot be had, however, if the linear dimension describing the pressure-tap layout is used as the abscissa of the plot.

Finally, note that quasiconical interaction symmetry is an approximate framework of understanding rather than a precise law. It breaks down near the fin leading edge in the inception zone, and also along the intersection of the fin and the flat plate (which cannot lie on a generating ray of the conical flow). It is subject to the second-order 3-D influence of the spanwise growth of  $\delta_0$ , mentioned earlier. It is a mean-flow framework for the description of interactions which are known to have some time-dependent characteristics. In extremely weak interactions (Refs. 34 and 35) the conical spreading of the flow may be so small as to be undetectable. In extremely strong interactions the approximation may once again break down, though experimental limitations prevent such a case from being observed. Between these two limits, and subject to the qualifications listed, all known dimensionless fin interactions exhibit quasiconical symmetry.

#### 4.2 Boundary-Layer Separation

All shock/boundary-layer interactions, whether 2-D or 3-D, involve the separation of the boundary-layer when the shock wave is of sufficient strength to bring this about. Despite some controversy over the semantics of the word "separation," the literature cited thus far leaves no room for doubt that it is a distinct and recognizable phenomenon in swept interactions. Due to the nature of such flows, when separation does occur it is necessarily three-dimensional and highly swept with respect to the oncoming flow.

A proper treatment of the topological criteria for 3-D flow separation is well beyond the present scope. The reader is directed to Ref. 12 for a thorough coverage of this topic. Briefly, the present discussion accepts the Legendre-Lighthill view of 3-D separation as the convergence of limiting streamlines of the flow upon a particular (swept) streamline which connects singular points of separation located, in this case, somewhere on the flat plate. The exact nature of these singular points is a secondary issue for present purposes. What is important is the observation (eg Ref. 26) that the noticeable effects of separation develop gradually in sharp fin interactions, and that occurrence of separation is clearly a function of Mach number and shock wave strength.

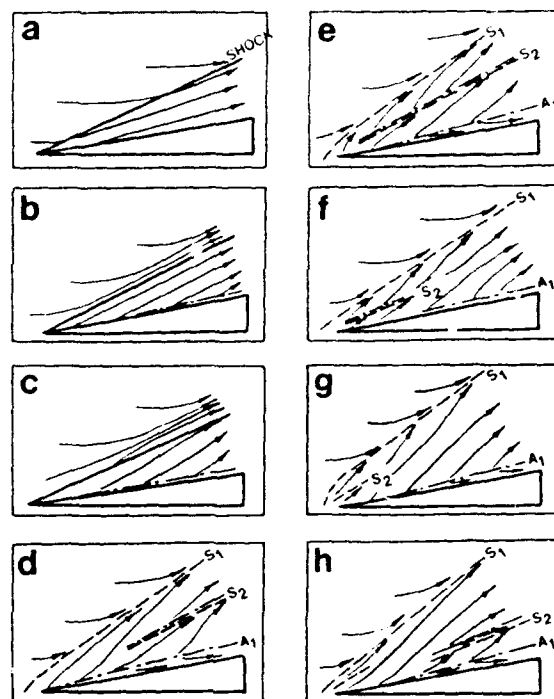


Fig. 6 Stages in the Development of the Interaction Footprint (per Zheltovodov *et al.*).

Fig. 6, from Ref. 26, shows 8 stages in the development of the limiting streamlines of the interaction footprint on the flat plate as a function of increasing shock wave strength. Such patterns are obtained by surface-flow visualization techniques, and will be discussed further in later sections. For the moment, one sees in Fig. 6a the case of a weak, unseparated interaction in which the limiting streamlines veer underneath the inviscid shock wave but do not form a convergence line. With increasing shock strength, Fig. 6b, the separation line moves outward and eventually lies underneath the inviscid shock, with limiting streamlines on either side running essentially parallel to it. (Stanbrook (Ref. 36) defined this condition rather arbitrarily as incipient swept separation of the boundary layer.) A further increase of shock strength, Fig. 6c, leads to asymptotic convergence of the limiting streamlines upon the line of 3-D separation. Finally, in Fig. 6d, a sufficiently-strong shock produces an explicit convergence line,  $S_1$ , which lies well outboard of the inviscid shock position.

This gradual development of the flow points out the disparity between the strict topological definition of 3-D separation, for which the present flow is always separated (Ref. 37), and more practical definitions which find no evidence of lift-off of the boundary-layer from the flat plate until the condition in Fig. 6d is reached. Should there be any doubt on this point, Fig. 7 shows the kerosene-lampblack footprint trace of a weak fin interaction (Mach 2,  $\alpha = 6^\circ$ ), in which the



primary separation line lies well inside the zone bounded by the fin and the inviscid shock. (This pattern was obtained by placing surface-tracer material on the flat plate only *upstream* of the fin prior to the experiment.) Since a line of 3-D separation is clearly present in Fig. 7, Stanbrook's criterion (Ref. 36) must be strictly incorrect. It serves, nonetheless, to indicate the approximate condition where sizable or significant 3-D separation occurs, insofar as effects on the outer flowfield are concerned. More will be said about this below.

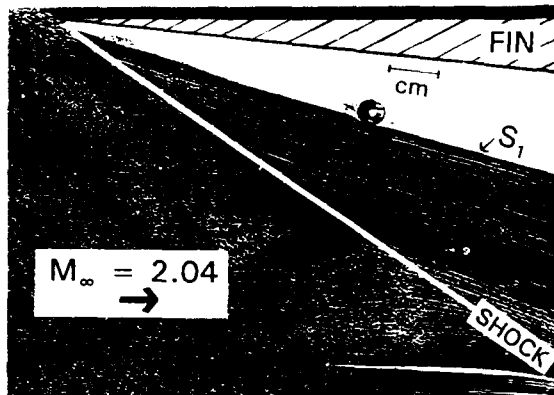


Fig. 7 - Footprint Trace of a Weak Separated Fin Interaction.

Based on arguments put forward by McCabe, (Ref. 38) Korkegi (Refs. 39 and 40) proposed a practical criterion for incipient swept separation in the form:

$$M_\infty \alpha_i = 0.3 \quad (1)$$

for  $M_\infty > 1.6$  and  $\gamma = 1.4$ , where  $\alpha_i$  is measured in radians. Lu (Ref. 41) recently re-derived this result on a somewhat firmer ground. As the most well-known and popular criterion for incipient swept separation, Eqn. (1) is illustrated here in Fig. 8. It corresponds to the flow condition shown in Fig. 6b and determines the condition in which the limiting streamlines run parallel to the inviscid shock wave, not true incipient separation, as was already mentioned in connection with Fig. 7 (see also Refs. 21, 37, and 42).

It may be seen from Fig. 8 that the practical condition of incipient swept separation not only occurs for weaker shocks than does incipient 2-D separation at the same  $M_\infty$ , but also happens even more readily as  $M_\infty$  increases. Early on, the lack of a physical explanation for this was the source of some consternation and disbelief. However, the physical explanation is not difficult to understand if one accepts that it makes no sense to compare 2-D and 3-D separation at the same value of  $M_\infty$ . According to the above quasi-conical symmetry discussion, it is the *normal* Mach number,  $M_n$ , which is significant in determining the properties of a swept interaction, rather than  $M_\infty$ .

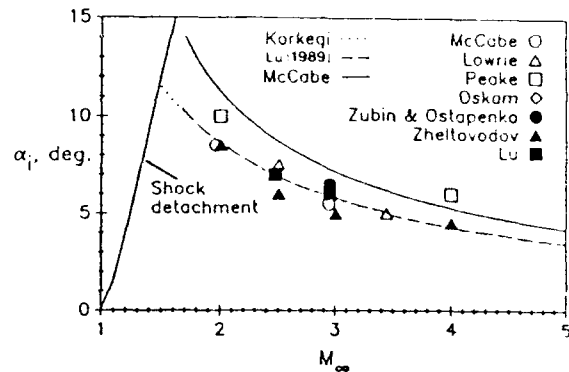


Fig. 8 - Incipient Separation Criterion for Sharp-Fin Interactions.

When compared on this basis, 2-D and swept incipient separation criteria are in close agreement. For example, in broad terms, incipient turbulent boundary layer separation is found at normal Mach numbers between 1.2 and 1.3 in a wide variety of swept and unswept shock/boundary-layer interactions (Refs. 26, 41, and 43). The corresponding inviscid-shock pressure ratios,  $(p_2/p_1)_i$ , in air are between 1.5 and 1.8. Thus the seeming anomaly of incipient separation becoming more likely with increasing Mach number is explainable in terms of the higher sweepback angle of the shock wave. No discrepancy between 2-D and swept separation criteria occurs, so long as one pays attention to the proper coordinate frame.

The recent work of Zheltovodov *et al.* (Refs. 26 and 43) has developed this approach considerably. In re-working the classical free-interaction analysis of Chapman *et al.* (Ref. 44), they obtained the following expression for the "plateau" pressure in a separated interaction:

$$p_p - p_\infty = K M_n^2 (M_n^2 - 1)^{-1/4} c_f^{1/2} + 1 \quad (2)$$

where  $\gamma = 1.4$  is assumed,  $K = 5.94$  for turbulent and 1.46 for laminar flows, and  $M_n$  is the Mach number normal to the separation line. This expression was verified by comparison with experimental data for 2-D turbulent interactions. It embodies the pressure-rise required to produce incipient separation, if one accepts this to be equal to the plateau pressure rise of a well-separated interaction. When combined with the classical expression for oblique-shock pressure ratio in terms of  $M_n$ , Eqn. 2 can be used to predict incipient swept separation as well. Zheltovodov *et al.* found the result to be in good agreement with the data for what they call incipient "small angle" separation, *i.e.* the condition represented by Fig. 6b where surface streamlines run parallel to



the shock but noticeable lift-off of the boundary-layer from the flat plate has yet to develop.

These authors then proposed an additional, new criterion for incipient "large-scale" separation. Plots of the angle between the upstream-influence and primary separation lines of the interaction show that it decreases with increasing interaction strength, eventually tending toward a constant value. Once this constancy occurs, it is argued that the interaction has reached a condition (Fig. 6d) where the swept separation is fully developed and where its gross effects are clearly manifested in the interaction flowfield.

Finally, Zheltovodov *et al.* used the above quasi-2-D free-interaction analysis to demonstrate that  $(p_2/p_1)_i$  tends to decrease from 1.7 to 1.5 as  $Re_\theta$  increases from  $10^3$  to  $5 \times 10^4$ , as illustrated in Fig. 9. Variations in the shape parameter of the incoming boundary-layers in the experimental data points shown (numbered symbols 4-9) further required that  $K$  in Eqn. 2 be varied over the range 5.9 to 9.4, producing the band shown in the Figure. This view of incipient separation is clearly an improvement over Eqn. 1, Korkegi's criterion, which embodies the simple implicit assumption that  $(p_2/p_1)_i = 1.5$ , and thus ignores the Reynolds number and shape factor dependence inherent in the characteristics of the incoming boundary layer. Korkegi's criterion is also shown in Fig. 9 for comparison.

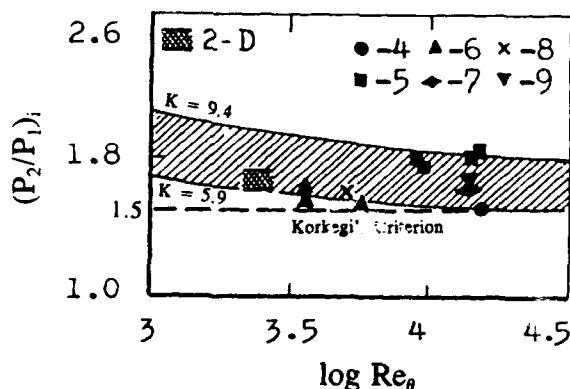


Fig. 9 - Incipient Separation Criteria vs.  $Re_\theta$  (per Zheltovodov *et al.*).

### 4.3 The Interaction Footprint

#### 4.3.1 Limiting Streamline Pattern

Returning to Fig. 4, the "footprint" of a shock-generated swept interaction, *ie* its pattern of limiting streamlines on the flat plate, is illustrated with definitions of nomenclature. Four important features are identified by their conical angles: the upstream influence line  $U$ , the primary separation line  $S_1$ , the primary attachment line  $A_1$ , and the secondary separation line  $S_2$ . The upstream influence line, being the forwardmost extent of the interaction, has been the

subject of various attempts to relate the response of the interaction footprint to changes in Mach number, Reynolds number, and fin angle (Refs. 1, 15, 17-22, 26, 27, 34, 45, and 46). Similar but more limited attempts have been made to correlate the positions of the primary separation and attachment lines. Primary attachment, which first appears in the shock-strength progression in Fig. 6d, marks the position where the flow, having left the surface of the flat plate at the primary separation line, reattaches to the plate (though the stream-surface which separates is not the one which reattaches). Between these two lines lies a region of reverse flow in the conical projection, which also has a strong spanwise ( $r$ -direction) component. This leads to a helical separation vortex. One may view this vortex as a reorganization of the spanwise vorticity of the incoming boundary layer. Zheltovodov *et al.* (Ref. 26) noted an inflection in the primary separation line which they ascribed to transition from laminar to turbulent reverse-flow within the separated region.

The angular difference  $\beta_U - \beta_{S1}$  between the upstream influence and primary separation lines is sizable for weak interactions, but shrinks quickly to a small value as the interaction grows stronger. The achievement of this asymptotic value (Refs. 26 and 43) has been used as an indicator of incipient "large-scale" flow separation, as noted earlier. In fact, the region between these two defining lines of the interaction has been found to be highly unsteady. Since the current discussion concerns only mean-flow properties, this unsteadiness is covered elsewhere in this report by D. S. Dolling.

If the definition of primary separation has caused some past confusion, as noted earlier, this is doubly the case for secondary separation. According to Zheltovodov *et al.* (Refs. 18, 26), the footprint feature known as secondary separation first appears once the interaction has achieved a certain strength (Fig. 6d), showing up in the conical region of the flow but not in the inception zone. Its spanwise extent grows with increasing shock strength (Fig. 6e) but then diminishes again (Fig. 6f), eventually appearing only in the inception zone and then disappearing altogether (Fig. 6g). Secondary separation then reappears in the strongest interactions observed to date (Fig. 6h), but in a different position, noticeably closer to the fin than previously. Zheltovodov *et al.* were the first to observe this behavior, and have invested considerable effort in trying to understand it. Their experiments with sand-grain roughness applied to the interaction region appear to demonstrate that the initial behavior of secondary separation is related to laminar, transitional, and then turbulent reverse-flow in the swept separation bubble. They also ascribe the reappearance of secondary separation (Fig. 6h) to the development of supersonic reverse flow in the separat-



ed region with an imbedded normal shock wave. This was first reported by Zubin and Ostapenko (Ref. 16), though no clear image of it was shown. Very clear images confirming this hypothesis have recently been obtained by Alvi and Settles (Refs. 16 and 47).

Another, even more serious, problem with secondary separation is that it usually appears without the visible accompaniment of secondary attachment! This topologically-impossible situation is probably due to a very small angle between secondary separation and attachment, such that they appear as a single feature. Zheltovodov (Ref. 48) has obtained evidence of both secondary separation and attachment in an extremely-strong fin-induced turbulent boundary-layer interaction at Mach 4 and  $\alpha = 30.6^\circ$ . The surface flow pattern of this interaction, shown in Fig. 10, was traced directly from an enlargement of an oil-flow photograph provided by Zheltovodov, since the photo itself would not be likely to reproduce well enough to show the features described. Nonetheless, distinct secondary separation and secondary attachment lines are clearly visible with an angle of 1 or 2 degrees between them. This evidence confirms, in the opinion of the present author, that secondary separation actually can occur in this class of interactions, given the proper circumstances. A local maximum appears at this secondary separation/attachment location in measured skin-friction distributions (Refs. 49 and 50). A local flowfield disturbance also appears in the vicinity of this location in conical shadowgrams and interferograms of the flowfield (Refs. 24, 25, and 47).

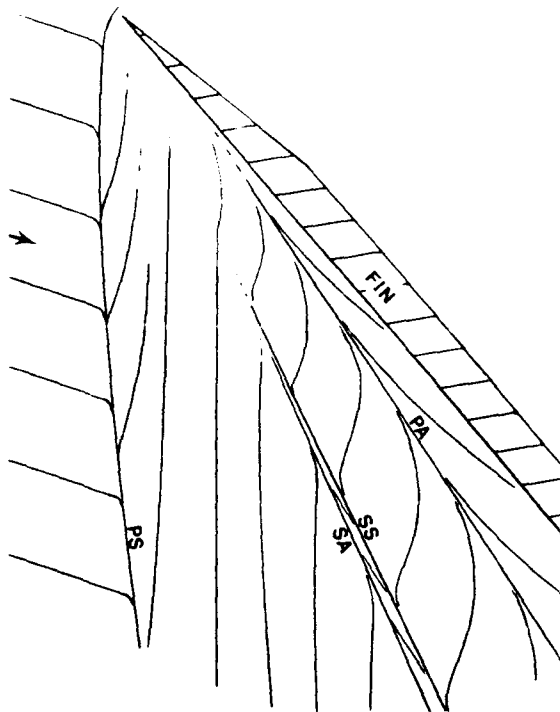


Fig. 10 - Tracing of Surface Pattern of Zheltovodov's Mach 4,  $\alpha = 30.6^\circ$  Interaction.

Fig. 4 illustrates how the conical lines of the interaction footprint all emanate from a common vertex, the virtual conical origin or VCO. This origin, which is the center of the spherical coordinate frame shown in Fig. 2, lies somewhat ahead of the actual fin leading-edge due to the presence of the inception region, which is also indicated in Fig. 4 by its length,  $L_i$ .

Zheltovodov *et al.* (Ref. 26) proposed correlations for the conical angles of upstream influence  $\beta_w$  and primary separation  $\beta_{s1}$  in terms of the inviscid shock angle  $\beta_0$ . Incipient "small-scale" separation, as defined in the previous section (Fig. 9), is used as a basis for these correlations, and is denoted by an asterisk. The correlations are:

$$\beta_w - \beta_{w*} = 1.53(\beta_0 - \beta_{0*}) \quad (3)$$

$$\beta_{s1} - \beta_{s1*} = 2.15(\beta_0 - \beta_{0*}) - 0.0144(\beta_0 - \beta_{0*})^2 \quad (4)$$

one confusing factor is that two forms of the  $\beta_{s1}$  correlation were given, one for laminar and the second for turbulent reverse-flow. Since it may not be easy to determine which form to use, it is suggested here that supersonic interactions with freestream unit Reynolds numbers on the order of  $10^7/\text{m}$  or higher use only the turbulent form, which is the one given above as Eqn. 4. The correlations of Eqns. 3 and 4 are based upon many experimental points obtained at Novosibirsk in the Mach 2-4 range. However, Schmisser (Ref. 51) also compared them with his data, obtained at Mach 5, and found good agreement.

#### 4.3.2 Surface Pressure Distribution

Many investigators have measured the surface pressure beneath the footprint of the interaction. Its classical shape, measured in the proper crossflow coordinate frame for a well-separated interaction, was already shown in Fig. 5. The peak pressure, just ahead of the fin, is of interest because it overshoots the maximum pressure,  $p_2$ , expected behind the inviscid shock wave. Several attempts have been made to derive expressions for the peak pressure ratio,  $p_{pk}/p_\infty$ . For example, according to Hayes (Ref. 52):

$$p_{pk}/p_\infty = M_\infty^{2.4} \quad (5)$$

Scuderi (Ref. 53), Zheltovodov (Ref. 18), and Lu (Ref. 27) proposed similar expressions. Most recently, Lu (Ref. 54) has reexamined this issue in the light of current knowledge, to be discussed below, about the detailed structure of the fin interaction flowfield. He arrived at a physically more meaningful, though less explicit, approach to predicting  $p_{pk}/p_\infty$ . His summary graph is reproduced here as Fig. 11, which shows a comparison of available data and prediction methods for this quantity.



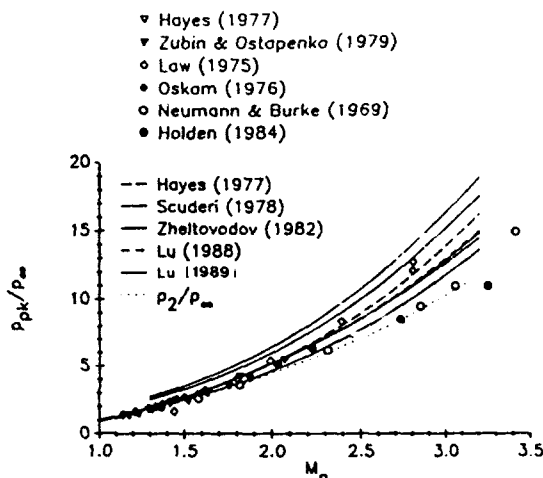


Fig. 11 - Interaction Peak Pressure Ratio vs. Normal Mach Number (per Lu).

Zheltovodov *et al.* (Ref. 55) also proposed a new expression for the peak pressure ratio based on their quasi-2-D free interaction analysis:

$$p_{pk}/p_{\infty} = 1.3(p_2/p_1) - 0.3(p_2/p_1)_i \quad (6)$$

They developed a method to predict not only  $p_{pk}$ , but also the entire shape of the interaction-footprint pressure distribution.

### 4.3.3 Heat Transfer Distribution

The peak heat transfer rate in the interaction footprint occurs at the same location as  $p_{pk}$ , and is often linked to it by simple calculation schemes. For example, Holden (Ref. 13) correlated the results of several swept-interaction heat transfer experiments with:

$$c_{h,pk}/c_{h,\infty} = (p_{pk}/p_{\infty})^{0.85} \quad (7)$$

While such expressions lack a fundamental basis, they are of practical importance in predicting high aerothermal loading due to interacting flows on high-speed flight vehicles. One difficulty lies in the fact that the knowledge of peak heat transfer can be no better than that of the peak pressure in an expression such as Eqn. 7. A somewhat more fundamental peak heating correlation was developed by Neumann and Hayes (Ref. 56), which gives the peak heating as a function of both normal Mach number  $M_n$  and position  $x/\delta$  downstream of the leading-edge of the fin. The initial variation of heat transfer near the fin leading edge is now easy to recognize as a 3-D effect of the growth of the interaction inside its inception zone. The work of Neumann and Hayes was done before the quasiconical

nature of the fin interaction was generally recognized, so they cannot be faulted for overlooking this.

In light of the present knowledge of quasiconical interaction symmetry, Lee *et al.* (Ref. 57) assumed that  $c_h$  asymptotes to a constant value along a conical ray outside the interaction inception zone, as was shown experimentally by Rodi and Dolling (Ref. 58). This enabled them to propose a much-simpler data correlation in terms of  $c_{h,peak}/c_{h,\infty}$  vs.  $M_n$  only. This correlation is demonstrated in the graph of Fig. 12. The data of Lee (Refs. 57 and 59) are shown by solid symbols, while other available data (cited by Lee *et al.* in Ref. 57) are shown by open symbols. Taken together, these data approximately describe a linear relationship within their overall scatter. The equation of the line shown in Fig. 12 is:

$$C_{h,peak}/C_{h,\infty} = 3.7M_n - 2.7 \quad (8)$$

This relationship was proposed by Lee *et al.* as a simple empirical guide for peak heating in sharp-fin-generated interactions with turbulent boundary layers outboard of the inception zone near the fin leading edge. No such simple relationship is possible inside the inception zone.

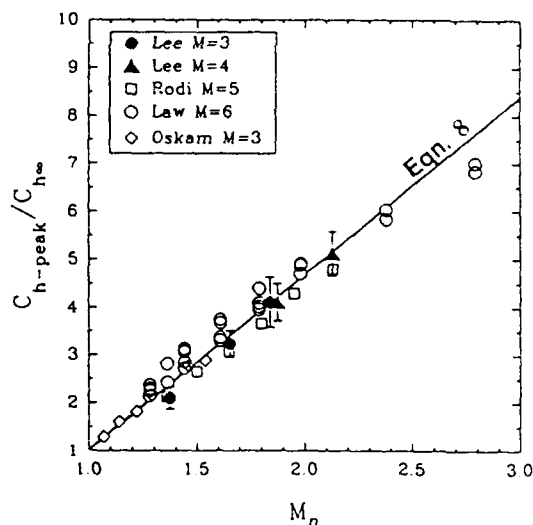


Fig. 12 - Interaction Peak Heating Correlation (per Lee *et al.*).

The data shown in Fig. 12, from which Eqn. 8 is derived, were chosen from the available literature because their accuracy is reasonably documented and because it can be demonstrated that they were obtained outside the interaction inception zone. Heat transfer data at hypersonic freestream Mach numbers are available (eg Refs. 60 and 61), but are not included in Fig. 12 because, unfortunately, this latter condition cannot be satisfied. The reason for this appears



to be that very high Reynolds numbers, and consequently long distances downstream of a flat-plate leading edge, are generally required to produce an equilibrium turbulent boundary-layer in hypersonic wind tunnel testing. For this reason such a boundary-layer tends to be comparatively thick at the location of the swept interaction, which naturally leads to a large inception zone (see the next section). The dimensional limits of the hypersonic test models used so far have thus precluded the taking of data outside the inception zone.

#### 4.3.4 Skin Friction Distribution

Finally, the skin friction distribution in the interaction footprint is of similar interest. Until recently, no suitable instrument was available to make such measurements accurately. The development of the Laser Interferometer Skin Friction (LISF) meter (eg. Ref. 49) is discussed later in this paper. For the present, only the results of this instrument are presented.

LISF skin friction measurements have thus far been made in both supersonic (Ref. 50) and hypersonic (Ref. 61) turbulent fin interactions. The inherent quasiconical symmetry of these flows has been taken advantage of in order to limit the number of measurement points and to present the results conveniently in terms of the angle  $\beta$ . An example from Ref. 50 is shown in Fig. 13.

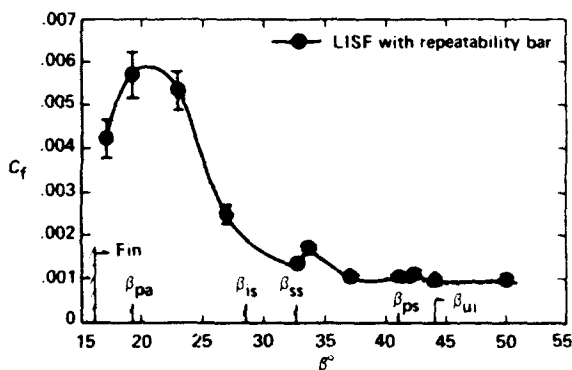


Fig. 13 - Skin Friction Coefficient vs.  $\beta$  for Mach 4,  $\alpha = 16^\circ$  Interaction.

This Figure shows that the skin friction rises dramatically from its incoming level to a peak at the rear of the interaction, near the fin. It thus behaves in much the same way as do the surface pressure and heat transfer. For the moderately-strong interaction case shown, the peak skin friction is about six times the incoming flat-plate value. A small discontinuity in  $C_f$  is also seen near the secondary-separation line.

Results of several computational simulations of this flow were also presented in Ref. 50. A discussion of such computations is given elsewhere in this report by

D. D. Knight. It should be noted here, notwithstanding, that no serious discrepancy between measured and computed peak  $C_f$  values occurs in such comparisons. In Ref. 50 a stronger interaction case (Mach 4,  $\alpha = 20^\circ$ ) was shown, in which the computations appeared to underpredict the data by 50%. This led the authors to conclude that the computations failed systematically as the interaction strength increased. This conclusion was an unfortunate one, as it has since been learned (Ref. 62) that it was the measurements, not the computations, which were in error in this instance. In fact, reasonable agreement of skin friction data and CFD prediction occurs irrespective of interaction strength.

#### 4.4 Reynolds Number Effects

As it happens, the effect of Reynolds number on swept interactions in general is simpler than was first imagined. According to the dimensional argument given earlier, only the inception length to quasiconical flow will be affected by Reynolds number (provided, of course that  $Re$  is high enough to ensure that the interaction remains fully turbulent). Early concerns about the fact that  $\delta$  varies along the swept interaction line were essentially unfounded to first order, as demonstrated by both the swept-leading-edge-plate experiments of Dolling *et al.* (Ref. 63) and computations by Knight (Ref. 64). Apparently only the freestream Reynolds number and the incoming boundary-layer thickness at the fin leading-edge location are involved in the dimensional interplay which establishes  $L_i$ , beyond which the interaction becomes purely conical. Newcomers are cautioned that normalizing any linear dimension that one may arbitrarily define in the conical-flow region of the interaction by the local incoming boundary-layer thickness is not only incorrect according to present understanding, but also highly misleading.

The original Reynolds number scaling law (Refs. 44, 45, and 46) for the upstream influence of general swept interactions at Mach 3 was given in terms of nondimensional lengths tangential and normal to the swept shock as:

$$(L_n / \delta Re_\delta^{1/3})_U / M_\infty = f [(L_s / \delta Re_\delta^{1/3})_U] \quad (9)$$

or

$$(L_n)_U / M_\infty = f [(L_s)_U] \quad (10)$$

This general rule is compatible with all quasiconical sharp fin interactions, though it may appear somewhat clumsy. However, since the sharp-fin interactions under present consideration have no other characteristic length dimension, Eqns. 9 and 10 apply only to the inception length. Further, since the scaling



by  $(1/\delta)Re_\delta^{1/3}$  is applied uniformly in two orthogonal directions in the interaction footprint, it amounts to a simple scale transformation. That is, the dimensional scale of the footprint expands or shrinks *without geometric distortion* due to changes in the values of  $Re$  and  $\delta$ . Since it is intuitively obvious that conical flows are invariant to a scale transformation (see, eg, Ref. 65), we see once again that only the inception length can be affected by such changes in the values of  $Re$  and  $\delta$ . Thus Eqns. 9 & 10 simplify to:

$$\frac{L_i/\delta}{M_\infty} \propto Re_\delta^{-1/3} \quad (11)$$

for the special case of sharp fin interactions.

Examining Eqn. 11, we see that small dimensional inception lengths will result when the Reynolds number is high and the initial boundary-layer is thin. Similarly, flows with thick boundary-layers at comparatively-low Reynolds numbers can require rather large dimensional distances outboard of the fin leading-edge to achieve conical symmetry. This simple distinction has been widely misunderstood, resulting in confusion over whether or not a particular experiment or computation extended far enough outboard to reach beyond the inception zone into the region of conical flow symmetry. So, for purposes of illustration, a classic example adapted from Oskam *et al.* (Ref. 66) is reproduced here in Fig. 14. The experiment by Token (Ref. 67), though performed with an enormous 1-meter-long fin, remains firmly imbedded in the inception zone near the fin leading edge! The experiments of Oskam and Zheltovodov (Refs. 66 and 26), while carried out in much smaller test facilities with smaller physical models, nonetheless covered a far broader region of the interaction footprint in nondimensional terms.

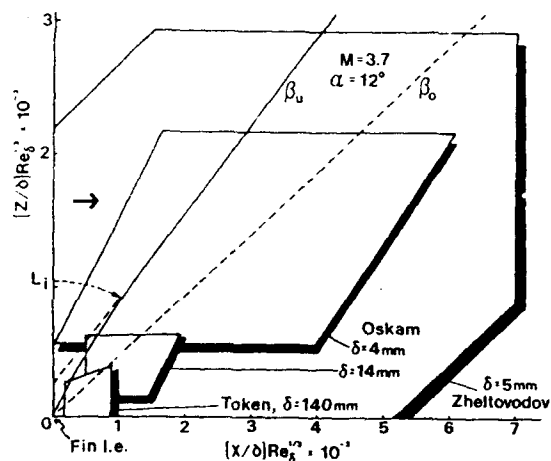


Fig. 14 - Plot of Dimensionless Interaction Footprint Showing Measurement Zones of Various Studies.

The same Reynolds-number scaling philosophy has been shown to be effective for the *flowfield* features of sharp fin interactions (Ref. 68) and other swept interactions, as well as for their footprints. Eqns. 9-11 were even applied successfully to a laminar interaction (Ref. 20), though with a different (negative) value of the scaling exponent. Recent work (Ref. 69) further reveals that the empirical 1/3 exponent for turbulent interactions in Eqns. 9-11 is essentially constant within the Mach number range of 2.5 to 4.0, so long as equilibrium flat-plate boundary layers are solely considered. Inger (Ref. 70) has noted that this exponent is expected to vary if significant variations in the wake-strength parameter of the incoming boundary layer occur.

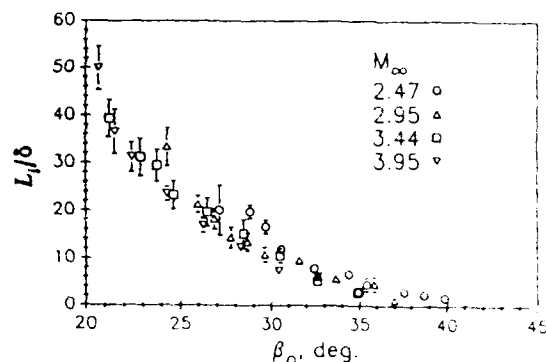


Fig. 15 - Inception Length Scaling in Terms of Inviscid Shock Angle.

Finally, the detailed behavior of the inception length in sharp fin interactions in the Mach number range  $2.5 \leq M_\infty \leq 4.0$  was examined by Lu and Settles (Ref. 71), and was found to be primarily a function of the shock angle,  $\beta_0$ , when  $Re_\delta \sim \text{constant}$ . (This is compatible with Eqn. 11, since  $M_\infty$ ,  $M_\infty$ , and  $\beta_0$  are intimately related.) As illustrated in Fig. 15, for strong interactions (large  $\beta_0$ ) the inception length almost vanishes, producing an interaction with nearly complete conical flow everywhere. Since  $L_i$  describes an asymptotic change from a curved to a straight line of upstream influence, major differences in its level have been reported due to differences in the philosophy of data analysis of various investigators (or even co-authors of a single work). Ref. 71 also gives data on the location, relative to the fin leading-edge, of the virtual conical origin (see Fig. 4). Note that Fig. 15 should not be expected to hold outside its Mach number range of validity.

#### 4.5 Mach Number Effects and Interaction Strength

Per the discussion of conical symmetry,  $M_\infty$  is the first-order strength parameter of swept interactions which combines the effects of both  $M_\infty$  and  $\alpha$ . Either an increase of  $M_\infty$  at fixed  $\alpha$  or of  $\alpha$  at fixed  $M_\infty$  produces a stronger shock and thus a stronger interaction, since  $M_\infty$  grows larger in both cases.



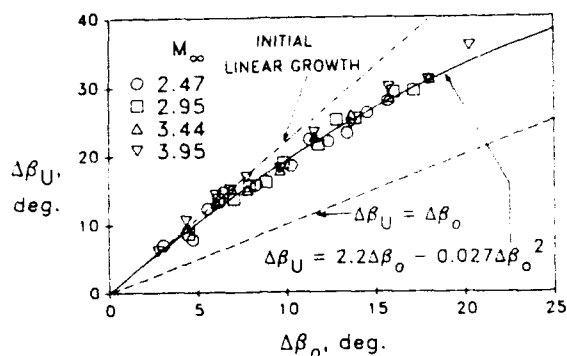


Fig. 16 - Scaling of Reduced Upstream Influence with Inviscid Shock Angle (per Lu *et al.*)

Unfortunately, few systematic interaction experiments have been performed with variable Mach number, due primarily to wind-tunnel nozzle limitations. Prior to the last decade or so, most of the available data were at Mach 3 only. However, two significant variable Mach number supersonic datasets have recently become available, one from ITPM- Novosibirsk (Refs. 15, 18, 26, 43, and 55) and the other from the Penn State Gas Dynamics Lab (Refs. 21, 27, 34 and 47).

Lu, Settles, and Horstman (Ref. 34) examined the relative behavior of the inviscid shock wave and the upstream influence line over the range  $2.5 \leq M_\infty \leq 4.0$ , and found that the Mach number effect could be most simply accounted for by referencing both  $\beta_U$  and  $\beta_0$  to the freestream Mach angle,  $\mu_\infty$ , and then observing their behavior with respect to the fin angle-of-attack. This demonstrated clearly that upstream influence cannot vary linearly with shock angle, though such a linear relationship had been assumed in previous studies due to insufficient data.

Fig. 16 shows the accumulated data of Ref. 34 in terms of a reduced upstream influence parameter,  $\Delta\beta_U = (\beta_U - \mu_\infty)$ , plotted vs. the reduced shock strength parameter  $\Delta\beta_0 = (\beta_0 - \mu_\infty)$ . A least-squares curvefit through the data yields the following relationship

$$\Delta\beta_U = 2.2\Delta\beta_0 - 0.027\Delta\beta_0^2 \quad (12)$$

Though based on data in the Mach 2.5 to 4.0 range, this relationship has been compared with Mach 5 sharp-fin data by Schmisser (Ref. 51). He found that it underpredicted his data somewhat, while the upstream-influence correlation of Zheltovodov *et al.* (Eqn. 3) did a better job. The latter correlation covers a similar Mach and Reynolds-number range as in Ref. 34, but extends to significantly higher values of  $\alpha$  (ie stronger interactions).

Once a nonlinear growth rate of upstream influence with inviscid-shock angle is accepted, the paradox of very weak interactions with large upstream influence angles (Ref. 17) is immediately removed. Instead, the upstream influence angle is seen to grow regularly, though nonlinearly, from a value of zero at zero shock strength in Fig. 16. In this immediate vicinity, however, there now exists the possibility of a linearized solution for weak interactions, where experimental data are sparse. This initial linear growth rate of the interaction is indicated in Fig. 16

Ref. 34 also confirmed Morkovin's hypothesis (Refs. 72 and 73) over the Mach number range investigated: The effects observed were entirely due to inviscid constraints imposed by the outer stream, with no noticeable effect of compressibility on the turbulent nature of the interaction up to at least Mach 4.

#### 4.6 Conical Similarity Law

A parametric study of 24 different swept- and unswept-leading-edge fin interactions at Mach 3 was carried out by Settles and Lu (Ref. 21). The analysis of these results showed that the conical footprint angles of the entire set of interactions depended only on the angle,  $\beta_0$ , of the inviscid shock wave irrespective of either  $\alpha$  or the leading-edge sweepback angle. This simple similarity of interactions due to geometrically-dissimilar shock generators was unique at the time, and was dubbed "conical similarity." It has since been extended to other geometries, including semicones and swept compression corners (Ref. 1). The principle of conical similarity allows the scaling laws discussed in this paper for the archetypical sharp-fin interaction to be applied to a broader context of quasiconical swept interactions.

Zheltovodov *et al.* (Refs. 26 and 55) and Stollery *et al.* (Ref. 74) have recently done extensive experiments with swept-leading-edge fins, achieving similar results. All such investigations require knowledge of the angle at which the inviscid shock intersects the flat plate, since this is the reference line for the entire interaction. These shock angles are not known *a priori* for swept-leading-edge fins, and were measured in each of the above studies by way of delta-wing models mounted in the freestream flow.

#### 5.0 FLOWFIELD STRUCTURE

Early models of the off-the-surface flowfield structure of sharp fin interactions, eg Refs. 15 and 66, identified some salient features such as the bifurcation of the inviscid shock into a "λ-foot" and the development of a helical separation vortex. However, the lack of optical flowfield visualization in such highly-swept flows was sorely missed, and the flowfield models were crude and incomplete. Zubin and Ostapenko carried out the first conical shadowgraphy experiments in fin interactions, but their results were only briefly



reported in the open literature (Ref. 16), and only became available in the West in complete form (Ref. 75) within the last 3 years. Recently, extensive optical studies have been carried out at Penn State (Refs. 24, 25, 47, 76, and 77) using conical shadowgraphy, conical holographic interferometry, and planar laser scattering (PLS) techniques. These studies have produced a very clear view of the detailed flowfield structure.

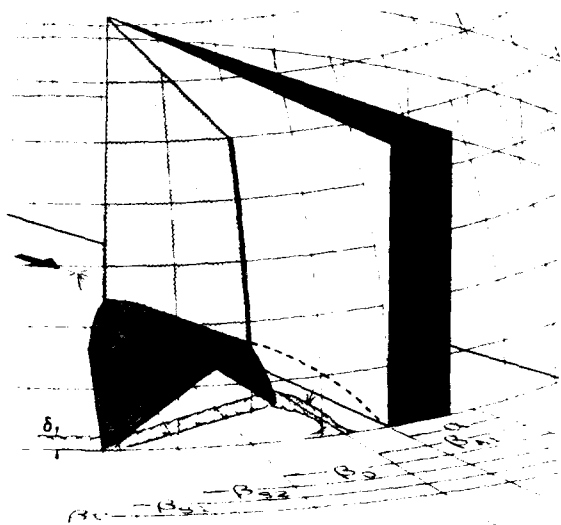


Fig. 17 - Projection of Quasiconical Interaction Flowfield onto Spherical Polar Coordinate Surface.

To avoid confusion, a 3-D sketch of the conical flowfield projection onto the spherical coordinate surface is shown in Fig. 17. This view, of course, is normal to the conical rays of the interaction, and may be seen as a closeup view of the interaction in the coordinate frame shown earlier in Fig. 2. If the conical projection is peeled from the sphere and pressed flat, one obtains the current model of the flowfield structure. In such a case the Mach number normal to the inviscid shock, for example, will be the normal component  $M_n$  which is tangent to the sphere. Although the direction of  $M_n$  is left-to-right in Fig. 17, all succeeding pictures of the interaction structure will be rendered with the flow in a right-to-left orientation.

Figs. 18-20 show a conical shadowgram, a conical holographic interferogram and a PLS image, respectively, of the detailed flowfield structure typical of a separated sharp-fin interaction (from Refs. 24, 25, and 47). Fig. 18 depicts the Mach 3,  $\alpha = 20^\circ$  interaction while Figs. 19 and 20 depict the Mach 3,  $\alpha = 16^\circ$  case. The techniques used to obtain these images are described in later sections of this paper. For comparison purposes, Fig. 21 presents the Mach 3,  $\alpha = 16^\circ$  physical flowfield model in  $(\beta, \phi)$  coordinates from Ref. 47.

The inviscid shock is seen to bifurcate into a "λ-foot" in Figs. 18-21. The forward leg of the λ, known as the

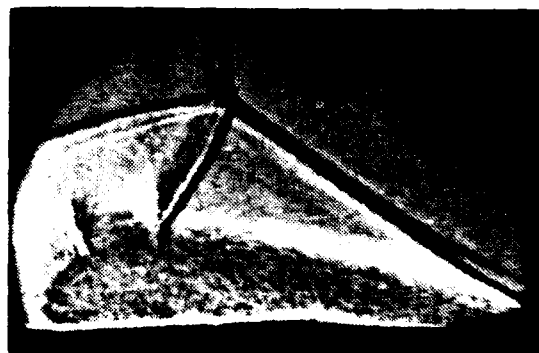


Fig. 18 - Conical Shadowgram of Mach 3,  $\alpha = 20^\circ$  Interaction Structure.

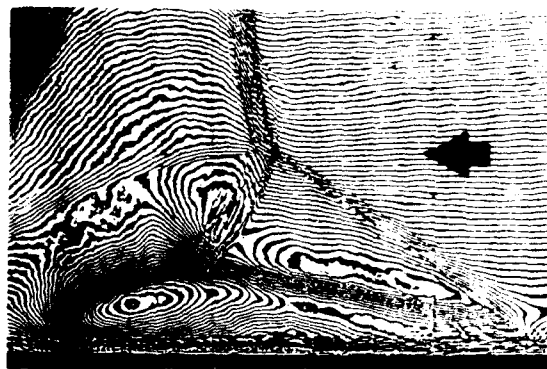


Fig. 19 - Conical Holographic Interferogram of Mach 3,  $\alpha = 16^\circ$  Interaction Structure.

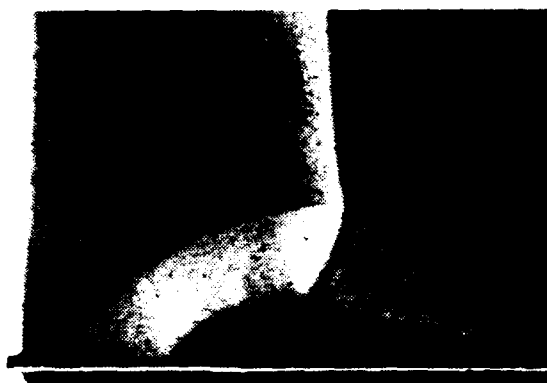


Fig. 20 - Planar Laser Scattering (PLS) Image of Mach 3,  $\alpha = 16^\circ$  Interaction Structure.

separation shock, causes the separation of the incoming turbulent boundary layer at the primary separation line,  $S_1$  (indicated in Fig. 21). The separated free shear layer is deflected away from the flat plate by the separation shock, then back toward it by the rear leg of the λ-shock. The separated free shear layer then rolls up into a tight vortex, the core of which is clearly seen in Fig. 19 and indicated in Fig. 21. Note that the *entire* incoming boundary-layer is separated from the flat plate and rolled up in this vortex, a fact which has strong implications for the



performance of high-speed inlets with such interactions occurring on their sidewalls.

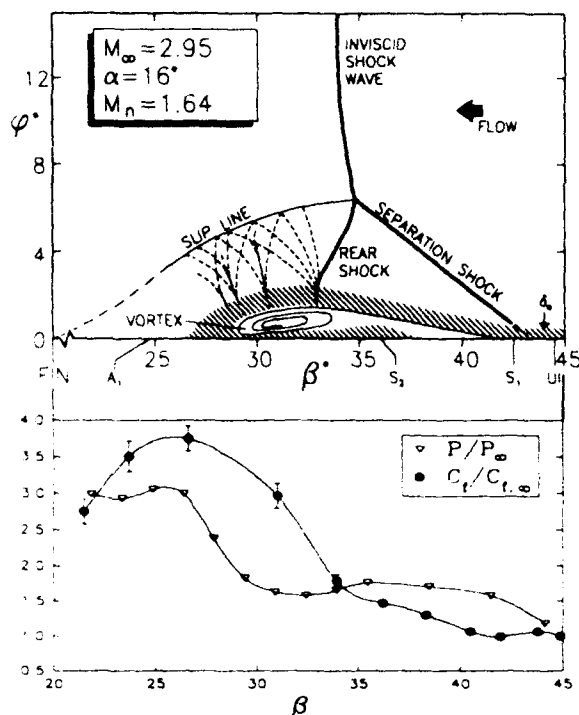


Fig. 21 - Mach 3,  $\alpha = 16^\circ$  Flowfield Map and Surface Distributions (per Alvi & Settles).

Aft of the separation bubble in Figs. 18-21, the flow is observed to impinge upon the flat plate, forming the line of attachment  $A_1$ , where some flow is directed back upstream in the normal plane. This reverse-flow then encounters secondary separation at  $S_2$  as indicated in Fig. 21.

Beneath the flowfield map of Fig. 21, the corresponding surface distributions of static pressure and skin friction are plotted to the same  $\beta$ -scale. These distributions show a gradual rise from the freestream values of  $c_f$  and  $p/p_\infty$  in the forward part of the interaction, followed by a rapid climb to peak values to the rear. For even stronger interactions (Fig. 13 and Ref. 47), the surface properties display a long, gentle rise leading up to a rapid climb to a strong peak near primary flow attachment. These features become even more exaggerated at hypersonic freestream Mach numbers (Refs. 60 and 61).

What is really new in the flowfield images and model of Figs. 18-21 is the fate of the streamtube of outer, inviscid flow subtended by the separation shock below its triple-point intersection with the main shock wave. This streamtube is also deflected upward by the separation shock, then downward by the rear lambda-foot shock. Having no place else to go, the streamtube curves downward and impinges directly upon the flat plate, as seen unequivocally in Fig. 20. This is accomplished, since the nature of the flow is

hyperbolic, by reflected Prandtl-Meyer expansion and compression fans. The appearance of this impinging streamtube is strongly reminiscent of a curved high-speed jet, and is henceforth referred to as the "impinging-jet" phenomenon. Given the reduction in Mach number through the two oblique shocks of the lambda-foot, starting from an initial value of  $M_\infty$ , the local Mach number in this jet is transonic in the normal plane for the supersonic-freestream interactions under scrutiny.

The structure of this jet impingement is highly reminiscent of that produced by an Edney (Ref. 78) type-IV leading-edge shock impingement. Upon comparison, the shock bifurcation and jet impingement of the two interactions are observed to be closely similar (Ref. 79). The reason for the peak heating, pressure, and skin friction in the rear part of the fin interaction is now clear: Edney-type jet impingement is known to produce peak heating rates which can be at least an order of magnitude above normal. The swept-interaction surface-pressure peak discussed earlier (see Figs. 5 and 21) is therefore actually imposed upon the flat-plate surface by the outer flow structure. High peak fluctuating-pressure loads up to 160 dB have also been measured near the attachment-line of these interactions (Ref. 80).

In the reverse-flow direction, the strong favorable pressure gradient ahead of the wall-pressure peak beneath the impinging jet accelerates the reverse-flow forward. For sufficient interaction strengths, this reverse flow goes locally supersonic and then "shocks down," generating a small internal normal-shock (see Ref. 24 for illustration) and producing the aft-located secondary-separation first described by Zheltovodov (Ref. 18). Also, for sufficient interaction strengths, the impinging-jet itself becomes sufficiently supersonic that an internal normal shock wave is seen before the jet impinges on the plate (Refs. 24 and 47).

Using  $M_\infty$  and  $p_2/p_1$  as interaction strength parameters, as described earlier, the test matrix of the optical flowfield investigations of Alvi and Settles (Refs. 24 and 47) is shown in Fig. 22. The curve shown is simply that of the pressure ratio across an oblique shock, but the points indicate the relative strengths of the six distinct interactions studied, which span the range from weak (*ie* barely separated) to very strong. Four flow-regime boundaries are also indicated in Fig. 22, corresponding to incipient primary and secondary separation, the appearance of a normal shock in the impinging jet, and the onset of a supersonic region in the reversed-flow bubble.

The flowfield features of Figs. 18 and 19 line up so well under properly-aligned conical optical probing (a technique to be described later in this paper) that there can be little doubt about the almost-perfect



conicity of strong sharp-fin interactions outside the inception zone. In support of this assertion, Fig. 23 shows excellent agreement in spherical polar coordinates between the Mach 4,  $\alpha = 20^\circ$  flow-field structure derived from two Planar Laser Scattering "cuts" separated by 33 mm of conical ray length. Both cuts were taken outside the inception zone and the VCO location was 21 mm ahead of the fin leading edge in this example.

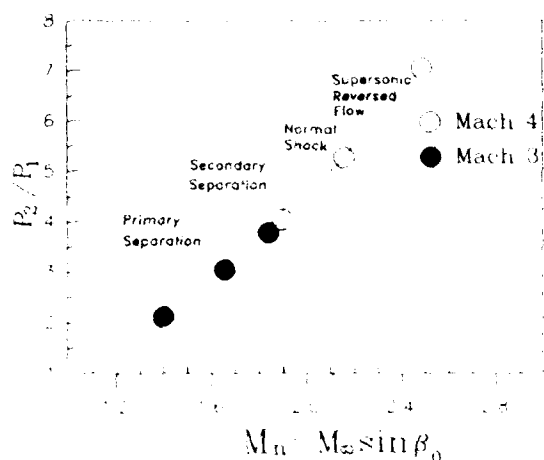


Fig. 22 - Interaction Test Matrix of Alvi and Settles.

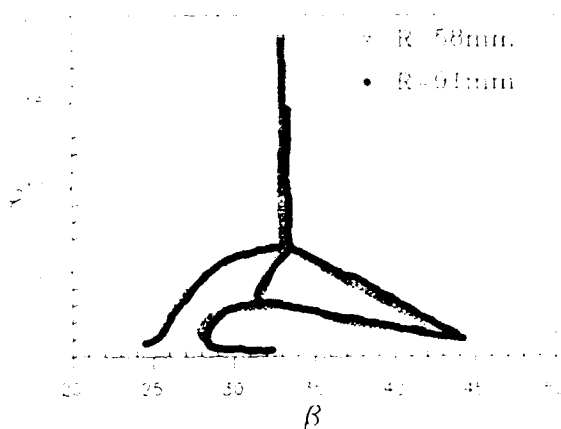


Fig. 23 - Overlay of PLS Cuts at Different Locations.

A significant conclusion of the Penn State optical studies of sharp-fin interactions reviewed here (Refs. 24, 25, 47, 76, and 77) is that the interaction structure (ie lambda-foot, vortical separation, and impinging jet) develops very rapidly once the shock strength for incipient boundary-layer separation has been exceeded. On the other hand, once these features are present, further increases in shock strength cause only second-order structural changes in the flowfield, such as those discussed in relation to Fig. 22. Strong interactions tend to have very long regions of comparatively gradual flow changes from the separation line up to the inviscid shock. The rear shock and impinging jet, being "cramped" into tight

quarters near the fin-plate intersection in high-Mach-number interactions, then lead to a spectacular peak in pressure, wall shear, and heat transfer at the rear of the interaction. Such an example is shown in Fig. 24 (from Ref. 60), though it should be noted that this hypersonic interaction is atypical of those shown thus far, since the entire lambda-foot structure is embedded within the boundary layer.

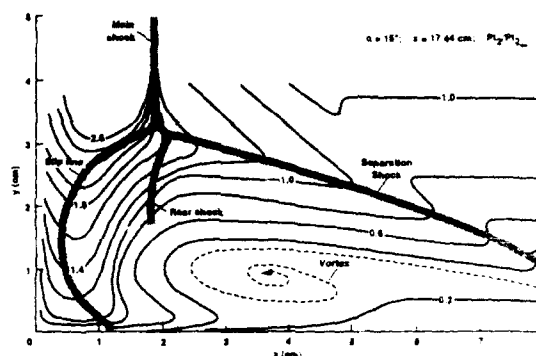


Fig. 24 - Pitot-Pressure Contours for Mach 8.2,  $\alpha = 15^\circ$  Interaction (per Kussoy *et al.*)

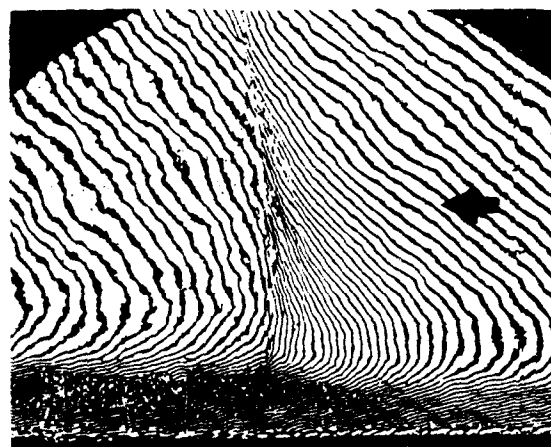


Fig. 25 - Conical Holographic Interferogram of Mach 2.35,  $\alpha = 7^\circ$  Interaction Structure.

Conical holographic-interferometry visualizations (Refs. 25 and 76) have also revealed the flowfield structure in weak interaction cases, as illustrated here in Figs. 25 and 26. Fig. 25 shows a case below the incipient separation limit whose flowfield structure is almost featureless. There is some gradual compression prior to the inviscid shock meeting the boundary layer, but the overall effect upon the latter seems minimal. Slightly beyond incipient separation, Fig. 26, the lambda-foot is clearly seen but the core of the separation vortex, curiously, is located well aft of the rear lambda-foot shock. In such a case the impinging jet structure is quite long and approaches the flat plate at a shallow angle. For somewhat stronger interactions, Figs. 18-21, the archetypical separated-interaction structure, discussed earlier, is observed.





Fig. 26 - Conical Holographic Interferogram of Mach 3,  $\alpha = 10^\circ$  Interaction Structure.

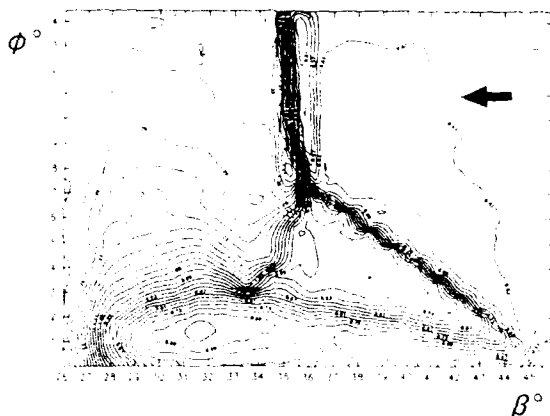


Fig. 27 - Flowfield Density Map of Mach 3,  $\alpha = 16^\circ$  Interaction.

Quantitative flowfield density maps were extracted (Ref. 76) from conical holographic interferograms such as those just shown. An example is reproduced here as Fig. 27, corresponding to the interferogram shown previously in Fig. 19 for the Mach 3, 16 degree interaction. These results are believed to be the first quantitative, non-intrusive flowfield data ever obtained in a swept shock/boundary-layer interaction. The highest density level in the flowfield occurs at the jet-impingement location in Fig. 27. In contrast, the core of the separation vortex, consisting of "warm" air originally from the boundary layer, is a zone of comparatively low density.

Comparisons of these flowfield data with computational Navier-Stokes solutions have been made, *eg*, in Refs. 28 and 81. The details of such comparisons are discussed by D.D. Knight elsewhere in this report.

Finally, Alvi (Ref. 82) examined the quantitative growth of the flowfield structure with shock strength for turbulent interactions at Mach 3 and 4. He found

that the separation shock wave angle for all interactions studied at Mach 3 and 4 corresponds to a flow-deflection angle between 8 and 12 degrees, as predicted by "free interaction" theory (Refs. 26, 83, and 84). This fact contributes to the rapid lateral spread of the interaction structure with increasing Mach number, since the separation-shock angle grows smaller. The angular height of the lambda-foot triple-shock intersection point,  $\phi_{TP}$ , was then found by Alvi to be related to  $M_\infty$  and the freestream Mach angle by:

$$\phi_{TP}/\mu_\infty = -0.17 + 0.30M_\infty \quad (13)$$

However, the lateral angular extent of the interaction failed to correlate simply in terms of  $M_\infty$ . This is because, Alvi found, the aft section of the interaction, between the triple-point and the fin, is quite sensitive to the fin proximity. By dividing the lateral spread of the interaction into two segments ( $\Delta\beta_1$  and  $\Delta\beta_2$ , shown in Fig. 28), he was able to show that this aft segment, characterized by  $\Delta\beta_1$ , scales according to:

$$\Delta\beta_1/(\beta_0 - \alpha) = -0.6 + 0.63M_\infty - 0.12M_\infty^2 \quad (14)$$

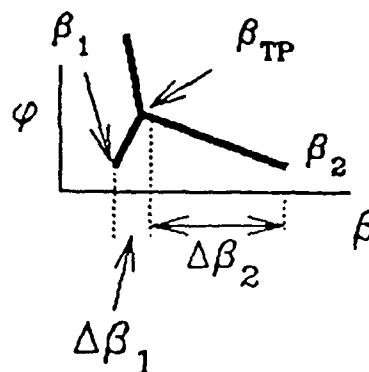


Fig. 28 - Flowfield Diagram Defining  $\Delta\beta_1$  and  $\Delta\beta_2$ .

In contrast, the forward segment of the interaction structure, characterized by  $\Delta\beta_2$ , scales purely with  $M_\infty$  according to:

$$\Delta\beta_2 = -23.1 + 26.0M_\infty - 4.4M_\infty^2 \quad (15)$$

When thus considered in a "piecemeal" or zonal fashion, the scaling of the interaction structure with Mach number and fin angle becomes clear. The reader should note that  $M_\infty$  has been taken as a first-order indicator of interaction strength in this paper, and is the principal independent variable in Eqns. 13-15 as well. However, Eqn. 14 clearly shows that the interaction has a residual dependence upon  $\alpha$  as well as upon  $M_\infty$ , so that the use of  $M_\infty$  alone as a scaling parameter for interaction strength is an over-



simplification. The reader should also note that Eqs. 13-15 are not necessarily expected to apply outside the range of Alvi's (Ref. 82) experiments, upon which they are based.

## 6.0 EXPERIMENTAL METHODS

### 6.1 Wall Pressure Measurements

Of all measurements in shock/boundary-layer interactions, mean wall static pressure measurements are the most straightforward. Traditionally, miniature pressure taps consisting of holes drilled normal to the test surface are used to sense the mean wall static pressure. According to Prandtl's boundary-layer approximation of the y-momentum equation, static pressure is propagated without change across a thin viscous layer at a wall. The technique is used in practice even when the boundary-layer is separated, in which case it is the near-wall static pressure of the separation bubble which is being sensed. Examples of such surface pressure distributions in swept interactions have already been shown in Figs. 5 and 21.

The pressure taps in the test surface are connected by tubing to individual pressure transducers or, more often, to a single transducer by way of a rotating pressure scanner such as the Scanivalve.<sup>TM</sup> A typical Scanivalve installation can sense 48 pressure taps in a few seconds, making it suitable for intermittent as well as continuous wind tunnel testing. Electronic pressure scanners have also become available recently. Pressure measurements are both time-honored and central to high-speed wind tunnel technique. They are only mentioned here, the reader being referred to a text such as Pope and Goin (Ref. 85) for more detail.

The measurement of time-dependent wall pressures by way of miniature piezoelectric transducers is outside the scope of the present paper, and is covered elsewhere in this report in the paper by Dolling. One should also bear in mind that the mean-pressure measuring method just described produces an ill-defined response when the pressure tap lies beneath a bimodal phenomenon such as an intermittent separation region. Excellent examples of this are given in the paper by Dolling.

### 6.2 Surface Flow Visualization

One of the simplest but most useful of all flow visualization methods is that of surface streakline tracing using liquid indicators (Refs. 86 and 87). At one time a mixture of fluorescent dye and machine oil was so commonly used for this purpose that the entire class of surface-flow visualization techniques came to be referred to by the term "oil flow." Today, however, this class of techniques comprises a wide variety of carrier fluids and pigments.

While generally effective, the oil-flow technique nonetheless suffers drawbacks under certain testing

conditions. For example, an oil film often remains wet throughout a wind tunnel test and then smears upon tunnel shutdown. One must consequently photograph the oil-flow pattern during the test through available tunnel windows, which often introduces optical distortion and resolution loss. Further, a buildup of oil occurs at flow separation lines which can produce anomalous patterns due to competing wall shear and pressure-gradient-induced buoyancy forces (Ref. 83, Appendix).

Thus a particular dry-transfer technique has evolved for the visualization and measurement of surface streaklines beneath swept shock interactions and similar flows (Refs. 88 to 90). This technique produces a streakline pattern which dries during a brief wind tunnel test and is subsequently preserved without photography.

A thick mixture (between 1:4 and 1:1, depending on test conditions) of a dry pigment and a volatile carrier fluid is applied to wind tunnel surfaces *upstream* of the region to be visualized. The flow spreads this mixture over the test surfaces, forming streaks which dry before the airflow is stopped. The very thin coating of pigment remaining on the surface is then lifted off and preserved using ordinary transparent matte-acetate adhesive tape. Because the pattern is extremely thin, problems with buoyancy forces on liquid accumulations on the test surfaces are avoided. Surface-flow visualization of nominally steady boundary-layer flows using an evaporating carrier fluid can therefore be considered to be nonintrusive.

The most suitable carrier fluid for supersonic testing in cold tunnels is found to be ordinary kerosene (Refs. 88 to 90). Kerosene is quite volatile at the near-ambient surface temperatures and sub-ambient static pressures typical of such facilities, so that it typically evaporates within 5-20 seconds of the beginning of a wind tunnel run, this time being determined by observing the pattern formation. (Gasoline was also tried, but was observed to boil away immediately upon the static-pressure drop which accompanies tunnel startup.) Other wind tunnel facilities with different operating conditions may require more or less volatile carrier fluids, for which purpose a wide variety of hydrocarbon distillates is readily available. For example, the heated hypersonic flow of Ref. 61 resulted in a model temperature well above ambient, which required the use of a less-volatile carrier fluid (vacuum-pump oil).

The pigment material may be, in principle, almost any finely-divided powder. However, experience (Refs. 88 to 90) has shown that ultra-fine particle diameters in the range of a few  $\mu\text{m}$  and smaller do not produce the best patterns. Similarly, large particles on the order of 100  $\mu\text{m}$  diameter or larger disturb the boundary



layer excessively. There is thus a range of particle sizes where this method is most successful. The extremely-fine particles of oil-paint pigments or food dyes do not streak properly, resulting instead in a featureless smear. Ground carbon-black or powdered, colored chalk seem to produce the best results.

For complex flows, combinations of different color mixtures are helpful in following the surface streakline pattern development (Ref. 91). This reference includes a printed comparison of a color and a monochrome image of the same shock/boundary-layer interaction footprint for comparison. Contrasting colors are used, for example, to highlight the primary flow separation line. Color offers several advantages in pattern visibility and interpretation which, unfortunately, must be weighed against the expense of reproducing color images.

Once a pattern is formed, it is conveniently preserved using a large rectangle of matte-acetate adhesive tape, which is commercially available in widths up to at least 20 cm. Such a square of tape is placed carefully upon the dry pattern, rubbed vigorously with a soft cloth, peeled off, and preserved by pressing on white paper. The result is an undistorted, full-scale pattern of the surface streaks, from which quantitative measurements may be made.

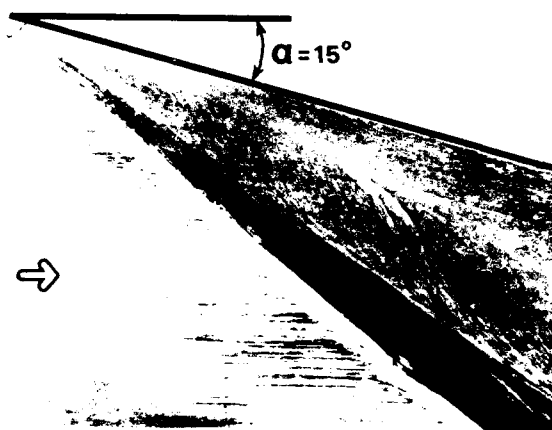


Fig. 29 - Kerosene-Lampblack Footprint Trace of Mach 3,  $\alpha = 15^\circ$  Interaction.

An example of such a pattern, formed by a swept shock/boundary layer interaction, was shown previously in Fig. 7. Another example is given in Fig. 29. In this separated sharp-fin interaction footprint, fine streaking of the indicator material gives an excellent rendition of surface limiting-streamline features and directions. In order to produce this pattern, the kerosene-lampblack mixture was applied both upstream of the interaction and near the fin-plate junction, since the primary separation line is a line of exclusion preventing upstream material from reaching downstream locations. The primary separation, secondary separation, and primary attachment lines of the flow are clearly visible in the example of Fig. 29.

While the fine detail of this pattern is beyond the resolution of the printing process, measurements with  $200 \mu\text{m}$  or  $0.1 \text{ deg}$  accuracy can be made from the full-sized original. Such patterns have been instrumental in the swept-interaction research which was reviewed earlier in this paper. They constitute the single most important source of data from which the Reynolds number and Mach number scaling laws and the conical similarity principle for swept interactions were first derived (Refs. 21, 26, 27, 34, 46, 69, and 71). Topological rules are applied to interpret such surface patterns (eg Refs. 7 and 12).

### 6.3 Conical Shadowgraphy

Optical shadowgraphy (see eg Ref. 87) is a well-known and widely-used tool for the visualization of high-speed flows. The technique is usually straightforward and inexpensive, and is notable for its ability to reveal strong refractive index gradients produced by such flow phenomena as shock waves or turbulent eddies. Ordinary shadowgraphy is usually done with a collimated light beam originating from a "point" source (ie a source of high spatial coherence). The information in the shadowgram results from an integration across the flow through which this beam passes. Thus the shadowgram interpretation can be straightforward only for those flow disturbances which lie parallel to the light-beam axis, namely, planar two-dimensional flows. However, it is well-known that disturbances in a uniform, inviscid supersonic flow exhibit conical rather than planar symmetry. The usefulness of parallel-light shadowgraphy to investigate such conical flowfields is thus quite limited.

For some time it has been known that the optical diagnosis of conical flows depends critically upon placing the illumination in the proper conical framework, without which little or nothing is likely to be seen. Love and Grigsby (Ref. 92) first accomplished this by arranging for their conical delta-wing flow and a conical light beam to have common vertices. Subsequent work (Refs. 93 and 94) similarly dealt with flows over conical wing planforms. The use of conical shadowgraphy for the optical diagnosis of swept shock/boundary layer interactions was first reported by Zubin and Ostapenko (Refs. 16 and 75). It was subsequently used by Settles and Teng (Ref. 88). None of this early work, however, was able to simultaneously achieve accurate alignment and high resolution, nor was a broad range of interaction strengths investigated.

The key difficulty with the early attempts at conical shadowgraphy for the imaging of swept shock/boundary layer interactions had to do with alignment. Since the interactions were known to be, at best, quasiconical, it was unclear exactly how the light beam should be matched up with the actual flow. Some insight on this issue was gained in Ref. 95,



where benchtop simulation experiments showed both axial and transverse misalignment to be significant problems, though axial misalignment was found to be comparatively less serious. Fortunately, the quasiconical nature of the flow (*ie* the presence of a nonconical inception zone) was not discovered to be an overriding issue. Apparently the conical nature of the majority of the flowfield predominates over its non-conical inception zone, insofar as conical shadowgraphy is concerned.

These results were put to practice by Alvi and Settles (Ref. 24), who produced the first clear images of the sharp-fin-generated swept-interaction structure by conical shadowgraphy. This was accomplished by focusing a light beam at the interaction VCO and aiming it such that the resulting conical beam coincided with the rays of the swept interaction under study. A special optical setup with its axis in the plane of the flat plate was assembled for this purpose. As shown in top view in Fig. 30, a xenon arc lamp (GenRad 1431AB Strobotac) is used as a white-light source. The output of this lamp is focused on a pinhole or an adjustable aperture (set to approximately 0.5x0.5 mm) to generate an effective "point" light source. An achromatic lens,  $L_1$ , collimates this beam, which is then focused near the fin leading edge using a second achromatic lens  $L_2$ . The axis of the resulting conical light beam is aimed along the interaction sweep line, which corresponds to the trace of the inviscid shock wave.

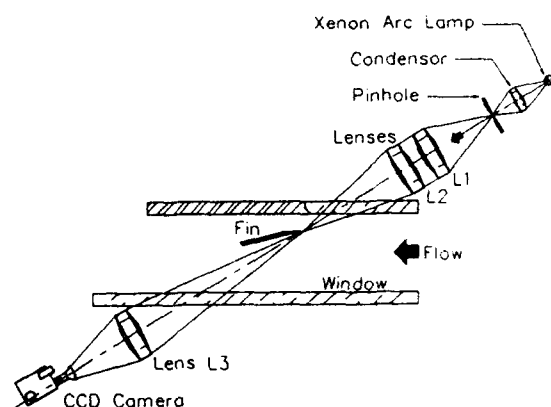


Fig. 30 - Schematic Diagram of Conical Shadowgraphy Setup (Top View).

For proper alignment, the axis of the light beam must lie on the surface of the flat plate. In practice this requires that the beam actually reflect off the highly-polished flat plate. When the alignment is correct, this reflected beam is conical with rays aligned with the conical rays of the interaction itself. This conical light beam exits through a special 3.75 cm-thick acrylic tunnel sidewall and is focused by a third lens,  $L_3$ , into the zoom-lens of a CCD video camera.

The resulting video image, recorded by Alvi and Settles in the S-VHS format, is displayed on a high-resolution television monitor. Automatic line-synchronization occurs between the individual flashes of the arc-lamp light source and the video frames, such that each frame receives 2-3  $\mu$ s of exposure. However, the framing rate of the video equipment used here is only 30 Hz. Single-image still photography could have been used in place of the video equipment just described, with either the xenon flashlamp source already described or a small continuous-light source in use.

The conical shadowgram shown earlier in this paper (Fig. 18) was taken from the original video record using a microcomputer-based frame grabber which has a 512x464x8-bit pixel resolution. This image was then halftoned and printed directly on a laser printer using desktop-publishing software, thus avoiding photographic processing. Many other examples of the results thus obtained can be found in Ref. 24 and 82. In addition, the Penn State Gas Dynamics Laboratory has produced a videotaped compilation of these results (Ref. 96).

As previously shown by Lu and Settles (Ref. 71), the inception length to conical symmetry in swept interactions decreases as the interaction strength increases, such that, for moderate to strong interactions, the VCO is essentially coincident with the junction of the fin leading edge and the flat plate. Consequently, the conical light beam is roughly focused near the fin leading edge along the inviscid shock sweep line before a wind tunnel test. Fine alignment of the light beam with the interaction is then done during one or more test runs. The criterion for "perfect" conical shadowgraphy beam alignment is the collapse of the shock wave image into its characteristic lambda-foot shape with as little spreading of the structure as possible. This often requires multiple alignment runs to achieve. In all cases the fact that the fin-plate junction does not lie along a ray of the quasiconical interaction prevents the imaging of the extreme rear segments of the interactions under study.

Some limitations of this approach include the standard caution that a shadowgram is a picture of a shadow, *not* a focused image. Geometric distortions are possible. Another difficulty encountered in the work of Refs. 24 and 82 was that a suitable lens of sufficiently-large aperture, high quality, and short focal length was not available for  $L_3$ , so that the larger interactions had to be imaged piecemeal. Finally, due to the effect of reflecting the entire test beam from the polished flat plate surface, optical aberrations were produced which thwarted attempts to convert the conical shadowgraph apparatus to conical schlieren by the addition of a knife-edge cutoff.



#### 6.4 Conical Holographic Interferometry

While conical shadowgraphy provided extremely valuable flow visualizations in the above-cited studies, it nonetheless suffered the traditional limitations of shadowgraphy, which is a purely-qualitative tool. No published record has been found of any attempt prior to 1989 to apply a more sophisticated optical diagnostic, such as interferometry, to such swept conical flows. This was first attempted in the experiments of Hsu and Settles (Ref. 76), which were preliminary, but pointed the way for their later quantitative pulsed-laser holographic interferometry measurements of swept sharp-fin-generated shock-boundary layer interactions (Ref 25).

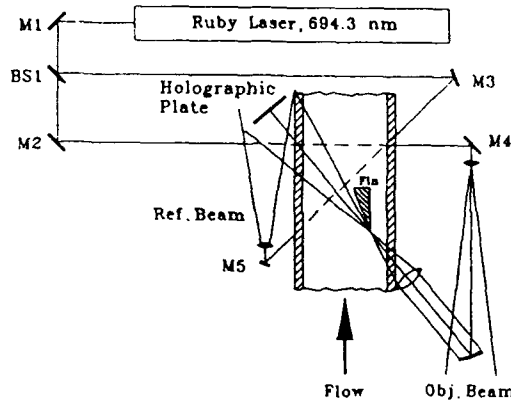


Fig. 31 - Schematic Diagram of Conical Holographic Interferometry Setup (Top View).

The advantages of holographic interferometry for this purpose are well known (Refs. 87 and 97), and include the capture of several different types of flow information on a single holographic plate. Quantitative density measurements are possible, as is a systematic study of flow unsteadiness (by varying the interval between laser pulses, though this has not been done in the cited work of Hsu and Settles). Further, holographic interferograms do not require schlieren-quality glass windows, allowing the use of the acrylic wind tunnel test section sidewall window, mentioned earlier, for purposes of broad optical access.

In Ref. 25 a conical holographic object beam, focused at the virtual origin of the interaction and aimed along the swept shock wave, was used to produce double-pulsed holographic interferograms of a range of swept-interaction flowfields, examples of which were already given in Figs. 19, 25, and 26. As in the conical shadowgraphy discussed earlier, the optical rays diverging from the VCO integrate the properties of the flow conically through the whole interaction. (Of course, the inception zone is non-conical, but its deviation from conicity typically produces only a second-order effect.) The resulting interferograms were then analyzed to yield conical flowfield density maps, an example of which was already given in Fig. 27. Here, the experimental technique and data reduction procedure will next be described.

#### 6.4.1 Optical Apparatus

A pulsed ruby laser (693.4 nm wavelength) was used as the light source for holographic interferometry. The maximum energy output of this laser was 300 mJ/pulse and the pulse width was 20 ns. Though the laser has a double-pulse capability, it was used only in single-pulse mode in this study. Because of its excellent coherence, the ruby laser has been respected as the best available source for holographic imaging despite its rather poor reputation in terms of ease of operation and upkeep. (An alternative laser source for this purpose is a pulsed, frequency-doubled Nd:YAG laser.)

The layout of the optical apparatus with respect to the wind tunnel test section and fin shock generator is depicted schematically in Fig. 31. M1-M5 are beam-folding mirrors and BS1 is a beamsplitter in this figure. A 1.2 x 2.4 meter optical table was positioned beneath the wind tunnel test section in order to support both the laser and its associated optical components. A 15 mW helium-neon laser, aimed through the ruby-laser cavity, was used for optical setup and alignment. AGFA 8E75 holographic plates of 10x12.5 cm size were used as the recording medium.

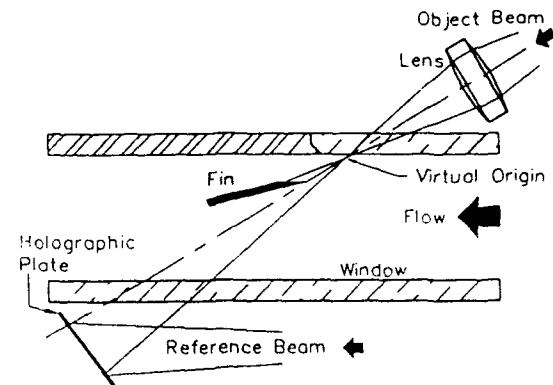


Fig. 32 - Diagram of Object-Beam Alignment with Fin (Top View).

The manner in which the holographic object beam is aligned with the quasiconical flow structure is crucial to this experimental technique. When perfectly aligned as shown in Fig. 32, the conical object beam is partially blocked by the leading edge of the fin itself, so that no features of the interaction downstream of the shock wave may be observed. Thus a slight deviation of the focus of the object beam from the true VCO becomes necessary, as was the case in the conical shadowgraphy described previously. In Ref. 76 a horizontal misalignment was used, but this was later found to be a wrong approach. Instead, positioning the object-beam focus closer to the fin leading edge than the VCO, so as to avoid beam blockage by the fin, was found more effective in Ref. 25. This approach works according to the rule



discovered by Schmidt and Settles (Ref. 95), that axial misalignment is relatively innocuous compared to transverse (horizontal or vertical) displacement in conical shadowgraphy. In any case, other results (Ref. 71) show that the fin leading edge and the VCO become practically coincident for sufficient-high interaction strengths.

As in conical shadowgraphy, in order to achieve proper vertical alignment it is necessary to reflect the object beam focus from the surface of the flat plate. Accordingly, a high polish on the flat plate in the vicinity of the fin leading edge was produced for specular reflection.

The reference beam remains outside the wind tunnel and is directed to interfere with the object beam on the holographic plate. This plate is positioned normal to the object beam to minimize the distortion of the conical projection, and is located immediately outside the wind tunnel window, as shown in Fig. 32. A sharp shadow of the interaction structure is thus cast on the plate by the object beam, making this optical arrangement the logic 1 equivalent of image-plane holography. During the experiment, each holographic plate is exposed twice; once immediately before the wind tunnel test and then a second time after the flow is established. Interference thus occurs between the two exposures, since the object beam wavefront, which creates the second exposure, is distorted by its passage through the flow.

Following the development of the plate an optical reconstruction of the holographic interferogram is performed. While this is usually done with coherent light, it proved more convenient to use a white-light reconstruction technique. This technique was simple to implement, produced bright interferogram images, and eliminated any coherent artifact noise associated with the reconstruction process. Since the optical arrangement described above produces what amounts to an image-plane interferogram (where the fringe pattern is "locked into" the emulsion), any means of reconstruction will yield the same fringe pattern.

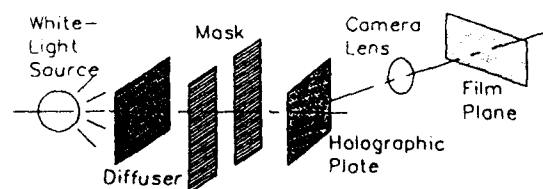


Fig. 33 - White-Light Hologram Reconstruction Setup.

Fig. 33 illustrates the setup for white-light reconstruction. The light source is an incandescent bulb with a 4800 K color temperature. This bulb is positioned so that the angle of the incident beam is the same as the angle of the reference beam in the hologram exposure process. The light reaches the holographic plate

through a diffusing screen and a rectangular mask. A camera placed at the proper diffraction angle to the plate records the holographic interferogram. Either monochrome or color images may be recorded, though the colors are purely artifacts of the white-light reconstruction method.

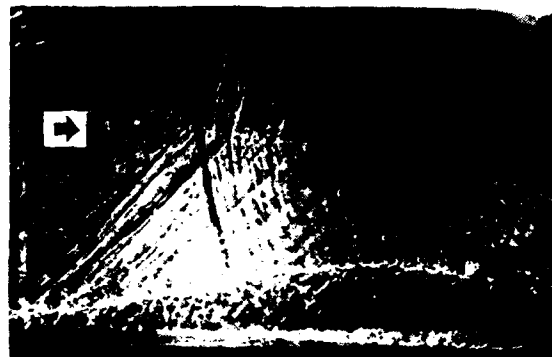


Fig. 34 - Conical Laser Shadowgram of Mach 2.43,  $\alpha = 15^\circ$  Interaction.



Fig. 35 - Conical Holographic Interferogram of Mach 2.43,  $\alpha = 15^\circ$  Interaction.

Since the conical object beam projects a direct shadow of the interaction onto the holographic plate, a laser shadowgram may be obtained simply by contact-printing the plate on photographic paper. Such an example is shown in Fig. 34 for a Mach 2.43,  $\alpha = 15^\circ$  interaction from Ref. 76. It is followed by the corresponding holographic interferogram reconstruction from the same plate, shown in Fig. 35. (Note that the flow direction in these images is left-to-right.) The alignment of the object beam with the interaction is obviously not so good as in the previous examples shown here (note the lateral spreading and "ghost" images of the  $\lambda$ -foot in Fig. 34). Nonetheless, these figures show an interesting contrast between two different visualizations obtained from the same plate. Fig. 34 is similar to the white-light conical shadowgram shown earlier in Fig. 18, but is less clear due to exposure variations across the plate and coherent artifact noise. It reveals the turbulence in the separated region, the slip line emanating from the triple-shock intersection, and "shocklets" in the jet region aft of the  $\lambda$ -foot. The interferogram, Fig. 35, is generally less revealing in terms of qualitative flowfield phenomenology. It does show clearly, how-



ever, the core of the separation vortex (located at bottom mid-frame in Fig. 35).

#### 6.4.2 Data Reduction Procedure

The data reduction process used to obtain flowfield density data from the present holographic interferograms assumes that both the flow and the object beam are conical (*ie* two-dimensional in spherical polar coordinates). Thus, end effects being assumed negligible, the data reduction may thus proceed according to the classical procedure for 2-D interferograms (Ref. 97). This involves the following five major steps:

- 1) Select a series of closely-spaced vertical "cuts" through the interferograms along which fringes will be evaluated. The number of cuts is chosen to yield adequate data resolution, and is a direct function of the angular extent in  $\beta$  of the particular interaction being evaluated.
- 2) Digitize the fringe centers. For this process, a digitizing pad is used to manually locate the fringe centers as they cross each vertical cut on an enlarged interferogram image. A relative fringe order number is then assigned to each fringe.
- 3) Calculate the optical path length. The integrated optical path length is not a constant because the swept interaction structure intersects the flat tunnel sidewall at an oblique angle (see Fig. 32). Hence, the optical path length of each ray through the VCO varies from position to position throughout the entire interferogram. Using the VCO, the fin leading edge, and fiducial marks on the downstream tunnel window as reference points, the optical path length at the position of each registered fringe center is calculated trigonometrically.
- 4) Cancel the superimposed constant phase shift. (Although the present results should be infinite-fringe interferograms in principle, a minute shift in the flat plate, upon which the object beam reflects, due to wind tunnel loads between exposures superimposes a regular finite-fringe background on the results.) The constant fringe spacing observed in the undisturbed freestream flow region characterizes this fixed phase shift over the entire interferogram. The phase shift is removed by a calculated correction at this point. Absolute phase shifts  $S_{1,i}$  are then reassigned to every registered fringe location.
- 5) Calculate the density distribution of the flowfield. Based on the farfield conical structure, the refractive index along each ray emanating from the VCO is constant if the end effects are small. Eqn. 16 below, using the known freestream conditions as an initial reference point, calculates the density of each digitized point. (Note that fringe discontinuities across shock waves were resolved, where necessary, using the ideal-gas

shock wave theory evaluated at the local normal Mach number.)

$$S_{1,i} \cdot \lambda = K [(\rho_1 l_1 - \rho_i l_i) - \rho_{ref}(l_1 - l_i)] \quad (16)$$

Where  $S_{1,i}$  = corrected fringe shift between a point selected for evaluation and a known local reference point,  $\lambda$  = laser wavelength,  $K$  = Gladstone-Dale Constant,  $\rho_{ref}$  = constant free-stream reference density,  $l_1$  = optical path length through the local reference point,  $\rho_1$  = density at the local reference point,  $l_i$  = optical path length through the point selected, and  $\rho_i$  = density at the point selected.

The solution of Eqn. 16 yields the value of the local density ( $\text{kg/m}^3$ ) at each of typically several hundred points within each interferograms which is evaluated. In view of the quasiconical nature of the flow, the positions of these points may only be given properly in angular coordinates measured from the VCO location. Both the azimuth angle  $\beta$  and the elevation angle  $\phi$  are referenced to the freestream direction and are given in degrees. A typical example of a conical interaction flowfield density map, obtained from the interferogram of Fig. 19, was shown earlier in Fig. 27.

#### 6.5 Planar Laser Scattering

The planar laser scattering technique, also known as light-screen, light-sheet, or vapor-screen imaging, is a standard experimental technique which originated in the early 1960's (Ref. 98). Though early difficulties were experienced in collimating non-coherent light, the availability of powerful lasers now enables high-quality images to be obtained without undue difficulty. Usually the flow is seeded with water vapor, either naturally or deliberately by injecting water into the airstream (Ref. 99), though other seeding materials have been tried as well. Light is scattered by the aerosol particles as the flow passes through the light-screen. Since it is unclear in general that this scattering is either of the Mie type (produced only by comparatively-large spherical particles) or of the Rayleigh type (denoting scattering from molecules), it was decided by the present author to call it simply "planar laser scattering," or PLS.

Different scattering intensities in PLS imaging indicate, in principle, different flow densities, assuming that the aerosol was initially evenly-distributed in the flow. However, at least two difficulties arise which prevent a quantitative density measurement. Boundary-layers, which form upon relatively-hot solid surfaces in the flow, tend to re-evaporate any condensing moisture. Further, a high-speed boundary-layer, being less dense than the freestream, contains a smaller particle number-density than the freestream. Finally, the static-temperature rise across



a shock wave can be sufficient to re-evaporate condensed moisture particles as well. It is thus observed that such boundary-layers and post-shock regions appear unnaturally dark in PLS images. Boundary-layer fluid which leaves the surface during flow separation appears dark as well (Refs. 98 and 99). Though quantitative use has certainly been made of the PLS technique (*eg* Ref. 100), it will here be treated purely as a means of qualitative flow visualization.

One drawback of the PLS technique arises from condensing moisture in a supersonic wind tunnel nozzle, which can adversely affect the flow (Ref. 101). Some previous studies have used moist air with a frostpoint as high as  $-4^{\circ}\text{C}$ , which jeopardizes the results due to the possibility of condensation shock formation (Ref. 101). The procedure followed by Lu and Settles (Ref. 77) to prevent this is as follows. The dewpoint (or, more correctly, the frost point) of the air in the blowdown wind tunnel storage tank was kept below  $-22^{\circ}\text{C}$ , measured at atmospheric pressure. This dewpoint results in an error due to moisture condensation of less than one percent of the freestream static pressure, or the freestream Mach number, for Mach numbers in the 2.5-4 range (Refs. 101, 102, and 27, Appendix A). This amount of water vapor was also sufficient to yield good PLS images. In order to achieve this moisture level, the air, after being compressed, is sent directly to the storage tank without passing through the drying equipment (which, under normal operating conditions, dries the air to a dewpoint of  $-37^{\circ}\text{C}$  or lower by passing it through a silica-gel bed).

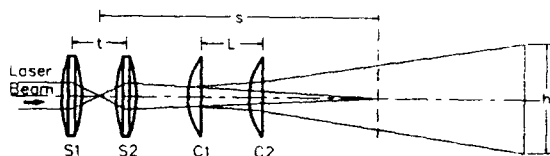


Fig. 36 - Diagram of Laser Sheet Generator (per J. T. Kegelmann).

#### 6.5.1 Optical Apparatus and Procedure

The specific PLS technique used to obtain the image shown previously in Fig. 20, as well as the other PLS images shown in Refs. 47 and 82, will now be discussed. Fig. 36 shows the optics used to generate a thin planar light sheet. A 10-Watt pulsed Copper-vapor laser (MVL-2000, CJ Laser Corp.) was used as a light source. More recently, a 5-Watt Argon-Ion laser has also been used successfully for this purpose. The laser beam is first focused in the center of the wind tunnel test section using the two spherical lenses S1 and S2. These lenses have typical focal lengths of 100 and 75 mm, respectively, and are both 50 mm in diameter. The output of S2 is then expanded into a sheet using a combination of two cylindrical lenses C1

and C2, both of which have 50 mm focal lengths and are 50 mm in width. The two spherical lenses allow the focus of the laser beam to be changed by varying the spacing,  $t$ , between them. Similarly the sheet height,  $h$ , can be controlled by adjusting the spacing,  $L$ , between C1 and C2. In the resulting optical setup the light-sheet thickness is less than 2 mm throughout the region of interest.

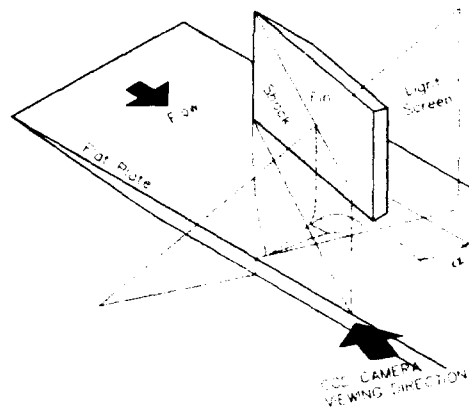


Fig. 37 - Diagram of PLS Setup and Test Geometry (per Alvi and Settles).

Any flow imaging technique used to examine fin interactions must take the quasispherical symmetry of the flow into account. Consequently several cuts, *normal to the undisturbed inviscid shock*, were made at various distances from the interaction VCO as illustrated in Fig. 37. The PLS images were recorded on S-VHS videotape (standard 30 Hz framing rate and approximately a 1/30 sec exposure) using a high-resolution color CCD camera. Some 20 ns images were also obtained with a Xybion ISG-250 electronically intensified and gated video camera to "freeze" the turbulent motion in the flow. The angular coordinates of flow features observed in the PLS imagery were obtained by way of "tare" images of a precise grid placed in the plane of the laser screen. By overlaying the flowfield and tare images in proper registration, an accurate scaling of the former was accomplished.

When aerosols such as the present ice crystals are used to seed the flow, care must be taken to ensure that: a) the seeding is uniform so as not to bias the image brightness, and b) the seed particles are small enough not to disturb the flow. It was confirmed that the flow was well-mixed in the wind tunnel stilling chamber by capturing uniform PLS images of the supersonic freestream without a model in place.

#### 6.5.2 Particle Size Measurements

Two independent techniques were used to measure the size of ice crystals entrained in this flowfield. The first method, known as a two-wavelength transmissometer technique, has been used extensively in



the past (Refs. 103 to 105) to determine the size of seeding particles in high speed flows. It involves the transmittance measurement of laser light through the seeded flow at two different wavelengths. The ratio of the transmittances at the two wavelengths is then used to calculate the mean particle size. Refs. 103-105 discuss the application of the technique in detail.

In the second particle sizing technique, the seeded flow is illuminated by unpolarized light and the degree of polarization of light scattered at  $90^\circ$  is measured. The degree of polarization in this case is inversely proportional to particle size and thus gives an estimate of the size of the ice crystals (Refs. 106 to 108).

The results of both these measurements indicate that the mean radius of the ice crystals used for seeding the flow was 0.04 microns. Further, the measurements indicated that the largest ice crystals were 0.25 microns in diameter. Numerical simulations performed using modified Stokes drag show that particles of this size follow the mean flow satisfactorily in that they accurately reveal the shock structure in the present flowfield. For a detailed description of the particle size measurements and particle trajectory analysis, the reader should consult Appendix B of Ref. 82.

#### 6.6 Skin Friction Measurements

Until recently, no instrument existed with which to measure with confidence the skin friction distribution beneath a shock/boundary-layer interaction of the sort described here (see Refs. 109 and 110). Other than the direct measurement of wall shear stress,  $\tau_w$ , by a balance, the available techniques infer skin friction from some other measured quantity, such as heat transfer or pitot pressure. The validity of such inferential methods is doubtful in complex interacting flows. Further, floating-element balances themselves have serious problems in such flows, especially due to pressure gradients and poor spatial resolution.

A recent development, the Laser Interferometer Skin Friction (LISF) meter, promises to resolve this problem. The LISF meter was invented by Tanner and Blows (Ref. 111), and was subsequently refined by Tanner (Ref. 112), Monson and Higuchi (Ref. 113), Monson, Driver and Szodruch (Ref. 114), Monson (Refs. 115 and 116), Westphal, Bachalo, and Houser (Ref. 117), and Kim and Settles (Refs. 49 and 118). The LISF meter was used to measure skin friction in supersonic sharp-fin-generated swept interactions by Kim *et al.* (Refs. 49 and 50) and in hypersonic interactions by Kussoy, Kim, and Horstman (Ref. 61). An Example of the results of such measurements was given earlier in Fig. 13. The most recent work on this topic has been published by Bandyopadhyay and Weinstein (Ref. 119), Kornilov *et al.* (Ref. 120), and Seto and Hornung (Ref. 121).

The LISF meter interferometrically senses the time rate of thinning of an oil film on a polished surface subjected to aerodynamic shear. In two-dimensional (2-D) flows without pressure gradients, oil lubrication theory then gives  $\tau_w$  directly without any reference to the properties of the overlying boundary layer. While some corrections are required in pressure-gradient and shear-gradient flows, the instrument nonetheless delivers essentially a direct measurement of  $\tau_w$ .

#### 6.6.1 The LISF Meter in High-Speed 3-D Flows

The underlying theory of the LISF technique and examples of its application, mainly in incompressible flows, are thoroughly documented in Refs. 111 to 117. Other than in a supersonic delta-wing demonstration experiment by Monson, *et al.* (Ref. 114), the LISF meter had not been used in compressible 3-D flows prior to the work of Kim and Settles (Refs. 49 and 118). They found that the major limitation of the technique in compressible flows was due to surface-wave phenomena on the oil film in cases of high  $\tau_w$ , about which more will be said below.

Kim and Settles (Ref. 118) performed an experimental calibration over a range of Mach numbers using zero-pressure-gradient supersonic turbulent boundary layers. This calibration showed that the typical error of the technique (compared to such standards as Preston-tube data and eddy-viscosity computations) ranged from -3% to -8% with Mach number. A recent repeat of this calibration using improved equipment and procedures (Ref. 122) over the range  $2.5 \leq M_\infty \leq 4$  showed that the LISF meter readings were within 1-2% of the mean of the calibration standards except at Mach 4.

It is generally necessary in 3-D laser skin friction measurements to know the direction of the wall shear stress vector *a priori*, since an accurate knowledge of the distance,  $\Delta s$ , from the oil-film leading edge to the laser-beam measuring spot is required. Alternatively, when the dual-beam LISF adaptation is used, Refs. 113-117,  $\Delta s$  need not be measured. However, in that case, either the dual beam spots must still be aligned with the local  $\tau_w$  direction, or else two components of  $\tau_w$  must be measured with considerable extra effort. Recent trends have been in favor of single- rather than dual-beam skin friction interferometry on grounds of reduced complexity.

Local  $\tau_w$  directions may be determined directly from surface-flow visualization results, assuming that these are obtained in a quantitatively-usable manner. Also, it is known that small-amplitude, broadband fluctuations occur in shock wave/turbulent boundary layer interactions, though the overall flow structure has been observed to be nominally stationary (see the paper by D. S. Dolling elsewhere in this report).



Since surface-flow visualization methods have little or no frequency response, they clearly perform some sort of averaging process. In the absence of evidence to the contrary, it is assumed that such patterns generally yield a true representation of the local mean direction of the wall  $\tau_w$  vector.

The kerosene-lampblack-adhesive tape technique described earlier in this paper is particularly suitable for determining  $\tau_w$  directions, in that it yields undistorted full-scale surface-streak patterns. Angular measurements of local  $\tau_w$  directions are possible with  $\pm 0.5^\circ$  routine accuracy. During LISF tests, full-scale transparent overlays of these surface-flow patterns were used to identify the surface-flow direction corresponding to a given position of the laser-beam measuring spot.

After applying the oil film to the flat plate, an optical cathetometer (least count: 0.025 mm) aligned normal to the surface-flow direction was used by Kim and Settles to measure  $\Delta s$  with a repeatability of  $\pm 0.6\%$ . The leading edge of the oil film was highlighted for this purpose by reflected light from a spotlight positioned outside the wind tunnel. Still, uncertainty of the exact oil-film leading-edge position was the major contributor to uncertainty in  $\Delta s$ . Checks were made to insure that  $\Delta s$  did not shift due to wind tunnel startup. With practice,  $\Delta s$  was measured with an overall accuracy of  $\pm 2\%$  using the optical cathetometer.

Recognizing that the  $\Delta s$  measurement error is likely to be the single most important issue in the accuracy of the instrument, Kim *et al.* (Ref. 50) recommended and Garrison and Settles (Ref. 122) implemented the use of a Questar DR1 telemicroscope to obtain a more accurate  $\Delta s$  measurement. The latter authors succeeded in achieving a  $\Delta s$  measurement error of only  $\pm 0.5\%$  by this means. Accurate  $\Delta s$  measurements along the local surface-flow direction enable, at least in the present circumstances, the use of the relatively-simple single-beam LISF meter arrangement shown in Fig. 38 rather than the dual-beam method of Monson *et al.* (Refs. 113-116).

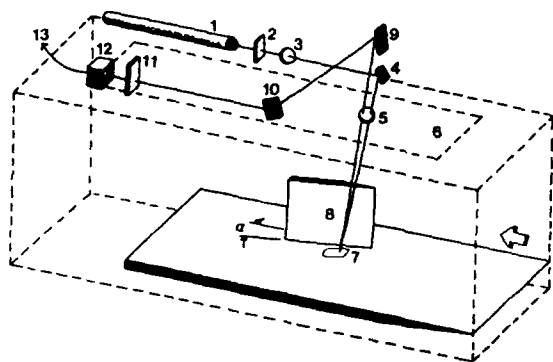


Fig. 38 - Diagram of LISF Meter

### 6.6.2 Apparatus and Data Acquisition

Fig. 38 illustrates the components of the single-beam LISF meter as used by Kim *et al.* (Refs. 49, 50, and 118). The beam from a 5-milliwatt linearly-polarized helium-neon laser (1) first passes through a 50% neutral-density filter (2) and an iris diaphragm (3). The beam is then directed downward by a folding mirror (4), and focused by a lens (5), passing through the clear acrylic ceiling window (6) of the wind tunnel to form a spot of about 450  $\mu\text{m}$  diameter at an appropriate point (7) on the flat plate. During experiments, a thin film of  $\nu = 500$  centistokes Dow-Corning "200" silicone oil applied to a local region (7) of the flat plate is sheared by the  $\tau_w$  distribution of the shock/boundary-layer interaction due to the fin (8). The incident laser beam is reflected by both the surface of the oil film and the polished plate beneath it. This produces a reflected, two-component, interfering laser beam directed out of the wind tunnel through the ceiling window. (The beam angles of incidence and reflection are kept to about  $1^\circ$ .) The reflected beam is intercepted by two first-surface aiming mirrors (9) and (10), whence it is directed through a ground-glass diffuser (11) and a 6328 Å filter onto a photodiode (12).

The photodiode senses a time-dependent light intensity due to the interference of light reflected from the oil film and test surface. The photodiode output (13) is raised to a level of 8 volts by an internal operational amplifier, low-pass filtered with a 10 Hz cutoff to remove high-frequency, vibration-induced optical noise above the oil-film response range, and recorded. Several other channels of data are recorded simultaneously, including wind tunnel stagnation properties and wall pressures and temperatures. These analog data channels are then digitized by a microcomputer-controlled A/D converter, and stored in the computer memory. (Current practice employs a multi-channel 12-bit LeCroy waveform recorder for this purpose.)

Kim *et al.* (Refs. 49, 50, and 118) used a 20Hz data rate, later upgraded to 50Hz. Garrison and Settles (Ref. 122) later found that a significantly-higher data rate (200 Hz) helps to distinguish the initial fringe pattern from random noise, thus improving the signal. They also achieved a better focus of the incident laser beam on the flat plate by attaching a beam expander (composed of a microscope objective and an output lens) to the laser, as done by Westphal *et al.* (Ref. 117).

A photograph of the physical implementation of the LISF instrument is given in Fig. 39. The instrument is mounted on a platform supported by pedestal legs whose lower ends are attached to an optical table. The test section sidewall has been removed to reveal the flat plate and white-painted fin. Shown adjusting



the instrument in Fig. 39 is the late Dr. Kwang-Soo Kim, who developed this version of it at Penn State University. The details of this development may be found in his Ph.D. Thesis, Ref. 123.



Fig. 39 - Photo of LISF Meter Installed Above Wind Tunnel Test Section.

### 6.6.3 Data Reduction

The occurrence of surface waves on the oil film under conditions of high shear limits the number of useful interference fringes which can be obtained (Refs. 118 and 124). This calls for a somewhat-different data reduction scheme than that reported by the cited earlier investigators for incompressible flows. Given only a few good fringes, it becomes necessary to determine  $\tau_w$  based on the entire signal within the usable fringe record. Merely determining the time interval corresponding to 3 arbitrary fringe peaks (minima and maxima), as was often done in incompressible flow, does not yield sufficient accuracy here.

Thus, as described in Ref. 118, it is necessary to define that part of the fringe record which is usable. The last fringe in the record is often a partial one, obtained when the oil-film has become extremely thin. It is usually discarded. The initial fringes "emerge" from noise induced by the surface capillary waves, which migrate downstream as the oil-film begins to thin. In high-shear flows where each additional fringe is valuable, it is very important to make use of as many of these initial fringes as is practical. Unfortunately, no explicit rules can be stated other than the fact that experience is required to make this choice properly. The approach given in Refs. 49, 118, and 123 has, to some extent, been superseded. Interested readers are referred to Ref. 122 (still in preparation at the time of this writing) for more information on this issue.

Occasionally, distorted or corrupted fringe records occur with this instrument for no obvious reason.

This is suspected to be due to dust particles on the oil film, etc. Corrupted fringe records are usually easy to identify by visual inspection, and should be discarded. Even the best fringe records, however, are subject to random electronic noise, vibration-induced noise, etc. It is fortunate that most of this noise is well above the comparatively-low frequency of the fringes, so filtering is effective. Digitized fringe records are thus routinely smoothed by repeated application of an adjacent-point averaging algorithm until a "clean" signal remains.

The LISF data reduction equation (Ref. 113), derived from the Navier-Stokes equation and assuming constant wall shear stress, is:

$$\tau_w = \frac{2n\rho\nu\cos(r)}{\lambda} [\Delta s/N't'] \quad (17)$$

where  $N'$  = effective fringe number,  $t'$  = effective oil flow time,  $n$  = oil refractive index,  $\rho$  = oil density,  $\lambda$  = laser wavelength,  $\nu$  = oil viscosity, and  $r$  = oil refraction angle.

Eqn. 17 requires a correction for the effect of variable wall temperature on  $\nu$ , such as that described in Ref. 118. This correction is critical to LISF measurements in high-speed flows, since a 1° C change in  $T_w$  causes about a 2% change in  $\nu$ . It is likewise important to know your oil, whence Kim *et al.* had the viscosity-temperature characteristics of a sample of 500-centistoke silicone oil determined by a professional testing laboratory to an accuracy of better than 1% over their wall-temperature range.

In Ref. 118, Kim and Settles found that the wall temperature in the interaction region of interest was, to first order, dependent only upon time from the beginning of the wind tunnel run. It was thus possible to fit an expression to the temperature-time data and use this to form an expression for  $\nu(t)$ . This was next used to "correct" the time base of the LISF fringe record in order to produce a distorted fringe record with constant effective  $T_w$  conditions. That approach was workable, but not as straightforward as it might be. A more direct approach is to rederive from first principles an expression similar to Eqn. 17, but in which it is assumed *a priori* that  $\nu = \nu(t)$ . This was done by Monson (Ref. 125), with the result:

$$\tau_w = \frac{2n\rho\nu_r\cos(r)}{\lambda} [\Delta s/N'] \int_0^t \frac{\nu(t)}{\nu_r} dt \quad (18)$$

where  $\nu_r$  is a known reference viscosity at a certain temperature. Eqn. 18 can be integrated numerically when  $\nu(t)$  is known, thus effecting a more direct solution to the issue of the variable  $T_w$  effect than that



of Ref. 118. (For more information on this approach, see Ref. 122.)

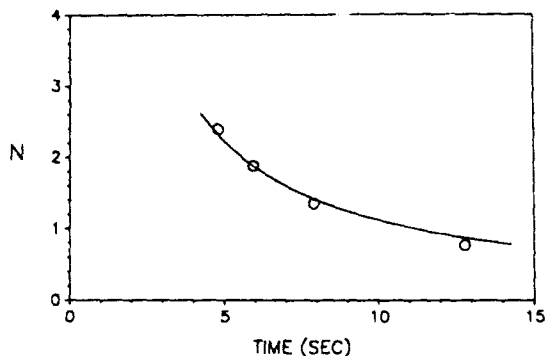


Fig. 40 - Fringe Number vs. Time, Comparing Data and Curvefit.

The experimental data of fringe number vs. time are next compared with oil lubrication theory, as shown in the example of Fig. 40 for a high-shear case where  $\tau_w = 577 \text{ N/m}^2$ . A least-squares curvefit of the data to the lubrication theory ( $N \propto 1/t$ ) is performed, followed by a computation of the "goodness-of-fit" of the curve to the data. The inclusion of additional, possibly-questionable fringes at the beginning or end of the fringe record may be judged by their effect on the overall goodness-of-fit. Finally, the essence of the data as represented by the curvefit of fringe number vs. time (or related quantities), is used in Eqn. 18 to calculate  $\tau_w$ . The 4 fringes represented in Fig. 40 are the smallest number required for acceptable  $\tau_w$  accuracy according to Ref. 122, despite the earlier claim of Ref. 49 that 2 fringes could be made to suffice.

Before  $\tau_w$  is found, however, two further corrections (Refs. 113 and 114) are required in principle, since the oil film in swept interaction experiments is subject to both pressure- and shear-gradients. The pressure-gradient correction, per Ref. 113, was evaluated in the work of Kim *et al.* through interpolation of  $p_w$  measured at pressure taps near the constant-radius LISF measurement arc on their flat plate. It was found that the pressure-gradient correction for the experiments of Kim *et al.* amounted at most to  $\pm 0.1\%$ , which is negligible. This fact is significant in that pressure-gradient errors are controlling factors in most other methods of skin friction measurement (Refs. 109 and 110). However, it cannot be stated categorically that the LISF pressure-gradient correction will always be negligible in all experiments. Two-dimensional interactions, for example, could produce pressure gradients large enough to make this correction significant.

Per Monson, Driver, and Szodrich (Ref. 114), the shear-gradient correction is quite simple for the single-beam LISF technique. The correction is required if there is a significant change in  $\tau_w$  from the

oil-film leading-edge to the laser-beam measurement spot. This correction has a form (see Refs. 114 and 118) such that it is accomplished by an effective shift of the measurement point along the surface streamline direction. However, for the experiments of Kim *et al.* wherein  $\Delta s \sim 2 \text{ mm}$ , the required shift is only 0.5 mm, which is negligible. In general, a shear-gradient correction may always be avoided in single-beam LISF measurements if  $\Delta s$  is kept small, which it should be anyhow for purposes of surface-wave avoidance in most cases.

#### 6.6.4 Preston-Tube Comparison

Simple experimental techniques like the Preston-tube (Refs. 109 and 110) were decried at the beginning of this section for purposes of skin friction measurement beneath swept interactions. This was because the Preston-tube, actually a surface-pitot tube, depends upon the logarithmic law-of-the-wall for the calibration which relates its output to  $c_f$ . One may not necessarily expect the log-law to hold in the complex swept-interaction flows described in this paper.

Nonetheless, M. Rubesin of NASA-Ames Research Center suggested that it would be enlightening to determine, by comparison with LISF data, whether or not the Preston-tube has any validity in a shock/boundary-layer interaction. This challenge was accepted by Kim, Lee, and Settles (Ref. 126), who applied the Preston tube to estimate  $c_f$  in a sharp-fin-generated swept interaction at Mach 4 and  $\alpha = 16^\circ$ . The LISF skin friction data for this case had already been obtained as described previously and shown in Fig. 13.

For the Preston tube, a stainless steel hypodermic tube having a circular, squared-off end was used. The inner diameter was 0.457 mm and the outer diameter was 0.813 mm, yielding a diameter ratio of about 0.6. The ratio of the Preston tube outer diameter to the incoming boundary layer thickness was about 0.27. The Preston-tube impact pressure and the corresponding wall pressure were measured at each of eleven locations within the interaction.

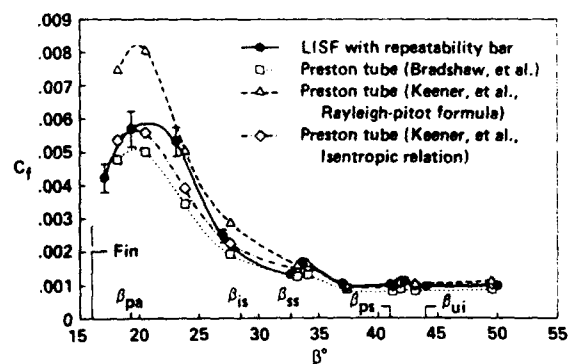


Fig. 41 - Comparison of LISF and Preston Tube  $c_f$ .



A comparison of Preston-tube skin friction results, obtained using the Bradshaw-Unsworth (Ref. 127) and Keener-Hopkins (Ref. 128) calibrations, with the LISF data is shown in Fig. 41. Both Preston-tube methods are in reasonable agreement with the LISF data, so long as isentropic flow rather than the Rayleigh pitot formula is used in calculating the Preston-tube Mach number in the case of the Hopkins-Keener calibration. This is surprising, since the validity of these calibrations in separated flows is highly questionable.

Unfortunately, this comparison of techniques is thus rendered somewhat anticlimactic. The evidence shown in Fig. 41 is not strong enough to warrant a general recommendation that the Preston tube may be usable in compressible separated flows, even with restrictions on the choice of calibration. More experiments of this sort in a wider range of interactions would be required to decide the general applicability of Preston tube in such flows.

### 6.7 Heat Transfer Measurements

Experimental heat transfer is a very broad field. Many techniques have been developed by previous investigators to measure aerodynamic heat transfer, no single approach having clearly gained the upper hand. General references (Refs. 129-132) are available on these conventional heat transfer measurement techniques and instruments. The present scope only allows a discussion of certain techniques of interest in cold-flow facilities, where the heat transfer signal being measured may sometimes be quite weak, and in blowdown facilities where the testing time is limited.

#### 6.7.1 Thin-Film Gages

The development of evaporated metallic-film coating technology in other fields has spawned thin-film gages which are becoming widely used in aerodynamic testing. Because of its high sensitivity and fast response, the thin-film gage is applied in a variety of ways. It can measure highly-transient surface temperatures, it can be used as a calorimeter gage, or it can constitute the sensing element in a multilayer "sandwich" gage. Epstein *et al.* (Ref. 133) used such gages to measure the heat flux to a transonic turbine, while Hayashi *et al.* (Ref. 134) first used them to measure heat flux in a shock/boundary layer interaction. Thin-film gages have also been used in transition detection studies (*eg* Johnson *et al.*, Ref. 135). Although the thin-film technique has versatility, accuracy, and fast response, its fabrication by microlithographic techniques is expensive. The resulting thin-film sensors further need care in handling, annealing to prevent drift, and highly-accurate calibration procedures.

#### 6.7.2 Resistance Heater Methods

For heat transfer measurements in unheated, cold-flow facilities it is apparent that external heating or

cooling is needed, since a sufficient difference between the surface temperature and the adiabatic wall temperature is critical to the signal-to-noise ratio of the measurement. (Such was the case in the experiments of Lee *et al.*, Refs. 57 and 59, discussed earlier.) Though cooling by way of a circulated refrigerant has been attempted in the past, Lee *et al.* chose heating by an embedded resistance heater as the simplest means to vary the surface temperature.

The resistance heater method is the most widely-used technique to apply external heating for steady-state heat flux measurements. A heating element inside the surface of a test model generates enough heat to raise the surface temperature significantly. During a test the electrical power input to the heater equals the convective heat transfer from the model surface at steady-state. By measuring the local surface temperature and applying the heat convection equation (Newton's law of cooling), the heat transfer coefficient can thus be calculated.

For example, Simonich and Moffat (Ref. 136) used a thin gold-film resistance heater to generate a uniform heat flux, and cholesteric liquid crystals to sense the resulting surface temperature distribution. Hippensteele *et al.* (Ref. 137) evaluated commercially-available elements for use in the resistance heater technique. Abuaf *et al.* (Ref. 138) used a resistance heater/liquid crystal combination to measure the heat transfer distribution in a jet impingement experiment. Eibeck and Eaton (Ref. 139) used thermocouple measurements beneath a foil heater element to investigate the heat transfer effect of a longitudinal vortex in a turbulent boundary layer.

However, these methods had been used only for relatively-low-speed flows until recently. Higher heat generation rates and accurate multipoint surface temperature measurements are needed for high-speed flow experiments. In the work of Lee *et al.* (Refs. 57 and 59), it was attempted to combine the above heat transfer measurement technologies to obtain a high-resolution, steady-state measurement technique for high-speed flow in a near-adiabatic wind tunnel facility. Further, in order to obtain high-spatial-resolution data with a modest number of discrete gages, the inherent quasicircular symmetry of sharp-fin-generated interactions was exploited as well.

#### 6.7.3 Flat Plate for Heat Transfer Measurements

The Penn State flat plate for heat transfer measurements, discussed in Refs. 57 and 59 and diagrammed in Fig. 42, is a "sandwich" consisting of a top sheet of RTD (Resistance Temperature Detector) sensors, a foil heater, an insulation board, and a stainless steel supporting plate. A few thermocouples are also distributed inside the insulation board. Heat is generated by the foil heater and the surface



temperature distribution is measured by the RTD sensors. The heat convected to the flow at steady-state equals the total heat generated by the heater ( $V^2/R$ ) minus the heat loss through the insulation board. However, the adiabatic wall temperature is also needed in the calculation of a heat transfer coefficient, and is indirectly measured as described in a later section.

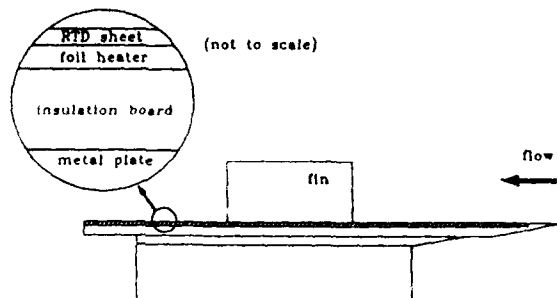


Fig. 42 - Diagram of Multilayer Construction of Flat Plate for Heat Transfer.

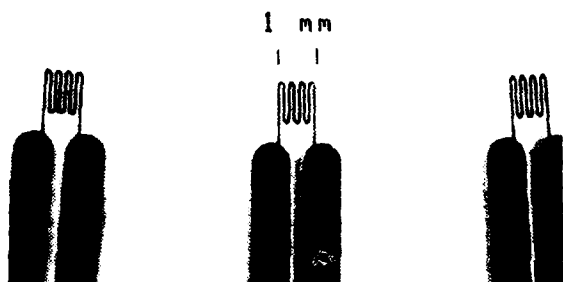


Fig. 43 - Magnified Image of RTD Sensor Geometry.

#### 6.7.4 RTD Surface Temperature Sensors

Custom-made thin-film RTD sensors were vacuum-deposited on a plastic substrate by NASA-Langley Research Center staff using microlithographic fabrication techniques. These thin-film sensors can measure accurate surface temperatures without disruption of the flowfield and have a high frequency response. However, only steady-state measurements were carried out by Lee *et al.*

Each of the 37 RTD sensors consists of a Nickel-film resistance thermometer of about  $1000\text{\AA}$  thickness deposited on the  $50\text{ }\mu\text{m}$  thick Kapton polyimide substrate sheet. The sheet itself is then attached to the flat surface of the foil heater using laminating epoxy cement. Nickel is chosen as the sensing element because of its relatively-high sensitivity and its excellent adhesion characteristics in thin-film applications. The sensor geometry is the square  $1\times 1\text{ mm}$  serpentine pattern shown in Fig. 43. This pattern maximizes the sensor length in a small surface area, thus producing a high room-temperature resistance ( $65\text{ }\Omega$ ), a high signal-to-noise ratio, and effectively a "point" surface temperature measurement. Low-resistance  $6\text{ }\mu\text{m}$ -thick copper-film leads are also deposited from each sensor to the edge of the

polyimide sheet. These leads are individually soldered to a 37-conductor coaxial cable, which is then connected to a specially-designed 37-channel signal-conditioner outside the wind tunnel test section.

To utilize the quasiconical nature of the fin interaction, a double-circular-arc distribution of the 37 temperature sensors (at radii of 86.4 mm and 91.4 mm from the fin leading edge) is chosen, as shown in Fig. 44. In terms of the azimuthal angle  $\beta$ , these gages are spaced at a  $2^\circ$  angular separation from  $\beta = 6^\circ$  to  $78^\circ$ , allowing high spatial-resolution data to be obtained.

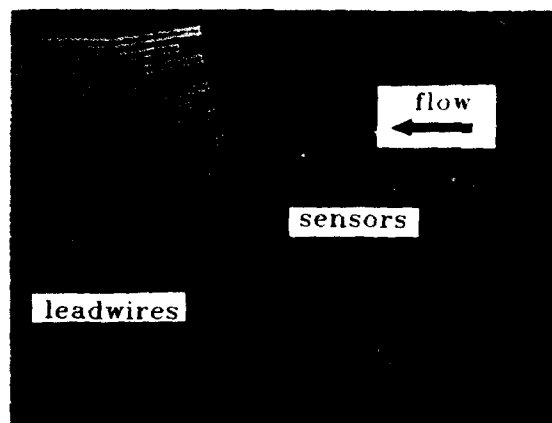


Fig. 44 - Image of 37-RTD Sensor Arc on Flat Plate.

#### 6.7.5 Heater

Two types of heating methods are commercially available: the surface resistance heater method and the radiation method. The radiation method utilizes external quartz lamps placed outside the test section and focused upon the model. In general it is a costly and difficult technique. Surface resistance heaters, on the other hand, are widely used because of their relatively-low cost and easy application. With this approach the model is heated by a resistance foil imbedded in the model surface.

There were four major requirements for the heater in the experiments of Lee *et al.*: (1) High heat flux should be generated because of the large convective heat transfer expected in high-speed flows. (2) The heat efflux should be uniform over the surface of interest. (3) For quick heating during a typical wind tunnel run of about 30 seconds, the thermal mass of the heater should be as small as possible. (4) The surface of the heater should be flat and smooth, since the RTD sheet is mounted upon it and is exposed to the flow.

Commercially-manufactured "unetched-foil" heaters, as used in a variety of experiments (Refs. 136-139), showed quite satisfactory results in terms of uniform heat flux and easy application. However, all these heaters were thought to be unsuitable for present purposes because their resistances were too low to



generate sufficient heat flux without requiring an unreasonable electrical current flow. Instead, Lee *et al.* (Refs. 57 and 59) used an Inconel "etched-foil" heater. This heater is thin and flexible, consisting of an etched-foil resistive element laminated between layers of flexible insulation. It also has a thin aluminum foil over the top surface of the heating element to enhance uniform heating. Custom-made by Minco Products Inc., it is 0.25 mm thick and its room temperature resistance is 21.6  $\Omega$ . Using a laminating epoxy cement, it is "sandwiched" between the RTD sheet and the insulation board (see Fig. 42). In retrospect, the choice of this etched-foil heater may have been ill-advised, since later results indicated that its uniformity of heat efflux was poor.

The foil heater is powered through leadwires connected to an AC variable transformer which is capable of an output voltage up to 280 V and a current up to 15 A. The voltage applied to the heater is recorded during testing.

#### 6.7.6 Insulation Board

The heat generated by the heater can be transferred to the surroundings by conduction, convection and radiation. However, in the experiment of Lee *et al.* radiation was negligible because the temperature is near-ambient. Thus a portion of the heat energy at steady-state is assumed to be convected to the flow over the plate while the remainder is conducted through the insulation board underlying the heater. (1-D heat flow with no lateral conduction is presumed.) A good insulator is thus needed to minimize the conduction loss. The insulator should further be rigid enough to support the heater during exposure to high-shear flows, and should be machined for surface flatness.

"Rexolite" plastic was chosen for this purpose. It has a low thermal conductivity (0.00035 cal/sec/cm/ $^{\circ}$ C) and also satisfies the stated mechanical requirements. A 4.76 mm-thick "Rexolite 1422" sheet was purchased from Almac Plastic Corp. and was machined to size. After attaching the heater and RTD sheet to the insulation board using the "vacuum bagging" technique (see Ref. 59), the entire assembly was installed on the stainless-steel flat plate. Also, to measure the temperature change of the insulation board, three quick-response thermocouples were installed on its top face and two more on its bottom face.

#### 6.7.7 Signal Conditioning

The RTD sensors, which are at the heart of this experiment, measure temperature by the change of resistance of a sensing element according to a prior calibration. To measure the resistance, it is necessary to provide a constant current flow to the RTD during an experiment. A signal-conditioning instrument was designed and fabricated for this purpose, consisting of

37 sets of constant-current sources (1.5 mA), amplifiers, and low-pass-filters for each of the 37 RTD channels. For the calibration of the RTDs, the internal heater of the plate and a precision thermocouple are used. The heater elevates the temperature of the RTDs and this temperature is measured by the thermocouple. To maintain a uniform temperature over all sensors, a large aluminum block in which the thermocouple is installed is placed on top of the plate and the entire assembly is allowed to reach thermal equilibrium before calibration data are read.

#### 6.7.8 Data Acquisition

A LeCroy digital waveform recorder controlled by a 386-class microcomputer is used for data acquisition. This system has 12 channels of high-speed sampling capability at rates up to 5 Mhz and 32 channels of relatively-low-speed data sampling at rates up to 5 KHz. All these channels utilize 12-bit digitization. The "ASYST" software package is employed for data handling. During experiments, signals from the RTD sensors and thermocouples of the heat transfer model, as well as signals from the wind tunnel stilling chamber, are all simultaneously recorded on the LeCroy system.

#### 6.7.9 Data Reduction

The present heat transfer measurement technique requires an accurate determination of all the terms in the definition of the Stanton number,  $c_h$ :

$$c_h = \frac{h}{\rho_{\infty} V_{\infty} c_p} = \frac{q''_{\text{conv}}}{\rho_{\infty} V_{\infty} c_p (T_w - T_{aw})} \quad (19)$$

where  $h$  is the convective heat transfer coefficient,  $T_w$  is the surface temperature of the flat plate,  $T_{aw}$  is the adiabatic wall temperature,  $\rho_{\infty}$ ,  $V_{\infty}$ ,  $c_p$  are the density, velocity and specific heat of the freestream, respectively, and  $q''_{\text{conv}}$  ( $\text{W}/\text{m}^2$ ) is the heat convected to the flow. Except for  $T_w$ , which is directly measured by the RTD sensors, all terms in Eqn. 19 must be determined indirectly from measured values. In particular, the accurate determination of both  $q''_{\text{conv}}$  and  $T_{aw}$  is essential, since these parameters principally determine the accuracy of the Stanton number. They are, however, not easy to measure.  $T_{aw}$  is usually never reached during the brief tests characteristic of a blowdown wind tunnel facility, even on an insulating model. Further, the variation of temperature within the insulation board is quite complex during a test due to changing stagnation temperature and heater voltage, requiring that a special calculation be performed.

#### 6.7.10 Conduction Loss Calculation

From the measured voltage applied to the foil heater and its resistance, its heat efflux is easily calculated.



However, it was already noted that not all of this heat efflux is convected to the flow. There is also a conduction loss through the insulation board which must be determined.  $q''_{\text{conv}}$  is then calculated by subtracting this conduction loss from the heat efflux produced by the heater. The conduction loss is calculated using the measured RTD temperature and the bottom temperature of the insulation board by solving the time-dependent 1-D heat diffusion equation with an imbedded heat-source layer:

$$\frac{\partial T}{\partial t} = \frac{\partial}{\partial x} \left( D \frac{\partial T}{\partial x} \right) + \rho c_p \dot{g} \quad (20)$$

where  $t$  is time,  $x$  is depth into the plate measured normal to the top surface of the RTD sheet (see Fig. 45), and  $D$ ,  $\rho$ , and  $c_p$  are the thermal diffusivity, density, and specific heat of the multi-layered components of the plate, respectively. Also  $\dot{g}$  ( $\text{W}/\text{m}^3$ ) is the rate at which heat is generated per unit volume of the foil heater. The measured time-dependent RTD and insulator-bottom temperatures serve as boundary conditions, and a constant-temperature initial condition throughout the plate is both assumed in the solution and forced in the actual experiment by allowing adequate time for thermal equilibration between tests.

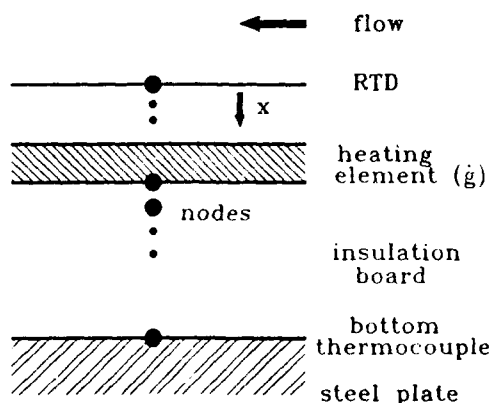


Fig. 45 - Diagram for Computation of Conduction Loss into Flat Plate.

The numerical solution of Eqn. (20) yields temperature vs. time for 49 nodes within the plate, from which the time-dependent conduction loss to the insulation board,  $q''_{\text{loss}}$  ( $\text{W}/\text{m}^2$ ), is obtained from Fourier's law:

$$q''_{\text{loss}} = -k \frac{dT}{dx} \quad (21)$$

using the first two node temperatures at the top of the insulation board to form the gradient. ( $k$  is the thermal conductivity of the insulation board.) Of course, this procedure accounts only for conduction

normal to the plate surface. Lateral conduction effects were estimated in Ref. 59 and found to be, at worst, 20% to 30% of the normal conduction, which is itself on the order of 10% of the total heat produced by the heater. Accordingly, no correction has been carried out for lateral conduction.

#### 6.7.11 Adiabatic Wall Temperature

In the experiments of Lee *et al.*, an accurate evaluation of  $T_{\text{aw}}$  was a most critical step, since  $T_w - T_{\text{aw}}$  was relatively small at the location of peak heat transfer in the swept shock/boundary-layer interactions under study. Although most previous experimental studies have assumed that  $T_{\text{aw}}$  is constant beneath such interactions, it was necessary to check that assumption in order to maintain the accuracy of the heat transfer results.

There are two methods generally used to measure  $T_{\text{aw}}$ : the "direct" method and the "indirect" or extrapolation method. The direct method measures  $T_{\text{aw}}$  directly upon an insulated model after thermal equilibrium is reached (Refs. 140-142). However, in most of these cited cases the required tunnel run time was quite long, which is not possible for tests in a blowdown wind tunnel.

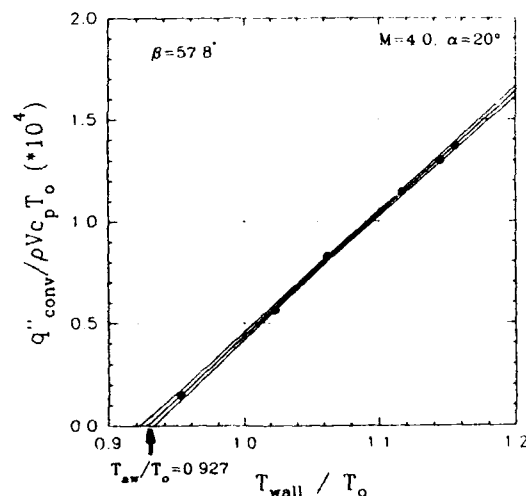


Fig. 46 - Example of the Determination of Adiabatic Wall Temperature.

Neumann and Hayes (Ref. 56) discuss the general problem of recovery temperature measurement and present a classical way to solve it. This method involves making several heat flux measurements at different wall temperatures. Since the heat flux is linear with  $T_w$  so long as the heat convection coefficient is constant, a linear fit to the data can be extrapolated to the temperature at which zero heat is convected to the flow, which is identically  $T_{\text{aw}}$ . Lee *et al.* (Refs. 57 and 59) employed this "indirect" method, obtaining results which are typified by Fig. 46 for the case of a sensor located in the flat plate boundary-



layer at  $M_\infty = 4.0$ . Six different heating rates show the expected linear variation with wall temperature which, upon extrapolation, yields a flat-plate recovery factor of 0.90. This is sufficiently close to the classical value of 0.89 which is expected for supersonic turbulent boundary-layers. A 95% confidence interval is also shown on the data in Fig. 46, which is used for the error analysis of the measurements.

#### 6.7.12 Data Reduction Program

A heat transfer data reduction program was written by Lee (Ref. 59) to implement the procedures described above. The program was written in the FORTRAN language, and runs on a 386-class microcomputer. It accepts as input 42 data channels and processes data for 6 different heating rates of the imbedded foil heater, thus producing a total of 252 data files. The program then calculates the distribution of  $c_h$  at 35 different locations of the RTD sensors in the swept interaction under study. For each RTD location the calculation procedure is executed in time, with 0.05 sec time steps beginning at the start of the wind tunnel run. The calculation procedure is as follows:

- 1) The heat efflux generated by the heater,  $\dot{q}$ , is calculated.
- 2) Eqn. 20 is solved for 49 nodal temperatures in the flat plate.
- 3) The heat loss to the insulation board is obtained by solving Eqn. 21.
- 4) From  $\dot{q}$ ,  $q''_{\text{heater}}$  is determined by multiplying by the surface area of the heater. The heat convected to the flow is then calculated by subtracting the calculated conduction loss from  $q''_{\text{heater}}$ .
- 5)  $T_{aw}$  is calculated by the indirect method described above.
- 6) The wind tunnel freestream properties are calculated.
- 7) Finally, mean  $c_h$  values are calculated at each sensor  $\beta$ -location by averaging the data over a 5 sec period near the end of the wind tunnel run, where it is assumed that a steady-state condition exists.

#### 6.7.13 Error Analysis

The uncertainty of each variable in the above process contributes to the total uncertainty of the final result. As Coleman and Steele (Ref. 143) suggest, the total uncertainty of the present measurements is determined by calculating and combining the "root-sum-squares" of the uncertainties of each variable in the data reduction equation. This calculation indicates a maximum total uncertainty in  $c_h$  of about  $\pm 10\%$  for the 5 different swept interaction cases which were measured by Lee *et al.* The error bars which were shown on Lee's data points in Fig. 12 reflect this uncertainty estimate.

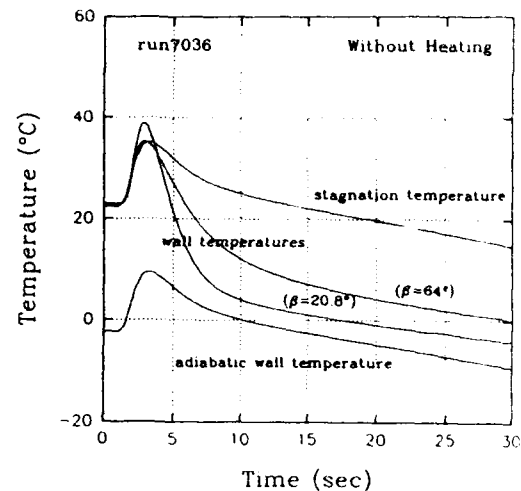


Fig. 47 - Temperature Variations Without Heating for Mach 4,  $\alpha = 16^\circ$  Interaction.

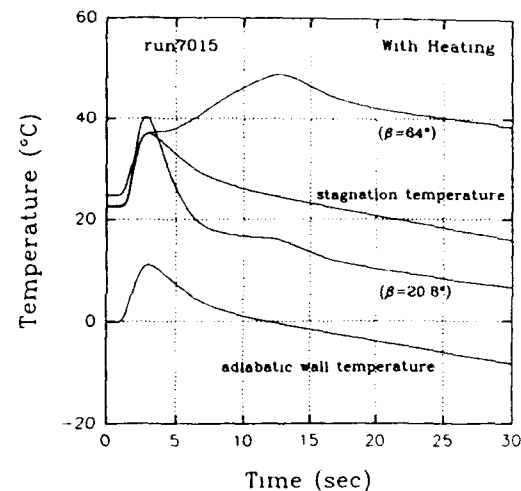


Fig. 48 - Temperature Variations With Heating for Mach 4,  $\alpha = 16^\circ$  Interaction.

#### 6.7.14 Results

Fig. 47 shows the time variations of wall temperature at two representative RTD sensor locations ( $\beta = 64^\circ$ , located outside the interaction, and  $20.8^\circ$ , located at the point of peak heat transfer) in the Mach 4,  $\alpha = 16^\circ$  fin interaction *without* heating. Fig. 48 shows the corresponding case *with* heating, where the two wall temperatures are elevated well above the adiabatic wall temperature. The "knees" in the variation of the wall temperatures in Fig. 48 (at 12.5 sec) are due to a deliberately-abrupt change of the heating rate during the run, which was required to raise the plate temperature rapidly at the beginning of the run in order to save testing time. The tunnel stagnation and adiabatic wall temperature variations (calculated under the assumption that the recovery factor equals 0.89 based on many measurements of high-speed turbulent boundary-layers) are also shown.



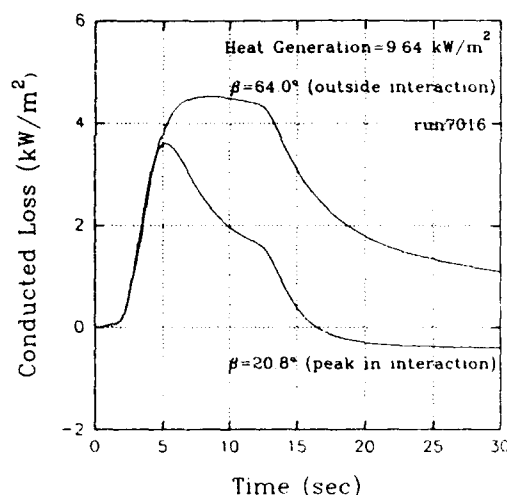


Fig. 49 - Comparison of Conduction Loss Calculations for Mach 4,  $\alpha = 16^\circ$  Interaction.

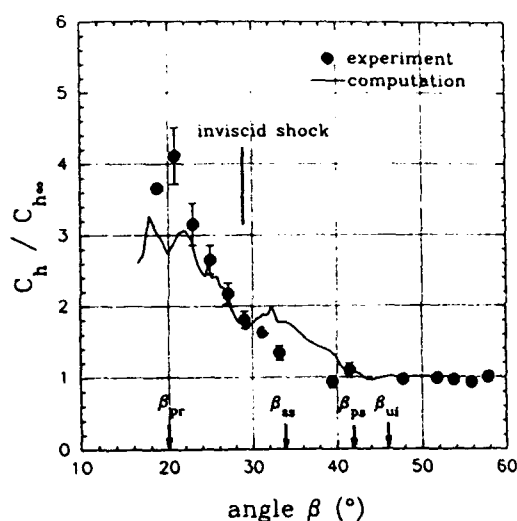


Fig. 50 - Normalized Heat Transfer Distribution for Mach 4,  $\alpha = 16^\circ$  Interaction.

Fig. 49 shows a comparison of the computed conduction loss through the insulation board at the same two sensor locations ( $\beta = 64.0^\circ$  and  $20.8^\circ$ ) for the same interaction. Similar "knees" at 12.5 sec are also seen here. At the location of peak heat transfer ( $\beta = 20.8^\circ$ ) the conduction loss is actually negative at the end of the tunnel run because heat is so strongly convected to the flow there.

Fig. 50 shows the measured heat transfer distribution in the Mach 4,  $16^\circ$  fin interaction as a function of the azimuthal interaction angle. The computation by Horstman (Ref. 57) is shown for comparison. Four other interactions were similarly measured in the work of Lee *et al.* The indicated error bars reflect the error analysis described above. Peak heat transfer rates from this set of data were discussed earlier in this paper and shown in Fig. 12.

## 7.0 ACKNOWLEDGEMENTS

The sponsorship of that part of the research reviewed here which was carried out at Penn State came primarily from AFOSR (J. D. Wilson and L. Sakell) and the NASA-Ames Research Center (C. C. Horstman). The author owes much to a long-standing research collaboration with D. S. Dolling, C. C. Horstman, D. D. Knight, and A. A. Zheltovodov. The work of current and former graduate students F. S. Alvi, S. Garg, T. J. Garrison, J. C. Hsu, K.-S. Kim, Y. Lee, F. K. Lu, and M. C. Schmidt has been invaluable, and has been used freely in this paper. Finally, the author thanks L. J. Dodson and J. D. Miller, the staff of the Penn State Gas Dynamics Laboratory, for their loyal support.

## 8.0 REFERENCES

1. Settles, G. S., and Dolling, D. S., "Swept Shock Wave/Boundary-Layer Interactions," in *AIAA Progress in Aeronautics and Astronautics: Tactical Missile Aerodynamics*, edited by M. Hemsch and J. Neilsen, Vol. 104, AIAA, New York, 1986, pp. 297-379.
2. Settles, G. S., and Dolling, D. S., "Swept Shock/Boundary-Layer Interactions--Tutorial and Update," AIAA Paper 90-0375, January 1990.
3. Ferri, A., "Experimental Results with Airfoils Tested in the High-Speed Tunnel at Guidonia," NACA TM 946, 1940 (translation).
4. Stalker, R. J., "Sweepback Effects in Turbulent Boundary-Layer Shock-Wave Interaction," *J. Aero. Sci.*, Vol. 27, May 1960, pp. 348-356.
5. Green, J. E., "Interactions between Shock Waves and Turbulent Boundary Layers," *Progress in Aerospace Sciences*, Vol. 11 edited by D. Kuchemann, 1970, pp.235-340.
6. Korkegi, R. H., "Survey of Viscous Interactions Associated with High Mach Number Flight," *AIAA Journal*, Vol. 9, No. 5, May 1971, pp. 771-784.
7. Peake, D. J. and Tobak, M., "Three-Dimensional Interactions and Vortical Flows with Emphasis on High Speeds," NASA TM 81169, March 1980.
8. Delery, J. M. and Marvin, J. G., "Shock-Wave Boundary-Layer Interactions," AGARDograph No. 280, Feb. 1986.
9. Stollery, J. L., "Glancing Shock-Boundary Layer Interactions," AGARD - FDP - VKI Special Course on Three-Dimensional Supersonic and Hypersonic Flows Including Separation, May 1989.
10. Settles, G. S., and Dodson, L. J., "Hypersonic Shock/Boundary-Layer Interaction Database," NASA CR 177577, April 1991.
11. Settles, G. S., and Dodson, L. J., "Hypersonic Shock/Boundary-Layer Interaction Database," AIAA Paper 91-1763, to be published in *AIAA Journal*.



12. Tobak, M., and Peake, D. J., "Topology of Three-Dimensional Separated Flows," *Ann. Rev. Fluid Mech.*, Vol. 14, 1982, pp. 61-85.
13. Law, C. H., "Three-Dimensional Shock Wave Turbulent Boundary Layer Interactions at Mach 6," ARL-TR-75-0191, June 1975.
14. Korkegi, R. H., "On the Structure of Three-Dimensional Shock-Induced Separated Flow Regions," *AIAA Journal*, Vol. 14, May 1976, pp. 597-600.
15. Zheltovodov, A. A., "Properties of Two- and Three-Dimensional Flows at Supersonic Velocities," *Izvestiya Akademii Nauk SSSR, Mekhanika Zhidkosti i Gaza*, Vol. 14, May-June 1979, pp. 42-50.
16. Zubin, M. A., and Ostapenko, N. A., "Structure of the Flow in the Separation Region Resulting from Interaction of a Normal Shock Wave with a Boundary Layer in a Corner," *Izvestiya AN SSSR, Mekhanika Zhidkosti i Gaza*, Vol. 14, May-June 1979, pp. 51-58.
17. Dolling, D. S. and Bogdonoff, S. M., "Upstream Influence in Sharp Fin-Induced Shock Wave Turbulent Boundary-Layer Interaction," *AIAA Journal*, Vol. 21, No. 1, Jan. 1983, pp. 143-145.
18. Zheltovodov, A. A., "Regimes and Properties Three-Dimensional Separated Flows Initiated by Oblique Shock Waves," *Zhurnal Prikladnoi Mekhanika i Tekhnicheskoi Fiziki*, May-June 1982, pp. 116-123.
19. Goodwin, S. P., "An Exploratory Investigation of Sharp Fin-Induced Shock Wave-Turbulent Boundary-Layer Interactions at High Shock Strengths," MSE Thesis, Mechanical and Aerospace Engineering Department Report No. 1687-T, Princeton University, Princeton NJ, November 1984.
20. Degrez, G. and Ginoux, J. J., "Surface Phenomena in a Three-Dimensional Skewed Shock Wave/Laminar Boundary-Layer Interaction," *AIAA Journal*, Vol. 22, Dec. 1984, pp. 1764-1769.
21. Settles, G. S. and Lu, F. K., "Conical Similarity of Shock/Boundary-Layer Interactions generated by Swept and Unswept Fins," *AIAA Journal*, Vol. 23, No. 7, July 1985, pp. 1021-1027.
22. Dolling, D. S., "Upstream Influence in Conically Symmetric Flow," *AIAA Journal*, Vol. 23, June 1985, pp. 967-969.
23. Knight, D. D., Horstman, C. C., Bogdonoff, S. M. and Shapey, B. L., "Structure of Supersonic Turbulent Flow Past a Sharp Fin," *AIAA Journal*, Vol. 25, 1987, pp. 1331-1337.
24. Alvi, F. S. and Settles, G. S., "Structure of Swept Shock Wave/Boundary-Layer Interactions Using Conical Shadowgraphy," AIAA Paper 90-1644, June, 1990.
25. Hsu, J. C. and Settles, G. S., "Holographic Flowfield Density Measurements in Swept Shock Wave/Turbulent Boundary-Layer Interactions," AIAA Paper 92-0746, Jan. 1992.
26. Zheltovodov, A. A., Maksimov, A. I. and Shilein, E. K., "Development of Turbulent Separated Flows In The Vicinity of Swept Shock Waves," *The Interactions of Complex 3-D Flows*, edited by A. M. Kharitonov, USSR Academy of Sciences, Inst. Theoretical and Applied Mechanics, Novosibirsk, 1987, pp. 67-91.
27. Lu, F. K., "Fin Generated Shock-Wave Boundary-Layer Interactions," Ph.D. Thesis, Mechanical Engineering Dept., Pennsylvania State University, 1988.
28. Knight, D. D., Badekas, D., Horstman, C. C. and Settles, G. S., "Quasiconical Flowfield Structure of the Three-Dimensional Single Fin Interaction," *AIAA Journal*, Vol. 30, Dec. 1992, pp. 2809-2816.
29. Busemann, A., "Infinitesimale kegelige Überschallströmung," *Jahrbuch Luftfahrtforschung*, Vol. 7B, 1943, pp. 105-122.
30. Lighthill, M. J., "The Shock Strength in Supersonic Conical Fields," *Philosophical Magazine*, Vol. 40, Series 7, 1949, pp. 1202-1223.
31. Inger, G. R., "Spanwise Propagation of Upstream Influence in Conical Swept Shock Boundary-Layer Interactions," *AIAA Journal*, Vol. 25, February 1987, pp. 287-293.
32. T. R. Bewley, private communication, July, 1990.
33. Smith, J. H. B., "Remarks on the Structure of Conical Flow," *Progress in Aerospace Sciences*, Vol. 12, ed. D. Kuchemann, Pergamon Press, 1972, pp. 241-272.
34. Lu, F. K., Settles, G. S. and Horstman, C. C., "Mach Number Effects on Conical Surface Features of Swept Shock Boundary/Layer Interactions," *AIAA Journal*, Vol. 28, Jan. 1990, pp. 91-97.
35. Stalker, R. J., "A Characteristics Approach to Swept Shock Wave Boundary Layer Interactions," *AIAA Journal*, Vol. 22, Nov. 1984, pp. 1626-1632.
36. Stanbrook, A., "An Experimental Study of the Glancing Interaction Between a Shock Wave and a Turbulent Boundary-Layer," British A. R. C. CP No 555, July 1960.
37. Degrez, G., and Settles, G. S., "A Reexamination of the Concept of 3-D Separation in Swept Shock Wave/Boundary Layer Interactions," (in press).
38. McCabe, A., "The Three-Dimensional Interaction of a Shock Wave with a Turbulent Boundary-Layer," *The Aeronautical Quarterly*, Vol. 17, Aug. 1966, pp. 231-252.
39. Korkegi, R. H., "A Simple Correlation for Incipient Turbulent Boundary-layer Separation Due to Skewed Shock Wave," *AIAA Journal*, Vol. 11, No. 11, Nov. 1973, pp. 1578-1579.



40. Korkegi, R. H., "Comparison of Shock Induced Two- and Three-Dimensional Incipient Turbulent Separation," *AIAA Journal*, Vol. 13, April 1975, pp. 534-535.
41. Lu, F. K., "Semi-Empirical Extension of McCabe's Vorticity Model for Fin-Generated Shock-Wave Boundary-Layer Interactions," presented at the 4th Asian Congress of Fluid Mechanics, Hong Kong, Aug. 21-25, 1989.
42. Kubota, H. and Stollery, J. L., "An Experimental Study of the Interaction Between a Glancing Shock Wave and a Turbulent Boundary Layer," *J. Fluid Mech.*, Vol. 116, Pt. 1, 1982, pp. 431-458.
43. Zheltovodov, A. A., Maksimov, A. I., Shilein, E. K., Dvorak, R., and Safarik, P., "Development of Two-Dimensional Analogies Conformably to Three-Dimensional Separated Flows," in *Separated Flows and Jets*, ed. V.V. Kozlov and A. V. Dovgal, IUTAM Symposium, Novosibirsk, USSR, July, 1990, Springer-Verlag, Berlin, 1991 pp. 365-368.
44. Chapman, D. R., Kuehn, D. M., and Larson, H. K., "Investigation of Separated Flows in Supersonic and Subsonic Streams with Emphasis on the Effect of Transition," NACA TN 3869, March 1957.
45. Settles, G. S., Perkins, J. J. and Bogdonoff, S. M., "Upstream Influence Scaling of 2D and 3D Shock/Turbulent Boundary Layer Interactions at Compression Corners," AIAA Paper 81-0334, 1981.
46. Settles, G. S. and Bogdonoff, S. M., "Scaling of Two- and Three-Dimensional Shock/Turbulent Boundary Layer Interactions at Compression Corners," *AIAA Journal*, Vol. 20, June 1982, pp. 782-789.
47. Alvi, F. S., and Settles, G. S., "Physical Model of the Swept Shock Wave/ Boundary-Layer Interaction Flowfield," *AIAA Journal*, Vol. 30, Sept. 1992, pp. 2252-2258.
48. Zheltovodov, A. A., private communication, May 1989.
49. Kim, K.-S., and Settles, G. S., "Skin Friction Measurements by Laser Interferometry in Swept Shock/Turbulent Boundary-Layer Interactions," *AIAA Journal*, Vol. 28, Jan. 1990, pp. 133-139.
50. Kim, K.-S., Lee, Y., Alvi, F. S., Settles, G. S., and Horstman, C. C., "Skin-Friction Measurements and Computational Comparison of Swept Shock/Boundary-Layer Interactions," *AIAA J.*, Vol. 29, No. 10, Oct. 1991, pp. 1643-1650.
51. Schmisser, J. D., "An Experimental Study of Fluctuating Wall Pressures in a Highly Swept, Sharp Fin-Induced, Mach 5 Shock Wave/Turbulent Boundary Layer Interaction," M.S.E. Thesis, Aerospace Engineering and Engineering Mechanics Dept., University of Texas at Austin, May 1992.
52. Hayes, J. R., "Prediction Techniques for the Characteristics of Fin-Generated Three Dimensional Shock Wave Turbulent Boundary Layer Interactions," USAF AFFDL-TR-77-10, May 1977.
53. Scuderi, L.F., "Expressions for Predicting 3-D Shock Wave-Turbulent Boundary Layer Interaction Pressures and Heating Rates," AIAA Paper 78-162, 1978.
54. Lu, F. K., "The Peak Surface Pressure in Fin-Generated Shock-Wave Boundary-Layer Interactions," presented at the 17th Symp. on Shock Waves and Shock Tubes, Bethlehem, PA, July 17-21, 1989.
55. Zheltovodov, A. A., and Shilein, E. K., "3-D Interactions of Swept Shock Waves with Turbulent Boundary Layers in Corner Configurations," Preprint No. 34-86, Inst. of Theoretical and Applied Mechanics, USSR Academy of Sciences, Novosibirsk, 1986.
56. Neumann, R. D. and Hayes, J. R., "Introduction to Aerodynamic Heating Analysis of Supersonic Missiles," in *AIAA Progress in Astronautics and Aeronautics: Tactical Missile Aerodynamics*, Vol. 104, AIAA, New York, Sept. 1986, pp. 421-479.
57. Lee, Y., Settles G. S., and Horstman, C. C., "Heat Transfer Measurements and CFD Comparison of Swept Shock Wave/Boundary-Layer Interactions," AIAA Paper 92-3665, July, 1992, submitted to *AIAA Journal*.
58. Rodi, P. E., and Dolling, D. S., "An Experimental/Computational Study of Sharp Fin Induced Shock Wave/Turbulent Boundary Layer Interactions at Mach 5: Experimental Results," AIAA Paper 92-0749, Jan. 1992.
59. Lee, Y., "Heat Transfer Measurements in Swept Shock Wave/Turbulent Boundary-Layer Interactions," Ph.D. Dissertation, Mechanical Engineering Dept., Penn State University, June 1992.
60. Kussoy, M. I., and Horstman, K. C., "Documentation of Two- and Three-Dimensional Shock-Wave-/Turbulent-Boundary-Layer Interaction Flows at Mach 8.2," NASA TM 103838, May 1991.
61. Kussoy, M. I., Kim, K.-S., and Horstman, K. C., "An Experimental Study of a Three-Dimensional Shock-Wave-/Turbulent-Boundary-Layer Interaction Flows at a hypersonic Mach Number," AIAA Paper 91-1761, June 1991.
62. Garrison, T. J., unpublished work, Nov. 1992.
63. Dolling, D. S., Cosad, C. D., Bogdonoff, S. M. and Vas, I.E., "A Three-Dimensional Study of Fin-Induced Shock Wave Turbulent Boundary Layer Interaction, Army Research Office Report ARO-14026, 1977.
64. Knight, D. D., private communication, January 1987.



65. Hayes, W. D., "Linearized Supersonic Flow," Ph.D. Thesis, Calif. Inst. of Technology, 1947.
66. Oskam, B., Vas, I. E. and Bogdonoff, S. M., "Mach 3 Oblique Shock Wave/Turbulent Boundary Layer Interactions in Three Dimensions," AIAA Paper 76-336, 1976.
67. Token, K. H., "Heat Transfer Due To Shock Wave Turbulent Boundary Layer Interactions On High Speed Weapon Systems," AFFDL-TR-74-77, 1974.
68. McClure, W. B., "An Experimental Study into the Scaling of the Interaction of an Unswept Sharp Fin-Generated Shock/Turbulent Boundary Layer Interaction," M.S.E. Thesis, MAE Dept., Princeton University, January 1983.
69. Lu, F. K., and Settles, G. S., "Upstream-Influence Scaling of Sharp Fin Interactions," *AIAA Journal*, Vol. 29, July 1991, pp. 1180-1181.
70. Inger, G. R., "The Role of Law of the Wall/Wake Modeling in Validating Shock-Boundary Layer Interactions," AIAA Paper 88-3580, July 1988.
71. Lu, F. K., and Settles, G. S., "Inception Length to a Fully-Developed Fin-Generated Shock Wave Boundary-Layer Interaction," *AIAA Journal*, Vol. 29, May 1991, pp. 758-762.
72. Morkovin, M. V., "Effects of Compressibility on Turbulent Flows," *The Mechanics of Turbulence*, Gordon & Breach Sci. Pub., 1964, pp. 367-380.
73. Morkovin, M. V., "Mach Number Effects on Free and Wall Turbulent Structures in Light of Instability Flow Interactions," *J. L. Lumley 60th Festschrift*, Springer-Verlag, 1991, pp. 1-16.
74. Stollery, J. L., Fomison, N. R., and Hussain, S., "The Effects of Sweep and Bluntness on Glancing Interactions at Supersonic Speeds," *Proc. 5th ICAS Symposium*, London, Sept. 7-12, 1986, pp. 172-182.
75. Zubin, M. A., and Ostapenko, N. A., "Experimental Study of the Structure of Three-Dimensional Supersonic Flows with Separation of the Boundary Layer in Corners," in *Jets and Separated Flows. Transactions of Moscow University*, 1979, pp. 14-42.
76. Hsu, J. C. and Settles, G. S., "Measurements of Swept Shock Wave/Turbulent Boundary-Layer Interactions by Holographic Interferometry," AIAA Paper 89-1849, June 1989.
77. Lu, F. K., and Settles, G. S., "Structure of Fin-Shock/Boundary Layer Interactions by Laser Light-Screen Visualization," AIAA Paper 88-3801, July 1988.
78. Edney, B., "Anomalous Heat Transfer and Pressure Distributions on Blunt Bodies at Hypersonic Speeds in the Presence of an Impinging Shock," Swedish FFA Report 115, 1968.
79. Settles, G. S., Alvi, F. S., and Hsu, J. C., "On the Shock-Bifurcation/Jet-Impingement Structure of Swept Interactions and Related Flowfields," in *Separated Flows and Jets*, ed. V.V. Kozlov and A. V. Dovgal, IUTAM Symposium, Novosibirsk, USSR, July, 1990, Springer-Verlag, Berlin, 1991, pp. 255-262.
80. Garg, S. and Settles, G. S., "An Experimental Investigation of Fluctuating Pressure Loads Beneath Swept Shock Wave/Boundary-Layer Interactions," AIAA Paper 93-0384, Jan. 1993.
81. Zheltovodov, A. A., Borisov, A. V., Knight, D. D., Horstman, C. C., and Settles, G. S., "The Possibilities of Numerical Simulation of Shock Waves/Boundary layer Interaction in Supersonic and Hypersonic Flows," *Proc. Intl. Conf. on the Methods of Aerophysical Research*, Inst. of Theoretical and Applied Mechanics, Russian Academy of Sciences, Siberian Div., Novosibirsk, Russia, August 31- Sept. 4, 1992, pp. 164-170.
82. Alvi, F. S., "An Experimental Study of Swept Shock Wave/Turbulent Boundary-Layer Interactions," Ph.D. Thesis, Mechanical Engineering Dept., Penn State University, 1992.
83. Chapman, D.R., Kuehn, D.M. and Larson, H.K., "Investigation of Separated Flows in Supersonic and Subsonic Streams with Emphasis on the Effect of Transition," NACA Rept. 1356, 1958.
84. Settles, G. S. and Kimmel, R. L., "Similarity of Quasiconical Shock Wave/Turbulent Boundary-Layer Interactions," *AIAA Journal*, Vol. 24, No. 1, Jan. 1986, pp. 47-53.
85. Pope, A. Y., and Goin, K. L., *High-Speed Wind Tunnel Testing*, Krieger Pub. Co., Huntington, NY, 1978.
86. Maltby, R. L., ed., AGARDograph 70, "Flow Visualization in Wind Tunnels Using Indicators," April 1962.
87. Merzkirch, W., *Flow Visualization*, 2nd Ed., Academic Press, Orlando, 1987.
88. Settles, G. S. and Teng, H-Y., "Flow Visualization Methods for Separated Three-Dimensional Shock Wave/Boundary-Layer Interactions," *AIAA Journal*, Vol. 21, March 1983, pp. 390-397.
89. Settles, G. S., "Modern Developments in Flow Visualization," *AIAA Journal*, Vol. 24, No. 8, August, 1986, pp. 1313-1323.
90. Settles, G. S., Metwally, O. M., Hsu, J. C., and Lu, F. K., "Visualization of High-Speed Flows at the Penn State Gas Dynamics Laboratory," *Proc. 1988 International Conference on Applications of Lasers and Electro-Optics*, Santa Clara, Oct. 30, 1988, Laser Inst. of America Vol. 67, pp. 95-101.
91. Lu, F. K., and Settles, G. S., "Color Surface-Flow Visualization of Fin-Generated Shock-Wave Boundary-Layer Interactions," *Experiments in Fluids*, March 1990, Vol 8, No. 6, pp 352-354.



92. Love, E. S., and Grigsby, C. E., "A New Shadowgraph Technique for the Observation of Conical Flow Phenomena in Supersonic Flow and Preliminary Results Obtained for a Triangular Wing," NACA TN 2950, 1953.
93. Pierce, D., and Treadgold, D., "Some Examples of the Use of a Conical Shadowgraph Technique," British ARC CP-763, 1964.
94. Alekseev, V. N., and Gonor, A. L., "Optical Investigation of Three-Dimensional Supersonic Flow," *Fluid Dynamics*, Vol. 9, Jan.-Feb. 1974, pp. 148-152.
95. Schmidt, M. C., and Settles, G. S., "Alignment and Application of the Conical Shadowgraph Flow Visualization Technique," *Experiments in Fluids*, Vol. 4, 1986, pp. 93-96.
96. Alvi, F. S. and Settles, G. S., "Swept Shock Wave/Boundary-Layer Interaction Structure Using Conical Shadowgraphy and Planar Laser Scattering," 20-minute color VHS videotape, Penn State Gas Dynamics Laboratory, 1991.
97. Vest, C. M., *Holographic Interferometry*, Wiley, New York, 1979.
98. McGregor, I., "Development of the Vapour Screen Method of Flow Visualization in a 3ft x 3ft Supersonic Tunnel," in AGARDograph 70, "Flow Visualization in Wind Tunnels Using Indicators," ed. R. L. Maltby, April 1962.
99. Snow, W. L., and Morris, O. A., "Investigation of Light Source and Scattering Medium Related to Vapor-Screen Flow Visualization in a Supersonic Wind Tunnel," NASA TM 86290, 1984.
100. Naughton, J. W., and Settles, G. S., "Experiments on the Enhancement of Compressible Mixing via Streamwise Vorticity, Part I - Optical Measurements," AIAA Paper 92-3549, July 1992.
101. Wegener, P. P. and Mack, L. M., "Condensation in Supersonic and Hypersonic Wind Tunnels," *Advances in Applied Mechanics*, Vol. V, ed. H. L. Dryden and Th. von Karman, Academic Press, New York, 1958, pp. 307-447.
102. Monaghan, R. J., "Tests of Humidity Effects on Flow in a Wind Tunnel at Mach Numbers between 2.48 and 4," British A.R.C. CP No. 247, January 1955.
103. Ariessohn, P. C., Self, S. A. and Eustis, R. H., "Two-Wavelength Laser Transmissometer for Measurements of the Mean Size and Concentration of Coal Ash Droplets in Combustion Flows," *Applied Optics*, Vol. 19, No. 22, 1980, pp. 3775-3781.
104. Durbin, E. J., "Optical Methods Involving Light Scattering for Measuring Size and Concentration of Condensation Particles in Supercooled Hypersonic Flow," NACA TN 2441, 1951.
105. Clemens, N. T., Mungal, M. G., "A Planar Mie Scattering Technique for Visualizing Supersonic Mixing Flows," *Experiments in Fluids*, Vol. 11, 1991, pp. 175-185.
106. Bohren, C. F., "On the Size, Shape, and Orientation of Noctilucent Cloud Particles," *Tellus*, Vol. 35B, 1983, pp. 65-72.
107. Bohren, C. F., private communication, Aug. 1990.
108. Bohren, C. F. and Huffman, D. R., *Absorption and Scattering of Light by Small Particles*, John Wiley and Sons, New York, 1983.
109. Winter, K. G., "An Outline of the Techniques Available for the Measurement of Skin Friction in Turbulent Boundary Layers," *Progress in the Aerospace Sciences*, Vol. 18, 1977, pp. 1-57.
110. Settles, G. S., "Recent Skin Friction Techniques for Compressible Flows," AIAA Paper 86-1099, May 1986.
111. Tanner, L. H., and Blows, L. G., "A Study of the Motion of Oil Films on Surfaces in Air Flow, with Application to the Measurement of Skin Friction," *Journal of Physics E. Scientific Instruments*, Vol. 9, March 1976, pp. 194-202.
112. Tanner, L. H., "The Application of Fizeau Interferometry of Oil Films to the Study of Surface Flow Phenomena," *Optics and Lasers in Engineering*, Vol. 2, 1981, pp. 105-118.
113. Monson, D. J., and Higuchi, H., "Skin Friction Measurements by a Dual-Laser-Beam Interferometer Technique," *AIAA Journal*, Vol. 19, June 1981, pp. 739-744.
114. Monson, D. J., Driver, D. M., and Szodruch, J., "Application of a Laser Interferometer Skin-Friction Meter in Complex Flows," *Proc. Intl. Congress on Instrumentation in Aerospace Simulation Facilities*, Sept. 1981, pp. 232-243 (IEEE Publication 81CH1712-9).
115. Monson, D. J., "A Nonintrusive Laser Interferometer Method for Measurement of Skin Friction," *Experiments in Fluids*, Vol. 1, 1983, pp. 15-22.
116. Monson, D. J., "A Laser Interferometer for Measuring Skin Friction in Three-Dimensional Flows," *AIAA Journal*, Vol. 22, April 1984, pp. 557-559.
117. Westphal, R. V., Bachalo, W. D., and Houser, M. H., "Improved Skin Friction Interferometer," NASA TM 88216, March 1986.
118. Kim, K.-S., and Settles, G. S., "Skin Friction Measurements by Laser Interferometry," in *A Survey of Measurements and Measurement Techniques in Rapidly Distorted Compressible Turbulent Boundary Layers*, eds. Fernholz, H. H., Smits, A. J., and Dussauge, J. P., AGARDograph 315, Nov. 1988, Ch. 3.
119. Bandyopadhyay, P. R., and Weinstein, L. M., "A Reflection-Type Oil-Film Skin-Friction Meter," *Experiments in Fluids*, Vol. 11, 1991, pp. 281-292.
120. Kornilov, V. I., Pavlov, A. A., and Shpak, S. I., "On the Techniques of Skin Friction Measurement Using Optical Methods," *Proc. Intl. Conf. on the Methods of Aerophysical*



- Research, Inst. Theor. and Appl. Mechanics, Russian Academy of Sciences, Novosibirsk, 1992, pp. 71-74.*
121. Seto, J. and Hornung, H., "Two-Directional Skin Friction Measurement Utilizing a Compact Internally-Mounted Thin-Liquid-Film Skin Friction Interferometer," AIAA Paper 93-0180, Jan. 1993.
  122. Garrison, T. J., and Settles, G. S., "Improved Methods for Skin Friction Measurements in Compressible Flows by Laser Interferometry," to be submitted for publication in 1993.
  123. Kim, K.-S., "Skin Friction Measurements by Laser Interferometry in Supersonic Flows," Ph.D. Thesis, Mechanical Engineering Dept., Penn State University, May 1989.
  124. Murphy, J. D., and Westphal, R. V., "The Laser-Interferometer Skin-Friction Meter--A Numerical and Experimental Study," *Proc. Third Symposium on Numerical and Physical Aspects of Aerodynamic Flows*, Long Beach, CA, Jan. 1985, Paper 7-1.
  125. Monson, D. J., "Rederivation of Variable Viscosity Oil-Flow Skin Friction Equations," private communication, August 1984.
  126. Kim, K.-S., Lee, Y., and Settles, G. S., "Laser Interferometer/Preston Tube Skin-Friction Comparison in Shock Boundary-Layer Interaction," *AIAA Journal*, Vol. 29, June 1991, pp. 1007-1008.
  127. Allen, J. M., "Reevaluation of Compressible-Flow Preston Tube Calibrations," NASA TM X-3488, Feb. 1977.
  128. Keener, E. R. and Hopkins, E. J., "Use of Preston Tubes for Measuring Hypersonic Turbulent Skin Friction," NASA TN D-5544, Nov. 1969.
  129. Schultz, D. J., and Jones, T. V., "Heat Transfer Measurements in Short-Duration Hypersonic Facilities," AGARD-AG-165, Feb. 1973.
  130. Moody, H. L., and Jechel, K., "Heat Transfer Measurements in Cold Wind Tunnels," AFWAL-TR-81-3176, Sept. 1982.
  131. Neumann, R. D., "Aerothermodynamic Instrumentation," AGARD publication in press.
  132. Thompson, W. P., "Heat Transfer Gages," *Methods of Experimental Physics: Fluid Dynamics*, Vol. 18B, Academic Press, 1981, pp. 663-685.
  133. Epstein, A. H., Guenette, G. R., Norton, R. J. G., and Yuzhang, C., "High-Frequency Response Heat-Flux Gage," *Rev. Sci. Instrum.*, Vol. 57, No. 4, April 1986.
  134. Hayashi, M., Sakurai, A., and Aso, S., "Measurements of Heat-Transfer Coefficients in the Interaction Regions between Oblique Shock Waves and Turbulent Boundary Layers with a Multi-Layered Thin Film Heat Transfer Gage," *Trans. Japan Society Aero. Space Sci.*, Vol. 30, No. 88, Aug. 1987.
  135. Johnson, C. B., Carraway, D. L., Hopson, P., Jr., and Tran, S. Q., "Status of a Specialized Boundary Layer Transition Detection System for Use in the U.S. National Transonic Facility," ICIASF 1987 Record, pp. 141-155.
  136. Simonich, J. C., and Moffat, R. J., "New Technique for Mapping Heat-Transfer Coefficient Contours," *Rev. Sci. Instrum.*, Vol. 53, No. 5, 1982, pp. 678-683.
  137. Hippensteele, S. A., Russell, L. M., and Stepka, F. S., "Evaluation of a Method for Heat Transfer Measurements and Thermal Visualization Using a Composite of a Heater Element and Liquid Crystals," *Journal of Heat Transfer*, Vol. 105, 1983, pp. 184-189.
  138. Abuaf, N., Urbaetis, S. P., and Palmer, O. F., "Convection Thermography" Technical Report No. 85CRD168, General Electric Co., Sept. 1985.
  139. Eibeck, P. A., and Eaton, J. K., "An Experimental Investigation of the Heat Transfer Effects of a Longitudinal Vortex Embedded in a Turbulent Boundary Layer," Report MD-48, Thermosciences Division, Dept. of Mechanical Engineering, Stanford University, November 1985.
  140. Johnson, C. B., and Adcock, J. B., "Measurement of Recovery Temperature on an Airfoil in the Langley 0.3m Transonic Cryogenic Wind Tunnel," AIAA Paper 81-1062, June 1981.
  141. Mack, L. M., "An Experimental Investigation of the Temperature Recovery Factor," Report No. 20-80, Jet Propulsion Laboratory, California Institute of Technology, Aug. 1954.
  142. Stalder, J. R., Rubesin, M. W., Tendeland, T., "A Determination of the Laminar-, Transitional-, and Turbulent Boundary Layer Temperature Recovery Factors on a Flat Plate in Supersonic Flow," NACA TN 2077, June 1950.
  143. Coleman, H. W. and Steele W. G., *Experimentation and Uncertainty Analysis for Engineers*, John Wiley & Sons, 1989.



# Swept shock wave/laminar boundary layer interactions, experimental and numerical results

G. DEGREZ\*

von Karman Institute for Fluid Dynamics, Aerospace Department,  
Chaussée de Waterloo 72, B-1640 Rhode St-Genèse, Belgium

## 1 SUMMARY

Experimental and numerical investigations of swept shock wave / laminar boundary layer interactions are reviewed. Experimental investigations show that the flowfield is characterized by an extensive primary separation of the boundary layer upstream of the inviscid shock wave, which then rolls up into a very elongated vortex. This is often accompanied by secondary and sometimes higher order separations. Similar to turbulent interactions, the flowfield is essentially conical as far as the surface flow data are concerned (surface pressures, heat transfer and skin friction patterns). Also, the free-interaction concept introduced for turbulent interactions is shown to apply to laminar interactions as well.

Recent LDV flowfield data for a supersonic interaction are presented. They nicely confirm the vortical structure of the interaction deduced from the surface data as well as the important thickening of the viscous layer due to separation. They also show that the vertical dimension of the interaction does not obey a conical similarity rule but rather follows the classical boundary layer scaling.

Numerical investigations confirm these experimental findings. None of these has however been carried out with sufficient grid resolution so as to demonstrate grid convergence and code validity, in particular concerning the location of separation lines.

## 2 INTRODUCTION

The interaction of shock waves with boundary layers is one of the basic problems of supersonic and hypersonic aerodynamics, and has both fundamental and practical importance. From a practical standpoint, it is really ubiquitous and strongly influences the drag of airfoils and airframes in general, the efficiency of controls, the efficiency of air intakes, and the wall heat transfer to hypersonic vehicles, to name just a few. From the fundamental point of view, it represents one of the simplest occurrences of a strong viscous/inviscid interaction involving separation, and therefore an ideal test case for Navier-Stokes solvers.

For all these reasons, this problem has attracted considerable attention over the last fifty years. Initially, the focus has been on two-dimensional flow, which can now be considered to be relatively well understood, although some difficulties remain in their numerical prediction especially at hypersonic speeds [1] and also in the understanding of

the unsteadiness (see companion paper by D. Dolling) and of the turbulence behaviour (see companion papers by J. Détery and by D. Vandromme). Subsequently, interest has shifted towards three-dimensional interactions, in particular swept interactions, the simplest of those being produced by a wedge mounted normal to a flat plate (Fig. 1). The research in this area has been presented

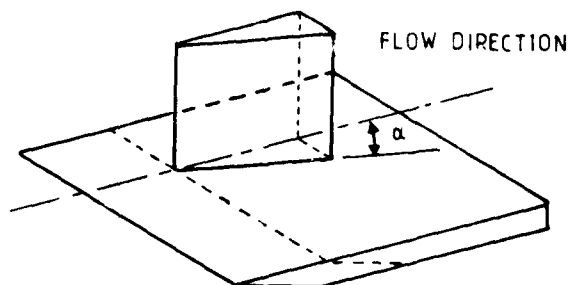


Fig. 1: Simplest swept shock wave/boundary layer interaction configuration : wedge mounted normal to a flat plate

in two major reviews by Settles and Dolling [2, 3]. Now, despite extensive research in this field, these interactions are still only partially understood and important contributions are still coming out [4, 5]. In two companion lectures, Profs G. Settles and D. Knight present the major results concerning interactions between swept shock wave and *turbulent* boundary layers from the experimental and numerical points of view, while the present paper will deal with their laminar counterpart.

Now, contrary to 2D interactions where laminar interactions are extensively documented in the supersonic as well as in the hypersonic régimes, there exist very little data about supersonic laminar interactions and only little more in the hypersonic régime. In addition, most of the hypersonic results concern symmetric corner flow configurations which have a somewhat different character. As a matter of fact, the scarcity of the data for laminar interactions was pointed out by Settles and Dodson [6] in their review of hypersonic shock wave/boundary layer interactions data sets.

In the present paper, we shall thus review the existing work on swept shock wave/laminar boundary layer interactions, including flow along axial corners, as well as some recent unpublished VKI work. From the limited amount of experimental and numerical data, the flow structure will be discussed and compared to the turbulent flow counterpart and finally areas where additional work is needed will be identified.

\*Associate Professor



### 3 FLOWFIELD CONFIGURATIONS

Swept shock wave/boundary layer interactions may exist in various flow configurations. As mentioned previously, the most simple is probably the case of the wedge mounted normal to a flat plate parallel to the flow (Fig. 1). This may be generalized by substituting the wedge by any conical shock generator, as shown in Fig. 2. Particular cases, in addition to the normal wedge, are the

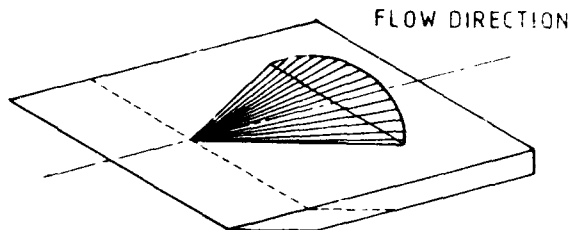
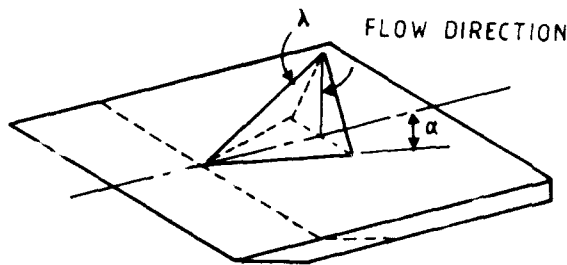
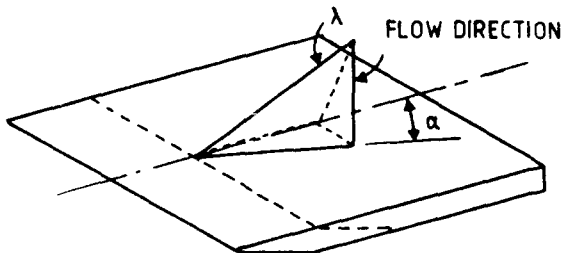


Fig. 2: Arbitrary conical shock generator

symmetric dihedron (Fig. 3a), the asymmetric dihedron (Fig. 3b) and the half circular cone (Fig. 4). For all



(a) Symmetric dihedron



(b) Asymmetric dihedron

Fig. 3: Dihedron shock generators

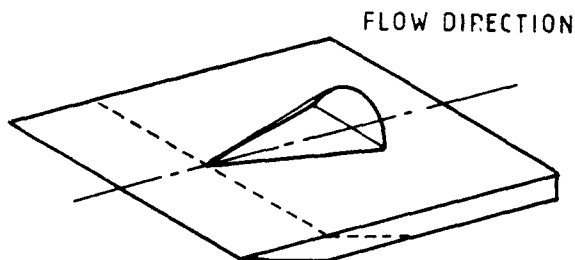


Fig. 4: Half circular cone shock generator

these configurations, there is only one inviscid shock wave

produced by the shock generator which impacts on the boundary layer developing on the flat plate, which, being parallel to the flow, does not produce a shock wave except the (weak) shock due to leading edge viscous/inviscid interaction. This class of configurations can further be subdivided into two subclasses depending on whether the shock generator apex lies at the flat plate leading edge<sup>1</sup> or downstream of it. The former case will be called an intake-type configuration, while the latter will be called a fin-type configuration. This problem is characterized by an extra parameter, i.e. the flat plate boundary layer thickness at the location of the shock generator apex or, more appropriately, the Reynolds number based on this thickness.

Another class of configurations is obtained from the intake-type configuration by setting the flat plate at incidence with or without leading edge sweepback. Such configurations have been studied exclusively with planar conical shock generators and are known in the literature as corner flows. Because the flat plate is now at incidence, it also produces an inviscid shock wave, so that the flow produced by such configurations is characterized by a shock/shock interaction in addition to shock wave/boundary layer interactions on both planar surfaces. These configurations have been mostly studied for symmetric cases, i.e. when both planar surfaces have the same incidence with respect to the flow and leading edge sweepback angle. It is clear from the previous discussion that the intake-type configuration is a particular case of an asymmetric corner flow configuration.

The characteristics of the three classes of configurations is summarized in Table 1. Although all three types of con-

Configuration	Fin-type	Intake-type	Corner
# of shock generator surfaces	1	1	2
Nature of shock generator surfaces	any	any	planar
Incoming boundary layer	Yes	No	No

Table 1: Summary of swept shock wave/boundary layer interaction configurations

figurations will be discussed, the present paper will emphasize the fin-type and intake-type configurations. Full details about the corner configurations may be found in the excellent review paper by Hummel [7].

## 4 EXPERIMENTAL RESEARCH

### 4.1 Literature survey

Initial investigations of swept shock wave/laminar boundary layer interactions were carried out by Stainback [8, 9] in the early sixties at about the same time turbulent interactions were first studied [10, 11]. Stainback considered corner configurations where both surfaces were set

<sup>1</sup> Such configurations are those of Fig. 1-4 where the flat plate leading edge is moved downstream as indicated by the hatched lines



at zero incidence with respect to the flow and performed surface pressure and heat transfer measurements at Mach 5 and 8. He observed strong increases of both parameters in the corner region with respect to flat plate data.

Charwat and Redekopp [12] in the late sixties performed extensive measurements in a few symmetrical and asymmetrical corner configurations at Mach numbers ranging from 2.5 to 4. Experimental results included surface flow visualizations, surface pressure measurements and pitot pressure surveys. The emphasis of the research was mainly to characterize the outer inviscid flow structure. Despite the presence of strong viscous effects due to shock wave/boundary layer interactions, Charwat and Redekopp found the flow structure to be conical - this behaviour should be expected for pure inviscid flow - except close to the leading edge, where the hypersonic interaction parameter was large. Upon analysis of their experimental data, they proposed the following flowfield model (Fig. 5). The individual wedge shocks interfere to

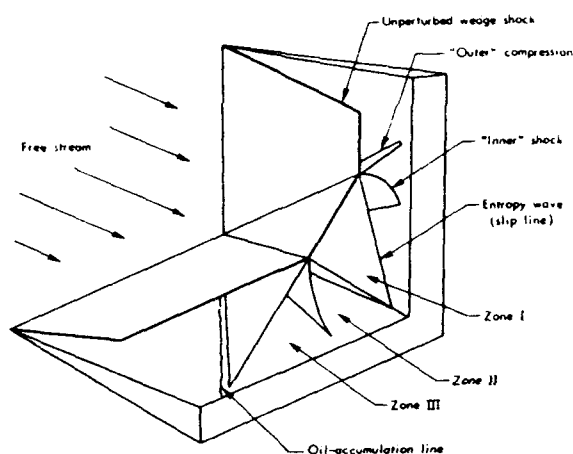


Fig. 5: Corner flow structure according to Charwat and Redekopp [12]

create a corner shock. This corner shock interacts with each unperturbed wedge shock at a so-called triple point, producing an embedded transmitted shock impinging on the wedge and a slip line running into the intersection of wedges. On each wedge, an oil-accumulation (separation) line was identified. Charwat and Redekopp include in their model an additional (separation) shock emanating from this accumulation line and running into the triple point, although it does not clearly appear in their experimental data. After discussing this feature, they conclude that it must be an essentially inviscid phenomenon.

Corresponding investigations were carried out at hypersonic speeds by Cresci et al. [13] ( $M = 11.2$ ) and by Watson and Weinstein [14] ( $M = 20$ ) on symmetrical corner configurations. The same patterns as in the supersonic investigation of Charwat and Redekopp were observed, except that, because hypersonic boundary layers are much thicker and shock waves lie much closer to the corner, there is a much larger viscous influence on the shock system location. Also, because of increased shock intensities, more extensive separations were observed.

In his 1971 survey paper, Korkegi [15] reexamined the Charwat and Redekopp results and suggested that the interference flow between the embedded transmitted shock and the oil accumulation line was due to boundary

layer separation rather than to an inviscid interaction as proposed by the original investigators.

To clarify this issue and also to find out the purely inviscid flow structure, West and Korkegi [16] studied corner flows at Mach 3 over a wide range of Reynolds numbers (from 0.4 to  $60 \cdot 10^6$ ). They observed that for turbulent interactions corresponding to Reynolds numbers larger than  $3 \cdot 10^6$ , the wave structure determined from pitot pressure surveys was virtually independent of Reynolds number, from which they concluded that it represents the purely inviscid flow structure. The correctness of this conclusion was later confirmed by the numerical studies of Kutler [17] and Marconi [18], whose inviscid results are in close agreement with the experimental data of West and Korkegi as will be shown in section 5.1. On the contrary, for a lower Reynolds number corresponding to laminar flow, displacement effects due to the extensive separation were shown to result in an outward displacement of the wave structure.

Another major finding of their study was the confirmation of Korkegi's [15] earlier suggestion that the interference flow region outboard of the embedded shock resulted from flow separation due to the interaction of the embedded shock with the boundary layer rather than from an inviscid phenomenon. This is demonstrated by the much greater extent of this region for laminar flow, which is typical of the much greater spread of separated laminar flow. It is worthwhile noting that, notwithstanding this viscous nature, the flow pattern in this region was essentially conical, whether the boundary layer was laminar or turbulent.

All previous investigations concerned corner flow configurations and most of them were symmetrical. The first investigation of an intake-type configuration (if one excepts the plate/plate configurations studied by Stainback [8, 9]) was performed by Cooper and Hankey [19] under hypersonic ( $M = 12.5$ ) flow conditions. The shock generator was an unswept 15 degree wedge. The objective of their investigation was to determine the flow structure for a case in which the dominant phenomenon is the shock wave/boundary layer interaction rather than the shock/shock interaction for corner configurations, and to identify regions of local intense heating, a very significant issue for hypersonic flows. Measurements included oil flow visualizations, surface pressure distributions and pitot pressure surveys. The results of the pitot pressure surveys revealed that the interaction of the weak shock generated by the viscous interaction at the flat plate leading edge with the strong wedge shock did not result in a wave pattern involving a corner shock with two triple points as observed earlier for symmetric corners ([12, 16] - see also Fig. 5) but rather in a pattern involving a single triple point (Fig. 6). Such a pattern was later to be observed as well by Rao in a fin-type configuration at Mach 6 (unpublished results shown in [20] - see Fig. 7). The pattern proposed by Cooper and Hankey (Fig. 6) also includes two weak ( $\xi = \text{pressure ratio} = 1.3$ ) compression waves due to the separation of the plate boundary layer which rolls up into an elongated vortex. Rao's vapour screen visualization (Fig. 7) also shows the elongated vortical structure due to the separation of the incoming boundary layer but no separation compression wave is visible. Just as for the previous studies of symmetrical corners, oil flow visualizations revealed an essentially conical flow pattern for Cooper and Hankey's intake-type configuration, including a primary and, clearly identified for the first time, a secondary separation line. Actually, a close look at Charwat and Redekopp's results allows



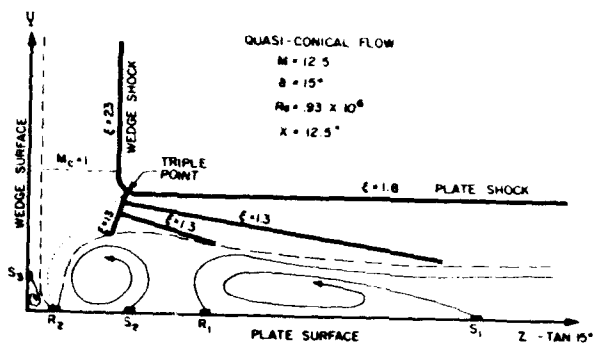


Fig. 6: Flow structure in intake-type configuration according to Cooper and Hankey [19]

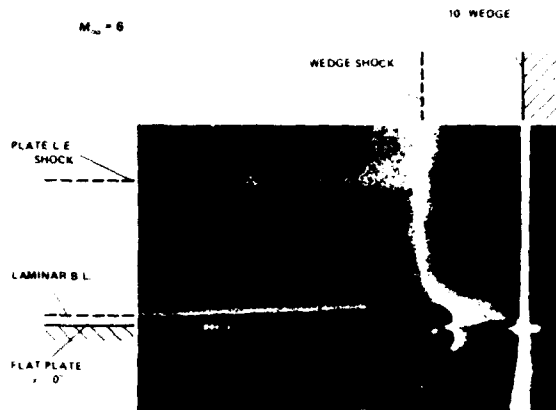


Fig. 7: Vapour screen visualization in swept shock wave/ laminar boundary layer interaction (from [20])

to identify a secondary separation in their case as well. The interpretation of the separation pattern as in Fig. 6 was however later shown to be incorrect by Korkegi [21], the correct pattern being shown in Fig 8. The high heat transfer rates encountered in such interactions [22] is then explained by the attachment process of fresh outer fluid along the reattachment line A1.

A systematic study of hypersonic corner flow configurations was then performed at the Institut für Strömungsmechanik of the Technical University of Braunschweig [23, 24, 25, 26, 7]. Experimental results included surface pressure and heat transfer measurements, oil flow visualizations and, most importantly, detailed pitot pressure surveys. The studies, mostly carried out at Mach 12.3, examined the effect of several parameters including wedge deflection, leading edge sweepback and axial corner angle (also called dihedral in [12]). The results of the flow surveys were analyzed in detail and compared with the flow structure reconstructed from a few key data and the shock wave relations. A typical example of such a comparison is shown in Fig. 9. The agreement is seen to be excellent. The identified flow pattern confirms and refines the earlier results of Charwat and Redekopp [12] and West and Korkegi [16], clearly exhibiting clearly the embedded shock (which for this hypersonic flow is oblique rather than essentially normal in the former supersonic experiments), the slip line from the triple points as well as the primary and secondary vortices due to shock-induced boundary layer separation. Worth noticing are the reflec-

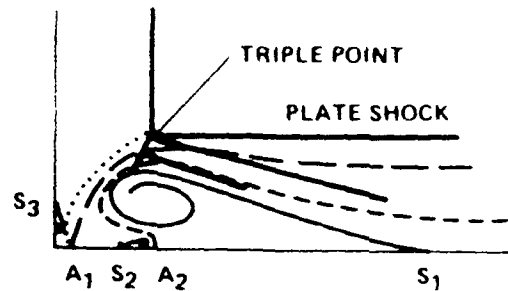


Fig. 8: Flow structure in intake-type configuration (from [20])

tion of the embedded shock on the separated shear layer as an expansion fan and also the absence of a compression shock due to separation but rather the existence of a smooth compression fan. The very high heat transfer rates around reattachment are then explained by the impact of the cross flow through the embedded shock accelerated by the reflected expansion, much like in the Edney Type IV interaction [27]. With respect to the conical character of the flow, the measurements confirm that the flow is fairly conical for values of the hypersonic parameter  $\chi = \frac{M^2 \sqrt{C}}{\sqrt{Re}}$  greater than around 3 or 4. Increasing leading edge sweepback and axial corner angles were found to reduce the shock strengths of respectively the primary or interference shocks, thereby reducing pressure and heat transfer peaks.

Although the fin-type configuration had been extensively studied in the turbulent régime for many years (see for instance the review papers of Settles and Dolling [2, 3]) - actually it is the most studied swept shock wave/boundary layer interaction in the turbulent régime this configuration had not been studied in the laminar régime before the experimental and numerical investigations by Degrez [28, 29, 30]. The shock generator was a wedge mounted normal to a flat plate (Fig. 1). Experimental results included surface flow visualizations and surface pressure distributions for a relatively limited test matrix of wedge incidence angles ( $4^\circ \leq \alpha \leq 8^\circ$ ) and  $Re_\delta$  at the shock generator apex. Flow visualizations revealed the presence of an extended separation even for the smallest wedge incidence (and therefore the weakest shock), in contrast with turbulent flow, for which the incipient separation wedge incidence would be around  $10^\circ$  for the current value of Mach number (2.25), according to a criterion due to Korkegi [31]. The separation line determined by the oil flow visualizations was straight near the shock generator apex, indicating a conical pattern but bent downstream. Whether this was a genuine phenomenon, an edge effect or an artefact of the experimental technique was not determined. Also, because only the flow upstream of the primary separation line was visualized, nothing could be said about the existence of a secondary separation. Pressure distributions exhibited a characteristic mild pressure rise upstream of the inviscid shock followed by a steep increase slightly downstream of the shock, a peak near reattachment and a smooth relaxation towards the inviscid post-shock level, very much like the distributions obtained by Charwat and Redekopp [12] for their corner configuration. The pressure rise upstream of the inviscid shock wave was found to be essentially independent of shock wave strength and the pressure distributions agreed reasonably well with a conical scaling.



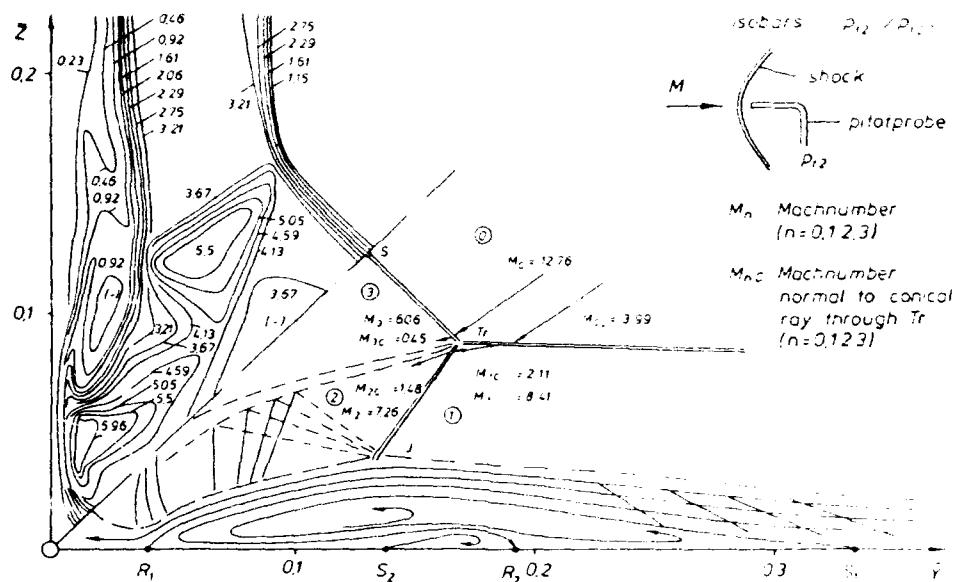






Fig. 11: Half circular cone model

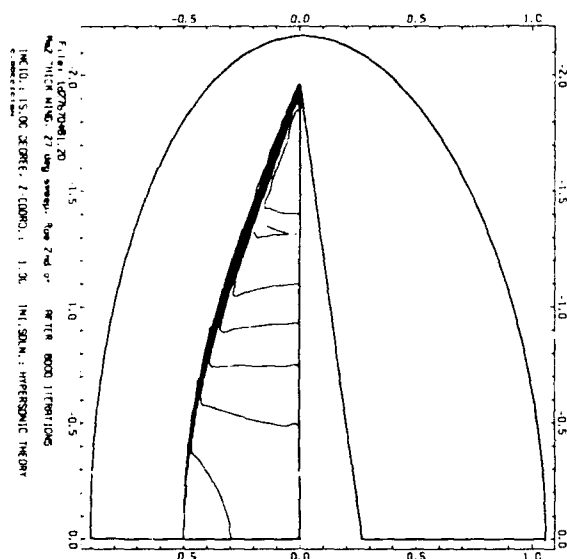


Fig. 12: Inviscid flow over asymmetric dihedral : pressure contours in crossflow plane

The hypersonic shock generators were unswept wedges with incidence angles  $\alpha = 3, 6, 9, 12$  and  $15^\circ$ , as well as an asymmetric dihedral with  $\alpha = 15^\circ$ ,  $\lambda = 80.5^\circ$ . Just as for the supersonic experiment, the leading edge sweep-back was chosen in such a way that the resulting shock wave impacts the flat plate at the same location as that produced by the  $12^\circ$  unswept wedge.

#### 4.2.2 Surface flow visualization (skin friction patterns)

##### Supersonic flow

Surface flow visualizations were carried out only for the unswept wedge shock generators and for only one Reynolds number, since this parameter did not prove to have a significant effect in previous studies. In all cases, a primary separation line (oil convergence line) clearly appeared as well as a herringbone pattern associated with primary attachment. Fig. 13 shows for instance the flow visualization obtained for the  $9^\circ$  wedge. To demonstrate without ambiguity that the oil convergence line is indeed a separation line, a second visualization in which only the fore part of the model was covered with oil was performed. One observes that the oil runs only up to the

Fig. 13: Surface flow visualization,  $M = 2$ , unswept shock generator,  $\alpha = 9^\circ$ 

separation line, with the aft part of the model remaining clean, inaccessible by the oil flow from upstream. Another interesting observation from Figs. 13-14 is that the primary separation line is essentially straight, suggesting a conical behaviour as observed in former studies [19]. Coming back to Fig. 13, one observes also a region of sluggish oil flow immediately downstream of the primary separation line. The extent of such a region of sluggish fluid is seen to increase as the wedge incidence is increased (see Fig. 15). This suggests that this region may be associated with the existence of a secondary separation. To provide some support to this hypothesis, the same kind of technique used in Fig. 14 was applied. Specifically, oil was introduced only near the flat plate leading edge and near the primary attachment line. The resulting pattern (Fig. 16) shows the existence of a clean region between the two regions covered with oil, which nicely confirms the existence of secondary separation. Secondary separation was observed for  $\alpha = 9, 12$  and  $15^\circ$ .

As the flow visualization features appeared mostly conical, their angle was determined. Because of the qualitative character of the visualization technique and of the photographic recording, the uncertainty on the angle values was estimated to be  $\pm 2$  degrees. Angles of the upstream influence line, defined as the line where the skin friction lines first deviate from the free stream direction, and of the primary and secondary separation lines with respect to the free stream Mach line are displayed in Fig. 17 as a function of the shock wave intensity as represented by the normal Mach number  $M_n = M_\infty \sin \beta_0$ . It is seen that the upstream influence line angle increases slowly with shock strength whereas the separation line angle first increases rapidly, until it gets close to the upstream influence line angle, after which it follows the evolution of the upstream influence line angle.

##### Hypersonic flow

Surface flow visualizations exhibited the same qualitative features as for supersonic flow: the patterns were conical and an extensive primary separation was observed in





Fig. 14: Surface flow visualization,  $M = 2$ , evidence of primary separation

all cases. Because of the higher Mach number, angles of all characteristic lines (upstream influence, separations, attachments) are of course considerably smaller than for their supersonic counterparts. Secondary separation is observed already for the weakest shock, as demonstrated in Fig. 18 which shows the existence of a clean region downstream of the primary separation line. As the wedge angle is increased, additional features are observed. For  $\alpha = 6^\circ$  (Fig. 19), one distinguishes three dark lines originating from the wedge apex. The most upstream one is the primary separation line, the most downstream one is the secondary separation line, but the nature of the third line is not clear from the oil flow visualization. A mixed oil flow/oil dot visualization (Fig. 20) allows to identify it as a tertiary separation line. Although this may not appear obvious from the figure, it becomes much clearer for stronger interactions such as that produced by the unswept  $12^\circ$  wedge as shown in Fig. 21 which compares oil flow and oil dot flow visualizations for this case. It is believed that this is the first time a tertiary separation has been observed in a swept shock wave/boundary layer interaction, although tertiary separations have been observed in other circumstances as for instance flows over cones at angle of attack [20]. Actually, looking attentively at Fig. 21a, one can identify a fourth dark line between the tertiary and secondary separation lines suggesting the presence of a quaternary separation, although it is not clearly distinguishable from Fig. 21b. Additional support to this hypothesis is given by heat transfer measurements performed by Papuccuoglu [38] in the same configuration for  $\alpha = 9^\circ$ . Fig. 22 shows the heat transfer coefficient (Stanton number) distribution on a line perpendicular to the freestream at 7.5 cm from the wedge apex. One observes four peaks which can be attributed to 4 attachment lines. As a matter of fact, their location is seen to correspond fairly well with the location of attachment lines as determined from surface flow visualizations (Table 2). It should be mentioned however that the innermost heat transfer peak can also be explained by the presence of a corner vortex, as proposed



Fig. 15: Surface flow visualization,  $M = 2$ , unswept shock generator,  $\alpha = 15^\circ$

Attachment lines		Peak heat transfer
Order	angle	angle
A1	$13.5^\circ$	$11.3^\circ$
A3	$17.5^\circ$	$14.9^\circ$
A4	$19.9^\circ$	$19.5^\circ$
A2	$25.1^\circ$	$23.1^\circ$

Table 2: Comparison of attachment line angles and peak heat transfer angles

by Hummel [7]. In summary, primary and secondary separation lines were observed for all wedges, tertiary separation appeared for  $\alpha = 6^\circ$  and quaternary separation for  $\alpha = 9^\circ$ . The evolution of upstream influence, primary and secondary separation line angles with shock strength is shown in Fig. 23. It is seen to exhibit the same trends as observed in Fig. 17 for supersonic flow. Finally, the surface flow visualizations performed for the asymmetric dihedral shock generator are displayed in Fig. 24. The upstream influence, primary and secondary separation, as well as primary reattachment line angles are observed to be very close to those observed for the unswept  $12^\circ$  wedge. This point will be further discussed in section 4.2.4.

#### 4.2.3 Surface pressure measurements

##### Supersonic flow

Surface pressure measurements were obtained for the unswept shock generator at 6, 9 and 12 degrees, for the swept asymmetric dihedral and for the half circular cone





Fig. 16: Surface flow visualization,  $M = 2$ , evidence of secondary separation

configurations. Tunnel blockage problems prevented to make the pressure measurements with the unswept shock generator at 15 degrees incidence. The model was instrumented with three rows of pressure taps perpendicular to the free stream direction at respectively 5 cm, 10 cm and 15 cm from the flat plate leading edge.

Fig. 25 shows the pressure distributions on the three rows for the unswept wedge at 9° incidence. The pressures non-dimensionalized by the freestream static pressure are plotted as a function of the reduced coordinate  $y/x$  where  $y$  is the transverse coordinate and  $x$  the distance of the row from the leading edge. Although all three distributions are relatively close in this conical coordinate system, the differences are too large to be attributed solely to experimental scatter. As a matter of fact, a general trend is observed, especially for the part of the interaction out-

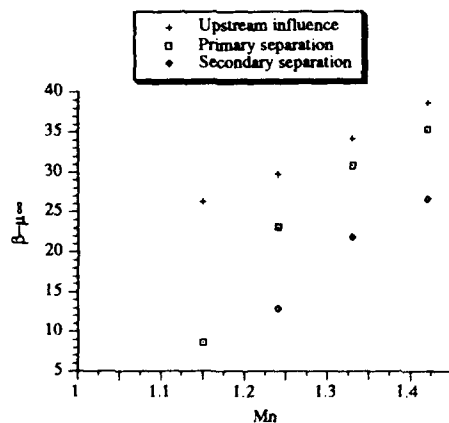


Fig. 17: Separation line angles as a function of shock strength (Mach 2)



Fig. 18: Surface flow visualization,  $M = 6$ , unswept shock generator,  $\alpha = 3^\circ$

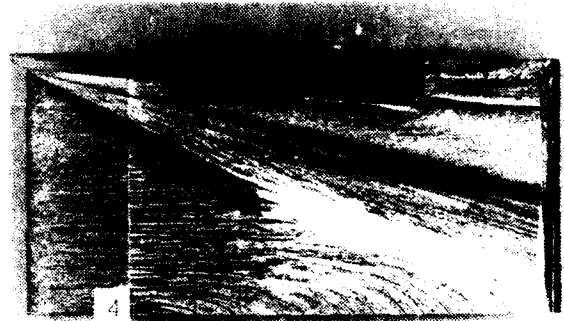


Fig. 19: Oil flow visualization,  $M = 6$ , unswept shock generator,  $\alpha = 6^\circ$

board of the inviscid shock wave location ( $y/x > 0.8$ ): the pressure is seen to decrease as the axial distance from the leading edge is increased. This is due to the flat plate leading edge viscous interaction effect and suggests that it might be better to non-dimensionalize the pressure by the flat plate pressure at the same axial location<sup>2</sup> to remove the leading edge interaction effect. Unfortunately, the pressure taps did not extend far enough laterally to reach the fully undisturbed flow region, so that this alternative scaling could not be attempted. Fig. 25 also displays the locations of the upstream influence, primary and secondary separation, and primary reattachment lines as determined from the surface flow visualizations, as well as the inviscid pressure distribution. The location of the upstream influence line is seen to coincide with the initial pressure rise while the primary reattachment coincides with the pressure peak.

The effect of shock strength is shown in Fig. 26 which displays the pressure distributions on the second row for the three unswept shock generator configurations. Whereas for the  $\alpha = 6^\circ$  case the pressure increase appears monotonic, for the  $\alpha = 9$  and  $12^\circ$  cases, there is an initial modest pressure rise followed by a plateau, a small dip and then an abrupt pressure rise leading to a peak before the pressure relaxes to the inviscid value. It is interesting to note that the existence of a local pressure minimum coincides with the observation of secondary separation in the flow visualizations. However, the resolution of the pressure measurements should be increased to provide more details around the local minimum before a definite

<sup>2</sup>This is actually what has been done by some previous authors, e.g. Hummel [7].





Fig. 20: Mixed surface flow visualization,  $M = 6$ , unswept shock generator,  $\alpha = 6^\circ$

statement can be made about the relation of the pressure minimum with secondary separation. Another interesting observation is the fact that the amplitude of the initial pressure rise appears to depend very little on shock strength, as was already observed by Degrez [28] for his fin-type configurations, with a maximum pressure level upstream of the shock around 1.2.

Pressure distributions measured with the asymmetric dihedron and half circular cone shock generators will be presented and discussed in section 4.2.4.

#### Hypersonic flow

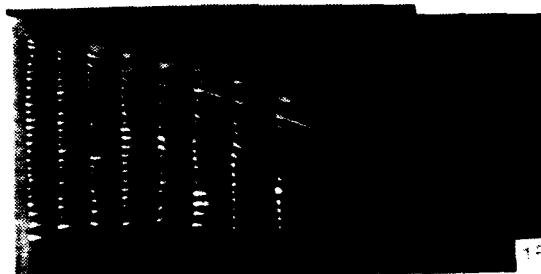
Surface pressure measurements were obtained for all unswept wedges ( $3^\circ \leq \alpha \leq 15^\circ$ ). The flat plate was instrumented with 44 pressure taps distributed on three rows perpendicular to the free stream direction at respectively 4.5, 6.5 and 8.5 cm from the flat plate leading edge.

The general shape of pressure distributions was the same as observed for supersonic flow, i.e. an initial smooth and modest pressure rise outboard of the inviscid shock wave is followed by an abrupt increase near the inviscid shock wave location, a peak near primary reattachment and a relaxation towards the inviscid post-shock level. This is illustrated in Fig. 27 which shows the pressure distributions measured with the  $15^\circ$  wedge. As for the supersonic case, the surface pressure is normalized by the freestream static pressure but the coordinate in abscissa is the argument  $\beta$  in a polar coordinate system centred at the wedge apex and whose reference direction is the freestream direction. This is related to the reduced coordinate  $y/x$  used for supersonic flow (Fig. 25) by  $y/x = \tan \beta$ . The pressure distributions on the three rows are seen to be in much better agreement than for supersonic flow. This confirms the quasi-conical behaviour of the interaction. Unfortunately, because of the limited resolution of the pressure tapping, the details of the pressure distributions, in particular near the inviscid shock wave could not be determined.

The effect of shock strength on the pressure distributions is shown in Fig. 28 which shows pressure distributions at  $x=8.5$  cm for different wedge incidences. Again, one observes the weak dependance of the initial pressure rise with shock strength, with a maximum value of normalized pressure upstream of the inviscid shock wave around 1.5 (against 1.2 for the supersonic experiments). Pressure undershoots near the inviscid shock wave, which were associated with the existence of secondary separation in supersonic flow are also observed in most instances, e.g.



(a) Oil flow technique



(b) Oil dot technique

Fig. 21: Surface flow visualization,  $M = 6$ , unswept shock generator,  $\alpha = 12^\circ$

the curve corresponding to  $\alpha = 12$  and  $15^\circ$  in Fig. 28. In other cases, no undershoot is visible but one may have been missed due to the lack of resolution of the pressure tapping.

#### 4.2.4 Effect of shock generator geometry - Free interaction

As mentioned in section 4.2.1, the asymmetric dihedron and half circular cone shock generators studied in the recent experimental investigations at the VKI were designed in such a way that they produce inviscid shock waves whose strength at their impact on the plate was

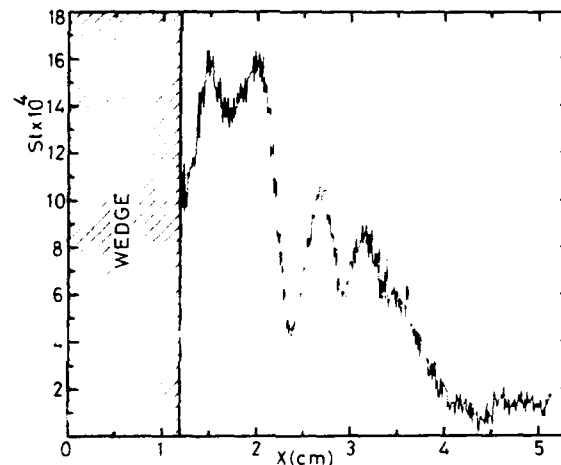


Fig. 22: Spanwise Stanton number distribution at  $x = 7.5$  cm,  $M = 6$ , unswept shock generator,  $\alpha = 9^\circ$



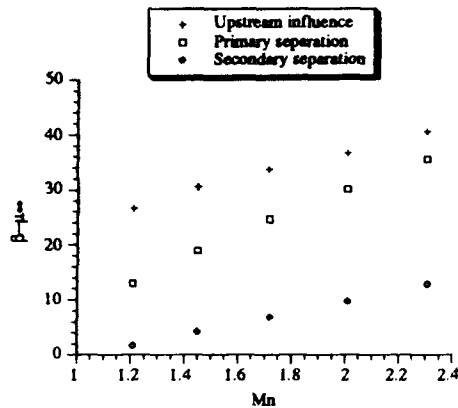


Fig. 23: Separation line angles as a function of shock strength (Mach 6)

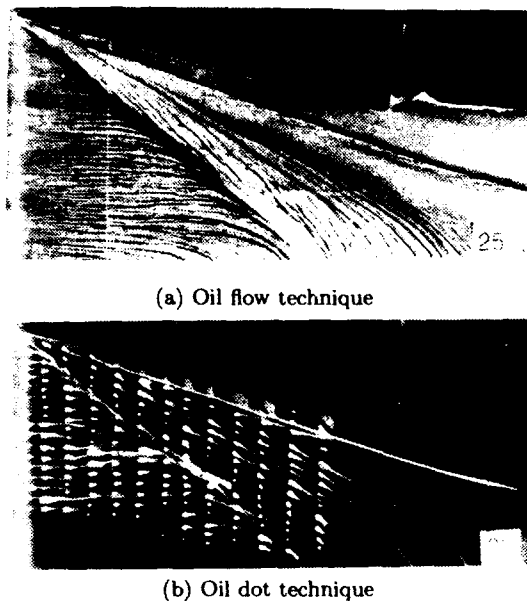


Fig. 24: Surface flow visualization,  $M = 6$ , asymmetric dihedral,  $\alpha = 15^\circ$ ,  $\lambda = 80.5^\circ$

identical to that of the shock generated by a  $12^\circ$  unswept wedge. The motivation behind this design was to determine whether the so-called free interaction concept applies to laminar interactions. This concept first formulated by Settles and Lu [39] for turbulent interactions and initially dubbed 'conical similarity' signifies that the upstream part of conical interactions does not depend on the particular shock generator geometry but only on the incident shock strength. Support for this concept was given by the study of Settles and Kimmel [40] as well as by some recent experiments [41] and computations [42], also in the turbulent régime.

In section 4.2.2, it was shown (Fig. 21 & 24) that surface flow visualizations obtained at Mach 6 for the unswept wedge and the equivalent asymmetric dihedral were nearly identical and in particular, the separation and reattachment line angles were found to match closely. In Fig. 29, spanwise pressure distributions at  $x=5$  cm in supersonic flow are compared for the three equivalent shock generators. The agreement of the curves outboard of the

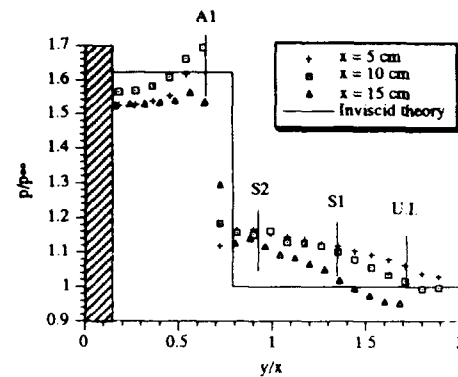


Fig. 25: Spanwise pressure distributions,  $M = 2$ , unswept wedge,  $\alpha = 9^\circ$

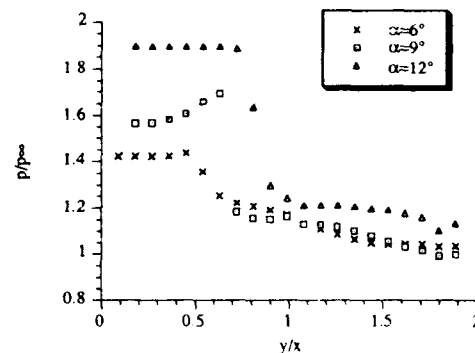


Fig. 26: Effect of shock strength on spanwise pressure distributions (Mach 2)

inviscid shock wave is seen to be excellent. Both results give evidence that the conical free interaction concept applies to the present class of laminar interactions.

#### 4.2.5 Velocity measurements

Longitudinal velocity measurements were performed in the interaction produced by a  $6^\circ$  unswept wedge at Mach 2 using single component Laser Doppler Velocimetry (LDV). The LDV system is a dual beam fringe mode system with forward scatter light collection. Special care has been taken to optimize the seeding material and delivery system for the extremely severe circumstances encountered in the present test conditions (extremely high velocity gradients - up to  $600 \text{ ms}^{-1}$  per mm -, high velocities and low densities), which make particle lag problems particularly serious. The optimization process, as well as the validation of the set up is discussed in detail in [36, 43]. Traverses were performed along two rows parallel to the flat plate leading edge at respectively  $x = 100$  mm and  $x = 250$  mm. In total, 11 traverses were obtained at 10 different locations. Because of this very limited number of traverses, and also because a malfunction of the tunnel drying system resulted in variations in the test conditions between runs, the results give only qualitative information about the flow and are of limited use.



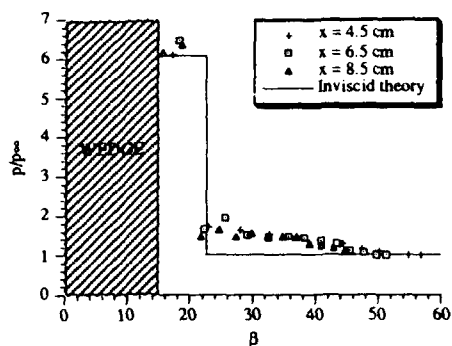


Fig. 27: Spanwise pressure distributions,  $M = 6$ , unswept wedge,  $\alpha = 15^\circ$

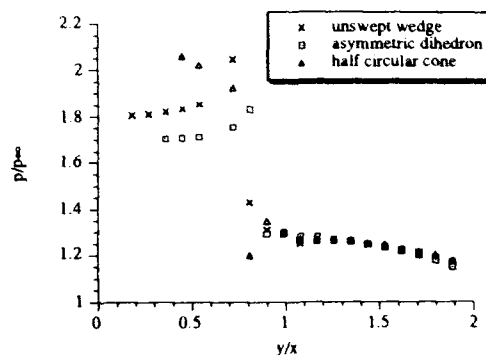


Fig. 29: Effect of shock generator geometry on spanwise pressure distributions (Mach 6)

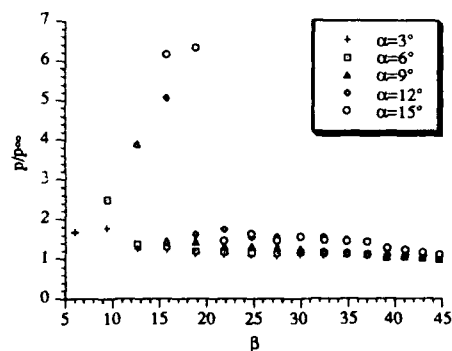


Fig. 28: Effect of shock strength on spanwise pressure distributions (Mach 6)

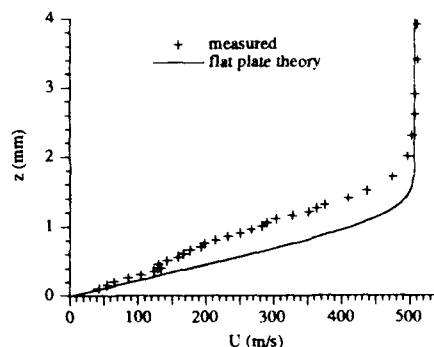


Fig. 30: Velocity profile at  $y/x = 1.4$

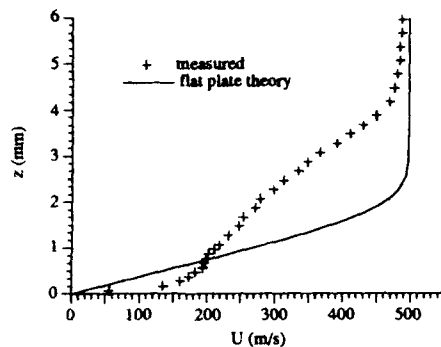
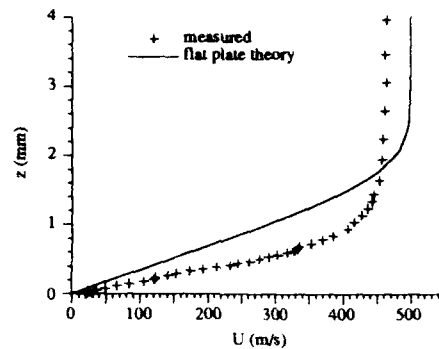
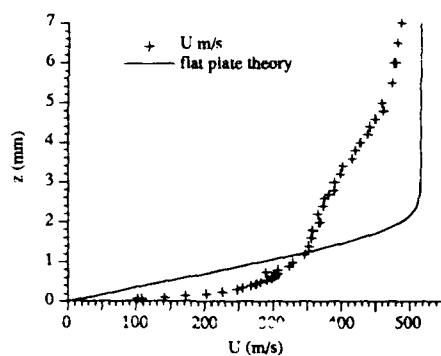
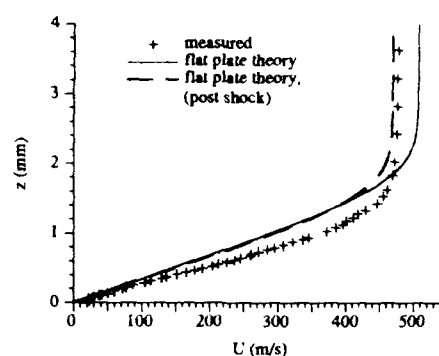
fulness for quantitative analysis, e.g. for code validation purposes.

Surface flow visualizations and pressure measurements having demonstrated the quasi-conical symmetry of the interaction, the velocity profiles are displayed and analyzed as a function of the reduced coordinate  $y/x$ . They are plotted together with the flat plate velocity profiles under the same flow conditions as calculated from the Chapman-Rubens theory [44]. This allows to observe the effect of the interaction with respect to the undisturbed flow case.

The most outboard velocity profile (Fig. 30) was measured at  $y/x = 1.4$  or equivalently at  $\beta = \tan^{-1}(y/x) = 54.5^\circ$ . This is slightly downstream of the upstream influence line as determined from surface flow visualizations ( $\beta_u = 58.5^\circ$ ). One observes that the velocity profile is indeed perturbed, although quite moderately, by the interaction. With respect to the undisturbed flat plate profile, the essential differences are a 50 % increase in the boundary layer thickness and the appearance of a small inflection in the profile. Getting deeper in the interaction region (for a smaller value of  $y/x$ ), the boundary layer thickens and develops a typical S-shape, as illustrated in Fig. 31 which shows a velocity profile measured at  $y/x = 0.8$ , i.e. near the inviscid shock wave location.

The S-shape of the velocity profile is associated with the presence of the vortical structure produced by the boundary layer separation, and was also observed in turbulent interactions [45, 46, 47]. The thickening of the boundary layer and the amplification of the S-shape of the velocity profile continues as one progresses to the next exploration station at  $y/x = 0.65$  (Fig. 32). At this point, the viscous layer has become three times thicker than the corresponding flat plate boundary layer. One can also observe that the velocity profile does not reach the free stream velocity value. This should be expected as the present value of  $y/x$  corresponds to a station downstream of the inviscid shock wave. The measured asymptotic velocity indeed corresponds quite closely to the post-shock value computed from oblique shock relations ( $u_2 = 480 \text{ ms}^{-1}$ ). This close agreement indicates that, at this location, there is no noticeable particle lag due to the oblique shock wave. At the next station corresponding to  $y/x = 0.5$  (Fig. 33), one observes a drastic change: the viscous layer has become considerably thinner than the undisturbed flat plate boundary layer and has completely lost its S-shape, resembling rather an accelerated boundary layer profile. Both of these features are indicative of an attachment phenomenon, which agrees with the surface flow visualization results since primary reattachment was observed around an angle of  $26^\circ$ , close to the present station. Finally, at  $y/x = 0.38$ , the boundary layer is seen to be relaxing towards a flat plate boundary layer corre-



Fig. 31: Velocity profile at  $y/x = 0.8$ Fig. 33: Velocity profile at  $y/x = 0.5$ Fig. 32: Velocity profile at  $y/x = 0.65$ Fig. 34: Velocity profile at  $y/x = 0.38$ 

sponding to post-shock conditions (Fig. 34).

To check whether the quasi-conical symmetry of the interaction applies to the velocity profiles, for two values of  $y/x$  (0.8 and 0.5), traverses were measured at the two longitudinal locations and compared. The comparison was performed by non-dimensionalizing the vertical coordinate by the flat plate similarity parameter  $(\sqrt{\frac{2\nu_{\infty}C_C z}{u_{\infty}}})$ , where  $C_C$  is Chapman's viscosity constant,  $\nu_{\infty}$  and  $u_{\infty}$  are respectively the freestream kinematic viscosity and velocity) and the velocity  $u$  by the local outer flow velocity. Fig. 35 shows the results of the comparison for  $y/x = 0.5$ . The agreement is seen to be quite good. This gives additional support to the validity of the conical scaling in the  $x-y$  plane, while in the vertical direction, the correct scaling seems to be the classical laminar boundary layer scaling. Additional measurements are however needed to confirm this observation.

## 5 NUMERICAL RESEARCH

### 5.1 Inviscid flow

As mentioned in section 2, corner flow configurations differ essentially from intake or fin-type configurations by the fact that they involve two shock generators. The in-

viscid flowfield is therefore complicated by the interaction of these two shocks and this interaction has been shown in section 4.1 to play an essential role also for real viscous flows. Inviscid analyses therefore present a real interest for corner flows and were performed initially.

Kutler [17] solved the conical Euler equations using a shock capturing technique for the configuration studied by West and Korkegi [16]. The resulting shock pattern was in very good agreement with the experimental results when the boundary layer was turbulent as shown in Fig. 36 which compares the experimental results of West and Korkegi with numerical results of Kutler and of Marconi [18], to be discussed below. The same numerical approach was subsequently used by Shankar et al. [48] and by Anderson and Nangia [49] to study a variety of corner flow configurations, including swept and asymmetric configurations.

Shankar et al. compared their results with the experimental data of Charwat and Redekopp [12]. Although the shock patterns qualitatively agreed, the actual position of shock waves did not agree, lying further outboard in the experimental results. This is due to the outward displacement of the shock structure due to laminar boundary layer separation as shown by the experimental study of West and Korkegi [16]. Anderson and Nangia compared their results with their own experimental data obtained for turbulent flow at Mach 2. Despite the



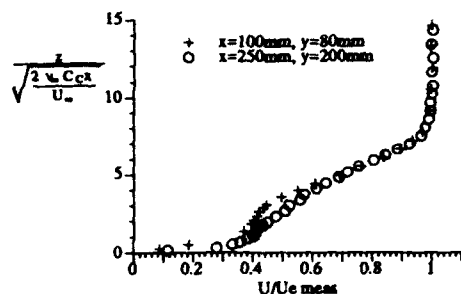


Fig. 35: Comparison of velocity profiles at  $y/x = 0.5$

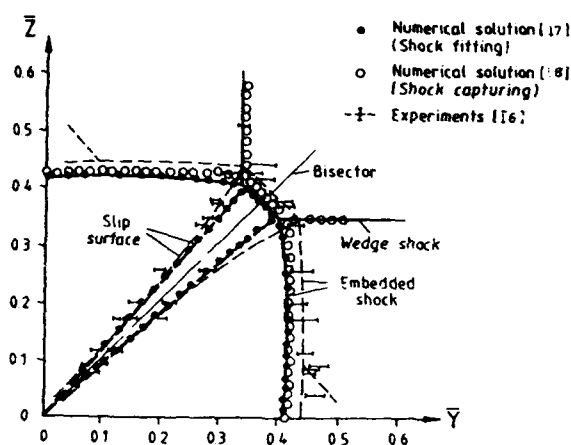


Fig. 36: Wave pattern in corner flow configuration: comparison of experimental results of West and Korkegi [16] and computational results of Kutler [17] and of Marconi [18]

coarseness of the computational mesh, good agreement was found between computed and experimental wave patterns.

Marconi [18] used a shock fitting approach to solve the conical Euler equations for unswept symmetric corner flow configurations. He studied the effect of Mach number and wedge deflection and found the existence of two flow régimes. For small wedge deflections, the wedge shocks intersect and no slip line is present whereas for larger deflections, the structure described above with a corner shock, two triple points and two slip lines is observed. An example of such a case is West and Korkegi's configuration for which Marconi's results are seen to be in good agreement with both the experimental data and Kutler's computation (Fig. 36).

Some experimental [14, 7] and theoretical [50] studies suggest that in some instances the slip lines originating from the triple point do not run into the intersection of wedges but terminate somewhere in the flow. Such patterns were recently shown to exist in numerical solutions of the Euler equations by Marsilio [32] and Degrez et al. [33]. Both analyses used a shock capturing finite volume approach but the former used a 3D space marching

method whereas the latter compared this method with the conical time-dependent method developed at the VKI [37, 51]. It was found that when the slip lines terminated inside the flow, this was associated with the existence of vortices within the inviscid flow and moreover that this vortical pattern could be asymmetric even for symmetric configurations. This is illustrated in Fig. 37 which displays crossflow streamlines in a symmetric cor-

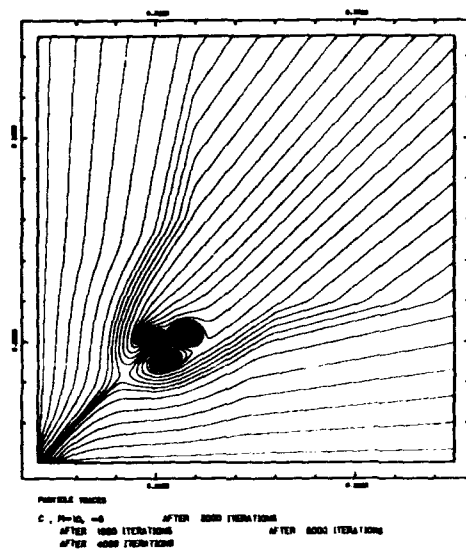


Fig. 37: Crossflow streamlines in asymmetric vortical flow in a corner,  $M = 10$ ,  $\delta = 8^\circ$

ner at Mach 10 with a wedge deflection  $\delta = 8^\circ$ .

Fin and intake-type configurations exhibit a much simpler inviscid flow pattern. For unswept wedge and half circular cone shock generators, the inviscid flow even has an analytical or semi-analytical solution. However, for more general shock generators such as symmetric or asymmetric dihedrons, the inviscid flow and in particular the shock shape can only be determined by numerical solutions of the Euler equations. Such solutions were obtained by Salas [52] and by Bewley [53] for symmetric dihedrons, and by the present author for asymmetric dihedrons (unpublished results - see Fig. 12).

## 5.2 Viscous flow

The first numerical computation of a swept shock wave/laminar boundary layer interaction was performed by Shang and Hankey [54]. They implemented the explicit predictor-corrector scheme of MacCormack [55] to solve the 3D time-dependent Navier-Stokes equations for the intake-type configuration studied experimentally by Cooper and Hankey [19]. They used a series of rather coarse meshes with the finest being made of  $8 \times 32 \times 36$  points. The mesh was conically expanding in the axial direction to reflect the quasiconical nature of the flow observed experimentally. Despite the coarseness of the grid, the essential flow features were correctly captured as seen in Fig. 38 which shows a comparison of measured and computed pitot pressure contours. The effect of grid coarseness however shows up clearly in the smearing of the wedge shock and of most of the flowfield details. Similar to the experimental results, the computed skin friction pattern (Fig. 39) shows the presence of a primary and a



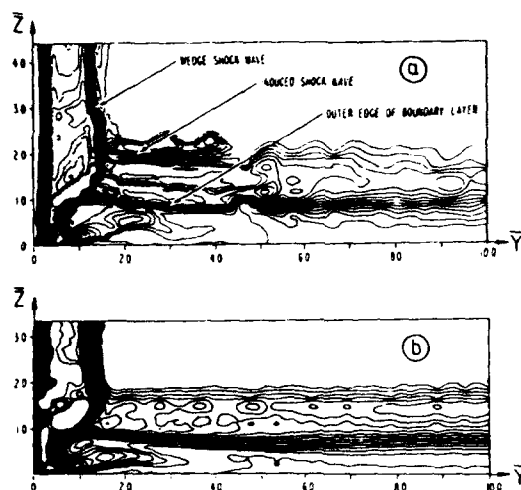


Fig. 38: Comparison of measured [19] (a) and computed [54] (b) pitot pressures in intake configuration ( $\delta_w = 15^\circ$ ,  $M_\infty = 12.5$ )

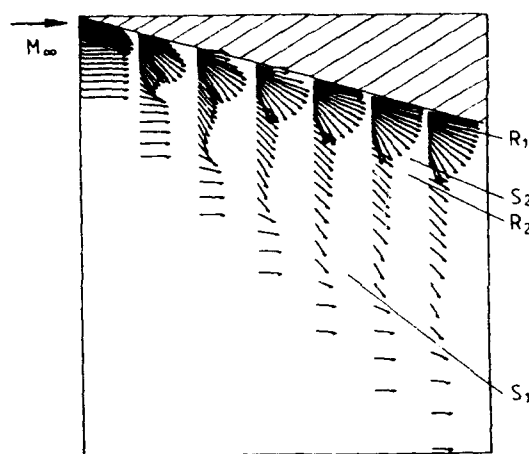


Fig. 39: Computed [54] flat plate skin friction pattern in intake configuration ( $\delta_w = 15^\circ$ ,  $M_\infty = 12.5$ )

secondary separation. The extent of the secondary separation is however not captured properly because of the excessive numerical dissipation due to the coarseness of the grid. One also observes the nearly conical nature of the computed flowfield. It should be kept in mind however that the conical nature and the coarseness of the mesh would prevent to capture properly moderate departures from conicity as for example in the strong interaction region near the flat plate leading edge. Finally, Fig. 40 shows that the computed surface pressure distribution is in excellent agreement with the experimental results, the pressure peak at reattachment being perfectly captured by the computation. Notice also the close resemblance of this pressure distribution with the distribution measured in recent VKI experiments (Fig. 27).

Later, Shang et al. [56] introduced a mixing length eddy viscosity model and a transition model in their code and computed West and Korkegi's [16] corner flow configuration with  $Re_L = 1.1 \cdot 10^6$ . This corresponds to a transitional flow case with the upstream region  $Re_x \leq 0.5 \cdot 10^6$

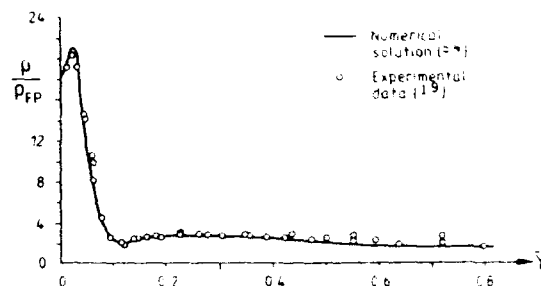


Fig. 40: Comparison of measured [19] and computed [54] pressure distribution on flat plate in intake configuration ( $\delta_w = 15^\circ$ ,  $M_\infty = 12.5$ )

being laminar and the downstream region turbulent. As in the previous study, the mesh was conically expanding in the axial direction with  $17 \times 33 \times 33$  points. The numerical results nicely reproduced the experimental observations including the S-bend of the primary separation line due to the transition from laminar to turbulent flow (Fig. 41). The outward displacement of the wave pat-

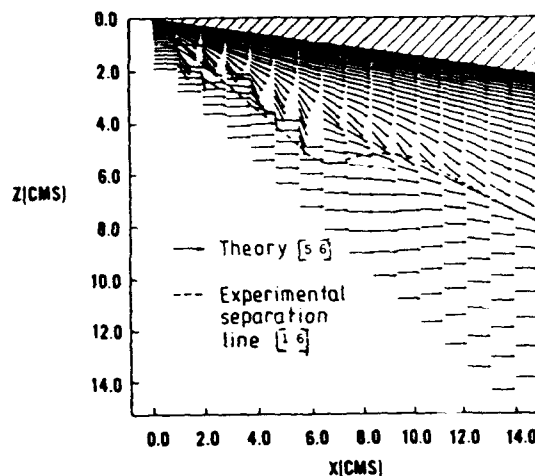


Fig. 41: Computed [56] skin friction pattern in symmetric corner configuration ( $\delta = 9.5^\circ$ ,  $M_\infty = 3.0$ ), together with experimental [16] separation line

tern due to the extensive boundary layer separation in the laminar flow region was also correctly simulated as seen in Fig. 42 which compares the computed and measured wave patterns in the laminar and turbulent flow regions. The slip lines emanating from the triple points are also seen to be well captured by the numerical solution.

At about the same period, Hung and MacCormack [57] solved the 3D time-dependent Navier-Stokes equations using the hybrid explicit/implicit scheme of MacCormack [58] for a three-dimensional compression corner configuration. The configuration was made out of a 2D compression corner mounted normal to a flat plate. This configuration is considerably more complex than the ones considered in this paper as it involves both a 2D interaction at the compression corner and a 3D swept interaction on the flat plate. No experimental data were available for comparison. The same flow solver was later extended to turbulent flows and used to study turbulent interactions [59, 47]. These will be described in the companion



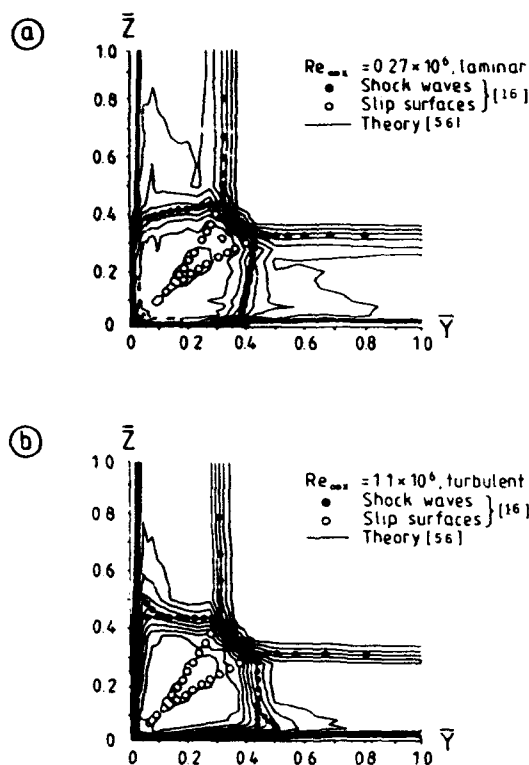


Fig. 42: Comparison of computed [56] and measured [16] wave patterns in symmetric corner configuration ( $\delta = 9.5^\circ$ ,  $M_\infty = 3.0$ ); (a) laminar flow, (b) turbulent flow

paper by D. D. Knight which concerns the computation of turbulent interactions.

Degrez [29, 30] solved the 3D time-dependent Navier-Stokes equations using the implicit scheme of Beam and Warming [60] for a fin-type configuration previously studied experimentally by the same author [28]. The Mach number was 2.25, the shock generator was an unswept  $6^\circ$  wedge and the Reynolds number based on the distance between the wedge apex and the flat plate leading edge was  $1.08 \times 10^5$ . A coarse ( $35 \times 36 \times 20$ ) and a finer ( $65 \times 49 \times 25$ ) mesh were successively used. Contrary to the calculations of Shang et al. [54, 56], the meshes were not conically expanding from the wedge apex but were rather generated by conformal mapping in the  $x-y$  plane. The pressure contours on the plate surface (Fig. 43 - fine mesh) confirm the quasiconical symmetry of the interaction, although some departures from conicity are observed, namely a curving in of the outermost pressure isolines and the development of a pressure trough when progressing away from the wedge apex. This latter phenomenon was also recently observed in the numerical computation of a turbulent interaction by Panaras and Stanewsky [5]. A quantitative comparison of computed and measured pressure distributions on a line parallel to the free stream at 5 cm from the wedge apex is shown in Fig. 44. The fine mesh result is seen to be in quite good agreement with the experimental data except for the downstream pressure level, which is due to a difference in free stream Mach numbers between theory and experiment, and for the presence of the pressure trough around  $x = 15$  cm. The computed skin friction patterns are shown in Fig. 45-46 for respectively the coarse and

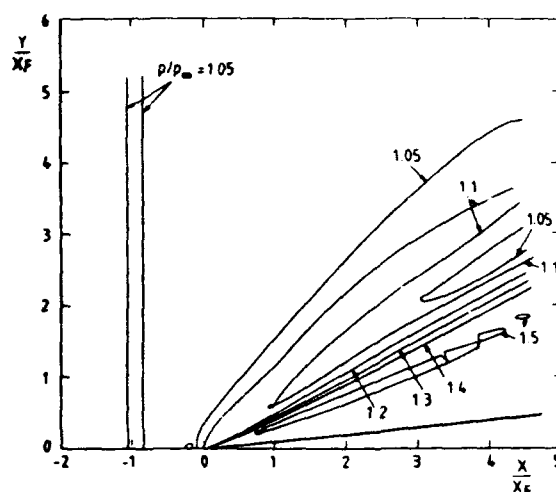


Fig. 43: Computed [30] pressure contours on flat plate in fin-type configuration ( $\delta = 6^\circ$ ,  $M_\infty = 2.25$ ,  $Re_{x_F} = 1.08 \times 10^5$ )

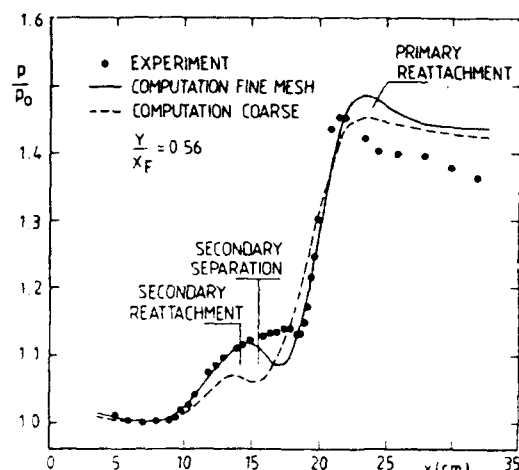


Fig. 44: Comparison of computed [30] and measured [28] pressure distribution on flat plate ( $y = 5$  cm) in fin-type configuration ( $\delta = 6^\circ$ ,  $M_\infty = 2.25$ ,  $Re_{x_F} = 1.08 \times 10^5$ )

fine meshes. Again, the pattern is nearly conical. Both include a primary separation but the fine mesh results also include a secondary separation. This is consistent with the observation of a trough in the computed pressure distribution (Fig. 44). Whether this is actually a physical phenomenon is not clear as a recent computation by Hung [61] of the same flow configuration did not show the presence of a secondary separation nor of a trough in the wall pressure distribution (Fig. 47). Also, no secondary separation was observed for  $\alpha = 6^\circ$  in the recent experimental investigation of an intake-type configuration at Mach 2 by Piepsz [34] described in section 4.

The quasiconical nature of swept shock wave/laminar boundary layer interactions suggests that they may be amenable to analysis using the conical Navier-Stokes equations. Although supersonic inviscid flows over conical geometries are rigorously conical, this is not true for viscous flows. For high Reynolds number flows though, it was shown theoretically [62] and numerically [63] that the



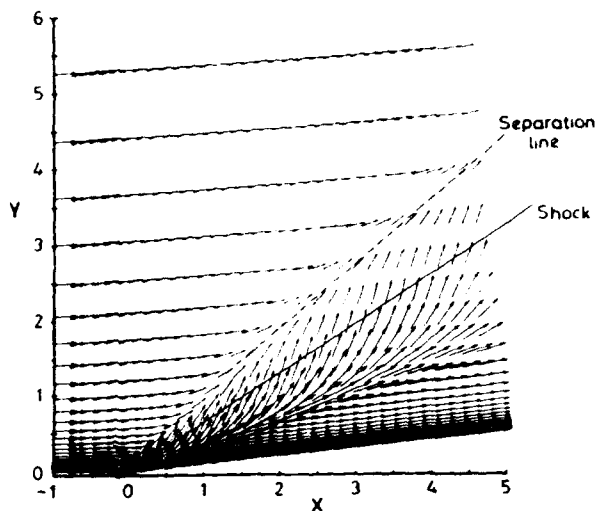


Fig. 45: Computed [30] flat plate skin friction pattern in fin-type configuration ( $\delta = 6^\circ$ ,  $M_\infty = 2.25$ ,  $Re_{x_F} = 1.08 \cdot 10^5$ ), coarse mesh

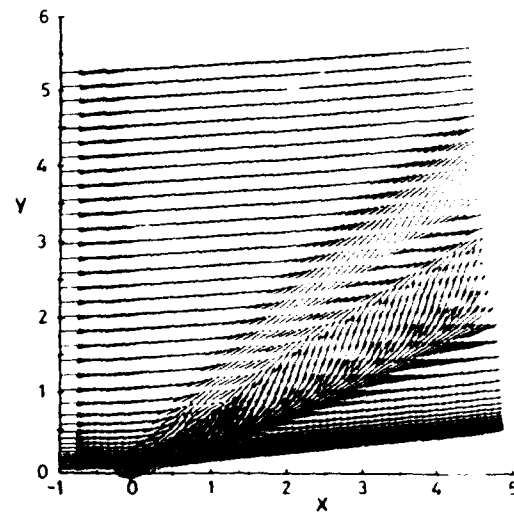


Fig. 46: Computed [30] flat plate skin friction pattern in fin-type configuration ( $\delta = 6^\circ$ ,  $M_\infty = 2.25$ ,  $Re_{x_F} = 1.08 \cdot 10^5$ ), fine mesh

conical Navier-Stokes equations represent a good approximation of the real 3D equations. Such conical Navier-Stokes computations were performed by Scriba [64] for the corner flow configuration studied by Möllenstadt [25]. Although the overall flow patterns were in excellent agreement (Fig. 48), there existed important quantitative differences in the surface pressure and heat transfer distributions. It is worth mentioning that conical Navier-Stokes computations were also performed for turbulent interactions [65].

## 6 FINAL COMMENTS ABOUT THE STRUCTURE OF SWEEPED SHOCK WAVE/LAMINAR BOUNDARY LAYER INTERACTIONS

It appears from the previous discussions that an essential difference exists between corner flow configurations on the one hand and intake and fin-type configurations on the other. The former are dominated by the shock/shock interaction which produces slip lines emanating from the triple points (Fig. 9) whereas the latter are dominated by the viscous/inviscid interaction produced at the impingement of the shock wave with the boundary layer. Details of the flow structure in this case are not completely known. For intake-type configurations, the plate leading edge shock still intersects the wedge shock wave at a triple point, producing a slip line as illustrated in Figs. 6 and 8, but this cannot be a dominant feature since the leading edge shock can be made as weak as desired by reducing the hypersonic parameter or by moving the flat plate leading edge upstream (for fin-type configurations).

The structure of turbulent interactions is far better known [4] and might be used as a model for the structure of laminar interactions. Let us thus examine briefly the turbulent interaction flow structure. As shown by Alvi and Settles [4], it is basically conical and can therefore be represented in the spherical coordinate system centred at the virtual conical origin as shown in Fig. 49. The turbulent boundary layer separation is seen to induce a separation

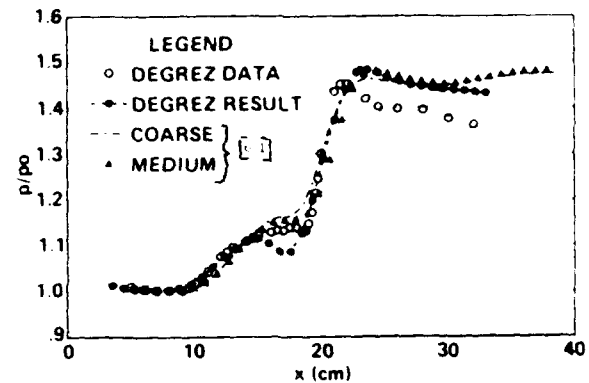


Fig. 47: Comparison of computed [61, 30] and measured [28] pressure distribution on flat plate ( $y = 5 \text{ cm}$ ) in fin-type configuration ( $\delta = 6^\circ$ ,  $M_\infty = 2.25$ ,  $Re_{x_F} = 1.08 \cdot 10^5$ )

shock which intersects the outer inviscid shock at a triple point, producing a slip line. The pattern is seen to be very similar to the corner flow pattern except that the triple point is now produced by the separation shock rather than by the wedge shock.

It is believed by the present author that this pattern does not apply to laminar interactions for the following reason: the thickening and separation of laminar boundary layers is a much smoother phenomenon than for turbulent boundary layers. The compression outboard of the inviscid shock wave is therefore much more likely to be spread in a compression fan than concentrated in a separation shock, as suggested in Fig. 9 taken from [7]. Such a wave pattern at separation would in fact correspond to the behaviour at separation in 2D interactions as sketched in Fig. 50. The interaction of a compression fan with the outer inviscid shock wave would then produce a region of varying entropy rather than a slip line. The remaining of the flow structure, i.e. the vortical structure beneath the shock leg exists also in laminar interactions but it has been shown to be much more elongated than for turbulent interactions because of the much greater extent of laminar separation.



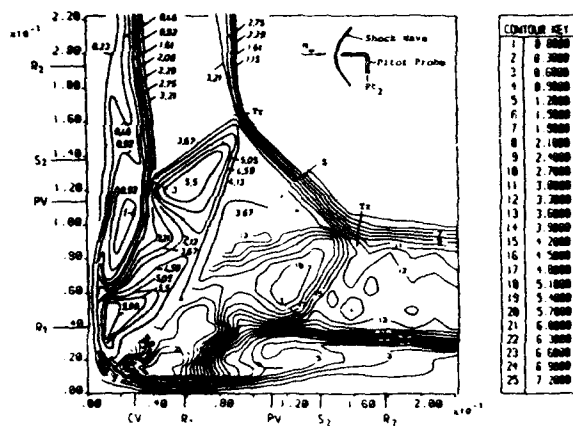


Fig. 48: Comparison of computed [64] and measured [25] pitot pressure contours in a symmetrical corner configuration ( $\delta = 8^\circ$ ,  $M_\infty = 12.8$ ) with  $30^\circ$  swept leading edges - experiments above the bisector, computation below)

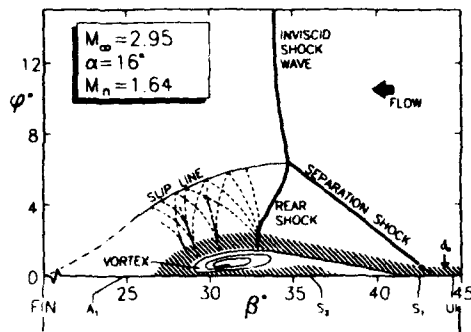


Fig. 49: Swept shock wave/turbulent boundary layer structure (after [4])

## 7 CONCLUSIONS

The experimental and numerical studies on swept shock wave/laminar boundary layer interactions have been reviewed. Three classes of flow configurations were identified, named respectively fin-type, intake-type and corner configurations. Although the amount of experimental and computational results is much more limited than for turbulent interactions, they nevertheless allow one to draw the following conclusions :

- For all three types of configurations, the flow is of quasiconical nature,
- For corner flows, the outer wave structure is essentially the same as for turbulent flows but is displaced outboard due to the extensive boundary layer separations,
- All cases under review exhibited an extensive separation of the upstream boundary layer which then rolls up into an elongated vortex,
- This primary separation is accompanied most of the time by a secondary separation and it has been shown that in some instances higher order separations may even be present,

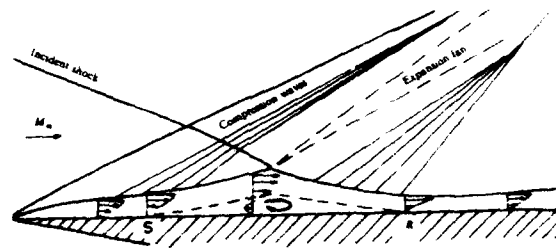


Fig. 50: Structure of 2D incident shock wave/laminar boundary layer interaction

- The free interaction concept which applies to turbulent interactions has been shown to apply to laminar interactions as well,
- Numerical results are in good agreement with the experimental results but no numerical computation so far has demonstrated a sufficient mesh resolution to capture all flowfield details.

Some unanswered questions still remain, which indicate the need for additional research.

- The outer wave structure of fin and intake-type configurations is not yet fully understood. Additional experimental/numerical investigations should clarify this point,
- The existence of multiple separations should be confirmed and the circumstances in which they occur should be identified,
- Departures from conicity should be further investigated and analyzed,
- The effect of wall temperature, which is known to be important for 2D interactions is completely unknown for swept interactions,
- A comprehensive flowfield survey in a swept shock wave/laminar boundary layer interaction is badly needed to serve as a benchmark for the validation of 3D Navier-Stokes solvers,
- New numerical computations should be carried out with a demonstrated sufficient grid resolution in order to capture the flowfield details, in particular secondary and possibly higher order separations.

## ACKNOWLEDGEMENTS

The research on supersonic swept shock wave/laminar boundary layer interactions reviewed in section 4.2 was supported by the Commission of the European Communities through research contract AERO-0027C within the Brite-Euram programme, monitored by D. Knörzer. The VKI work reported in this review owes much to the contributions of L. Bertuccioli, P. Jacqy and O. Piepsz, which are gratefully acknowledged.



## REFERENCES

- [1] G. Simeonides, W. Haase, and M. Manna. Experimental, analytical and computational methods applied to hypersonic compression ramp flows. In *Theoretical and experimental methods in hypersonic flows*. AGARD CP 514, May 1992.
- [2] G. S. Settles and D. S. Dolling. Swept shock wave / boundary layer interactions. In M. Hemsch and J. Nielsen, editors, *AIAA Progress in Astronautics and Aeronautics, Vol. 104, Tactical Missile Aerodynamics*, pages 297-379. AIAA, New York, 1986.
- [3] G. S. Settles and D. S. Dolling. Swept shock wave / boundary layer interactions - Tutorial and update. AIAA Paper 90-0375.
- [4] F. S. Alvi and G. S. Settles. Physical model of the swept shock wave/boundary-layer interaction flow-field. *AIAA Journal*, 30(9):2252-2258, September 1992.
- [5] A. G. Panaras and E. Stanewsky. Numerical study of secondary separation in a glancing shock/turbulent boundary layer interaction. AIAA Paper 92-3666.
- [6] G. S. Settles and L. J. Dodson. Hypersonic shock/boundary layer interaction database. AIAA Paper 91-1763.
- [7] D. Hummel. Axial flow in corners at supersonic and hypersonic speeds. In *Special Course on Three-dimensional supersonic/hypersonic Flows including Separation*. AGARD R 764, 1989.
- [8] P. C. Stainback. An experimental investigation at a Mach number 4.95 of flow in the vicinity of a 90 degrees interior corner aligned with the free stream velocity. TN D-184, NASA, 1960.
- [9] P. C. Stainback. Heat transfer measurements at a Mach number of 8 in the vicinity of a 90 degrees interior corner aligned with the free stream velocity. TN D-2417, NASA, 1960.
- [10] R. J. Stalker. Sweepback effects in turbulent boundary layer shock wave interaction. *Journal of the Aeronautical Sciences*, 27(5):348-356, 1960.
- [11] A. Stanbrook. An experimental study of the glancing interaction between a shock wave and a turbulent boundary layer. CP 555, Aeronautical Research Council, July 1960.
- [12] A. F. Charwat and L. G. Redekeopp. Supersonic interference flow along the corner of intersecting wedges. *AIAA Journal*, 5(3):480-488, March 1967.
- [13] R. J. Cresci, S. G. Rubin, C. T. Nardo, and T. C. Lin. Hypersonic interaction along a rectangular corner. *AIAA Journal*, 7:2241-2246, 1969.
- [14] R. D. Watson and L. M. Weinstein. A study of hypersonic corner flow interactions. *AIAA Journal*, 9:1280-1286, 1971.
- [15] R. H. Korkegi. Survey of viscous interactions associated with high Mach number flight. *AIAA Journal*, 9(5):771-784, May 1971.
- [16] J. E. West and R. H. Korkegi. Supersonic interaction in the corner of intersecting wedges at high Reynolds numbers. *AIAA Journal*, 10(5), May 1972.
- [17] P. Kutler. Supersonic flow in the corner formed by two intersecting wedges. *AIAA Journal*, 12:577-578, 1974.
- [18] F. Marconi. Supersonic, inviscid, conical corner flowfields. *AIAA Journal*, 18:78-84, 1980.
- [19] J. R. Cooper and W. L. Hankey. Flowfield measurements in an asymmetric axial corner at  $M=12.5$ . *AIAA Journal*, 12(10):1353-1357, October 1974.
- [20] D. J. Peake and M. Tobak. Three-dimensional interactions and vortical flows with emphasis on high speeds. AGARDograph 252, 1980.
- [21] R. H. Korkegi. On the structure of three-dimensional shock-induced separated flow regions. *AIAA Journal*, 14(5):597-600, May 1976.
- [22] H. D. Schultz and R. C. Baker. Pressure and heat transfer measurements in regions of three-dimensional shockwave-boundary layer interactions. Technical Report LMSC-D157341, Lockheed Missiles and Space Co., Sunnyvale, Calif., March 1972.
- [23] K. Kipke. Untersuchungen an längsangeströmten Ecken im Hyperschallbereich. Vorabdruck 73-114. DGLR, 1973.
- [24] K. Kipke and D. Hummel. Untersuchungen an längsangeströmten Eckenkonfigurationen im Hyperschallbereich, Teil I: Ecken zwischen ungepfeilten Keilen. *Z. Flugwiss.*, 23:417-429, 1975.
- [25] W. Möllenstadt. Untersuchungen an längsangeströmten Eckenkonfigurationen im Hyperschallbereich, Teil II: Ecken zwischen gepfeilten Keilen. *Z. Flugwiss. Weltraumforsch.*, 8:405-414, 1984.
- [26] D. Hummel. Experimental investigations on blunt bodies and corner configurations in hypersonic flow. In *Aerodynamics of hypersonic lifting vehicles*. AGARD CP 428, 1987.
- [27] B. E. Edney. Anomalous heat transfer and pressure distributions on blunt bodies at hypersonic speeds in the presence of an impinging shock. Technical Report FFA Report 115, The Aeronautical Research Institute of Sweden, Stockholm, Sweden, February 1968.
- [28] G. Degrez and J. J. Ginoux. Surface phenomena in a three-dimensional skewed shock wave / laminar boundary layer interaction. *AIAA Journal*, 22(12):1764-1769, December 1984.
- [29] G. Degrez. Numerical solution of a 3D skewed shock wave laminar boundary layer interaction. In J. J. H. Miller, editor, *Proceedings of the IIIrd International Boundary and Interior Layers Conference*, Dublin, June 1984.
- [30] G. Degrez. Computation of a three-dimensional skewed shock wave laminar boundary layer interaction. AIAA Paper 85-1565.
- [31] R. H. Korkegi. A simple correlation for incipient turbulent boundary layer separation due to a skewed shock wave. *AIAA Journal*, 11:1578-1579, November 1973.
- [32] R. Marsilio. Vortical solutions in supersonic corner flows. AIAA Paper 93-0760.



- [33] G. Degrez, P.-G. Spazzini, R. Marsilio, and M. Pandolfi. Asymmetric vortical flows in supersonic corners : steady 3D space-marching versus time-dependent conical results. *AIAA Paper* 93-2957.
- [34] O. Piepsz. Etude paramétrique de l'interaction tridimensionnelle entre onde de choc et couche limite laminaire en régime supersonique. Travail de fin d'études, Université Libre de Bruxelles, 1992.
- [35] P. Jacquy. Etude expérimentale de l'interaction dérapée entre une onde de choc et une couche limite laminaire en régime hypersonique. Travail de fin d'études, Université Libre de Bruxelles, 1992.
- [36] L. Bertuccioli. Improvement and validation of an LDV system to perform measurements in supersonic flows. Project Report 1992-16, VKI, 1992.
- [37] R. Schricke. Solution of the conical Euler equations. Project Report 1988-13, VKI, 1988.
- [38] H. Papuccuoglu. An experimental study of hypersonic axial corner flow. Project Report 1991-22, VKI, 1992.
- [39] G. S. Settles and F. K. Lu. Conical similarity of shock/boundary layer interactions generated by swept and unswept fins. *AIAA Journal*, 23:1021-1027, July 1985.
- [40] G. S. Settles and R. L. Kimmel. Similarity of quasi-conical shock wave/turbulent boundary layer interactions. *AIAA Journal*, 24:47-53, 1986.
- [41] X. Y. Deng and J. H. Liao. Correlative behaviours of shock/boundary layer interaction induced by sharp fin and semicone. *AIAA Paper* 91-1756.
- [42] X. Zang and D. D. Knight. Computation of sharp fin and swept compression corner shock/turbulent boundary layer interactions. *AIAA Paper* 89-1852.
- [43] L. Bertuccioli and G. Degrez. Application of LDV to supersonic laminar boundary layer flows. *AIAA Paper* 93-3069.
- [44] D. R. Chapman and M. W. Rubesin. Temperature and velocity profiles in the compressible boundary layer with arbitrary distribution of surface temperature. *Journal of the Aeronautical Sciences*, 16(9):547-565, September 1949.
- [45] D. J. Peake. *Three dimensional swept shock/turbulent boundary layer separation with control by air injection*. PhD thesis, Carleton University, Ottawa, 1975.
- [46] B. Oskam. Three dimensional flowfields generated by the interaction of a swept shock wave with a turbulent boundary layer. Technical Report 1313, Princeton University, Gas Dynamics Laboratory, December 1976.
- [47] C. C. Horstman and C. M. Hung. Computation of 3D turbulent separated flows at supersonic speeds. *AIAA Paper* 79-0002.
- [48] V. Shankar, D. Anderson, and P. Kutler. Numerical solutions for supersonic corner flow. *Journal of computational physics*, 17:160-180, 1975.
- [49] D. A. Anderson and R. K. Nangia. Comparison of numerical and experimental conical flow fields in supersonic corners with compression and/or expansion. *Aeronautical Quarterly*, 28:293-306, 1977.
- [50] T. P. Goebel. *A theoretical study of inviscid supersonic flow along the corner formed by the intersection of two wedges*. PhD thesis, University of California, Los Angeles, 1969.
- [51] P. G. Spazzini. Improvement and acceleration of a conical solver and applications to super hypersonic flows. VKI PR 1992-25, von Karman Institute, June 1992.
- [52] M. D. Salas. A careful numerical study of flowfields about external axial corners: Part I symmetric configurations. *AIAA Paper* 79-1511.
- [53] T. R. Bewley. Swept fin induced shock wave / laminar boundary layer interactions. An analytical, computational and experimental study. Project Report 1990-31, VKI, 1990.
- [54] J. S. Shang and W. L. Hankey. Numerical solution of the navier-stokes equations for a three-dimensional corner. *AIAA Journal*, 15:1575-1582, 1977.
- [55] R. W. MacCormack. The effect of viscosity in hypervelocity impact cratering. *AIAA Paper* 69-0354.
- [56] J. S. Shang, W. L. Hankey, and J. S. Petty. Three-dimensional supersonic interacting turbulent flow along a corner. *AIAA Journal*, 17:706-713, 1979.
- [57] C. M. Hung and R. W. MacCormack. Numerical solution of supersonic laminar flow over a three-dimensional compression corner. *AIAA Paper* 77-0694.
- [58] R. W. MacCormack. An efficient numerical method for solving the time-dependent compressible Navier-Stokes equations at high Reynolds number. TM X-73, NASA, July 1976.
- [59] C. M. Hung and R. W. MacCormack. Numerical solution of three-dimensional shock wave and turbulent boundary-layer interaction. *AIAA Journal*, 16:1090-1096, 1978.
- [60] R. M. Beam and R. F. Warming. An implicit factored scheme for the compressible Navier-Stokes equations. *AIAA Journal*, 16(4):393-402, 1978.
- [61] C. M. Hung. Computation of Navier-Stokes equations for three-dimensional separation. *AIAA Journal*, 29:1659-1667, 1991.
- [62] G. R. Inger. Spanwise propagation of upstream influence in conical swept shock/boundary layer interactions. *AIAA Journal*, 25:287-293, 1987.
- [63] S. N. Mc Millin, J. L. Thomas, and E. M. Murman. Navier-Stokes and Euler solutions for leeside flows over supersonic delta wings. Technical Publication 3035, NASA, 1990.
- [64] K. W. Scriba. Exploration of the importance of viscous effects on waverider configurations in simulated re-entry flow. Technical report, University of Glasgow, Dept. of Aeronautics and Fluid Mechanics, March 1988.
- [65] D. D. Knight and D. Badekas. On the quasi-conical flowfield structure of the swept shock wave-turbulent boundary layer interaction. *AIAA Paper* 91-1759.



# Numerical Simulation of 3-D Shock Wave Turbulent Boundary Layer Interactions

Doyle D. Knight

Department of Mechanical and Aerospace Engineering  
Rutgers University - The State University of New Jersey  
PO Box 909 · Piscataway NJ 08855-0909

## Abstract

The paper assesses the capability for numerical simulation of 3-D shock wave turbulent boundary layer interactions. Specific configurations examined include the sharp fin, blunt fin, cylinder/flare, swept compression corner and crossing shock. Future needs in improved computational methods, collaborative experimental/computational efforts and incorporation of knowledge of flowfield structure into more effective designs are discussed.

## 1 Nomenclature

$c_f$	skin friction coefficient
$c_h$	heat transfer coefficient
$c_p$	specific heat at constant pressure
$k$	turbulence kinetic energy
$k - \epsilon$	Jones-Launder turbulence model
$M$	Mach number
$p$	static pressure
$p_p$	pitot pressure
$q_w$	heat transfer at wall
RANS	Reynolds-averaged Navier-Stokes
$Re_{\delta_\infty}$	$\rho_\infty U_\infty \ell_\infty / \mu_\infty$
$T_{aw}$	adiabatic wall temperature
$T_w$	wall temperature
$U_\infty$	freestream velocity
$W$	separation between fins (crossing shock)
$\alpha$	fin angle (sharp fin) cone angle of attack (cylinder-flare)
$\beta$	conical angle (Appendix B)
$\delta$	boundary layer thickness
$\phi$	spherical angle (Appendix B)
$\rho$	density
$\theta$	shock angle
$\infty$	evaluated in freestream

## 2 Introduction

The interaction of shock waves and turbulent boundary layers is a common phenomenon in aerodynamics and aeropropulsion, and significantly impacts the performance of aeronautical systems. Shock wave turbulent boundary layer interactions occur at wing- and tail-fuselage junctures, deflection of control surfaces, high speed inlets, transonic compressors, rotorcraft and many other applications.

The objective of the paper is to review the status of numerical simulation of 3-D shock wave-turbulent boundary layer interactions (also denoted as "3-D turbulent interactions"). The paper considers five fundamental 3-D turbulent interactions, assesses the capability for prediction of the flowfield through comparison with experiment, and briefly describes the principal features of the mean flowfield structure.

The focus of the paper is necessarily restricted due to practical limitations. Several decisions, admittedly a matter of personal taste, are reflected in the paper. First, the paper has been deliberately restricted to 3-D flows. Certainly, 3-D turbulent interactions are far more common in application than 2-D/axisymmetric turbulent interactions. However, knowledge of 2-D turbulent interactions is important to the understanding of 3-D turbulent interactions<sup>1</sup>, and research in 2-D/axisymmetric turbulent interactions bears some importance. Second, a limited number of 3-D configurations were selected based on the availability of both experimental and numerical results. To be sure, the selection

<sup>1</sup> E.g., the quasi-conical model of the sharp fin [1] is a two dimensional model of an ostensibly three dimensional flow.



is not exhaustive, and other 3-D configurations could be chosen with equal regard. In particular, the selected configurations are all in the Mach 2 to 8 regime. There is a substantial body of experimental and computational results on 3-D transonic shock wave turbulent boundary layer interactions, and their omission from this paper is due simply to practical limitations. Third, substantial effort has been made to provide an appropriate representation of computed results for the configurations chosen including extensive use of the AIAA Aerospace Database and consultation with colleagues. Any errors or other inaccuracies are inadvertent and, of course, the sole responsibility of this author. Fourth, since the paper focuses on assessing the capability for numerical simulation, it does not present a review of all experiments for those configurations selected. References [2], [3], [4] and [5] may be consulted for further information. Finally, numerical algorithms are not discussed. A reasoned consideration of numerical methods for 3-D turbulent interactions alone would constitute a separate paper. However, some discussion is focused on the need for further research in numerical methods for 3-D turbulent interactions.

### 3 Governing Equations

#### 3.1 Reynolds-Averaged Equations

The Reynolds-averaged equations for conservation of mass, momentum and energy are (see Appendix A),

$$\begin{aligned}\frac{\partial \bar{\rho}}{\partial t} + \frac{\partial \bar{\rho} \bar{u}_k}{\partial x_k} &= 0 \\ \frac{\partial \bar{\rho} \bar{u}_i}{\partial t} + \frac{\partial \bar{\rho} \bar{u}_i \bar{u}_k}{\partial x_k} &= \\ -\frac{\partial \bar{p}}{\partial x_i} + \frac{\partial}{\partial x_k} \left( -\overline{\rho u_i'' u_k''} + \bar{\tau}_{ik} \right) & \\ \frac{\partial \bar{\rho} \bar{e}}{\partial t} + \frac{\partial (\bar{\rho} \bar{e} + \bar{p}) \bar{u}_k}{\partial x_k} &= \\ \frac{\partial}{\partial x_k} \left( -c_p \overline{\rho T'' u_k''} - \bar{q}_k \right) + & \\ \frac{\partial}{\partial x_k} \left( -\overline{\rho u_i'' u_k''} \bar{u}_i + \bar{u}_i \bar{\tau}_{ik} \right) &\end{aligned}$$

where the Einstein summation convention is employed, and the overbar represents ensemble averaging, i.e.,

$$\bar{f} = \lim_{n \rightarrow \infty} \frac{1}{n} \sum_{\nu=1}^n f^{(\nu)}$$

where  $f^{(\nu)}$  are the individual realizations of the variable  $f(x, y, z, t)$ . The mass-averaged variable  $\bar{f}$  is defined as the density-weighted ensemble average,

$$\bar{f} = \frac{1}{\bar{\rho}} \lim_{n \rightarrow \infty} \frac{1}{n} \sum_{\nu=1}^n (\rho f)^{(\nu)}$$

and the fluctuating variable  $f''$  in the mass-averaged expansion is

$$f'' = f - \bar{f}$$

Alternately, the fluctuating variable  $f'$  in the unweighted expansion is

$$f' = f - \bar{f}$$

In the above,  $\bar{\rho}$  is the mean density,  $\bar{u}_i$  is the mass-averaged velocity,  $\bar{p}$  is the mean pressure, and  $\bar{e}$  is the mass-averaged total energy per unit mass,

$$\bar{e} = c_v \bar{T} + \frac{1}{2} \bar{u}_i \bar{u}_i + k$$

where  $k$  is the mass-averaged turbulence kinetic energy

$$\bar{\rho} k = \frac{1}{2} \overline{\rho u_i'' u_i''}$$

The equation of state is

$$\bar{p} = \bar{\rho} R \bar{T}$$

The mean molecular viscous stress  $\bar{\tau}_{ij}$  is

$$\bar{\tau}_{ij} = -\frac{2}{3} \bar{\mu} \frac{\partial \bar{u}_k}{\partial x_k} \delta_{ij} + \bar{\mu} \left( \frac{\partial \bar{u}_j}{\partial x_i} + \frac{\partial \bar{u}_i}{\partial x_j} \right)$$

where  $\bar{\mu} \equiv \mu(\bar{T})$ . Similarly, the molecular heat flux is

$$\bar{q}_k = -\frac{c_p \bar{\mu}}{Pr} \frac{\partial \bar{T}}{\partial x_k}$$

where  $Pr$  is the molecular Prandtl number.



### 3.2 Turbulence Models

Closure of the Reynolds-averaged Navier-Stokes equations requires additional equations for the turbulent stresses  $-\rho \overline{u_i'' u_k''}$  and turbulent heat flux  $-c_p \rho \overline{T'' u_k''}$ , collectively denoted as the "turbulent correlations". Following Reynolds [6], a taxonomy of turbulence closure models can be described:

#### Zero Equation

The turbulent correlations are expressed in terms of an eddy viscosity which is obtained from the mean field (*i.e.*, the velocity  $\bar{u}_k$ , density  $\bar{\rho}$  and temperature  $\bar{T}$ ) and a prescribed physical length scale which depends on the specific geometry of the problem. No additional partial differential equations are employed (hence the name "zero-equation").

#### One Equation

One additional partial differential equation is specified for a turbulence quantity (*e.g.*,  $k$ ). An eddy viscosity is typically employed for the turbulent correlations. A length scale is also prescribed which is geometry dependent.

#### Two Equation

Two additional partial differential equations are specified for two turbulence quantities (*e.g.*,  $k$  and the rate of dissipation of  $k$ ). An eddy viscosity is typically employed for the turbulent correlations. No additional length scale is needed.

#### Reynolds Stress Equation

Partial differential equations are specified for the components of the Reynolds stress  $-\rho \overline{u_i'' u_k''}$ . The turbulent heat flux  $-c_p \rho \overline{T'' u_k''}$  may be similarly modeled using a partial differential equation, or modeled using an turbulent eddy viscosity. No additional length scale is needed.

#### Large Eddy Simulation

These simulations involve a time-dependent, three-dimensional computation of the large-eddy structure and a model for the small-scale turbulent motions.

#### Direct Numerical Simulation

The direct numerical simulation involves the computation of all scales in a turbulent flow. These calculations are currently infeasible except for low Reynolds numbers and relatively simple geometries due to limitations on computer resources.

Numerical simulations of 3-D shock wave-turbulent boundary layer interaction have employed zero-, one- and two-equation turbulence closure models. The principal reasons for this trend have been simplicity and cost. It is reasonable to assess first the capability of simple turbulence models for the prediction of 3-D turbulent interactions. Also, the more sophisticated turbulence models (*e.g.*, Reynolds Stress Equation) require substantially greater computer resources than simpler models. As our knowledge of the capabilities and limitations of various turbulence closure models improves, and cost of computation decreases, the trend is towards more sophisticated models of turbulence.

The development of turbulence models for moderately compressible flows has been based on a straightforward extension of their incompressible counterparts, *i.e.*, allowing the density to be variable. The justification for this action is Morkovin's hypothesis [7]. For turbulent boundary layers, Morkovin's hypothesis states that the turbulence structure is unaffected by compressibility provided that the Mach number is less than approximately 5 (*i.e.*, non-hypersonic) and the wall is adiabatic or near-adiabatic. A detailed discussion of Morkovin's hypothesis is provided by Bradshaw [8].

The recent renewed interest in hypersonic flight has focused attention on the need to understand the effects of compressibility for hypersonic turbulent boundary layers and supersonic shear layers, and the inadequacy of simple extensions of incompressible turbulence models to these cases. Perhaps the most widely cited example is the supersonic free shear layer wherein the rate of growth is significantly affected by compressibility [9].

In the following sections, the overscripts  $'$  and  $''$  are omitted for clarity.

## 4 Results

A representative group of 3-D turbulent interactions are reviewed in this section. The choices are intended to be illustrative, and certainly do not include all configurations studied. Also, the selection reflects, to some extent, the interests and research of the author. Nonetheless, the specific examples manifest the general trends of



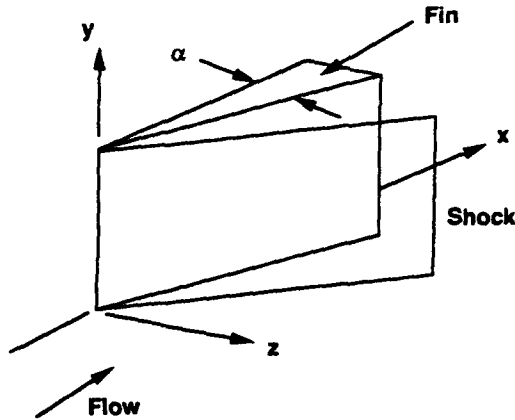


Figure 1: Geometry of sharp fin

numerical simulation of 3-D turbulent interactions.

#### 4.1 Sharp Fin

The sharp fin geometry is a wedge attached normal to a flat plate (Fig. 1) on which an equilibrium turbulent boundary layer has developed. The wedge generates an oblique shock wave which interacts with the boundary layer on the flat plate. The flow parameters are the Mach number  $M_\infty$ , Reynolds number  $Re_{\delta_\infty}$ , fin angle  $\alpha$  and wall temperature ratio  $T_w/T_{aw}$ .

A representative group of computations of the sharp fin are listed in Table 1, ordered by the magnitude of the normal shock Mach number  $M_n = M_\infty \sin \theta$  as suggested by Alvi and Settles [1] where  $M_\infty$  is the freestream Mach number and  $\theta$  is the shock angle. Equivalently, the cases could be ordered on the basis of the inviscid pressure ratio

$$\frac{p_2}{p_1} = \frac{2\gamma M_n^2 - (\gamma - 1)}{\gamma + 1}$$

where  $p_1$  and  $p_2$  are the static pressure upstream and downstream, respectively, of the inviscid shock. The computations have employed a variety of zero-, one- and two-equation turbulence models. While most of the calculations employed the three-dimensional Reynolds Averaged Navier-Stokes equations, the sharp fin has also been computed using the conical Reynolds Averaged Navier-Stokes equations based on the

observed conical behavior<sup>2</sup> of certain aspects of the single fin interaction outside of an inception region at the fin leading edge (see, for example, refs. [10, 1, 11, 2, 5, 3, 12, 13]).

Table 1 Sharp Fin Computations

$M_n$	$M_\infty$	$\alpha$	Model	Type	Eqns	Ref
1.13	2.9	4°	Esc	0	3-D	[14]
			B-L	0	3-D	[15]
1.21	2.0	8°	Esc	0	3-D	[14]
1.36	2.9	10°	Esc	0	3-D	[14]
			B-L	0	3-D	[15]
1.38	3.0	10°	J-L	2	3-D	[16]
1.44	5.9	6°	Esc	0	3-D	[17]
1.50	4.9	8°	B-L	0	Con	[18]
1.65	3.0	16°	J-L	2	3-D	[16]
1.82	2.9	20°	B-L	0	3-D	[19]
			J-L	2	3-D	[19]
			B-L	0	3-D	[20]
1.84	3.0	20°	J-L	2	3-D	[16]
1.88	4.0	16°	B-L	0	3-D	[21]
			J-L	2	3-D	[21],[16]
1.99	5.9	12°	Esc	0	3-D	[17]
2.12	4.9	16°	B-L	0	Con	[18]
2.15	4.0	20°	B-L	0	3-D	[21]
			J-L	2	3-D	[21, 16]
			B-L	0	Con	[12]
2.18	8.2	10°	Rodi	2	3-D	[22]
			$k - \omega$	2	3-D	[23]
			B-L	0	3-D	[23]
2.90	8.2	15°	Rodi	2	3-D	[22]
			$k - \omega$	2	3-D	[23]

Legend:

$M_n$	normal Mach number ( $\equiv M_\infty \sin \theta$ )
$M_\infty$	freestream Mach number
$\alpha$	fin angle
Model	turbulence model
B-L	Baldwin-Lomax model [24]
Esc	Escudier model [25]
J-L	Jones-Launder model [26]
Rodi	Rodi model [27]
$k - \omega$	$k - \omega$ model [28]
Type	type of turbulence model (0 = Zero Equation, etc)
Eqns	equations solved
3-D	3-D RANS equations
Con	conical RANS equations

<sup>2</sup>See Appendix 2 for definition of conical flow.



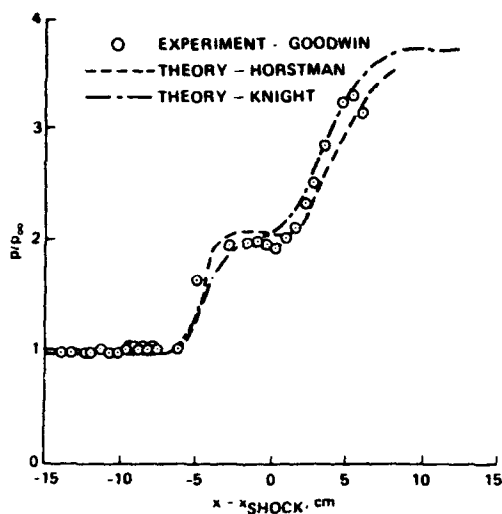


Figure 2: Surface pressure for sharp fin at  $M_\infty = 2.9, \alpha = 20^\circ, Re_{\delta_\infty} = 9 \times 10^5$

Many of the principal features of the surface pressure are predicted with reasonable accuracy by all of the turbulence models examined. In Fig. 2, results are shown for  $M_n = 1.82$  ( $M_\infty = 2.9, \alpha = 20^\circ$ ) for the Baldwin-Lomax model ("Theory-Knight") and the Jones-Launder model ("Theory-Horstman"). The abscissa is the streamwise distance measured from the inviscid shock location at a spanwise distance  $6.8\delta_\infty$  from the plane of symmetry. The computed profiles are in close agreement with the experimental data of Goodwin [29].

In Fig. 3, results are shown for  $M_n = 2.15$  ( $M_\infty = 4.0, \alpha = 20^\circ$ ) for the Baldwin-Lomax model. The abscissa is the conical angle  $\beta$  (see Appendix 2). The computed profiles display general agreement with the experimental data of Settles *et al* [10, 1, 11] with regards to the peak corner pressure and plateau pressure. However, the angle of the line of upstream influence, defined as the location of the inception of the pressure rise, is underestimated by approximately 10%, and the slight decrease in surface pressure near  $\beta = 29^\circ$  (which is associated with secondary separation) is not predicted. Similar results have been observed using the Baldwin-Lomax model for other sharp fin cases (*e.g.*, [30]).

In Fig. 4 results are shown for  $M_n = 2.90$  ( $M_\infty = 8.2, \alpha = 15^\circ$ ) for the Jones-Launder

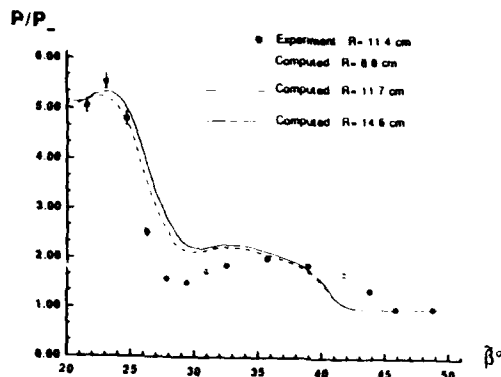


Figure 3: Surface pressure for sharp fin at  $M_\infty = 4.0, \alpha = 20^\circ, Re_{\delta_\infty} = 2.2 \times 10^5$

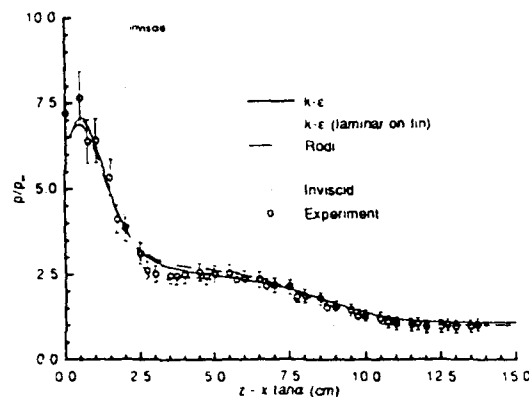


Figure 4: Surface pressure for sharp fin at  $M_\infty = 8.2, \alpha = 15^\circ, Re_{\delta_\infty} = 1.9 \times 10^5$

and Rodi models<sup>3</sup>. The abscissa is the spanwise distance measured from the fin surface at  $x = 4.9\delta_\infty$ . The agreement between the computation and experiment [31] is good. Similar close agreement was obtained for the  $k-\omega$  model [23].

The pitot pressure and yaw angle profiles within the interaction flowfield are predicted with reasonable accuracy by all of the turbulence models examined except close to the surface. The yaw angle is defined as  $\tan^{-1}(w/u)$  where  $u$  and  $w$

<sup>3</sup>Computations have also been performed for this configuration using the Baldwin-Lomax model and the conical RANS [22]. Recent results [23] suggest, however, that the assumption of conical flow within the region of experimental measurements is incorrect for this case, and therefore the conical RANS computations using the Baldwin-Lomax model are not presented herein.



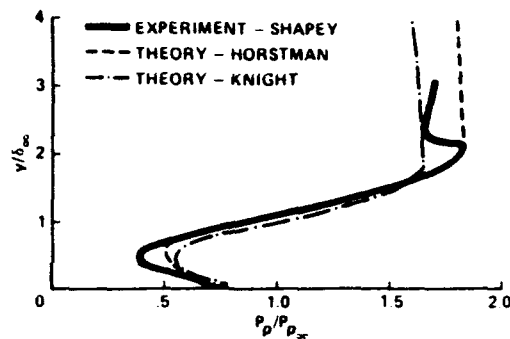


Figure 5: Pitot pressure for sharp fin at  $M_\infty = 2.9, \alpha = 20^\circ, Re_{\delta_\infty} = 9.0 \times 10^5$

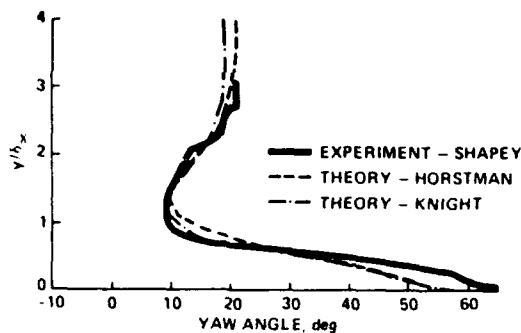


Figure 6: Yaw angle for sharp fin at  $M_\infty = 2.9, \alpha = 20^\circ, Re_{\delta_\infty} = 9.0 \times 10^5$

are the velocity components in the  $x$  and  $z$  directions, respectively (Fig. 1). In Fig. 5, computed and experimental pitot pressure profiles are shown for  $M_n \approx 1.82$  ( $M_\infty = 2.9, \alpha = 20^\circ$ ). Results are shown for the Baldwin-Lomax model ("Theory-Knight") and Jones-Launder model ("Theory-Horstman"). The profile location is immediately beneath the inviscid shock at a spanwise location of  $5.3 \delta_\infty$ . The agreement between the computations and experiment is generally good<sup>4</sup>. The minimum pitot pressure at  $y/\delta_\infty \approx 0.5$  is associated with the core of the vortex generated by the shock boundary layer interaction [19].

In Fig. 6, computed and experimental yaw angle

<sup>4</sup>The differences in computed pitot pressure for  $y/\delta_\infty > 2$  are associated with the shock capturing nature of the numerical algorithms, as the profile location coincides with the inviscid shock.

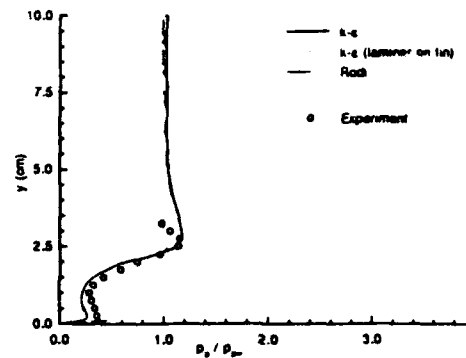


Figure 7: Pitot pressure for sharp fin at  $M_\infty = 8.2, \alpha = 15^\circ, Re_{\delta_\infty} = 1.9 \times 10^5$

profiles are displayed at the same location as Fig. 5. Except in the immediate vicinity of the wall, the comparison between the computed and experimental profiles is generally good. Near the surface, typical differences of 10% are observed between the computation and experiment, and between the two computations themselves<sup>5</sup>.

In Fig. 7, computed and experimental pitot pressure profiles are shown for  $M_n = 2.90$  ( $M_\infty = 8.2, \alpha = 15^\circ$ ) for the Jones-Launder and Rodi models. The location is within the 3-D turbulent interaction, and upstream of the inviscid shock wave. The agreement with experiment is good, and no significant difference is seen between the computations.

In Fig. 8, computed and experimental yaw angle profiles are displayed at the same position. Generally, the computations show reasonable agreement with experiment, except in the immediate vicinity of the surface where significant discrepancies are evident. In particular, the Rodi model overestimates the surface yaw angle by 17%, while the Jones-Launder model exceeds the experimental value by 31%.

The principal features of the heat transfer distribution on the flat plate are predicted with reasonable accuracy by the turbulence models examined, although a detailed comparison displays significant discrepancies in some cases. In Fig. 9, the computed and measured heat transfer coefficient  $c_h$  on the flat plate, normalized by

<sup>5</sup>In the latter case, the differences are very close to the surface and not readily visible in the figure.



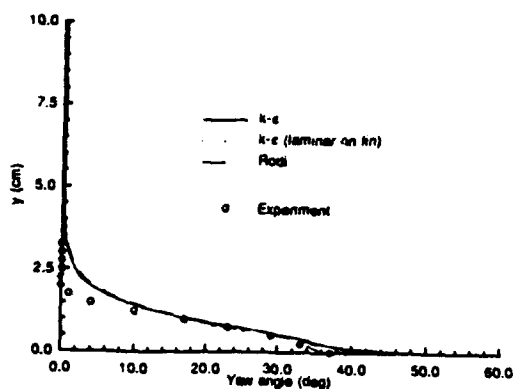


Figure 8: Yaw angle for sharp fin at  $M_\infty = 8.2, \alpha = 15^\circ, Re_{\delta_\infty} = 1.9 \times 10^5$

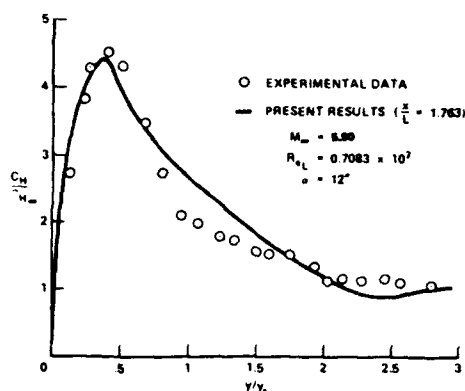


Figure 9: Heat transfer for sharp fin at  $M_\infty = 5.9, \alpha = 12^\circ, Re_{\delta_\infty} = 1.3 \times 10^5$

the upstream value  $c_{h_\infty}$ , are shown for  $M_n = 2.0$  ( $M_\infty = 5.9, \alpha = 12^\circ$ ). The computations employed the Escudier model. The abscissa is the spanwise distance measured from the fin surface and normalized by the spanwise distance between the fin and inviscid shock at the measurement location. The computed profile displays the general trend of the experimental data. The peak heat transfer, a particularly important parameter in design, is accurately predicted. However, the computed  $c_h$  overpredicts the experiment within the region surrounding the inviscid shock wave ( $y/y_s \approx 1$ ).

In Fig. 10, the computed and measured heat transfer coefficient  $c_h$ , normalized by the upstream value  $c_{h_\infty}$ , are displayed for  $M_n = 2.12$  ( $M_\infty = 4.92, \alpha = 16^\circ$ ). The computations em-

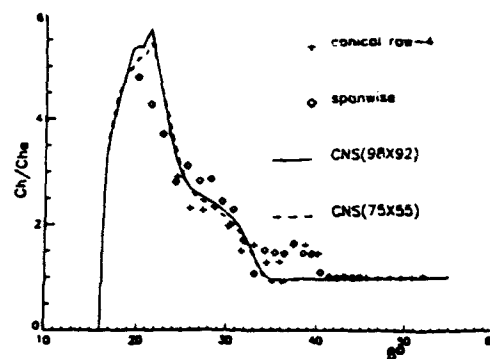


Figure 10: Heat transfer for sharp fin at  $M_\infty = 5.0, \alpha = 16^\circ, Re_{\delta_\infty} = 2.4 \times 10^5$

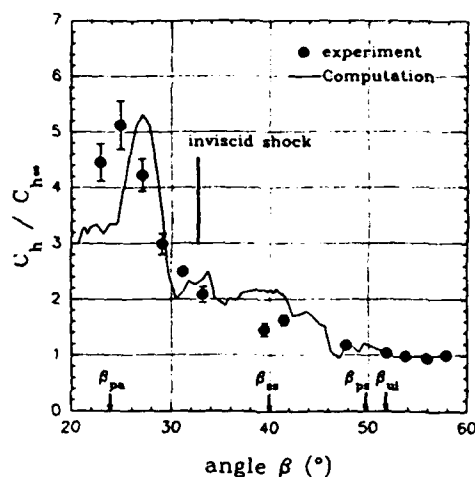


Figure 11: Heat transfer for sharp fin at  $M_\infty = 4.0, \alpha = 20^\circ, Re_{\delta_\infty} = 2.0 \times 10^5$

ployed the Baldwin-Lomax model and the conical RANS. The abscissa is the polar angle  $\beta$  (see Appendix 2). The computed profile displays the general trend of the experimental data, and predicts the peak  $c_h$  within 15%; however, the initial increase in  $c_h$  near the line of upstream influence at  $\beta = 43^\circ$  is not observed in the computations.

In Fig. 11, the computed and measured  $c_h$ , normalized by the upstream value  $c_{h_\infty}$  are shown for  $M_n = 2.15$  ( $M_\infty = 4.0, \alpha = 20^\circ$ ). Results are shown for the Jones-Launder model. The abscissa is the polar angle  $\beta$  (see Appendix 2), and the results are shown at a radial distance of  $31\delta_\infty$  from the fin leading edge. The computed profile displays the general trend of the



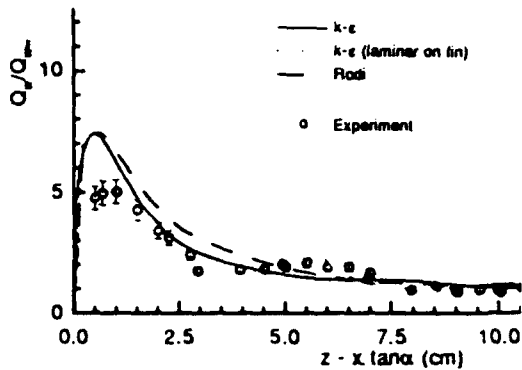


Figure 12: Heat transfer for sharp fin at  $M_\infty = 8.2, \alpha = 15^\circ, Re_{\delta_\infty} = 9 \times 10^5$

experimental data and accurately estimates the peak value of  $c_h$ ; however, the location of the computed peak  $c_h$  differs from the experiment by 10% in  $\beta$ , and the computed  $c_h$  significantly underestimates the experiment near the corner. The small drop in  $c_h$  in the vicinity of the secondary separation line at  $\beta = 40^\circ$  is not observed in the computation.

In Fig. 12, the computed and measured wall heat transfer  $q_w$ , normalized by the upstream wall heat transfer  $q_{w_\infty}$ , is displayed for  $M_n = 2.9$  ( $M_\infty = 8.2, \alpha = 15^\circ$ ). Results are shown for the Jones-Launder and Rodi models. The abscissa is the spanwise distance measured from the fin surface at the experimental measurement location  $x = 4.5\delta_\infty$ . The computed profiles display the general trend of the experiment; however, the peak heat transfer coefficient is overestimated by 48%.

In Fig. 13, the computed and measured wall heat is shown for the same conditions as Fig. 12 for the  $k - \omega$  model. The computed profiles exhibit similar trends as the experiment. The peak heat transfer is predicted within 10%; however, differences elsewhere as large as 40% are evident elsewhere.

The principal features of the skin friction distribution on the flat plate are predicted with a level of accuracy similar to the surface heat transfer. In Fig. 14, the computed and measured skin friction coefficient  $c_f$  on the flat plate are shown for  $M_n = 1.88$  ( $M_\infty = 4, \alpha = 16^\circ$ ). Results

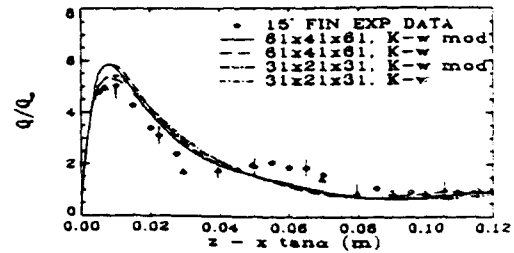


Figure 13: Heat transfer for sharp fin at  $M_\infty = 8.2, \alpha = 15^\circ, Re_{\delta_\infty} = 9 \times 10^5$

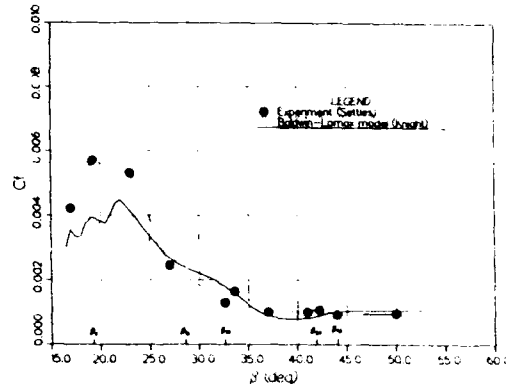


Figure 14: Skin friction for sharp fin at  $M_\infty = 4.0, \alpha = 16^\circ, Re_{\delta_\infty} = 2.0 \times 10^5$

are shown for the Baldwin-Lomax model. The abscissa is the polar angle  $\beta$  (see Appendix 2), and the results are shown at a radial distance of  $30\delta_\infty$  from the fin leading edge. The computed profile displays the basic trend of the experimental data; however, the peak  $c_f$  is underestimated by 22%. The small drop in  $c_f$  associated with the secondary separation line at  $\beta = 32.5^\circ$  is not observed in the computation.

In Fig. 15, the computed and measured  $c_f$  are shown for  $M_n = 2.18$  ( $M_\infty = 8.2, \alpha = 10^\circ$ ). Results are presented for the Jones-Launder model. The abscissa is the spanwise distance measured from the fin surface at  $x = 4.2\delta_\infty$ . The computed profiles display good agreement with experiment; in particular, the peak  $c_f$  is predicted within the experimental uncertainty.

In Fig. 16, the computed and measured  $c_f$  are shown for  $M_n = 2.9$  ( $M_\infty = 8.2, \alpha = 15^\circ$ ). Results are presented for the Jones-Launder and



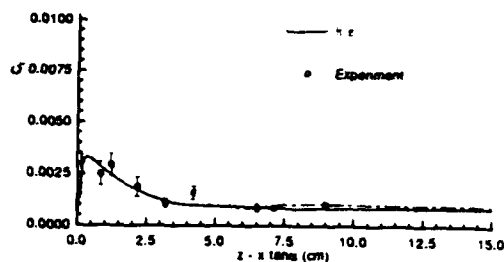


Figure 15: Skin friction for sharp fin at  $M_\infty = 8.2, \alpha = 10^\circ, Re_{\delta_\infty} = 1.9 \times 10^5$

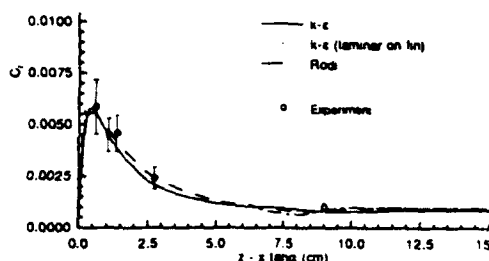


Figure 16: Skin friction for sharp fin at  $M_\infty = 8.2, \alpha = 15^\circ, Re_{\delta_\infty} = 1.9 \times 10^5$

Rodi models. The abscissa is the spanwise distance measured from the fin surface at  $z = 4.2\delta_\infty$ . The computed profiles again display good agreement with experiment, and predict the peak  $C_f$  within the experimental uncertainty.

In Fig. 17, the computed and measured skin friction is shown for the same conditions as Fig. 16 for the  $k - \omega$  model. The computed profiles exhibit similar trends as the experiment. The skin friction is predicted within the experimental uncertainty.

The results described above indicate that the computed pitot pressure and yaw angle are relatively insensitive to the particular choice of turbulence model, except in the immediate vicinity of the surface. Similarly, the computed surface pressure is insensitive to the turbulence

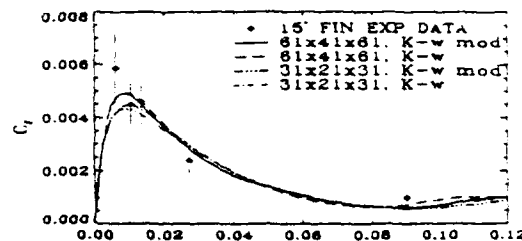


Figure 17: Skin friction for sharp fin at  $M_\infty = 8.2, \alpha = 15^\circ, Re_{\delta_\infty} = 1.9 \times 10^5$

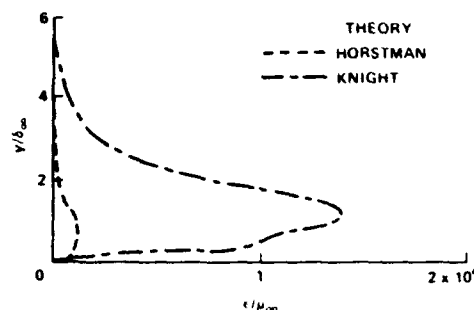


Figure 18: Turbulent eddy viscosity for sharp fin at  $M_\infty = 3.0, Re_{\delta_\infty} = 9.0 \times 10^5, \alpha = 20^\circ$

model. A detailed comparison of the computed turbulent eddy viscosity was conducted for  $M_\infty = 1.84$  ( $M_\infty = 3, \alpha = 20^\circ$ ). An example is shown in Fig. 18 at  $z = 11\delta_\infty$  at a spanwise distance of  $6\delta_\infty$  from the fin which corresponds to a location within the 3-D interaction. The computed eddy viscosities for the Baldwin-Lomax (denoted "Knight") and Jones-Launder (denoted "Horstman") models differ by as much as a factor of 14, while the computed pitot pressure, yaw angle and pitch angle<sup>6</sup> profiles agree to within a few percent except very close to surface (i.e., within approximately the lowest 10% of the boundary layer) [19].

These results indicate that the flowfield is predominantly rotational and inviscid, except in a thin region<sup>7</sup> adjacent to the flat plate. This result is conceptually similar to the triple-deck

<sup>6</sup>The pitch angle is defined as  $\tan^{-1}(v/\sqrt{u^2 + w^2})$ , and represents the angle of the mean velocity vector measured vertically from the flat plate.

<sup>7</sup>I.e., thin compared to the upstream boundary layer thickness  $\delta_\infty$ .



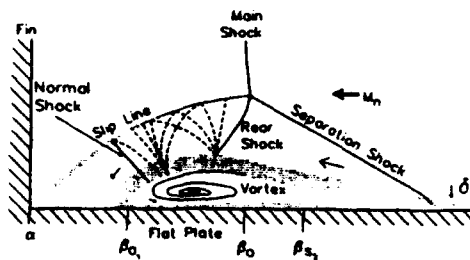


Figure 19: Quasi-conical flowfield model for single fin [1]

theory developed for interacting boundary layers (e.g., Stewartson [32]) and extended to non-separated 3-D shock wave-turbulent boundary layer interactions by Inger [33, 34, 35]. The first region ("deck") is immediately adjacent to the flat plate. In this region, the flow dynamics are governed by both viscous and inviscid effects. The turbulent stresses and heat transfer (and hence, the turbulence model) are important to the flow physics. The second region, immediately above the first deck, is rotational and inviscid to a first approximation, i.e., turbulent stresses and heat transfer are higher order effects. This region comprises most of the boundary layer<sup>8</sup>. The third region is the two-dimensional inviscid, irrotational wedge flow.

These observations imply that the turbulence model is important for the prediction of surface skin friction and heat transfer. The majority of the computed flowfield, however, is relatively insensitive to the turbulence model provided the proper upstream boundary layer profile is prescribed.

The mean flowfield has been found in both experiment and computation to be quasi-conical outside an inception region near the fin leading edge (see, for example, refs. [10, 1, 11, 2, 5, 3, 12, 13]). This allows a substantial simplification in the description of the flowfield structure

<sup>8</sup> It is difficult to prescribe a precise definition of the local boundary layer thickness in a 3-D turbulent interaction. Nonetheless, it is possible to envision the boundary layer region for the 3-D single fin as the domain wherein the flowfield differs significantly from the 2-D inviscid wedge flow.

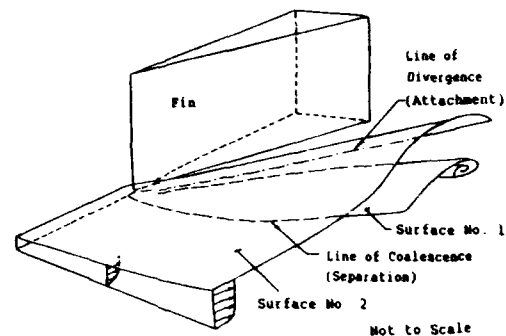


Figure 20: Entrainment into vortex for sharp fin

for strong interactions as shown in Fig. 19. The main shock bifurcates into a separation and rear shock. A portion of the incoming flow is entrained into the vortex (Fig. 20). The level of entrainment depends on  $M_n$ . The incoming flow originating above the entrainment surface flows over the vortex and attaches obliquely on the flat plate, causing enhanced skin friction and heat transfer. The wave structure associated with the attaching flow includes compression by the separation and rear shocks, expansion over the leeside of the vortex, and recompression near the flat plate.

## 4.2 Blunt Fin

The blunt fin geometry is a fin of constant thickness with rounded leading edge, and attached normal to a flat plate (Fig. 21) on which an equilibrium turbulent boundary layer has developed. The blunt leading edge generates a shock wave which interacts with the boundary layer on the flat plate. The flow parameters are the Mach number  $M_\infty$ , Reynolds number  $Re_{\delta_\infty}$ , ratio of boundary layer thickness  $\delta_\infty$  to leading edge diameter  $D$ , and wall temperature ratio  $T_w/T_{aw}$ .

The computations of the blunt fin are listed in Table 2. Computations have been performed for  $M_\infty = 2.95$  and  $3.71$  at Reynolds numbers from  $Re_{\delta_\infty} = 0.8 \times 10^5$  to  $9 \times 10^5$  and approximately adiabatic wall temperatures. The only turbulence model employed is Baldwin-Lomax.



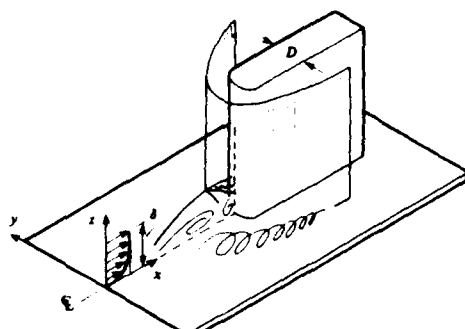


Figure 21: Geometry for blunt fin

Table 2 Blunt Fin Computations

$M_\infty$	$\delta_\infty/D$	$Re_{\delta_\infty}$	Model	Type	Ref
2.95	0.10	$0.8 \times 10^5$	B-L	0	[36]
	0.26	$2.1 \times 10^5$	B-L	0	[36]
	1.00	$8.0 \times 10^5$	B-L	0	[36]
3.71	1.00	$4.3 \times 10^5$	B-L	0	[37]

Legend:

$M_\infty$  freestream Mach number  
 $\delta_\infty$  boundary layer thickness  
 $D$  diameter of fin leading edge  
 Model turbulence model  
 B-L Baldwin-Lomax model [24]  
 Type type of turbulence model  
 (0 = Zero Equation, etc)

The computed surface pressure shows good agreement with experiment. The computed pressure on the fin surface for  $M_\infty = 2.95$  and  $\delta_\infty/D = 1.0$  is shown in Fig. 22 at  $\phi = 0^\circ$  and  $45^\circ$ , where  $\phi$  is the polar angle measured from the leading edge of the blunt fin. The ordinate is the distance normal to the flat plate, and the abscissa is the surface static pressure normalized by the total pressure  $p_{t2}$  behind a normal shock at the freestream Mach number. Overall, there is close agreement between the computation and experiment. The peak pressure at  $z/D \approx 1.2$  is due to the supersonic jet formed by the Edney Type IV interference associated with the intersection of the separation shock (Fig. 23) and bow shock [38], although no such supersonic region was observed in the computation due possibly to inadequate grid resolution.

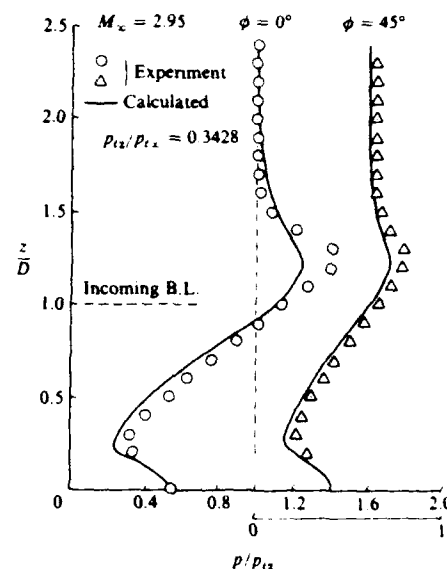
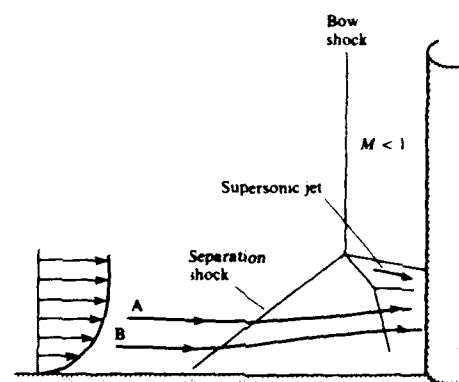
Figure 22: Static pressure for blunt fin on  $\phi = 0^\circ$  and  $45^\circ$ 

Figure 23: Shock structure for blunt fin



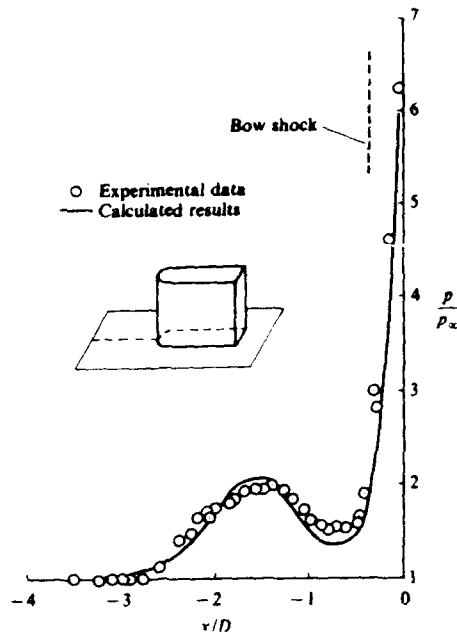


Figure 24: Static pressure for blunt fin on centerline

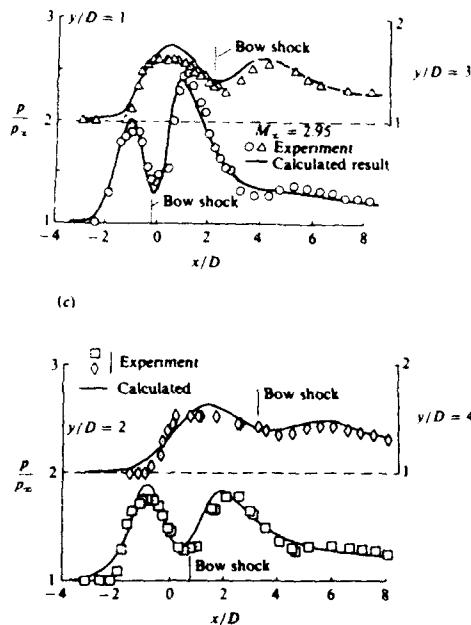


Figure 25: Static pressure for blunt fin on  $y/D = 1, 2, 3$  and  $4$

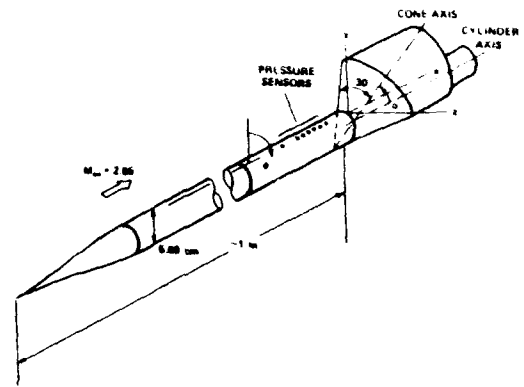


Figure 26: Geometry for cylinder/flare

The surface pressure on the symmetry plane (Fig. 24) shows similar close agreement between computation and experiment. It is known, however, that the separation shock wave is unsteady with substantial motion on the scale of the fin diameter  $D$  [39, 40], and thus the upstream portion of the mean experimental surface pressure distribution represents the average signal associated with a moving shock. Since  $D$  may be large or comparable to  $\delta_\infty$ , the Reynolds-averaged Navier-Stokes equations may be formally capable of resolving the unsteady shock motion provided the effects of turbulence are properly modeled and sufficient grid resolution is employed. To date, computations of the blunt fin have been found to be steady. This discrepancy may be attributable to inadequate grid refinement and/or inaccuracies in the turbulence model. The surface pressure at  $y/D = 1, 2, 3$  and  $4$ , shown in Fig. 25, show similar close agreement between computation and experiment.

#### 4.3 Cylinder/Flare

The asymmetric cylinder/flare geometry, shown in Fig. 26, is a cylinder and a frustum of a cone (flare) whose centerline is offset relative to the cylinder axis. The cone generates a three-dimensional shock wave which interacts with the boundary layer on the cylinder. The flow parameters are the Mach number  $M_\infty$ , Reynolds number  $Re_{\delta_\infty}$ , cone half-angle  $\beta$ , cone angle of attack  $\alpha$  and wall temperature ratio  $T_w/T_{aw}$ .

The computations of the cylinder/flare are listed in Table 3. A single study of the asymmetric



cylinder/flare has been performed [41, 42, 43] at  $M_\infty = 2.85$ ,  $Re_{\delta_\infty} = 1.8 \times 10^5$ ,  $\beta = 30^\circ$ ,  $\alpha = 5^\circ$  and  $10^\circ$ , and approximately adiabatic wall conditions. The computations employed the Jones-Launders turbulence model with the Viegas-Rubens wall functions [44].

**Table 3 Cylinder/Flare Computations**

$M_\infty$	$\alpha$	$\beta$	Model	Type	Ref
2.85	5°	30°	J-L	2	[42, 43]
	10°	30°	J-L	2	[42, 43]

Legend:

$M_\infty$  freestream Mach number  
 $\alpha$  cone angle of attack  
 $\beta$  cone half-angle  
 Model turbulence model  
 J-L Jones-Launders model [26]  
 Type type of turbulence model  
 (0 = Zero Equation, etc)

The basic flow structure on the windward plane of symmetry is shown in Fig. 27. The flare deflects the flow by an angle  $\alpha + \beta$  through a shock system. Within the neighborhood of the boundary layer, a bifurcated shock is formed whose upstream and downstream segments are denoted the separation and reattachment shocks. The adverse pressure gradient associated with the shock system causes separation of the turbulent boundary layer and formation of a recirculation vortex. High speed shadowgraph movies synchronized with wall pressure measurements have demonstrated that the entire shock system is unsteady with streamwise excursions on the order of  $\delta_\infty$  which increase in amplitude with increasing  $\alpha$ . Therefore, the flow structure in Fig. 27 represent an instantaneous image.

The computed and experimental mean surface pressure on the windward symmetry plane are displayed in Fig. 28 for  $\alpha = 5^\circ$  and  $10^\circ$ . The upstream influence point (i.e., the location of the initial rise in surface pressure) is underpredicted by  $1.1\delta_\infty$  and  $1.2\delta_\infty$  for  $\alpha = 5^\circ$  and  $10^\circ$ , respectively. The experimental surface pressure distribution represents the time average of a pressure signal caused by a shock system moving on the scale of the mean flow (i.e.,  $\delta_\infty$ ). The computed flowfield flowfield was found to be steady, in

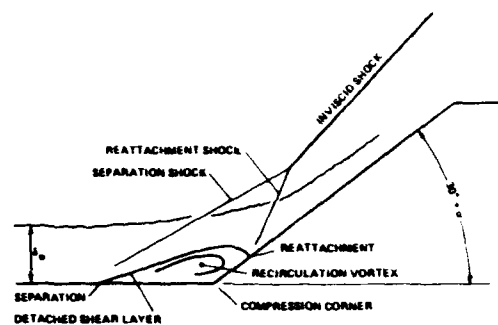


**Figure 27: Flowfield for cylinder/flare**

contrast to the experiment, and therefore close agreement with the experimental surface pressure in the vicinity of the upstream influence point is not expected. The computed profile overestimates the plateau pressure by typically 15% to 20%. The rapid pressure rise downstream of the corner ( $x > 0$ ) is accurately predicted.

The mean velocity profiles in the  $x$ -direction are not accurately predicted. The computed and measured mean velocity are displayed in Fig. 29 for  $\alpha = 10^\circ$ . In the vicinity of the upstream limit of the surface pressure plateau region (e.g.,  $x = -3.0$  and  $-2.5$  cm), significant differences are evident. These may be attributable to the lack of unsteadiness in the computed shock system. Downstream of the corner ( $x > 0$ ), the calculated profiles show substantial disagreement with experiment.

The turbulence kinetic energy  $k$  profiles are also inaccurately predicted. The computed and measured  $k$  are shown in Fig. 30 for  $\alpha = 10^\circ$ . The calculated profiles differ substantially from the experiment at all locations within the interaction.

In summary, the computed flowfield displays significant differences with experiment. The most important defect in the numerical simulation may well be the absence of unsteadiness in the computed shock system. Since the scale of the unsteadiness ( $\approx 1\delta_\infty$ ) is comparable to overall size of the interaction ( $\approx 8\delta_\infty$ ), a substantial fraction of the experimental flowfield may arguably be regarded as strongly influenced by the shock unsteadiness. Further research is needed



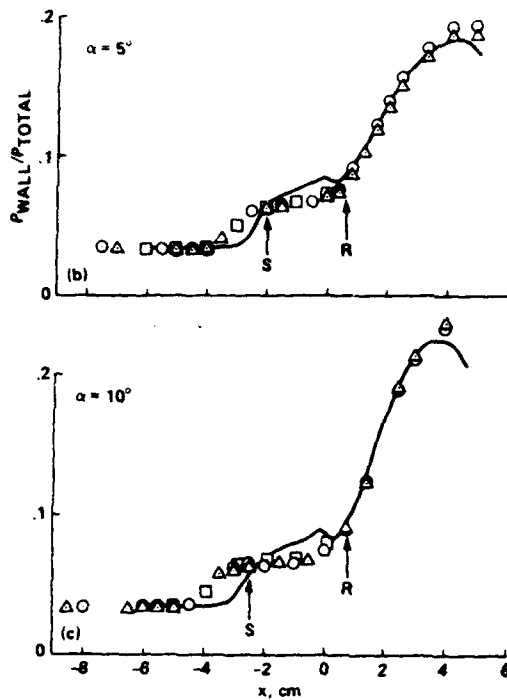


Figure 28: Surface pressure for cylinder/flare

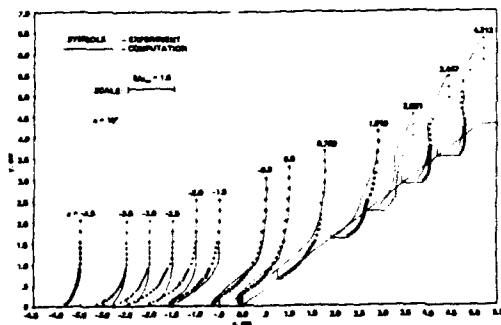


Figure 29: Velocity for cylinder/flare

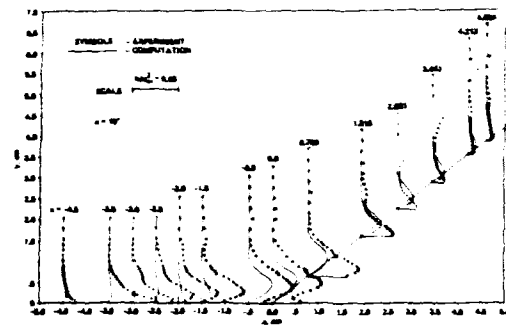


Figure 30: Turbulence kinetic energy for cylinder/flare

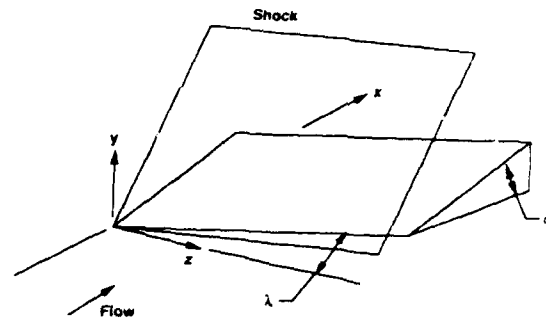


Figure 31: Geometry for swept compression corner

to improve the accuracy of the numerical simulation.

#### 4.4 Swept Compression Corner

The swept compression corner geometry, shown in Fig. 31, is a compression corner swept downstream. The compression corner generates a shock wave which interacts with the boundary layer on the flat plate. There is a symmetry plane at the apex of the swept corner ( $z = 0$ ). The flow parameters are the Mach number  $M_\infty$ , Reynolds number  $Re_{\delta_\infty}$ , compression angle  $\alpha$  measured in the streamwise  $x$ - $y$  plane, sweep angle  $\lambda$ , and wall temperature ratio  $T_w/T_{aw}$ . The sharp fin is the limiting case  $\alpha = 90^\circ$ .

The computations of the swept compression corner are listed in Table 4. All computations known to the author have been performed for  $M_\infty = 2.95$ . The Reynolds numbers vary from



$Re_{\delta_{\infty}} = 1.4 \times 10^5$  to  $9 \times 10^5$ . The wall temperature is approximately adiabatic.

**Table 4 Swept Compression Corner Computations**

$M_{\infty} = 2.95$

$\alpha$	$\lambda$	Model	Type	Ref
24°	40°	C-S	0	[45, 46]
		J-L	2	[45, 46]
				[47, 48]
24°	60°	B-L	0	[47, 48]
		B-L	0	[48, 49]
		J-L	2	[48, 49]
30°	60°	B-L		[50]
5° → 24°	0 → 60°	J-L	2	[51]

Legend:

$M_{\infty}$  freestream Mach number  
 $\alpha$  compression angle  
 $\lambda$  sweep angle  
Model turbulence model  
B-L Baldwin-Lomax model [24]  
C-S Cebeci-Smith model [52]  
J-L Jones-Launder model [26]  
Type type of turbulence model  
(0 = Zero Equation, etc)

There is general agreement between the computed and experimental surface pressure. In Figs. 32, results are shown for  $M_{\infty} = 2.95$ ,  $\alpha = 24^\circ$  and  $\lambda = 40^\circ$ . The abscissa is the streamwise distance measured from the corner line  $x_{\text{corner}} = z \tan \lambda$ . Results are shown at a spanwise location  $z/\delta_{\infty} = 10$ . The computations employed the Cebeci-Smith model (Case 3), Jones-Launder model integrated to the wall (Case 4) and Baldwin-Lomax model (Case 5). The computed profiles using all three turbulence models are in general agreement with experiment. (No experimental data was available downstream of the corner line). Except in the immediate vicinity of the line of upstream influence (i.e., the location of the initial pressure rise), the calculated pressure for all cases is within 14% of the experiment. The Baldwin-Lomax model underestimates the upstream influence, but predicts the level of pressure plateau with greater accuracy. The Cebeci-Smith and Jones-Launder models agree more closely with

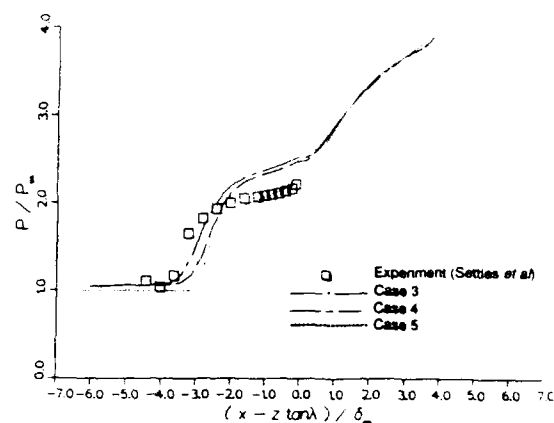


Figure 32: Surface pressure for swept compression corner for  $\alpha = 20^\circ$  and  $\lambda = 40^\circ$

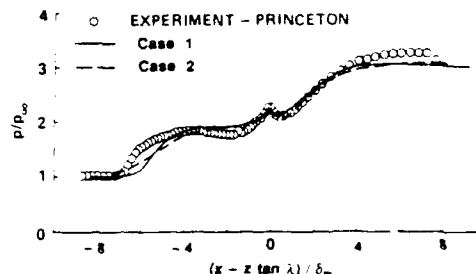


Figure 33: Surface pressure for swept compression corner for  $\alpha = 20^\circ$  and  $\lambda = 60^\circ$

the experimental upstream influence line, but overestimate the plateau pressure.

In Fig. 33, results are shown for  $\alpha = 24^\circ$  and  $\lambda = 60^\circ$  at a spanwise location  $z/\delta_{\infty} = 7.85$ . The computations employed the Baldwin-Lomax model (Case 1) and Jones-Launder model with the Viegas-Rubens [44] wall functions (Case 2). The computed profiles using both turbulence models display good agreement with experiment. Notwithstanding the underestimation of the upstream influence line, the computed surface pressure agrees with experiment to within 10%.

The pitot pressure is predicted with reasonable accuracy by all turbulence models examined. The computed and experimental pitot pressure for  $M_{\infty} = 2.95$ ,  $\alpha = 24^\circ$ , and  $\lambda = 40^\circ$  are displayed in Figs. 34 to 36 at  $z = 7\delta_{\infty}$  and



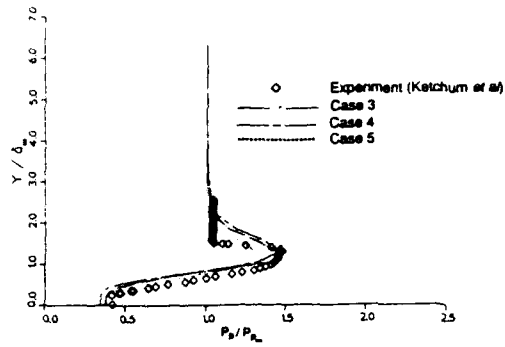


Figure 34: Pitot pressure for swept compression corner for  $\alpha = 20^\circ$  and  $\lambda = 40^\circ$

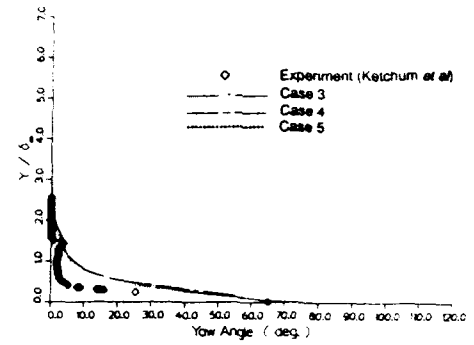


Figure 37: Yaw angle for swept compression corner for  $\alpha = 20^\circ$  and  $\lambda = 40^\circ$

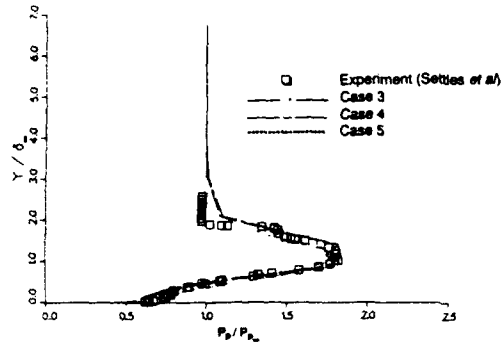


Figure 35: Pitot pressure for swept compression corner for  $\alpha = 20^\circ$  and  $\lambda = 40^\circ$

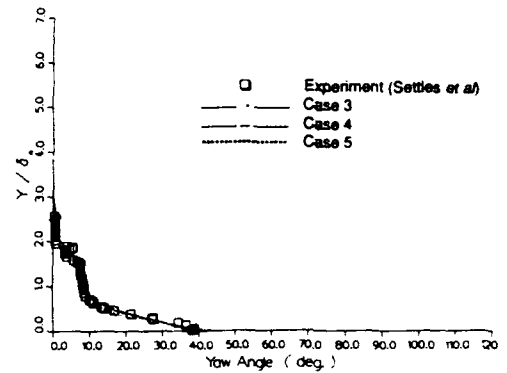


Figure 38: Yaw angle for swept compression corner for  $\alpha = 20^\circ$  and  $\lambda = 40^\circ$

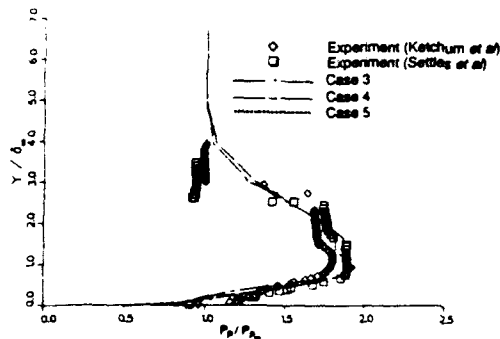


Figure 36: Pitot pressure for swept compression corner for  $\alpha = 20^\circ$  and  $\lambda = 40^\circ$

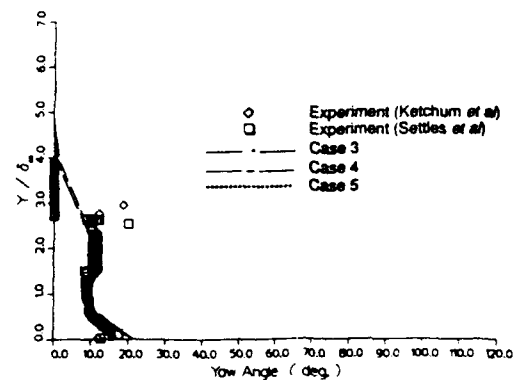


Figure 39: Yaw angle for swept compression corner for  $\alpha = 20^\circ$  and  $\lambda = 40^\circ$



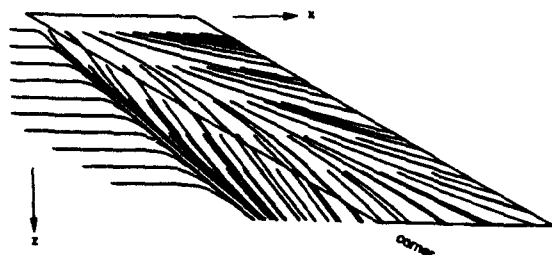


Figure 40: Skin friction lines for swept compression corner

$x - z \tan \lambda = 0.4\delta_\infty$ ,  $2.6\delta_\infty$  and  $6.0\delta_\infty$ , respectively. The first profile ( $x - z \tan \lambda = 0.4\delta_\infty$ ) is located approximately at the corner line. The second profile ( $x - z \tan \lambda = 2.6\delta_\infty$ ) is located near the line of divergence (line of attachment) on the compression surface. The third profile ( $x - z \tan \lambda = 6.0\delta_\infty$ ) is located far downstream of the corner interaction. The computed profiles display general agreement with the experiment, and exhibit minor differences associated with the specific turbulence model.

The yaw angle is similarly predicted with reasonable accuracy. Computed and experimental profiles are displayed in Figs. 37 to 39 for the same flow conditions and locations as the pitot pressure. At  $x - z \tan \lambda = 0.4\delta_\infty$ , the computed profiles overestimate the yaw angle by as much as 20°; however, the computed yaw angle near the surface agrees with the experiment to within 10%. Near the line of divergence (Fig. 38) and downstream of the corner (Fig. 39), all models predict the yaw angle within the experimental uncertainty. Except within the lowest 10% of the boundary layer where the computed yaw angles differ typically by 10%, the calculated profiles are virtually identical.

The computed skin friction lines for  $M_\infty = 2.95$ ,  $\alpha = 24^\circ$ , and  $\lambda = 60^\circ$  using the Baldwin-Lomax model are displayed in Fig. 40. A line of coalescence (line of separation in the sense of Lighthill [53]) forms upstream of the corner. The angle of the computed line of coalescence, measured relative to the spanwise coordinate direction, is approximately 10% greater than the experimental surface flow visualization [47], implying that the computed extent of upstream influence is smaller than observed in the experiment. This

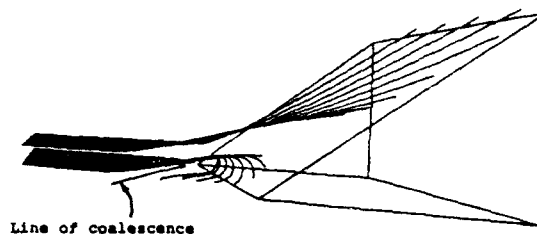


Figure 41: Streamlines for swept compression corner

observation is consistent with the results for surface pressure (Figs. 32 and 33). The line of divergence (line of attachment) is located on the compression surface.

The general agreement between the computation and experiment permits determination of the flowfield structure using the calculated flowfields. A series of computed mean streamlines are shown in Fig. 41 for  $M_\infty = 2.95$ ,  $\alpha = 24^\circ$ , and  $\lambda = 60^\circ$ . The two families of streamlines originate at  $y/\delta_\infty = 0.2$  and  $0.8$  at  $x - z \tan \lambda = -12.2\delta_\infty$ . The streamlines originating at  $y/\delta_\infty = 0.2$  are entrained into a vortex whose axis is approximately aligned with the corner line. The streamlines originating at  $y/\delta_\infty = 0.8$  move over the vortex and continue downstream over the compression ramp. A similar structure is observed at  $\alpha = 24^\circ$  and  $\lambda = 40^\circ$ .

The general mean streamline model, deduced from the computations, is shown in Fig. 42. The principal feature is a large vortex approximately coincident with the corner line. A three dimensional surface of separation originates from the line of separation and spirals into the core of the vortex. The streamlines in this surface are strongly skewed in the spanwise direction. Another three dimensional surface, originating within the upstream boundary layer, intersects the compression surface at the line of attachment. This surface marks the extent of the flow entrained into the vortex. Within the upstream boundary, fluid beneath this surface is entrained into the vortex, while fluid above this surface passes over the vortex and up the compression ramp. The general features of the streamline structure is similar to the 3-D single fin (Fig. 20).



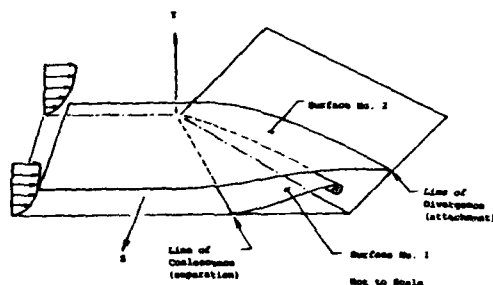


Figure 42: Flowfield model for swept compression corner

The nature and extent of the computed entrainment of the incoming boundary layer into the vortex is dependent on  $M_\infty$ ,  $\alpha$  and  $\lambda$ . For  $M_\infty = 2.95$ , the height of the computed entrainment surface is shown in Fig. 43 for  $(\alpha, \lambda) = (24^\circ, 40^\circ)$  and  $(24^\circ, 60^\circ)$  at  $Re_{\delta_\infty} = 8 \times 10^5$  and  $9 \times 10^5$ , respectively. The ordinate is the height of the entrainment surface measured within the undisturbed boundary layer, and the abscissa is the spanwise location. Two lines are shown for each case representing the lower and upper estimates of the height of the entrainment surface [48]. For the  $(24^\circ, 40^\circ)$  case, the height appears to asymptote  $y/\delta_\infty = 0.15$ , while for  $(24^\circ, 60^\circ)$  the height continues to increase in an approximately linear manner. However, the limited spanwise extent of the computations does not permit a definitive statement concerning the asymptotic behavior at large spanwise distances.

A computational study of the contributions of inviscid and viscous effects to the evolution of the mean kinetic energy was performed [54] for  $M_\infty = 2.95$ ,  $\alpha = 24^\circ$ , and  $\lambda = 40^\circ$ . The results suggest that the flow is principally rotational and inviscid throughout the boundary layer except within a thin layer adjacent to the surface and in an isolated region near the corner.

#### 4.5 Crossing Shock

The crossing shock geometry is two wedges attached normal to a flat plate (Fig. 44) on which an equilibrium turbulent boundary layer has de-

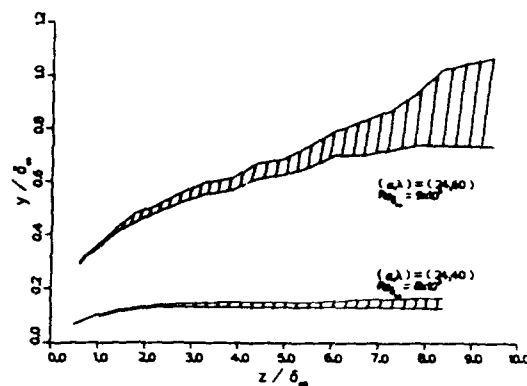


Figure 43: Height of entrainment surface for swept compression corner

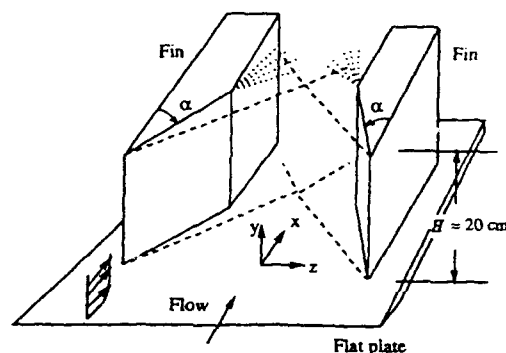


Figure 44: Geometry of crossing shock

veloped. The two wedges generate intersecting shock waves which interact with the boundary layer on the flat plate. The geometry is a natural extension of the single sharp fin (Fig. 1). The flow parameters are the Mach number  $M_\infty$ , Reynolds number  $Re_{\delta_\infty}$ , fin angles  $(\alpha_1, \alpha_2)$ , fin leading edge separation ratio  $W/\delta_\infty$  and wall temperature ratio  $T_w/T_{aw}$ .

The computations of the crossing shock are listed in Table 5, ordered by the magnitude of the inviscid shock pressure ratio  $p_3/p_1$ , where  $p_1$  and  $p_3$  are the static pressure upstream and downstream of the shock intersection, respectively. All computations are for symmetric shocks ( $\alpha_1 = \alpha_2$ ).



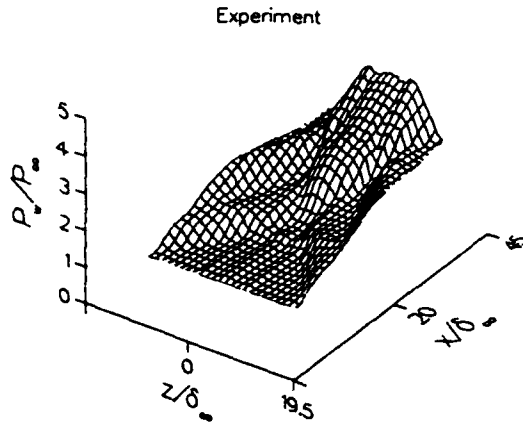


Figure 45: Surface pressure for crossing shock at  $M_\infty = 3.0$ ,  $\alpha = 11^\circ$ ,  $Re_{\delta_\infty} = 2.6 \times 10^5$  for experiment

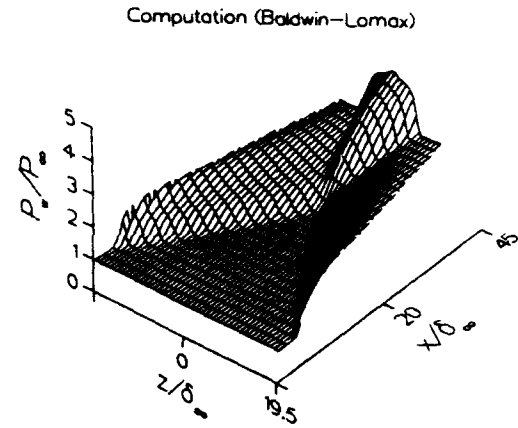


Figure 46: Surface pressure for crossing shock at  $M_\infty = 3.0$ ,  $\alpha = 11^\circ$ ,  $Re_{\delta_\infty} = 2.6 \times 10^5$  for Baldwin-Lomax model

Table 5 Crossing Shock Computations

$p_3/p_1$	$M_\infty$	$\alpha$	Model	Type	Ref
1.7	1.85	$5^\circ$	B-L	0	[55]
2.6	3.5	$6^\circ$	B-L	0	[56]
3.0	4.0	$6^\circ$	B-L	0	[56]
3.4	2.95	$9^\circ$	B-L	0	[57, 58]
4.2	2.95	$11^\circ$	B-L	0	[57, 59, 58]
			J-L	2	[59]
4.6	3.5	$10^\circ$	B-L	0	[56]
10.2	4.0	$15^\circ$	B-L	0	[60]
19.2	8.3	$10^\circ$	B-L	0	[61]
44.1	8.3	$15^\circ$	B-L	0	[62]
			Rodi	2	[62]

Legend:

$p_3/p_1$	inviscid pressure ratio across crossing shocks
$M_\infty$	freestream Mach number
$\alpha$	fin angle
Model	turbulence model
B-L	Baldwin-Lomax model [24]
J-L	Jones-Launder model [26]
Rodi	Rodi model [27]
Type	type of turbulence model (0 = Zero Equation, etc)

There is general agreement between the computed and measured surface pressure for all of the turbulence models examined. In Figs. 45,

46 and 47 results are shown for  $M_\infty = 2.95$ ,  $\alpha = 11^\circ$ ,  $W/\delta_\infty = 39$  for experiment and computations using the Baldwin-Lomax and Jones-Launder models. The extent of upstream influence is moderately underestimated by both turbulence models, and the computed spanwise pressure distribution near the outflow boundary ( $x = 47\delta_\infty$ ) exhibits differences with the experiment.

The pressure distributions on two streamwise cuts are shown in Figs. 48 and 49 corresponding to the centerline ( $z = 0$ ) and off-centerline ( $z = 3.81\delta_\infty$ ) locations, respectively. Differences of typically 15% between the Baldwin-Lomax and Jones-Launder computations are observed. The computed surface pressure on the centerline underestimates the upstream influence, and overestimates the pressure downstream of the approximate plateau region.

In Fig. 50, results are displayed for  $M_\infty = 8.3$ ,  $\alpha = 15^\circ$ ,  $W/\delta_\infty = 4.7$  for the Baldwin-Lomax and Rodi models corresponding to the geometry shown in Fig. 51. Both computations show close agreement<sup>9</sup>. The peak pressure is predicted by both models within 20%, and is substantially

<sup>9</sup>Except for  $x/\delta_\infty > 9$ . In this region, the difference may be attributable to the absence of separation, in the computation using the Rodi model, for the sidewall (fin) shock-boundary layer interaction. This interaction involves a reflected shock which emanates from the intersection of the two incident shock waves.



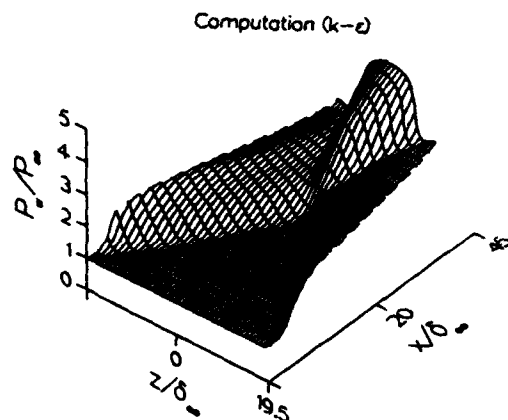


Figure 47: Surface pressure for crossing shock at  $M_\infty = 3.0$ ,  $\alpha = 11^\circ$ ,  $Re_{\delta_\infty} = 2.6 \times 10^5$  for Jones-Launder model

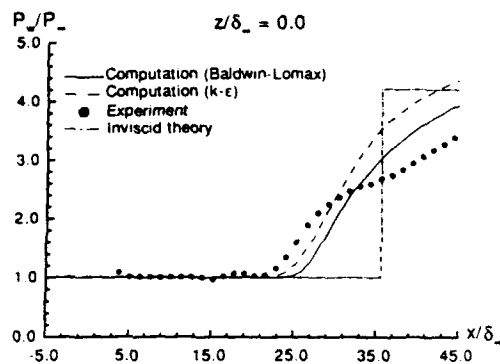


Figure 48: Surface pressure for crossing shock at  $M_\infty = 3.0$ ,  $\alpha = 11^\circ$ ,  $Re_{\delta_\infty} = 2.6 \times 10^5$

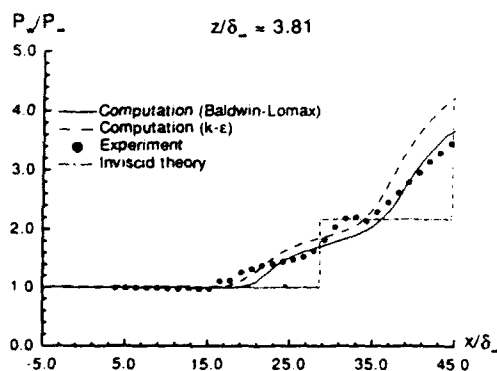


Figure 49: Surface pressure for crossing shock at  $M_\infty = 3.0$ ,  $\alpha = 11^\circ$ ,  $Re_{\delta_\infty} = 2.6 \times 10^5$ ,

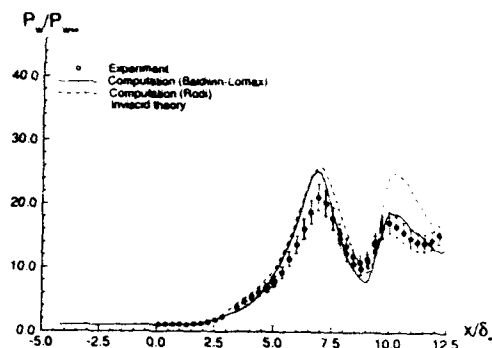
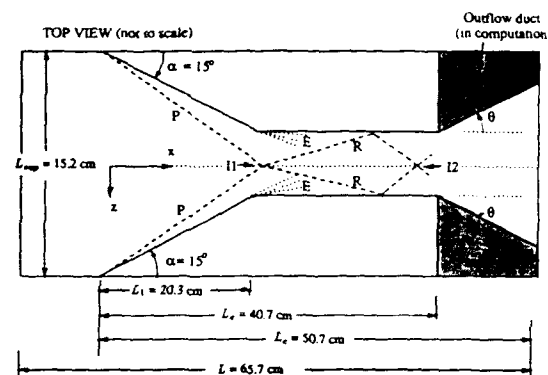


Figure 50: Surface pressure for crossing shock at  $M_\infty = 8.3$ ,  $\alpha = 15^\circ$ ,  $Re_{\delta_\infty} = 1.7 \times 10^5$





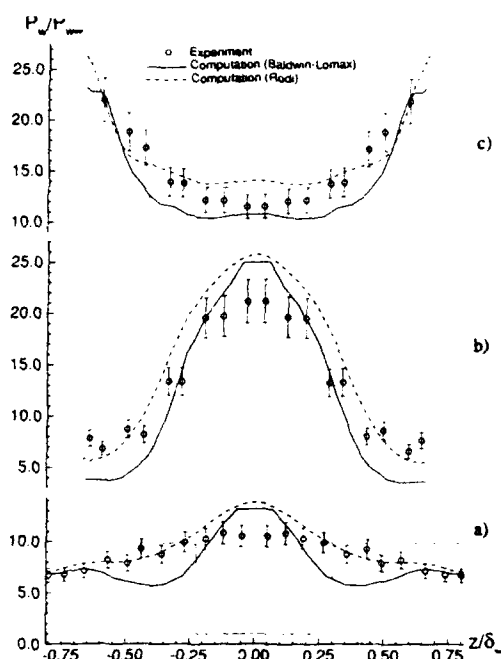


Figure 52: Surface pressure for crossing shock at  $M_\infty = 8.3$ ,  $\alpha = 15^\circ$ ,  $Re_{\delta_\infty} = 1.7 \times 10^5$

below the theoretical (inviscid) value due the combined effects of the shock wave-turbulent boundary layer interaction and the expansion fan originating from the change in slope of the fin surface. In Fig. 52, computed and experimental surface pressure are shown (bottom to top) at  $x/\delta_\infty = 5.6$ ,  $6.92$  and  $8.31$  (see Fig. 51 for the relative location of the measurements). The computed profiles agree generally with the experiment.

The pitot pressure is predicted with reasonable accuracy for  $M_\infty = 8.3$ ,  $\alpha = 15^\circ$ ,  $W/\delta_\infty = 4.7$  using the Baldwin-Lomax and Rodi models. Figs. 53 and 54 display the experimental and computed results for  $p_p/p_{p_\infty}$  using the Baldwin-Lomax and Rodi models, respectively, at  $x = 5.6\delta_\infty$ . Figs. 55 and 56 show the corresponding results at  $x = 8.3\delta_\infty$ . The computations display general agreement with the experiment. The formation of a large low  $p_p$  region on the centerline near the flat plate is evident. This structure corresponds to a low total pressure jet comprising two counter-rotating vortices.

The yaw angle is similarly predicted with reasonable accuracy for  $M_\infty = 8.3$ ,  $\alpha = 15^\circ$ ,  $W/\delta_\infty$

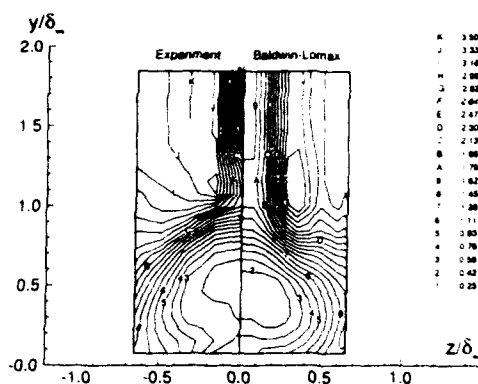


Figure 53: Pitot pressure for crossing shock at  $M_\infty = 8.3$ ,  $\alpha = 15^\circ$ ,  $Re_{\delta_\infty} = 1.7 \times 10^5$ ,  $x = 5.6\delta_\infty$ , Baldwin-Lomax model

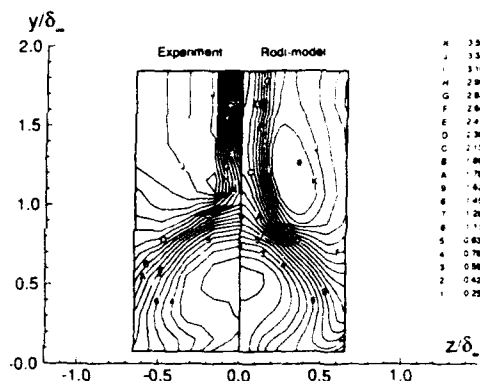


Figure 54: Pitot pressure for crossing shock at  $M_\infty = 8.3$ ,  $\alpha = 15^\circ$ ,  $Re_{\delta_\infty} = 1.7 \times 10^5$ ,  $x = 5.6\delta_\infty$ , Rodi model

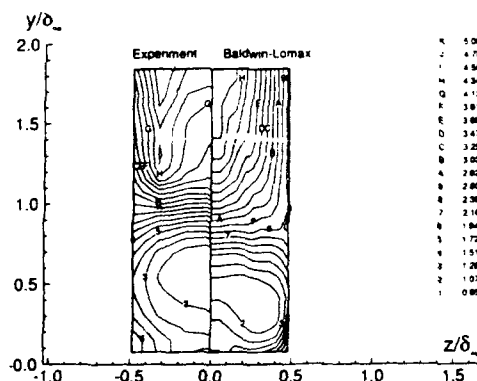


Figure 55: Pitot pressure for crossing shock at  $M_\infty = 8.3$ ,  $\alpha = 15^\circ$ ,  $Re_{\delta_\infty} = 1.7 \times 10^5$ ,  $x = 8.3\delta_\infty$ , Baldwin-Lomax model



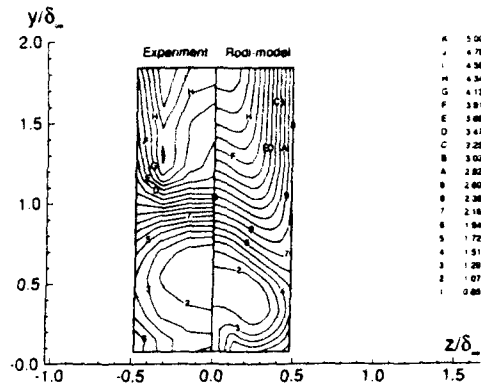


Figure 56: Pitot pressure for crossing shock at  $M_\infty = 8.3$ ,  $\alpha = 15^\circ$ ,  $Re_{\delta_\infty} = 1.7 \times 10^5$ ,  $x = 8.3\delta_\infty$ , Rodi model

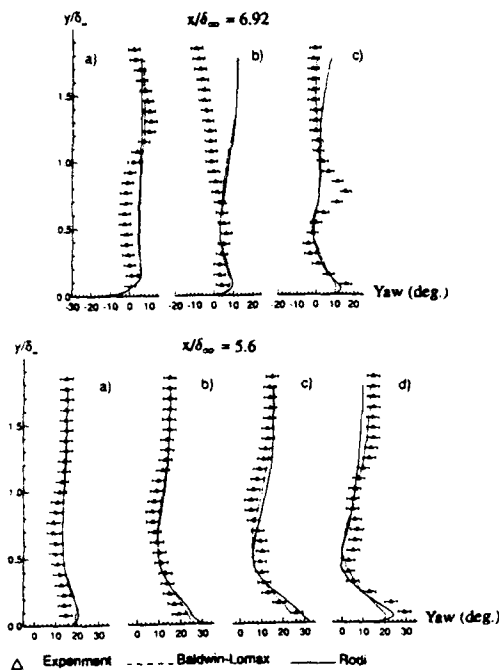


Figure 57: Yaw angle for crossing shock at  $M_\infty = 8.3$ ,  $\alpha = 15^\circ$ ,  $Re_{\delta_\infty} = 1.7 \times 10^5$ ,  $x = 5.6\delta_\infty$  and  $6.9\delta_\infty$

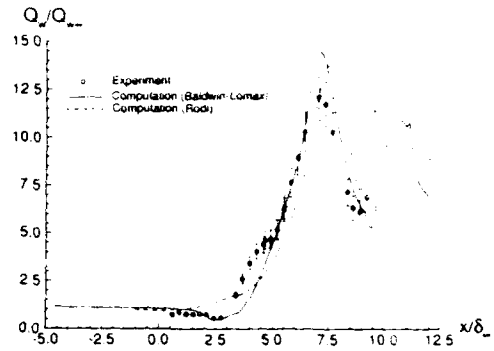


Figure 58: Heat transfer for crossing shock at  $M_\infty = 8.3$ ,  $\alpha = 15^\circ$ ,  $Re_{\delta_\infty} = 1.7 \times 10^5$

= 4.7 using the Baldwin-Lomax and Rodi models. In Fig. 57, results are shown for the Baldwin-Lomax and Rodi models at  $x/\delta_\infty = 5.6$  for four spanwise locations a) to d) of  $z/\delta_\infty = -0.65, -0.49, -0.33$  and  $-0.16$ , respectively, and at  $x/\delta_\infty = 6.9$  for three spanwise locations a) to c) of  $z/\delta_\infty = -0.48, -0.32$ , and  $-0.15$ , respectively. The computations show close agreement with each other, and general agreement with the experiment.

The predictions of surface heat transfer show substantial disagreement with experiment. In Fig. 58 and 59, results are shown using the Baldwin-Lomax and Rodi models for  $M_\infty = 8.3$ ,  $\alpha = 15^\circ$ ,  $W/\delta_\infty = 4.7$ . The centerline results display general agreement with experiment, although significantly overestimating the heat transfer in the initial stages of the interaction ( $x/\delta_\infty = 3.5$  to  $5.0$ ). The off-centerline predictions are substantially in error (Fig. 59) and overestimate the heat transfer up to 85%.

The results described above indicate that the computed surface pressure, pitot pressure and yaw angle are relatively insensitive to the specific turbulence model, similar to the observations for the sharp fin. In contrast, the computed surface heat transfer is affected more significantly by the choice of the turbulence model. A detailed comparison of the computed eddy viscosity was performed for  $M_\infty = 8.3$ ,  $\alpha = 15^\circ$ ,  $W/\delta_\infty = 4.7$ . An example is shown in Fig. 60. The computed peak values of the eddy viscosity differ by a factor of seven, while at the same location the pitot pressure and yaw angle profiles are in reasonable agreement (e.g., the yaw angle



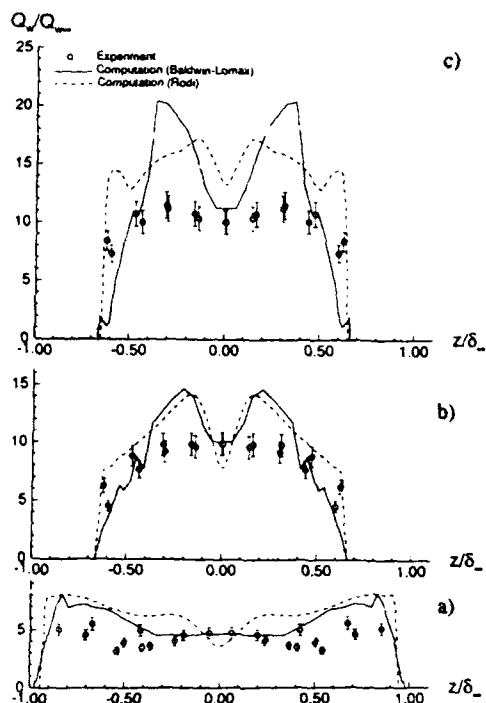


Figure 59: Heat transfer for crossing shock at  $M_\infty = 8.3$ ,  $\alpha = 15^\circ$ ,  $Re_{\delta_\infty} = 1.7 \times 10^5$ ,  $x/\delta_\infty = 5.08, 6.4$  and  $7.8$

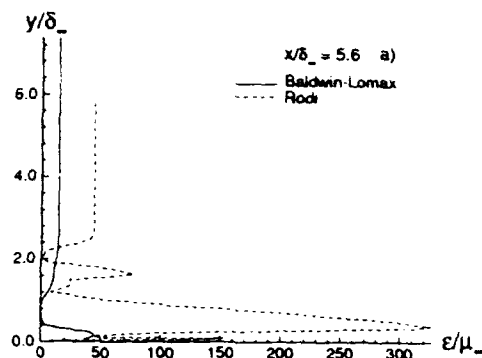


Figure 60: Eddy viscosity for crossing shock at  $M_\infty = 8.3$ ,  $\alpha = 15^\circ$ ,  $Re_{\delta_\infty} = 1.7 \times 10^5$ ,  $x/\delta_\infty = 5.6$ ,  $z/\delta_\infty = -0.65$

profiles agree within 8% as indicated in Fig. 57) except within a thin region adjacent to the surface (i.e., within approximately the lowest 10% of the boundary layer).

These results imply that the flowfield is dominantly rotational and inviscid, except within a thin region adjacent to the flat plate. This result is similar to the observation for the sharp fin. Similar implications regarding turbulence modeling follow. Specifically, the turbulence model has a significant effect on the computed surface heat transfer<sup>10</sup>. The majority of the flowfield is rotational and inviscid, to a first approximation, and hence insensitive to the turbulence model employed.

The computed and experimental results can be employed to develop a model of the streamline and wave structure of the crossing shock interaction. The computed shock structure of the crossing shock interaction at  $M_\infty = 8.3$ ,  $\alpha = 15^\circ$ ,  $W/\delta_\infty = 4.7$  is shown in Fig. 61. Near the leading edge of the fins, the flowfield is comprised of two single fin interactions which are characterized by a classic  $\lambda$ -shock [1]. The individual components of the  $\lambda$ -shock are the inviscid shock '1', separation shock '2' and rear shock '3' (Fig. 61a). The separation shocks intersect, forming a reflected shock with two segments '4a' and '4b' (Fig. 61b). The "bridging" segment

<sup>10</sup>It is anticipated that the computed surface skin friction would also be sensitive to the particular turbulence model employed, although no comparisons have been published for the crossing shock. Measurements of skin friction have recently been obtained for the Mach 4,  $\alpha = 15^\circ$  crossing shock [63] and comparison with previous computations [60] is in progress.



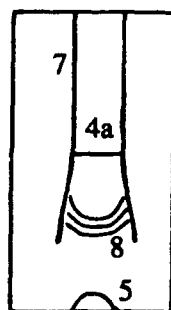
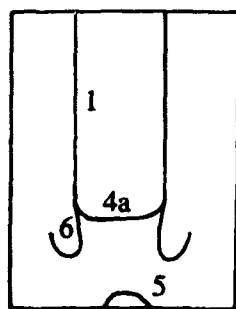
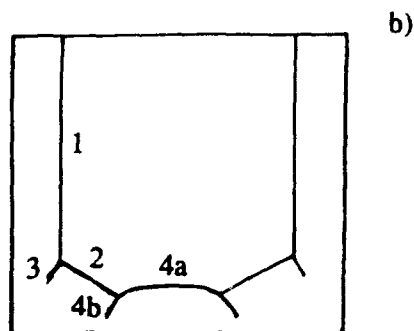
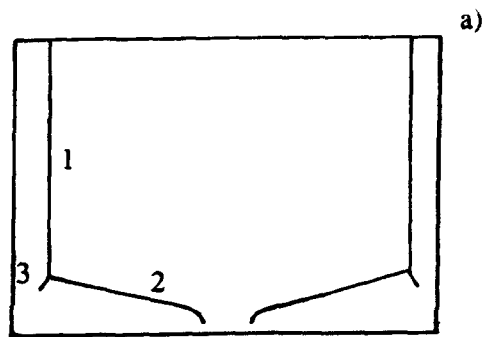


Figure 61: Shock structure for crossing shock at  $M_\infty = 8.3$ ,  $Re_{\delta_\infty} = 1.7 \times 10^5$ ,  $\alpha = 15^\circ$

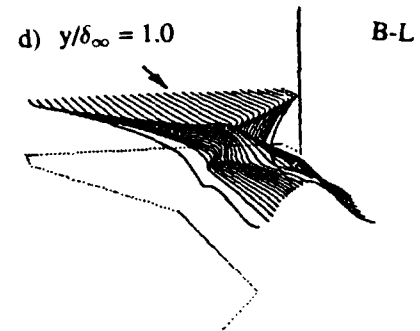
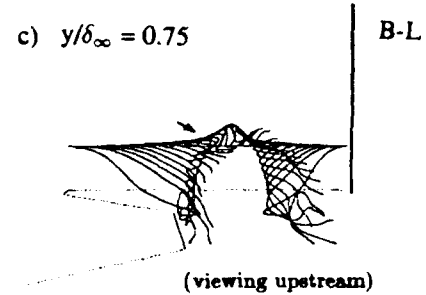
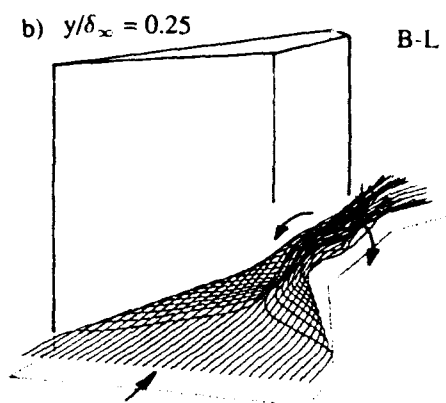
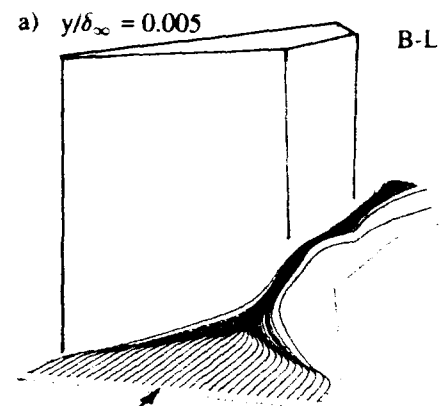


Figure 62: Streamline structure for crossing shock at  $M_\infty = 8.3$ ,  $Re_{\delta_\infty} = 1.7 \times 10^5$ ,  $\alpha = 15^\circ$



'4a' rises with increasing downstream distance. The remaining segment '4b' moves towards the fins and interacts with the rear segment '3' of the original  $\lambda$  shock, forming a localized high pressure region '6'. A separate curved shock '5' forms on the centerline near the surface, and is associated with the turning of the flow near the surface along the plane of symmetry (Fig. 61c). Downstream of the intersection of the inviscid shocks '1', an expansion region forms '8', while the separate shock '5' remains (Fig. 61d). The reflected shocks '7' move towards the fins.

A shock similar structure was observed experimentally and computationally [60] at Mach 4. However, the experimental visualization indicated a continuation of the reflected shock segment '4b' which was not observed in the computations. The discrepancy may be associated with insufficient grid resolution within the trajectory of segment '4b'.

The computed mean streamline structure for the crossing shock interaction at  $M_\infty = 8.3$ ,  $\alpha = 15^\circ$ ,  $W/\delta_\infty = 4.7$  is shown in Fig. 62. The principal feature is a pair of counter-rotating vortices, generated by the individual single fin interactions, which intersect at the plane of symmetry and rise above the surface.

The flowfield structure has significant implications for the use of the crossing shock interaction as a supersonic diffuser (inlet). Downstream of the crossing shock interaction, the counter-rotating vortex pair forms a core of low total pressure, low Mach number fluid [57, 59, 61, 62]. In effect, the individual vortices generated by the single fin interactions scavenge the low energy fluid (originating near the surface in the incoming boundary layer) and collide at the symmetry plane, forming a counter-rotating vortex pair with a low total pressure core.

## 5 Conclusions

Considerable progress has been achieved in the capability for prediction of 3-D shock wave-turbulent boundary layer interactions. Five specific configurations have been examined - sharp fin, blunt fin, cylinder/flare, swept compression corner and crossing shock. Numerical simulations of these configurations have been compared with experimental data at Mach num-

bers from two to eight. With some risk of overgeneralization, the following conclusions may be reached.

- The pitot pressure, yaw angle, and surface pressure are predictable with reasonable accuracy using algebraic or two equation turbulence models, except in certain cases exhibiting significant shock unsteadiness (e.g., cylinder/flare). This success is attributable to the generally asymptotic "triple-deck" structure of 3-D turbulent interactions. In a thin layer adjacent to solid boundaries, the flow is governed by both viscous (molecular and turbulent) and inviscid effects. The remainder of the boundary layer is effectively rotational and inviscid to a first approximation, thereby explaining the relative insensitivity of the pitot pressure, yaw angle and surface static pressure to the turbulence model employed.
- The mean flowfield structure (i.e., mean streamlines and wave structure) is therefore generally predictable. Some details of the computations, however, may not necessarily be correct (e.g., the absence of a continuation of the reflected shock segment '4b' in the crossing shock interaction at Mach 4). Such discrepancies may be associated with insufficient grid resolution and/or the turbulence model employed.
- The surface heat transfer is not accurately predicted in strong 3-D shock wave turbulent boundary layer interactions (e.g., crossing shock). Differences as large as 85% have been noted. Reasonable agreement has been found, however, for the sharp fin. Further research in development of turbulence models and additional heat transfer measurements are needed.
- Experimental data for the turbulence structure are rare for 3-D shock wave turbulent boundary layer interactions. Of all configurations considered in the present paper, there has been a comparison of computed and experimental data for only one case (i.e., cylinder/flare), and the predictions were uniformly poor.



## 6 Future Work

Substantial additional research in 3-D shock wave turbulent boundary layer interactions is needed to achieve greater understanding of the fluid physics and to improve the accuracy of numerical simulations. Among these needs are improved computational methods, collaborative experimental/computational efforts and incorporation of knowledge of flowfield structure into more effective design.

### Computational Methods

The complex shock structures developing from ostensibly simple geometries (*e.g.*, crossing shocks) pose difficulties for numerical algorithms based on structured grids. Resolution of these shocks requires refinement in one or more coordinate directions, thereby increasing the density of grid points both within the region of high gradients and also outside. This approach becomes computationally inefficient as more grid points are added where unneeded. Recent efforts in the development of algorithms based on unstructured grids hold promise for improved resolution in regions of large gradients at reasonable computational cost (see, for example, refs. [64, 65, 66, 67]).

### Collaborative Experimental/Computational Efforts

#### *Unsteady Interactions*

In a wide range of aerospace systems, 3-D shock wave turbulent boundary layer interactions are inherently unsteady on the spatial and temporal scales of the mean flow. Examples include high speed inlet unstart [68], inlet buzz (Dailey-type) [69] and transonic rotorcraft [70]. The knowledge of these unsteady turbulent interactions is minimal, and further collaborative experimental and theoretical (computational) research is needed.

#### *Turbulence Models*

Improvement in turbulence models is needed to remedy inadequacies in at least two critical areas. First, surface heat transfer is poorly predicted in strong 3-D shock wave turbulent boundary layer interactions (*e.g.*, the crossing shock interaction using the algebraic Baldwin-Lomax and two-equation Rodi turbulence models). Second, the unsteady flow behavior of the blunt

fin and cylinder-flare have not been accurately modeled by either algebraic or two-equation turbulence models. The large spatial scale and low frequency shock oscillations can, in principle, be represented by the Reynolds-averaged equations. However, all computations have converged to steady state solutions.

The effort in turbulence model development needs to be closely coordinated with new experiments. Experience has shown that surface pressure, pitot pressure and yaw angle measurements provide a relatively weak test of the accuracy of turbulence models in 3-D shock wave turbulent boundary layer interactions. The principal data needed for evaluation of turbulence models is surface heat transfer, surface skin friction and Reynolds stress measurements.

#### *Non-Equilibrium Upstream Conditions*

Virtually all fundamental experimental data on 3-D shock wave-turbulent boundary layer interactions have been obtained for configurations with incoming equilibrium, flat plate boundary layers. This provides a relatively simple, experimentally reproducible upstream condition, and isolates the 3-D turbulent interaction from outside effects. This approach is essential for understanding the fundamental behavior of a specific 3-D turbulent interaction. Once understood, the next step is to consider non-equilibrium upstream boundary layers which are more common in practice.

#### *Specific Configurations*

In addition to the generic needs described above, many additional areas of research can be identified. In the interests of brevity, only two will be mentioned herein. First, the understanding of the sharp fin interaction in the presence of surface bleed is critical to the performance of many mixed compression inlet designs. The available experimental data is inadequate. The experimental data of Barnhart *et al* [71] is a useful first step; however, the local bleed flow rate was not measured and consequently the local boundary conditions for computation are not known accurately. Computed results [55, 72] suggest that the primary vortex is not significantly affected by surface suction.

Second, there is little experimental data for the asymmetric crossing shock. Experimental flowfield data (*e.g.*, pitot pressure, yaw angle, flow-



field) for the crossing shock interaction has been restricted to symmetric configurations. Surface mean and fluctuating pressure data has been obtained for three asymmetric configurations at Mach 3 by Bogdonoff [73]. Further experimental data for asymmetric configurations is needed.

### Impact on Design

It is been shown that existing computational methods are capable of predicting the mean flow structure (e.g., surface pressure, pitot pressure, yaw angle) of 3-D shock wave turbulent boundary layer interactions with a reasonable level of accuracy. This knowledge can be incorporated into the design process. For example, the crossing shock interaction is characterized by a low total pressure jet comprising two counter-rotating vortices. The low momentum fluid near the wall in the incoming boundary layer is effectively scavenged by the two vortices formed by the single fin interactions and entrained into the jet. Can this information be employed to design a more effective scramjet combustor?

## 7 Acknowledgments

This research was sponsored by the Air Force Office of Scientific Research under Grant F49620-93-1-0005 monitored by Dr. Len Sakell. The author acknowledges, with sincere appreciation, scientific collaborations with D. Badekas, S. Bogdonoff, D. Dolling, D. Gaitonde, C. Horstman, N. Narayanswami, D. Raufer, G. Settles, A. Smits, and A. Zheltovodov.

## References

- [1] F. Alvi and G. Settles, "Physical Model of the Swept Shock / Boundary Layer Interaction Flowfield," *AIAA Journal*, vol. 30, pp. 2252-2258, 1992.
- [2] G. Settles and D. Dolling, "Swept Shock Wave Boundary Layer Interactions," in *Tactical Missile Aerodynamics*, pp. 297-379, AIAA, 1986.
- [3] G. Settles and D. Dolling, "Swept Shock / Boundary-Layer Interactions - Tutorial and Update." AIAA Paper 90-0375, 1990.
- [4] M. Holden, "Aerothermal Problems Associated with Viscous / Inviscid Interaction over Hypersonic Flight Vehicles," in *Turbulent Shear-Layer / Shock-Wave Interactions*, pp. 323-338, New York: Springer-Verlag, 1986.
- [5] A. Zheltovodov, A. Maksimov, and E. Shilein, "Development of Turbulent Separated Flows in the Vicinity of Swept Shock Waves," in *The Interaction of Complex 3-D Flows*, pp. 67-91, Novosibirsk, Russia: Institute of Theoretical and Applied Mechanics, USSR Academy of Sciences, 1987.
- [6] W. Reynolds, "Computation of Turbulent Flows," *Annual Review of Fluid Mechanics*, vol. 8, pp. 183-208, 1976.
- [7] A. Favre, ed., *The Mechanics of Turbulence*, p. 367. New York: Gordon and Breach, 1964.
- [8] P. Bradshaw, "Compressible Turbulent Shear Layers," *Annual Review of Fluid Mechanics*, vol. 9, pp. 33-54, 1977.
- [9] O. Zeman, "Dilatation Dissipation: The Concept and Application in Modeling Compressible Mixing Layers," *Physics of Fluids A*, vol. 2, pp. 178-188, 1990.
- [10] F. Alvi and G. Settles, "Structure of Swept Shock Wave / Boundary Layer Interactions Using Conical Shadowgraphy." AIAA Paper 90-1644, 1990.
- [11] G. Settles and F. Lu, "Conical Similarity of Shock / Boundary Layer Interactions Generated by Swept and Unswept Fins," *AIAA Journal*, vol. 23, pp. 1021-1027, 1985.
- [12] D. Knight and D. Badekas, "On the Quasi-Conical Flowfield Structure of the Swept Shock Wave-Turbulent Boundary Layer Interaction." AIAA Paper 91-1759, 1991.
- [13] D. Knight, D. Badekas, C. Horstman, and G. Settles, "Quasi-conical Flowfield Structure of the Three-Dimensional Single Fin Interaction," *AIAA Journal*, vol. 30, pp. 2809-2816, 1992.
- [14] C. Horstman and C. Hung, "Computation of Three-Dimensional Turbulent Separated Flows at Supersonic Speeds." AIAA Paper 79-0002, 1979.



- [15] D. Knight, "A Hybrid Explicit - Implicit Numerical Algorithm for the Three - Dimensional Compressible Navier-Stokes Equations," *AIAA Journal*, vol. 22, pp. 1056-1063, 1984.
- [16] Y. Lee, G. Settles, and C. Horstman, "Heat Transfer Measurements and CFD Comparison of Swept Shock Wave/Boundary Layer Interactions." AIAA Paper 92-3665, 1992.
- [17] C. Hung and R. MacCormack, "Numerical Solution of Three-Dimensional Shock Wave and Turbulent Boundary-Layer Interaction," *AIAA Journal*, vol. 16, pp. 1090-1096, 1978.
- [18] P. Rodi, D. Dolling, and D. Knight, "An Experimental/Computational Study of Heat Transfer in Sharp Fin Induced Turbulent Interactions at Mach 5." AIAA Paper 91-1764, 1991.
- [19] D. Knight, C. Horstman, B. Shapey, and S. Bogdonoff, "Structure of Supersonic Turbulent Flow Past a Sharp Fin," *AIAA Journal*, vol. 25, pp. 1331-1337, 1987.
- [20] A. Panaras, "Numerical Investigation of the High-Speed Conical Flow Past a Sharp Fin," *Journal of Fluid Mechanics*, vol. 236, pp. 607-633, 1992.
- [21] D. Knight, C. Horstman, and G. Settles, "Three Dimensional Shock Wave - Turbulent Boundary Layer Interactions Generated by a Sharp Fin at Mach 4." AIAA Paper 91-0648, 1991.
- [22] D. Knight, C. Horstman, and D. Monson, "The Hypersonic Shock Wave-Turbulent Boundary Layer Interaction Generated by a Sharp Fin at Mach 8.2." AIAA Paper 92-0747, 1992.
- [23] J. Bardina, T. Coakley, and J. Marvin, "Two Equation Turbulence Modelling for 3-D Hypersonic Flows." Fourth International Aerospace Planes Conference, December 1992.
- [24] B. Baldwin and H. Lomax, "Thin Layer Approximation and Algebraic Model for Separated Flows." AIAA Paper 78-257, 1978.
- [25] M. Escudier, "The Distribution of Mixing Length in Turbulent Flows Near Walls." Report TWF/TN/1, Mech Engr Dept, Imperial College, London, 1965.
- [26] W. Jones and B. Launder, "The Prediction of Laminarization with a Two-Equation Model of Turbulence," *Int. Journal of Heat and Mass Transfer*, vol. 15, pp. 301-304, 1972.
- [27] W. Rodi, "Experience with Two-Layer Models Combining the  $k - \epsilon$  with a One-Equation Model Near the Wall." AIAA Paper 91-0216, 1991.
- [28] T. Coakley and P. Huang, "Turbulence Modelling for High Speed Flows." AIAA Paper 92-0436, 1992.
- [29] S. Goodwin, "An Exploratory Investigation of Sharp-Fin Induced Shock Wave-Turbulent Boundary Layer Interaction at High Shock Strengths," Master's thesis, Princeton University, Dept Mech and Aero Engr, 1984.
- [30] D. Knight, C. Horstman, G. Settles, and A. Zheltovodov, "3-D Shock Wave-Turbulent Boundary Layer Interactions Generated by a Single Fin," *The Russian Journal of Theoretical and Applied Mechanics*, vol. 2, no. 3, 1992.
- [31] M. Kussoy and K. Horstman, "Documentation of Two- and Three Dimensional Shock-Wave/Turbulent Boundary Layer Interaction Flows at mach 8.2," Tech. Rep. NASA TM 103838, NASA Ames Research Center, May 1991.
- [32] K. Stewartson, "Some Recent Studies in Triple-Deck Theory," in *Numerical and Physical Aspects of Aerodynamic Flows* (T. Cebeci, ed.), p. 142, Springer-Verlag, 1981.
- [33] G. Inger, "Supersonic Viscous-Inviscid Interaction of a Swept Ramp with a Turbulent Boundary Layer." AIAA Paper 85-1669, 1985.
- [34] G. Inger, "Incipient Separation and Similitude Properties of Swept Shock/Turbulent Boundary Layer Interactions." AIAA Paper 86-0345, 1986.



- [35] G. Inger, "Spanwise Propagation of Upstream Influence in Conical Swept Shock / Boundary Layer Interactions," *AIAA Journal*, vol. 25, pp. 287-293, 1987.
- [36] C. Hung and P. Buning, "Simulation of Blunt Fin Induced Shock Wave Turbulent Boundary-Layer Interaction," *Journal of Fluid Mechanics*, vol. 154, pp. 163-185, 1985.
- [37] B. Lakshmanan, S. Tiwari, and M. Hussaini, "Control of Supersonic Intersection Flowfields Through Filletting and Sweep." AIAA Paper 88-3534, 1988.
- [38] D. Dolling and S. Bogdonoff, "Blunt Fin-Induced Shock Wave / Turbulent Boundary Layer Interaction," *AIAA Journal*, vol. 20, pp. 1674-1680, 1982.
- [39] D. Dolling and S. Bogdonoff, "An Experimental Investigation of the Unsteady Behavior of Blunt Fin-Induced Shock Wave Turbulent Boundary Layer Interaction." AIAA Paper 81-1287, 1981.
- [40] D. Dolling and L. Brusniak, "Separation Shock Motion in Fin, Cylinder, and Compression Ramp-Induced Turbulent Interactions," *AIAA Journal*, vol. 27, pp. 734-742, 1989.
- [41] J. Brown, *Two-Component L D V Investigation of Shock-Related Turbulent Boundary Layer Separation with Increasing Three-Dimensionality*. PhD thesis, University of California, Berkeley, 1986.
- [42] J. D. Brown, J. L. Brown, M. Kussoy, M. Holt, and C. C. Horstman, "Two-Component LDV Investigation of 3-Dimensional Shock / Turbulent Boundary Layer Interactions." AIAA Paper 87-0553, 1987.
- [43] C. Horstman, M. Kussoy, and W. Lockman, *Computation of Three-Dimensional Shock-Wave/Turbulent Boundary-Layer Interaction Flows*, ch. 24. Springer-Verlag, 1986.
- [44] J. Viegas, M. Rubesin, and C. Horstman, "On the Use of Wall Functions as Boundary Conditions for Two-Dimensional Separated Compressible Flows." AIAA Paper 85-0180, 1985.
- [45] G. Settles, C. Horstman, and T. McKenzie, "Flowfield Scaling of a Swept Compression Corner Interaction - A Comparison of Experiment and Computation." AIAA Paper 84-0096, 1984.
- [46] G. Settles, C. Horstman, and T. McKenzie, "Experimental and Computational Study of a Swept Compression Corner Interaction Flowfield," *AIAA Journal*, vol. 24, pp. 744-752, 1986.
- [47] D. Knight, D. Raufer, C. Horstman, A. Ketchum, and S. Bogdonoff, "Supersonic Turbulent Flow Past a 3-D Swept Compression Corner at Mach 3 - Part II." AIAA Paper 88-0310, 1988.
- [48] D. Knight, C. Horstman, and S. Bogdonoff, "Structure of Supersonic Turbulent Flow Past a Swept Compression Corner," *AIAA Journal*, vol. 30, pp. 890-896, 1992.
- [49] D. Knight, C. Horstman, R. Ruderich, M. F. Mao, and S. Bogdonoff, "Supersonic Turbulent Flow Past a 3-D Swept Compression Corner." AIAA Paper 87-0551, 1987.
- [50] Y. Zang and D. Knight, "Computation of Sharp Fin and Swept Compression Corner Shock/Turbulent Boundary Layer Interactions." AIAA Paper 89-1852, 1989.
- [51] C. Horstman, "A Computational Study of Complex Three-Dimensional Turbulent Flow Fields." AIAA Paper 84-1556, 1984.
- [52] T. Cebeci and A. Smith, *Analysis of Turbulent Boundary Layers*. New York: Academic Press, 1974.
- [53] L. Rosenhead, ed., *Laminar Boundary Layers*, pp. 46-113. New York: Oxford, 1963.
- [54] N. Narayanswami and D. Knight, "Viscous / inviscid Effects in 3-D Shock-Wave Turbulent Boundary Layer Interactions." AIAA Paper 89-0358, 1989.
- [55] D. Gaitonde and D. Knight, "Numerical Experiments on the 3-D Shock-Wave Boundary Layer Interaction Generated by a Sharp Fin." AIAA Paper 88-0309, 1988.
- [56] D. Reddy, "3-D Navier-Stokes Analysis of Crossing, Glancing Shocks/Turbulent



- Boundary Layer Interaction." AIAA Paper 91-1758, 1991.
- [57] N. Narayanswami, D. Knight, S. Bogdonoff, and C. Horstman, "Crossing Shock Wave-Turbulent Boundary Layer Interactions." AIAA Paper 91-0649, 1991.
- [58] N. Narayanswami, *A Numerical Investigation of the Interaction Between Crossing Oblique Shocks and a Turbulent Boundary Layer*. PhD thesis, Rutgers University, 1992.
- [59] N. Narayanswami, D. Knight, S. Bogdonoff, and C. Horstman, "Interaction Between Crossing Oblique Shocks and a Turbulent Boundary Layer," *AIAA Journal*, vol. 30, pp. 1945-1952, 1992.
- [60] T. Garrison, G. Settles, N. Narayanswami, and D. Knight, "Structure of Crossing-Shock Wave/Turbulent Boundary Layer Interactions." AIAA Paper 92-3670, 1992.
- [61] N. Narayanswami, D. Knight, and C. C. Horstman, "Investigation of a Hypersonic Crossing Shock Wave / Turbulent Boundary Layer Interaction." *Shock Waves*, 1992. to appear.
- [62] N. Narayanswami, C. Horstman, and D. Knight, "Numerical Simulation of Crossing Shock / Turbulent Boundary Layer Interaction at Mach 8.3 - Comparison of Zero- and Two- Equation Turbulence Models." AIAA Paper 93-0779, 1993.
- [63] T. Garrison and G. Settles, "Private Communication," 1992.
- [64] T. Barth, "Numerical Aspects of Computing Viscous High Reynolds Number Flows on Unstructured Meshes." AIAA Paper 91-0721, 1991.
- [65] J. Batina, "A Fast Implicit Upwind Solution Algorithm for Three-Dimensional Unstructured Dynamic Meshes." AIAA Paper 92-0447, 1992.
- [66] D. Knight, "A Fully Implicit Navier-Stokes Algorithm Using an Unstructured Grid and Flux Difference Splitting." AIAA Paper 93-0875, 1993.
- [67] L. Martinelli and A. Jameson, "Validation of a Multigrid Method for the Reynolds Averaged Equations." AIAA Paper No. 88-0414, 1988.
- [68] C. Domack, "A Preliminary Investigation of Inlet Unstart Effects on a High Speed Civil Transport Concept." AIAA Paper 91-3327, 1991.
- [69] E.-O. Krohn, "Inlet Buzz in Ramjets and its Suppression," in *8th International Symposium on Air-Breathing Engines*, pp. 110-117, June 1987.
- [70] R. Strawn and T. Barth, "A Finite-Volume Euler Solver for Computing Rotary-Wing Aerodynamics on Unstructured Meshes." 48th Annual Forum of the American Helicopter Society, 1992.
- [71] P. Barnhart, I. Greber, and W. Hingst, "Glancing Shock Wave-Turbulent Boundary Layer Interaction with Boundary Layer Suction." AIAA Paper 88-0308, 1988.
- [72] D. Gaitonde and D. Knight, "Numerical Investigation of Bleed on Three-Dimensional Turbulent Interactions Due to Sharp Fins," *AIAA Journal*, vol. 29, pp. 1878-1885, 1991.
- [73] S. Bogdonoff, "Preliminary Data Report, Cross Shock Configuration." Department of Mechanical and Aerospace Engineering, Princeton University, 1989.
- [74] F. Owen, C. Horstman, and M. Kussoy, "Mean and Fluctuating Flow Measurements of a Fully-Developed, Non-Adiabatic, Hypersonic Turbulent Boundary Layer," *Journal of Fluid Mechanics*, vol. 70, pp. 393-413, 1975.
- [75] A. Laderman and A. Demetriades, "Mean and Fluctuating Flow Measurements in the Hypersonic Boundary Layer Over a Cooled Wall," *Journal of Fluid Mechanics*, vol. 63, pp. 121-144, 1974.
- [76] R. Courant and K. Friedrichs, *Supersonic Flow and Shock Waves*. New York: Springer-Verlag, 1948.



## A Reynolds Averaged Equations

The exact Reynolds-averaged Navier-Stokes equations are,

$$\begin{aligned}\frac{\partial \bar{p}}{\partial t} + \frac{\partial \bar{p} \bar{u}_k}{\partial x_k} &= 0 \\ \frac{\partial \bar{p} \bar{u}_i}{\partial t} + \frac{\partial \bar{p} \bar{u}_i \bar{u}_k}{\partial x_k} &= \\ -\frac{\partial \bar{p}}{\partial x_i} + \frac{\partial}{\partial x_k} \left( -\overline{\rho u_i'' u_k''} + \bar{\tau}_{ik} \right) \\ \frac{\partial \bar{p} \bar{e}}{\partial t} + \frac{\partial (\bar{p} \bar{e} + \bar{p}) \bar{u}_k}{\partial x_k} &= \\ \frac{\partial}{\partial x_k} \left( -c_p \overline{\rho T'' u_k''} - \bar{q}_k \right) + \\ \frac{\partial}{\partial x_k} \left( -\overline{\rho u_i'' u_k''} \bar{u}_i + \bar{u}_i \bar{\tau}_{ik} \right) + \\ \frac{\partial}{\partial x_k} \left( -\frac{1}{2} \overline{\rho u_j'' u_j'' u_k''} + \bar{u}_j'' \bar{\tau}_{ik} \right)\end{aligned}$$

The mean molecular viscous stress  $\bar{\tau}_{ij}$  can be approximated by<sup>11</sup>

$$\bar{\tau}_{ij} = -\frac{2}{3} \bar{\mu} \frac{\partial \bar{u}_k}{\partial x_k} \delta_{ij} + \bar{\mu} \left( \frac{\partial \bar{u}_j}{\partial x_i} + \frac{\partial \bar{u}_i}{\partial x_j} \right)$$

where  $\bar{\mu} \equiv \mu(\bar{T})$ . By similar argument, the mean molecular heat flux is

$$\bar{q}_k = -\frac{c_p \bar{\mu}}{Pr} \frac{\partial \bar{T}}{\partial x_k}$$

where  $Pr$  is the molecular Prandtl number.

The triple velocity correlation  $(1/2) \overline{\rho u_j'' u_j'' u_k''}$  is small compared to  $\bar{p} \bar{k} \bar{u}_k$ , which is one of the terms in  $\bar{p} \bar{e} \bar{u}_k$ , and can therefore be neglected<sup>12</sup>. Also, the velocity-molecular shear correlation  $\bar{u}_i'' \bar{\tau}_{ik}$  can be demonstrated to be small<sup>13</sup>.

<sup>11</sup>The analysis is based on the experimental data of Owen *et al* [74] for non-adiabatic hypersonic boundary layers

<sup>12</sup>Using the data of Owen *et al* [74], it can be shown that  $|(1/2) \overline{\rho u_j'' u_j'' u_k''}| \leq 0.1 \bar{p} \bar{k} |\bar{u}_k|$

<sup>13</sup>The analysis is based on the experimental data of Laderman and Demetriades [75] and the assumption that the rms molecular fluctuations  $\sqrt{\tau_{ik}''}$  are no larger than the mean molecular shear stress  $\bar{\tau}_{ik}$ .

The Reynolds-averaged Navier-Stokes equations may therefore be assumed, under practical circumstances, to be

$$\begin{aligned}\frac{\partial \bar{p}}{\partial t} + \frac{\partial \bar{p} \bar{u}_k}{\partial x_k} &= 0 \\ \frac{\partial \bar{p} \bar{u}_i}{\partial t} + \frac{\partial \bar{p} \bar{u}_i \bar{u}_k}{\partial x_k} &= \\ -\frac{\partial \bar{p}}{\partial x_i} + \frac{\partial}{\partial x_k} \left( -\overline{\rho u_i'' u_k''} + \bar{\tau}_{ik} \right) \\ \frac{\partial \bar{p} \bar{e}}{\partial t} + \frac{\partial (\bar{p} \bar{e} + \bar{p}) \bar{u}_k}{\partial x_k} &= \\ \frac{\partial}{\partial x_k} \left( -c_p \overline{\rho T'' u_k''} - \bar{q}_k \right) + \\ \frac{\partial}{\partial x_k} \left( -\overline{\rho u_i'' u_k''} \bar{u}_i + \bar{u}_i \bar{\tau}_{ik} \right)\end{aligned}$$

## B Conical Flow

A conical flow is a steady flowfield whose velocity, pressure and temperature are invariant with radial distance from a common vertex [76]. Consider the spherical polar coordinate system  $(R, \beta, \phi)$  shown in Fig. 63. Thus,

$$\begin{aligned}\frac{\partial \bar{u}_k}{\partial R} &= 0 \\ \frac{\partial \bar{p}}{\partial R} &= 0 \\ \frac{\partial \bar{T}}{\partial R} &= 0\end{aligned}$$

where  $R$  is the spherical polar radius

$$R = \sqrt{(x - x_0)^2 + (y - y_0)^2 + (z - z_0)^2}$$

where  $(x_0, y_0, z_0)$  is the Virtual Conical Origin. For the sharp fin, the VCO is close to the intersection of the fin with the flat plate. The velocity, pressure and temperature are functions of the spherical polar coordinates

$$\begin{aligned}\beta &= \tan^{-1} ((z - z_0) / (x - x_0)) \\ \phi &= \tan^{-1} ((y - y_0) / \sqrt{(x - x_0)^2 + (z - z_0)^2})\end{aligned}$$



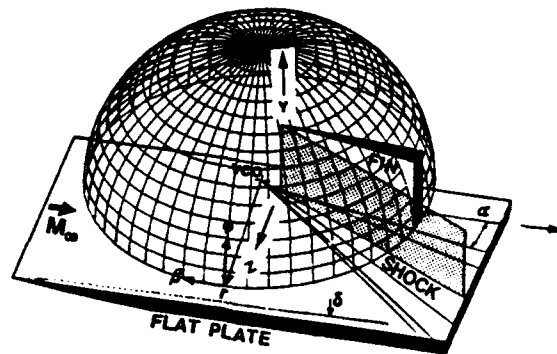


Figure 63: Spherical polar coordinates

Figs. 21-25 reprinted with permission of  
the *Journal of Fluid Mechanics*.



# Unsteady Phenomena in Shock Wave/ Boundary Layer Interaction

D. S. Dolling

Center for Aeromechanics Research  
The University of Texas at Austin  
Austin, Texas 78712

## ABSTRACT

A brief review is given of the unsteadiness of shock wave/turbulent boundary layer interaction. The focus is on interactions generated by swept and unswept compression ramps, by flares, steps and incident shock waves, by cylinders and blunt fins, and by glancing shock waves. The effects of Mach number, Reynolds number, and separated flow scale are discussed as are the physical causes of the unsteadiness. The implications that the unsteadiness has for interpreting time-averaged surface and flowfield data, and for comparisons of such experimental data with computations, is also briefly discussed. Finally, some suggestions for future work are given. It is clear that there are large gaps in the data base and that many aspects of such phenomena are poorly understood. Much work remains to be done.

## 1 INTRODUCTION

### 1.1 Engineering Implications of Flowfield Unsteadiness

Airbreathing transatmospheric vehicles will be exposed to severe aeroacoustic loads generated by the unsteady flowfields associated with airbreathing engines, by separated turbulent flows, and by engine-generated acoustic loads (Pozefsky et al., 1989; Zorumski, 1987; Holden, 1986). Whereas conventional hypersonic configurations such as ballistic missiles are essentially axisymmetric shells which are *efficient* structures, several proposed hypersonic vehicles are much larger and substantial areas will consist of flat panels. Flat panels are generally inefficient in reacting pressure loads, and the low resonant frequencies associated with their reduced stiffness may fall within the frequency range of unsteady shock-induced aeroacoustic loads.

The ascent phase, during which the engines will be running continuously and the vehicle will be exposed to high dynamic pressures, is critical.

At orbital cruise altitude, the engines will be off and the flow will probably be laminar. Similarly during descent, engines are off, dynamic pressures will be lower reducing the windside loading, and only low levels of laminar heating are expected on the leeside. Predictions indicate that regions subjected only to the loading generated by attached turbulent boundary layers will be relatively fatigue-free and have long structural lifetimes (Pozefsky, et al., 1989). In contrast, regions subjected to shock wave boundary layer interaction will experience the most intense loading up to 185 dB or more, and the time to failure of conventional structures is estimated to be orders of magnitude lower. Some examples of where shock/shock and shock boundary layer interactions can occur on a generic hypersonic vehicle are shown in Fig. 1. Engineering methods to predict loading levels and their frequency spectra are clearly needed, as are methods to reduce loading levels and alter their frequency spectra.

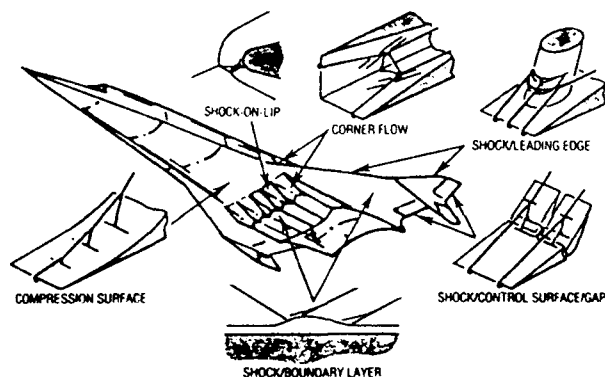


Fig. 1. Possible shock/shock and shock wave/boundary layer interactions on a hypersonic vehicle (from Jackson et al., 1987).



## 1.2 Implications of Unsteadiness for Flowfield Computation

It is generally accepted that the key element in CFD validation is comparison with experiment. However, drawing meaningful conclusions from such comparisons is not a trivial exercise. The problem is that the bulk of the experimental data base consists of time-averaged measurements which provides no information about flowfield steadiness or the lack of it. A discussion, with some examples of the problem, is given in Sec. 6.

## 1.3 Focus

The objective of this paper is to review briefly the salient features of the unsteadiness generated by supersonic and hypersonic shock wave/turbulent boundary layer interaction. On account of their practical importance, the emphasis is on the fluctuating loads generated by such flows, the physical causes of the unsteadiness, and the implications for CFD. There is no discussion of the fluctuating loads generated by turbulent boundary layers. The latter has received considerable attention in the past, and the reader is referred to Laganelli et al. (1976, 1983), Dolling and Dussauge (1989) and Pozefsky et al. (1989) for details. Dolling and Dussauge discuss the measuring techniques and their problems, the data and their deficiencies, while Laganelli et al. and Pozefsky et al. focus on engineering correlations for rms pressure levels and power spectral density. Extensive bibliographies are given in all three references.

The work cited in this paper is largely experimental. To the author's knowledge, no unsteady computations of shock-induced turbulent separation and reattachment have been made from which fluctuating load levels and spectra can be extracted. Further, the majority of the work is in the supersonic region ( $M_\infty \leq 5$ ). Holden (1991) reported plans to obtain fluctuating wall pressures in interactions at Mach numbers between 8 and 16 but, to the author's knowledge, results are not yet published.

Loading levels in this paper are expressed both in terms of the rms of the pressure fluctuations  $\sigma p$ , (in either absolute or normalized form) or in terms of *sound pressure level* (SPL) where  $\text{SPL} = 20 \log_{10} (\sigma p / 0.00002) \text{ dB}$ . The reference pressure in the denominator,  $20 \mu \text{ Nm}^{-2}$ , is the acute threshold of hearing. Since  $\sigma p$  in a given experiment depends on the freestream static pressure,  $P_\infty$ , meaningful values of SPL for design purposes can only be generated if  $\sigma p$  is referenced to the design  $P_\infty$ . Similarly, meaningful comparisons of SPL from different experiments can

only be obtained if  $\sigma p$  is scaled using a common value of  $P_\infty$ . The value of  $P_\infty$  at 50,000 feet altitude, namely 1.69 psia ( $1.165 \times 10^4 \text{ Nm}^{-2}$ ) is used throughout this paper.

Interest in shock wave/boundary layer interactions has been sustained for more than forty years, largely because of their importance in such a wide variety of internal and external aerothermodynamics problems. There have consequently been many studies of such phenomena, with computation playing an increasingly important role since the mid 1970s. An excellent review of much of the early work was compiled by Green (1970). More recent reviews, focusing mainly on work of the past ten years in swept interactions have been written by Settles and Dolling (1990, 1992). Hamed and Shang (1989) present a survey and assessment of the data base of shock wave boundary layer interactions relevant to supersonic inlets. A survey of recent developments in 2-D shock wave boundary layer interactions and their control is given by Viswanath (1988). Recommendations for hypersonic building-block experiments for CFD validation have recently been presented by Marvin (1992), and some remarks on the implications that flowfield unsteadiness has with respect to CFD are discussed by Dolling (1992). Most recently, data bases of hypersonic experiments have been compiled by Settles and Dodson (1991) and by Holden and Moselle (1992). However, neither contain any details about flow unsteadiness.

Fluctuating surface and flow field data are far less common, particularly prior to 1980. Digital data acquisition systems capable of sampling at MHz rates and of acquiring millions of highly resolved data points now render such measurements much easier. Even so, fluctuating wall pressure measurements have not been made in such a wide variety of flows as have mean measurements, nor over such a broad range of flow conditions. Most of the data are from interactions generated by unswept or swept compression ramps, forward facing steps, flares, sharp and blunt fins, cylinders, and by impinging shocks. Discussion of what has been learned from these experiments is the focus of this review.

Only flows which are naturally unsteady are included. Forced unsteadiness, induced by oscillating boundaries or from time-varying upstream or downstream boundary conditions, is largely excluded. The rich field of self-sustaining coherent oscillations of impinging shear layers is excluded, as is the sub-class of unstable shock patterns associated with shock oscillations induced by spiked blunt bodies. Reviews of these fields are given by



Rockwell (1983) and Calarese and Hankey (1985), respectively. Further, since the emphasis is on supersonic and hypersonic flows, forced and self-excited oscillations in transonic diffuser flows are also excluded.

## 2 DISCUSSION

The discussion is split into several parts. For organizational reasons more than physical ones, 2-D and 3-D flows are largely discussed in separate sections. However, since they do have a great deal in common, they are discussed together where appropriate. Before focusing on turbulent flows, some brief remarks are made concerning the steadiness of laminar flows.

### 2.1 Shock-Induced Laminar Separation

It cannot be said with absolute certainty that shock-induced laminar separated flows are always steady. Nevertheless, the preponderance of evidence suggests that laminar separation induced by ramps, steps, and glancing and incident shocks is steady. In most experimental studies, it was implicitly assumed that the flow was steady, and the question was never addressed directly. However, there have been some checks. In the early studies of Chapman et al. (1958) it was reported that "high speed motion pictures (taken at  $M_\infty = 2.3$  with 2000 to 6000 frames per sec.) indicate the pure laminar separation over a step to be steady." In contrast, in the transitional case (i.e., transition occurs relatively far downstream of separation and relatively close to reattachment) Chapman et al. report that "high speed motion pictures indicated the flow to be unsteady in the region between transition and reattachment on the step." They also noted that, as the Reynolds number increased and transition moved closer to separation, "the angle of separation appeared unsteady in the motion pictures as did the flow downstream of transition."

Degrez and Ginoux (1983, 1984) examined the laminar interaction generated by a sharp fin at angle of attack at  $M_\infty = 2.2$ . A Kulite pressure transducer was installed flush with the test surface downstream of the fin trailing edge. Degrez and Ginoux state that "for the highest Reynolds number, fluctuating pressures were recorded, clearly indicating transition. Other transducer signals were steady." Although this is not direct proof of the steadiness of the upstream flowfield, it is unlikely that a transducer under the outgoing boundary layer would generate a steady output if the upstream interaction was unsteady.

In addition, circumstantial evidence supports the view that laminar interactions are steady. For

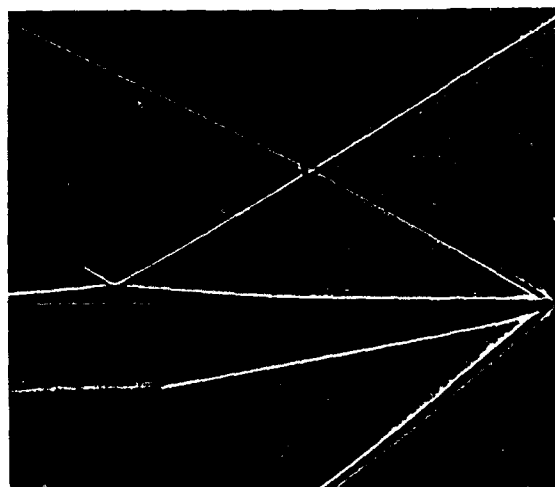


Fig. 2. Typical shadow photograph of a separated laminar interaction generated by an incident shock at Mach 2.2 (from Burgio, 1970).

example, Kaufman and Johnson (1974) report results from a study of incident shock interactions with a Mach 8 laminar boundary layer. Schlieren photographs of the interaction are composites from two different tunnel runs. One photograph includes the leading edges of the plate and shock generator, their shock waves, and the separating plate boundary layer; the other shows the downstream flowfield. The waves on each photograph are straight and intersect where the two photographs overlap, attesting to a steady flow. Indeed, shadow photographs of laminar interactions are typically characterized by smoothly varying *white lines* (indicative of the boundary layer edge) and straight shocks at reattachment and separation (Fig. 2). If the separated bubble was undergoing either periodic pulsations or random variations, rippled shocks and wavy boundary layer edges might be expected.

The only experimental evidence of unsteadiness of a supersonic laminar separation known to the author is the work of Ozcan and Holt (1984). LDV measurements were made on the plane of symmetry upstream of a circular cylinder at  $M_\infty = 2.36$ . It was reported that separation occurred about 6.8 diameters upstream of the cylinder "where it was difficult to make repeatable velocity measurements due to the unsteadiness of the flow." At the interface between the boundary layer edge and reversed flow, the variation in velocity was "between 80 and 440 m/s" for a data point with an average velocity of 292 m/s. Whether the separated shear layer or root vortex was transitional which fed distur-



bances upstream inducing motion of the separation point, or whether the unsteadiness was due to a natural instability, is not clear. The flow-field generated by a cylinder in a laminar boundary layer is a complex one, with both steady and unsteady regimes depending on Reynolds number. Recent numerical work by Visbal (1991;1,2) discusses many of these issues and presents simulations of both steady and unsteady flows. The reader is referred to these references for details.

## 2.2 Shock-Induced Turbulent Separation—2-D Flows

A useful departure point is the separated interaction generated by an unswept compression ramp. Although such flows exhibit an increasing degree of three-dimensionality near the wall as the bubble grows (variations in wall shear produce the classic node-saddlepoint pattern seen in flow visualization), the time-averaged flow-field is essentially 2-D. Detailed measurements by Nordyke (1987), Marshall (1989), and Marshall and Dolling (1990, 1992) show that such pronounced three-dimensionality in the wall shear stress field has no significant effects on the fluctuating wall pressures near separation; there is no evidence of any cyclic spanwise variations in rms levels. Thus this flowfield not only serves as a useful example for bringing out the salient features of the unsteadiness of shock-induced turbulent separated flows, but also serves as a useful reference against which to compare results from three-dimensional flows.

In separated compression ramp flows (or its axisymmetric or 3-D analog, the flare), the separated flow undergoes a large-scale, low-frequency motion, which can best be described as an *expansion/contraction* or *breathing* motion (Kussoy et al., 1987; Gramann, 1989; Gramann and Dolling, 1990,1). In this context, *low frequency* means low relative to the characteristic frequency,  $U_\infty/\delta_o$  of the incoming turbulent boundary layer. Typically the expansion/contraction process occurs at frequencies of a few hundred Hz to several kHz, even in flows in which  $U_\infty/\delta_o$  is order tens of kHz or higher. More is said about this in Sec. 2.2.4.

"Breathing" of the bubble results in large variations in flowfield scale. Kussoy et al. made wall pressure fluctuation measurements under the unsteady separation shock simultaneously with high speed shadow movies and LDV measurements. The model consisted of a tilted 30-deg. half-angle cone attached to a circular cylinder. Tests were made in a Mach 2.85 flow. Mean streamlines were deduced from the LDV data for the overall time-averaged case and for separation shock-forward

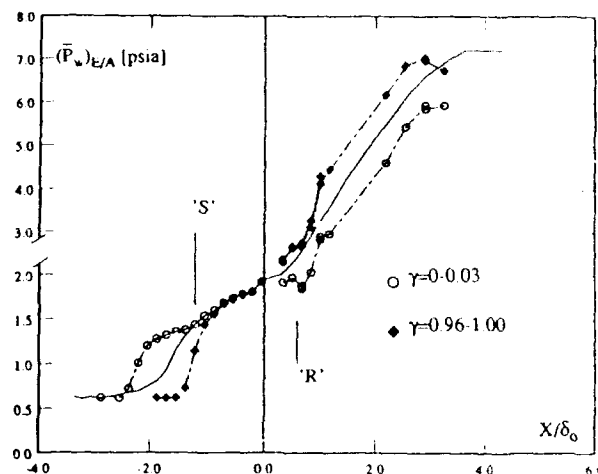


Fig. 3. Ensemble-averaged wall pressure corresponding to furthest upstream and furthest downstream locations in a Mach 5, 28-deg. compression ramp interaction (from Gramann, 1989).

and shock-back positions. Results on the plane of symmetry for the cone tilted 5 deg. showed that the separated bubble "expanded and contracted like a balloon." From data presented in Fig. 6 of Kussoy et al., Gramann and Dolling estimated that the variation in bubble length was from 1.5 to  $2.4\delta_o$ . In fact, because of the algorithm used by Kussoy et al. to determine the shock-back and shock-forward cases, the variation in bubble-size is probably underestimated (see Gramann and Dolling, 1990,1 for details).

Gramann (1989) and Gramann and Dolling (1990,1) made wall pressure fluctuation measurements in a 28-deg. ramp interaction at Mach 5. Using a conditional cross-correlation technique, it was shown that the instantaneous separation point occurred at the separation shock foot and the bubble size ranged from about  $1.7\delta_o$  to  $3.6\delta_o$ . In a flowfield whose time-averaged streamwise length is only about  $5\delta_o$ , this is clearly a significant variation in scale. Gramann (1989) also measured wall pressures throughout a Mach 5 compression ramp interaction when the separation shock was at its furthest upstream position (intermittency,  $\gamma$ , less than about 0.03) and furthest downstream position ( $\gamma$  about 0.96–1.00). The intermittency is simply the fraction of time the separation shock spends upstream of a given station. Ensemble-averaged wall pressures (Fig. 3) show quite clearly the expansion/contraction process. The solid line is the mean wall pressure measured using conventional means (i.e., wall pressure taps) or by averaging the unsteady signals, whereas the dashed lines correspond to the extremes of



the separation shock motion. Erengil (1989) and Erengil & Dolling (1989, 1991,2) have used a similar technique to look in detail at the flow structure upstream of the ramp corner. Some further remarks, focusing on implications for CFD, are given in Sec. 6.

Figure 4 shows mean and rms wall pressure distributions at  $M_\infty = 3$  and 5 measured by Murphy (1983) and Gramann (1989), respectively.

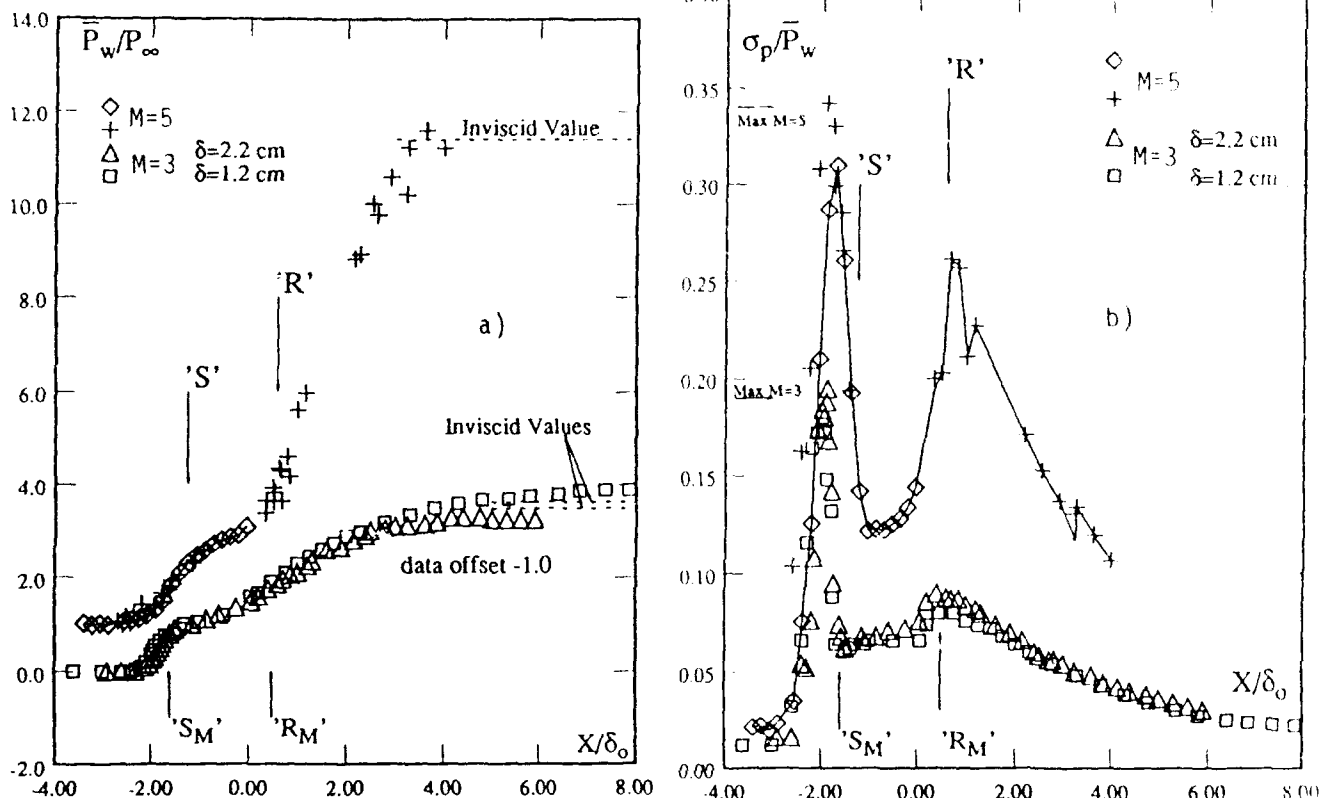


Fig. 4. Comparison of surface properties in Mach 5, 28-deg. and Mach 3, 24-deg. compression ramp interactions a) mean wall pressures, b) rms normalized by local mean wall pressure (from Gramann & Dolling, 1990).

Both interactions have about the same scale separated flow. Note, in the mean pressure distributions, that the Mach 5 data are shifted 1 unit of  $(\bar{P}_w/P_\infty)$  vertically. The rms distributions are shown normalized by the local mean wall pressure,  $\bar{P}_w$ , and "S" and "R" denote separation and reattachment, respectively, as indicated by the kerosene-lampblack surface tracer method. The reason why a well-defined separation line is obtained under an expanding/contracting bubble, and where it occurs in the intermittent region, are discussed in the Appendix. In the rms distributions, there are two local maxima, one just upstream of "S" and the other in the vicinity of "R." Both are caused by the expansion/contraction of

the bubble. Wall pressure signals show that the upstream maximum is generated by the unsteady separation shock foot. The moving shock generates an intermittent wall pressure signal  $P_w(t)$ , whose level fluctuates between the range characteristic of the undisturbed boundary layer (time  $t_1$  in Fig. 5) and that of the disturbed flow downstream of the shock (time  $t_2$ ). Kistler (1964) was probably the first to observe this behavior in his

studies of fluctuating wall pressures in forward-facing step flows at  $M_\infty = 3$  and 4.5. This characteristic *intermittent* signal has since been measured in interactions generated by unswept and swept compression ramps, blunt fins, circular cylinders, sharp fins at angle of attack, and by incident shock waves. Similarly shaped distributions of  $\sigma_p$  near separation have also been reported in studies in which the pressure signal was not shown or discussed explicitly, and include circular cylinders at transonic speed and axisymmetric flares and steps over a wide range of flow conditions. Intermittent wall pressure signals and a rapid rise in  $\sigma_p$  upstream of "S" appear to be universal features of supersonic and hypersonic



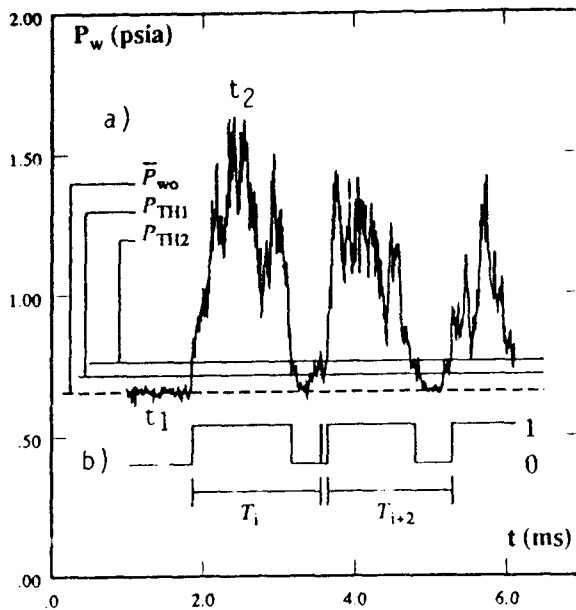


Fig. 5. Intermittent wall pressure signal upstream of separation "S" and conversion to boxcar representation (from McClure, 1992).

shock-induced turbulent separation. Indeed, they also occur in transonic diffusers and on transonic airfoils. Downstream of separation, the rms levels depend on the type and scale of the separated flow and are dependent on shock wave generator geometry. More will be said about that later.

As seen in Fig. 3, the streamwise wall pressure near reattachment is a function of separation shock position. At a fixed point on the ramp face, the instantaneous pressure therefore undergoes large variations as the bubble expands and contracts and the instantaneous reattachment point moves up and down the ramp face. It is this phenomenon, combined with turbulence amplification, which is responsible for the large fluctuating loads near reattachment. In the Mach 5 ramp flow, the maximum SPL in the vicinity of reattachment is of order 170 dB.

The intermittency  $\gamma$ , which was mentioned earlier, is a very useful parameter and is simply the fraction of time that the flow at a point is upstream of the separation shock wave. Thus  $\gamma$  varies from 0 to 1. Its magnitude can be calculated by first converting the pressure signal (Fig. 5a) into a boxcar function (Fig. 5b) and then calculating the fraction of the signal with level '1'. The conversion to the boxcar signal is based on the amplitude of the raw signal relative to some pre-established thresholds. A complete description of the conversion process, the logic behind it, the precautions necessary, and the sensitiv-

ity of the results to the threshold settings can be found in Dolling et al. (1990). Experimental results show that distributions of  $\gamma$  are good fits to the error function [Erengil and Dolling (1991,1)].

Distributions of  $\gamma$  can be used to estimate the length scale of the separation shock motion,  $L_s$ . In compression ramp flows and on centerline in blunt fin interactions,  $L_s$  spans the region from the upstream influence line,  $X_o$ , which is usually where  $\bar{P}_w$  first rises, to "S." In a given boundary layer, it can vary from a fraction of  $\delta_o$  to several  $\delta_o$ . Up to this point there is no evidence that  $L_s$  correlates simply with any incoming flow parameter. The effects of interaction sweepback on  $L_s$  are discussed later.

An important point relevant to flow physics and numerical modeling concerns the mechanism of upstream influence. The gradual increase in mean wall pressure downstream of  $X_o$ , seen in Fig. 4a, is not the result of upstream propagation of disturbances in a nominally steady flow, but is a direct result of shock motion. Upstream influence varies continuously with the maximum and minimum values corresponding to the furthest upstream and downstream locations of the shock wave. Conventionally, upstream influence is measured from  $X_o$  to the downstream reference position and has a fixed value. Pressure signals show that the conventionally defined  $X_o$  is simply the furthest upstream station at which an increment in  $\bar{P}_w$  is detectable using conventional instrumentation. Actually, at  $X_o$ ,  $\gamma$  is already about 0.03–0.05, and the skewness and flatness coefficients of the pressure signals already have very large values. In this sense, this length scale is somewhat arbitrary and is probably not a good test of a numerical method.

Having described briefly some of the results in compression ramp flows, pertinent questions at this point with respect to the flowfield unsteadiness include:

- (i) How are rms levels near separation influenced by Mach number, Reynolds number, boundary layer properties, separated flow scale, wall temperature condition, shock generator geometry, interaction sweepback, etc.?
- (ii) What are the frequencies and streamwise length scales of the separation shock motion, and how do they depend on incoming flow properties and shock generator geometry?
- (iii) What is the physical cause of the separation shock wave unsteadiness, and can it be controlled (or at least influenced favorably) through active or passive means?



- (iv) What are the rms levels under the separated flow and near reattachment, and how are they influenced by shock generator geometry and incoming flow conditions? What is the frequency content of the fluctuations in these regions, and on what does it depend?
- (v) How rapidly does the loading and spectral content of the outgoing boundary layer recover to the values characteristic of a zero pressure gradient flow at the new downstream conditions?

The remainder of this paper is largely an attempt to address these issues. It should be emphasized that there are few satisfactory answers to any of these questions. Answers require detailed parametric studies which have not been performed. Nevertheless, examination of the work of the late 1960s and early 1970s combined with the work of the mid 1980s to the present does provide partial answers to some of the questions raised. Moreover, it indicates very clearly where the knowledge base is inadequate and where future efforts should be directed.

### 2.2.1 RMS Levels Near Separation

Consider the intermittent pressure signal shown in Fig. 5. A relatively simple expression for the overall variance of the signal,  $\sigma^2 p$ , in terms of the contributions of the upstream and downstream pressure fields is given by Debiève and LaCharme (1986):

$$\frac{\sigma^2 p}{(\Delta P)_s^2} = (1-\gamma) \frac{\sigma p_u^2}{(\Delta P)_s^2} + \gamma \frac{\sigma p_d^2}{(\Delta P)_s^2} + (1-\gamma)\gamma \quad (1)$$

where  $(\Delta P)_s$  is the pressure rise across the separation shock, and subscripts  $u$  and  $d$  refer to the wall pressure fields upstream and downstream of the shock, respectively. The only inherent assumption is that the upstream and downstream fields are statistically homogeneous. If  $\sigma p_u$  and  $\sigma p_d$  are small compared to  $(\Delta P)_s$ , which, based on experimental evidence (Fig. 5), is a reasonable approximation, then the expression can be simplified to:

$$\frac{\sigma^2 p}{(\Delta P)_s^2} \approx \gamma(1-\gamma) \quad (2)$$

According to this expression, the maximum rms,  $(\sigma p)_{\max}$ , occurs at  $\gamma = 0.5$  (i.e., the midpoint of the intermittent region) and has a value of  $0.5 (\Delta P)_s$ . Although this is obviously a very simple formulation, its use as a prediction tool is limited since  $(\Delta P)_s$  is usually not known a priori. Of greater concern is whether such a simplified expression actually provides an accurate prediction of  $(\sigma p)_{\max}$ . Gonzalez and Dolling (1993)

attempted to assess the validity of this expression by calculating the ratio of the measured  $(\sigma p)_{\max}$  to  $(\Delta P)_s$  in a variety of flows including those induced by swept and unswept ramps, swept and unswept blunt fins, and sharp fins at angle of attack. In each case,  $(\Delta P)_s$  was taken as the difference between the mean pressure close to the downstream boundary of the intermittent region (i.e.,  $\gamma = 0.95$ ) and the undisturbed boundary layer pressure. Results are shown in Fig. 6. Although the data are plotted versus interaction sweepback angle, this is for convenience and is not meant to imply that  $(\sigma p)_{\max}/(\Delta P)_s$  is a function of sweepback. In fact, as indicated by Eq. (2),  $(\sigma p)_{\max}/(\Delta P)_s$  should be a constant. The experimental results show some scatter, but the bulk of the data fall within the range of about 0.4 to 0.6. In fact, for the blunt fins, the average value is 0.49, with a standard deviation of 0.04. The sharp fin and swept ramp averages and standard deviations are smaller and larger, respectively, than the blunt fin results. Overall, the average is 0.46, and the standard deviation is 0.085.

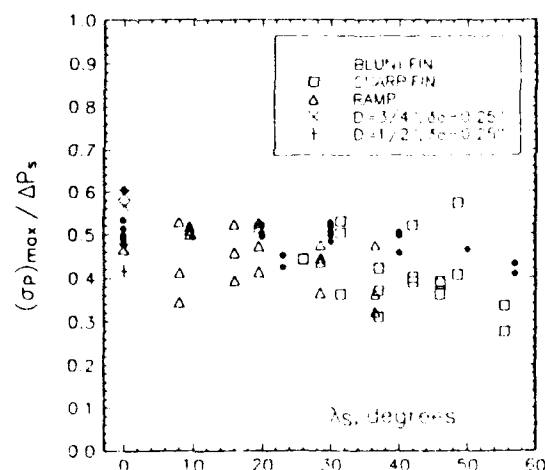


Fig. 6. Variation of  $(\sigma p)_{\max}/(\Delta P)_s$  for different interactions (from Gonzalez & Dolling, 1993).

Bearing in mind the difficulties both in locating and measuring  $(\sigma p)_{\max}$  as well as estimating  $(\Delta P)_s$ , particularly in highly swept flows where  $(\Delta P)_s$  was small, these results provide reasonable support for Eq. (2). As a first cut, Eq. (2) could provide an approximate estimate of the separation shock wave loading level. If the mean wall pressure and surface flow visualization were available for a given flow, then  $(\Delta P)_s$  could be taken as the mean value at separation minus the undisturbed boundary layer pressure. However, as discussed later, whereas "S" is at the downstream boundary of the intermittent region in unswept



flows, it moves upstream within the intermittent region with increasing sweepback; so it is likely that  $(\Delta P)_s$  would be underestimated in highly swept flows. Alternatively,  $(\Delta P)_s$  could be obtained from computation, although this could lead to some uncertainty in the estimate of  $(\sigma p)_{\max}$ , since the agreement between measurement and simulation is very much a function of the flowfield under study, as well as the turbulence model, etc.

### 2.2.2 Effects of Mach and Reynolds Number on RMS Pressure Levels and Intermittent Heating Near Separation

Since the flow turning angle at separation is typically of order 5–10 deg., irrespective of ramp angle, the separation shock strength increases with increasing Mach number. Thus it might be expected that, although  $(\sigma p)_{\max}$  would be approximately constant in terms of  $(\Delta P)_s$ , the absolute value of  $(\sigma p)_{\max}$  would be an increasing fraction of  $P_\infty$  with increasing Mach number. The Mach 3 and 5 flows of Fig. 4 appear to confirm this; the values of  $(\sigma p)_{\max}/P_\infty$  are 0.25 and 0.52, respectively. In terms of  $P_\infty$ , loading levels are everywhere higher at Mach 5, particularly on the ramp face. Table 1 gives values of  $\sigma p/P_\infty$  at four different locations in the interaction.

	Mach 3	Mach 5
Max. near "S"	0.25 (163)	0.52 (170)
At Corner	0.14 (158)	0.43 (168)
At "R"	0.23 (162)	0.95 (175)
Max. on Ramp	0.26 (163)	1.60 (180)

Table 1. Loading levels,  $\sigma p/P_\infty$ , at selected locations in compression ramp flows.

The values in parentheses following each value of  $\sigma p/P_\infty$  are the corresponding values of SPL in dB. It can be seen that very high loading levels occur on the ramp face.

Similar effects of Mach number are also seen in blunt fin and cylinder flows. Table 2 lists measured values of  $\sigma p/P_\infty$  near "S" and at the fin root at Mach numbers of 3, 4 and 5. The data are from Dolling and Bogdonoff (1981), Aso et al. (1991), and Brusniak (1991), respectively. At the fin root, the peak loading is very difficult to resolve accurately, due to steep gradients. Nevertheless, there is evidence of a large increase with Mach number. Again, the values in parentheses are dB, scaled to 50,000 feet. No values of SPL can be computed at Mach 4, since values of freestream static pressure were not provided. The most intense loads are produced at the root and exceed 180 dB.

Location	Mach No.	$\sigma p/P_\infty$
Near "S"	3	0.23 (160)
	4	0.52 ( )
	5	0.50 (170)
Fin Root	3	0.60 (170)
	4	3.07 ( )
	5	2.60 (184)

Table 2. Loading levels,  $\sigma p/P_\infty$ , at selected locations in blunt fin/cylinder flows.

Since separation shock strength is largely controlled by Mach number, then it might be anticipated that, in a given flow type,  $(\sigma p)_{\max}/P_\infty$  would only be a weak function of Reynolds number. This appears to be confirmed by experiment. Figure 7 shows the 24-deg. compression ramp at two values of  $Re_\delta$  at Mach 3; the two rms maxima near separation differ by only a few percent.

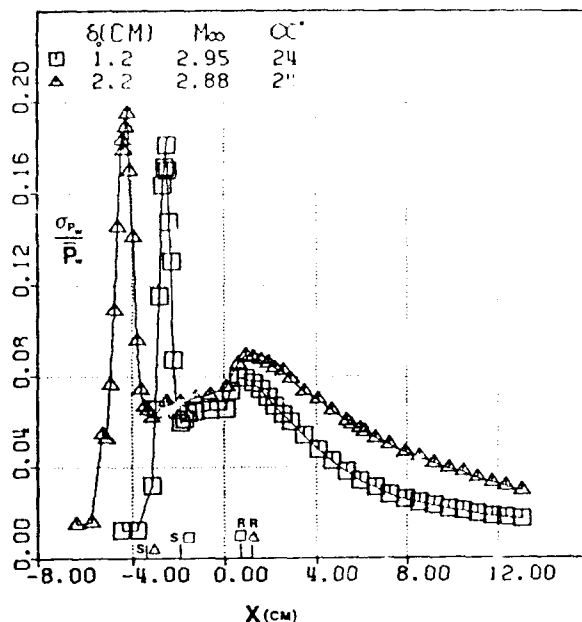


Fig. 7. Effect of  $Re_\delta$  on  $\sigma p/\bar{P}_w$  in a Mach 3, 24-deg. compression ramp interaction (from Murphy, 1983).

In terms of  $\sigma p/P_\infty$  near separation, the increase in  $Re_\delta$  resulted in an increase from 0.24 to 0.25. Experiments by Dolling and Bogdonoff (1981) in which wall pressure signals were measured upstream of blunt fins also show a similar weak variation. A sixfold increase in  $Re_\delta$  with a fixed diameter fin resulted in a decrease in  $(\sigma p/\bar{P}_w)_{\max}$  near separation of about 25 percent. However, in this case, part of this change can be attributed to the varying ratio of  $D/\delta$  since, even at a fixed  $Re_\delta$ ,  $(\sigma p/\bar{P}_w)_{\max}$  is a function of  $D$ . For exam-



ple, increasing  $D$  from 1.27 to 2.54 cm at fixed  $Re_\delta$  increased  $(\sigma p/\bar{P}_w)_{\max}$  from 0.18 to 0.23. For large  $D/\delta$ , as explained in Sec. 3.3,  $(\sigma p/\bar{P}_\infty)_{\max}$  should reach a constant value.

Hayashi et al. (1989) measured fluctuating heat transfer in an incident shock/turbulent boundary layer interaction at Mach 4. Measurements of the mean (in terms of Stanton number) and fluctuating heat transfer are shown in Fig. 8. Similar to the wall pressure, the heating rate is also intermittent with a large maximum near separation. In this experiment, the maximum value of  $\sigma q_w/\bar{q}_w$  is about 0.22. The only other fluctuating heat transfer data known to the author is that of Shifen and Qingquan (1992) in interactions induced by circular cylinders at Mach numbers of 5 and 7.8. The maximum value of  $\sigma q_w/\bar{q}_w$  near separation was about 0.5, twice the value at Mach 4, suggesting that this ratio may also increase with Mach number.

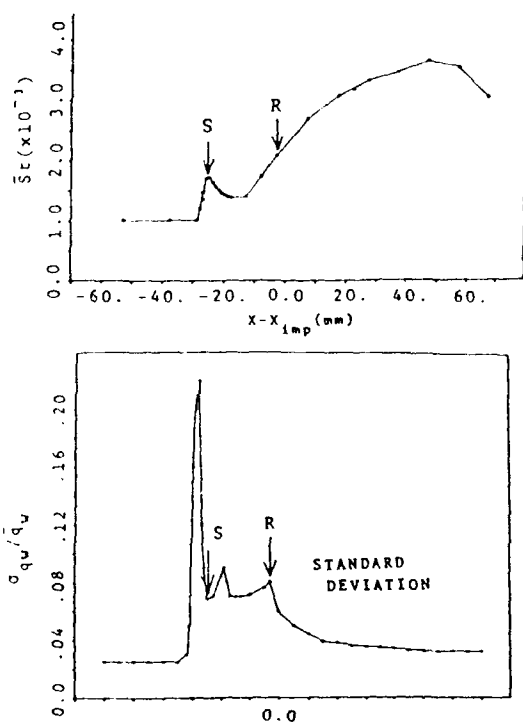


Fig. 8. Mean and fluctuating heat transfer in an incident shock interaction at Mach 4 (from Hayashi et al., 1989).

Shifen and Qingquan (1990) also made measurements of heat transfer fluctuations upstream of a step at Mach 7.8. Both wall pressure and heat transfer were intermittent, with frequencies in the range of 1–3 kHz. The standard deviation of the heat transfer rate increased rapidly in the

intermittent region reaching a maximum where the mean had increased by a factor of about two. The maximum was about 10 times the standard deviation in the incoming flow.

### 2.2.3 Effects of Separated Flow Scale on RMS Pressure Levels Near Separation

Experiments by Dolling and Or (1985) at Mach 3 showed that  $(\sigma p)_{\max}/P_\infty$  increased with increasing scale of the separated flow. As the compression ramp angle was increased from 16 deg. (incipient separation) to 24 deg. (separated bubble with a streamwise scale,  $L_{\text{sep}}$ , of about  $2\delta_o$ ),  $(\sigma p)_{\max}/P_\infty$  increased from about 0.11 to 0.20. These observations are consistent with the results of Coe et al. (1973) using a variable height, 45 deg. compression corner at Mach 2. Although  $(\sigma p)_{\max}$  was not well resolved, it is clear that it increased with increasing separated flow scale.

In the ramp experiment of Dolling and Or, the separated bubble size increased because the ramp angle was increased, and hence the overall inviscid pressure rise increased. The question of how the fluctuating load level near separation depends on overall inviscid pressure rise is not entirely clear. Experiments at Mach 5, using a compression ramp and circular cylinder for which the inviscid pressure ratios were about 11.5 and 29, respectively, have exactly the same maximum loading levels at separation. Other experiments using blunt fins (see Gonzalez and Dolling, 1993) result in the same levels of loading at a given spanwise station for fin angles of attack of zero and ten degrees. On the other hand, in glancing shock interactions, maximum loading at separation increases by about 75 percent, as the inviscid pressure ratio is increased from 5 to almost 12, whereas, in swept ramp flows, the loading increases by 100 percent as the inviscid pressure ratio is increased from about 11 to 12 (Schmisser, 1992). There is no consistent pattern from one configuration to another, suggesting that, in general, inviscid pressure ratio is not the appropriate parameter for correlating maximum loading near separation. As seen earlier,  $(\sigma p)_{\max}$  actually correlates with  $(\Delta P)_s$ .

Recent work at Mach 5 (Erengil 1991,3, McClure 1992) suggests that the actual behavior of  $(\sigma p)_{\max}$  may be asymptotic, once  $L_{\text{sep}}$  increases beyond some large value,  $(\sigma p)_{\max}$  remains fixed. First, in experiments using a 28-deg. compression ramp at Mach 5, it was observed that if disturbances such as a shear layer manipulator or a fishing line (see Fig. 9) were introduced into the flowfield, the separated flow length scale increased substantially. Rms distributions (Fig. 9a) show



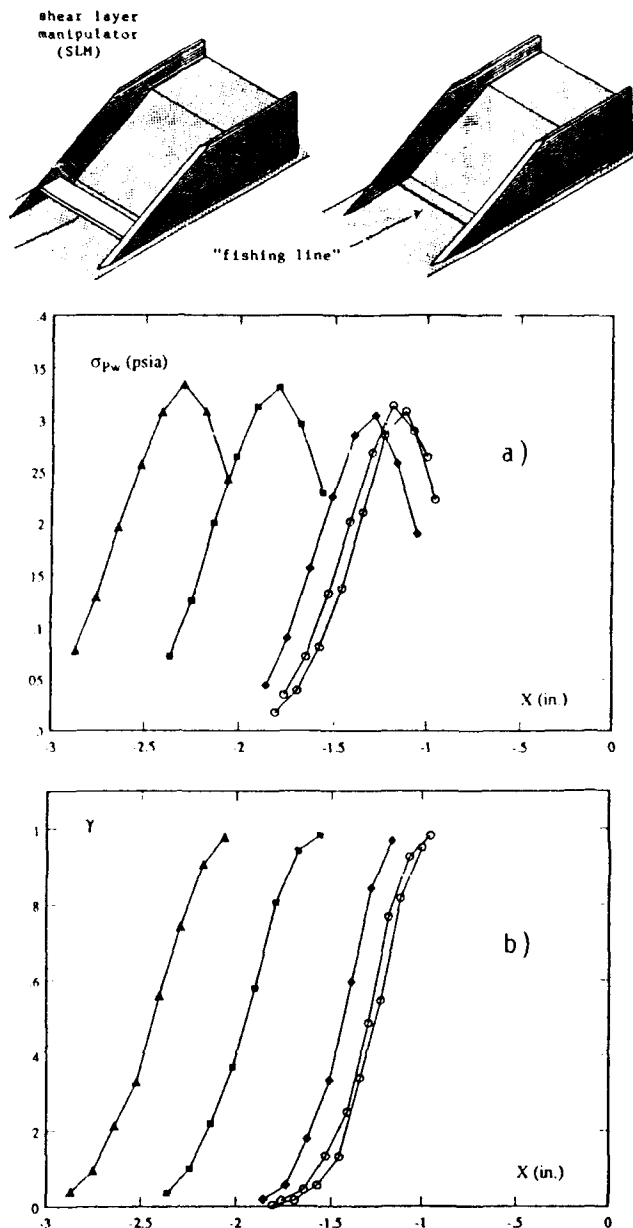


Fig. 9. Effects of separated flow length scale in a Mach 5, 28-deg. compression ramp interaction on a) rms pressure levels, b) intermittency distributions.

that  $(\sigma p)_{\max}$  increases only very slightly as  $L_{\text{sep}}$  doubles. Intermittency distributions (Fig. 9b) show that the region of shock motion shifts progressively upstream, but the shock motion length scale is essentially unchanged. Second, the results of McClure and Dolling (1992) using a boundary-layer manipulator (BLM), shown opposite, are also consistent with the idea that decreasing separated flow scale results in a decrease in load-

ing level for a constant overall inviscid pressure rise. Rms distributions for the baseline flow and with two BLM's (with 15-deg. and 35-deg. leading edges) are shown in Fig. 10. Flow conditions and baseline geometry are the same as for Fig. 9. However, in studies of the effects of suction using the same ramp model, also at Mach 5, McClure and Dolling (1991) found contradictory results. Suction was applied through a 6.8 mm slot spanning most of the ramp face and located at the mean reattachment location. With slot-alone (no suction), separation shifted about  $1\delta_o$  upstream compared to the baseline case, and  $(\sigma p)_{\max}$  increased about 15 percent. With suction, separation moved downstream, as expected, but in this case  $(\sigma p)_{\max}$  did not decrease but was 10–12 percent above the baseline value.

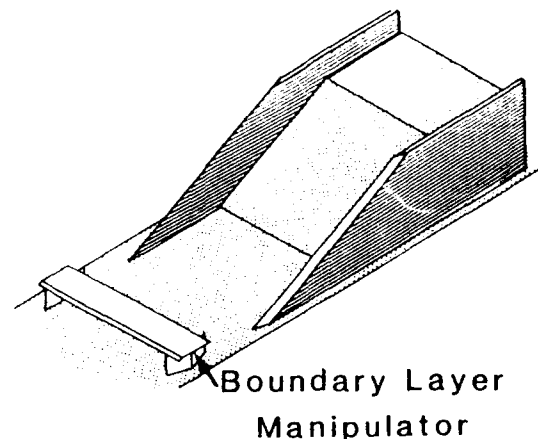


Figure 11 sums up the results from all of these studies. The value of  $P_\infty$  is the same in all cases, and the abscissa,  $X'$ , is the location of  $\sigma p_{\max}$  upstream of the corner (normalized by  $\delta_1$ , the incoming boundary layer mass flux thickness) and reflects the scale of the separated flow. If the suction study results are ignored, the general trend is that  $(\sigma p)_{\max}$  increases rapidly initially, but beyond  $X' \approx 1\delta_1$  reaches an almost constant value. The reasons for the discrepancy are presently not clear.

#### 2.2.4 Separation Shock Frequency

None of the optical or other studies provide any evidence that the shock motion is periodic. High speed schlieren cinematography by Degrez (1981) in blunt fin flows at Mach 3 has shown that the probability density distributions of the shock foot position are Gaussian. Shock foot histories deduced from multi-channel simultaneously sampled wall pressure signals in both swept and unswept compression ramp interactions also have a Gaussian distribution (Erengil & Dolling, 1992). Normalized power spectra presented by Dolling and



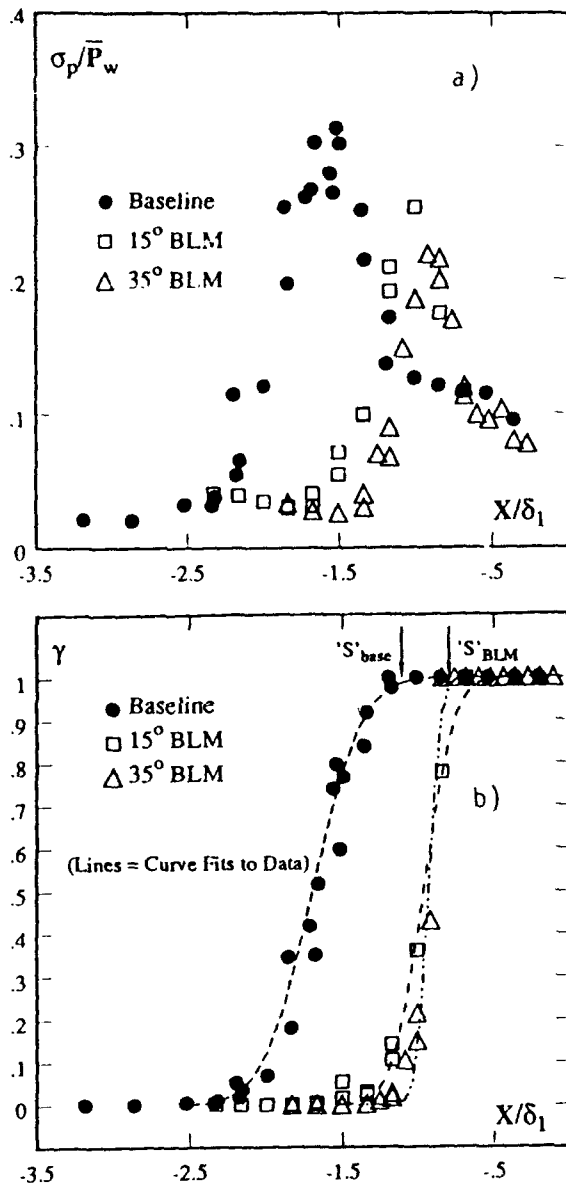


Fig. 10. Effects of boundary layer manipulators (BLM) on a) rms wall pressure, b) intermittency in a Mach 5, 28-deg. compression ramp interaction (from McClure & Dolling, 1992).

Brusniak (1989) for a variety of flow types are all broadband, with a large fraction of the energy at relatively low frequencies, as mentioned earlier. An example from Erengil and Dolling (1991,1) in Fig. 12 shows power spectra in the undisturbed boundary layer and under the translating shock in a 28 deg., Mach 5 compression ramp interaction. The ratio  $U_\infty/\delta_o$  for this flow is about 50 kHz. At  $x/\delta = -2.22$  and  $-1.55$ , the intermittency is low and the spectrum is bimodal, reflecting the contributions from both the shock-induced fluctua-

tions (about 0.2–2 kHz) and the undisturbed and separated boundary layer. Within the intermittent region, the power spectrum retains the same shape with a large fraction of the energy below 2 kHz. In the separated flow, the increased contribution from high frequencies is again evident. This general trend is typical of all the spectral results given in the literature.

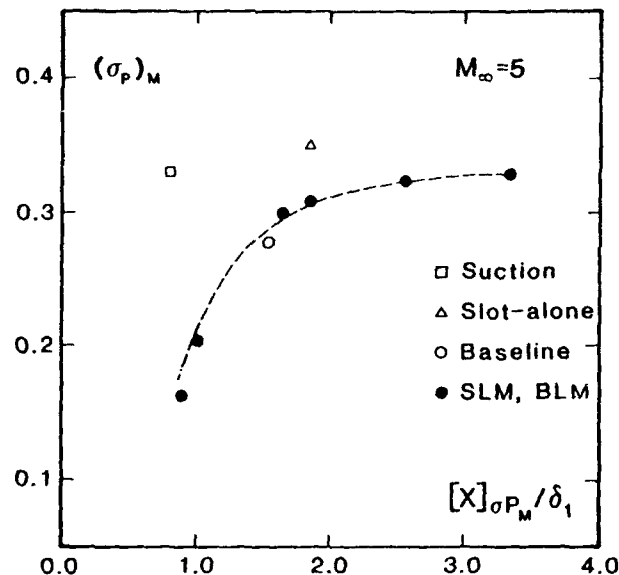


Fig. 11. Variation of  $(\sigma p)_{\max}$  with separated flow length in a Mach 5 compression ramp flow.

In cylinder or hemicylindrically blunted fin interactions, shock frequencies increase with decreasing leading edge diameter and decrease with increasing incoming boundary layer thickness (Smith, 1987). This result and some comments on appropriate correlating parameters for the power spectrum are discussed further in Sec. 3.3. With compression ramps, Dolling and Or (1985) noted that the shock frequencies decrease as the ramp angle and extent of separation increase. In the light of more recent studies showing how  $(\sigma p)_{\max}$  increases with increasing scale of separation, it is probable that the power spectrum also behaves asymptotically.

Robertson (1971) correlated intermittent region power spectra from a Mach 2, 45-deg. compression ramp experiment and from upstream of circular cylinders at  $M = 1.4$  and 1.6 in the form  $G(f)U_\infty/q_\infty^2\delta_o$  versus  $f\delta_o/U_\infty$ .  $G(f)$  is the power spectral density in units of (pressure)<sup>2</sup>/Hz, and  $f$  is the frequency in Hz. The results of Dolling and Or (1985) compared poorly with this correlation, particularly for  $f\delta_o/U_\infty < 0.1$ , the dominant range of shock motion. Robertson also scaled spectra using the separated flow length,  $L_{sep}$ , instead of  $\delta_o$  and obtained a marginally superior



correlation. Use of  $L_{sep}$  to correlate the spectra of Dolling and Or resulted in increased scatter compared to  $\delta_o$ . If relatively simple parameters describing the model geometry and incoming flow are to be used for correlations, it is probable that different parameters will be required in different interactions. In 3-D interactions, the problem is particularly complex. For example, in blunt-fin induced flows, the shock frequencies increase with increasing spanwise distance (i.e., increasing flow-field sweep) such that power spectra cannot be collapsed using simple parameters such as  $D$  or  $\delta_o$ , but will require parameters which reflect the local flowfield properties. Further comments on this subject are given in Sec. 3.3. Appropriate parameters for collapsing spectra is an area important in practical applications and one requiring substantially more work.

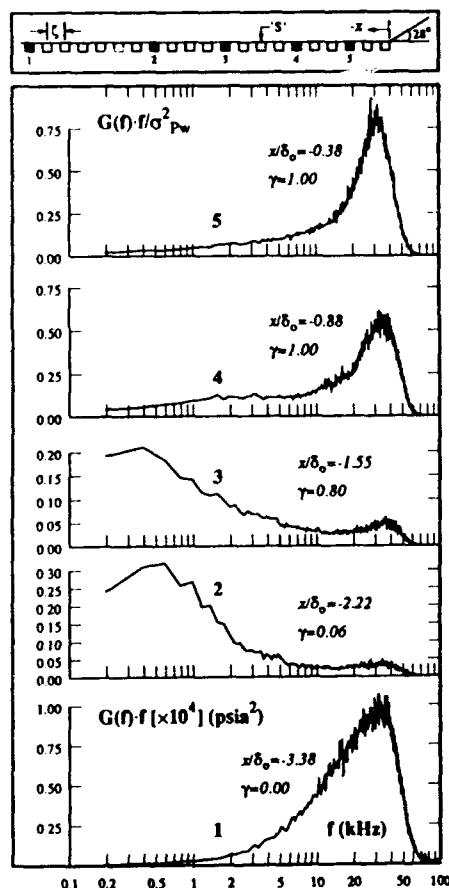


Fig. 12. Power spectra in the intermittent region of a Mach 5 compression ramp interaction.

To isolate the shock component of the pressure signal, several authors have employed conditional sampling algorithms [Dolling and Murphy (1983), Andreopoulos and Muck (1987), Narlo

(1986), Dolling and Smith (1989), Dolling et al. (1992)]. Their common feature is the conversion of the pressure signal into a *boxcar* of amplitude unity and varying frequency. The time  $T_i$  between consecutive passages of the shock over the transducer can be determined and statistics performed to obtain the probability distribution of  $T_i$  and the mean value  $T_m (\equiv \frac{1}{N} \sum_{i=1}^N T_i)$ , where  $N$  is the number of periods. It should be noted the  $1/T_m$  is the shock zero-crossing frequency,  $f_c$ , not the mean shock frequency.  $f_c$  is simply the number of crossings per second of the transducer by the shock wave, whereas the mean shock frequency is  $\frac{1}{N} \sum_{i=1}^N f_i$  where  $f_i = 1/T_i$ . Since the pressure signal is of a turbulent flow, precautions must be taken to ensure that high-frequency turbulent fluctuations are not inadvertently counted as shock waves. This problem and others are discussed by Dolling (1990). The utility of  $f_c$  is that shock motion can be characterized by a single frequency and rapid comparisons can be made between flows. Caution is required, however, since  $f_c$  is sensitive to threshold settings and thus comparisons should only be made between results obtained using the same algorithm and threshold settings. Also, the shock motion is broadband, and characterization by a single value can be misleading.

The zero-crossing frequency distribution upstream of a 28-deg. compression ramp at Mach 5 is shown in Fig. 13. Recall that the power spectra were shown earlier in Fig. 12. The intermittency distribution is also shown. The solid lines pass through the average values at each station. The dashed line is the error function fit to the intermittency data. The good fit shows that separation shock crossings are distributed in Gaussian fashion within the intermittent region. Thus the probability of finding a shock passage is at a maximum near  $\gamma = 0.5$ , and it decreases to zero upstream of *UI* and downstream of *S*. This result is also seen in the zero-crossing frequency distribution that has a maximum value of about 1.0 kHz at  $\gamma \approx 0.5$ .

### 2.2.5 Separated Flow Region

At *S*, or just downstream of it, the highly skewed pressure signals of the intermittent region are again essentially Gaussian. If the separation length is large enough, both  $\sigma p$  and  $\bar{P}_w$  reach constant plateau levels [Chyu and Hanly (1969), and Coe et al. (1973)]. Compared to the undisturbed flow,  $\sigma p$  is significantly higher. The measurements of Coe et al. upstream of a forward-facing step at 5 Mach numbers ranging from 1.7 to 3.5 show only a weak effect of  $M_\infty$  on the ratio



$\sigma p/q_\infty$ . The latter varied from about 0.03 to 0.04 with "a slight increase in intensity with increasing Mach number." At Mach 5 in an unswept compression ramp interaction, Gramann (1989) obtained a value of about 0.02 for  $\sigma p/q_\infty$ . The same value was measured by Murphy at Mach 3 in a 24-deg. compression ramp flow. However, in both cases the separation was relatively small ( $\approx 2-3\delta_o$ ) and the flow was still undergoing compression.

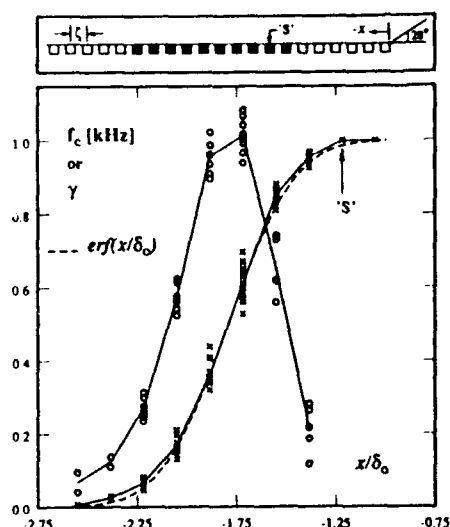


Fig. 13. Zero-crossing frequency and intermittency distributions in a Mach 5 compression ramp flow.

Coe et al. (1973) tried several combinations of length and velocity for the reduced frequency parameter and for the abscissa of the power spectrum. These included  $\delta_o/U_\infty$ ,  $\delta/U_\infty$ ,  $\delta/U$ ,  $\delta^*/U_\infty$ ,  $L_{sep}/U$ ,  $(L_{sep} - X_s)/U$ , and  $(S_s - X_s)/U$ , where  $\delta$ ,  $\delta^*$ , and  $U$  are local values,  $X_s$  is the distance upstream of the corner, and  $S_s$  is the length of separation measured upstream of the corner. No single reduced frequency or spectral density parameter was more effective over the full range of frequencies and for the different models tested (axisymmetric flares and forward facing steps, and 2-D forward facing steps). The best parameters were  $f\delta/U$  and  $f(S_s - X_s)$ . Generally,  $U$  is not known; but this is not critical, since the use of  $U$  or  $U_\infty$  produces only minor changes. The same applies to the use of  $q$  or  $q_\infty$  in the power axis scaling. Overall, a reasonably good correlation was obtained by plotting  $G(f)U/q_\infty^2\delta$  versus  $f\delta/U$ . However, the data used were all at  $M_\infty = 2$ .

Dolling and Or (1985) scaled their Mach 3 compression ramp data the same way, but using  $U_\infty$  and  $\delta_o$  rather than local values. The spec-

tra fell below the data band of Coe et al., although, as the separated flow length increased, the Mach 3 data came progressively closer to the band. Whether these are universal parameters is not clear, and more work is needed to clarify the issue.

## 2.2.6 Outgoing Boundary Layer

There are few data in the outgoing boundary layer, largely due to tunnel constraints. Compression ramp models must be long enough to avoid trailing edge effects on reattachment but short enough to avoid tunnel blockage. In compression ramp flows,  $\sigma p$  continues to increase downstream of reattachment, although  $\sigma p/\bar{P}_w$  (Fig. 4) reaches a maximum close to reattachment. The slow readjustment of the boundary layer is evident from the rms distributions and from the evolution of the skewness coefficient of the wall pressure fluctuations (Fig. 14). At both Mach 3 and 5, the skewness passes through zero about  $3\delta_o$  downstream of the corner and appears to level off at a value of about  $-0.2$ .

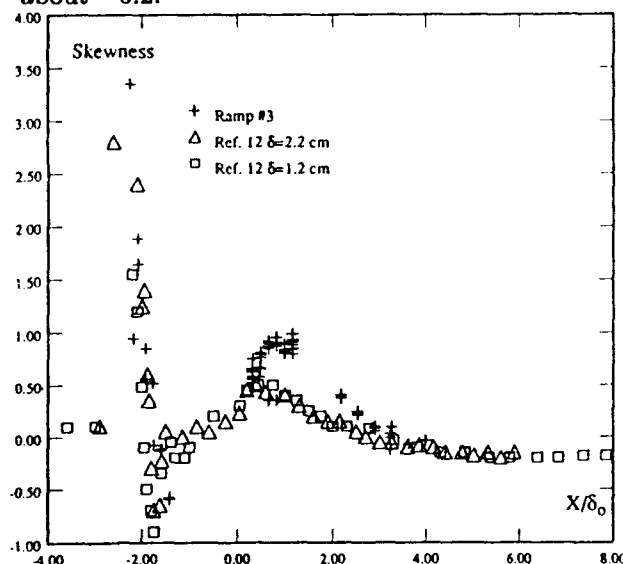


Fig. 14. Skewness coefficient distributions in Mach 5 and Mach 3 compression ramp interactions (from Gramann, 1989).

The effects of expansion/contraction of the separated flow are felt far downstream on the ramp face. The low-frequency flapping motion of the outgoing boundary layer is quite evident in conditionally sampled pitot surveys made by McClure & Dolling (1991). By simultaneous acquisition of fluctuating wall pressures under the unsteady separation shock and fluctuating pitot pressures above the ramp face, McClure & Dolling generated frozen pitot pressure profiles. This was



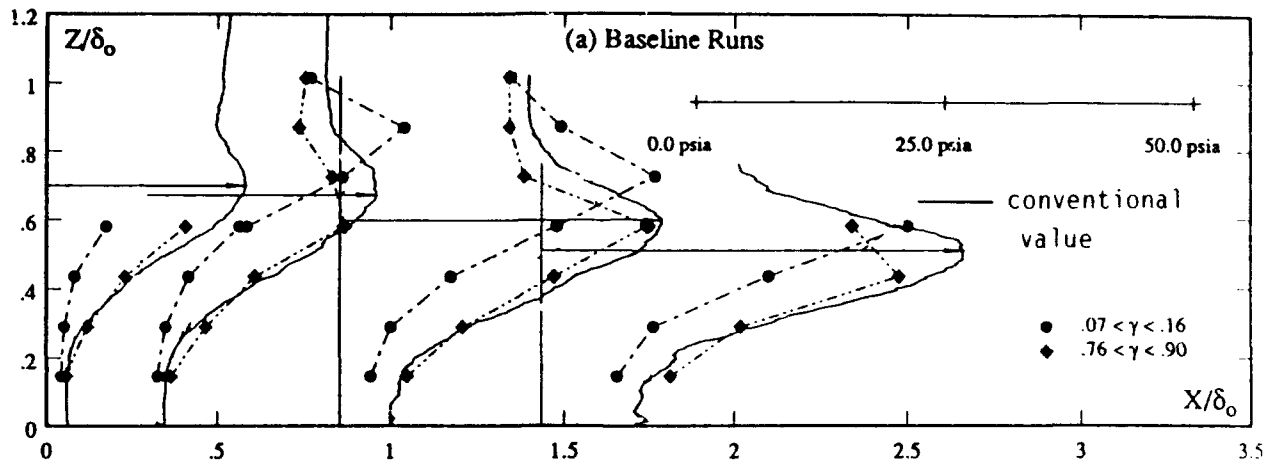


Fig. 15. Mean and conditionally sampled pitot pressure surveys in the outgoing boundary layer of a Mach 5, 28-deg. compression ramp interaction (from McClure & Dolling, 1991).

done by averaging pitot pressures only when the separation shock was located between two pre-selected pressure transducers (i.e., shock bracketed in a narrow range of intermittencies). Results for high and low intermittency ranges are shown in Fig. 15, together with the conventionally measured, time-averaged pitot survey. Data are shown at four streamwise stations on the ramp. As the separation shock moves downstream (to a location of higher intermittency), the downstream extent of the interaction shrinks, and vice-versa.

The low-frequency flapping is also evident in power spectra measured by Gramann and Dolling (1990,2) under the outgoing boundary layer in a Mach 5 compression ramp interaction. Although they are qualitatively similar to spectra of an undisturbed boundary layer, there is a much larger contribution to the variance from low frequencies (those in the range of the separation shock motion) than in an undisturbed boundary layer. Coherence function measurements between streamwise separated transducers on the ramp face show high coherence in the broadband of frequencies characteristic of shock motion. With increasing distance downstream, the coherence at higher frequencies increases as the outgoing flow becomes more like an attached turbulent boundary layer. Gramann also shows cross-correlations between wall pressure signals under the translating separation shock wave and on the ramp surface. As seen in the conditionally sampled wall pressure distribution of Fig. 3, as the shock moves forward (i.e., rising pressure on upstream channel), pressures on the ramp fall, and vice versa; so

the maximum cross-correlation coefficient is negative. As would be expected, the effect of the shock motion decreases with increasing distance downstream.

Gramann also examined the relative contributions to the overall rms from the low-frequency pressure fluctuations (due to flapping of the outgoing boundary layer) and high frequency fluctuations (due to turbulence). In Fig. 16, the solid line shows the rms pressure calculated the usual way (i.e., based on 100 records of 1024 data points with a single mean value). The dotted line employs the same 100 data records, but is calculated using 16-point data records, each with its own mean. The effect of using 16-point records is to filter out the lower frequency component of the signal. All of the rms values of the 16-point records were then averaged to give the dotted line. Thus, the difference between the solid and dashed lines provides a measure of the influence of the separation shock motion on the overall rms. Even with the contribution from the low-frequency flapping removed, the rms values are quite large, showing that pressure fluctuations due to turbulence amplification are significant.

Gramann also calculated the variation of the rms with separation shock position, and these results are shown by the symbols in Fig. 16. For  $X/\delta_0 < 1.2$ , rms levels are lower than the dashed line for the shock upstream ( $\gamma < 0.5$ ) and equal to or larger than the dashed line for the shock downstream ( $\gamma > 0.5$ ). These trends are reversed further downstream. Gramann explains this reversal using a flowfield model in which the fluc-



tuation statistics are fixed and the flowfield slides up and down the ramp in the opposite direction to the separation shock wave motion.

### 3 THREE-DIMENSIONAL FLOWS

Fewer measurements of fluctuating loads have been made in 3-D flows compared to 2-D flows, and the data are far more difficult to interpret since the flowfield above the transducers may be highly skewed. Much of the work has been done in the past seven years. The interactions studied include flows induced by (i) swept planar shocks from sharp fins at angle of attack [Tran et al. (1985), Tran (1987), Tan et al. (1987), Gibson (1990), Gibson and Dolling (1992), Schmis-seur (1992), Schmis-seur and Dolling (1992), and Garg and Settles (1993)]; (ii) crossing planar shocks generated by sharp fins at angle of attack [Batcho et al. (1989)]; (iii) swept compression ramps [Tran (1987), Boitnott (1990), Dolling et al. (1991), Erengil and Dolling (1992)]; (iv) unswept circular cylinders [Robertson (1969, 1971), Narlo (1986), Dolling and Narlo (1987), Smith (1987), Dolling and Smith (1988, 1989), Brusniak (1991), Bibko et al. (1991), Shifen and Qingquan (1992)]; (v) unswept hemicylindrically blunt fins [Dolling and Bogdonoff (1981), Dolling and Narlo (1987), Dolling and Brusniak (1991), Gonzalez and Dolling (1993), and Barnhart (1993)]. Barnhart's work is as yet unpublished. To the author's knowledge, only Kleifges

and Dolling (1993) have examined the effects of leading edge sweepback on fluctuating loads on centerline upstream of the fin. This section focuses primarily on what has been learned about the unsteadiness from these studies. A review of the mean surface properties and flowfield structure in such interactions is given by Settles and Dolling (1990).

Almost all of the work cited above was carried out at or below Mach 5. The only exception is the work of Shifen and Qingquan, which was carried out at Mach numbers of 5 and 7.8. The latter study also included measurements of fluctuating heat transfer near separation. In the discussion below, the swept ramp results are presented first, followed by the sharp and blunt fins. For the reasons mentioned earlier, there are few measurements in the outgoing boundary layer, and thus little is known about the downstream flowfield.

#### 3.1 Swept Compression Ramps

Boitnott (1990) made fluctuating wall pressure measurements upstream of the corner line in interactions generated by unswept, 10-deg. and 20-deg. swept models at Mach 5. Erengil and Dolling (1992) extended this study to include sweeps of 25, 30, 40, and 50 deg. In both studies the ramp streamwise angle was fixed at 28 deg. In the earlier work of Tran (1987) at Mach 3, data are presented for a 60-deg. swept model with streamwise ramp angles of 24 and 30 deg. Since measurements were made only along a single line perpendicular to the ramp corner line, no information can be gleaned concerning spanwise variations. To the author's knowledge, there are no measurements of fluctuating pressures on the surface of swept ramps.

Wall pressure rms distributions upstream of the corner are generally qualitatively similar to those in the unswept case (Fig. 7). The data are plotted versus  $(X+X_0)/(Z+Z_0)$ , which is the tangent of a conical ray from the virtual conical origin. There is a local maximum generated by the unsteady separation shock and a relatively constant value under the separated flow. The cause of the rapid rise in rms near the corner is unclear. Quantitatively, rms levels generally decrease with increasing sweep.

In the experiments of Erengil and Dolling, the 10-deg. swept ramp interaction converged to cylindrical symmetry. In this cylindrical case, the maximum rms generated by the separation shock was only slightly lower than in the unswept case and was constant spanwise. However, the intermittent region was about 20 percent shorter and the band of shock frequencies higher.

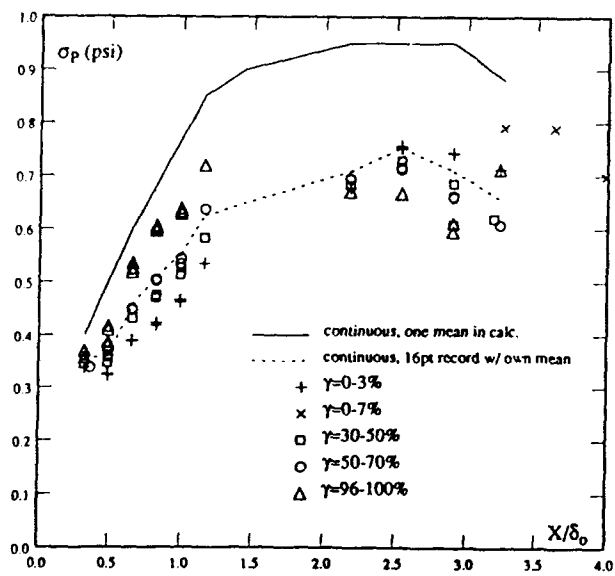


Fig. 16. Rms wall pressures as a function of separation shock position in a Mach 5 compression ramp interaction (from Gramann, 1989).



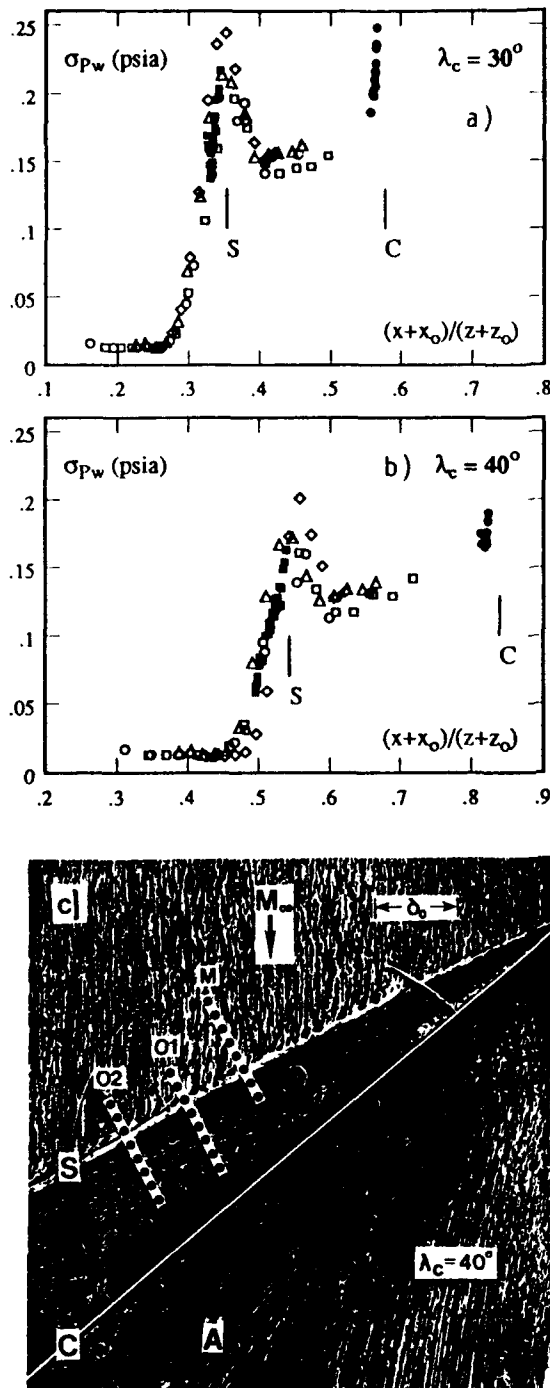


Fig. 17. Rms wall pressure distributions in conical coordinates in swept compression corner interactions a) corner sweepback,  $\lambda_c = 30^\circ$ , b)  $\lambda_c = 40^\circ$ , and c) kerosene-lampblack surface traces for  $\lambda_c = 40^\circ$  with instrumentation rows indicated (from Erengil & Dolling, 1992).

The entire measurement region was within the inception region for the 20-deg. model. The maximum standard deviation increased spanwise but did not exceed the unswept maximum value. Shock frequencies spanned a broader range than either the unswept or 10-deg. cases. In the highly swept interactions (corner line sweeps greater than 25 deg. at Mach 5), the rms distributions were conically symmetric, as were the mean distributions.

Figure 18 shows  $(\sigma p)_{\max}$  in the intermittent region from several rows at different distances from the ramp apex plotted versus the local sweepback angle of the separation line,  $\lambda_s$ . The rms decreases by a factor of about 2 as the separation line is swept back from 0 to 36.5 deg. Inspection of the wall pressure signals near separation highlights the physical effects of sweepback. Sample signals at  $\lambda = 0, 20$  and 40 deg. (with their corresponding amplitude probability density distributions) are shown in Fig. 19. The signal from the highly swept flow ( $\lambda_c = 40^\circ$ ) differs from the other two; although it is still intermittent, it has lower amplitude fluctuations at higher frequency, and the secondary peak in the probability distribution is no longer present. In general, the amplitude of the wall pressure fluctuations decreases, and the frequencies increase with increasing sweep. The change is initially gradual with increasing sweep, but becomes more

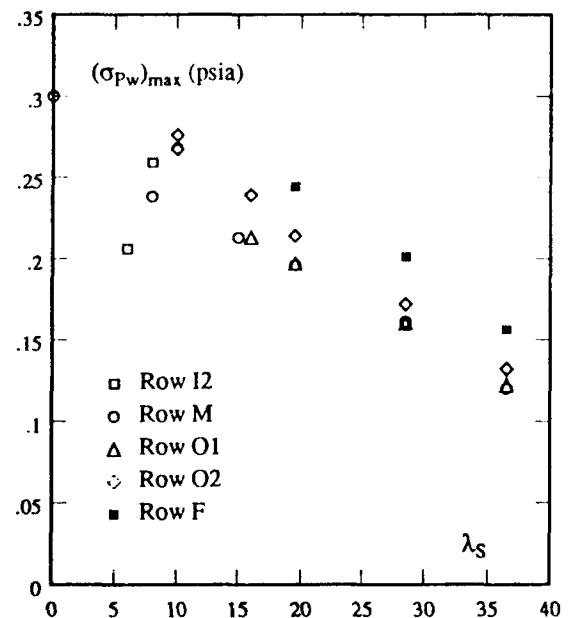


Fig. 18. Maximum rms level near separation in Mach 5 swept compression ramp interactions as a function of separation line sweepback (from Erengil & Dolling, 1992).



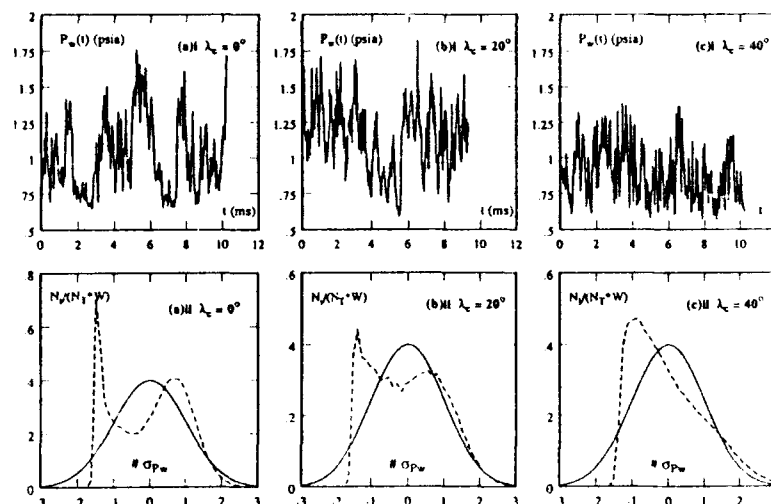


Fig. 19. Sample wall pressure signals and corresponding probability density distributions in unswept and swept compression ramp interactions (from Erenkil & Dolling, 1992).

rapid as sweep increases ( $> 25$  deg.). Power spectra at the location of the maximum rms for all seven sweep angles (Fig. 20) show this trend very clearly. The range of separation shock frequencies increases from about 0.3–0.5 kHz for unswept flow to about 2–7 kHz in highly swept flows. Note that, for a fixed sweep, the frequency content of signals in the intermittent region is independent of position.

Figure 21a shows the normalized length of the intermittent region,  $L_i/\delta_o$ , as a horizontal line for the unswept and the moderately swept interactions ( $\lambda_c \leq 20$  deg.). Since highly swept interactions ( $\lambda_c \geq 25$  deg.) are quasi-conically symmetric, it is more appropriate to define the intermittent region length in terms of an angular increment rather than in terms of  $\delta_o$ . Figure 21b shows the angular extent of the intermittent region by a vertical line drawn from  $\lambda_0$  to  $\lambda_1$ . Here,  $\lambda_0$  and  $\lambda_1$  are the sweepback angles of rays along which the intermittency is about 0.02 and about 0.98, respectively. In this representation, each line forms a scale ranging from  $\gamma \approx 0.98$  to  $\gamma \approx 0.02$ . The relative position of the separation line from the flow visualization is also indicated on each of these lines by  $\lambda_s$ . The decreasing length of the horizontal lines in Fig. 21a (and the vertical ones in highly swept interactions in Fig. 21b) shows quite clearly the shrinking of the intermittent region as the interaction is progressively swept back. Note, however, that in a given quasi-conical interaction the length of the intermittent region grows spanwise. Furthermore, the changing position of the marker (i.e.,  $\lambda_s$ ) indicating the location of the separation line shows

that the separation location from surface flow visualization moves upstream in the intermittent region towards lower and lower values of intermittency. A possible explanation of this phenomenon is given in the Appendix.

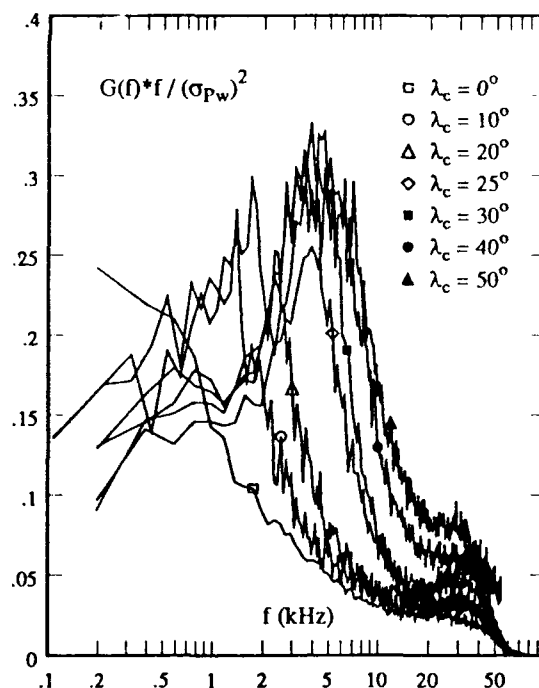


Fig. 20. Power spectra at position of maximum rms near separation in unswept and swept compression ramp interactions (from Dolling & Erenkil, 1992).



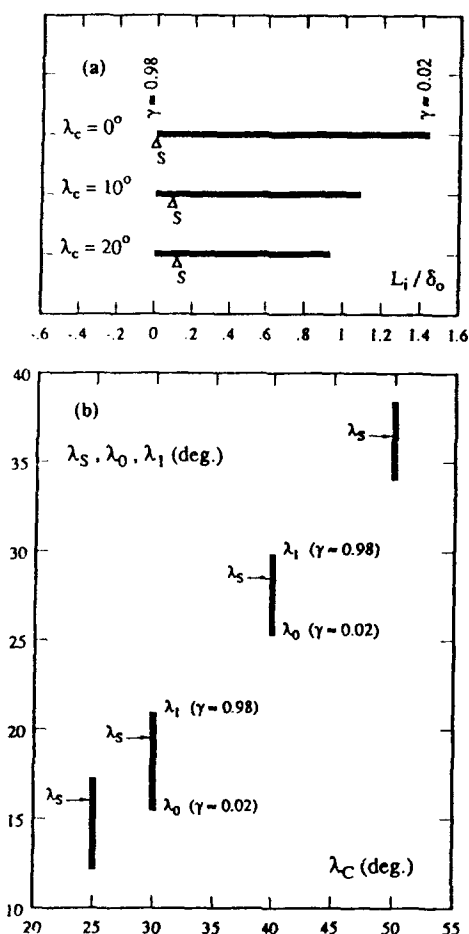


Fig. 21. Variation of intermittent region length and relative location of the separation line with ramp sweepback angle a) unswept and moderately swept flow, and b) conically-symmetric (i.e., highly swept) flow.

Erengil and Dolling (1992) examined the shock dynamics directly, using shock foot position and velocity histories deduced from simultaneously sampled wall pressure signals. They found that the separation shock dynamics, defined in terms of the shock foot history and its statistics, are essentially the same in all swept ramp interactions. The separation shock foot position is normally distributed, and the mean shock velocities are essentially equal. The only difference between flows is in the length of the region in which the separation shock moves. Higher shock frequencies are therefore a direct result of the decrease in the length scale of the separation shock motion.

### 3.2 Glancing Shock Interactions

The work of Tran et al. (1985), Tran (1987), and Tan et al. (1987), was performed at Mach 3

for fin angles of attack of 10, 12, 16, and 20 deg. The Mach number normal to the shock,  $M_n$ , which is a measure of interaction strength, varied from about 1.37 to 1.82. Measurements were made along a single survey line in the undisturbed freestream direction. Gibson (1990), Gibson and Dolling (1992), Schmisser (1992), and Schmisser and Dolling (1992) made measurements at Mach 5 for fin angles of attack from 16 to 28 deg.  $M_n$  varied from 2.1 to 3.2. Gibson's work was done on a flat plate test surface with a transducer layout which took advantage of the quasi-conical structure of sharp fin flowfields. Transducers were arranged along rays from the virtual conical origin. Schmisser's work was done under the same freestream conditions but on the tunnel floor, in order to take advantage of the improved spatial resolution associated with a thicker boundary layer. The only other experiments known to the author are those of Garg and Settles (1993) at Mach numbers of 3 and 4. The angle of attack range was 10–20 deg. at Mach 3 and 16–20 deg. at Mach 4, resulting in values of  $M_n$  from 1.4 to 2.16. Again, to take advantage of the conical symmetry, the transducers were installed along a circular arc centered at the fin leading edge.

The results of Gibson and Schmisser show that, within engineering accuracy, rms wall pressure distributions (like the mean wall pressure) are consistent with the view that quasi-conicity is the salient feature of the interaction footprint. No other topography describes the results as well. Distribution of the mean ( $\bar{P}_w/P_\infty$ ) and normalized rms wall pressures ( $\sigma p/\bar{P}_w$ ) as a function of conical angle  $\beta$  shown in Fig. 22 illustrates the collapse. The angle  $\beta$  and subscripts associated with separation, etc. are defined in the sketch above Fig. 22. In this case, the transducer rows labeled A, B, and C in Fig. 22 were perpendicular to the inviscid shock wave and located at different distances along the shock. The shapes of the distributions are the same as those obtained by Garg and Settles at lower Mach numbers.

Garg and Settles attempt to explain the features of the mean and rms distributions using detailed flowfield maps developed in earlier work (Alvi and Settles, 1992). An example of their measurements and a sketch of the corresponding flowfield map are shown in Fig. 23. They point out that the local peak in rms near "S" is almost certainly generated by the translating separation shock, as in other interactions. Schmisser's work at Mach 5 confirms this. Aft of separation,  $\sigma p/\bar{P}_w$  remains almost constant for a considerable angular distance and corresponds to the plateau region in the mean pressure distribution. This behavior,



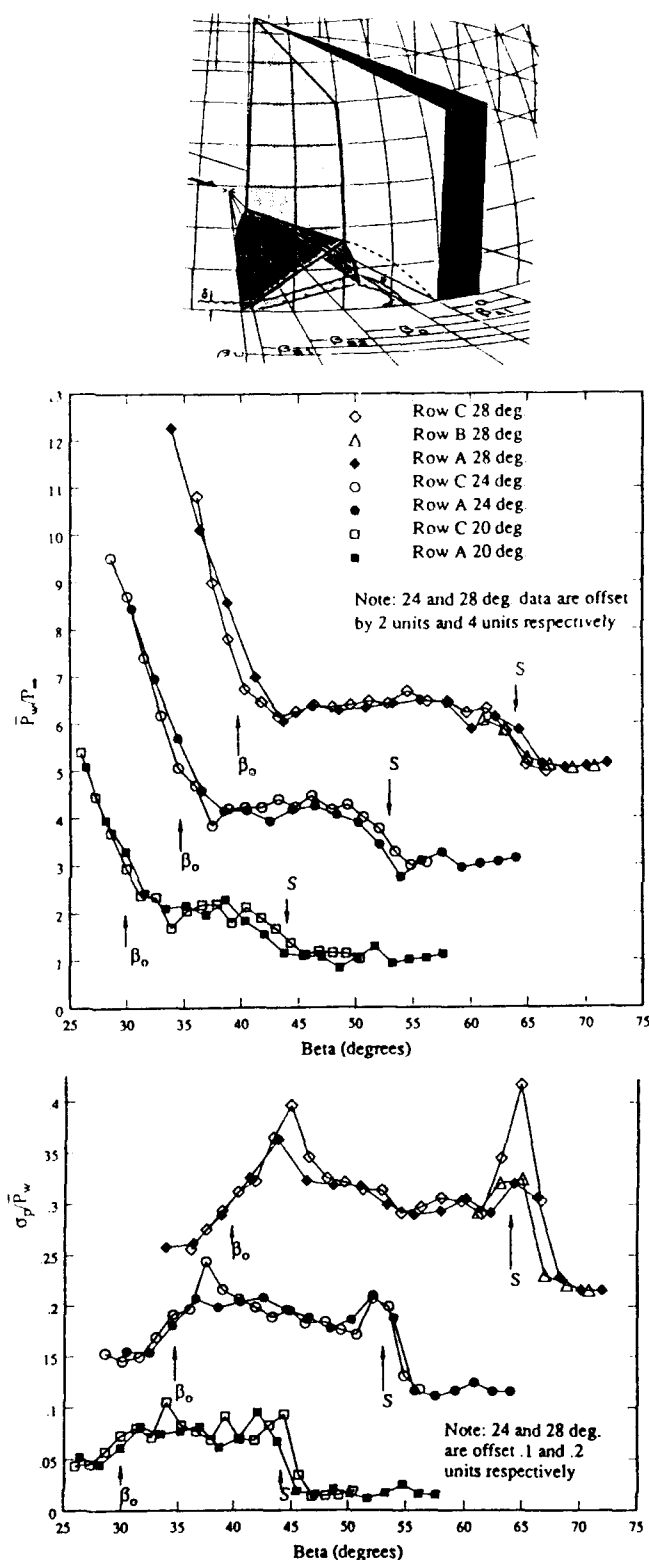


Fig. 22. Mean and rms pressure distributions in glancing shock interactions at Mach 5 (from Schmisser, 1992).

as noted earlier, also occurs in 2-D flows. They note next that the second rms peak occurs close to the dip in the mean pressure distribution. The dip is more noticeable in the Mach 3 and 4 experiments than at Mach 5 and may be a function of incoming boundary layer thickness, which was smaller in In Garg and Settles' experiment. At Mach 3 and 4, this second peak is directly underneath the core of the separation vortex. In the Mach 5 experiments, this peak is upstream of the inviscid shock (Fig. 22), whereas at Mach 3 and 4 it is downstream. Garg and Settles suggest that the trend of the vortex core approaching the inviscid shock location (as evident in their flow-field maps) may continue as interaction strength increases. Thus, at Mach 5, the vortex core may actually lie upstream of the inviscid shock.

The highest absolute fluctuation levels in the glancing shock interaction are at locations closest to the fin although, in terms of  $\bar{P}_w$  (Fig. 23), the normalized levels are only a factor of 2 or 3 larger than in the undisturbed boundary layer. In Garg and Settles' work, the highest rms levels nearest the fin correspond to a sound pressure level of 160 dB. The Mach 5 experiments give similar levels.

In Schmisser's work at angles of attack of 16–28 deg., the wall pressure signals near separation were clearly intermittent and qualitatively similar to those in unswept flows. Thus, as noted above, the local maximum in the rms near separation is generated by the translating separation shock, as in other interactions. In the earlier work of Gibson and Dolling, intermittency was not evident in the pressure signals, and the local flowfield near separation was described as a *shuddering compression* rather than a *translating shock*. This conclusion now appears to be incorrect. As explained independently by Schmisser and Dolling (1992) and Garg and Settles (1993), it is probable that this result can be attributed to inadequate spatial resolution.

Power spectra near separation show that for the same incoming flow conditions the frequency band of the translating shock is significantly higher than in unswept flow. This is consistent with the results from swept compression ramp flows. At 16-deg. angle of attack, with the separation line swept back 25 deg., Schmisser observed that the shock frequencies were in the range 4–5 kHz and that they did not increase further with increased sweep. This observation is also consistent with results from swept ramp flows. As seen in Fig. 20, the increase in shock frequency occurs rapidly as the flowfield is initially swept back and does not change much beyond 25–30



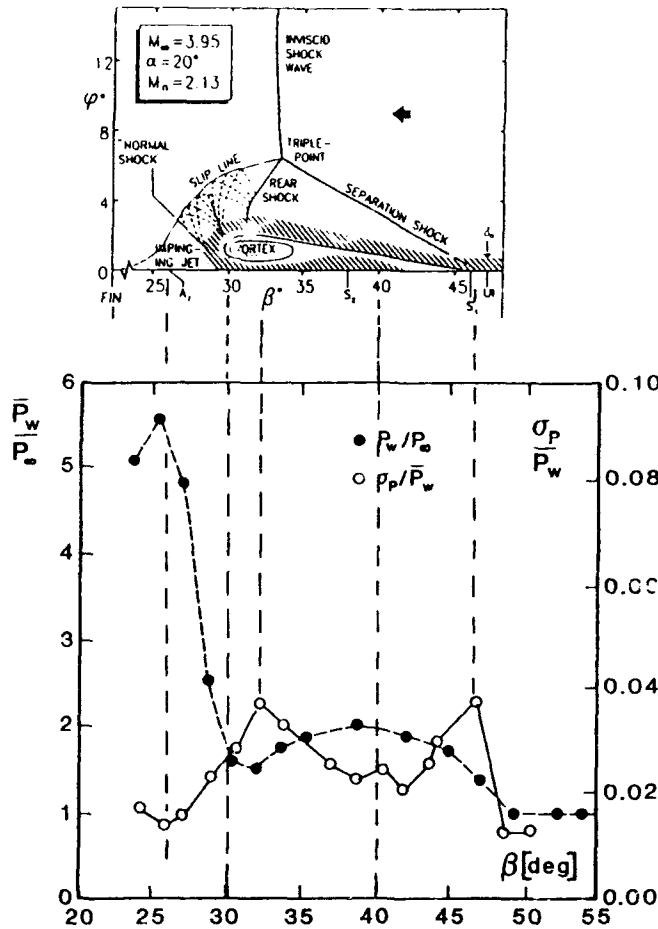


Fig. 23. Mean and rms pressure distributions in a Mach 4, 20-deg. glancing shock interaction (from Garg & Settles, 1993).

deg. of sweepback. Appropriate parameters for scaling power spectra in the intermittent region are not entirely clear. In the studies of Schmisser and Gibson at Mach 5, separation shock frequencies were of order 5 kHz and 8–10 kHz, respectively, whereas in Tran's work at Mach 2 they were around 2 kHz. Schmisser plotted the power spectral densities versus Strouhal number, " $S$ ," defined as  $f \delta / U_\infty$  (Fig. 24). At Mach 5, the spectra are centered at a Strouhal number of about 0.08–0.10 while, at Mach 3, it is centered around 0.06. Whether this is a Mach number influence or physically incorrect scaling parameters, or both, is not clear. More data over a wider range of conditions are needed to resolve this question.

Under the separated flow, spectra are similar to those of an undisturbed boundary layer with increased frequency content at lower levels. Closer to the fin, under the *impinging jet* (Fig. 23), a shift

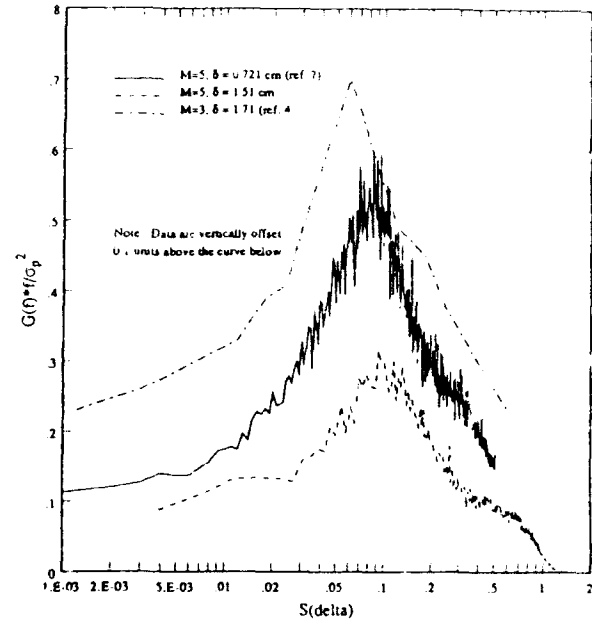


Fig. 24. Power spectra at maximum rms near separation at Mach 5 and at Mach 3 using  $\delta_0$  as a scale for reduced frequency (from Schmisser, 1992).

to lower frequencies occurs. In Schmisser's work spectra are centered around 15 kHz, compared to 5 kHz in the intermittent region and 20–40 kHz in the undisturbed boundary layer. Garg and Settles suggest this shift to lower frequencies is due to the fact that "these locations are relatively isolated from the influence of the turbulent separated shear layer, which wraps around the vortex core and becomes a part of the reverse flow upstream of these locations." Closest to the fin, where the highest rms levels occur, Garg and Settles show a further decrease in frequency—in their case, to about 5 kHz. They suggest that this may be due to the flapping of the slip layer, observed previously in flow visualization studies.

Appropriate correlating parameters for the rms levels associated with the plateau and the maximum near the fin are not clear. The same remark applies to the power spectra. As noted earlier,  $(\sigma p)_{\max}$  near separation is typically about 0.4–0.5  $(\Delta P)_s$ , but how  $(\Delta P)_s$  varies with  $M_\infty$ ,  $M_n$ , or  $Re$  is not known in any rigorous fashion. Garg and Settles plot  $(\sigma p / P_\infty)_{\max}$  near the fin as a function of normal Mach number; but this simple scaling would not appear to be universal, since the Mach 5 data of Schmisser fall far above it.

Batcho et al. (1989) report fluctuating wall pressure data in a Mach 3 crossing-shock interaction. Both fins were set at angle of attack of either 7 or 11 deg. Measurements were made only



along the centerline of the flowfield. For the 7-deg. case, the rms pressure levels are low (1 to 2 percent of  $P_\infty$ ) along the survey line, while, at 11 deg., a peak rms level of about 15-20 percent of  $P_\infty$  was measured downstream of the shock crossing point. At this stage, the paucity of data in this type of flowfield make it difficult to draw any general conclusions.

### 3.3 Blunt Fins and Cylinders

Interactions induced by hemicylindrically blunted fins and circular cylinders have much in common. The boundary layer separates about two to three diameters upstream of the leading edge and rolls up in a vortical structure which then develops spanwise and rearward as a horseshoe vortex system. The streamwise scale of the flowfield and spanwise flow development depend largely on  $D$  and only weakly on  $\delta_o$  (Dolling and Bogdonoff, 1982).

The data base is fairly extensive, spanning the range from transonic [Robertson, (1969, 1971)] to Mach 7.8 [Shifen and Qingquan, (1992)]. Other than Dolling and Bogdonoff (1981) at Mach 3, Aso et al. (1991) at Mach 4, Gonzalez and Dolling (1993) at Mach 5, and Barnhart (1993) at Mach numbers of 2-5, most of the data are on centerline upstream of the cylinder or fin. As noted earlier, the work of Barnhart is still in progress and has not yet been published. Shifen and Qingquan also made fluctuating heat transfer measurements on centerline at Mach numbers of 5 and 7.8.

Between the upstream influence line and "S," the wall pressure signal is intermittent and  $\sigma p$  increases rapidly, with a maximum upstream of "S" (Fig. 25). The distribution shape in the vicinity of "S" is the same as in other interactions and is generated by the unsteady separation shock. At a given Mach number, the magnitude of  $(\sigma p)_{\max}$  depends on the ratio of  $D/\delta_o$ , as shown in Fig. 26. Physically, for small  $D/\delta_o$ , the separation shock structure is completely immersed in the nonuniform incoming boundary layer. As  $D/\delta_o$  increases, a larger fraction of the shock forms in the more uniform external stream. At large  $D/\delta_o$ , when the shock is predominantly outside of the boundary layer, constant conditions prevail.

Measurements made by Brusniak (1991) show that a cylinder or fin with the same  $D$  generates the same distribution of  $\sigma p$  on centerline upstream of the model. Thus the centerline flow is unaffected by the cylinder wake. Since the length of the streamwise region between the upstream influence line and  $S$  scales with  $D$ , not  $\delta_o$ , the separation shock motion may be a fraction of  $\delta_o$  or several  $\delta_o$ . In terms of  $D$ ,  $L_s/D$  is typically

about 0.5-0.8.

The magnitude of  $(\sigma p)_{\max}$  near separation decreases spanwise, but not rapidly. For a fin at zero angle of attack at Mach 4, Aso et al. (1991) report that  $(\sigma p/P_w)_{\max}$  decreases from about 0.26 on centerline to about 0.2 at  $Y/D = 3$ , a 20 percent reduction. At Mach 3, Dolling and Bogdonoff (1981) report a 30 percent decrease from 0.18 to 0.12. In absolute terms, the decrease in  $(\sigma p)_{\max}$  was also about 30 percent. The heat transfer near separation is also intermittent. In the work of Shifen and Qingquan, the ratio of  $\sigma q$  to  $q_w$  in the intermittent region reaches a maximum value of about 0.5.

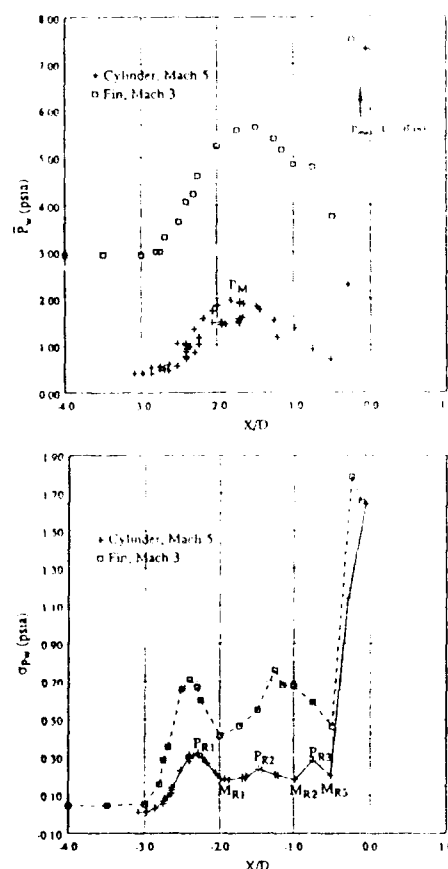


Fig. 25. Mean and rms pressure distributions on centerline upstream of blunt fins at Mach 3 and Mach 5.

A series of seven power spectra on centerline in a Mach 5 cylinder interaction on centerline are shown in Fig. 27. The data are for a 0.5-inch diameter cylinder in a boundary layer approximately 0.25-in. thick and have a frequency resolution of 195 Hz. These results are typical of the spectral evolution seen in several studies at Mach 3 and Mach 5. At station 1 in the undisturbed boundary layer, there is little energy at



low frequencies, as expected. Station 2 is at an intermittency of about 50 percent, and Station 3 is at, or slightly downstream of, "S." Spectra in the intermittent region all have the same shape, with large energy contributions at 0.2–5 kHz, due to the unsteady separation shock. Such low shock frequencies are typical. There appears to be relatively little influence of Mach number, cylinder diameter, or incoming boundary layer on the shock frequencies. Shifen and Qingquan, at Mach 5 and 7.8, report that "most of the separation shock oscillation frequencies are below 2.5 kHz."

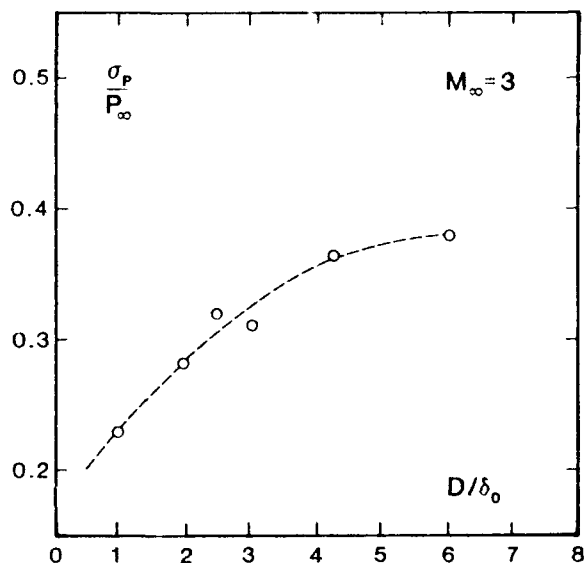


Fig. 26. Variation of  $(\sigma p)_{\max}/P_{\infty}$  near separation for blunt fin interactions at Mach 3.

Robertson (1971) correlated power spectra measured at the mean shock location in cylinder-induced flows at  $M = 1.4$  and  $1.6$ , and from an unswept compression ramp flow at  $M = 2$  by plotting  $G(f)U_{\infty}/q_{\infty}^2\delta_0$  versus  $f\delta_0/U_{\infty}$  and  $G(f)U_{\infty}/q_{\infty}^2L_{\text{sep}}$  versus  $fL_{\text{sep}}/U_{\infty}$ , where  $L_{\text{sep}}$  is the separated flow length. A better collapse was obtained using  $L_{\text{sep}}$  than with  $\delta_0$ . However, it does not appear that these correlating parameters are generally appropriate, as explained below. Power spectra at Mach 5 for different cylinder diameters and boundary layer thicknesses are shown in Fig. 28. Spectra for cases 2 and 3 correspond to flows in which  $L_{\text{sep}}$  is  $2.4D$  in both cases; but, due to the differences in  $D$ ,  $L_{\text{sep}}$  is 3.05 cm and 4.6 cm, respectively. Since  $q_{\infty}$  and  $U_{\infty}$  are the same for both flows, normalization using  $L_{\text{sep}}$  would separate the curves rather than collapse them. Further, it can be seen in Fig. 28 that, for a given incoming boundary layer, a larger diameter cylinder generates lower shock frequen-

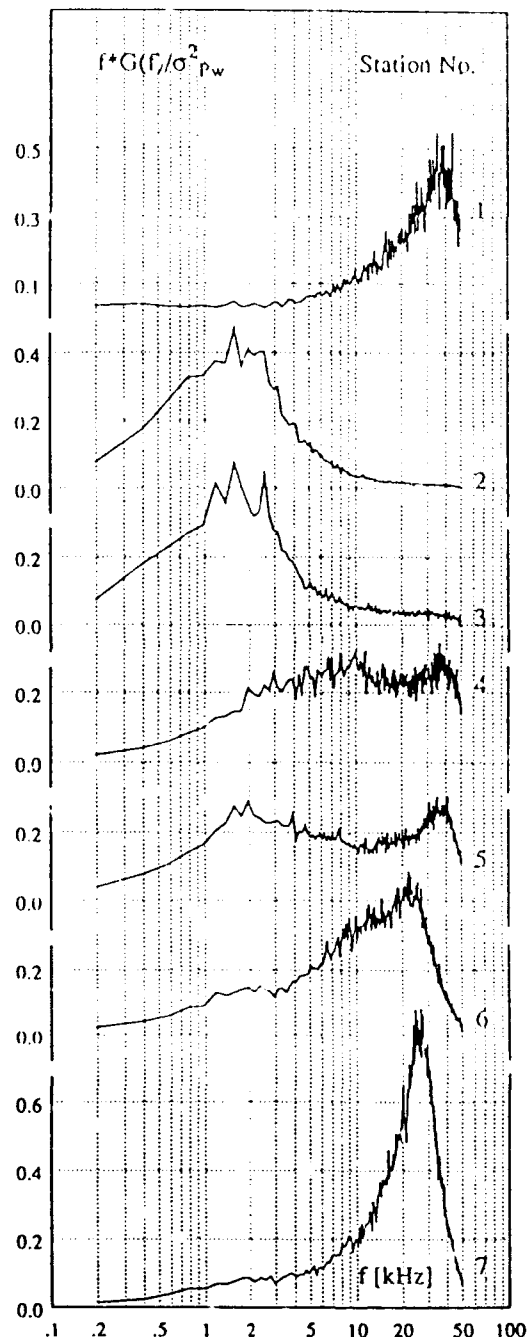
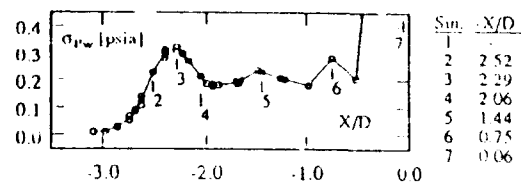


Fig. 27. Typical power spectra on centerline in a Mach 5 blunt fin interaction (from Brusniak & Dolling, 1992).



cies. This suggests that the separation shock frequencies are also influenced by the downstream separated flow, since the incoming conditions are fixed and only  $D$  is altered. More is said about this in Sec. 4. Thus, neither  $\delta_o$  nor  $L_{sep}$  is appropriate as a normalizer by itself, since both play a role in setting the shock frequency.

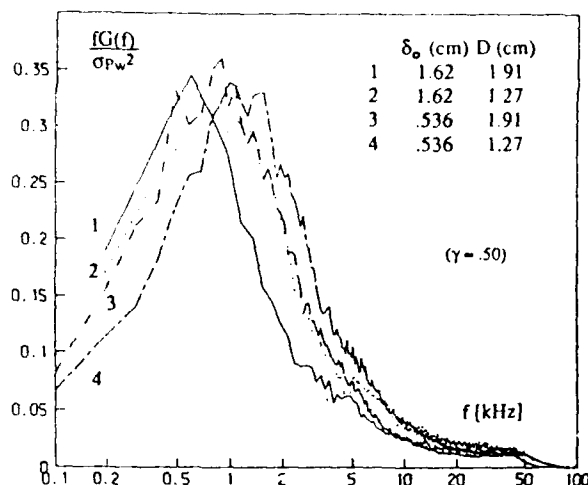


Fig. 28. Effects of cylinder diameter and boundary layer thickness on power spectra at maximum rms near separation in Mach 5 interactions (from Dolling & Smith, 1989).

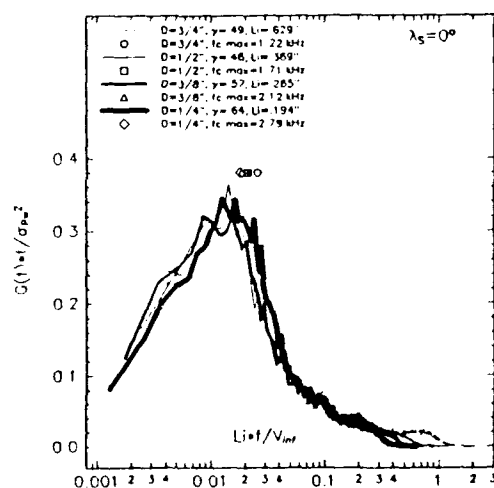


Fig. 29. Correlation of power spectra at maximum rms near separation using  $L_i$  as a scale for the reduced frequency (from Gonzalez & Dolling, 1993).

Gonzalez and Dolling (1993) show that spectra in the intermittent region, generated by different diameter cylinders, can be collapsed by plot-

ting  $G(f) \cdot f / \sigma_p^2$  versus  $f L_i / U_\infty$ , where  $L_i$  is the intermittent region length (Fig. 29). Similarly, power spectra measured at a given separation line sweepback angle can be collapsed in the same way. This scaling using  $L_i$  appears to have a firm foundation, but the use of  $U_\infty$  should be viewed as tentative, since all of the experiments were carried out at the same  $U_\infty$ . Further, it is not a very practical formulation since the parameter  $L_i$  is not usually known a priori. However, the results from the parametric study of Gonzalez and Dolling at Mach 5 show that  $L_i/D \approx 0.8$  for separation line sweepback angles less than about 30 deg.; between 30 and 60 deg.,  $L_i/D$  increase linearly to about 1.15D. First-order estimates of power spectra could probably be obtained using these values for  $L_i$ .

Returning to Fig. 27, station 4 is at the upstream end of the separated flow and has a bimodal spectrum. The energy concentration around 30 kHz is caused by the passage of separated, large-scale turbulent structures which originated in the incoming boundary layer. Station 5, under peak 2 in the  $\sigma p$  distribution (Fig. 25), is almost bimodal; but the lower frequency is now centered around 2 kHz, the shock frequency. Station 6, at peak 3 in the  $\sigma p$  distribution, has some energy centered around the shock frequencies, but most is around 25 kHz. Finally, at the cylinder base, when the absolute maximum loading levels occur under the root vortex, the bandwidth is relatively narrow and at high frequency ( $\approx 25$  kHz). In the work of Brusniak at Mach 5, rms levels of up to 260 percent of the local mean wall pressure were measured at the fin root. These correspond to the most intense levels known to the author, about 184 dB.

Kleifges and Dolling (1993) have measured mean and rms wall pressure distributions on centerline upstream of blunt fins with leading edges sweptback 8, 18 and 30 deg. in a Mach 5 flow. This study is still in progress and, thus, only preliminary results are available. As expected, upstream influence decreased from about 3.4D (unswept case) to about 1.2D (30 deg. swept back). The rms levels associated with the translating separation shock decreased by only about 20 percent, while the shock zero-crossing frequency increased by about 20 percent. However, loading levels at the fin root decreased by about 75 percent.

At this point, it is appropriate to note that a large variety of separated flow structures can exist, depending on the cylinder geometry and orientation, and incoming flow parameters such as Reynolds number and Mach number. The quali-



tative structure can best be understood in terms of vortex systems; these include vortices that form in the upstream separated flow, the stretching of these vortices around the leading edge in a horse-shoe shape, and, in the case of cylinder flows, the near-wake spiral vortices. This pattern is common to both laminar and turbulent flows, as well as to Mach numbers up to the hypersonic range. How many vortices occur appears to be primarily a function of Reynolds number, certain dimensionless parameters, and flow type [Sedney (1973)]. Since these vortices generate large streamwise and spanwise pressure gradients, it is obvious they will play a dominant role in the wall pressure fluctuation behavior. This behavior is likely to be very complex. The examples cited above should be considered in this context.

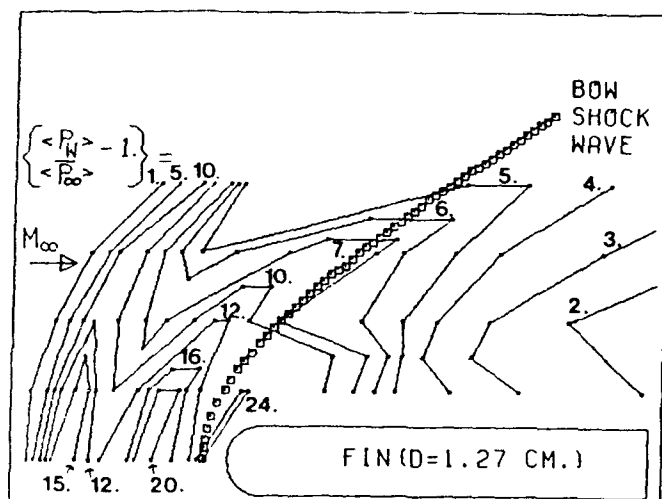


Fig. 30. Rms pressure contours in a Mach 3 blunt fin interaction (from Dolling & Bogdonoff, 1981).

There are relatively few results from under the separated flow. Those of Dolling and Bogdonoff at Mach 3, Aso et al. at Mach 4, and Brusniak at Mach 5 all show essentially the same features. As seen in Fig. 25,  $\sigma p$  continues to increase downstream of "S." It reaches a second peak whose magnitude is somewhat smaller than that caused by the unsteady separation shock. The peak in the intermittent region maintains its position relative to the upstream influence line with increasing distance spanwise; the second peak is swept back and crosses underneath the inviscid shock at  $X/D = 3$  (Fig. 30). On centerline, the second peak is about one diameter upstream of the fin leading edge, approximately at the upstream limit of the embedded supersonic reversed flow region predicted in a numerical study by Hung and

Buning (1985). As seen in Fig. 30, the second peak decays rapidly and, further spanwise than  $X/D = 4$ , is no longer detectable.

#### 4 MECHANISM OF UNSTEADINESS

There have been relatively few studies focusing on the cause of the unsteadiness of shock-induced turbulent separation. One of the first was that of Andreopoulos and Muck (1987), who analyzed wall pressure signals measured in Mach 3 compression ramp interactions. They reported that the mean separation shock period,  $T_m$ , was independent of position in the intermittent region and independent of the ramp angle. The value of  $T_m$  corresponded to a value of  $f_c (\equiv 1/T_m)$  of  $0.13U_\infty/\delta_o$ , which the authors claimed was the same order as the estimated bursting frequency in the incoming boundary layer. They also argued that, since the measured shock speeds were the same order as velocity fluctuations in the flowfield, this "represents further evidence that the turbulence of the incoming boundary layer is largely responsible for the shock motion."

Although later experiments (see below) have shown that turbulence in the incoming boundary layer plays an important role, doubts were originally raised about the above conclusions. First, if the shock frequency was controlled by turbulent bursts, then in a given boundary layer it might be anticipated that the shock frequency and streamwise length scale of the motion,  $L_s$ , would be fixed. This is certainly not the case. As noted earlier, for a circular cylinder of diameter,  $D$ , the shock frequency decreases as  $D$  increases, and  $L_s$  increases as  $D$  increases, all in a given boundary layer. Doubts also arose about the validity of the data analysis procedure used by Andreopoulos and Muck. A one-threshold algorithm was used to convert the intermittent pressure signals into boxcars, which are subsequently analyzed to provide information on shock frequency, period, etc. One-threshold algorithms are known to overestimate shock frequencies significantly because of their inability to discriminate consistently between shock-induced and turbulent pressure fluctuations.

Moreover, the later work of Tran (1987) appeared to contradict the findings of Andreopoulos and Muck. Tran's work was done in the same Mach 3 blowdown facility in the same boundary layer, but with a 20-deg. compression ramp rather than a 24-deg. model. One transducer was placed on the upstream influence line and the other further upstream in the incoming boundary layer. Tran found little correlation between events detected on the upstream channel, using the VITA



technique, and the shock-induced pressure pulses on the downstream channel. He concluded that the pressure pulses in the intermittent region were *independent* of the large-scale structures in the upstream boundary layer which are convected into the interaction. Tran's conclusions, however, must also be treated with some caution. In his experiment, only a single transducer was placed in the intermittent region, close to its upstream edge. It is quite possible that the separation shock moved upstream and downstream in response to the incoming turbulence, but remained downstream of the transducer whose output was being recorded. With hindsight, it might have been more appropriate to use the large shock-induced pressure rise on the downstream channel as a *trigger* and ensemble average on the upstream channel in the undisturbed boundary layer. The *trigger* is then a very well-defined and well-understood event.

This was the approach adopted by Erengil and Dolling (1991,2) and later refined by McClure (1992). Erengil and Dolling made simultaneous fluctuating wall pressure measurements in the incoming undisturbed boundary layer and under the unsteady separation shock wave in a Mach 5 compression ramp interaction. Conditional sampling algorithms and a variable-window-ensemble-averaging technique were used to investigate the correlation between specific separation shock motions (i.e., upstream or downstream sweeps, turnarounds) and pressure fluctuations in the incoming flow. In these exploratory experiments, there was uncertainty in the interpretation of some of the results, due to an insufficient number of ensembles for certain types of shock motion. This has since been clarified by McClure (1992), as explained below. Nevertheless, to the current author's knowledge, these results were the first to show a *direct* correlation between pressure fluctuations in the incoming flow and separation shock motion.

McClure's experimental arrangement was the same as that of Erengil and Dolling (see the inset of Fig. 31). The primary difference in the analysis procedure was in the selection criterion for ensemble extraction. McClure used shock sweep length alone, not sweep length and location, as used by Erengil and Dolling. For example, a 3-channel upstream sweep from channel 6 to channel 4 provided ensembles which were subsequently averaged with ensembles from upstream sweeps from channels 3 to 1. Phase alignment accounted for differences in transducer locations. This simply involved mapping the ensembles to a set of pseudo channels so that the beginning of the trig-

gering event (say an upstream sweep) was mapped to the same pseudo channel. All remaining channels had the same position relative to the starting channel as in the physical layout. The characteristics of the ensembles were further brought out by combining ensemble-averages from several runs.

Results for 3-channel downstream and upstream sweeps are shown in Figs. 31 and 32, respectively. A characteristic wall pressure signature (labeled *sig*) is seen on the channels upstream of the shock. Note that the signature appears at successively later times for channels closer to the shock and that the signature is coincident with the shock foot at  $t = 0$ . Note also that the characteristic signatures on the upstream channels are *different* for the different shock motions; it is a fall-rise-fall sequence for an upstream sweep and a rise-fall-rise for a downstream sweep. The convection velocity, based on tracking the leading peak of the signatures, is  $0.75U_\infty$ . The peak-to-peak amplitude of the pressure signature is about 1.5 percent of the boundary layer mean pressure. The pulse itself has a duration of about 75–100  $\mu\text{s}$ , corresponding to a length scale of about  $3.2\text{--}4.3\delta_1$ . McClure also noted that the pressure signatures continued to move downstream after passing through the shock; thus, they are generated by fairly robust structures. In an extension of McClure's work, Gramann and Dolling (1992) reported that these characteristic pressure signatures could be detected as far as 20 boundary layer thicknesses upstream of the interaction. Their clarity decreased significantly with increasing distance, indicative of evolving turbulent structures.

McClure (1992) and Gramann & Dolling (1992) also examined the relationship between pitot pressure fluctuations in the incoming boundary layer and separation shock motion. The pitot probe tip was located from 0.33 to  $1.31\delta_1$  above the wall at  $13.3\delta_1$  upstream of the ramp corner. Separation shock motion was again used as a trigger for extraction of ensembles. The results (Figs. 33 and 34) showed no evidence of a characteristic pitot signal corresponding to specific shock motions. However, for  $Y/\delta_1 < 0.98$ , there is a general decrease in pitot pressure for an upstream shock sweep and an increase in pitot pressure for a downstream shock motion. Cross-correlations between the pitot pressure signal and the wall pressure signal under the unsteady shock showed a weak (but increasing) correlation as the probe tip approached the wall. The power spectrum showed that an increasing fraction of the overall signal variance was generated by lower frequencies as the wall is approached. At this stage, the relationship between the pitot pressure fluctuations



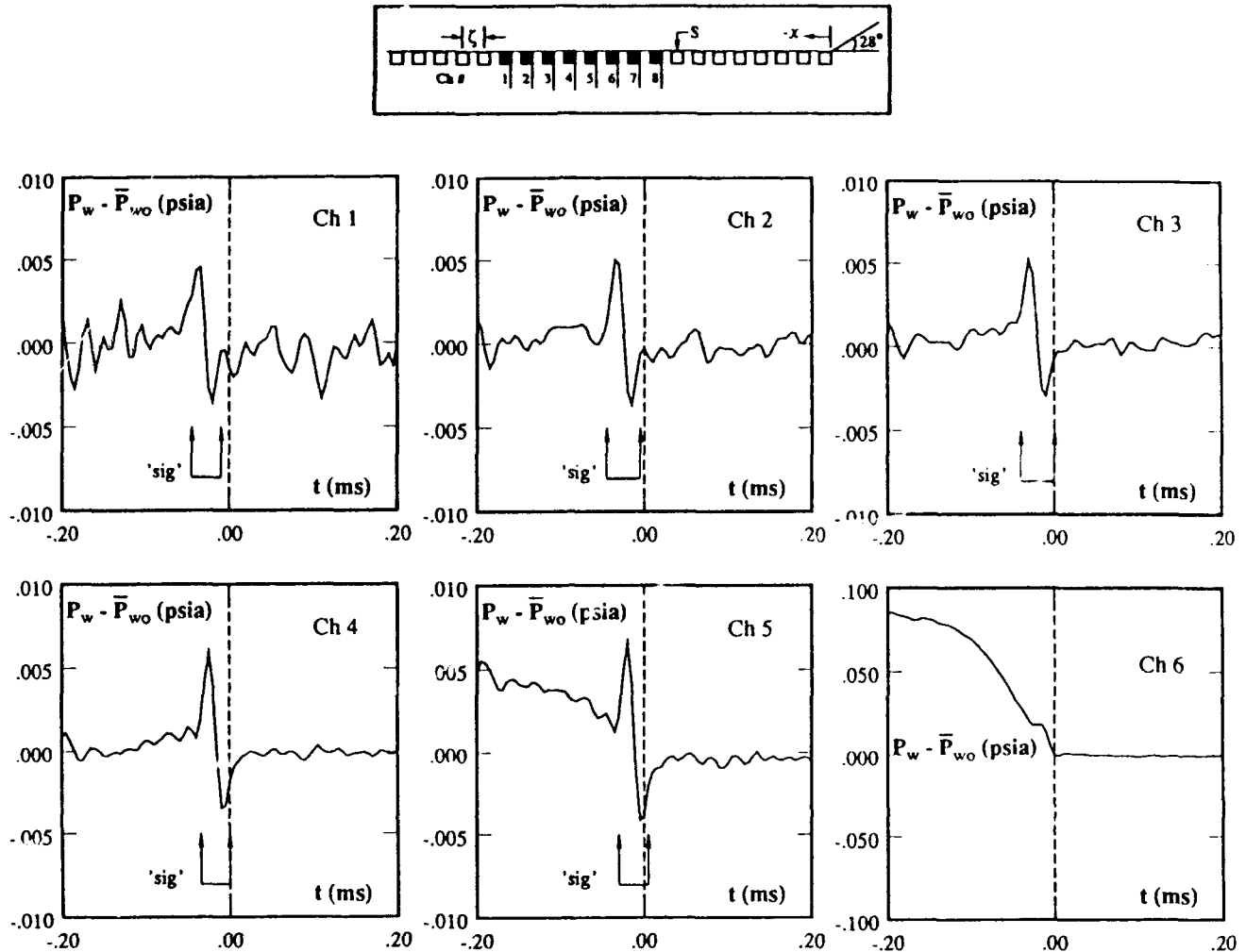


Fig. 31. Ensemble-averaged wall pressure histories for a 3-channel downstream sweep (trigger on channel 7) (from McClure, 1992).

and the shock motion is still somewhat confusing. The role that the low-frequency pitot pressure fluctuations have on the shock motion is still under active investigation.

Erengil and Dolling (1990, 1991,2) have examined the correlations between the separation shock velocity history and wall pressure fluctuations upstream and downstream of the intermittent region. Results have been obtained in swept and unswept compression ramp interactions, sharp fin-induced flows, and in interactions generated by blunt fins with both swept and unswept leading edges. In each flow, up to eight wall pressure transducers were placed under the unsteady separation shock. From analysis of simultaneously sampled signals, the shock foot

history  $X_s(t)$  was generated from nested boxcar sequences (Fig. 35). Linear interpolation of the *bin* history yields a piecewise smooth function for  $X_s(t)$ . An example of  $X_s(t)$  over a 10 ms time interval is shown in Fig. 36. The shock velocity history is deduced by taking the derivative of  $X_s(t)$ . The velocity history corresponding to the position history shown in Fig. 36 is shown in Fig. 37. The shock foot behavior can best be described as consisting of a low-frequency motion superposed on which is a higher frequency jitter. These two components appear to have two different causes, as outlined below. It should be noted that the experiments described below are ongoing, and the results have not been presented or published. Pending presentation/publication, the



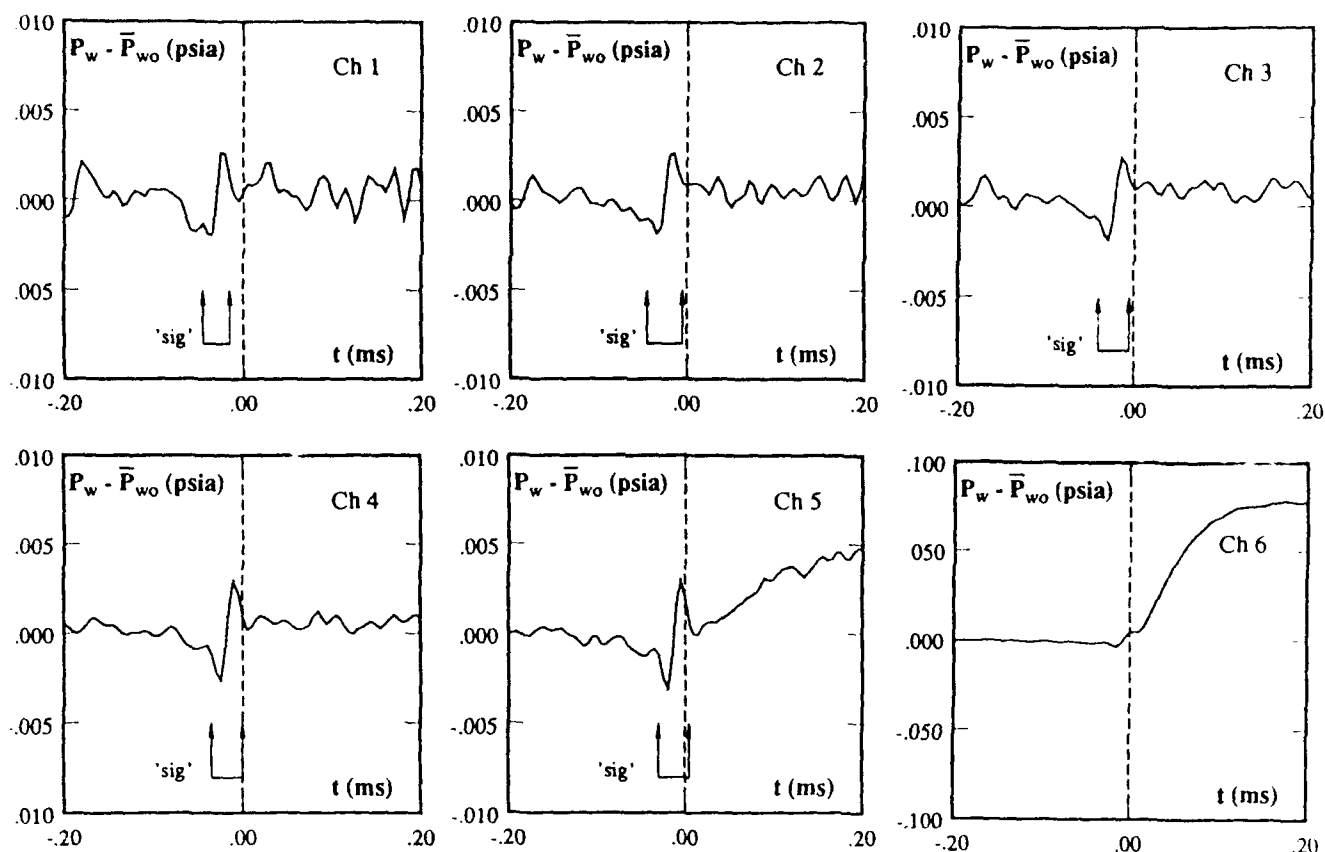


Fig. 32. Ensemble-averaged wall pressure histories for a 3-channel upstream sweep (trigger on channel 7) (from McClure, 1992).

results should be treated as tentative. They are reported here to provide up-to-date information on current ideas/approaches in understanding the physical mechanisms driving the unsteadiness.

Cross-correlations of the shock velocity history with wall pressure fluctuations under the incoming boundary layer have a well-defined peak at negative time. Thus, fluctuations in the incoming boundary layer *precede* shock velocity fluctuations. Furthermore, the same correlation was obtained in all of the different interactions listed above, indicating that the same physical mechanism occurs in all flows. Cross-correlations of the shock velocity history with wall pressure fluctuations downstream of the intermittent region are more difficult to interpret. This is because perturbations in the downstream flow may certainly perturb the upstream shock wave, but, at

the same time, shock wave unsteadiness causes fluctuations in the downstream quantities. Unlike the upstream correlations which were the same in all interactions, the downstream correlations are qualitatively similar but quantitatively different in different interactions. The correlation persists for a much longer time than observed in the upstream correlation. The time span of this longer period correlates well with the characteristic separated flow frequency of each of the different interactions (0.5 kHz for the unswept ramp, 4 kHz for the swept ramp, etc.). Within this time span of the correlations, there is in each case a second well-defined negative peak at negative time delay, showing that high-frequency wall pressure fluctuations under the separated flows precede shock velocity fluctuations.

These cross-correlations and earlier work give



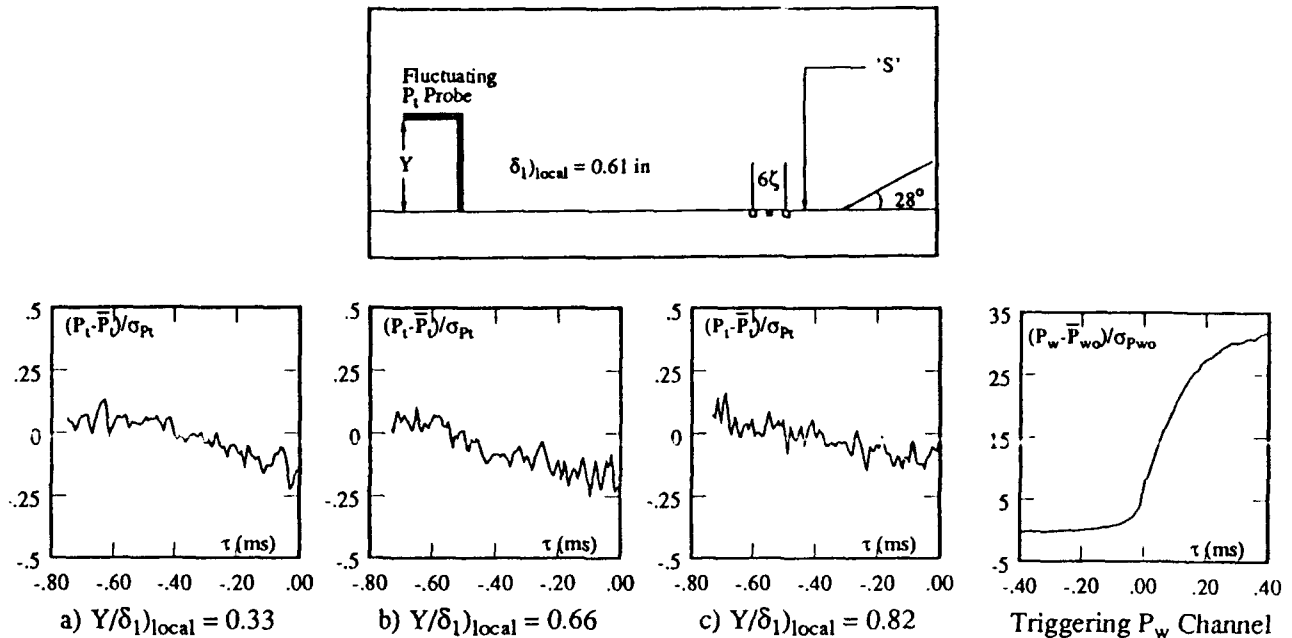


Fig. 33. Ensemble-averaged pitot pressures in the incoming boundary layer for an upstream shock sweep (from McClure, 1992).

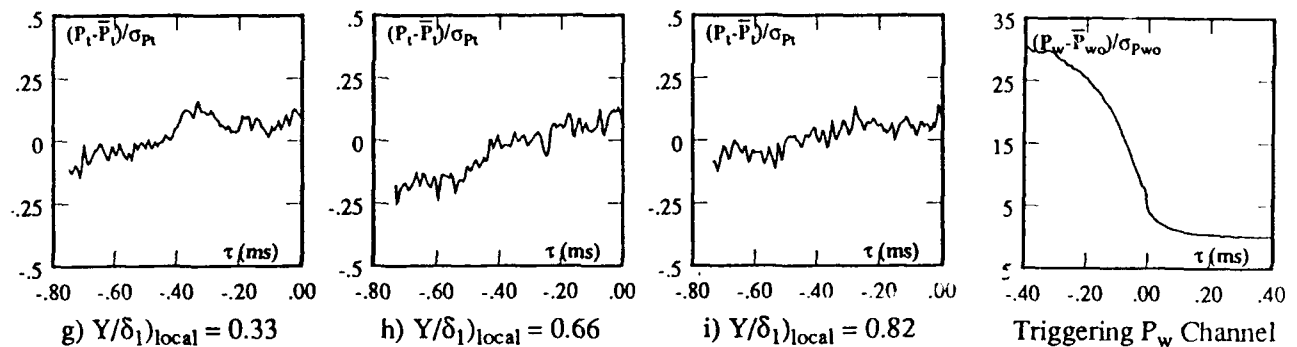


Fig. 34. Ensemble-averaged pitot pressures in the incoming boundary layer for a downstream shock sweep (from McClure, 1992).

rise to a tentative model in which the separation shock unsteadiness is attributed both to perturbations to the instantaneous ratio of static quantities across the separation shock and by the expansion/contraction or pulsation of the separated flow. High-frequency perturbations of the shock are driven by both upstream and downstream fluctuations; low-frequency perturbations only come from the downstream fluctuations. The implication is that the large-scale motion of the separation shock is caused by the *pulsation* of the separated region which occurs at different frequencies for different interactions, whereas

the small-scale motion of the separation shock is caused by the high-frequency perturbations in both upstream and downstream fluctuations in static quantities (i.e., by the passage of individual turbulent structures through the shock wave).

The available data, direct and circumstantial, suggest that it is the turbulent fluctuations close to the shock which drive the unsteadiness. McClure (1992) obtained detailed correlations of the flapping motion of the shear layer near reattachment with the separation shock motion. He used an event-relative-timing-analysis (ERTA) in which histograms are constructed of the time-



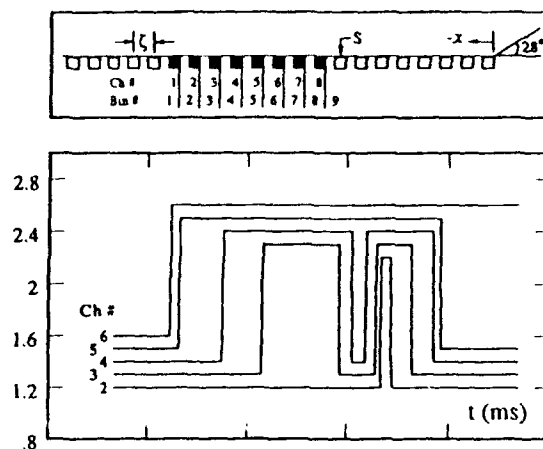


Fig. 35. Use of nested boxcar signals to obtain shock foot position history.

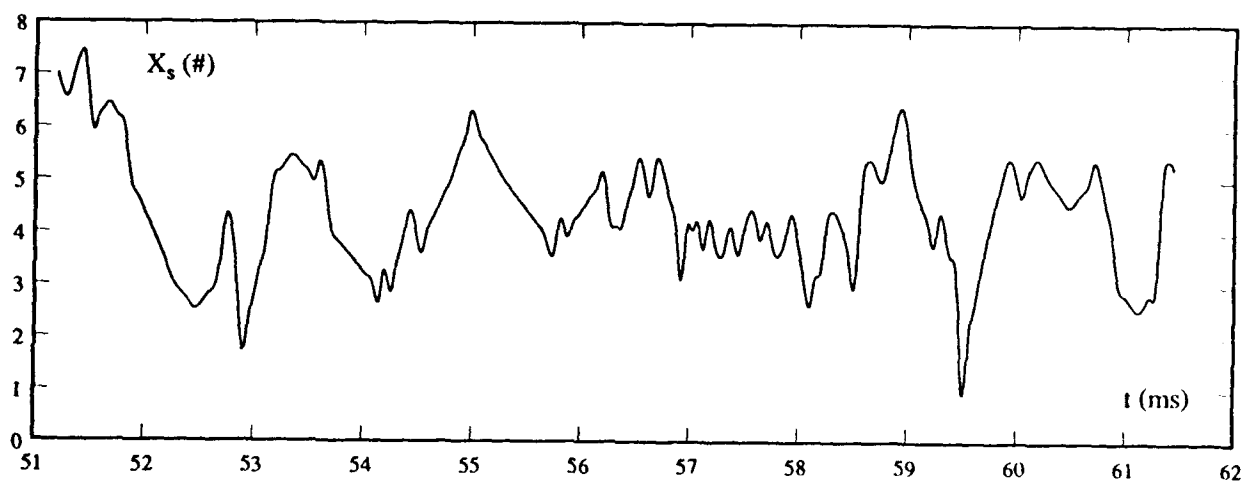


Fig. 36. Sample separation shock foot position history in a Mach 5 compression ramp interaction.

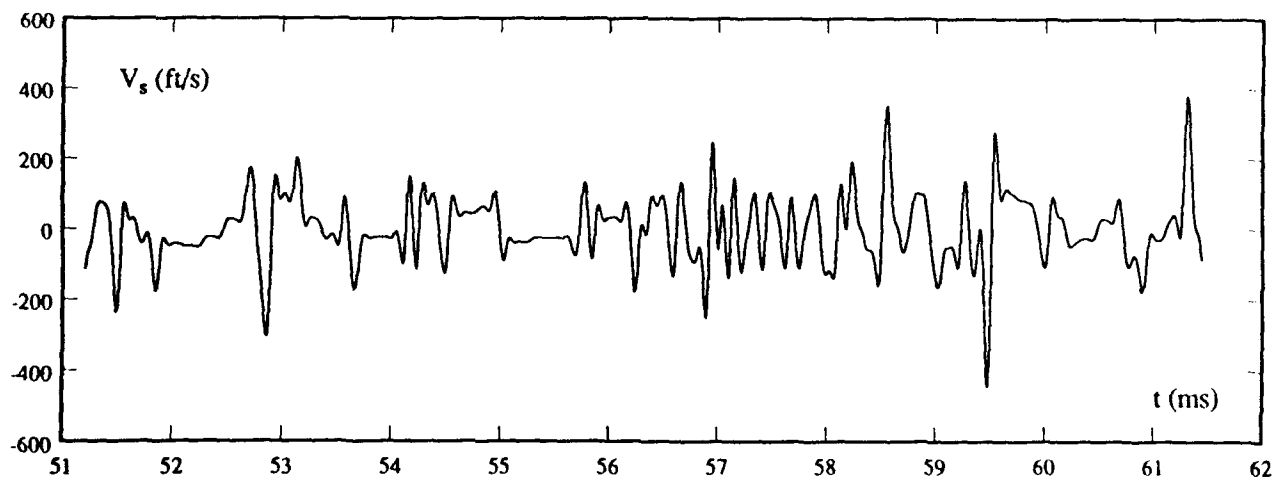


Fig. 37. Shock velocity history corresponding to the position history of Fig. 36.



delay between *events* near separation and the flapping of the shear layer. No evidence was found of any feedback from the reattachment region to the separation shock. Further, recalling Sec. 2.1, Chapman et al. noted that, if transition occurred between separation and reattachment, the shock did not become unsteady until transition moved close to separation. Thus, fluctuations in the vicinity of reattachment appear to have little effect on the separation shock.

Brusniak and Dolling (1991, 1992) have also been addressing the question of the mechanism and have focused on interactions generated by circular cylinders and blunt fins. In addition to cross-correlations and ensemble-averaging methods, a technique called RSED (Random Signal Event Detection) has been used in conjunction with the ERTA method described earlier. The RSED technique employs two wall transducers separated streamwise in the incoming boundary layer to detect *events* in the incoming flow which are convected into the interaction. The ERTA technique is then used to generate a histogram of the timing relationship between these *events* and specific separation shock motions further downstream. Alternatively, the two transducers can be placed under the separated flow to detect the passage upstream of specific pressure fluctuations and then examine the timing relation between them and the shock wave motion. This work is ongoing and has not yet been presented or published. Results to date have provided independent confirmation that the shock foot responds to pressure fluctuations under the incoming flow which convect into the interaction. It has also been shown that the separation shock motion is influenced by pressure variations under the separated flow and that *events* under the separated flow precede the shock motion. Moreover, the incoming turbulent structures apparently affect the shock motion twice—first, when they pass through the separation shock and, second, after they recirculate upstream from the fin root. The latter observation suggests that if the recirculation process could be altered, perhaps by fin leading edge geometry changes, then it might prove possible to influence the shock motion. Some exploratory experiments along this line have been performed by Kleifges and Dolling (1992) and are discussed briefly in the following section.

## 5 CONTROL OF UNSTEADINESS

For obvious, practical reasons, there has been a significant number of experimental and computational studies focusing on interaction management and control. Most of these have focused on

suppression of separation, and most have dealt only with the mean flowfield. The large majority of these efforts has involved mass transfer at the wall (injection or suction), with the objective of minimizing the extent of separation. Settles and Dolling (1990), Hamed and Shang (1989), and Viswanath (1988) give overviews of the work in swept flows and other interactions relevant to supersonic inlet design. To the author's knowledge, there have been few studies of passive control of supersonic/hypersonic flows. One of the earliest is probably that of Cooper and Korkegi (1975), who found that attempting "to reduce the size of the separated flow by channeling higher pressure air from behind the separated region to the boundary layer in front of the region is ineffective." The work of Glotov and Korontsvit (1983) and Goodman et al. (1985) are two more recent examples. Glotov and Korontsvit reduced the separated flow scale of a cylinder-induced interaction by placing a vertical "needle" in the separation. Goodman et al. examined the effect of an embedded plate placed parallel to the wall in the outer portion of the boundary layer in an incident shock interaction. If positioned to reflect the impinging shock wave flow, separation could be eliminated over a wide parameter range.

Passive techniques have been more widely studied in transonic flow. Raghunathan (1988) provides a detailed review of recent work. There have been few studies focusing directly on control of fluctuating loads, and this is a fruitful area for future research. The only studies known to the author are those of Selig (1988), Selig and Smits (1991), and McClure (1992).

Selig and Smits applied periodic blowing to the boundary layer surface at various locations within the separated flow generated by a 24-deg. compression ramp at Mach 3. Blowing was applied through a full span slot at a rate of either 2.5 percent or 9 percent of the freestream mass flux at frequencies up to 5 kHz. Wall pressure and mass flux fluctuation measurements were made; stroboscopic schlieren videography was used to observe the unsteady flowfield. As the slot was moved closer to the shock foot, the shock motion could be locked in to the blowing frequency and completely controlled by the periodic blowing. Note, however, that the mean shock location was shifted upstream (i.e., extent of separation increased). The rms levels in the vicinity of the shock did not change appreciably, nor did it appear (based on the rms distributions shown in Fig. 8 of Selig & Smits) that the length scale of the shock motion changed. Both of these findings are consistent with the remark made earlier about



the relationship between rms levels and separated flow scale.

Based on cross-correlations and the fact that the shock motion could be controlled in this manner, Selig and Smits concluded that "it seems probable that the unsteadiness of the shock for the 24-deg. compression corner is partially driven by large-scale fluctuations in the separated region." This is entirely consistent with the model proposed in the previous section.

McClure (1992) and McClure & Dolling (1991, 1992) investigated the effects of suction at reattachment and effects of boundary layer manipulators (BLM) placed in the incoming boundary layer on the separation shock dynamics in a Mach 5 compression ramp interaction. In this case, the BLM's were plates  $1.5\delta_1$  long, with sharp leading and trailing edges (beveled at 15 deg. for one plate and 35 deg. for the other) mounted parallel to the test surface and  $0.7\delta_1$  above it. The BLM trailing edge was  $3.2\delta_1$  upstream of the ramp corner. To examine whether or not the near wall structure of the boundary layer influenced the shock dynamics, McClure also investigated the effects of triangular riblets with a spacing  $s^+$  and height  $h^+$ , both equal to 15 wall units. In brief, the riblets had no measurable effect on the separation shock dynamics. The BLMs reduced the length of separation (defined as the distance from the ramp corner to the downstream limit of the separation shock motion) by 33-45 percent and reduced the streamwise extent of the separation shock motion by 36-74 percent. The physical cause is not entirely clear and could be due to the inviscid preturning of the flow by the BLM (hence weakening the interaction) and not due to changes in boundary layer structure. Further investigation is needed to clarify this issue.

Donovan (1992) has studied the effects of tangential mass injection on a nominally 2-D incident shock wave/turbulent boundary layer interaction. The Mach number was 3.4. The injection jet was one third of the height of the upstream boundary layer and was operated to provide ideal expansion to Mach 3.4 at the exit. The wedge angles were 5 deg., 8 deg. (incipient separation), 10 deg., and 12 deg. A video-schlieren system provided a qualitative record of the unsteadiness. Without injection, there was significant unsteadiness of the compression system at 10 and 12 deg. Not only was there a significant reduction (by factors of 4.7 and 5.5 at 10 deg. and 12 deg., respectively) in separation bubble length with injection, but "no fluctuations in any of the compression system were detected."

McCormick (1992) has examined the effects of

low-profile vortex generators and a passive cavity on the interaction generated by a normal shock wave in an axisymmetric tunnel at Mach numbers of 1.56-1.65. A large separation bubble was generated. The vortex generators produced significant suppression of separation, reducing the overall interaction length from about 57 to 23 $\delta_0$ . No fluctuating loads data were obtained, but, if significantly reduced separated flow length scales can be obtained, then the loading levels near separation can probably be reduced. However, it is possible that, with steeper pressure gradients near reattachment, the loading levels there may increase.

## 6 IMPLICATIONS OF UNSTEADINESS FOR CFD

Accurate predictions of the effects of shock wave turbulent boundary layer interactions are of particular importance in the design of supersonic and hypersonic vehicles. With increased reliance on computation, it is critical that the predictions are accurate. Thus, it is imperative that such codes be validated and calibrated and deficiencies be identified and rectified. For an overview on progress in this area, the reader is referred to the January and February 1992 editions of *Aerospace America* (a publication of the American Institute of Aeronautics and Astronautics) which were largely devoted to "a perspective on aerospace computational fluid dynamics." Articles authored by both practitioners and program managers discussed the military, industrial, and academic perspectives of CFD, not only in terms of the technical challenges, but also in terms of the economic and political issues. The objective of the current few remarks can probably best be introduced by extracting a few sentences from one of these recent articles. The author is Professor A. Jameson of Princeton University, New Jersey, who writes: "Code validation is increasingly being recognized as being vital to raising confidence in CFD use. In considering this requirement, it is important to distinguish between the correctness of the program and the suitability of the math model to the application. *Simply comparing experimental data with numerical results provides no way to distinguish the source of the discrepancies, whether they are due to faulty numerical approximation or programming, or to deviations between the math model and the true physics.*" (text italicized by current author) The difficulty of determining the deviation between the "math model and the true physics" is the focus of this section. It is suggested that a "fundamental deviation between the math model and the true physics," namely the global



unsteadiness of the experimental flowfield, which is not modelled numerically, may be a major contributor to the discrepancies between computation and experiment.

### 6.1 Comparisons of Computation with Experiment—Surface Properties

Figure 38 shows comparisons of the normalized wall pressure from computations and experiment for turbulent flow over a 34-deg. compression ramp at Mach 9.22. The data are those of Coleman (1973) and Coleman and Stollery (1972), and the computations were made by Horstman (1987) using the  $k$ - $\epsilon$ , Cebeci-Smith, and Baldwin-Lomax turbulence models. The computations employ the time-dependent, mass-weighted, Reynolds-averaged, Navier-Stokes equations for 2-D flow and are solved using the MacCormack explicit-implicit, second order predictor-corrector, finite volume method. The purpose of Horstman's study was to assess how well these turbulence models, which have been widely used in transonic and supersonic flows, fare in hypersonic flows. It was not assumed a priori that they were suitable for hypersonic flow. Indeed, as indicated on the figure, modifications were made to the  $k$ - $\epsilon$  model to include hypersonic effects. The modifications, indicated in the legend of Fig. 38, are as follows:

(i) Mod A – a correction to the  $\epsilon$  equation to account for the effect of rapid compression on the turbulent length scale; (ii) Mod B – corrections to both the  $k$  and  $\epsilon$  equations to model the additional terms which appear after mass-averaging; and (iii) Mod C – a correction to the turbulent stress terms for the density fluctuations. Details of each correction and its implementation can be found in Horstman (1987).

Before commenting on Fig. 38, one further set of comparisons is shown in Fig. 39. This figure shows comparisons of the same numerical approaches with the Mach 11.3 data of Holden (1984). In this case the flowfield is generated by an incident shock wave generated by a wedge. In both the Mach 9 and 11 experiments, the wall temperature ratios are similar ( $T_w/T_0 = 0.28$  and 0.19, respectively) and the Reynolds numbers differ only by a factor of two. In both cases, it can be seen that the major discrepancies occur upstream of the ramp corner. In Fig. 38 the Cebeci-Smith model predicts the wall pressure distribution quite well. The  $k$ - $\epsilon$  model underpredicts the upstream influence, whereas with Mods A, B, and C it is overpredicted. In contrast, at Mach 11 (Fig. 39) the Cebeci-Smith (and  $k$ - $\epsilon$ ) models are now the worst, and the  $k$ - $\epsilon$  with Mod C does the best. In fact, none of these predictions can be

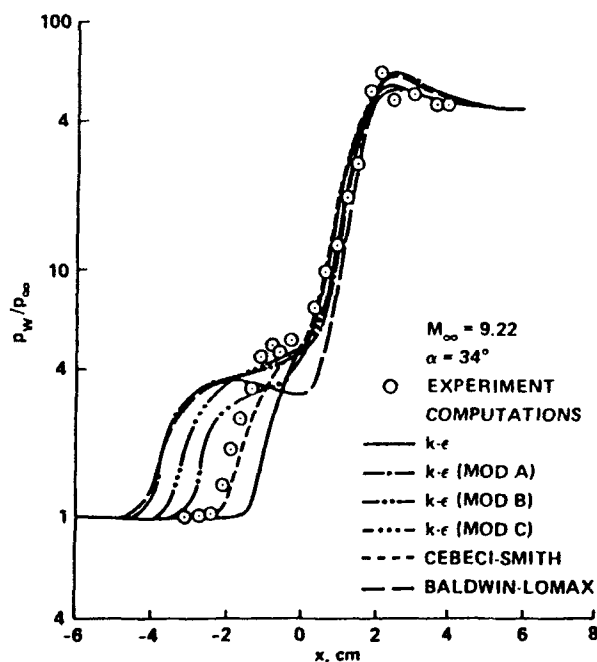


Fig. 38. Normalized wall pressure distributions in a compression ramp flow [ $M_\infty = 9.22$ ,  $\alpha = 34$  deg., data of Coleman (1973) and Coleman and Stollery (1972)]. Figure from Horstman (1987).

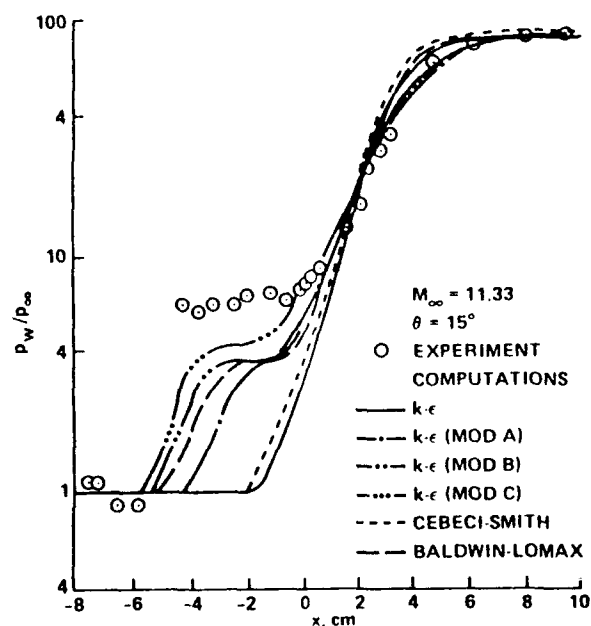


Fig. 39. Normalized wall pressure distributions in incident shock wave interaction [ $M_\infty = 11.33$ ,  $\theta = 15$  deg., data of Holden (1984)]. Figure from Horstman (1987).



considered satisfactory upstream of the corner for the Mach 11 flow.

Horstman (1987) states, "Two features of shock wave boundary layer interaction flows which are probably of most interest to the designer are the maximum heat transfer near reattachment and the length of the separation zone." Comparisons of the measured and predicted values of  $(q_{max}/q_{\infty})$  and the separation locations are shown in Figs. 40 and 41, respectively, for the Mach 9.22 compression ramp experiment. Note that the vertical axis in Fig. 40 is logarithmic. The  $k-\epsilon$  model and modifications do not even predict the right trend of  $(q_{max}/q_{\infty})$  with  $\alpha$ . The algebraic models predict the trend with  $\alpha$  better but underpredict the separated cases ( $\alpha > 30$  deg.). Figure 41 shows that the trends for the separation location are generally correct for all models, but only the Cebeci-Smith model predicts the values quantitatively. That the latter result is probably fortuitous is evident in Fig. 42, which shows similar comparisons at Mach 11. In this case, the Cebeci-Smith model is the worst. It is not just the maximum heating rate in the compression ramp interaction that is inadequately captured by any of the codes. The shape of the heat transfer rate throughout the interaction is also poorly predicted. The same remark applies to the heat transfer rate distribution in the incident shock wave experiment of Holden.

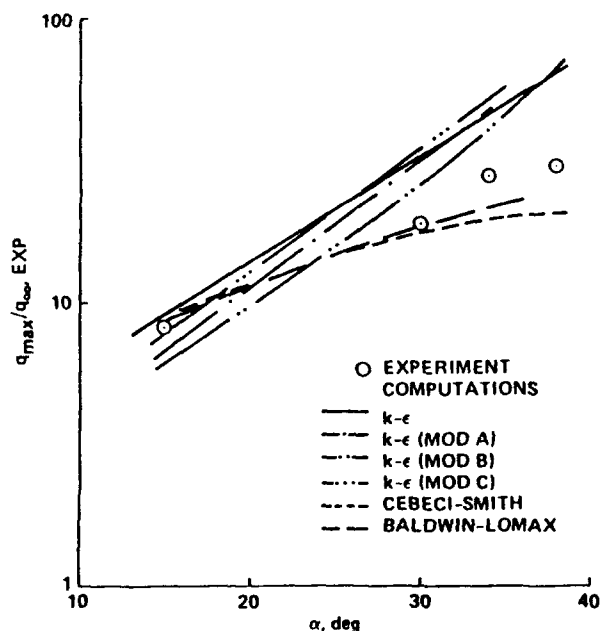


Fig. 40. Mach 9.22 compression ramp interaction: comparison of computed and experimental maximum heat transfer rates [from Horstman (1987)].

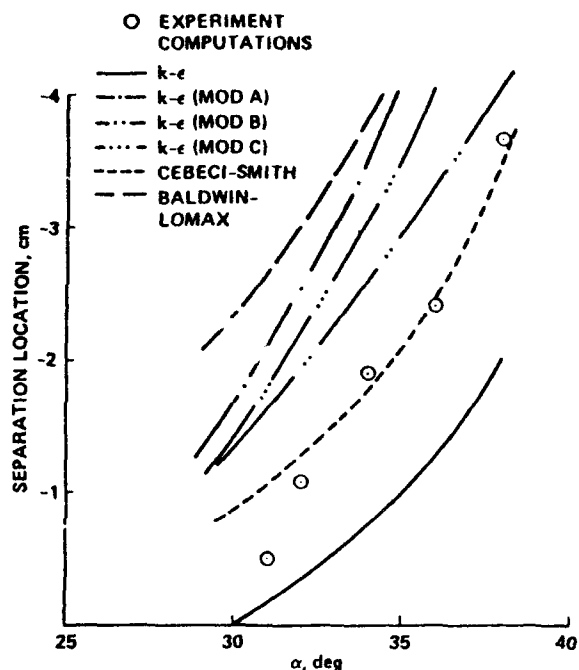


Fig. 41. Mach 9.22 compression ramp interaction: comparison of computed and experimental separation locations [from Horstman (1987)].

Horstman also points out that: "Experimenters have observed large unsteadiness for separated supersonic shock wave turbulent boundary layer interaction flows. There is no reason to doubt that unsteadiness is also present for the hypersonic test flows considered here. These unsteady effects can at times dominate the flowfield." He also pointed out that "the computations show no sign of unsteadiness. There is also no apparent mechanism in the present day eddy viscosity models for the observed unsteadiness. This may be an important factor that contributes to the discrepancies between the predicted and measured results."

The present author believes that the unsteadiness is indeed an important factor that contributes to the discrepancies between experiment and CFD, and that flowfields of this type cannot be understood in terms of mean measurements alone. Without understanding the dynamics of these flowfields, comparisons of mean surface and flowfield measurements with computations can lead to very misleading conclusions about a given algorithm or turbulence model. These statements are based on what is known of the unsteadiness of similar interactions at lower Mach numbers and which has been reported in earlier sections of this paper.



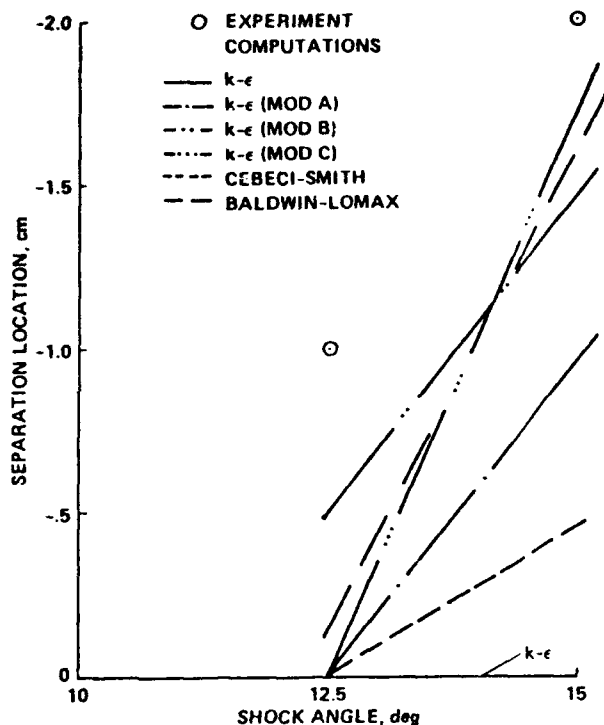


Fig. 42. Mach 11.3 incident shock wave interaction: comparison of computed and experimental separation locations [from Horstman (1987)].

Numerous computations, using a variety of turbulence models, have also been made of the 24-deg. Mach 3 unswept compression ramp experiment of Settles (1975). Four sets of computed pressure distributions for this flow are shown in Fig. 43. Similar to the hypersonic results of Figs. 38 and 39, the major discrepancies are upstream of the corner. Figure 43a shows those calculated by Viegas and Horstman (1979) using turbulence models available in 1979; Fig. 43b shows these calculated by Viegas et al. (1985) using the  $k-\epsilon$  model and employing both wall functions and integration to the wall (The experimental data of Dolling and Murphy (1983) are also shown in Fig. 43b. These data are time-averages of fluctuating wall pressure signals rather than single value mean measurements from scani-valves, as obtained by Settles.); Fig. 43c shows the results of Champney (1989), using more recent turbulence models; while Fig. 43d shows the most recent computations by Wilcox (1990), using his new "multi-scale" model and the  $k-\omega$  model. Champney's work includes calculations made using the turbulence model of Mansour and Shih, which was derived from direct simulation data for a channel flow and applied for the first time to a

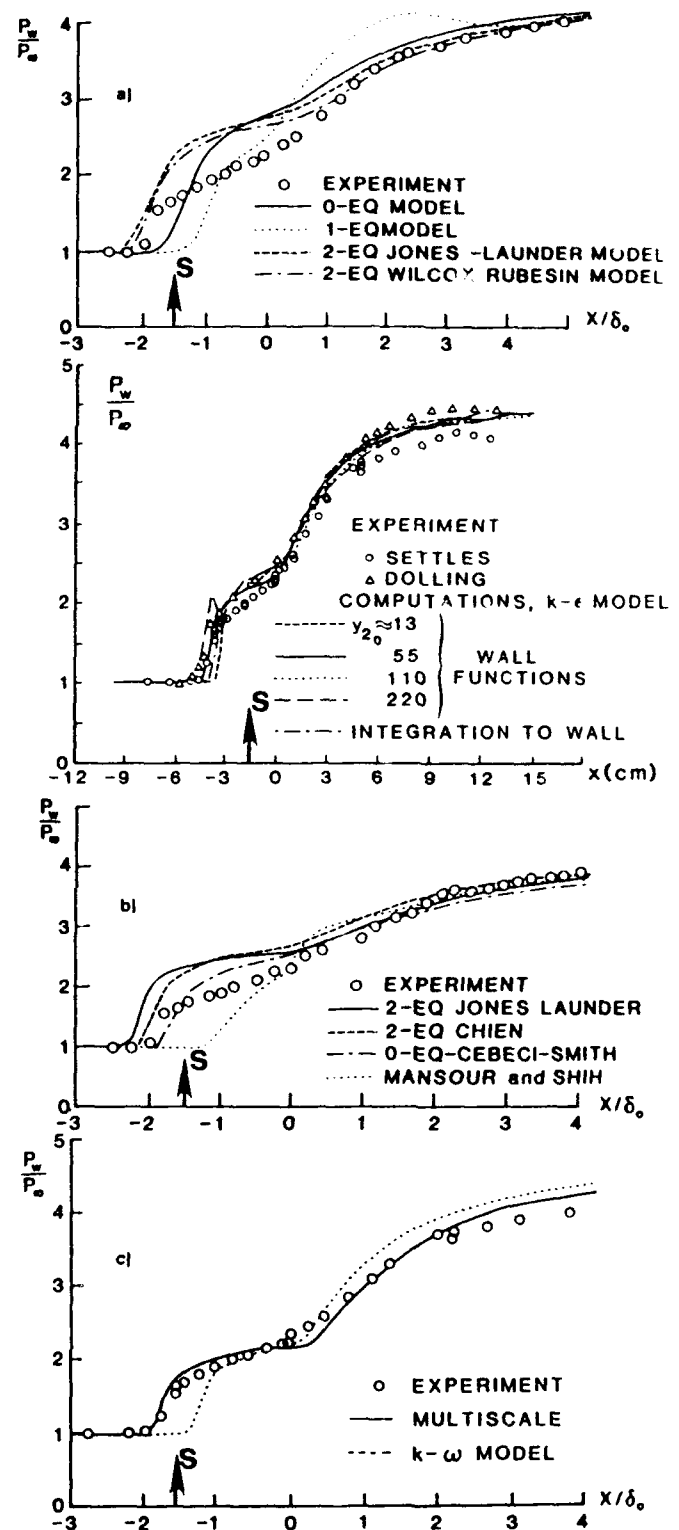


Fig. 43. Measured and computed wall pressure distributions in a 24-deg., Mach 3 compression ramp interaction: a) Viegas and Horstman (1979); b) Viegas, Rubesin and Horstman (1985); c) Champney (1989); d) Wilcox (1990).



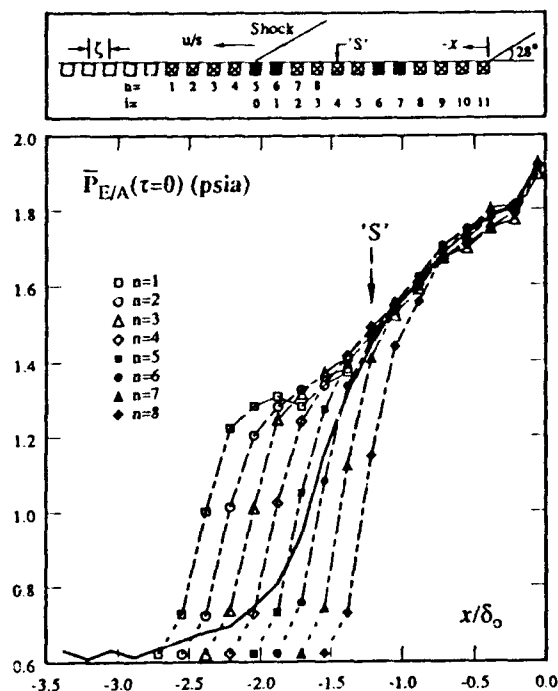


Fig. 44. Ensemble-averaged wall pressures upstream of the corner in a 28-deg., Mach 5 compression ramp interaction [from Erengil and Dolling (1991,1)].

compressible flow by Champney. The computations share certain common features—a generally steeper pressure gradient up through separation to the corner and a higher “plateau” level upstream of the corner than in the experiment. The  $k-\omega$  model of Fig. 43d is an exception to the latter and predicts the plateau pressure fairly well, but the upstream influence is substantially underpredicted. Of all the computations, Wilcox’s “multi-scale” model is superior; both upstream influence and plateau pressure levels are predicted quite well. The multi-scale model employs a physically more realistic description of the Reynolds stress tensor which is probably partly responsible for the overall improved comparison with the experiment. However, neither the multi-scale model nor any of the other methods model the low frequency unsteadiness of the separated flowfield. In this sense, as will be discussed later, the matching of the upstream influence by the multi-scale model can only be considered as fortuitous.

## 6.2 Implications of Unsteadiness for Computation of Surface Properties

It was stated earlier (Sec. 2.2) that Erengil and Dolling obtained ensemble-averaged pres-

ures  $\bar{P}_{E/A}$  from the separation shock foot to the corner in a Mach 5 compression ramp interaction. These distributions were generated by “freezing” the shock at various positions in the intermittent region and are plotted vs.  $X/\delta_0$  in Fig. 44. In the schematic at the top of the figure, filled markers shown an example of four simultaneously sampled transducer positions. (The “crossed” markers indicate the other positions at which ensemble-averaged pressures were obtained.) The symbol  $n$  represents the position of the shock in the intermittent region, and  $i$  is used to indicate the distance from the foot of the separation shock to the position of interest. The solid line in the Fig. 44 is the mean pressure distribution. Each one of the dashed-line curves was generated by freezing the shock at a given position in the intermittent region as it moved upstream and ensemble-averaging on each of the downstream channels.

Three features are evident. First,  $\bar{P}_{E/A}$  in the separated flow within about  $1\delta_0$  upstream of the ramp corner is relatively insensitive to the shock position in the intermittent region. Second, for the “shock-upstream” case, the ensemble-averaged pressure distribution has a well-defined plateau region, consistent with a large-scale separated flow. As the shock moves toward its most downstream position, the ensemble-averaged pressure distribution progressively changes, finally resembling that typical of a small-scale separated flow. The data presented are for upstream motion of the separation shock; similar results were obtained for downstream motion as well.

These results show clearly how the time-averaged results are generated. As noted earlier, it is the occasional presence of the unsteady shock at the upstream influence line (UI) which first increases the mean wall pressure above the undisturbed value. Most of the time the pressure at UI is within the undisturbed range typical of the incoming boundary layer. The mean pressure rises downstream of UI because the translating shock spends an increasing amount of time upstream of stations nearer the separation line. What is, in an instantaneous snapshot, an abrupt pressure rise across the separation shock, is smeared out from UI to S in the time-averaged picture by the shock motion.

Modeling the flowfield with a stationary separation shock cannot simultaneously generate the correct upstream influence (as usually defined) and the correct time-averaged wall pressure. Even if the upstream influence matches the experiment (as it does in several of the computations in Fig. 43), the pressure distribution is generally incor-



rect. This is because the stationary shock model essentially produces an instantaneous snapshot of the flowfield (i.e., one of the "shock frozen" distributions of Fig. 44). In the case just cited, the separation shock is close to the experimental upstream influence line. In the experiment, the mean pressure at any given point is the weighted average of a series of instantaneous flowfields, each for the separation shock at a different streamwise position. This is evident from Fig. 44, which showed ensemble-averaged streamwise pressures,  $\bar{P}_{E/A}$ , from the shock foot to the ramp corner, generated by "freezing" the separation shock at various positions in the intermittent region. Mean surface properties in an unsteady flowfield cannot be reproduced by a model in which the shock (even if successfully modeled as a discontinuity) is stationary. The only way in which both the correct upstream influence and pressure distribution can be generated is to include the translating shock front in the modeling. Time-averaging the computed wall pressures over many time steps (as is actually done in either digital or analog fashion in the experiment) should substantially improve the comparison with experiment, irrespective of the turbulence model.

### 6.3 Comparison of Computation with Experiment—Velocity Profiles

Wilcox also shows comparisons of the mean velocity profiles in the Mach 3, 24-deg. compression ramp interaction, with predictions from the  $k-\omega$  and multi-scale turbulence models. Examples are shown in Fig. 45. Downstream of the corner ( $y/\delta_o = 0.44$  to 6.13), the experimental data are much fuller than the computations below  $y/\delta_o$  of about 0.4. Wilcox also computed the outgoing mean velocity profiles for Brown's experiment (1986) of Mach 2.85 flow into a 30-deg. axisymmetric compression corner. These results are shown in Fig. 46. Again, below  $y/\delta_o$  of about 0.4, the measured profiles are much fuller than the computed profiles.

It was mentioned earlier that McClure and Dolling have examined how the outgoing mean pitot pressure profiles are actually generated in a Mach 5, 28-deg. compression ramp interaction. Three cases were studied: (i) ramp with suction applied along a 6mm-long slot spanning the ramp near the reattachment; (ii) ramp with suction slot exposed to the flow but without suction applied; (iii) baseline case (i.e., no slot or suction). Measurements were made using (i) a conventional pitot probe with a flattened tip (0.64 mm  $\times$  2.1 mm) with about 50 cm of pressure tubing between the probe tip and the pressure transducer, and

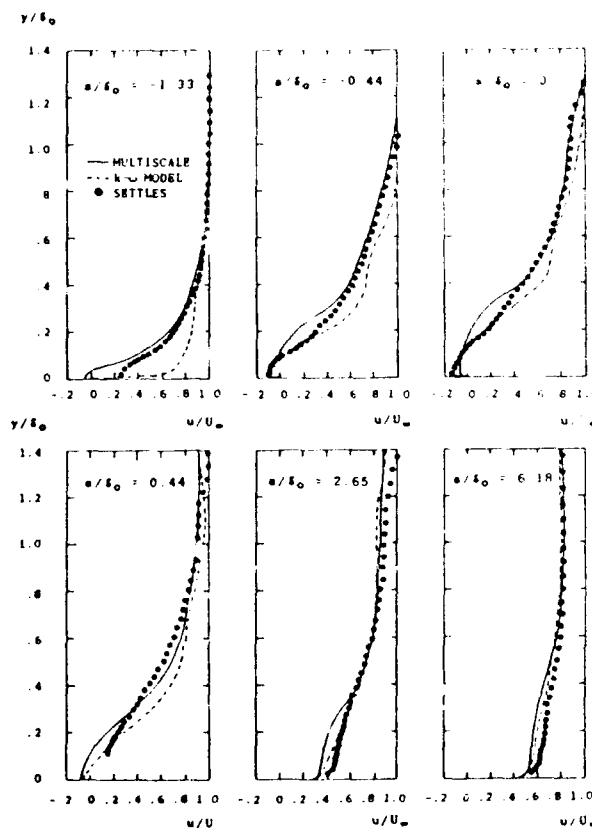


Fig. 45. Measured and computed mean velocity profiles downstream of the corner in a 24-deg., Mach 3 compression ramp interaction [from Wilcox (1990)].

(ii) a pitot probe with a single Kulite Model XCQ-062-100A miniature pressure transducer projecting upstream of the tip. The frequency response of the Kulite probe was about 50 kHz.

Results from the mean and fluctuating pitot surveys at four stations downstream of the corner are shown in Fig. 47 for the baseline and suction cases. Note that  $z$  is measured perpendicular to the ramp face. The solid lines are the mean profiles from the conventional probe. The dashed lines are "frozen" pitot profiles. "Frozen" profiles were obtained by averaging pitot pressure values only for the condition when the upstream separation shock was located between two specified surface transducers. The intermittencies of the surface transducer pair used are indicated in the figure keys. The two positions correspond to the separation shock far "upstream" and "downstream." Also indicated is the mean value from the fluctuating measurements.

Comparison of the mean pitot pressure values



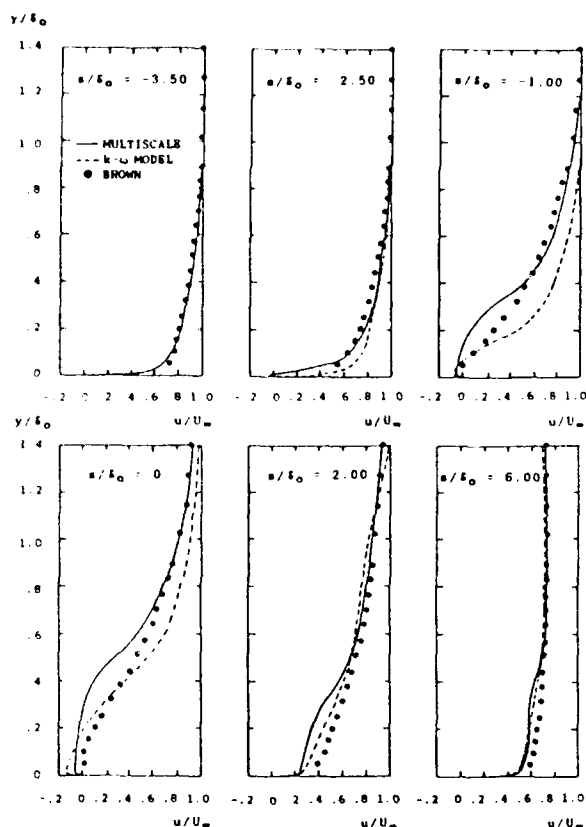


Fig. 46. Measured and computed mean velocity profiles downstream of the corner in a 30-deg., Mach 2.85 axisymmetric ramp flow [from Wilcox (1990)].

obtained from the conventional pitot probe with mean values from the fluctuating pitot pressure signal shows differences at each station. The differences have three possible causes. First, slight shifts in survey position show up as differences in pitot pressure. These differences should vary from ramp station to station but would be consistent for a given station. It is estimated that streamwise probe placement for a given ramp position varied by less than  $0.06\delta$  between *conventional* and *fluctuating* runs, and so should contribute only very slightly to  $P_t$  discrepancies. This possibility can therefore be disregarded. Second, the diameter of the fluctuating probe "tip" was 2.5 times greater than the conventional probe height, which would tend to integrate  $P_t$  over a larger distance and hence contribute to differences, particularly in regions of large gradients. It is probable that this integration has some effect. The third cause, which is almost certainly the major contributor, is the skewness of the fluctuat-

ing signal. Examination of the probability density distributions (pdd's) for the fluctuating pitot signals indicated that, close to the ramp surface ( $< 0.6\delta_0$ ), the pdd's had positive skewness and, in some cases, exhibited a bimodal shape with very large separation between peak values ( $\approx 32$  psi). Under conditions where the probability density values of these peaks were sufficiently different, *the conventional pitot reading was higher than the mean of the fluctuations*. Fig. 48 shows this effect for the data set with the largest disagreement, the suction survey at  $Z/\delta_0 \approx 1.45$ . The accompanying probability distributions for the fluctuating pitot pressure clearly show that the conventional pitot probe measurement is biased toward the higher mode in the fluctuating pitot pressure data for  $Z/\delta_0 \leq 0.43$ . This behavior reverses, though, for  $Z/\delta_0 = 0.58$ , where the probability density of the lower mode is six times greater than that of the higher mode. The 50 cm of tubing between the orifice and pressure transducer for the conventional pitot probe behaves as a *pressure sensitive* filter with an output dependent on the nature of the fluctuations (i.e., frequency and amplitude content).

In the experiments used for comparison with computation shown earlier, the pitot profiles from which mean velocity profiles were calculated were obtained using conventional probes. It is almost certain that these profiles are fuller than would

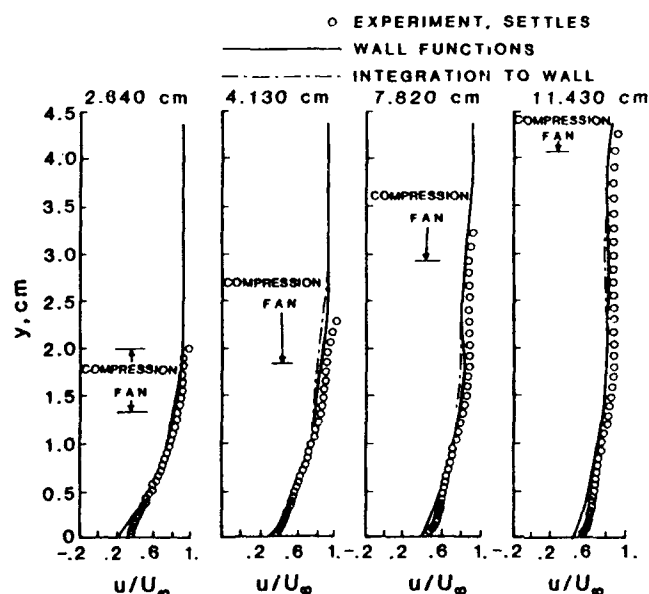


Fig. 47. Measured and computed mean velocity profiles downstream of the corner in a 20-deg., Mach 2.8 compression corner interaction [from Viegas, Rubesin and Horstman (1985)].



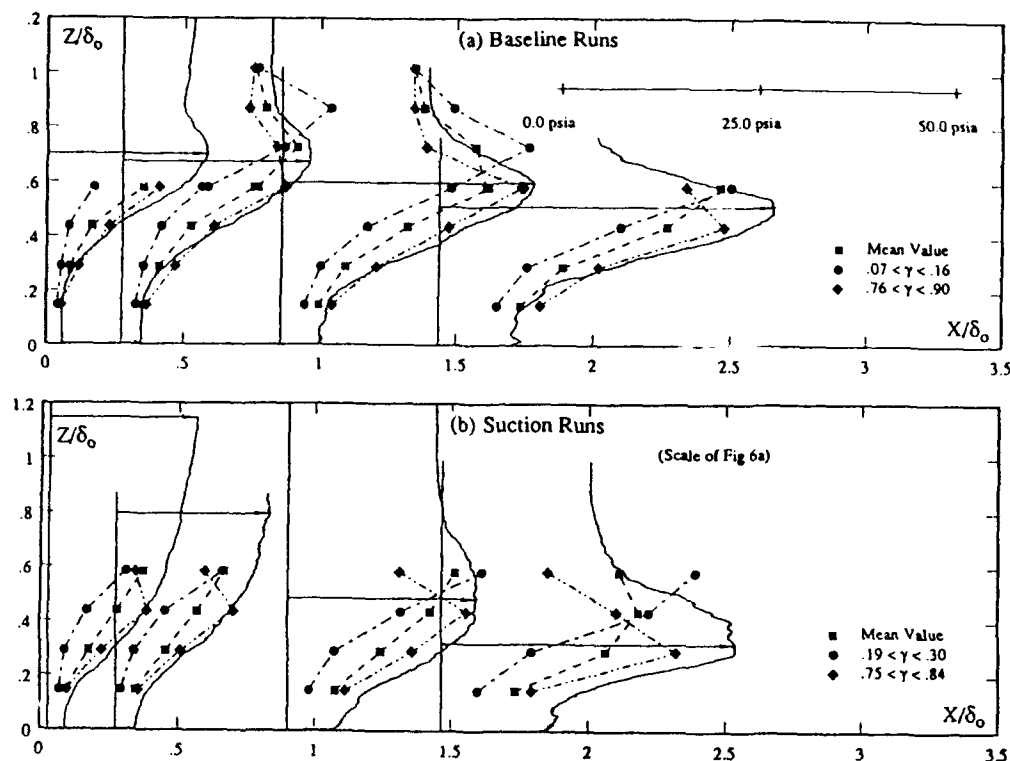


Fig. 48. Results from mean and fluctuating pitot surveys downstream of the corner in a 28-deg., Mach 5 compression ramp interaction: a) baseline; b) ramp with suction [from McClure & Dolling (1991)].

be obtained by time-averaging the corresponding fluctuating pitot pressure signals. If the mean velocity profile was computed using the mean of the fluctuating signal rather than the single time-averaged value from the conventional probe, the profiles would be much less full near the wall and would probably agree better with the computations.

#### 6.4 Concluding Remarks

It is clear that the measured mean surface and flowfield properties are controlled by the flowfield unsteadiness. The discrepancies between the predicted and measured properties are almost certainly not just due to inadequate turbulence modeling, but also due to neglect of the unsteadiness in the modeling. Without modeling the unsteadiness, it is unlikely that the codes can reproduce correct mean property distributions. For flows of this type, it is felt that equal emphasis should be placed on developing methods capable of modeling the unsteadiness as is placed on turbulence modeling.

#### 7 FUTURE WORK

Some suggestions as to the direction of future work are given below. The list is by no means exhaustive and focuses on control of unsteadiness, the development of better correlation/prediction schemes, additional experiments to confirm/discover causes of unsteadiness, and some remarks on the computation of unsteady flows.

- (i) Control of flowfield unsteadiness, particularly unsteady shocks with their attendant large amplitude loads, is a goal with significant practical returns. In the near term, however, a more realistic objective might be to develop methods to influence unsteadiness *favorably*. *Favorably* implies reducing peak loading levels, reducing the surface area exposed to high loads (i.e., reduce the length scale of shock motion), and developing means to shift shock frequencies out of one range and into another. Evidence exists that frequency shifts can be achieved using



active means, but these are likely to be complex, expensive, and bulky. Attention should initially be focused on passive means.

- (ii) There now exists, in the literature, a fairly large volume of fluctuating loads data for several different geometries. The range of flow conditions is fairly narrow but is probably sufficient to begin the development of engineering correlation and prediction schemes for loading levels and spectra. In the past, much of the effort has been devoted to determining flowfield physics, and relatively little attention has been given to correlating the results and developing easy-to-use prediction methods. It is probably an appropriate time to begin such work in earnest. Correlations which relate fluctuating load levels to local mean levels would be the most useful. There exists a large amount of mean flow data for many configurations over a wide range of flow conditions; thus, the mean properties of many flows are already known. Further, computational fluid dynamics is able, in many cases, to predict mean wall pressures accurately. Such an effort might also identify those flow regimes in which more data are required.
- (iii) Additional experiments are needed to confirm the physical mechanisms described in this paper and to examine their validity. An optimum approach might combine full flowfield visualization with quantitative measurements in the incoming and perturbed flows. As an example, specific large-scale turbulent structures entering the flow could be detected 5–10 $\delta_o$  upstream of the interaction using an array of hot wires and, after an appropriate delay, dual or multi-pulse flowfield images obtained to show the response of the shock/interaction to the passage of the structure. Such experiments would show directly and visually what must now be deduced from conditional sampling techniques.
- (iv) New efforts should be directed toward developing computational methods for modeling unsteady flowfields. Real time, fully 3-D, turbulent Navier-Stokes computations on a routine basis for engineering prediction are still in the distant future. A relevant question is whether simpler approaches can be developed which model the essential features of the unsteadiness. Can methods be developed which employ unsteady boundary conditions whose details are obtained from experiment? Would such an approach yield

an unsteady flowfield whose time-averaged surface properties matched experiment and from which approximate estimates of fluctuating load levels could be deduced? The author feels that, with the availability of parallel computers, this is a field ripe for exploitation by the CFD community.

## 8 ACKNOWLEDGMENTS

Much of the work cited here was conducted by the author, his colleagues, and his graduate students, and was supported by AFOSR (monitored by Dr. L. Sakell), by ARO (monitored by Dr. T. Doligalski), by NASA Lewis (monitored by W. Hingst), and by NASA Langley (monitored by Dr. W. Zorumski). Additional support was received from the Center of Hypersonics Training and Research supported by NASA (monitored by S. Wander). These sources of support are gratefully acknowledged.

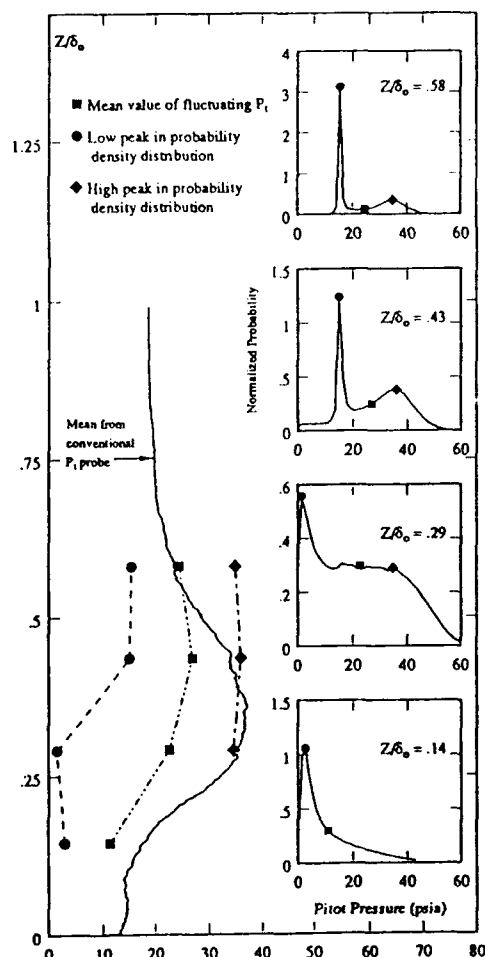


Fig. 49. Comparison of mean values from fluctuating and conventional mean pitot surveys [from McClure & Dolling (1991)].



## REFERENCES

- Alvi, F. S. and Settles, G. S. (1992), "Physical Model of the Swept Shock Wave/Boundary-Layer Interaction Flowfield," *AIAA Journal*, Vol. 30, Sep. 1992, pp. 2252-2558.
- Andreopoulos, J. and Muck, K. C. (1987), "Some New Aspects of the Shock-Wave/Boundary-Layer Interaction in Compression-Ramp Flows," *Journal of Fluid Mechanics*, Vol. 180, pp. 405-428.
- Aso, S., Tan, A., Hayashi, M. (1989), "The Structure of Aerodynamic Heating in Three Dimensional Shock Wave and Turbulent Boundary Layer Interactions Induced by Sharp Fins and Blunt Fins," AIAA Paper 89-1854, AIAA 20th Fluid Dynamics, Plasma Dynamics and Lasers Conference, Buffalo, NY, June 12-14, 1989.
- Aso, S., Kuranaga, S., Hayashi, M. (1991), "Detailed Measurements on Unsteady Properties in Three Dimensional Shock Wave/Turbulent Boundary Layer Interaction Induced by Blunt Fin at Mach Number 4," AIAA Paper 91-1755, AIAA 22nd Fluid Dynamics, Plasma Dynamics & Lasers Conference, Honolulu, HI, June 24-26, 1991.
- Batcho, P. F., Ketchum, A. C., Bogdonoff, S. M., Fernando, S. M. (1989), "Preliminary Study of the Interactions Caused by Crossing Shock Waves and a Turbulent Boundary Layer," AIAA Paper 89-0359, 27th Aerospace Sciences Meeting, Jan. 9-12, 1989, Reno, NV.
- Bibko, V. N., Efimtsov, B. M., Korkach, V. G., and Kuznetsov, V. B. (1991), "Oscillations of a Shock Wave Induced by Boundary Layer Separation," *Izvestiya Akademii Nauk SSSR, Mekhanika Zhidkosti i Gaza*, No. 4, pp. 168-170, July/Aug. 1990 (translation in *Fluid Dynamics*, Vol. 25, No. 4, Jan. 1991).
- Boitnott, T. (1990), "An Experimental Study of the Dynamics of Moderately Swept Compression Ramp-Induced Separation at Mach 5," M.S. Thesis, Dept. of Aerospace Engineering & Engineering Mechanics, The Univ. of Texas at Austin, Aug. 1990.
- Brown, J. D. (1986), "Two Component LDV Investigation of Shock Related Turbulent Boundary Layer Separation with Increasing Three-Dimensionality," PH.D. Thesis, University of California at Berkeley, 1986.
- Brusniak, L. (1991), "Experimental Investigation of the Driving Mechanism of the Unsteady Separation Shock Motion in a Cylinder-Induced Hypersonic Interaction," M.S.E. Thesis, Dept. of Aerospace Engineering & Engineering Mechanics, The Univ. of Texas at Austin, May 1991.
- Brusniak, L. and Dolling, D. S. (1992), data from an abstract entitled "Physical Causes of Unsteadiness in Blunt Fin-Induced Shock Wave/Turbulent Boundary Layer Interaction," submitted to 24th AIAA Fluid Dynamics Conference, July 1993. Copies available from second author.
- Burgio, C. (1970), "Comparison Between Shock Wave/Boundary Layer Interactions Caused Either by Incident Shocks or Ramps," Von Karman Institute for Fluid Dynamics, Project Report 1970-266, June 1970.
- Calarese, W. and Hankey, W. L. (1985), "Modes of Shock Wave Oscillations on Spike-Tipped Bodies," *AIAA Journal*, Vol. 23, No. 2, pp. 185-192, Feb. 1985.
- Champney, J. (1989), "Modelling of Turbulence for Compression Corner Flows and Internal Flows," AIAA Paper 89-2344, AIAA/ASME/SAE/ASEE 25th Joint Propulsion Conference, Jul. 1989.
- Chapman, D. R., Kuehn, D. M., and Larson, H. K. (1958), "Investigation of Separated Flows in Supersonic and Subsonic Streams with Emphasis on the Effect of Transition," NACA Report 1356, 1958.
- Chyu, W. J. and Hanly, R. D. (1969), "Power and Cross Spectra and Space-Time Correlations of Surface Fluctuating Pressures at Mach Numbers Between 1.6 and 2.5," NASA-TN-D-5440, Sept. 1969.
- Coe, C. F., Chyu, W. J., and Dods, J. B. (1973), "Pressure Fluctuations Underlying Attached and Separated Supersonic Turbulent Boundary Layers and Shock Waves," AIAA Paper 73-996, AIAA Aeroacoustics Conference, Seattle, WA, Oct. 15-17, 1973.
- Coleman, G. T. and Stollery, J. L. (1972), "Heat Transfer in Hypersonic Turbulent Separated Flow," Imperial College of Science and Technology Aero Rept. 72-05, London, Mar. 1972.
- Coleman, G. T. (1973) "A Study of Hypersonic Boundary Layers over a Family of Axisymmetric Bodies at Zero Incidence: Preliminary Report and Data Tabulation," Imperial College of Science and Technology Aero Rept. 73-06, London, Sep. 1973.
- Cooper, J. R. and Korkegi, R. H. (1975), "Investigation of Self-Induced Blowing and Suction Across a Region of Shock Wave Bound-



- ary Layer Interaction," ARL TR-75-0181, June 1975.
- Debieve, J. F. and LaCharme, J. P. (1985), "A Shock Wave/Free Turbulence Interaction," *Turbulent Shear Layer/ Shock Wave Interactions Conference Proceedings*, IUTAM Symposium, Palaiseau, 1985, Springer-Verlag.
- Degrez, G. (1981), "Exploratory Experimental Investigation of the Unsteady Aspects of Blunt Fin-Induced Shock Wave Turbulent Boundary Layer Interactions," M.S.E. Thesis 1516-T, Mechanical and Aerospace Engineering Dept., Princeton University, Princeton, NJ, June 1981.
- Degrez, G. and Ginoux, J. J. (1983), "Three Dimensional Skewed Shock Wave Laminar Boundary Layer Interaction at Mach 2.25," AIAA Paper 83-1755, AIAA 16th Fluid and Plasma Dynamics Conference, July 12-14, Danvers, MA.
- Degrez, G. and Ginoux, J. J. (1984), "Surface Phenomena in a Three Dimensional Skewed Shock Wave/ Laminar Boundary Layer Interaction," *AIAA Journal*, Vol. 22, No. 12, pp. 1764-1769, Dec. 1984.
- Dolling, D. S. and Bogdonoff, S. M. (1981), "An Experimental Investigation of the Unsteady Behavior of Blunt Fin-Induced Shock Wave Turbulent Boundary Layer Interactions," AIAA Paper 81-1287, AIAA 14th Fluid & Plasma Dynamics Conference, Palo Alto, CA, June 1981.
- Dolling, D. S. and Bogdonoff, S. M. (1982), "Blunt Fin-Induced Shock Wave Turbulent Boundary Layer Interaction," *AIAA Journal*, Vol. 20, No. 12, pp. 1674-1680, Dec. 1982.
- Dolling, D. S. and Murphy, M. T. (1983), "Unsteadiness of the Separation Shock Wave Structure in a Supersonic Compression Ramp Flowfield," *AIAA Journal*, Vol. 21, No. 12, pp. 1628-1634, Dec. 1983.
- Dolling, D. S. and Or, C. T. (1985), "Unsteadiness of the Shock Wave Structure in Attached and Separated Compression Corner Flowfields," *Experiments in Fluids*, Vol. 3, pp. 24-32.
- Dolling, D. S. and Narlo, J. C. (1987), "Driving Mechanism of Unsteady Separation Shock Motion in Hypersonic Interactive Flow," Ch. 7, AGARD CP428, (Aerodynamics of Hypersonic Lifting Vehicles), Nov. 1987.
- Dolling, D. S. and Smith, D. R. (1988), "Unsteady Shock-Induced Turbulent Separation in Mach 5 Cylinder Interactions," AIAA Paper 88-0305, AIAA 26th Aerospace Sciences Meeting, Reno, NV, Jan. 1988.
- Dolling, D. S. and Brusniak, L. (1989), "Separation Shock Motion in Fin, Cylinder and Compression Ramp Interactions," *AIAA Journal*, Vol. 27, No. 6, pp. 734-742, June 1989.
- Dolling, D. S. and Smith, D. R. (1989), "Separation Shock Dynamics in Mach 5 Turbulent Interactions Induced by Cylinders," *AIAA Journal*, Vol. 27, No. 12, pp. 1698-1706, Dec. 1989.
- Dolling, D. S. and Dussauge, J. P. (1990), "Fluctuating Wall Pressure Measurements," Ch. 8, Agardograph 315, *A Survey of Measurements and Measuring Techniques in Rapidly Distorted Compressible Turbulent Boundary Layers*.
- Dolling, D. S. (1990), "Unsteadiness of Supersonic and Hypersonic Shock Induced Turbulent Boundary Layer Separation," AGARD-R-764, Ch. 7, *Special Course on Three Dimensional Supersonic/ Hypersonic Flows Including Separation*, Jan. 1990.
- Dolling, D. S. and Brusniak, L. (1991), "Correlation of Separation Shock Motion in a Cylinder-Induced Interaction with Pressure Fluctuations Under the Separated Region," AIAA Paper 91-0650, 29th Aerospace Sciences Meeting, Reno, NV, Jan. 1991.
- Dolling, D. S., Boitnott, T., and Erengil, M. E. (1991), "Effects of Moderate Sweepback on the Separation Shock Wave Dynamics in a Mach 5 Compression Ramp Interaction," AIAA Paper 91-0254, AIAA 29th Aerospace Sciences Meeting, Reno, NV, Jan. 1991.
- Dolling, D. S. (1992), "Problems in the Validation of CFD Codes Through Comparison with Experiment," Paper 19, AGARD Symposium on Theoretical and Experimental Methods in Hypersonic Flows, Turin, Italy, May 4-8, 1992.
- Dolling, D. S., Brusniak, L., Erengil, M. E., and McClure, W. B. (1992), "Algorithms for Analysis of Unsteady Shock-Induced Turbulent Separated Flows," Center for Aeromechanics Research, Wind Tunnel Lab. Report, Apr. 1992. Copies available from first author.
- Donovan, J. F. (1992), "Preliminary Results from a Tangentially Injected Shock Wave/ Turbulent Boundary Layer Interaction," McDonnell Douglas Research Laboratories, MDRL 92-20, Sept. 1992.
- Erengil, M. E. and Dolling, D. S. (1989), "Separation Shock Wave Motion and Ensemble Averaged Wall Pressures in a Mach 5 Compression Ramp Interaction," AIAA Paper 89-1853,



- AIAA 20th Fluid Dynamics, Plasma Dynamics and Lasers Conference, Buffalo, NY, June 1989.
- Erengil, M. E. (1989), "Separation Shock Motion and Ensemble-Averaged Wall Pressures in a Mach 5 Compression Ramp Interaction," M.S. Thesis, Dept. of Aerospace Engineering and Engineering Mechanics, The Univ. of Texas at Austin, Aug. 1989.
- Erengil, M. and Dolling, D. S. (1990), "Correlation of Separation Shock Motion in a Compression Ramp Interaction with Pressure Fluctuations in the Incoming Boundary Layer," AIAA Paper 90-1646, AIAA 21st Fluid Dynamics, Plasma Dynamics and Lasers Conference, June 1990.
- Erengil, M. E. and Dolling D. S. (1991,1), "Separation Shock Wave Motion and Ensemble Averaged Wall Pressure in a Mach 5 Compression Ramp Interaction," *AIAA Journal*, Vol. 29, No. 5, pp. 728-735, May 1991.
- Erengil, M. E. and Dolling, D. S. (1991,2), "Correlation of Separation Shock Motion with Pressure Fluctuations in the Incoming Boundary Layer," *AIAA Journal*, Vol. 29, No. 11, pp. 1868-1877, Nov. 1991.
- Erengil, M. E. (1991,3), private communication.
- Erengil, M. E. and Dolling, D. S. (1992,1), "Effects of Sweepback on Unsteady Separation in Mach 5 Compression Ramp Interactions," AIAA Paper 92-0430, 30th Aerospace Sciences Meeting, Reno, NV, Jan. 6-9, 1992.
- Erengil, M. E. and Dolling, D. S. (1992,2), data from an abstract entitled "Physical Causes of Separation Shock Unsteadiness in Shock Wave Turbulent Boundary Layer Interaction," submitted to 24th AIAA Fluid Dynamics Conference, July 1993. Copies available from second author.
- Erengil, M. E. and Dolling, D. S., "Effects of Sweepback on Unsteady Separation in Mach 5 Compression Ramp Interactions," to be published by *AIAA Journal*.
- Garg, S. and Settles, G. S. (1993), "Wall Pressure Fluctuations Beneath Swept Shock/ Boundary Layer Interactions," AIAA Paper 92-0384, AIAA 30th Aerospace Sciences Meeting, Reno, NV.
- Gibson, B. G. (1990), "An Experimental Study of Wall Pressure Fluctuations Near Separation in a Mach 5, Sharp Fin-Induced Turbulent Interaction," M. S. Thesis, Dept. of Aerospace and Mechanical Engineering, The Univ. of Texas at Austin, Aug. 1990.
- Gibson, B. and Dolling, D. S. (1991), "Wall Pressure Fluctuations Near Separation in a Mach 5, Sharp Fin-Induced Turbulent Interaction," AIAA Paper 91-0646, AIAA 29th Aerospace Sciences Meeting, Reno, NV, Jan. 1991.
- Glotov, G. F. and Korontsvit, I. U. (1983), "An Investigation of a Method for Controlling a Three-Dimensional Separation Zone," *TsAGI, Uchenye Zapiski*, Vol. 14, No. 2, pp. 126-131, in Russian.
- Gonsalez, J. and Dolling, D. S. (1993), "Effects of Interaction Sweepback on the Dynamics of Shock-Induced Turbulent Separation," AIAA Paper 93-0776, AIAA 31st Aerospace Sciences Meeting, Reno, NV, Jan. 11-14, 1993.
- Goodman, W. L., Morrisette, E. L., Hussaini, M. Y., and Bushnell, D. M. (1985), "Control Plate for Shock Boundary Layer Interactions," AIAA Paper 85-0523, AIAA Shear Flow Control Conferences, Boulder, CO, Mar. 1985.
- Gramann, R. A. and Dolling, D. S. (1986), "Unsteady Separation in Shock Wave Turbulent Boundary Layer Interaction," AIAA Paper 86-1033, AIAA/ASME 4th Joint Fluid Mechanics, Plasma Dynamics and Lasers Conference, Atlanta, GA, May 12-14, 1986.
- Gramann, R. A. and Dolling, D. S. (1987), "Intermittent Separation in Shock Wave Turbulent Boundary Layer Interaction," *AIAA Journal*, Vol. 25, No. 12, pp. 1545-1546.
- Gramann, R. and Dolling, D. S. (1988), "Detection of Turbulent Boundary Layer Separation Using Fluctuating Wall Pressure Signals," AIAA Paper 88-4676, AIAA/ NASA/ AFWAL Conference on Sensors and Measurement Techniques for Aeronautical Applications, Atlanta, GA, Sep. 1988.
- Gramann, R. A. (1989), "Dynamics of Separation and Reattachment in a Mach 5 Unswept Compression Ramp Flow," Ph.D. Dissertation, Dept. of Aerospace Engineering and Engineering Mechanics, The Univ. of Texas at Austin, Dec. 1989.
- Gramann, R. A., and Dolling, D. S. (1990,1), "Dynamics of Separation and Reattachment in a Mach 5 Compression Ramp Flow," AIAA Paper 90-0380, AIAA 28th Aerospace Sciences Meeting, Jan. 8-11, 1990.
- Gramann, R. and Dolling, D. S. (1990,2), "Dynamics of the Outgoing Turbulent Boundary Layer in a Mach 5 Compression Ramp Interaction," AIAA Paper 90-1645, AIAA 21st Fluid



- Dynamics, Plasma Dynamics and Lasers Conference, June 1990.
- Gramann, R. A. and Dolling, D. S. (1992), "Examination of Turbulent Structures Associated with Unsteady Shock Motion in a Mach 5 Interaction," AIAA Paper 92-0744, AIAA 30th Aerospace Sciences Meeting, Reno, NV, Jan. 6-9, 1992.
- Green, J. E. (1970), "Interaction Between Shock Waves and Boundary Layers," *Progress in Aerospace Sciences*, Vol. 11, pp. 235-340, 1970.
- Hamed, A. and Shang, J. (1989), "Survey and Assessment of Validation Data Base for Shock Wave Boundary Layer Interactions in Supersonic Inlets," AIAA Paper 89-2939, AIAA/ASME/SAE/ASEE 25th Joint Propulsion Conference, Monterey, CA, July 10-12, 1989.
- Hayashi, M., Aso, S., and Tan, A. (1989), "Fluctuation of Heat Transfer in Shock Wave/Turbulent Boundary Layer Interaction," *AIAA Journal*, Vol. 27, No. 4, pp. 399-404, Apr. 1989.
- Holden, M. S. (1984), "Experimental Studies of Quasi-Two-Dimensional and Three-Dimensional Viscous Interaction Regions Induced by Skewed-Shock and Swept-Shock Boundary Layer Interaction," AIAA Paper 84-1677, Snowmass, CO, 1984.
- Holden, M. S. (1986), "A Review of Aerothermal Problems Associated with Hypersonic Flight," AIAA Paper 86-0267, 24th Aerospace Sciences Meeting, Reno, NV, Jan. 1986.
- Holden, M. S. (1991), "Studies of the Mean and Unsteady Structure of Turbulent Boundary Layer Separation in Hypersonic Flow," AIAA Paper 91-1778, AIAA 22nd Fluid Dynamics, Plasma Dynamics and Lasers Conference, Honolulu, HI, June 24-26, 1991.
- Holden, M. S. and Moselle, J. R. (1992), "A Database of Aerothermal Measurements in Hypersonic Flow for CFD Validation," AIAA 92-4023, AIAA 17th Aerospace Ground Testing Conference, Nashville, TN, July 6-8, 1992.
- Horstman, C. C. (1987), "Prediction of Hypersonic Shock Wave/Turbulent Boundary Layer Interaction Flows," AIAA Paper 87-1367, AIAA 19th Fluid Dynamics, Plasma Dynamics and Lasers Conference, Honolulu, HI, Jun. 8-10, 1987.
- Hung, C. M. and Buning, P. E. (1985), "Simulation of Blunt Fin-Induced Shock Wave and Turbulent Boundary Layer Interaction," *Jnl. of Fluid Mechanics*, Vol. 154, pp. 163-185, May 1985.
- Jackson, L. R., Dixon, S. C., Tenney, D. R., Carter, A. L., and Stephens, J. R. (1987), "Hypersonic Structures and Materials: A Progress Report," *Aerospace America*, pp. 24-30, Oct. 1987.
- Kaufman II, L. G. and Johnson, C. B. (1974), "Weak Incident Shock Interactions with Mach 8 Laminar Boundary Layers," NASA TN-D-7835, Dec. 1974.
- Kistler, A. L. (1964), "Fluctuating Wall Pressure Under a Separated Supersonic Flow," *J. Acoust. Soc. of America*, 36, pp. 543-550.
- Kleifges, K. and Dolling, D. S. (1992), data from abstract entitled "Control of Unsteady Shock-Induced Turbulent Boundary Layer Separation Upstream of Blunt Fins," submitted for presentation at AIAA 3rd Annual Shear Flow Control Conference, July 1993. Copies available from second author.
- Kussoy, M. L., Brown, J. D., Brown, J. L., Lockman, W. K., and Horstmann, C. C. (1987), "Fluctuations and Massive Separation in Three-Dimensional Shock Wave/Boundary Layer Interactions," 2nd International Symposium of Transport Phenomena in Turbulent Flows, Tokyo, Japan, Oct. 25-29, 1987.
- Laganelli, A. L., Martelluci, A., and Shaw, L. (1983), "Prediction of Turbulent Wall Pressure Fluctuations in Attached Boundary Layer Flow," *AIAA Journal*, Vol. 21, No. 4, Apr. 1983.
- Laganelli, A. L., Martelluci, A., and Shaw, L. (1976), "Prediction of Surface Pressure Fluctuations in Hypersonic Turbulent Boundary Layers," AIAA Paper 76-409, AIAA 9th Fluid Dynamics/Plasma Dynamics Conference, San Diego, CA, July 1976.
- Marshall, A. (1989), "An Experimental Investigation of the Spanwise Structure of the Unsteady Separation Shock in a Mach 5 Unswept Compression Ramp Interaction," M.S. Thesis, Dept. of Aerospace Engineering and Engineering Mechanics, The Univ. of Texas at Austin, May 1989.
- Marshall, T. A. and Dolling, D. S. (1990), "Spanwise Properties of the Unsteady Separation Shock in a Mach 5 Unswept Compression Ramp Interaction," AIAA Paper 90-0377, 28th Aerospace Sciences Meeting, Reno, NV.
- Marshall, A. and Dolling, D. S. (1992), "Comments on the Computation of Supersonic, Unswept, Turbulent Compression Ramp Interactions," *AIAA Journal*, Vol. 30, No. 8, pp. 2056-2065, Aug. 1992.



- Marvin, J. G. (1992), "CFD Validation Experiments for Hypersonic Flows," AIAA Paper 92-4024, AIAA 17th Aerospace Ground Testing Conference, Nashville, TN, July 6-8, 1992.
- McClure, W. B. and Dolling, D. S. (1991), "Exploratory Study of Effects of Suction Near Reattachment on the Unsteadiness of a Mach 5 Compression Ramp Interaction," AIAA Paper 91-1767, AIAA 22nd Fluid Dynamics, Plasma Dynamics and Lasers Conference, June 24-27, 1991.
- McClure, W. B. (1992), "An Experimental Study of the Driving Mechanism and Control of the Unsteady Shock-Induced Turbulent Separation in a Mach 5 Compression Corner Flow," Ph.D. Dissertation, Dept. of Aerospace Engineering and Engineering Mechanics, The Univ. of Texas at Austin, Aug. 1992.
- McClure, W. B. and Dolling, D. S. (1992), "An Examination of the Effects of Incoming Boundary Layer Modifications on the Dynamics of a Turbulent Compression Corner Interaction," AIAA/SAE/ASME/ASEE 28th Joint Propulsion Conference, Nashville, TN, July 6-8, 1992.
- McCormick, D. C. (1992), "Shock Boundary Layer Interaction Control with Low Profile Vortex Generators and a Passive Cavity," AIAA Paper 92-0064, AIAA 30th Aerospace Sciences Meeting, Reno, NV.
- Muck, K. C., Dussauge, J. P., and Bogdonoff, S. M. (1985), "Structure of the Wall Pressure Fluctuations in a Shock-Induced Separated Turbulent Flow," AIAA Paper 85-0179, AIAA 23rd Aerospace Sciences Meeting, Reno, NV, Jan. 1985.
- Muck, K. C., Andreopoulos, J., and Dussauge, J. P. (1988), "Unsteady Nature of Shock-Wave/Turbulent Boundary-Layer Interaction," *AIAA Journal*, Vol. 26, No. 2, pp. 179-187.
- Murphy, M. (1983), "An Experimental Investigation of the Separation Shock Wave Unsteadiness in a Compression Ramp Flowfield," M.S.E. Thesis 1605-T, Mechanical and Aerospace Engineering Dept., Princeton University.
- Narlo, J. C. (1986), "Experimental Investigation of the Driving Mechanisms of Separation Shock Wave Motion in Interactive Flows," M.S. Thesis, Dept. of Aerospace Engineering and Engineering Mechanics, The Univ. of Texas at Austin, Dec. 1986.
- Nordyke, R. J. (1987), "Spanwise Properties of the Unsteady Separation Shock in a Mach 5 Unswept Compression Ramp Interaction," M.S. Thesis, Dept. of Aerospace Engineering and Engineering Mechanics, The Univ. of Texas at Austin, May 1987.
- Ozcan, O. and Holt, M. (1984), "Supersonic Separated Flow Past a Cylindrical Obstacle on a Flat Plate," *AIAA Journal*, Vol. 2, pp. 611-617, May 1984.
- Pozefsky, P., Blevins, R. D., and Laganelli, A. L. (1989), "Thermo-Vibro-Acoustic Loads and Fatigue of Hypersonic Flight Vehicle Structures," AFWAL TR-89-3014, Feb. 1989.
- Raghunathan, S. (1988), "Passive Control of Shock-Boundary Layer Interaction," *Progress in Aerospace Sciences*, Vol. 25, pp. 271-296, 1988.
- Robertson, J. E. (1969), "Characteristics of the Static and Fluctuating-Pressure Environments Induced by Three-Dimensional Protuberances at Transonic Mach Numbers," Wyle Laboratories Research Staff Report WR-69-3, June 1969.
- Robertson, J. E. (1971), "Prediction of In-flight Fluctuating Pressure Environments Including Protuberance Induced Flow," Wyle Laboratories Research Staff Report WR-71-10, Mar. 1971.
- Rockwell, D. (1983), "Oscillations of Impinging Shear Layers," *AIAA Journal*, Vol. 21, No. 5, pp. 656-664, May 1983.
- Schmisser, J. D. and Dolling, D. S. (1992,1), "Unsteady Separation in Sharp Fin-Induced Shock Wave/Turbulent Boundary Layer Interaction," AIAA Paper 92-0748, AIAA 30th Aerospace Sciences Meeting, Reno, NV, Jan. 6-9, 1992.
- Schmisser, J. D. (1992,2), "An Experimental Study of Fluctuating Wall Pressures in a Highly Swept, Sharp Fin-Induced Shock Wave/Turbulent Boundary Layer Interaction," M.S.E. Thesis, Dept. of Aerospace Engineering and Engineering Mechanics, The Univ. of Texas at Austin, May 1992.
- Sedney, R. (1973), "A Survey of the Effects of Small Protuberances on Boundary Layer Flows," *AIAA Journal*, Vol. 11, No. 6, pp. 782-792, June 1973.
- Selig, M. S. (1988), "Unsteadiness of Shock Wave/Turbulent Boundary-Layer Interactions with Dynamic Control," M. S. E. Thesis 1801-T, Dept. of Mechanical and Aerospace Engineering, Princeton University.



- Selig, M. S. and Smits, A. J. (1991), "Effect of Periodic Blowing on Attached and Separated Supersonic Turbulent Boundary Layers," *AIAA Journal*, Vol. 29, No. 10, pp. 1651-1658.
- Settles, G. S. (1975), "An Experimental Study of Compressible Turbulent Boundary Layer Separation at High Reynolds Numbers," Ph.D. Dissertation, Mechanical and Aerospace Engineering Department, Princeton University, Sep. 1975.
- Settles, G. S. and Dolling, D. S. (1990), "Swept Shock/Boundary-Layer Interactions—Tutorial and Update," AIAA Paper 90-0375, 28th Aerospace Sciences Meeting, Reno, NV, Jan. 1990.
- Settles, G. S. and Dodson, L. J. (1991), "Hypersonic Shock/Boundary Layer Interaction Database," NASA Contractor Report 177577, Apr. 1991.
- Settles, G. S. and Dolling, D. S. (1992), "Swept Shock Wave Boundary Layer Interaction," AIAA Progress Series Volume on Tactical Missile Aerodynamics, Vol. 141, pp. 505-574, 1992.
- Shifen, W. and Qingquan, L. (1990), "Nature of the Surface Heat Transfer Fluctuation in a Hypersonic Turbulent Separated Flow," *ACTA MECHANICA SINICA*, Vol. 6, No. 4, pp. 296-302, 1990.
- Shifen, W. and Qingquan, L. (1992), "Hypersonic Turbulent Separated Flow Past an Unswept Circular Cylinder on a Flat Plate," *ACTA AERODYNAMICA SINICA*, Vol. 10, No. 1, pp. 38-44, 1992.
- Smith, D. R. (1987), "The Effects of Incoming Boundary Layer Thickness on Unsteady Shock-Induced Turbulent Separations Induced by Cylinders," M.S. Thesis, Dept. of Aerospace Engineering and Engineering Mechanics, The Univ. of Texas at Austin, Dec. 1987.
- Speaker, W. V. and Ailman, C. M. (1969), "Spectra and Space-Time Correlations of the Fluctuating pressures at a Wall Beneath a Supersonic Turbulent Boundary Layer Perturbed by Steps and Shock Waves," NASA CR-486, June 1969.
- Tan, D. K. M., Tran, T. T., and Bogdonoff, S. M. (1987), "Wall Pressure Fluctuations in a Three-Dimensional Shock-Wave/Turbulent Boundary Interaction," *AIAA Journal*, Vol. 25, pp. 14-21, Jan. 1987.
- Tran, T. T., Tan, D. K. M., and Bogdonoff, S. M. (1985), "Surface Pressure Fluctuations in a Three-Dimensional Shock Wave/Turbulent Boundary Layer Interaction at Various Shock Strengths," AIAA Paper 86-1562, AIAA 18th Fluid Dynamics and Plasma Dynamics and Lasers Conference, Cincinnati, OH, July 1985.
- Tran, T. T. (1987), "An Experimental Investigation of Unsteadiness in Swept Shock Wave/Turbulent Boundary Layer Interactions," Ph.D. Thesis, Mechanical and Aerospace Engineering Dept., Princeton University, Mar. 1987.
- Viegas, J. R. and Horstman, C. C. (1979), "Comparison of Multi-Equation Turbulence Models for Several Shock Boundary Layer Interaction Flows," *AIAA Journal*, Vol. 17, No. 8, pp. 811-820, 1979.
- Viegas, J. R., Rubesin, M. W., and Horstman, C. C. (1985), "On the Use of Wall Functions as Boundary Conditions for Two-Dimensional Separated Compressible Flows," AIAA Paper 85-0180, AIAA 23rd Aerospace Sciences Meeting, Reno, NV, Jan. 1985.
- Visbal, M. R. (1991,1), "The Laminar Horseshoe Vortex System Formed at a Cylinder/Plate Junction," AIAA Paper 91-1826, AIAA 22nd Fluid Dynamics, Plasma Dynamics and Lasers Conference, Honolulu, HI, June 24-26, 1991.
- Visbal, M. R. (1991,2), "Structure of Laminar Junction Flows," *AIAA Journal*, Vol. 29, No. 8, pp. 1273-1282, Aug. 1991.
- Wilcox, D. D. (1990), "Supersonic Compression Corner Applications of a Multi-Scale Model for Turbulent Flows," *AIAA Journal*, Vol. 78, No. 7, pp. 1194-1198, Jul. 1990.
- Zorumski, W. E. (1987), "Fluctuating Pressure Loads Under High Speed Boundary Layers," NASA TM-100517, Oct. 1987.

## APPENDIX

### Physical Interpretation of Separation Lines from Surface Tracer Patterns

Surface tracer techniques are widely used to locate *separation lines*. They are relatively easy to use and produce highly defined, repeatable *separation lines*. In the case of the kerosene lamp-black method, the pattern is lifted off the surface on large sheets of transparent tape, and full-scale, undistorted records are obtained. Since wall pressure signals show clearly that the separation shock wave moves well upstream of "S," the question of the physical meaning of "S" arises.

This question has been addressed by Gramann and Dolling (1988). Two pressure transducers with fixed streamwise separation were placed at



different positions in the intermittent region upstream of a circular cylinder. The Mach number was 5. Blocks of data corresponding to flow *downstream of the instantaneous shock wave* were extracted and cross-correlated. Cross-correlations at all of the stations in the intermittent region were essentially *the same as those measured downstream of "S"* where the flow is always separated. Maxima in the cross-correlation coefficient at both positive and negative time delays occurred at the same time, no matter where the transducer pair was located in the intermittent region. The results show that separation occurs at, or just downstream of, the instantaneous shock position and undergoes the same large-scale, low-frequency motion as the separation shock wave. Similar results have been obtained in a Mach 5 compression ramp flow. Thus the separation line indicated by surface tracers is actually the downstream boundary of a region of intermittent separation.

A plausible physical explanation for the latter is summarized below. If the shock motion over a point is modeled as a step function, then the instantaneous wall shear stress at that point has two possible values. One is the value corresponding to flow upstream of the shock wave (i.e., incoming boundary layer) which is large and positive, and the other corresponds to backflow and is considerably smaller and negative. Hence, even if there is backflow for a large fraction of the time (i.e., at high intermittency), the mean shear stress will still be positive. The surface tracer material, which has almost zero frequency response, will therefore move downstream. On this basis, the station at which the mean wall shear stress becomes zero and the tracer material accumulates will have a very high value of intermittency.

In swept compression ramp flows, experiments at Mach 5 show that the separation line moves upstream in the intermittent region with increasing sweepback (Erengil & Dolling, 1992). For a corner-line sweepback of 50 deg., the separation line is approximately in the middle of the intermittent region. This result lends some support to the physical explanation advanced above. In swept interactions, the upstream component of the wall shear stress is appreciably larger than in the unswept case with its subsonic recirculating flow. Hence, the relative position in the intermittent region where the time-averaged wall shear stress becomes zero changes. As a result, the line of coalescence of surface streaklines shifts progressively upstream in the intermittent region with increasing sweep.



# CONTRIBUTION OF LASER DOPPLER VELOCIMETRY TO THE PHYSICAL DESCRIPTION OF SHOCK WAVE / TURBULENT BOUNDARY LAYER INTERACTIONS WITH INCIDENCE ON TURBULENCE MODELLING

J. M. Délery

Aerodynamics Department  
ONERA - B.P. 72 - 92320 CHATILLON

## SUMMARY

With the advent of Laser Doppler Velocimetry in the 70s it has become possible to investigate high speed complex flows containing shock waves, separated regions and strong turbulent fluctuations. This powerful tool has allowed an unprecedented physical description of the flow fields resulting from shock wave/boundary layer interaction, both in two- and three-dimensional flows. It is remarkable that the development of LDV has accompanied the progress in CFD, thus permitting an in depth validation of the theoretical models. The Lecture focusses on the use of LDV to investigate typical transonic and supersonic interactions occurring, firstly in nominally 2D configurations, then in a 3D channel flow. The data thus obtained are used to provide a detailed description of the flow field and to validate several equilibrium and non-equilibrium turbulence models. In 2D flows, the calculations were executed by using an economical boundary layer type approach, for the 3D case the models were implemented in a Navier-Stokes code.

## 1. INTRODUCTION

The advent of Laser Doppler Velocimetry (LDV) in the 70s has operated a true break-through in our capacity to investigate complex turbulent flows, as those generated by the interaction between a shock-wave and a turbulent boundary layer. With LDV, it has become possible to perform reliable and accurate measurements in high speed flows containing shock-waves, large separated regions and strong turbulent fluctuations. Not only the mean flow structure can now be described in detail, but also the complete Reynolds stress tensor can be determined, even in three-dimensional configurations.

It is remarkable that the spectacular advances in experimental techniques were accompanied by the considerable development of the predictive tools which permit a local description of complex interacting flows. The large increase in computer performance and the parallel progress in numerical methods now render possible the solution of the full time averaged Navier-Stokes equations. However, purely numerical problems, like those posed by the definition of an adequate mesh, being excluded, the theoretical efforts are still hampered by the difficulty of representing the turbulent terms in the time averaged equations. In the domain of turbulence modelling, progress is much slower and important work has still to be done to obtain fully satisfactory results.

A real validation of numerical models must rely not only on confrontations between measured and computed wall quantities (pressure, skin-friction, heat-transfer in hypersonic flows) but also on *field properties* interesting both the mean and the turbulent fields. Classical measurement techniques, based on multi-hole pressure probes or temperature probes, can provide very useful results and, for this reason, must not be despised (Gaillard, 1983). Hot wire anemometry can give instructive information on the turbulent field, especially on its frequencies or length scales (Smits and Muck, 1987). Also, the highly fluctuating character of strong interactions must be investigated by using short response time surface transducers and/or probes (Sajben et al., 1985; Muck et al., 1988; Erengil and Dolling, 1991). These means of investigation suffer from their intruding nature which renders their use in transonic flows problematic, since then any obstacle, even small, can significantly affect the whole flow field, producing large displacements of the shock system. Furthermore, the probing of a separated zone with material probes is suspect because of their disturbing action and of the inherent difficulty to determine the direction of the velocity with such devices.

Interferometry, and more particularly: *holographic interferometry*, constitutes a powerful tool to analyze complex and sensitive flow fields because of its non intrusive nature (Surget et al., 1977; Hsu and Settles, 1989). In addition of spectacular visualizations of the flow, interferometry allows direct measurements of the local density by an adequate processing of the interferograms. Thus, interferometry has been, and is still, used to investigate shock wave/boundary layer interactions. However, interferometry suffers from three major disadvantages: 1) - In practice, its quantitative use is restricted to two-dimensional and axisymmetric flows, extension to truly three-dimensional flows requiring complex experimental procedures and ultra complicated processing techniques. 2) - It lacks sensitivity in separated flows since then, the velocity being small, the density is nearly constant. 3) - Turbulence measurements with interferometry does not seem possible, except a rough characterization of turbulent structures.

Laser Doppler Velocimetry does not suffer from these limitations. Performing a local measurement, having a high sensitivity and the ability to determine the velocity direction, LDV allows the survey of two-dimensional as well as three-dimensional, separated flows. Furthermore, the



nearly instantaneous measurement process permits turbulence measurements from an appropriate statistical treatment of a sample of instantaneous values recorded at one point. Of course, LDV has also limitations: 1) - It gives information at one point at a time, so that the probing of a vast field may require long, and sometimes prohibitive, test durations. On the opposite, interferometry operates the record of a whole flow field at once. 2) - The technique postulates that the velocity of the seeding particles is equal to the flow velocity, which may be not true in highly retarded or accelerated flows. 3) - Three-component LDV systems able to make measurements in high speed flows are expensive and delicate to operate.

The purpose of the present Lecture is to show the contribution of LDV to the investigation of shock wave/turbulent boundary layer interactions. This technique has been used by several investigators to obtain a faithful and reliable description of interacting flows containing more or less extended separated regions (East, 1976; Seegmiller et al., 1978; Ardonneau et al., 1980; Ardonneau, 1981; to cite the earlier LDV studies). Here, we will restrict ourselves to the studies of typical interactions which were conducted at ONERA, over the past 10 years. Emphasis will be placed on the crucial role played by LDV measurements in the physical understanding of interacting flows and in the critical examination of turbulence models. Firstly, two-dimensional interactions will be considered, then three-dimensional interactions will be discussed. The theoretical aspects of the question will be focussed on transonic and supersonic two-dimensional interactions which can be treated by using a simplified boundary-layer type approach, if the aim is to discuss turbulence modelling. Only a limited number of results obtained with Navier-Stokes calculations will be presented here, since this approach constitutes the main subject of other Lectures.

## 2. EXPERIMENTAL AND THEORETICAL TOOLS

### 2.1 The LDV System

All the field measurements presented in what follows were executed with a laser velocimeter developed by ONERA's Physics Department in collaboration with the Laser Measurement Group of the Aerodynamics Department (Boutier et al., 1984). The general arrangement of the velocimeter is shown in Fig. 1.

In its most advanced three-component capability, the velocimeter is equipped with two identical Argon lasers that can emit a maximum power of 15W in the all lines mode of operation. The first laser, in single-line violet (wave length  $\lambda = 0.4765\mu\text{m}$ ), operates at a power of 3W. The second is used in all lines mode at a power of 6W and the beam it emits is split by a set of semitransparent - or dichroic - mirrors into two colours: green ( $\lambda = 0.5145\mu\text{m}$ ) and blue ( $\lambda = 0.4880\mu\text{m}$ ). The three pairs of beams obtained from passing through the violet, blue and green beam splitters (see Fig. 1) are focussed by an appropriate lens assembling to constitute the probe volume, the diameter of which depends of the focal length of the focussing optics. This diameter can be as small as  $100\mu\text{m}$ , in the two-component version of the velocimeter; it is close to  $200\mu\text{m}$  in the three-component arrangement.

The blue and green beams are emitted in a horizontal plane at an angle  $\alpha$  from the spanwise axis of the test section. Their interferences produce two fringe patterns -

one horizontal and the other vertical - contained in a plane perpendicular to the emission line. The violet radiation is also emitted in a horizontal plane, but at an angle  $\beta$  with the spanwise axis. It sets up a vertical fringe pattern normal to this direction. These three fringe systems have their own fringe spacing  $l_i$ , which depends of the wave length. The velocity vector is thus measured in a system of axes in which one axis (Z) is vertical and the two others ( $X_1$  and  $X_2$ ) lie in a horizontal plane at an angle  $(\alpha + \beta)$  from each other. Maximum accuracy in the measurement of the velocity components is obtained when  $(\alpha + \beta)$  is equal to  $90^\circ$ , a condition impossible to realize because of the constraints imposed by the test section, in particular the size of its windows. In the reality, values of  $(\alpha + \beta)$  comprised between  $40^\circ$  and  $60^\circ$  are adopted. Elementary formulae can then convert these velocity components into the wind tunnel (X,Y,Z) coordinates in which the results are expressed.

For the velocimeter to determine the orientation of the measured velocity components, the six beams traverse Bragg cells inducing a shift of the fringes. With this device, the components are measured in a moving frame whose velocity is adjusted in such a way that all the components have the same direction, or sign. Thus, if  $f_{m_i}$  designates the measured frequency for component  $i$ ,  $f_B$ , the frequency associated with the Bragg shift,  $l_i$  the fringe spacing, then the velocity component  $u_i$  in the "laboratory" coordinate system is given by:

$$u_i = l_i(f_{m_i} - f_B)$$

The collecting part of the velocimeter includes two Cassegrain telescopes with a diameter of 200mm to collect the maximum light scattered by the particles passing through the probe volume. The light from the first of these telescopes passes through interference filters that select the green and blue from the incoming radiation. The second telescope selects the violet in the same way. The separated radiations are applied to three photomultipliers whose signals are processed by DISA55L counters connected through a simultaneity digitizer to the acquisition system. The digitizer checks that the three velocity measurements actually correspond to the same particle that has just crossed the probe volume.

The ONERA velocimeter works either in forward or back-scattering mode. For all the tests presented here, the forward-scattering mode was chosen because of its much better signal-to-noise ratio, which appears as essential to execute accurate measurements in high speed flows. In this arrangement, the emitting and collecting parts are mounted on two separate benches, placed on each side of the test section, each moving with a displacement uncertainty of  $0.05\text{mm}$  in three orthogonal directions. The benches are computer-controlled so that their motion coordinates with the collecting optics to follow the probe volume as it moves along.

To achieve an acceptable acquisition rate, especially in the separated regions, the flows were seeded with particles made of incense smoke or paraffin droplets injected in the wind tunnel settling chamber.

At each measurement point, the components of the instantaneous velocity were acquired on a sample of  $N$  events corresponding to  $N$  particles passing through the probe volume (most often,  $N = 2000$ ). Then, the mean velocity



and the Reynolds tensor components are computed by the following formulae:

$$\bar{u}_i = \frac{1}{N} \sum_{n=1}^{n=N} u_i^n$$

$$\overline{u_i u_j} = \frac{1}{N} \sum_{n=1}^{n=N} (u_i^n - \bar{u}_i) (u_j^n - \bar{u}_j)$$

The laser velocimeter can also operate as a two-component system, this version being used to probe nominally two-dimensional flows. In this case, only the blue and green colours are used and the beams are directed along the spanwise axis of the test section.

## 2.2 The Numerical Approach

Solution of the full time averaged Navier-Stokes equations is the most satisfactory way to compute complex flow fields, including both shock waves and large separated regions. However, in spite of dramatic progress, this approach is still expensive in terms of computer cost. Furthermore, experience shows that implementation of a new turbulence model, even in an already existing code, is a considerable task, especially for transport equation models. In these conditions, and if the aim of the study is simply to validate - or invalidate - turbulence models, to devise improvements to these models, or to develop new models, it may prove advantageous to use less "cumbersome" numerical tools. For instance, solving the first-order boundary layer equations can be a very interesting substitute to the use of the Navier-Stokes equations.

Of course, the use of the sole boundary layer equations does not allow a complete prediction of the flow, since part of the solution has to be provided, except if a coupling method treating the interaction between the boundary layer and the outer inviscid flow is adopted (see, for example, Le Balleur, 1987). In the usual boundary layer approach, the pressure or the velocity distribution at the boundary layer edge is prescribed. As it is now well known, this way of solving the problem breaks down if separation occurs, because of the so-called Goldstein's singularity met at the point where the skin friction vanishes. This singularity can be overcome by adopting an inverse mode of calculation in which the prescribed quantity pertains to the boundary layer development itself: it can be the distribution of the displacement thickness or of the skin friction (for more information on inverse methods, see Détery and Marvin, 1986).

In the "strategy" adopted here to validate turbulence models in two-dimensional flows, the first-order boundary layer equations have been solved in the inverse mode by prescribing the displacement thickness distribution deduced from experiment. In this case, the pressure distribution  $p(x)$  is an output of the calculation, as also all the other boundary layer properties, which can be compared to experimental data. The boundary layer equations, together with the energy and the transport equations for the turbulent quantities, when models with history effects were tested, were solved by an implicit finite difference method which will not be presented here (see Benay and Dupont, 1985). It was verified that this approach gave results in close agreement with Navier-Stokes calculations in transonic applications (Escande, 1986; Benay et al., 1987), which constitutes a guarantee of the soundness of the adopted approach.

Of course, in addition to its intrinsic limitation, the use of the boundary layer equations present disadvantages: 1) - The assumption of zero transverse pressure gradient ( $\partial p / \partial y = 0$ ) is questionable in regions where the flow properties vary rapidly (the shock foot region, for example). 2) - The accuracy will degrade as the Mach number increases, since at high Mach number the pressure gradients tend to be intense. 3) - Calculation of separated three-dimensional flows rapidly becomes inextricate, except in special situations like the infinite-swept wing assumption (Détery and Formery, 1983). Then, solution of the Navier-Stokes equations appears as necessary.

Nevertheless, as it will be seen in the coming Sections, the boundary layer approach can be extremely useful to test a large number of turbulence models, thus permitting a first selection before incorporating the most promising into a Navier-Stokes code.

## 2.3 Tested Turbulence Models

### 2.3.1 General Remarks

In usual computations of complex turbulent flows, one considers the time averaged version of the Navier-Stokes equations which result from an averaging of the time dependent equations over a time  $T$  long with respect to the time scales of the turbulent motion, but short compared to macroscopic unsteady motions. Two different averaging procedures can be applied. In the classical Reynolds averaging, any fluctuating variable  $f$  is split into:

$$f = \bar{f} + f' \text{ with } \bar{f}' = 0$$

the mean value  $\bar{f}$  being defined by:

$$\bar{f} = \frac{1}{T} \int_0^T f dt$$

Applied to an incompressible flow, the Reynolds averaging method leads to equations for the mean properties  $\bar{f}$  which are nearly identical to the starting equations, except for the presence of correlation terms of the form  $\overline{u_i' u_j'}$ , the so-called Reynolds stresses. In compressible flows, the Reynolds averaging procedure introduces several additional turbulent terms involving the fluctuations of density  $\rho'$  and temperature  $T'$ , which are hard to model. In order to avoid this complication, Favre (1965) introduced mass-averaged quantities which are frequently employed in the computation of compressible turbulent flows. According to this concept, a fluctuating variable, the velocity component  $u_i$  for example, is split into:

$$u_i = \bar{u}_i + u_i''$$

where the fluctuating part  $u_i''$  is defined in such a way that:

$$\overline{\rho u_i''} = 0$$

Now the fluctuating part  $u_i''$  is such that:

$$\overline{u_i''} = -\frac{\overline{\rho' u_i''}}{\bar{\rho}} \neq 0$$



The use of the mass-averaged variables gives the averaged Navier-Stokes equations a more compact form. As a counterpart, the turbulent terms now present in the averaged equations cannot be identified with measured quantities, which leads to other complications. However, at low to moderate Mach numbers, the difference between the Reynolds and Favre variables is immaterial, since then it is legitimate to neglect the fluctuations of density. In this case, which corresponds to the flows investigated here, it is more convenient to consider the classical time-averaged form of the Navier-Stokes equations, compressibility effects being taken into account by considering a variable mean density  $\bar{\rho}$ .

In the following Sections, a distinction is made between the equilibrium models and those taking into account a turbulence history effect which are called non-equilibrium models. The majority of these models is based on the eddy viscosity concept of Boussinesq. In the most sophisticated theories, the turbulent stresses are transported quantities; this constitutes the second-order closure. This last class of models was not considered in the present studies. With the Boussinesq concept, the Reynolds shear stress is expressed as:

$$-\bar{\rho} \overline{u'v'} = \mu_t \frac{\partial \bar{u}}{\partial y}$$

in the framework of the classical boundary layer assumption,  $\mu_t$  designating the turbulent viscosity. The averaging procedure applied to the energy equation introduces

a correlation term of the form:  $\bar{\rho} \overline{T'u'}$  which is represented by defining a turbulent thermal conductivity  $\lambda_t$  such that:

$$\bar{\rho} \overline{T'u'} = \lambda_t \frac{\partial \bar{T}}{\partial y}$$

Frequently, one introduces a turbulent Prandtl number:  $Pr_t = \mu_t C_p / \lambda_t$  which is assumed constant and equal to 0.9 ( $C_p$  is the constant pressure specific heat). This hypothesis, which was done in the calculations presented hereafter, greatly simplifies the problem of the modelling of the turbulent heat transfer term.

Classical notations are used throughout the paper:  $x$  and  $y$  designate the boundary layer coordinate system ( $x$  being along the wall and  $y$  normal to it),  $\bar{u}$  and  $\bar{v}$  are the mean velocity components, along  $x$  and  $y$  respectively,  $\bar{\rho}$  is the mean density,  $\mu$  the molecular viscosity,  $\mu_t$  the turbulent (or eddy) viscosity,  $\delta$  the boundary layer thickness.

### 2.3.2 Equilibrium Models

In these models, the turbulent quantities (in this case the shear stress) are completely determined from the local velocity distribution, which implies that turbulence adjusts itself instantly to the mean field. This assumption, called the equilibrium hypothesis, assumes that the variation undergone by the flow is gradual enough for there to be time for this adjustment. However, this is not always the case, in particular when the boundary layer is subjected to a strong adverse pressure gradient, such as is a shock wave/boundary layer interaction. The history or relaxation effects may then be very important, as it will be seen in Section 3.1.3.

Equilibrium models are also said algebraic, the eddy viscosity being expressed from the mean flow properties by purely algebraic equations. The first model of this kind examined here is that of Michel et al. (1969). It has been considered mainly as a reference since it is a standard model; similar models, that of Cebeci-Smith for instance, give identical results for strong interactions, as we were able to ascertain. The eddy viscosity  $\mu_t$  is given by the equation:

$$(1) \quad \mu_t = \bar{\rho} l^2 D^2 \left| \frac{\partial \bar{u}}{\partial y} \right|$$

where  $l$  is the mixing length and  $D$  the Van Driest damping function. The expression of  $l$  depends to a great extent of the nature of the flow considered. In the case of a boundary layer, Michel et al. suggested the following formula:

$$l = 0.085 \delta \tanh \left( \frac{0.41 y}{0.085 \delta} \right)$$

which ensures a continuous variation of  $l$  from the logarithmic region, where  $l$  has the form  $l = 0.41y$ , to the outer region where  $l$  becomes proportional to  $\delta$ .

In the present model,  $D$  is given by:

$$(2) D = 1 - \exp \left( -\frac{l}{26 \times 0.41 \mu} \sqrt{\frac{\bar{\tau}}{\bar{\rho}}} \right)$$

where  $\bar{\tau} = (\mu + \mu_t) \frac{\partial \bar{u}}{\partial y}$  is the total shear stress on the ordinate  $y$ . The above expressions lead to an implicit equation for  $\mu_t$  of the form  $\mu_t = f(\mu_t)$  which is most often solved by a fixed point technique.

The second model studied, due to Alber (1971), is an adaptation of the Cebeci-Smith's model to separated flows. The boundary layer is divided into an inner region and an outer region where  $\mu_t$  is given by different expressions designated by  $\mu_{t,i}$  and  $\mu_{t,e}$ , respectively. When the flow is attached, the following formulae are used:

$$(3) \mu_{t,i} = \bar{\rho} (0.41yD)^2 \left( \frac{\partial \bar{u}}{\partial y} \right)$$

$$\mu_{t,e} = 0.0168 \bar{\rho} \bar{u}_e \delta_i^* \gamma$$

where:

-  $\gamma$  is the Klebanoff intermittency function given here by:

$$\gamma = \left[ 1 + 5.5 \left( \frac{y}{\delta} \right)^6 \right]^{-1}$$

-  $\delta_i^*$  is the "incompressible" displacement thickness defined by:

$$\delta_i^* = \int_0^\delta \left( 1 - \frac{\bar{u}}{\bar{u}_e} \right) dy$$

As Alber remarked an expression such as (3) is incorrect in a region of reversed flow where the velocity profile exhibits a local minimum leading to  $\frac{\partial \bar{u}}{\partial y} = 0$  near the wall. According to (3) - or (1) - the result is that the turbulent shear stress vanishes in this point, leading to a laminar state in a region where the flow is highly turbulent. To remedy this unrealistic behaviour, Alber recommends adopting the following expressions after the boundary layer has separated:



and the Reynolds tensor components are computed by the following formulae:

$$\bar{u}_i = \frac{1}{N} \sum_{n=1}^N u_i^n$$

$$\overline{u_i u_j} = \frac{1}{N} \sum_{n=1}^N (u_i^n - \bar{u}_i) (u_j^n - \bar{u}_j)$$

The laser velocimeter can also operate as a two-component system, this version being used to probe nominally two-dimensional flows. In this case, only the blue and green colours are used and the beams are directed along the spanwise axis of the test section.

## 2.2 The Numerical Approach

Solution of the full time averaged Navier-Stokes equations is the most satisfactory way to compute complex flow-fields, including both shock waves and large separated regions. However, in spite of dramatic progress, this approach is still expensive in terms of computer cost. Furthermore, experience shows that implementation of a new turbulence model, even in an already existing code, is a considerable task, especially for transport equation models. In these conditions, and if the aim of the study is simply to validate - or invalidate - turbulence models, to devise improvements to these models, or to develop new models, it may prove advantageous to use less "cumbersome" numerical tools. For instance, solving the first order boundary layer equations can be a very interesting substitute to the use of the Navier-Stokes equations.

Of course, the use of the sole boundary layer equations does not allow a complete prediction of the flow, since part of the solution has to be provided, except if a coupling method treating the interaction between the boundary layer and the outer inviscid flow is adopted (see, for example, Le Balleur, 1987). In the usual boundary layer approach, the pressure or the velocity distribution at the boundary layer edge is prescribed. As it is now well known, this way of solving the problem breaks down if separation occurs, because of the so-called Goldstein's singularity met at the point where the skin friction vanishes. This singularity can be overcome by adopting an inverse mode of calculation in which the prescribed quantity pertains to the boundary layer development itself: it can be the distribution of the displacement thickness or of the skin friction (for more information on inverse methods, see Détery and Marvin, 1986).

In the "strategy" adopted here to validate turbulence models in two-dimensional flows, the first-order boundary layer equations have been solved in the inverse mode by prescribing the displacement thickness distribution deduced from experiment. In this case, the pressure distribution  $p(x)$  is an output of the calculation, as also all the other boundary layer properties, which can be compared to experimental data. The boundary layer equations, together with the energy and the transport equations for the turbulent quantities, when models with history effects were tested, were solved by an implicit finite difference method which will not be presented here (see Benay and Dupont, 1985). It was verified that this approach gave results in close agreement with Navier-Stokes calculations in transonic applications (Escande, 1986; Benay et al., 1987), which constitutes a guarantee of the soundness of the adopted approach.

Of course, in addition to its intrinsic limitation, the use of the boundary layer equations present disadvantages: 1) - The assumption of zero transverse pressure gradient ( $\partial p / \partial y = 0$ ) is questionable in regions where the flow properties vary rapidly (the shock foot region, for example). 2) - The accuracy will degrade as the Mach number increases, since at high Mach number the pressure gradients tend to be intense. 3) - Calculation of separated three-dimensional flows rapidly becomes inextricate, except in special situations like the infinite-swept wing assumption (Détery and Formery, 1983). Then, solution of the Navier-Stokes equations appears as necessary.

Nevertheless, as it will be seen in the coming Sections, the boundary layer approach can be extremely useful to test a large number of turbulence models, thus permitting a first selection before incorporating the most promising into a Navier-Stokes code.

## 2.3 Tested Turbulence Models

### 2.3.1 General Remarks

In usual computations of complex turbulent flows, one considers the time averaged version of the Navier-Stokes equations which result from an averaging of the time dependent equations over a time  $T$  long with respect to the time scales of the turbulent motion, but short compared to macroscopic unsteady motions. Two different averaging procedures can be applied. In the classical Reynolds averaging, any fluctuating variable  $f$  is split into:

$$f = \bar{f} + f' \text{ with } \bar{f}' = 0$$

the mean value  $\bar{f}$  being defined by:

$$\bar{f} = \frac{1}{T} \int_0^{t+T} f dt$$

Applied to an incompressible flow, the Reynolds averaging method leads to equations for the mean properties  $\bar{f}$  which are nearly identical to the starting equations, except for the presence of correlation terms of the form  $\overline{u_i' u_j'}$ , the so-called Reynolds stresses. In compressible flows, the Reynolds averaging procedure introduces several additional turbulent terms involving the fluctuations of density  $\rho'$  and temperature  $T'$ , which are hard to model. In order to avoid this complication, Favre (1965) introduced mass-averaged quantities which are frequently employed in the computation of compressible turbulent flows. According to this concept, a fluctuating variable, the velocity component  $u_i$  for example, is split into:

$$u_i = \tilde{u}_i + u_i''$$

where the fluctuating part  $u_i''$  is defined in such a way that:

$$\overline{\rho u_i''} = 0$$

Now the fluctuating part  $u_i''$  is such that:

$$\overline{u_i''} = - \frac{\overline{\rho' u_i''}}{\bar{\rho}} \neq 0$$



The use of the mass-averaged variables gives the averaged Navier-Stokes equations a more compact form. As a counterpart, the turbulent terms now present in the averaged equations cannot be identified with measured quantities, which leads to other complications. However, at low to moderate Mach numbers, the difference between the Reynolds and Favre variables is immaterial, since then it is legitimate to neglect the fluctuations of density. In this case, which corresponds to the flows investigated here, it is more convenient to consider the classical time-averaged form of the Navier-Stokes equations, compressibility effects being taken into account by considering a variable mean density  $\bar{\rho}$ .

In the following Sections, a distinction is made between the equilibrium models and those taking into account a turbulence history effect which are called non-equilibrium models. The majority of these models is based on the eddy viscosity concept of Boussinesq. In the most sophisticated theories, the turbulent stresses are transported quantities; this constitutes the second-order closure. This last class of models was not considered in the present studies. With the Boussinesq concept, the Reynolds shear stress is expressed as:

$$-\bar{\rho} \overline{u'v'} = \mu_t \frac{\partial \bar{u}}{\partial y}$$

in the framework of the classical boundary layer assumption,  $\mu_t$  designating the turbulent viscosity. The averaging procedure applied to the energy equation introduces

a correlation term of the form:  $\bar{\rho} \overline{T'u'}$  which is represented by defining a turbulent thermal conductivity  $\lambda_t$  such that:

$$\bar{\rho} \overline{T'u'} = \lambda_t \frac{\partial \bar{T}}{\partial y}$$

Frequently, one introduces a turbulent Prandtl number:  $Pr_t = \mu_t C_p / \lambda_t$  which is assumed constant and equal to 0.9 ( $C_p$  is the constant pressure specific heat). This hypothesis, which was done in the calculations presented hereafter, greatly simplifies the problem of the modelling of the turbulent heat transfer term.

Classical notations are used throughout the paper:  $x$  and  $y$  designate the boundary layer coordinate system ( $x$  being along the wall and  $y$  normal to it),  $\bar{u}$  and  $\bar{v}$  are the mean velocity components, along  $x$  and  $y$  respectively,  $\bar{\rho}$  is the mean density,  $\mu$  the molecular viscosity,  $\mu_t$  the turbulent (or eddy) viscosity,  $\delta$  the boundary layer thickness.

### 2.3.2 Equilibrium Models

In these models, the turbulent quantities (in this case the shear stress) are completely determined from the local velocity distribution, which implies that turbulence adjusts itself instantly to the mean field. This assumption, called the *equilibrium hypothesis*, assumes that the variation undergone by the flow is gradual enough for there to be time for this adjustment. However, this is not always the case, in particular when the boundary layer is subjected to a strong adverse pressure gradient, such as is a shock wave/boundary layer interaction. The history or relaxation effects may then be very important, as it will be seen in Section 3.1.3.

Equilibrium models are also said *algebraic*, the eddy viscosity being expressed from the mean flow properties by purely algebraic equations. The first model of this kind examined here is that of Michel et al. (1969). It has been considered mainly as a reference since it is a standard model; similar models, that of Cebeci-Smith for instance, give identical results for strong interactions, as we were able to ascertain. The eddy viscosity  $\mu_t$  is given by the equation:

$$(1) \quad \mu_t = \bar{\rho} l^2 D^2 \left| \frac{\partial \bar{u}}{\partial y} \right|$$

where  $l$  is the mixing length and  $D$  the Van Driest damping function. The expression of  $l$  depends to a great extent of the nature of the flow considered. In the case of a boundary layer, Michel et al. suggested the following formula:

$$l = 0.985 \delta \tanh \left( \frac{0.41 y}{0.085 \delta} \right)$$

which ensures a continuous variation of  $l$  from the logarithmic region, where  $l$  has the form  $l = 0.41y$ , to the outer region where  $l$  becomes proportional to  $\delta$ .

In the present model,  $D$  is given by:

$$(2) D = 1 - \exp \left( - \frac{l}{26 \times 0.41 \mu} \sqrt{\frac{\bar{\tau}}{\bar{\rho}}} \right)$$

where  $\bar{\tau} = (\mu + \mu_t) \frac{\partial \bar{u}}{\partial y}$  is the total shear stress on the ordinate  $y$ . The above expressions lead to an implicit equation for  $\mu_t$  of the form  $\mu_t = f(\mu_t)$  which is most often solved by a fixed point technique.

The second model studied, due to Alber (1971), is an adaptation of the Cebeci-Smith model to separated flows. The boundary layer is divided into an inner region and an outer region where  $\mu_t$  is given by different expressions designated by  $\mu_{t,i}$  and  $\mu_{t,e}$ , respectively. When the flow is attached, the following formulae are used:

$$(3) \mu_{t,i} = \bar{\rho} (0.41 y D)^2 \left( \frac{\partial \bar{u}}{\partial y} \right) \\ \mu_{t,e} = 0.0168 \bar{\rho} \bar{u}_e \delta^* \gamma$$

where:

-  $\gamma$  is the Klebanoff intermittency function given here by:

$$\gamma = \left[ 1 + 5.5 \left( \frac{y}{\delta} \right)^6 \right]^{-1}$$

-  $\delta_i^*$  is the "incompressible" displacement thickness defined by:

$$\delta_i^* = \int_0^\delta \left( 1 - \frac{\bar{u}}{\bar{u}_e} \right) dy$$

As Alber remarked an expression such as (3) is incorrect in a region of reversed flow where the velocity profile exhibits a local minimum leading to  $\frac{\partial \bar{u}}{\partial y} = 0$  near the wall. According to (3) - or (1) - the result is that the turbulent shear stress vanishes in this point, leading to a laminar state in a region where the flow is highly turbulent. To remedy this unrealistic behaviour, Alber recommends adopting the following expressions after the boundary layer has separated:



$$\mu_{t1} = 0.018 \bar{\rho} y D^2 \bar{u}_e$$

$$\mu_{t2} = 0.0168 \bar{\rho} \bar{u}_e \delta_i^* \gamma$$

In the equation giving  $\mu_{t1}$ ,  $\delta_i^*$  represents the displacement thickness above the discriminating streamline of the separation bubble, i. e. the streamline separating the recirculating flow from the flow streaming from upstream to downstream infinity. This avoids an abnormally high increase in turbulent quantities for a large separation where the boundary layer thickens considerably.

In addition, Alber introduced a modified form of the Van Driest damping function avoiding the cancellation of  $D$  at a point of zero skin friction. In the present applications of Alber's model, relation (2) has been adopted, since it presents similar advantages.

The models considered above use as length scale the thickness  $\delta$  of the boundary layer (or a displacement thickness whose computation requires the knowledge of  $\delta$ ) which is ill defined in interacting flows. Such a problem arises, for instance, at the foot of the shock where the velocity gradients along  $y$  remain large in the non-dissipative part of the field.

Baldwin and Lomax's model (1978), widely used in the Navier-Stokes codes, proposes to avoid this type of problem by defining the length scale without referring to a thickness related to  $\delta$ . It is also a two-layer model in which the inner and outer turbulent viscosities are computed by:

$$\mu_{t1} = \bar{\rho} (0.41 y D)^2 \left( \frac{\partial \bar{u}}{\partial y} \right)$$

$$\mu_{t2} = 0.0269 \bar{\rho} F_w \bar{\gamma}$$

In these expressions,  $F_w$  is a function of  $x$  alone given by whichever of the two equations below has the smallest value at the abscissa  $x$  considered:

$$F_w = y_M F_M, F_w = 0.25 y_M \frac{\bar{u}^2}{F_M}$$

The quantity  $F_M$  is the maximum of function  $F = y D \left( \partial \bar{u} / \partial y \right)$  and  $y_M$  is the ordinate at which this maximum is reached.

In this model, the vorticity distribution is used to define a length scale such that it is no longer necessary to locate the edge of the boundary layer. However, it may occur that function  $F$  has several maxima, which leads to other difficulties (see, for example, Visbal and Knight, 1984).

### 2.3.3 Non Equilibrium Models

The non equilibrium model of Johnson and King (1985) is an algebraic model with history effects offering the advantage of being mathematically simple. In this case, the kinematic eddy viscosity  $\nu_t = \mu_t / \bar{\rho}$  is given for the complete thickness of the boundary layer by the equation:

$$\nu_t = \nu_{t0} \left[ 1 - \exp \left( - \frac{\nu_{t1}}{\nu_{t0}} \right) \right]$$

where:

$$\nu_{t1} = 0.41 y D^2 \left[ - \left( \overline{u'v'} \right)_M \right]^{1/2}$$

and:

$$\nu_{t0} = \alpha y$$

The maximum shear stress at the abscissa  $x$  considered,

$\tau_{tM} = - \left( \overline{u'v'} \right)_M$ , satisfies an ordinary differential equation of the form:

$$\frac{L_M \bar{u}_M}{a_1 \tau_{tM}} \frac{d\tau_{tM}}{dx} + \sqrt{\tau_{tM}} + \frac{L_M D}{\tau_{tM}} = L_M \frac{\partial \bar{u}}{\partial y} \Big|_M$$

which is deduced from the transport equation for the turbulence kinetic energy  $k$  given below. The dissipation length  $L_M = \tau_{tM} / \epsilon_M$  and the turbulence diffusion rate  $D_M$  are computed by algebraic relations not given here.

A step towards greater sophistication consists of expressing  $\mu_t$  as a function of transported local turbulence quantities. The following expression, in which  $\mu_t$  is expressed in terms of the turbulence kinetic energy  $k$  and its dissipation rate  $\epsilon$ , is probably the most popular:

$$(4) \mu_t = \bar{\rho} C_\mu f_\mu \frac{k^2}{\epsilon}$$

Frequently used transport equations for  $k$  and  $\epsilon$  are those of Jones and Launder (1972) which are written (for a boundary layer flow):

$$(5) \bar{\rho} \bar{u} \frac{\partial k}{\partial x} + \bar{\rho} \bar{v} \frac{\partial k}{\partial y} = \bar{\rho} (P_k - \epsilon) - \boxed{2\mu \left( \frac{\partial \sqrt{k}}{\partial y} \right)^2} + \frac{\partial}{\partial y} \left[ \left( \mu + \frac{\mu_t}{\sigma_k} \right) \frac{\partial k}{\partial y} \right]$$

$$(6) \bar{\rho} \bar{u} \frac{\partial \epsilon}{\partial x} + \bar{\rho} \bar{v} \frac{\partial \epsilon}{\partial y} = -C_{\epsilon 1} \frac{\epsilon}{k} P_k - C_{\epsilon 2} \bar{\rho} \frac{\epsilon^2}{k} +$$

$$\boxed{\frac{2\mu\mu_t}{\bar{\rho}} \left( \frac{\partial^2 \bar{u}}{\partial y^2} \right)^2} + \frac{\partial}{\partial y} \left[ \left( \mu + \frac{\mu_t}{\sigma_\epsilon} \right) \frac{\partial \epsilon}{\partial y} \right]$$

where  $P_k$  designates the production term which, in the framework of the boundary layer approximation, reduces to:

$$P_k = - \overline{u'v'} \frac{\partial \bar{u}}{\partial y}$$

Taking the normal stresses into account (see Section 3.1.3),<sup>1</sup> leads to using the following form, which assumes that the mean flow is nearly incompressible:

$$P_k = - \overline{u'v'} \frac{\partial \bar{u}}{\partial y} - \left( \overline{u'^2} - \overline{v'^2} \right) \frac{\partial \bar{u}}{\partial x}$$

The surrounded terms are the so-called low Reynolds number terms introduced to have a correct behaviour of turbulent quantities on approaching the wall. In the same spirit,  $f_\mu$  is a damping function (not given here).

In the present applications, the constants had the following values:

$$\sigma_k = 1, \sigma_\epsilon = 1.3, C_{\epsilon 1} = 1.57, C_{\epsilon 2} = 2$$



Equations (5) and (6) are in principle valid down to the wall. However, it was demonstrated that the low Reynolds number terms gave poor results in the case of a separated flow. To improve the model a rather large number of adaptations have been proposed. Here we will consider a version in which a two layer representation is adopted:

- Near the surface, up to an ordinate  $y_R$ , the viscosity  $\mu_t$  is computed by the mixing length equation (1).

- In the outer region, where  $y > y_R$ , the transport equations (5) and (6), without the low Reynolds number terms, are solved and  $\mu_t$  is determined by (4) in which  $f_\mu \equiv 1$ .

The matching between the two layers is made at the ordinate at which the turbulence Reynolds number  $R_T = \bar{\rho} k^2 / \epsilon \sim \mu_t / \mu$  has become sufficiently large (the value  $R_T = 200$  was adopted).

The last non-equilibrium model considered here is the Algebraic Stress Model (ASM) proposed by Launder (1971) and Rodi (1972). It constitutes an intermediate step before a complete transport model - or Reynolds Stress Equation (RSE) model - in which the Reynolds stress tensor is transported.

The ASM is obtained from the RSE by assuming that the ratio  $\frac{\overline{u'v'}}{k}$  varies slowly. We can then write:

$$(7) \frac{D}{Dt} \left( \overline{u'u_j} \right) - \text{Diff} \left( \overline{u'u_j} \right) = \frac{\overline{u'u_j}}{k} \left( \frac{Dk}{Dt} - \text{Diff}(k) \right)$$

where  $D/Dt$  is the total derivative, Diff representing the diffusion term.

After proper modelling of the different terms of the Reynolds stress transport equation, the left hand side of (7) does not any longer contain stress derivatives (for details see Coët and Benay, 1986). In addition, we have:

$$\frac{Dk}{Dt} - \text{Diff}(k) = P_k - \epsilon$$

so that, one obtains an algebraic non linear system for the stresses  $\overline{u'u_j}$  which can be computed from  $k$ ,  $\epsilon$  and the space derivatives of the mean field. For a two dimensional flow this system is written:

$$\frac{1}{k} \overline{u'^2} \left( \overline{v'^2} - \overline{u'^2} \right) \frac{\partial \bar{u}}{\partial x} + \alpha_1 \overline{u'^2} + \alpha_2 \overline{v'^2} + \alpha_3 \overline{u'v'} -$$

$$\frac{\overline{u'^2} \overline{u'v'}}{k} \frac{\partial \bar{u}}{\partial y} - \frac{2}{3} \epsilon (C_1 - 1) = 0$$

$$\frac{1}{k} \overline{v'^2} \left( \overline{v'^2} - \overline{u'^2} \right) \frac{\partial \bar{u}}{\partial x} + \beta_1 \overline{u'^2} + \beta_2 \overline{v'^2} + \beta_3 \overline{u'v'} -$$

$$\frac{\overline{v'^2} \overline{u'v'}}{k} \frac{\partial \bar{u}}{\partial y} - \frac{2}{3} \epsilon (C_1 - 1) = 0$$

$$\frac{1}{k} \overline{u'v'} \left( \overline{v'^2} - \overline{u'^2} \right) \frac{\partial \bar{u}}{\partial x} + \gamma_1 \overline{u'^2} + \gamma_2 \overline{v'^2} + \gamma_3 \overline{u'v'} -$$

$$\frac{1}{k} \left( \overline{u'v'} \right)^2 \frac{\partial \bar{u}}{\partial y} = 0$$

The coefficients  $\alpha_i$ ,  $\beta_i$  and  $\gamma_i$  will not be explicit here, their expression can be found elsewhere (Bur, 1991)

Quantities  $k$  and  $\epsilon$  are computed from transport equations (5) and (6) with the wall region treated as in the previous model.

It can be shown that the Reynolds shear stress is given by:

$$-\bar{\rho} \overline{u'v'} = -\bar{\rho} \frac{k}{\epsilon} \frac{1 - C_2 \left( 1 - \frac{3}{2} f C_2' \right)}{\frac{P_k}{\epsilon} + C_1 - 1 + \frac{3}{2} f C_1'} \overline{v'^2} \frac{\partial \bar{u}}{\partial y} \equiv$$

$$\bar{\rho} C_\mu' \overline{v'^2} \frac{k}{\epsilon} \frac{\partial \bar{u}}{\partial y}$$

Since  $\overline{v'^2}$  is smaller than  $k$ , one sees that the length scale

$l = \overline{v'^2} \sqrt{k} / \epsilon$  attached to this model is shorter than that of the  $[k, \epsilon]$  model which is:  $l = k^{3/2} / \epsilon$ . Furthermore, an essential advantage of the ASM is that coefficient  $C_\mu'$  is a function of the ratio  $P_k / \epsilon$ , which is more realistic when the boundary layer is strongly out of equilibrium.

The constants of the model have the values:

$$C_1 = 1.8, C_2 = 0.6, C_1' = 0.5, C_2' = 0.3$$

the wall influence function  $f$  having the form:

$$f = 0.287 \frac{k^{3/2}}{\epsilon y}$$

### 3. TWO-DIMENSIONAL FLOWS

#### 3.1 Transonic Interactions

##### 3.1.1 General Flow Conditions

One of the first experimental investigations of transonic interaction making a thorough use of LDV to perform a detailed analysis of the flowfield was executed in the test set up represented in Fig. 2 (Délery, 1983). It is constituted by a nominally two-dimensional channel with a span  $b$  equal to 120mm and an entrance height of 100mm. Interchangeable nozzle blocks, or bumps, can be mounted in the working section with a view to accelerating the flow up to slightly supersonic velocities. A second throat, of adjustable cross section, is placed at the test section outlet making it possible, firstly to produce, by choking effect, a shock wave whose position, and hence intensity, can be adjusted in a continuous and precise manner, secondly to isolate the flowfield under study from pressure perturbations emanating from downstream ducts. Such a device notably reduces unwanted large shock oscillations. In these experiments, the two component version of the LDV system was used to probe the boundary layer along vertical lines, normal to the downstream rectilinear wall.

The channel was installed in the test section of the ON-ERA S8Ch continuous wind tunnel which is supplied with dessicated atmospheric air, with the stagnation conditions as follows: pressure  $p_{st} = 95kPa$ , temperature:

$T_{st} = 300K$ . The Reynolds number, computed with the sonic state and with a length  $L = 100mm$ , equal to the channel height in the entrance section, had the value:  $Re_L = 13.710^6$ .

The shock wave/boundary layer interactions under study took place on the lower wall of the channel at a station where the undisturbed turbulent boundary layer was fully turbulent with a thickness  $\delta_0$  of several millimeters (from 3 to 5mm, depending on the channel arrangement). The "aspect ratio"  $b/\delta_0$  is equal to 30. This value seems high enough to minimize three-dimensional effects in the case



of flows without large separation, where the thickening of the boundary layer during the interaction process is moderate. When an extended separated region forms, the local ratio  $b/\delta$  decreases more significantly, and surface flow visualizations show a rather strong distortion of the reattachment line. However, the presence of three-dimensional effects is not thought to alter radically the general features of the flow and the behaviour of turbulence. Thus, the information obtained can be used as a guide to improve the modelling of two-dimensional flows.

Four basic interactions, of variable strength, were investigated. Here we will consider only two of them, corresponding to incipient separation at the shock foot and to the formation of an extended separated zone. The "wall" Mach number distributions are plotted in Fig. 3 with indication of the locations of the vertical LDV explorations (the "wall" Mach number  $M_w$  is deduced from the pressure measured at the wall by assuming an isentropic relation and the reduced abscissa  $\tilde{X}$  is the distance from the interaction origin  $X_0$  scaled to the displacement thickness  $\delta_0^*$  of the boundary layer at  $X_0$ ).

**Flow A : Incipient Shock Induced Separation.** For this case, the test section was equipped with a symmetrical converging-diverging supersonic nozzle whose contour was designed to produce a uniform flow having a nominal Mach number equal to 1.4. The nearly normal shock wave is situated near the end of the diverging part of the nozzle at a station where the Mach number  $M_{e0}$  at the boundary layer edge is equal to 1.30. The values of  $M_{e0}$  and of the incompressible shape parameter of the boundary layer  $H_{i0}$ , in the present case, correspond to a situation which nearly coincides with incipient shock induced separation (Délery and Marvin, 1986).

**Flow C : Extended Separation.** Here, the transonic flow is produced in an asymmetrical channel where a bump is mounted on the lower wall of the wind tunnel test section. This bump has a maximum height of 12mm and a length of 286.4mm. Its contour is made up of a rectilinear upstream part with a slope of  $4^\circ$  connected to a circular arc extending down to the trailing edge of the bump. The interaction takes place at a location where the maximum Mach number in the flow is equal to 1.42. The shock is strong enough to induce boundary layer separation upstream of the bump trailing edge at a location where the Mach number at the boundary layer edge is  $M_{e0} = 1.37$ . An extended separation bubble forms due to the wall curvature effect as is evidenced by the plateau in the wall pressure distribution.

### 3.1.2 Mean Flow Properties

Some of the mean streamwise velocity profiles measured across the dissipative layers are shown in Figs. 4a and 4b. The distance to the wall  $Y$  is scaled to the displacement thickness  $\delta_0^*$  and the component  $\bar{u}$  to the value of  $\bar{u}$  at the boundary layer edge. The corresponding mean flow streamlines are represented in Figs. 5a and 5b. For flow A (incipient separation), one observes at first a strong distortion of the profiles; yet, no negative values of  $\bar{u}$  are measured. If separation actually occurs, it concerns a very small fraction of the flow too close to the wall to be detected by the present measurements. After a maximum retardation effect taking place at  $\tilde{X} = 56$ , turbulent viscous forces entail a gradual acceleration of

the fluid in the inner part of the boundary layer whose thickness increases continuously and moderately during the interaction process.

In flow C (extended separation), a large separated bubble exists with a maximum velocity  $\bar{u}/\bar{u}_e$  equal to  $-0.2$ . In the present situation, the vertical extent of the bubble is specially important, as shown by the tracing of the streamlines in Fig. 5b. Reattachment takes place at  $\tilde{X} = 135$ ; downstream of this station a rapid rehabilitation of the flow occurs with the filling of the profiles and the tendency of the dissipative layer towards a new equilibrium state. In this case, one observes a dramatic increase of the boundary layer thickness which is nearly multiplied by ten between  $X_0$  and the last downstream station.

### 3.1.3 Turbulence Properties

The profiles of the turbulence kinetic energy  $k$  are plotted in Figs. 6a and 6b ( $k$  is scaled to the square of the sound velocity for stagnation conditions  $a_{st}$ ). The kinetic energy  $k$  has been evaluated by the formula:

$$k = \frac{1}{2} \left( \overline{u'^2} + \overline{v'^2} + \overline{w'^2} \right)$$

where  $\overline{w'^2}$  was taken equal to  $\frac{1}{2} \left( \overline{u'^2} + \overline{v'^2} \right)$ , since the transverse velocity component  $w$  was not measured. For the two flows there is a very large increase of  $k$  in the first part of the interaction process, near the shock foot.

The profiles of the non dimensional Reynolds shear stress  $-\overline{u'v'}/a_{st}^2$  are plotted in Figs. 7a and 7b. Like the  $k$ -profiles, these distributions are characterized by a well defined maximum, which is well detached from the wall.

A more instructive idea of the variations of the turbulent properties during the interaction process is given by plotting the streamwise evolution of some typical quantities. Thus, Fig. 8 shows the X-wise variation of the maximum turbulence kinetic energy and Reynolds shear stress. The locations of the separation (S) and reattachment (R) points are indicated on the curves. There is a very large production of turbulence in the initial part of the interaction, near the shock foot. This production is enhanced when separation occurs; then  $k$  tends to a maximum level  $k_{max}$  which is between eight and nine times the initial level of the undisturbed boundary layer. For flow C,  $k_{max}$  starts to decrease upstream of the reattachment point R. Downstream of R, the turbulence kinetic energy diminishes rather slowly and tends gradually to a new equilibrium state. The shear stress grows at a slower pace than  $k$ , and reaches its maximum value downstream of the station where  $k$  culminates. For the separated flow, the location of maximum shear stress nearly coincides with the reattachment point; there the shear stress has reached a level which is ten times the maximum initial value.

Streamwise variations of the maximum RMS quantities  $\sqrt{\overline{u'^2}}/a_{st}$  and  $\sqrt{\overline{v'^2}}/a_{st}$  are plotted in Fig. 9. In the upstream part of the interaction, the streamwise fluctuations are seen to exceed the vertical fluctuations by a factor of 3, in contrast to a mixing layer where  $\sqrt{\overline{u'^2}}$  is



only 30% higher than  $\sqrt{v'^2}$ . The large increase in the normal stress  $\overline{u'^2}$  is to be expected if one considers the production term of the  $\overline{u'^2}$  transport equation (written here for an incompressible flow, compressibility effects being weak in transonic):

$$P_u = -2\overline{u'v'} \frac{\partial \overline{u}}{\partial Y} - \overline{u'^2} \frac{\partial \overline{u}}{\partial X}$$

In the first part of the interaction process, the term involving the streamwise derivative  $\partial \overline{u} / \partial X$  is as large as the term involving the strain rate  $\partial \overline{u} / \partial Y$  due to the strong retardation of the whole flow. Thus,  $P_u$  is here the sum of two large positive terms. On the other hand, the production mechanism for  $\overline{v'^2}$  involves terms whose magnitude is far less important since:

$$P_v = -2\overline{u'v'} \frac{\partial \overline{v}}{\partial X} - 2\overline{v'^2} \frac{\partial \overline{v}}{\partial Y}$$

The derivative  $\partial \overline{v} / \partial X$  is small,  $\partial \overline{v} / \partial Y$  is (nearly) equal to  $-\partial \overline{u} / \partial X$ , so that the second term tends to decrease  $\overline{v'^2}$  production in the first region of the interaction where  $\partial \overline{u} / \partial X$  is everywhere negative. Farther downstream, a larger and larger part of the dissipative layer is accelerated, which explains the latter growth of  $\overline{v'^2}$ . Further downstream,  $\overline{v'^2}$  is still increasing when  $\overline{u'^2}$  has started to diminish, so that  $\overline{v'^2}$  reaches its highest level well downstream of the maximum  $\overline{u'^2}$  location. Proceeding still further downstream,  $\overline{u'^2}$  and  $\overline{v'^2}$  become quite comparable.

Such a strong anisotropy of the flow can play a significant role in the mechanism of turbulence kinetic energy production. For an incompressible flow, and if the term involving the derivative  $\partial \overline{v} / \partial X$  is neglected, the production term of the  $k$  transport equation is:

$$P_k = -\overline{u'v'} \frac{\partial \overline{u}}{\partial Y} - \left( \overline{u'^2} - \overline{v'^2} \right) \frac{\partial \overline{u}}{\partial X}$$

The first term, representing production by shear stress, is most often predominant in shear layer and/or boundary layer flows so that it is only retained in predictive methods. An evaluation of the two production terms shows that production due to normal stresses is as high as production due to the shear stress over a streamwise distance which is of the order of 50% and which grossly corresponds to the region of steepest axial pressure gradient,

where there is a general retardation of the flow ( $\partial \overline{u} / \partial X$  negative). Downstream, the normal stresses contribution becomes rapidly negligible again.

The above turbulence measurements also show the necessity, in the shock foot region, to take into account the Reynolds normal stresses in the momentum equation. For an incompressible flow, the terms involving the Reynolds stresses are of the form:

$$-\frac{\partial}{\partial Y} \left( \overline{u'v'} \right) - \frac{\partial}{\partial X} \left( \overline{u'^2} - \overline{v'^2} \right)$$

In the very first part of the interaction, the X-derivatives of the normal stresses can be higher than the shear stress Y-derivatives. Far downstream, the normal stresses influence becomes negligible. Similar observations were made near the separation of an incompressible turbulent boundary layer (Simpson et al., 1977).

The whole history of the interacting dissipative layer can be depicted by plotting the square root of the maximum shear stress coefficient

$$C_r = \frac{2 \left( -\overline{\rho u'v'} \right)_{\max}}{\overline{\rho} \epsilon \overline{u}^2}$$

against the equilibrium shape parameter  $J = 1 - 1/H_i$ . A function  $G$  based on the maximum shear stress can be defined which will be constant for all equilibrium incompressible boundary layer flows and equal to the flat plate value (East and Sawyer, 1980). Thus  $G$ :

$$G \equiv \frac{H_i - 1}{H_i \sqrt{C_r/1}} = 6.55$$

specifies the straight line in Fig. 10. The unique relation between  $G$  and  $C_r$  expresses the fact that the shear stress depends only of the shape of the velocity distribution, which is the basic assumption of equilibrium models (see Section 2.3.1). If one plots  $\sqrt{C_r}$  against  $J$  for the present flows (a third interaction, not examined here, has been added in the figure), the experimental points fall below the equilibrium locus in the first part of the interaction, indicating that, during this rapid interaction process, there is a departure from equilibrium characterized by a lag of the shear stress. Then, as a consequence of the continuous increase of  $C_r$ , whereas  $J$  passes through a maximum and then decreases, the corresponding curve bend and cross the equilibrium locus at a point whose

location is a function of the intensity of the destabilizing agency. Thereafter, the points are above the equilibrium locus and reach a new situation of maximum departure from equilibrium. Downstream of this station, and in the absence of a new perturbation (no pressure gradient), the flows relax towards a new equilibrium state. In the course of this last process, the representative points follow a common trajectory leading to the equilibrium locus.

### 3.1.4 Validation of Turbulence Models

**Flow A : Incipient Separation.** The pressure distributions on the wall given by the algebraic equilibrium models (Michel et al., Alber, Baldwin-Lomax) are plotted in Fig. 11. For this moderately strong interaction, where no separated bubble of appreciable size forms, the three models lead to almost the same results for  $p(x)$  which are in poor agreement with experiment. Thus the steepness of the compression occurring in the initial part of the interaction is highly overestimated.

Let us now consider the models with history effects (Johnson-King, [k,ε] and ASM). The wall pressure distributions in Fig. 12 show a substantially improved prediction, in particular for the ASM which nearly coincides with the experimental results. The agreement is not as good for Johnson-King's model and the [k,ε] model whose



results are nearly the same here.

Figure 13 shows the reduced mean velocity distributions  $\bar{u} / \bar{u}_0$  ( $\bar{u}_0$  is the mean velocity corresponding to the Mach number  $M_{e0}$ ) for several stations spaced between  $\bar{X} = 15$  and  $\bar{X} = 202.5$ . The three equilibrium models lead to almost identical results and the profiles computed are - as regards their shape - in good agreement with the experimental results. However, the velocity level at the edge of the boundary layer is underestimated, which is the reason for the excessive recompression mentioned above. The defective form of the external part of the first computed profile (at  $\bar{X} = 15$ ), which belongs to a region located at the foot of the shock, should also be noted. In this case, the difference can be explained by the normal pressure gradient effect not taken into account in the equations used. The same deficiency is observed in all the other computations presented.

The velocity profiles obtained with the models including a history effect are shown in Fig. 14, where the following trends can be seen for the three models:

- In the initial part of the interaction, the computation predicts too strong a deceleration near the wall.
- Further downstream, in the so-called rehabilitation region, the computed profiles imperfectly reproduce the rapid filling of the experimental distributions in the immediate vicinity of the wall.
- Also, downstream, the real boundary layer thickens more than is predicted by computation.

Figure 15 shows the normalized Reynolds stress profiles  $-\bar{u}'v' / \bar{u}_0^2$  for the equilibrium models. As a general rule,

these models highly overestimate the growth of  $-\bar{u}'v'$  up to the abscissa  $\bar{X} = 40$ . The trends are then reversed, as the experimental results catch up with and overtake the theoretical results. Thus, the slow relaxation of turbulence downstream of the interaction region is poorly predicted, as the classical algebraic models predict too fast a decrease in the shear stress levels. The distributions of  $-\bar{u}'v'$  predicted by the models with history effect are shown in Fig. 16. In the upstream part of the interaction, a substantial improvement can be noted with respect to the previous models, which is probably a reason for a much better prediction of the wall pressure distribution. For instance, the highly overestimated maximum of  $-\bar{u}'v'$  in this region no longer occurs (on this point, the [k,e] model performs least well). However, no model satisfactorily reproduces the slow decrease of the turbulent shear stress in the downstream part of the interaction. The least unsatisfactory result is given by the ASM.

**Flow C : Extended Separation.** In this case, a large crosswise separation bubble forms, which constitutes a difficult case for predictive methods. The wall pressure distribution  $p(x)$  computed with algebraic equilibrium models are plotted in Fig. 17. The model of Michel et al. leads to much too high a recompression, and the beginning of the typical plateau of an interaction with separation is not visible. It should be mentioned that this model was developed to compute boundary layers subjected to moderately adverse or favorable pressure gradients and that it does not contain any special adaptation for representing separated flows. Because of its change in the formulation of  $\mu_t$  made as soon as separation occurs, Alber's model

substantially improves the prediction. The double inflection in the  $p(x)$  can now be seen. Baldwin-Lomax's model also leads to a certain improvement, but more limited. In a general way, the theoretical curves are far from the experiment, and they all indicate far too high a compression at the beginning of interaction. In addition, the level of the plateau - when it is predicted - is highly overestimated.

The wall pressure distributions predicted with the non-equilibrium models are plotted in Fig. 18. The theoretical results agree increasingly well with the measurements considering the Johnson-King model, the [k,e] model, the ASM in succession. The result obtained with the ASM is even spectacular, both the plateau and downstream levels being correctly predicted.

The velocity profiles  $\bar{u} / \bar{u}_0$  are plotted in Figs. 19 and 20. Their shape is predicted poorly by the three equilibrium models, both in the separated region where the amount of reversed flow is underestimated, and downstream of reattachment where the profiles are not enough filled. In spite of a clear improvement, the models with history effects also exhibit deficiencies such as an underestimation of the reversed flow amplitude, too slow a filling near the wall downstream of reattachment and a too small thickening of the boundary layer.

The shear stress distributions computed with the equilibrium models (see Fig. 21) exhibit the same defects as was already observed for flow A, but more pronounced. There is a relatively good agreement in the first part of the interaction up to  $\bar{X} = 77$  for the model of Michei et al.; beyond that, the theoretical levels start decreasing, whereas, in reality, the maximum shear stress  $-\left(\bar{u}'v'\right)_{max}$  continues to increase up to the station  $\bar{X} = 125.5$ . Further downstream, the difference between the theoretical and experimental results is even larger. The general level of shear stress is largely underestimated, as also the Y-wise diffusion of turbulence. As far as models with history effects are concerned (see Fig. 22), they are still far from being fully satisfactory. As for the [k,e] model and the ASM, the prediction, although good in the upstream part of the interaction, strongly underestimates the maximum levels reached during the interaction. In addition, the relaxation is still much too fast. However, in this case where the flow was explored down to stations far downstream of the interaction region, a good agreement between the computed and measured  $-\left(\bar{u}'v'\right)_{max}$  is again observed for the most distant stations, but the lateral diffusion remains poorly represented.

## 3.2 Supersonic Interactions

### 3.2.1 General Flow Conditions

The main objective of the present investigation was to characterize the effect of the wall temperature on the interaction resulting from the reflection of an oblique shock wave on a turbulent boundary layer. Information is available on interactions taking place on a cold wall, this case corresponding to the situation met on a hypersonic vehicle where the surface temperature  $T_w$  is much lower than the outer flow stagnation temperature  $T_{st}$ . Then, it is found that wall cooling tends to contract the streamwise extent of the interaction and to prevent the development of an extended separated region (Lewis et al., 1967; Kil-



burg and Kotansky, 1969; Spaid and Frisshett, 1972). The opposite case, where the wall is heated, has practically not been investigated, except for small temperature differences, although this situation may occur on an afterbody heated by hot propulsive jets, for example. For this reason, it was worthwhile to examine the interaction between an oblique incident shock wave and the boundary layer developing on a strongly heated plate. In fact, it is more usual to compare the wall temperature  $T_w$  with the recovery temperature  $T_r$ , which is the temperature of the wall when adiabatic equilibrium is reached.

These experiments have been executed in the ONERA S5Ch continuous wind tunnel on the experimental arrangement sketched in Fig. 23. The test section, whose span is equal to 300mm, was equipped with a contoured nozzle block producing a uniform supersonic flow of Mach number  $M_{\infty} = 2.4$ . The test section symmetry plane was in two parts:

- the upstream part was a flat plate made of aluminium alloy which took the equilibrium recovery temperature  $T_r$ ;
- the central part was a copper plate heated by 21 electrical resistors permitting to maintain the plate at a given temperature  $T_w$  with a maximum surface non-uniformity of 1%. The maximum allowable temperature level was equal to 600K. During the tests, the heating system was regulated so as to keep constant the value of the ratio  $T_w/T_r$ .

The working plate was equipped with 66 pressure taps and 24 thermocouples to check its temperature uniformity. Also, it comprised 8 orifices allowing the passage of pressure and temperature probes actuated by an automated displacement device. When not in operation, the passages were obturated by plugs. To insure a fully turbulent boundary layer in the interaction region, transition was triggered by a wire located 430mm upstream of the heated region.

The shock generator was constituted by a flat plate with a sharp leading edge mounted above the working wall with an angle of incidence  $\alpha$ . The shock generator had a length of 220mm and entirely spanned the test section. The strength of the shock could be varied by changing the incidence  $\alpha$  of the generator which could rotate about an axis coincident with its leading edge.

The flow in the interaction region has been thoroughly explored by means of surface flow visualizations (to check its two-dimensionality), surface pressure measurements, detailed probings by Pitot, static pressure, stagnation temperature probes and two-component LDV (for a more detailed information, see Détery, 1992). Thus all the flow quantities (static pressure, total pressure, stagnation temperature, velocity and Reynolds stresses) have been directly determined.

Four interactions were investigated, corresponding to the following conditions:

- Shock generator incidence :  $\alpha = 5^\circ$  ; temperature ratios:  $T_w/T_r = 1$  (adiabatic reference case) and 2. An angle of  $5^\circ$  corresponds to incipient shock induced separation in the adiabatic case.
- Shock generator incidence :  $\alpha = 8.75^\circ$  ; temperature ratios:  $T_w/T_r = 1$  and 2. In this case, an extended separated region forms at the shock foot.

The upstream flow conditions and the properties of the initial boundary layer are given in the following table.

$M_{\infty}$	$p_{\infty}(kPa)$	$T_{\infty}(K)$	$T_r(K)$	$R_{\infty}(m^{-1})$	$R_{\delta^*}$	$\delta^*(mm)$	$\theta(mm)$	$H$
2.4	74.9	317	300	$7.0110^6$	$1.2510^6$	1.78	0.454	1.40

$R_{\infty}$  designates the unit Reynolds number,  $\theta$  the boundary layer momentum thickness and  $H$ , its incompressible shape parameter.

### 3.2.2 Mean Flow Properties

**Surface Pressure Distributions.** The pressure distributions measured for  $\alpha = 5^\circ$  are plotted in Fig. 24. It is observed that the compression curve is much more spread when the plate is heated. In addition, this curve exhibits the three inflection points typical of an interaction with separation. In the downstream part of the interaction domain, the two distributions override the perfect fluid level before tending towards the theoretical perfect fluid pressure rise. This "overshoot", which is always observed in shock wave - boundary layer interactions of weak to moderate strength, is due to the coupling between the inviscid and viscous parts of the flow (see Détery and Marvin, 1986).

Figure 25 shows the wall pressure distributions corresponding to  $\alpha = 8.75^\circ$ . These curves are typical of an interaction with formation of an extended separated region, as indicated by the existence of a plateau following the rapid pressure rise accompanying the separation

process. One notes that the interaction domain is far more extended when the wall is heated, its origin being 30mm more upstream than in the adiabatic case, which represents 4 times the thickness  $\delta_0$  of the initial boundary layer. Then, the plateau extends on a longer distance, the pressure curve in the reattachment region being weakly affected. This deformation of the pressure distribution excludes a simple change in the scale of the phenomenon which would result from a thickening of the initial boundary layer displacement thickness  $\delta_0^*$ . Indeed, according to this interpretation, wall heating - as well as wall cooling - could be taken into account by normalizing the size of the interaction domain with  $\delta_0^*$ , which strongly depends on the wall temperature. This conclusion appears to be wrong (see Détery, 1992). In the two cases (adiabatic and heated wall conditions), the pressure distributions go through a maximum - nearly equal to the perfect fluid downstream level - before decreasing markedly. This decrease is due to the reflection on the working wall of the expansion fan emanating from the trailing edge of the shock generator. Furthermore, a closer examination of the results, shows that the pressure gradients are less intense when the wall is heated, especially at separation.

**Flow Field Mach Number.** From the measurement of the flow velocity, by means of the LDV system, and of its stagnation temperature  $T_{t1}$ , by temperature probes, it was possible to determine the local values of the Mach number, from which the lines of constant Mach number have been computed. The iso Mach-lines of the flow resulting from interactions at  $\alpha = 5^\circ$  are traced in Fig. 26, and those corresponding to  $\alpha = 8.75^\circ$  in Fig. 27. In each figure, a different mode of tracing allows to distinguish the subsonic part of the flow. On these figures, interest has been placed on the boundary layer part of the flow, which explains the poor definition of the inviscid flow structure, where the different wave systems are barely visible.



For the two incident shock intensities, wall heating provokes an obvious dilatation of the subsonic part of the boundary layer, the sonic line, which is very close to the wall in the adiabatic case, rising up in the boundary layer when heating is applied. This effect is explained by the fact that the velocity is almost unaffected by the wall temperature (except in the immediate vicinity of the surface), whereas the local speed of sound is much increased, hence a diminishing of the local Mach number. At reattachment, the compression is much more spread out when the wall is heated. Thus, a rise in the wall temperature tends to increase the streamwise extent of the interaction, as already noticed from the wall pressure distributions.

**Flow Streamlines.** The structure of the flow generated by the interaction is also well visualized by the tracing of the mean flow streamlines which are defined here as lines of constant value for the streamfunction:

$$\Psi(X, Y) = \int_0^{Y/\delta_0} \frac{\bar{\rho}}{\rho_{st0}} \frac{\bar{u}}{\bar{u}_0} d\left(\frac{Y}{\delta_0}\right)$$

where quantities  $\rho_{st0}$ ,  $\bar{u}_0$  and  $\delta_0$  are introduced for normalization purposes.

The streamlines relative to the case  $\alpha = 5^\circ$  are shown in Fig. 28. Here also, the more important dilatation of the boundary layer occurring when the wall is heated appears clearly. However, in this case, no negative values of  $\Psi$  are detected. On the other hand, for  $\alpha = 8.75^\circ$  (see Fig. 29), a recirculation region where streamlines are closed curves is well visible, the size of this "bubble" being amplified when the wall is heated.

The observed above tendencies are in agreement with observations made for cooled wall situations, in which the opposite trends are noted. In the framework of Chapman's Free Interaction Theory (Chapman's et al., 1958), the streamwise extent of a strongly interacting flow can be scaled by a length  $L$  obeying a law of the form:

$$L \sim \frac{\delta_0^*}{C_{f_0}^{1/2} (M_{\infty}^2 - 1)^{1/4}}$$

Thus, since heating the wall tends both to increase  $\delta_0^*$  and to decrease (weakly) the skin friction coefficient  $C_{f_0}$ , the observed trends are in agreement with this analysis. However, the real effect is far more important than that predicted by Chapman's theory. So that another mechanism must certainly be at work. It could be the thickening of the subsonic part of the boundary layer which permits a longer upstream propagation of the pressure rise induced by the reflected shock wave.

### 3.2.3 Validation of Turbulence Models

In the present investigation, the algebraic model of Baldwin-Lomax, the [k,ε] model and the ASM have only been considered, since they are the most representative and commonly used models for the prediction of separated flows. Also, this discussion will be restricted to the interaction leading to the formation of an extended separated region (case  $\alpha = 8.75^\circ$ ), which is the most severe and hence the most instructive (the complete results can be found in Benay, 1991).

**Adiabatic Case.** The computed and measured wall pressure distributions are plotted in Fig. 30. One sees that the [k,ε] model and the ASM yield comparable results in the first half of the separated region located between  $X = 100$  and  $160\text{mm}$ . However, the ASM seems to be more accurate in the plateau and reattachment regions. We observe, on the other hand, that the Baldwin-Lomax equilibrium model predicts the wall pressure far less well, the deficiencies being similar to those noted in transonic flows (see Section 3.1.4). The computed and measured mean velocity profiles for adiabatic conditions are compared in Fig. 31. As the two non-equilibrium models yielded almost identical predictions of the velocity distributions, only those of the ASM are plotted in Fig. 31. As far as the general shape of the profiles is concerned, agreement between theory and experiment can be considered as very good for both models, although discrepancies exist for example at station  $X = 110\text{mm}$  and in the immediate vicinity of the wall. Also, large differences exist for station  $X = 150\text{mm}$ , which corresponds to the location where the incident shock penetrates the boundary layer, thus making the basic boundary layer theory assumption of zero transverse pressure gradient questionable. This remark is also valid for the interaction onset, where the compression waves induced by the separation process, originate well inside the boundary layer.

The shear stress profiles are plotted in Fig. 32 (here  $-u'v'$  is normalized by  $\bar{u}_0^2$ ). For the present interaction, the algebraic model largely overpredicts the shear stress levels, particularly in the first part of the interaction. The ASM leads to a substantial improvement in the prediction up to the reattachment point, which is located at about  $X = 180\text{mm}$ . But this improvement becomes spectacular after the reattachment where the prediction is very satisfactory. The [k,ε] model, though it gives results close to those of the ASM in the separated region, becomes poor downstream of the reattachment point, with a ratio of two between the predicted and measured values. The ASM allowing also the prediction of the normal stresses,

the profiles of  $\bar{u}^2$  are compared in Fig. 33. If we overlook a large difference in the region just downstream of the point where the shock penetrates the boundary layer (station  $X = 160\text{mm}$ ) - where both the calculation and the experiment are suspect - there is a very satisfactory agreement between theory and experiment.

**Non Adiabatic Case.** The wall pressure distributions plotted in Fig. 34 show that, in this case where compressibility effects are larger because of heating, the accuracy of the two transport equation models is degraded with respect to the unheated case. On the other hand, the algebraic model seems to adapt to this situation unharmed, which is probably due to its greater simplicity. In effect, the parameters and relations defining the [k,ε] model and the ASM were defined for incompressible flows, which could explain why they do not behave as well in those cases. The cause of the bad behaviour of the models could also be the greater extension of the separated region. The Baldwin-Lomax algebraic model, which is more global and less accurate in the transonic domain, retains the same order of accuracy in the situation examined here. This proves that the existing closure relations in the case of the transport equation models, specialized



for low Mach numbers, have a lesser degree of generality than the turbulent viscosity law of the Baldwin-Lomax model.

Comparing the mean velocity distributions for the algebraic model (see Fig. 35), we come to the same conclusions as in the adiabatic case though with a smaller error in the localization of the separation point. The prediction of the profiles in the increasing part of the separated region is good. The error on the external velocity at  $X = 150\text{mm}$  (point of shock penetration into the boundary layer) no longer appears at the next station. This error is in fact due to an uncertainty on the outer boundary condition at this point. As far as the transport equation models are concerned, the ASM having only be considered), all the observations made for the unheated plate remain valid, on the whole, for the heated surface. The ASM is still a model that performs best here, in predicting the mean velocities, with the  $[k, \epsilon]$  model.

A comparative look at the Reynolds shear stress distributions (see Fig. 36) leads to the same remarks as in the case where the surface is not heated: the Baldwin-Lomax algebraic model gives poor prediction up to the shock impact, with gradual improvement in the reattachment region. The ASM yields a larger overestimation of the maximum shear stress than the Baldwin-Lomax model in the separated region. Yet the shape of the profiles is better.

That is the ordinate at which  $-u'v'$  vanishes is well predicted by the ASM throughout the domain, which is not true of the Baldwin-Lomax model, where a permanent shift is noted between computation and experiment for the location of this point. The  $[k, \epsilon]$  model aggravates the former disadvantage and yields an error of 100% between the experimental and computed levels after the reattachment. It must be emphasized that an uncertainty remains on the validity of the experimental results in the zone of maximum shear stress where the measured distributions exhibit discontinuities that were not explained.

The ASM predicts the normal tension distributions  $u'^2$  (see Fig. 37) quite well, except in the area between the incident shock and the reattachment, where the maximum level is largely overestimated. Interpreting these results, we must also take into account a certain amount of inaccuracy in the measurements.

All the observations made in the unheated case, concerning the effect of the Y-wise variation of the pressure in the region of the start of the interaction and at the location where the incident shock penetrates the boundary layer, hold here too. As the heating of the surface has the general effect of amplifying the spatial extent of the separated zones, the errors observed in the adiabatic case are increased, correlatively to the fact that the domains where the Prandtl approximation does not hold are now more extensive. In these conditions, it is probable that a Navier-Stokes code would offer better predictions, especially with the ASM.

## 4. THREE-DIMENSIONAL FLOWS

### 4.1 Introductory Remarks

Although some issues are still unsolved for two-dimensional - or axisymmetric - interactions, the problem of turbulence modelling in separated regions for instance, the physics of these flows is now well understood and there

exists a relative large number of well documented experiments to validate the theoretical models. However, one should be aware that in almost all existing nominally two-dimensional experiments, unwanted three-dimensional effects are present which can make questionable a precise validation of the models.

In reality, though, aside from a few devices exhibiting symmetry of revolution, such as nozzles or certain types of air-intake, the vast majority of the flows of practical interest are *three-dimensional*. The problem of the interaction then becomes more complex and, on the level of our physical understanding of the phenomena involved, clear pictures of interacting flow fields are not yet well established. The most typical three-dimensional situations are:

- The swept wedge, which represents the situation met at a control surface.
- The slanted shock creating an interaction on a plate normal to it, which corresponds to interactions occurring on the side wall of an air-intake. The shock is here generated by a sharp edged fin whose leading edge can be swept.
- The fin induced interaction, the fin having a rounded leading which can be either normal or swept. This configuration reproduces any situation where an obstacle, like a tail, is placed in a supersonic flow.
- The transonic channel, simulating the flow in the region of the terminal shock of a supersonic air-intake or in a compressor cascade.

The three first configurations have already been the subject of careful investigations who gave important information about the structure of such flows (Sednay and Kitchens, 1977; Settles et al., 1980; Degrez and Ginoux, 1983; Dolling, 1982; Alvi and Settles, 1990; Settles and Dolling, 1990, to cite only a few studies on these cases; see also other Lectures of this Special Courses). Here we shall concentrate on the fourth situation by considering an experiment in which the flow in a simple three-dimensional channel has been investigated in great detail.

In fact, investigation of three-dimensional flows is a complex operation since then the investigator is confronted with greater experimental difficulties and with a mass of results whose interpretation can be a hard task. The present Lecture will illustrate this last point. Also, as far as the theoretical prediction is concerned, its possibilities are still limited although rapid progress is made in modelling the phenomena by solving the Navier-Stokes equations.

## 4.2 Interaction in a Three-Dimensional Channel

### 4.2.1 General Flow Conditions

The geometrical definition of the tested channel is shown in Fig. 38. It consists of a converging - diverging section with three flat faces, the fourth face (lower wall) bearing a swept bump. The test section is 120mm wide and 100mm high in the inlet plane. The upstream part of the bump is flat and inclined at  $7^\circ$  with respect to the horizontal. This first portion is followed by a contour of variable slope, beginning with a circular convex part having a radius of curvature of 100mm, followed by a concave circular part with a radius of 180mm. The two circular arcs are defined so as to insure slope continuity at the points where they interconnect and at the points where they come to contact with the rectilinear upstream and downstream parts.



The three-dimensional effect is achieved by sweeping the bump crest line  $30^\circ$  from the upstream flow direction. The maximum height of the bump is 20mm and its length is equal to 355mm. The generation is cylindrical downstream of the crest line (for a more complete definition of the channel geometry, see Pot et al., 1991). The incoming subsonic flow accelerates in the converging part of the channel to reach a sonic state in the vicinity of the bump crest, which constitutes a throat. The flow becomes supersonic downstream and then, because of the choking effect caused by an adjustable second throat, it decelerates through shock waves interacting with the boundary layers of the channel walls. The test set up is installed in the ONERA S8Ch wind tunnel already used to perform two-dimensional transonic studies (see Section 3.1). Let us recall that the stagnation conditions are the following: pressure :  $p_{st} = 92000 \text{ Pa}$ , temperature :  $T_{st} = 300 \text{ K}$ . The Reynolds number computed with the sonic state and taking the throat height (80mm) as reference length is :  $1.1310^6$ . Under these conditions, the boundary layers are fully turbulent well upstream of the interactions.

The four channel walls were equipped with a total of 597 pressure orifices, 216 being installed on the lower wall bearing the bump, 181 on the top wall, and 100 on each side walls (for the pressure measurements, the side windows were replaced by metal plates equipped with the pressure tapping). The skin-friction line patterns on the four faces of the channel were visualized by the oil film technique. The field measurements were executed by using the three-component LDV system described in Section 2.1. The probe volume had a useful diameter of  $200 \mu\text{m}$ . In the present arrangement, the blue and green beams were emitted in a horizontal plane, at an angle of  $-24^\circ$  with respect to the Y spanwise axis and the violet component at an angle of  $+25^\circ$  with respect to the Y-axis. Thus the total angle ( $\alpha + \beta$ ) is here equal to  $49^\circ$ . The measurements have been executed along 220 vertical stations contained in 11 longitudinal planes, each comprising 96 points: hence a total of 21,120 measurement points.

#### 4.2.2 Surface Flow Properties

The skin-friction line pattern - or surface flow pattern - provides a precious and indispensable help in the understanding of the physics of separated three-dimensional flows. A careful examination of the skin friction lines and observation of the *critical points* in their pattern allows with the greatest certainty to define the concepts of *separation* and *attachment* in three-dimensional flows, where these concepts are trickier to grasp than in two-dimensional flows.

The interpretation of the surface flow patterns is based on the Critical Point Theory (Poincaré, 1882, Legendre, 1936). Let us simply recall here the possible existence of isolated critical - or singular - points where the wall shear-stress and rotational vector cancel each other out. Of these points we should distinguish (see sketches in Fig. 39):

- *Nodes*, through which pass an infinite number of skin friction lines, all but one of them being tangent to a common direction. If the skin friction lines are oriented towards the node, then the node is a *separation node*; if they flow from the node, it is called an *attachment node*.
- *Foci*, where there is no common tangent but an infinity of skin friction lines spiralling about this point.

- *Saddle points*, through which only two skin friction lines pass, with all the others avoiding the singular point by curving away from it into one or the other direction of the two particular skin friction lines.

The theory introduces also special lines, called *separators*, which are defined as skin-friction lines passing through a saddle point. From a physical point of view, a separator (S) is identified either with a separation line or with an attachment line, according to the flow behaviour in its vicinity. Also, one considers separation and/or attachment surfaces which are streamsurfaces intersecting an obstacle along a separator (for details, see Déleroy, 1992).

The above concepts will be used to interpret the surface flow visualizations on the four faces of the channel which allowed to draw the patterns shown in Fig. 40. These diagrams, which represent certain skin-friction lines with the critical points of the pattern, have been established from photographs and direct observation of the visualizations during the tests, which reveal information that is lost when the picture is taken. Here we will only examine the flow over the bump (see Fig. 40a) and on the top wall (see Fig. 40b). The lower wall pattern contains one focus  $F_1$  around which rolls up separator ( $S_1$ ) emanating from the half-saddle point  $C_1$  located at the junction between the lower wall and sidewall A. A second half-saddle point  $C_2$  exists downstream of  $C_1$  through which passes the separator ( $S_2$ ) which is in fact an attachment line. The skin-friction lines coming from upstream that are flowing between ( $S_2$ ) and sidewall A wind around  $F_1$  into which they "disappear"; those located above ( $S_2$ ) continue their way downstream. The spirals winding around  $F_1$  are the traces on the lower wall of a tornado-like vortex escaping into the flow with the separation line ( $S_1$ ) being the origin of a separation surface that winds around the axis of the vortex structure.

On the top wall, two foci  $F_4$  and  $F_3$  are clearly visible. The separation line ( $S_9$ ) passing through saddle point  $C_8$  and spiralling around  $F_4$  and  $F_3$  constitutes a "barrier" approximately at the foot of the nearly normal shock ( $\Gamma_3$ ) of the lambda system attached to the interaction (see Section 4.2.3 below). The skin friction lines that are coming from upstream and that are contained in the domain delimited by the separator ( $S_{11}$ ) passing through saddle point  $C_9$  are going to wind around either  $F_4$  or  $F_3$ , depending if they are located on one side or the other of separator ( $S_{10}$ ) which carries both  $C_8$  and  $C_9$ . One bundle of these lines goes around the barrier ( $S_{10}$ ) by curving backward abruptly. The skin friction lines from upstream divide into two families. The first, near face B, all flow continuously downstream. The other, near wall A, separates in turn into two families:

- Those lines included between ( $S_{11}$ ) and separator ( $S_{13}$ ) leading to the saddle point  $C_{10}$ , that continue their path downstream.
- Those lines between wall A and ( $S_{11}$ ) that wind around a third focus  $F_6$  to form a "vortex" delimited by separator ( $S_{13}$ ). The skin-friction lines winding around  $F_6$  all come from the node  $N_2$  at the junction between the top wall and wall A.

In such a situation, ( $S_9$ ) can be associated with a well characterized separation, with the flow in the vicinity of ( $S_9$ ) "leaving" the wall. Separator ( $S_{11}$ ) is an attachment line insofar as a little above ( $S_{11}$ ) the outer flow "dives" in the direction of the wall. This makes  $C_{10}$  a separation saddle point and  $C_9$  an attachment saddle point.



The attachment line ( $S_{11}$ ) is the trace on the wall of an attachment surface ( $\Sigma_{10}$ ) which is schematically represented in Fig. 41a. All the streamlines constituting this stream-surface stream into the attachment node  $N_{10}$  coincident with  $C_9$  on the wall. On the other hand, ( $S_9$ ) is the trace on the wall of a separation surface ( $\Sigma_9$ ) represented in Fig. 41b. This stream-surface is made of the streamlines originating at node  $N_9$  coincident with saddle-point  $C_4$ . Surface ( $\Sigma_9$ ) rolls up to constitute two vortical structures - or vortices - whose trace on the wall are the foci  $F_4$  and  $F_5$ . These structures are tornado like vortices which escape into the outer field where they bend under the action of the flow.

The two surfaces ( $\Sigma_9$ ) and ( $\Sigma_{10}$ ) intersect to constitute the structure sketched in Fig. 41c. The intersection of the two vortices emanating from  $F_4$  and  $F_5$  with the attachment surface ( $\Sigma_9$ ) gives rise to two foci contained in ( $\Sigma_9$ ) around which streamlines of ( $\Sigma_9$ ) wind to feed the vortices.

A similar description of the wall patterns in terms of singular points and separation/attachment lines can be made for the other faces of the channel, care being taken to insure continuity of patterns at the crossing of the corner lines between adjacent walls.

#### 4.2.3 Mean Flow Properties

**Velocity Field in Longitudinal Planes.** The fields of the velocity component in longitudinal planes XZ located at the spanwise locations  $Y = 10, 30, 60, 90$  and  $110\text{mm}$  are represented in Fig. 42. An examination of these results show the following trends:

- In the most upstream part of the explored domain, the flow - which has become supersonic - accelerates because of the divergence of the channel. Then, due to curvature effect, the velocity is greater in the vicinity of the bump. Just upstream of the interaction region, the boundary layer has a thickness of about 4mm on the bottom and top walls of the channel.

- Considering first the planes which are close to side wall A ( $Y = 10$  and  $30\text{mm}$ ), one notes that an important thickening of the boundary layer takes place downstream of  $X = 280\text{mm}$ . Then the velocity profiles present a large deficit down to  $X = 310\text{mm}$ . This behaviour must be correlated with the surface flow pattern in Fig. 40a where it can be seen that the two XZ planes cross the separated zone comprised between separators ( $S_1$ ) and ( $S_2$ ). Downstream, a rapid filling of the profiles takes place. One will note in plane  $Y = 10\text{mm}$  the considerable decrease of the amplitude of the velocity in the inferior half part of the channel. This phenomenon is due to the strong thickening of the side wall boundary layer resulting for the formation of a large separated zone (see surface flow pattern in Fig. 40c). An important thickening of the boundary layer also occurs on the top wall as a consequence of the strong interaction induced by the nearly normal shock ( $\Gamma_3$ ) (see next section).

- The behaviour of the longitudinal flow changes much at  $Y = 60\text{mm}$  and beyond. Then, on approaching side wall B, the thickening of the bottom wall boundary layer is less important, as if an interaction was no longer taking place. This tendency is confirmed by the surface flow pattern of Fig. 40b, where it is seen that beyond separator ( $S_2$ ), the skin friction lines flow from the inlet to the outlet section of the observed field. At the same time, these is a

clear intensification of the interaction taking place on the top wall. There, the velocity profiles thicken more and more while being "emptied", as one moves towards side wall B. Even, a small but well defined portion of reversed velocity is observed. This zone has to be correlated with the surface flow pattern in Fig. 40c, which shows that the skin friction lines are turned back between separators ( $S_9$ ) and ( $S_{11}$ ). Thus, there is a fair agreement between the field measurements and the surface flow properties.

- Very close to side wall B (plane  $Y = 110\text{mm}$ ), the region of reversed flow resorbs itself progressively, although the top wall boundary layer is still very thick. On the other hand, at large distance from the top wall, the velocity levels are still high, the plane  $Y = 110\text{mm}$  passing outside the boundary layer of the side wall B where the interactions are weak.

**Mach Number Distributions in Longitudinal Planes.** The experimental values of the Mach number have been determined from the mean velocity vector measurements made with the LDV system assuming a uniform stagnation temperature, even in the dissipative regions. This approximation is well verified in transonic adiabatic flows.

The iso-Mach lines relative to planes located at  $Y = 10, 30, 60, 90$  and  $110\text{mm}$  are shown in Fig. 43. The plane  $Y = 10\text{mm}$  traverses the interacting boundary layer of face A which explains the spreading of the Mach number distributions (peaks in the experimental iso-Mach lines near the bump are due to erroneous values). In planes located at  $Y = 30$  and  $60\text{mm}$ , a lambda shock pattern is clearly visible. This pattern is made of: a leading oblique shock ( $\Gamma_1$ ), a nearly normal shock ( $\Gamma_2$ ) occupying about half the channel, in its upper part, a "leg" ( $\Gamma_3$ ) consisting of a very weak shock hardly discernible in the experiment (the important thickening of the shocks in the experimental plottings is due to the spacing of the measurement points). In plane  $Y = 30\text{mm}$ , the tracings reveal the large region of separated flow starting from the foot of shock ( $\Gamma_1$ ), which was already detected from the surface flow visualizations. This zone disappears when one tends towards face B and is no more apparent in plane  $Y = 60\text{mm}$ . A separated zone induced by shock ( $\Gamma_2$ ) is also visible near the top wall, both in plane  $Y = 30, 60$  and  $90\text{mm}$ . At  $Y = 90\text{mm}$  the oblique shock ( $\Gamma_1$ ) is much weakened and replaced by a continuous compression.

**Flow in Transverse Planes.** The flow in ( $Y, Z$ ) planes is represented in Fig. 44 by tracings of the lines of constant value for the modulus of the velocity component in these planes. The explored region extends from  $Y = 10\text{mm}$  to  $Y = 110\text{mm}$  in the spanwise direction, the use of the LDV system close to the lateral glass windows being difficult because of important parasitic stray light.

The first station at  $X = 230\text{mm}$  is located upstream of the shock system. There, due to the strong acceleration of the flow, viscous effects are extremely weak so that the boundary layers are barely visible. The second station at  $X = 270\text{mm}$  nearly coincides with the origin of shock ( $\Gamma_1$ ), so that viscous effects are still unimportant. The third plane, at  $X = 310\text{mm}$ , crosses shock ( $\Gamma_1$ ) but is upstream of the nearly normal shock ( $\Gamma_2$ ). One sees in the field the trace of ( $\Gamma_1$ ), this shock being replaced by a continuous compression wave on approaching the side wall B. A region of intense interaction is visible in the vicinity of the corner line between the lower wall and the side



wall A. There, the boundary layer undergoes a rapid and important thickening which corresponds to the vortical structure originating at the combination of the two half-saddle points  $C_1 + C_2$  (see Figs. 40a and 40b). The trace of shock ( $\Gamma_1$ ) is well visible in plane  $X = 330\text{mm}$ .

The plane  $X = 350\text{mm}$  is very close to the transverse plane containing the strong shock ( $\Gamma_2$ ), which can explain some erratic behavior of the iso-lines in the central part of the channel. The last plane,  $X = 390\text{mm}$  is well downstream of the shock system. One notes the important thickness of the top wall boundary layer and the large dissipative region still existing at the corner line between the lower wall and the side wall A. In fact, as shown by the skin-friction line patterns in Fig. 40, this transverse plane still crosses the vortical flow comprised between the saddle point ( $C_1 + C_2$ ) and the node ( $N_2 + N_3$ ).

#### 4.2.4 Turbulence Properties

The use of the three-component LDV system has brought a large amount of information on turbulence, since the 6 distinct components of the Reynolds tensor were measured. So, to keep to this paper a reasonable size we will give here a synthetic presentation of these results by means of tracings of iso-value lines and by considering only the turbulence kinetic energy  $k$  and the cross-correlation  $\overline{u'w'}$ , these quantities being the most interesting (in the present experiment,  $w$  is the velocity component along axis  $Z$  normal to the flat part of the bottom wall).

**Turbulence Kinetic Energy.** The iso- $k$  lines in the longitudinal planes  $Y = 10, 30, 60, 90$  and  $110\text{mm}$  are shown in Figs. 45. The mode of tracing adopted emphasizes the region of strong interaction where turbulence increases much with a large correlative thickening of the dissipative regions. For this reason, the thin incoming boundary layers will be barely visible. Starting from plane  $Y = 10\text{mm}$ , the closest to side wall A, one sees a broad region where  $k$  takes large values, this plane traversing the boundary layer of side wall A where strong interactions occur, as revealed by the mean flow analysis. In the present tracing, the iso- $k$  lines seems to emanate from the foot of shock ( $\Gamma_1$ ) in the vicinity of the bottom wall, on the one hand, and from the region of birth of the compression waves whose coalescence will form the nearly normal shock ( $\Gamma_3$ ), on the other hand. The plane  $Y = 30\text{mm}$  still crosses the separated boundary layer of side wall A. The large "spot" visible in the middle of the channel can be attributed to an oscillation of shock ( $\Gamma_3$ ), the phenomenon being here exaggerated by the code used to compute the iso-lines which was applied to experimental points too distant from each other in the  $X$ -wise direction.

For plane  $Y = 60\text{mm}$  and beyond, the region of high turbulence corresponds to the interactions of shocks ( $\Gamma_1$ ) and ( $\Gamma_3$ ) with the boundary layers of the bottom and top walls. The size of the bottom wall interaction starts to shrink from plane  $Y = 50\text{mm}$  (not shown here) while the interaction occurring on the top wall keeps nearly constant dimensions. For  $Y = 60\text{mm}$ , the turbulent zone of the bottom wall is reduced to a thin layer whose thickness decreases on approaching side wall B. This behaviour agrees with the description provided by the mean flow. The central spot disappears almost completely for the next planes, except the last one. This fact can be interpreted, with precaution, as the consequence of a smaller unsteadiness of shock ( $\Gamma_3$ ) in this part of the channel.

The spot again appears on approaching side wall B (see plane  $Y = 110\text{mm}$ ). Here the phenomenon is due to the penetration of the exploration plane into the zone of interaction between shock ( $\Gamma_3$ ) and the boundary layer of side wall B.

In brief, the maximum levels of  $k$  are reached in the vicinity of the wall bearing the bump and in the planes close to side wall A; i.e., in the regions where the interactions are the strongest. Then the reduced kinetic energy  $k/a^2$ , is close to 0.11, which corresponds to a conventional turbulence rate equal to 0.33.

**Shear Stress Component  $\overline{u'w'}$ .** The spatial distributions of this component are shown in Fig. 46. The fact that the plane  $Y = 10\text{mm}$  traverses the thick boundary layer of side wall A leads to a rather complex distribution

of  $\overline{u'w'}$  which is first negative very close to the bottom wall before taking positive values. Close to the top wall,  $\overline{u'w'}$  takes only positive values which is in agreement with the behaviour of this stress in a classical boundary layer, the axis normal to the wall being here oriented opposite to the usual sense. From the plane  $Y = 30\text{mm}$  and beyond,

$\overline{u'w'}$  is negative near the bump, the exploration planes no longer traversing the boundary layer of side wall A.

The behaviour of  $\overline{u'w'}$  becomes more "normal" with a rapid increase from the foot of the shock ( $\Gamma_1$ ) and passage through a maximum (in absolute value) before a slow decrease in the downstream part of the interaction. In the other  $Y$ -planes, the region of high shear stress shrinks in correlation with the weakening of shock ( $\Gamma_1$ ). On the other hand, close to the top wall where the situation is close to a two-dimensional interaction, the evolution of the phenomena with the spanwise distance  $Y$  is much slower.

#### 4.2.5 Validation of Turbulence Models

**Numerical Method and Turbulence Models.** The flow in the channel has been computed by solving the full time-averaged Navier-Stokes equations (Couaillier et al., 1991). The adopted time-marching numerical method uses an explicit centered finite difference scheme applied to a finite-volume approach on a structured mesh. The mean flow and the turbulent transport equations are both discretized by using a two-step Lax-Wendroff scheme. The dissipation terms are taken into account according to Thommen's idea. The space discretization of the divergence terms at each time step is performed by using an integral contour formulation. The source terms are evaluated at each step of the predictor-corrector scheme at the centres and at the nodes of the basic cells respectively. A numerical viscosity is added to improve the stability of the scheme and to correctly capture the flow discontinuities in the inviscid flow regions. In the present calculations, the computational domain extends from  $X = -30\text{mm}$  to  $X = 560\text{mm}$ . Grid interpolation is made on surfaces constructed between the lower wall bearing the bump and the flat top wall. High refinements is introduced near the wall to properly resolve the boundary layers. The total number of mesh points is a little less than 700,000.

Two turbulence models have been tested (for detailed results and a more thorough discussion, see Cahen, 1993 and Cahen et al., 1993). The first one is the algebraic equilibrium model of Michel et al. (1969) presented in Section 2.3.2. The original formulation has been modified to extend its applicability to three-dimensional flows



and to treat the problem of corner flows. The turbulent viscosity is now given by:

$$\mu_t = \bar{\rho} l^2 D^2 \left| \bar{\Omega} \right| \text{ where: } \bar{\Omega} = \text{curl} \left( \vec{V} \right)$$

and the mixing length by:

$$l = 0.085 \tanh \left( \frac{0.41d}{0.085\delta} \right)$$

In the above expression,  $d$  denotes Buleev's "modified distance" which takes into account the influence of several walls in the case of corner flows and  $\delta$  is a "modified" boundary layer thickness (for details, see Cambier and Escande, 1991).

The second model is the non-equilibrium Jones-Launder model whose boundary layer type version has been presented in Section 2.3.3. The general form of these equations, with the low Reynolds number terms, will not be given here (see Cahen, 1993).

The accuracy of these models will be discussed by considering the same quantities as those already considered in the presentation of two-dimensional flows.

**Wall Pressure Distributions.** Some pressure distributions on the four channel walls are plotted in Fig. 47. On the wall bearing the bump and on the top wall, these distributions are plotted along the lines  $Y = 15\text{mm}$ , located near side wall A,  $Y = 60\text{mm}$ , in the vertical median plane and line  $Y = 105\text{mm}$ , close to side wall B. For the lateral walls, these distributions are relative to the line  $Z = 65\text{mm}$  which is close to the channel half-height. These distributions first exhibit a rapid expansion in the upstream converging part of the channel. On the bump the flow goes supersonic, reaching a maximum Mach number of 1.75 as denoted by the pressure measured at the wall. For the upper and lower walls, clear differences exist between the three distributions. Close to face A, one observes a steep pressure rise terminating the expansion process. This rise, which denotes the existence of a shock, is followed by a well defined plateau. Further downstream, a more progressive compression takes place, the expansion at the extremity of the domain being caused by the acceleration induced by the second throat. The shape of the pressure curves is typical of a transonic interaction with shock-induced separation, the rapid pressure rise being associated with the separation process, denoted by the separation line ( $S_1$ ) observed in Fig. 40a, and the pressure plateau with the large vortical structure extending between  $C_1$  and  $C_2$ .

In the median plane ( $Y = 60\text{mm}$ ), the first pressure rise is less rapid, the amplitude of the compression being however more important and the plateau having disappeared. A small pressure jump is observed at  $X$  close to  $300\text{mm}$ . In the immediate vicinity of face B ( $Y = 105\text{mm}$ ), the compression which follows the expansion on the first part of the bump is now progressive, no "separation shock" being observed. The pressure rise is followed by a moderate expansion which is terminated by a weak shock. This pressure distribution has to be placed in correspondence with the surface pattern observed in the vicinity of face B: in this part of the flow, the surface pattern is free of critical points and separators.

In the upstream part of the channel, where viscous effects are extremely weak, the two calculations are in excellent agreement with experiment. Considering the part of the flow where viscous effects are important, the calculations using the [k,  $\epsilon$ ] turbulence model are in very good agreement with experiment, especially along lines  $Y = 60\text{mm}$  and  $Y = 105\text{mm}$ . Major discrepancies exist close to side wall A where the pressure plateau is not captured by either calculations.

**Longitudinal Velocity Profiles.** An objective validation of the accuracy of the calculations is provided by a comparison of the velocity distributions across the channel. Thus, Fig. 48 shows the profiles of the streamwise velocity component in the median plane  $Y = 60\text{mm}$  for nine  $X$ -wise stations. The first profile at  $X = 290\text{mm}$  crosses the leading oblique shock ( $\Gamma_1$ ) close to the bump. Further downstream, the trace of ( $\Gamma_1$ ), well visible on the profiles, moves away from the lower surface. Section  $X = 350\text{mm}$  nearly coincides with the quasi normal shock ( $\Gamma_2$ ) which explains a certain scatter in the measured values. Downstream, the exploration lines traverse the subsonic part of the flow.

The interaction between the top wall boundary layer and shock ( $\Gamma_2$ ) gives rise to an important thickening of the dissipative layer. Close to the wall, negative values of the  $\bar{u}$  component are observed at  $X = 350\text{mm}$ , i.e. just downstream of the foot of ( $\Gamma_2$ ). The region of reversed flow extends down to  $X = 410\text{mm}$  where it vanishes. This region of backflow is in agreement with the pattern observed at the wall, its origin being coincident with the separation line ( $S_9$ ) and its resorption with the attachment line ( $S_{11}$ ).

In general, there is a good agreement between the computed and the measured profiles, the best results being obtained with the [k,  $\epsilon$ ] model. It will be noted that the location of shock ( $\Gamma_1$ ) is accurately predicted. However, relaxation of the boundary layer downstream of the strong interaction taking place on the upper wall at the foot of shock ( $\Gamma_2$ ) is ill predicted, even by the transport equation model. As a general rule, most turbulence models tend to predict a too fast relaxation process, the computed velocity distributions being fuller than the experimental ones

and the predicted reattachment occurring too rapidly. In the present case, the computed profile at  $X = 390\text{mm}$  is fully attached, whereas the measured profile still has a backflow region. Also the thickness of the relaxing boundary layer is underpredicted.

**Turbulence Properties.** The profiles of the turbulence kinetic energy  $k$  (normalized by  $a_{t1}^2$ ) in 5 longitudinal planes are shown in Fig. 49. In the most upstream station, at  $X = 230\text{mm}$ , the turbulence level is everywhere low, except inside the bottom and top wall boundary layers. At station  $X = 270\text{mm}$ , we note a rise in  $k$  close to the bottom wall. This peak is produced by the start of the interaction between the bump boundary layer and the oblique shock ( $\Gamma_1$ ). In the vicinity of the side wall A (plane  $Y = 10\text{mm}$ ), very high levels of  $k$  are measured downstream of  $X = 270\text{mm}$  (note the change in the scale for profiles beyond  $X = 270\text{mm}$ ). These important values of the turbulence kinetic energy are correlated with the strong interaction taking place on the side wall A in this region. The [k,  $\epsilon$ ] model reproduces this behaviour, although the predicted levels are below the experimental results. In the same way, the rise in turbulence occurring near the top wall because of the interaction produced by



the shock ( $\Gamma_2$ ) is underpredicted, especially in the downstream part of the interaction domain. This behaviour of the theoretical turbulence profiles has to be correlated with the evolution of the mean  $X$  wise velocity distributions presented in Fig. 48. As already mentioned, the classical turbulence models tend to predict a too fast relaxation process behind a region of strong interaction, thus a too rapid fall in the turbulence levels and a too rapid filling of the mean velocity profiles. The measured profiles located at  $X = 350\text{mm}$  exhibit a bump in the  $k$  distribution at some distance from the top wall. This phenomenon, which is completely ignored by the calculation, is in fact due to a slight oscillation of the shock ( $\Gamma_2$ ).

## 5. CONCLUDING REMARKS

Laser Doppler Velocimetry offers an unprecedented tool to investigate complex turbulent flows over a velocity domain ranging from low subsonic values up to several hundreds m/s, the maximum practical limit being now around 600m/s. Both two-dimensional, planar or axisymmetric, and three-dimensional flows can be explored without the perturbing effect of classical probes. With the advent of LDV, it has become possible to investigate in great details and with a fair degree of confidence shock wave/turbulent boundary layer interactions whose study was until then hampered by their high sensitivity to perturbations, especially in transonic streams. With LDV, it was possible to establish a clear and reliable physical description of interacting flows, including mean as well as turbulent properties. Presently, LDV is routinely used to investigate two-dimensional interactions, exploration a three-dimensional situations - although possible - remaining a long and complex task.

Thus, over the past 15 years, a rather complete set of two-dimensional - and axisymmetric - test cases has been constituted allowing an in depth validation of computer codes, and more particularly of the turbulence models used in them. Although the results obtained are most often spectacular - considering the state of the art 15 years ago - systematic comparative studies have shown that none of the most commonly used turbulence models are entirely satisfactory. Interaction with a shock wave imparts to a boundary layer a so strong and so rapid retardation that the present models are unable to represent this process, even those incorporating a history effect. In fact, experience shows that such an interaction involves phenomena, like unsteadiness and shock / turbulence interaction, which are not taken into account in these models. However, one has not to be unduly pessimistic, considering that existing simple models, implemented in accurate and efficient Navier-Stokes codes, already give results sufficient for many practical applications. The situation in three-dimensional flows is not so advanced, since probing and interpretation of such flows is a long and complex task. Due to the importance of the subject, and considering the very instructive results already obtained on a reduced number of configurations, in the coming years the main effort must be devoted to a thorough characterization of typical three-dimensional interactions. Because of the high cost of both experiment and computation applied to three-dimensional flows, this action will have to be conducted in close cooperation between experimentalists and theoreticians in order to properly define the configurations to be tested.

In spite of its great and numerous advantages, LDV suffers from shortcomings which restrict its use in situations of great interest. Seeding of the flow remains a critical issue, since LDV measures in fact the velocity of particles. Thus, in regions of high acceleration, or retardation, particle lag introduces errors which prevent the use of LDV in the immediate vicinity of a shock and render turbulence measurements suspect if the frequency of the velocity fluctuations is high. Time scales, or power spectra, measurements with LDV are still largely impossible, except at low frequencies, mainly because of the difficulty

to properly seed the flow. The problem of particle lag put also a bound to the maximum velocities which can be measured, all the attempts to use LDV in high Mach number flows (above 4) having failed. In spite of important progress, velocity measurements very close to a surface in tangential approach (e.g., below 0.1mm) are not possible - especially in three-component versions - which is a serious restriction, since many things occurs in this part of the boundary layer. The frontal approach of an obstacle, gives rise to parasitic stray light making measurements impossible below a distance of the order of 10mm, according to our experience. At last, but not the least, high speed multi-component LDV systems are still costly and delicate to operate which is a strong restriction to their general use. We have to hope that, in the coming years, most of these limitations will be overcome.

## ACKNOWLEDGEMENT

Most of the studies presented here have been executed with the financial support of the Direction des Recherches et Etudes Techniques and of the Service Technique des Plans et Programmes of the French Ministry of Defence. The author is very grateful to Claude Quélin for his help in the preparation of the figures.

## REFERENCES

- ALBER, I. E. (1971) "Similar solutions for a family of separated turbulent boundary layers". AIAA Paper 71-203
- ALVI, F. S. and SETTLES, G. S. (1990) "Structure of swept shock wave / boundary layer interactions using conical shadowgraphy". AIAA Paper 90-1644
- ARDONCEAU, P. (1981) "Etude de l'interaction onde de choc - couche limite supersonique". Ph. D. Dissertation, University of Poitiers, France
- ARDONCEAU, P.; LEE, D. H.; ALZIARY DE ROQUEFORT, T. and GOETHALS, R. (1980) "Turbulence behavior in a shock wave / boundary layer interaction". AGARD CP-271
- BALDWIN, B. S. and LOMAX, J. (1978) "Thin layer approximation and algebraic model for separated turbulent flows". AIAA Paper 78-257
- BENAY, R. (1991) "Modélisation de la turbulence dans une interaction onde de choc - couche limite sur une paroi chauffée". *La Recherche Aérospatiale*, N° 1991-5, pp. 45-68 (French and English editions)
- BENAY, R. and DUPONT, A. (1985) "Méthode aux différences finies pour le calcul d'une couche limite turbulente avec effets thermiques". ONERA Rapport Technique N° 63/7078AY
- BENAY, R.; COET, M.-C. and DELERY, J. (1987) "Validation de modèles de turbulence appliqués à l'interaction



- onde de choc - couche limite transsonique". *La Recherche Aérospatiale*, N° 1987-3, pp. 1-16 (French and English editions)
- BOUTIER, A.; d'HUMIERES, C. and SOULEVANT, D. (1984) "Three-dimensional laser velocimetry: a review". 2nd Int. Symposium on Application of Laser Anemometry to Fluid Mechanics, Lisbon, Portugal, 2-4 July 1984, see also: ONERA TP N° 1984-43
- BUR, R. (1991) "Etude fondamentale sur le contrôle passif de l'interaction onde de choc - couche limite turbulente en écoulement transsonique". Ph. D. Dissertation, University Pierre et Marie Curie, Paris
- CAHEN, J. (1993) "Modélisation de la turbulence pour la prédiction d'écoulements internes compressibles. Validation d'un modèle [k,ε] en configuration tridimensionnelle d'interaction onde de choc - couche limite turbulente". Ph. D. Dissertation, University of Rouen, France
- CAHEN, J.; COUAILLIER, V.; DELERY, J. and POT, T. (1993) "Validation of a Navier-Stokes code using a [k,ε] turbulence model applied to a three-dimensional transonic channel". AIAA Paper 93-0293
- CAMBIER, L. and ESCANDE, B. (1991) "Calculation of a three-dimensional shock wave - turbulent boundary layer interaction". AIAA Journal, Vol. 28, N° 11, pp. 1901-1908
- CHAPMAN, D. R.; KUEHN, D. M. and LARSON, H. K. (1958) "Investigation of separated flows in supersonic and subsonic streams with emphasis on the effect of transition". NACA TR-1356
- COET, M.-C. and BENAY, R. (1986) "Application de l'approche couche limite à la validation de six modèles de turbulence dans des interactions onde de choc - couche limite transsoniques". ONERA Rapport Technique N° 64/7078AN
- DEGREZ, G. and GINOUX, J. J. (1983) "Three-dimensional skewed shock wave - laminar boundary layer interaction at Mach 2.25". AIAA Paper 83-1755
- DELERY, J. (1978) "Analyse du décollement résultant d'une interaction choc - couche limite turbulente en transsonique". *La Recherche Aérospatiale*, N° 1978-6, pp. 305-320 (French and English editions)
- DELERY, J. (1981) "Investigation of strong shock/turbulent boundary layer interactions in 2D transonic flows with emphasis on turbulence phenomena". AIAA Paper 81-1245; see also: AIAA Journal, Vol. 21, N° 2, pp. 180-185
- DELERY, J. (1992) "Etude expérimentale de la réflexion d'une onde de choc sur une paroi chauffée en présence d'une couche limite turbulente". *La Recherche Aérospatiale*, N° 1992-1, pp. 1-23 (French and English editions)
- DELERY, J. (1992) "Physics of Vortical Flows". *Journal of Aircraft*, Vol. 29, N° 5, pp. 856-876
- DELERY, J. and FORMERY, M. (1983) "A finite difference method for inverse solution of 3-D turbulent boundary layer flows". AIAA Paper 83-0301
- DELERY, J. and MARVIN, J. G. (1986) "Shock wave/boundary layer interactions". AGARDograph N° 280
- DOLLING, D. S. (1982) "Comparison of sharp and blunt fin-induced shock wave / turbulent boundary layer interactions". AIAA Journal, Vol. 20, N° 10, pp. 1385-1391
- EAST, L. F. (1976) "The application of laser anemometry to the investigation of shock wave - boundary layer interactions". AGARD-CP-193
- EAST, L. F. and SAWYER, W. G. (1980) "An investigation of the structure of equilibrium turbulent boundary layers". AGARD CP-271, pp. 6.1-6.19
- ERENGIL, M. E. and DOLLING, D. S. (1991) "Correlation of separation shock motion with pressure fluctuations in the incoming boundary layer". AIAA Journal, Vol. 29, N° 11, pp. 1866-1877
- ESCANDE, B. (1986) "Modélisation de l'interaction onde de choc - couche limite turbulente. Comparaison calcul-expérience". Ph. D. Dissertation, Ecole Centrale de Lyon, France
- FAVRE, A. (1965) "Equations des gaz turbulents compressibles". *Journal de Mécanique*, Vol. 4, N° 3, pp. 361-421
- GAILLARD, R. (1983) "Etalonnage et utilisation de sondes cinq trous". Proceedings of the 7th Symposium on Measurement Techniques for Transonic and Supersonic Flow in Cascades and Turbomachines, Paper 19, pp. 1-17
- HSU, J. C. and SETTLES, G. S. (1989) "Measurements of swept shock wave/turbulent boundary layer interactions by holographic interferometry". AIAA Paper 89-1849
- JOHNSON, D. A. and KING, L. S. (1985) "A mathematically simple turbulence closure model for attached and separated flows". AIAA Journal, Vol. 23, N° 11, pp. 1684-1692
- JONES, W. P. and LAUNDER, B. E. (1972) "The prediction of laminarization with a two equation model of turbulence". *Journal of Heat and Mass Transfer*, Vol. 15, N° 2
- KILBURG, R. F. and KOTANSKY, D. R. (1969) "Experimental investigation of the interaction of a plane, oblique, incident-reflecting shock wave with a turbulent boundary layer on a cooled surface". NASA CR-66-841
- LAUNDER, B. E. (1971) "An improved Algebraic Stress Model". Mech. Eng. Dept., Imperial College, Rept. TM/TN/A8
- LE BALLEUR, J.-C. (1987) "Viscous inviscid interaction solvers and computation of highly separated flows". *Studies of Vortex Dominated Flows*, Chapter 3, pp. 158-192, Springer-Verlag
- LEGENDRE, R. (1956) "Lignes de courant d'un écoulement permanent. Décollement et séparation". *La Recherche Aérospatiale*, N° 54, Nov.-Dec. 1956
- LEWIS, J. E.; KUBOTA, T. and LEES, L. (1967) "Experimental investigation of supersonic laminar two-dimensional boundary layer separation in a compression corner with and without cooling". AIAA Paper 67-191; see also: AIAA Journal, Vol. 6, N° 1, pp. 7-14
- MICHEL, R.; QUEMARD, C. and DURANT, R. (1969) "Application d'un schéma de longueur de mélange à l'étude des couches limites d'équilibre". ONERA Note Technique N° 154
- MUCK, K. C.; ANDREOPOULOS, J. and DUSSAUGE, J.-P. (1988) "Unsteady nature of shock wave / turbulent boundary layer interaction". AIAA Journal, Vol. 26, N° 2, pp. 179-187
- POINCARÉ, H. (1882) "Les points singuliers des équations différentielles". *Comptes Rendus Académie des Sciences de Paris*, T. 94, Feb. 13, 1882, pp. 416-418
- POT, T.; DELERY, J. and QUELIN, Q. (1991) "Interaction onde de choc - couche limite dans un canal transsonique tridimensionnel". ONERA Rapport Technique N° 92/7078AY
- RODI, W. (1972) "The prediction of free boundary layers by use of a two-equation model of turbulence". Ph. D. Dissertation, University of London



- SAJBEN, M.; BOGAR, T. J. and KROUTIL, J. C. (1985) "Experimental study of flows in a two-dimensional inlet model". *Journal of Propulsion and Power*, Vol. 1, N° 2, pp. 109-117
- SEDNEY, R. and KITCHENS, C. W., Jr. (1977) "Separation ahead of protuberances in supersonic turbulent boundary layers". *AIAA Journal*, Vol. 15, N° 4, pp. 546-552
- SEEGMILLER, H. L.; MARVIN, J. G. and LEVY, L. L. Jr. (1978) "Steady and unsteady transonic flow". *AIAA Journal*, Vol. 16, N° 12, pp. 1262-1270
- SETTLES, G. S. and DOLLING, D. S. (1990) "Swept shock / boundary layer interactions. Tutorial and update". AIAA Paper 90-0375
- SETTLES, G. S.; PERKINS, J. J. and BOGDONOFF, S. M. (1980) "Investigation of three-dimensional shock - boundary layer interaction at swept compression corners". *AIAA Journal*, Vol. 18, N° 7, pp. 779-785
- SIMPSON, R. L.; STRICKLAND, J. H. and BARR, P. W. (1977) "Features of separating turbulent boundary layer in the vicinity of separation". *Journal of Fluid Mechanics*, Vol. 79, Part 3, pp. 553-594
- SMITS, A. J. and MUCK, K. C. (1987) "Experimental study of three shock wave / turbulent boundary layer interactions". *Journal of Fluid Mechanics*, Vol. 182, pp. 291-314
- SPAUD, F. W. and FRISHETT, J. C. (1972) "Incipient separation of a supersonic, turbulent boundary layer including effects of heat transfer". *AIAA Journal*, Vol. 10, N° 7, pp. 915-922
- SURGET, J.; DELERY, J. and LACHARME, J.-P. (1977) "Holographic interferometry applied to the metrology of gaseous flows". *Proceedings SPIE*, Vol. 136
- VISBAL, M. and KNIGHT, D. (1984) "The Baldwin-Lomax turbulence model for two-dimensional shock wave / boundary layer interactions". *AIAA Journal*, Vol. 22, N° 7, pp. 921-928

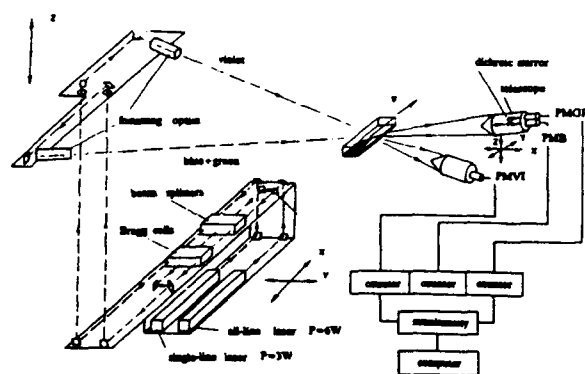


Fig. 1 - Schematic arrangement of the ONERA three-component LDV system

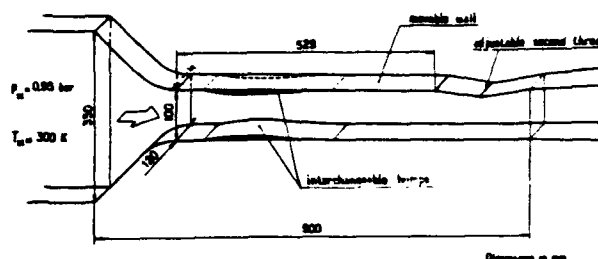


Fig. 2 - Arrangement of the two-dimensional transonic channel

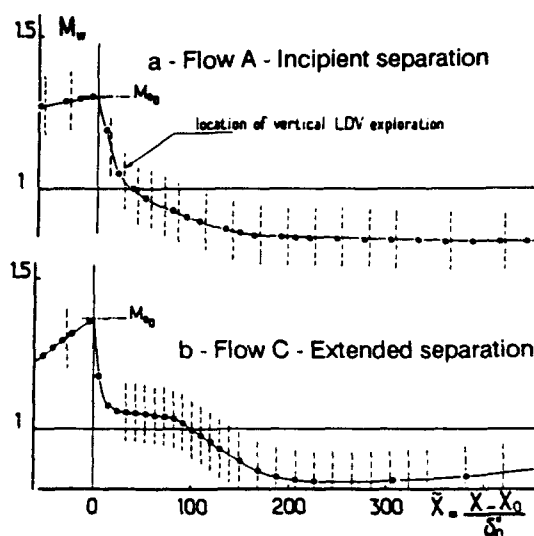


Fig. 3 - 2D transonic flow. "Wall" Mach number distributions

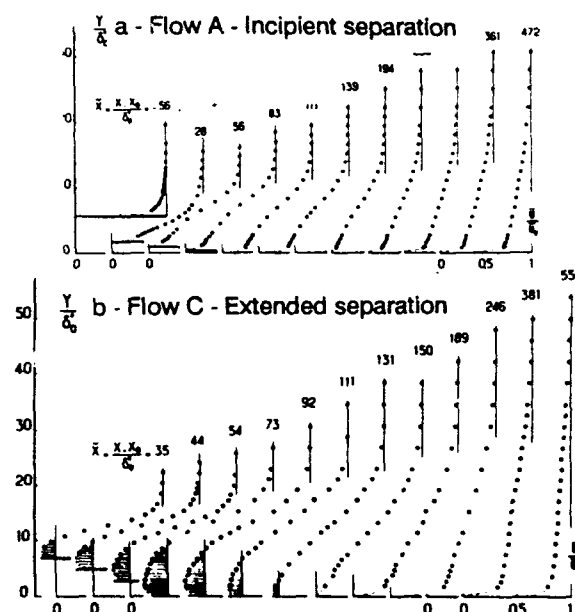


Fig. 4 - 2D transonic flow. Mean streamwise velocity profiles



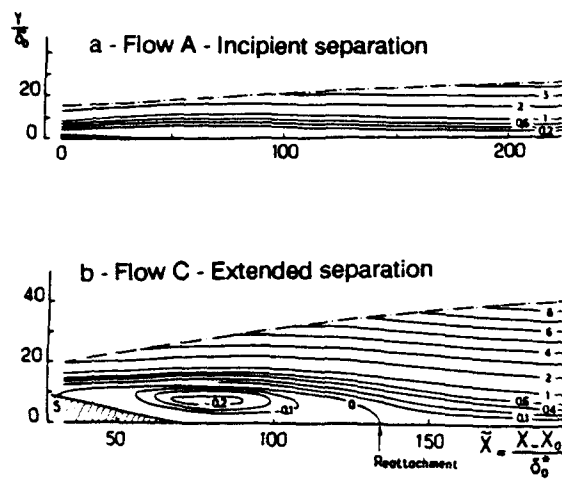


Fig. 5 - 2D transonic flow. Mean flow streamlines

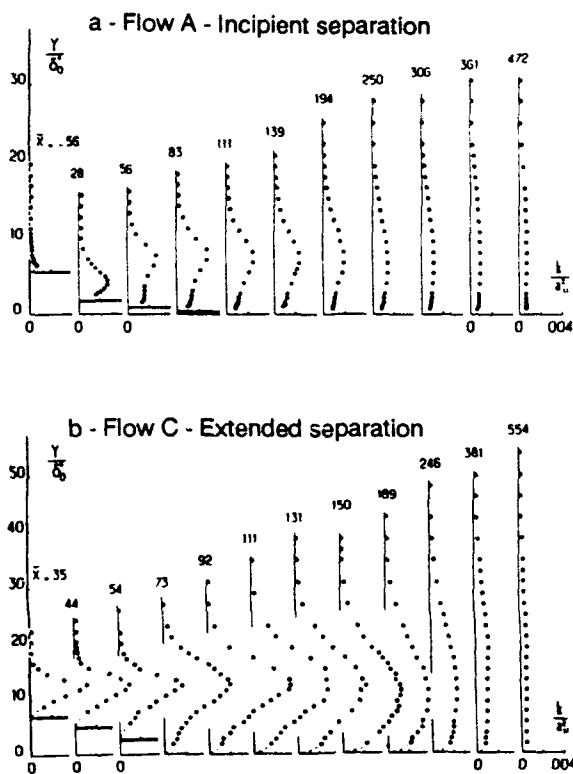


Fig. 6 - 2D transonic flow. Turbulence kinetic energy profiles

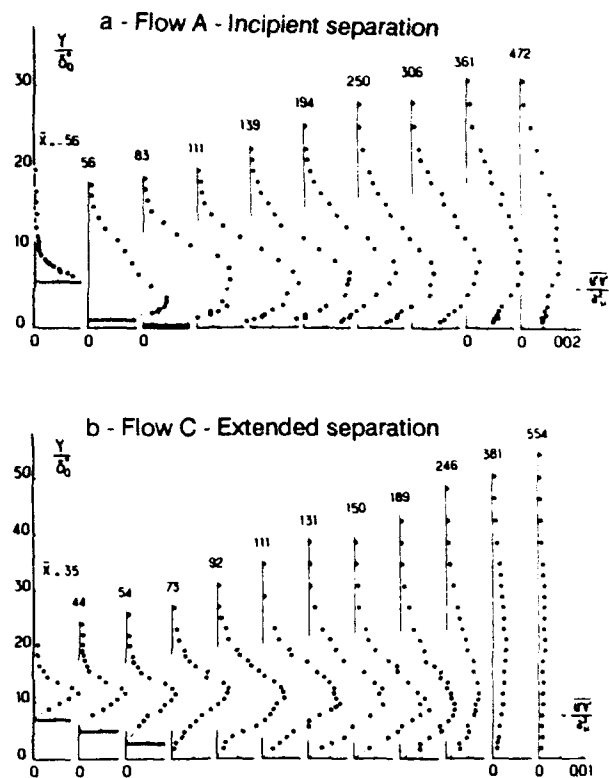


Fig. 7 - 2D transonic flow. Shear stress profiles

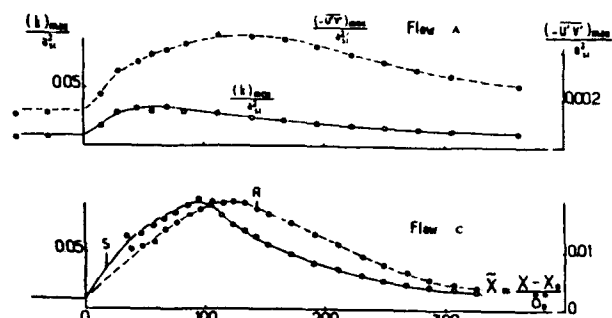


Fig. 8 - 2D transonic flow. Variation of maximum turbulence kinetic energy and shear stress.

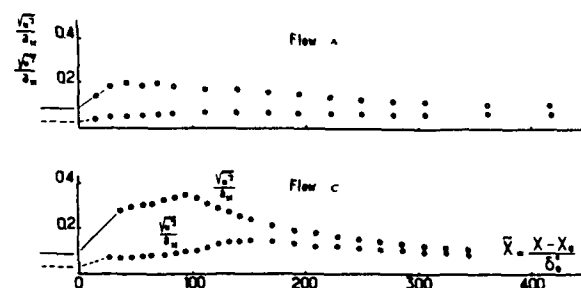


Fig. 9 - 2D transonic flow. Variation of maximum turbulence intensities



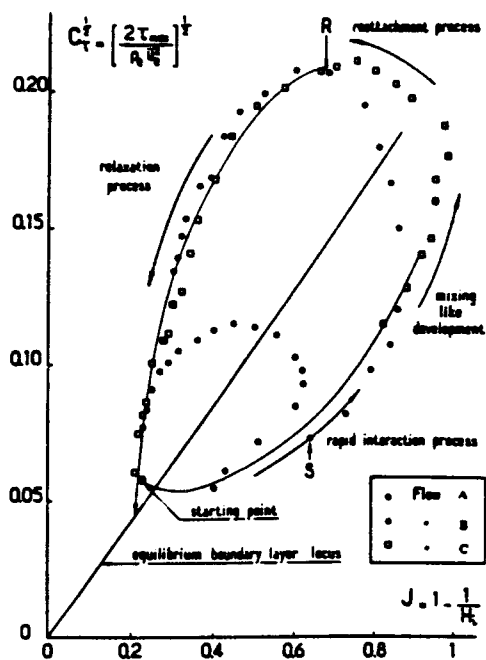


Fig. 10 - 2D transonic flow. Evolution of the maximum shear stress with the shape parameter

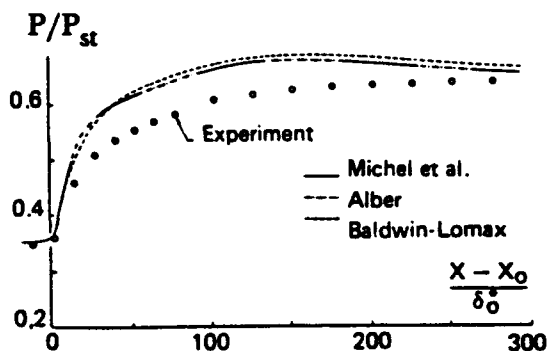


Fig. 11 - 2D transonic flow. Flow A. Wall pressure distributions. Equilibrium models

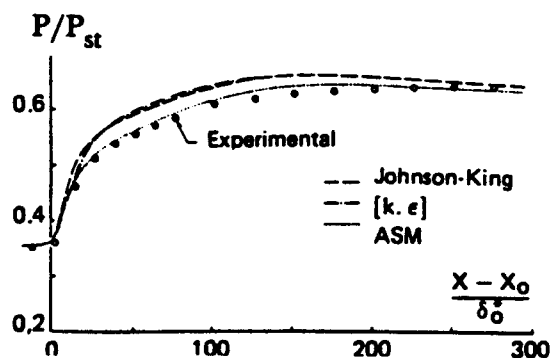


Fig. 12 - 2D transonic flow. Flow A. Wall pressure distributions. Non equilibrium models

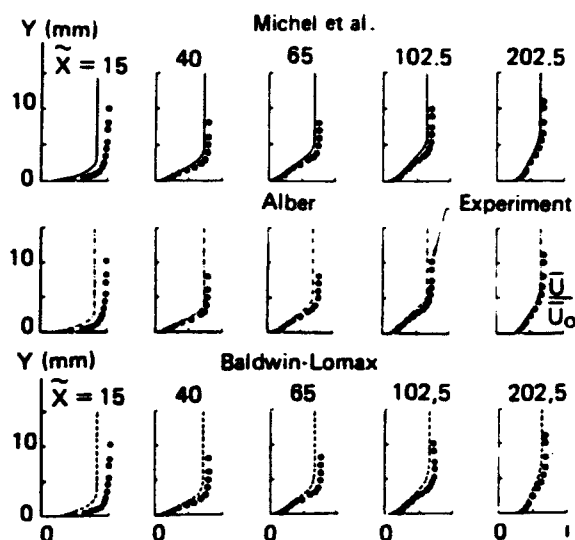


Fig. 13 - 2D transonic flow. Flow A. Mean velocity profiles. Equilibrium models

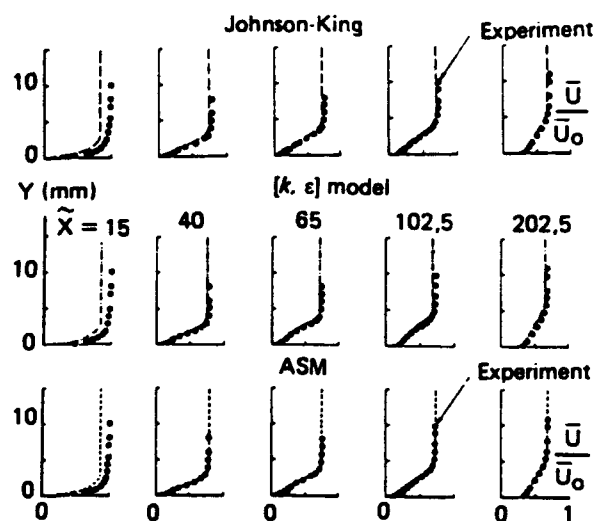


Fig. 14 - 2D transonic flow. Flow A. Mean velocity profiles. Non equilibrium models



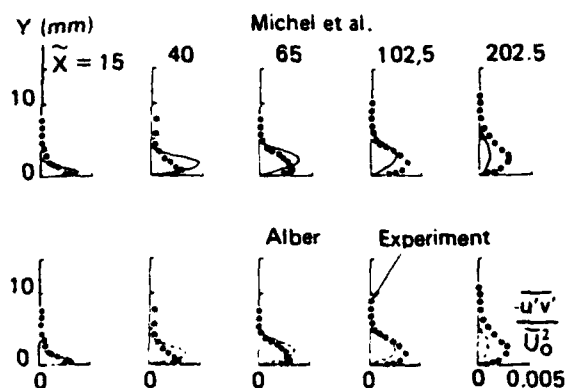


Fig. 15 - 2D transonic flow. Flow A. Shear stress profiles. Equilibrium models

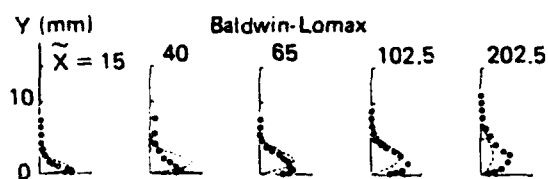


Fig. 16 - 2D transonic flow. Flow A. Shear stress profiles. Non equilibrium models

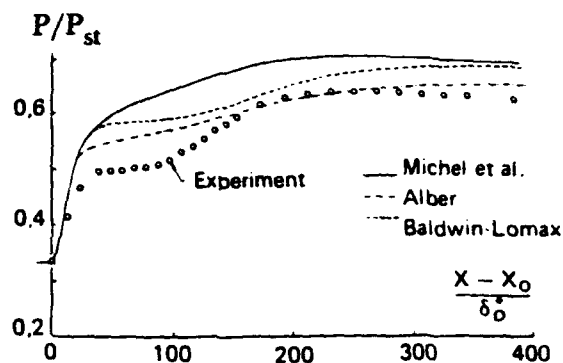


Fig. 17 - 2D transonic flow. Flow C. Wall pressure distributions. Equilibrium models

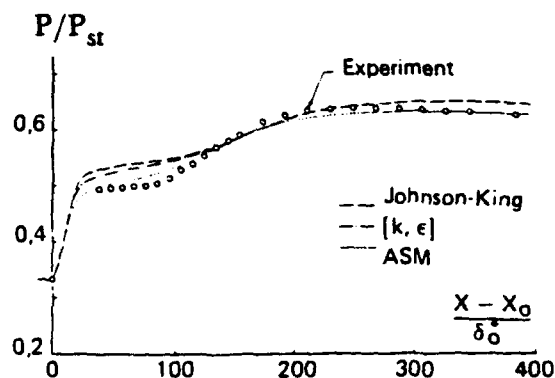


Fig. 18 - 2D transonic flow. Flow C. Wall pressure distributions. Non equilibrium models

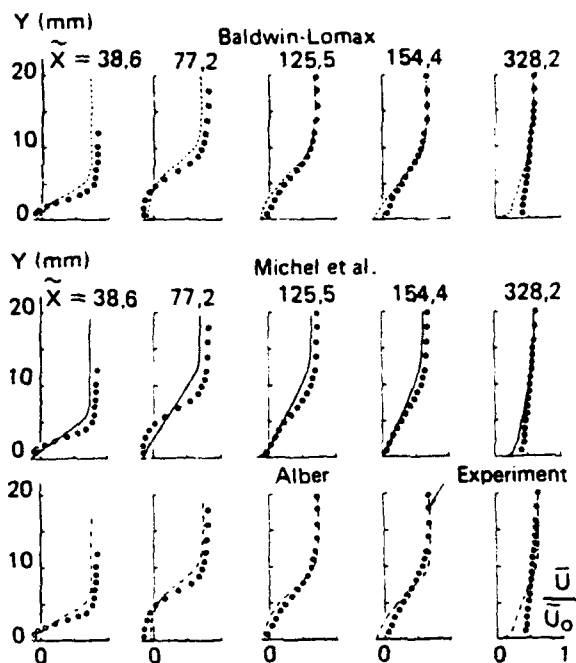
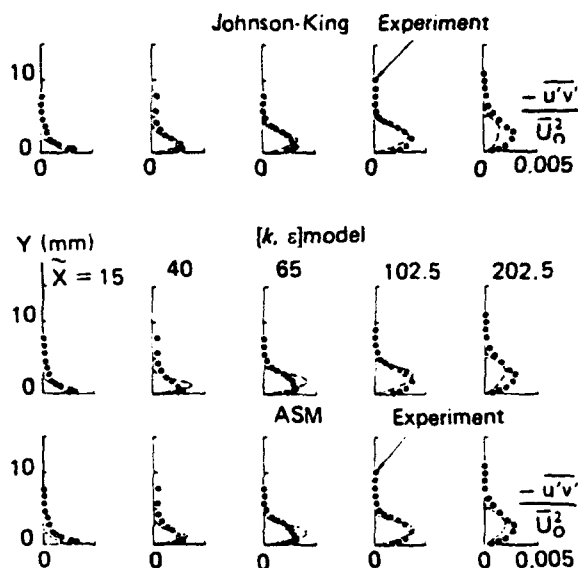


Fig. 19 - 2D transonic flow. Flow C. Mean velocity profiles. Equilibrium models



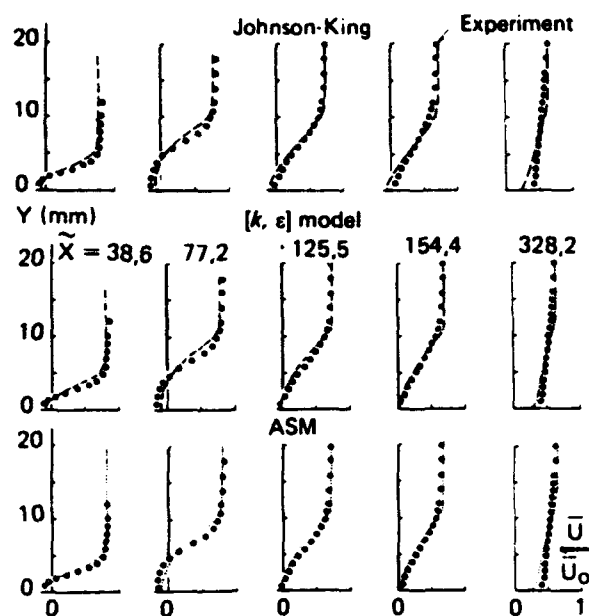


Fig. 20 - 2D transonic flow. Flow C. Mean velocity profiles. Non equilibrium models

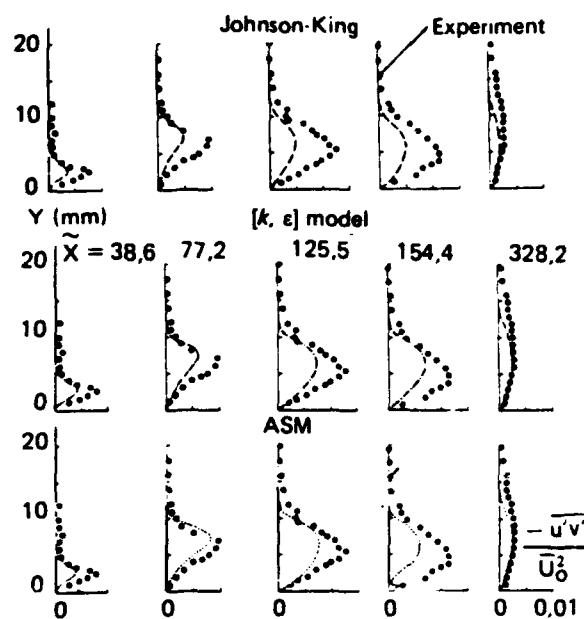


Fig. 22 - 2D transonic flow. Flow C. Shear stress profiles. Non equilibrium models

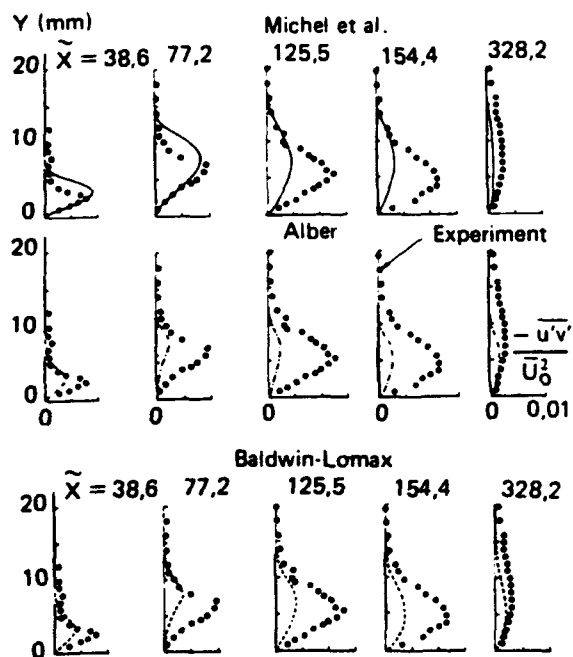
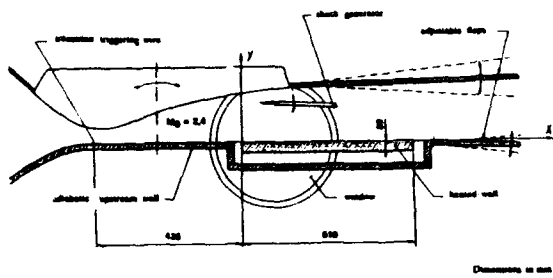


Fig. 21 - 2D transonic flow. Flow C. Shear stress profiles. Equilibrium models





**Fig. 23 - 2D supersonic flow. Test arrangement**

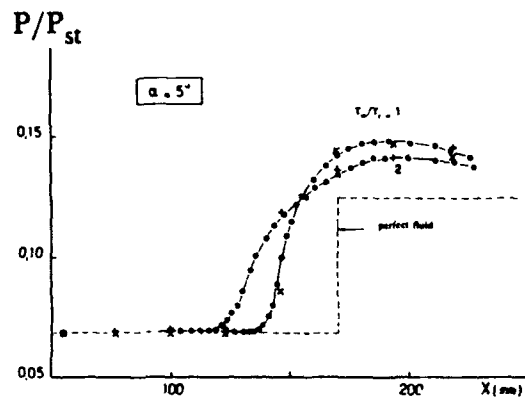
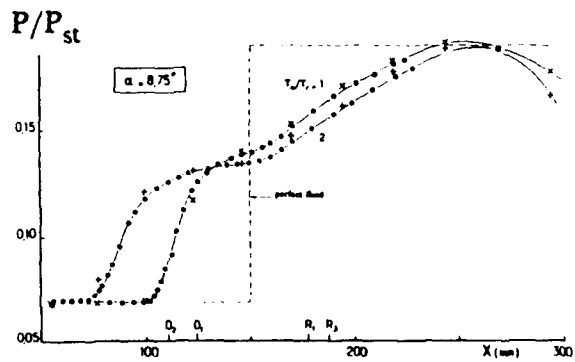


Fig. 24 - 2D supersonic flow. Wall pressure distributions. Interaction without separator



**Fig. 25 - 2D supersonic flow. Wall pressure distributions. Interaction with separation**

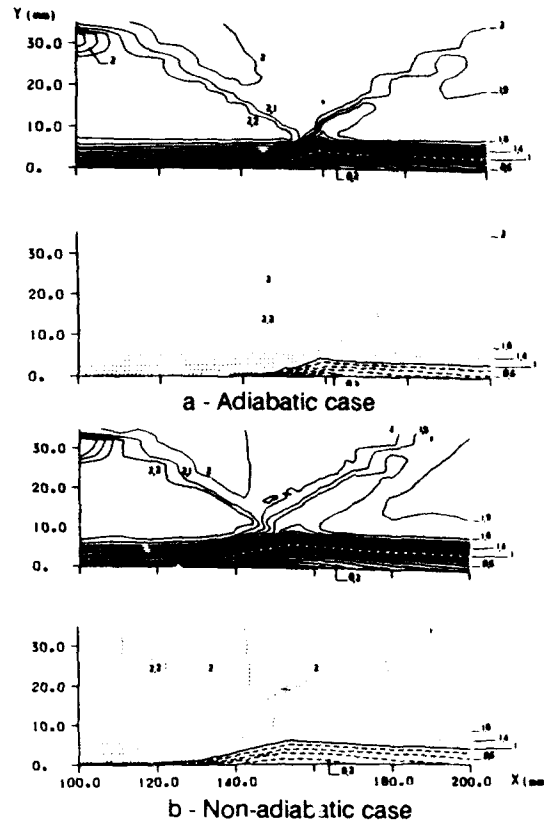
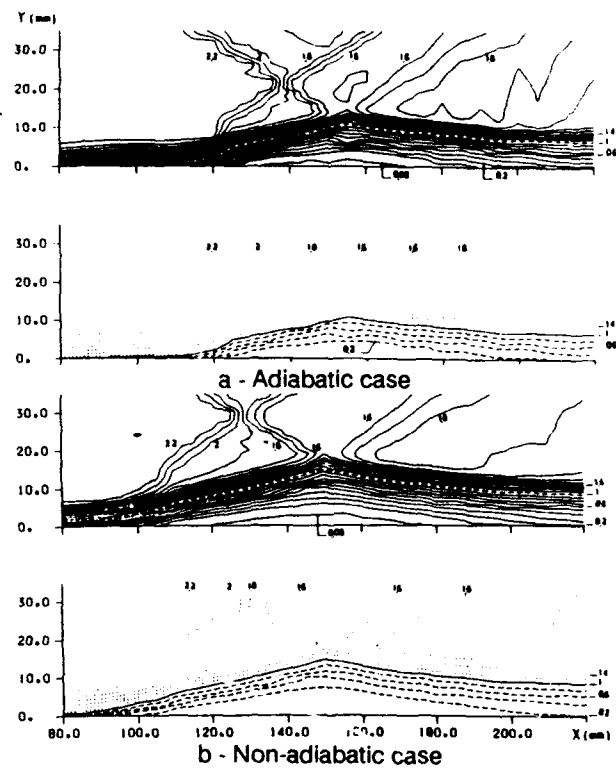


Fig. 26 - 2D supersonic flow. Iso-Mach lines. Interaction without separation.



**Fig. 27 - 2D supersonic flow. Iso-Mach lines. Interaction with separation.**



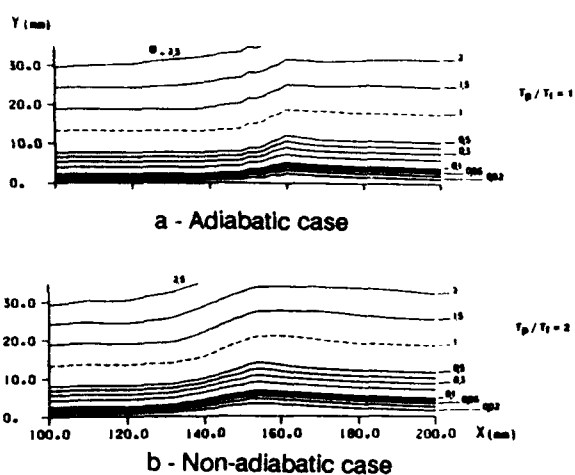


Fig. 28 - 2D supersonic flow. Mean flow streamlines. Interaction without separation.

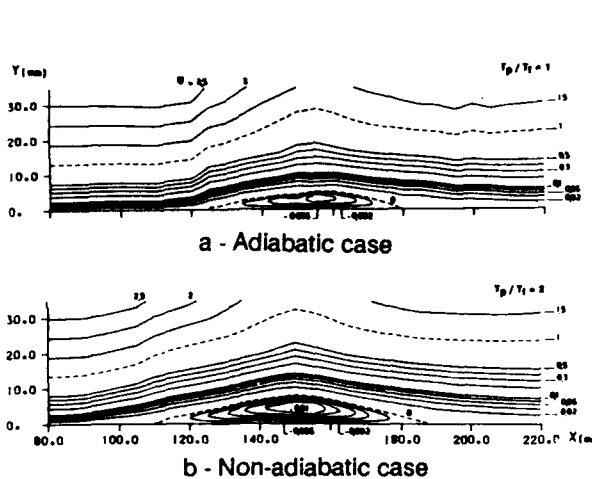
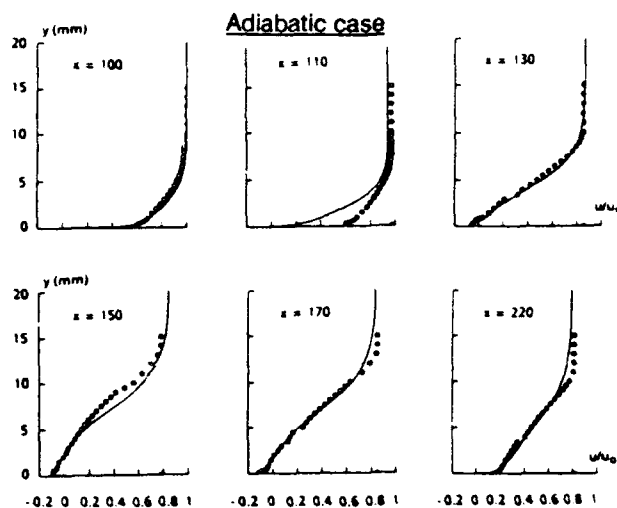


Fig. 29 - 2D supersonic flow. Mean flow streamlines. Interaction with separation.

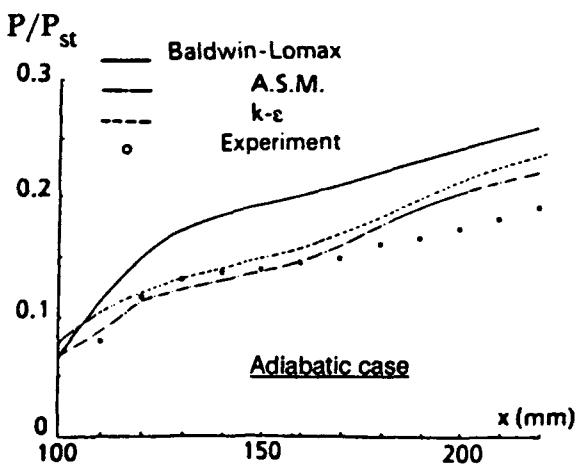
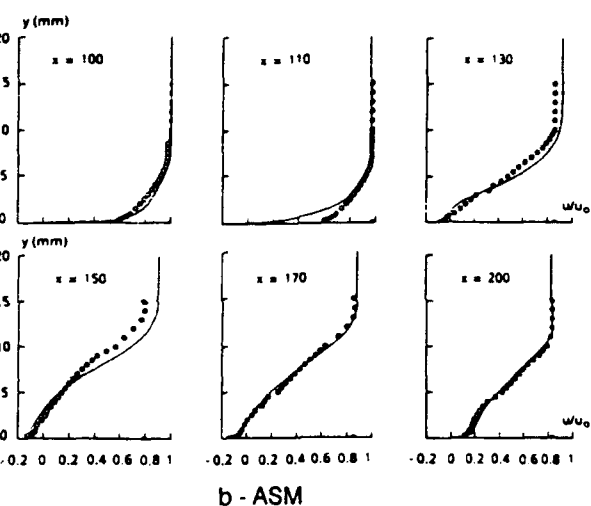
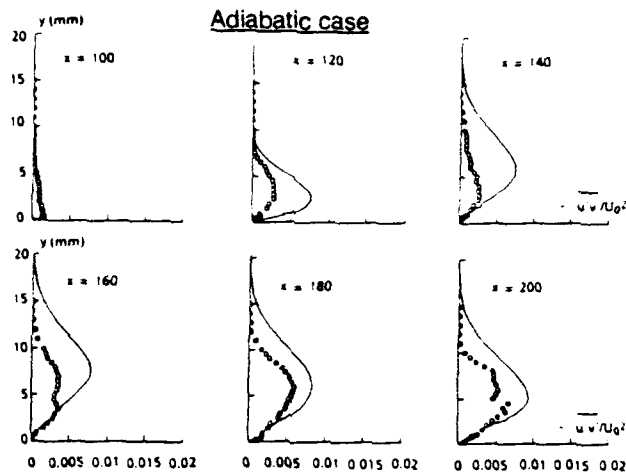


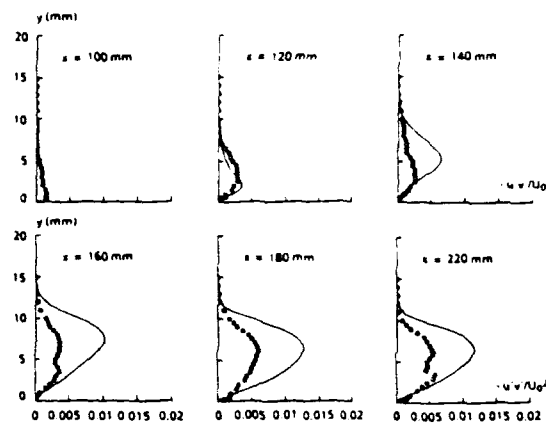
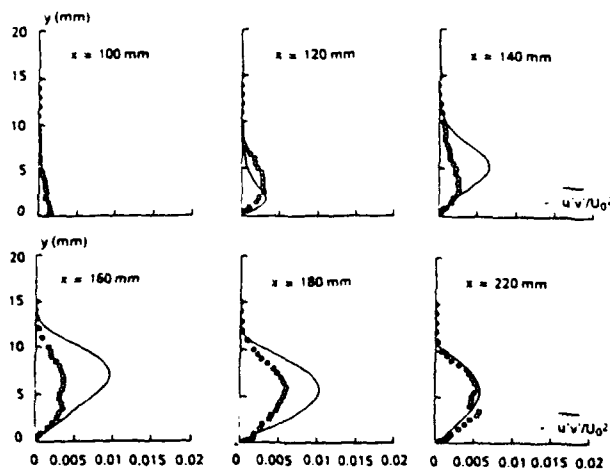
Fig. 31 - 2D supersonic flow. Mean velocity profiles. Interaction with separation.

Fig. 30 - 2D supersonic flow. Wall pressure distributions. Interaction with separation.

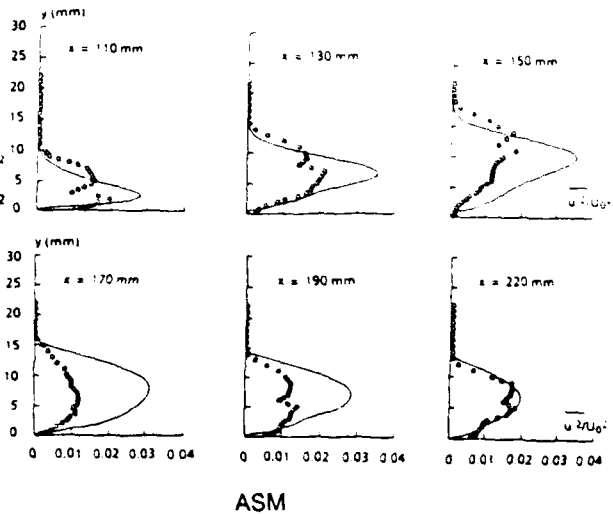




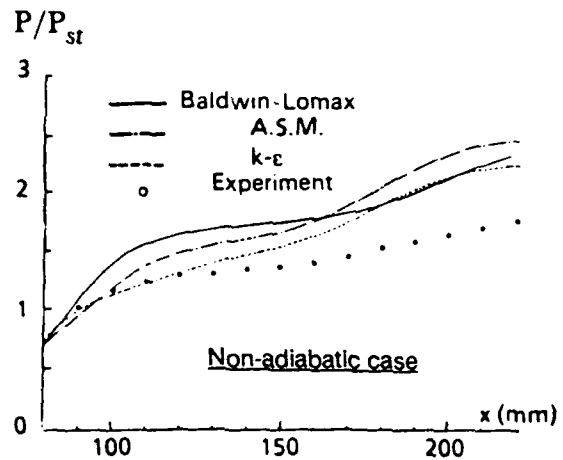
a - Baldwin - Lomax

Fig. 32 - Shear stress distribution  $T_{xy} = \mu(\partial u/\partial y)$ b -  $[k, \epsilon]$  model

c - ASM

Fig. 32 - 2D supersonic flow. Shear stress profiles. Interaction with separation.**Adiabatic case**

ASM

Fig. 33 - 2D supersonic flow. Normal stress profiles. Interaction with separation.Fig. 34 - 2D supersonic flow. Wall pressure distributions. Interaction with separation.



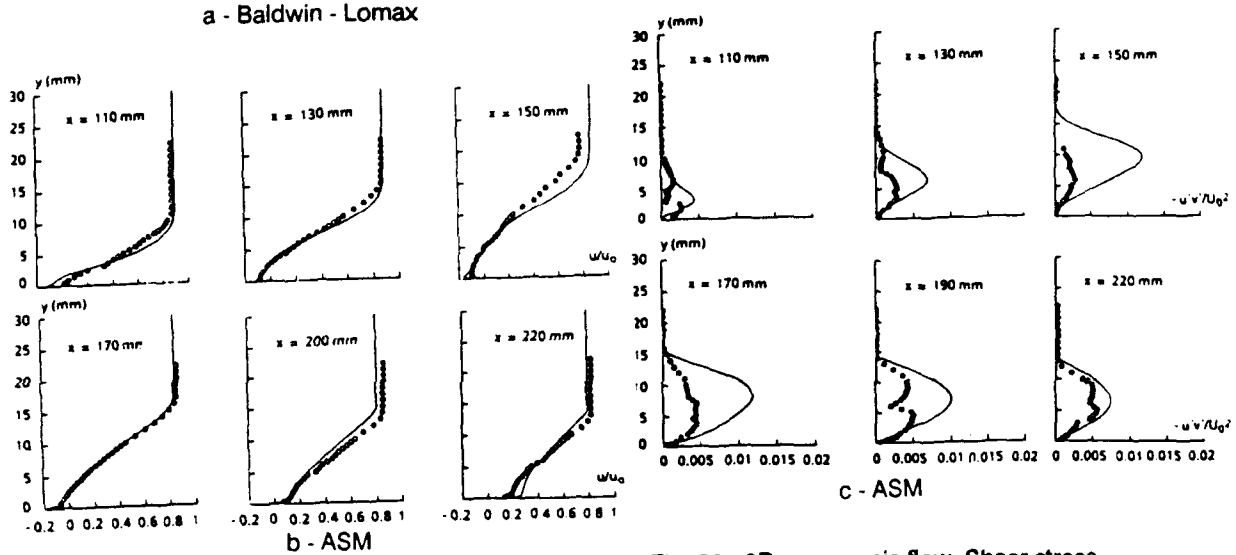
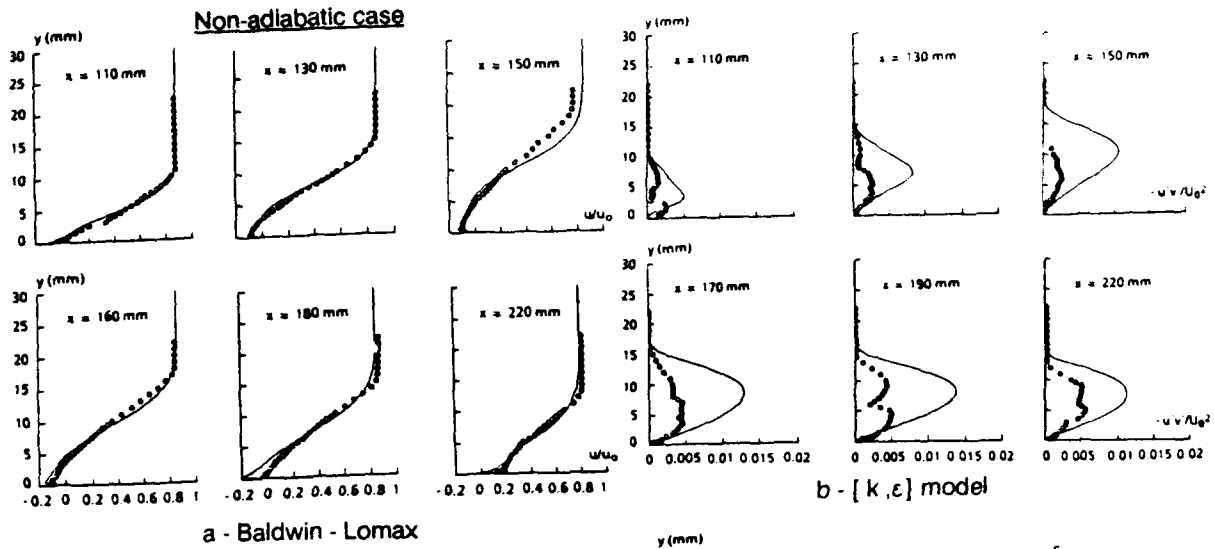


Fig. 35 - 2D supersonic flow. Mean velocity profiles. Interaction with separation.

Fig. 36 - 2D supersonic flow. Shear stress profiles. Interaction with separation.

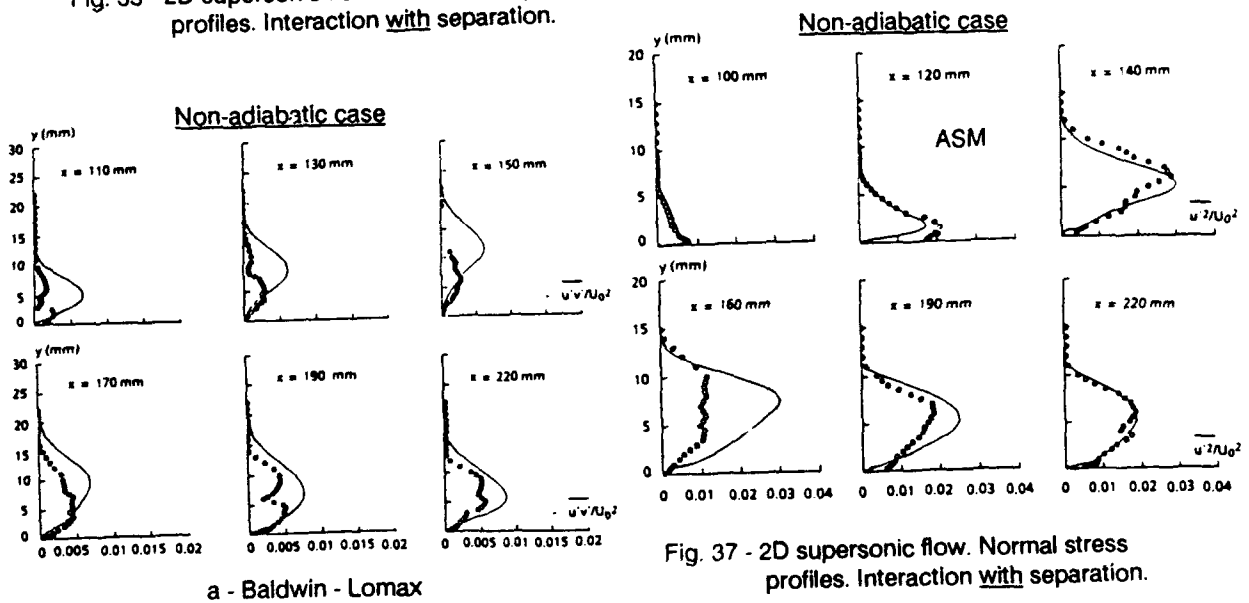


Fig. 37 - 2D supersonic flow. Normal stress profiles. Interaction with separation.



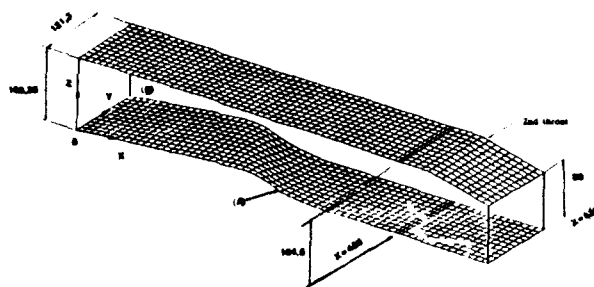


Fig. 38 - 3D transonic flow. Definition of the three-dimensional channel

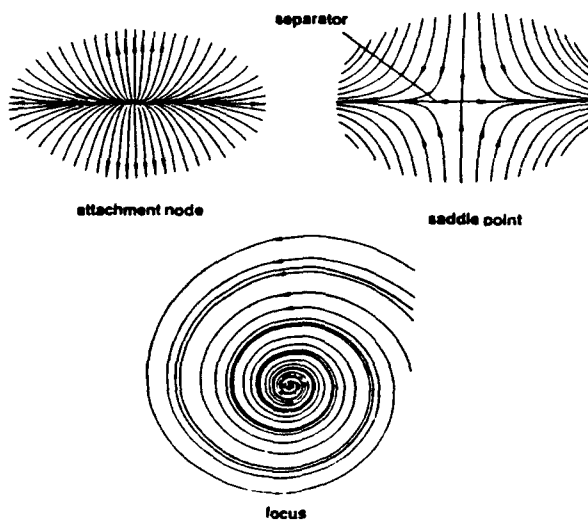
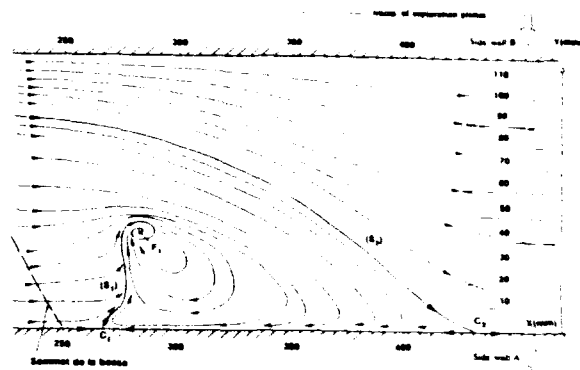
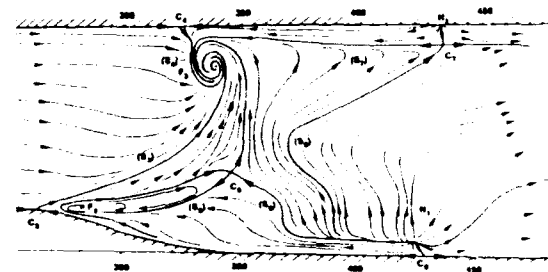


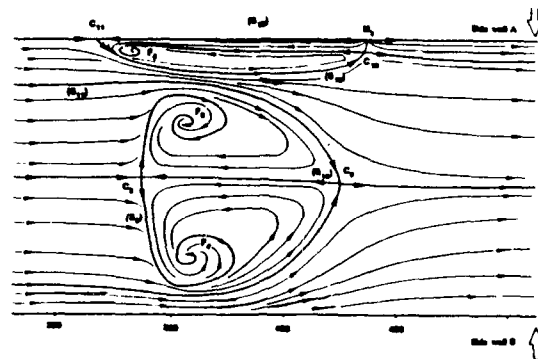
Fig. 39 - The main critical points



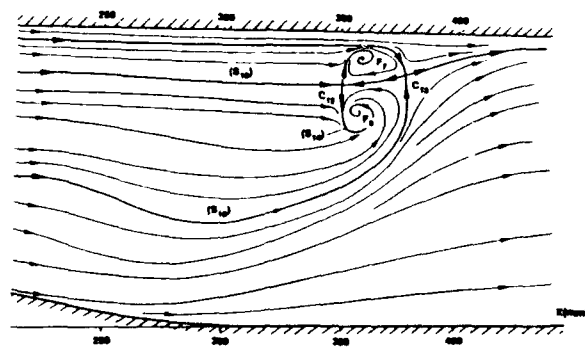
a - Bottom wall bearing the bump



b - Side wall A



c - Top wall



d - Side wall B

Fig. 40 - 3D transonic flow. Surface flow patterns



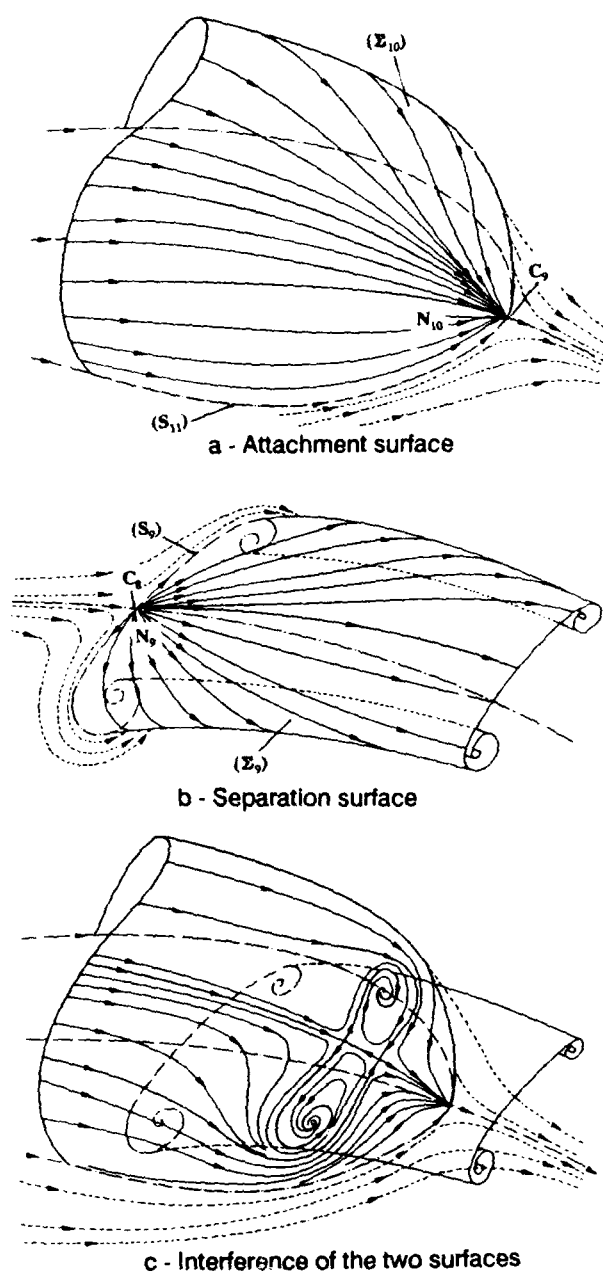
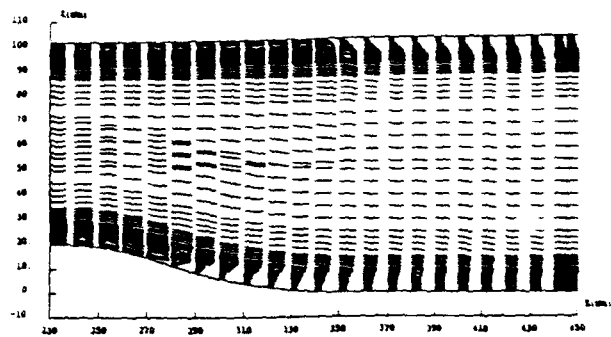
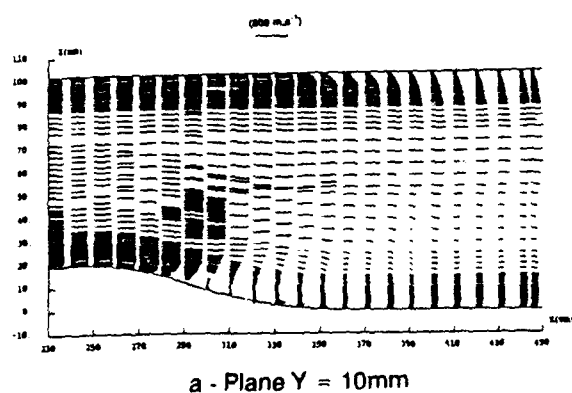
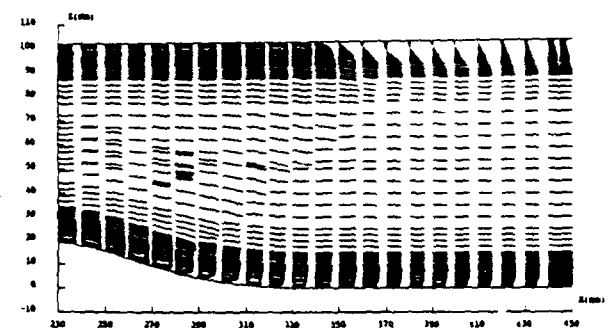


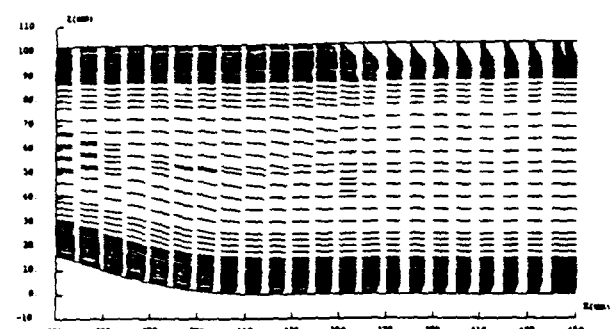
Fig. 41 - 3D transonic flow. Flow structure in the vicinity of the wall bearing the bump



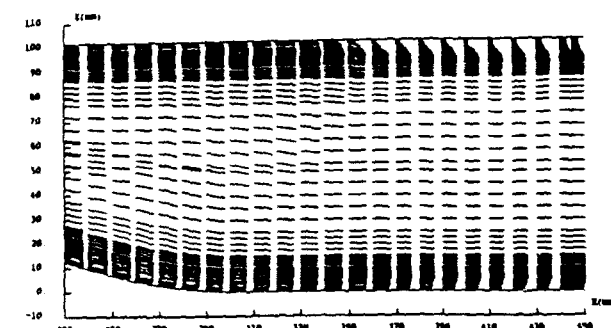
b - Plane Y = 30mm



c - Plane Y = 60mm



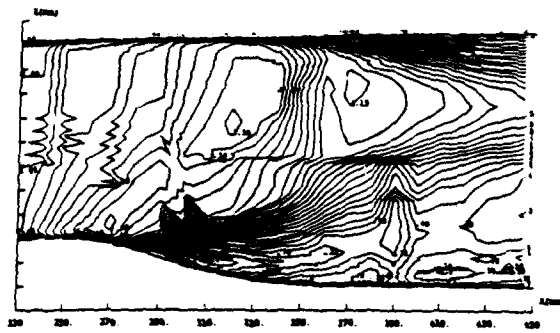
d - Plane Y = 90mm



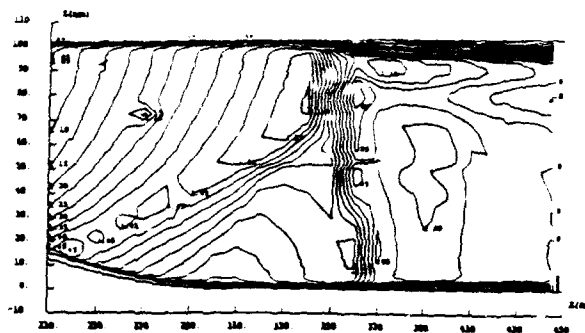
e - Plane Y = 110mm

Fig. 42 - 3D transonic flow. Mean velocity field in longitudinal planes



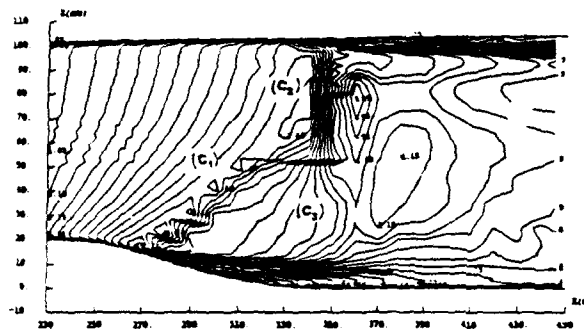


a - Plane Y = 10mm

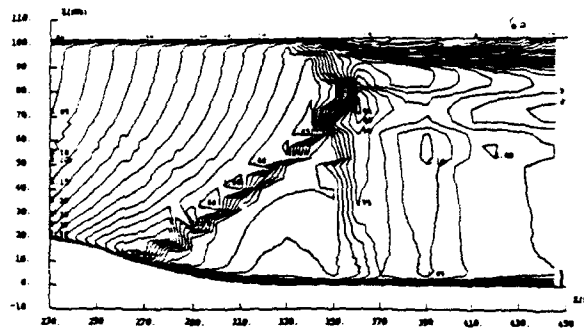


e - Plane Y = 110mm

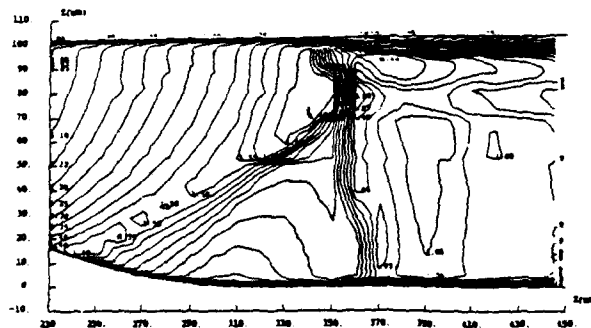
Fig. 43 - 3D transonic flow. Iso-Mach lines in longitudinal planes



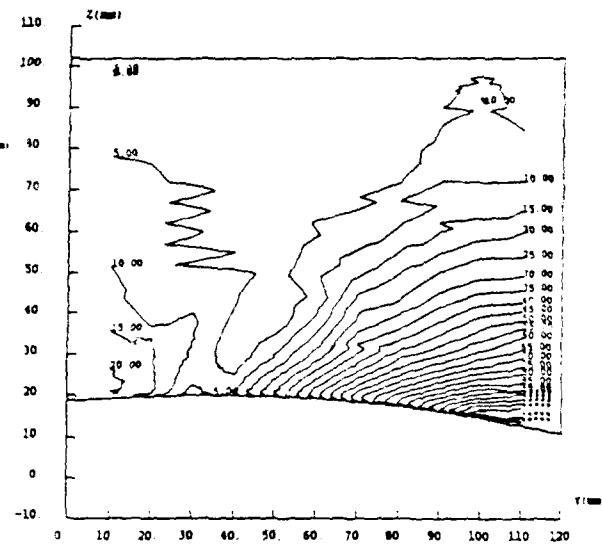
b - Plane Y = 30mm



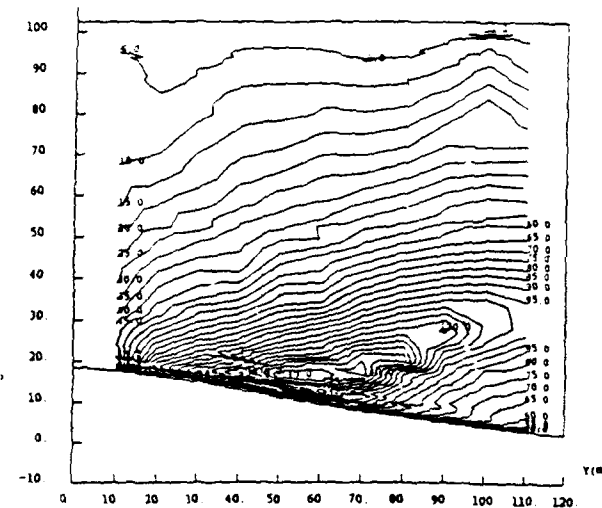
c - Plane Y = 60mm



d - Plane Y = 90mm

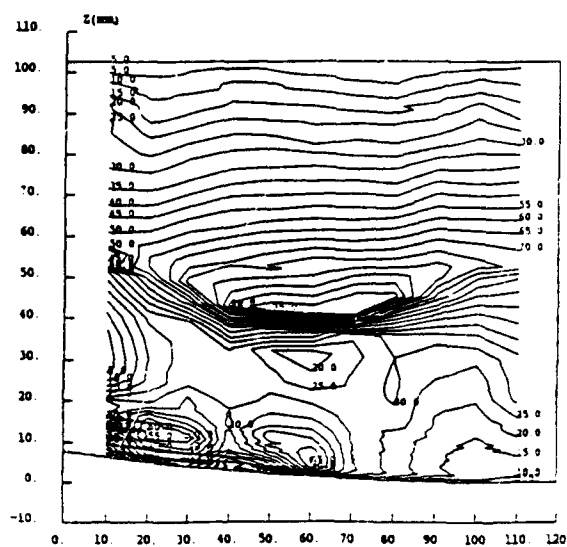


a - Plane X = 230mm

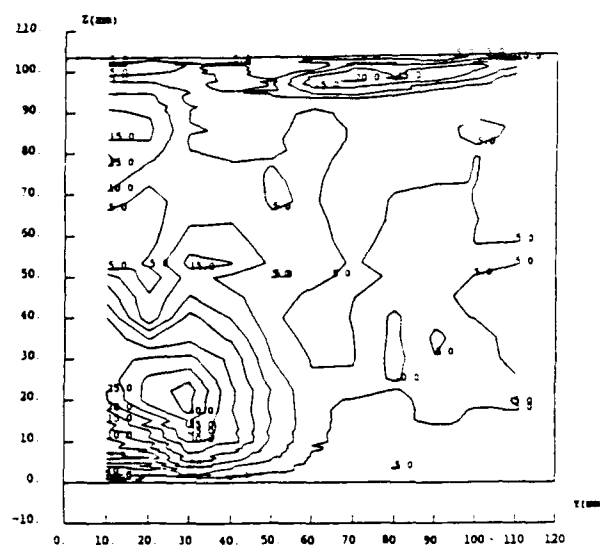


b - Plane X = 270mm

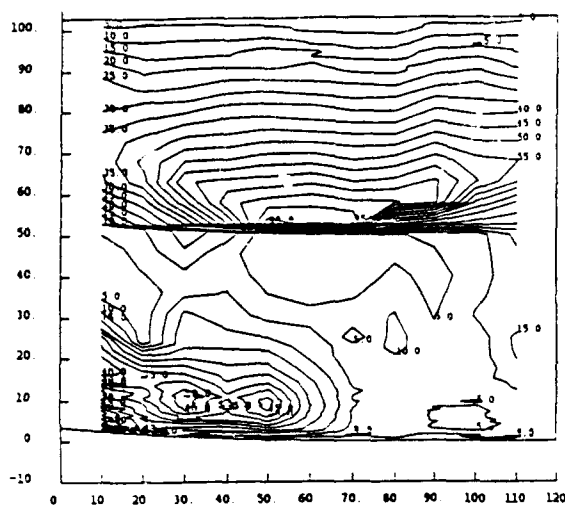




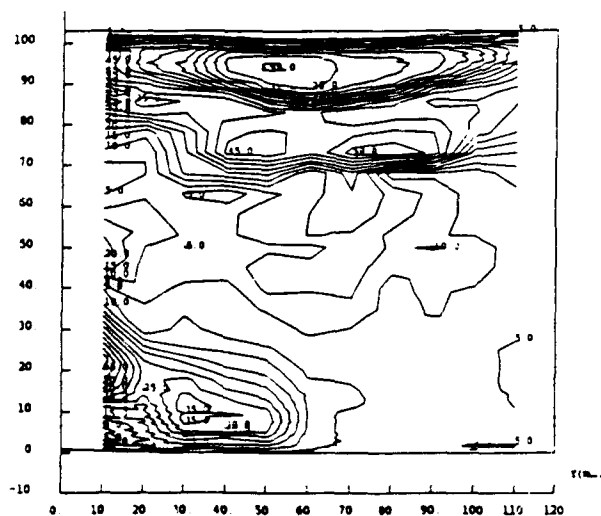
c - Plane X = 310mm



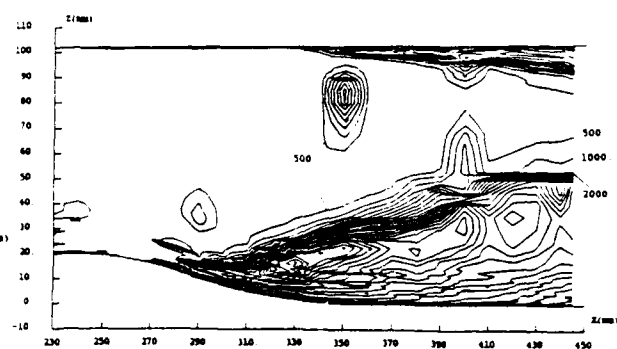
f - Plane X = 390mm



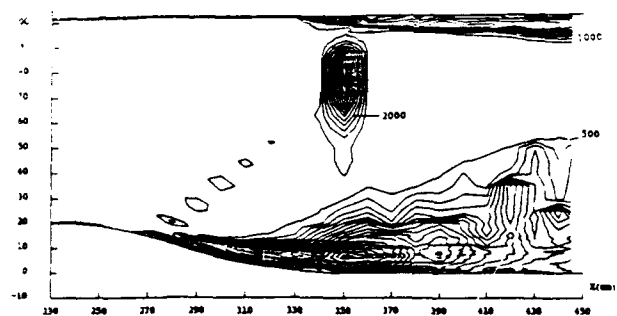
**d - Plane X = 330mm**



**e - Plane X = 350mm**



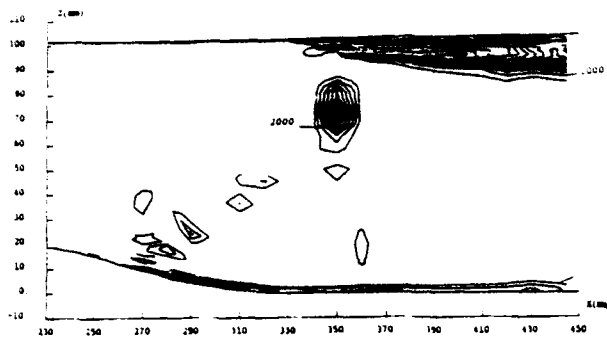
**a - Plane Y = 10mm**



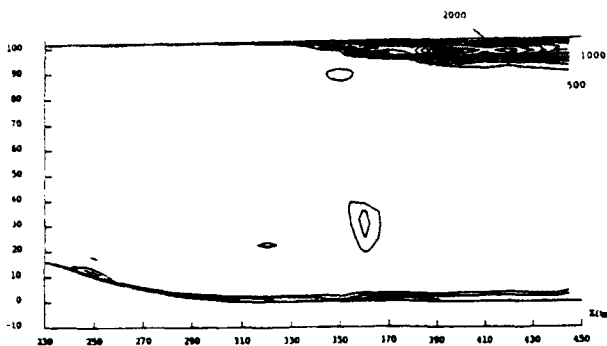
u - Plane Y = 30mm

Fig. 44 - 3D transonic flow. Amplitude of the velocity in transverse planes

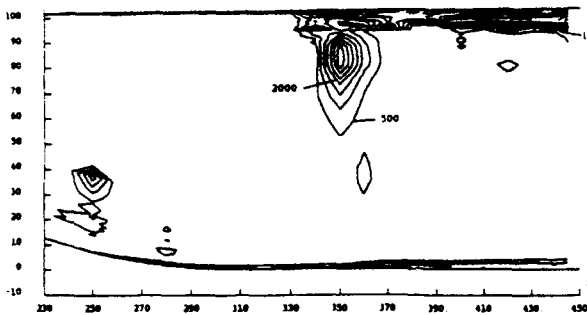




c - Plane Y = 60mm

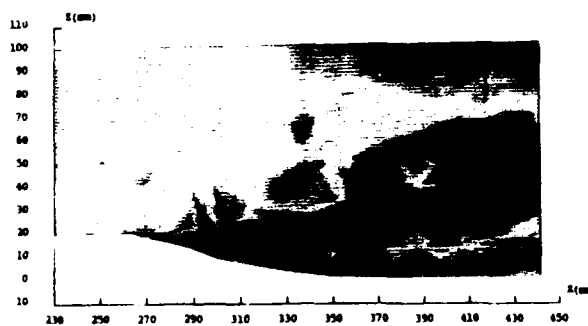


d - Plane Y = 90mm

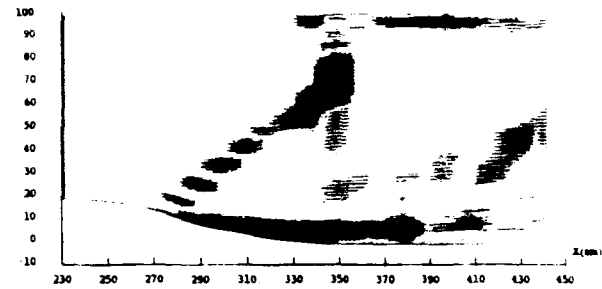


e - Plane Y = 110mm

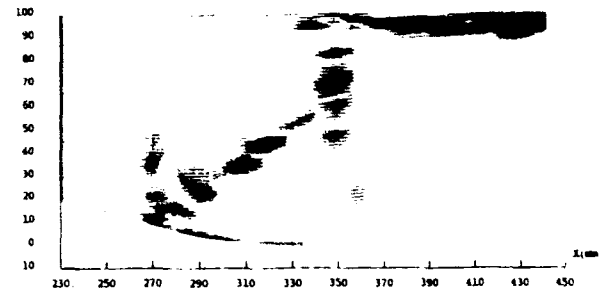
Fig. 45 - 3D transonic flow. Turbulence kinetic energy in longitudinal planes



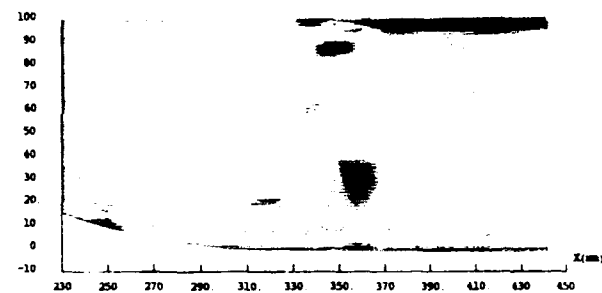
a - Plane Y = 10mm



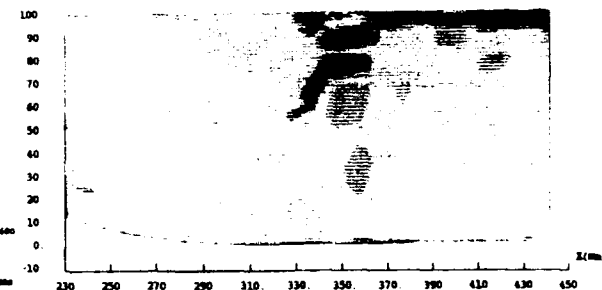
b - Plane Y = 30mm



c - Plane Y = 60mm



d - Plane Y = 90mm



e - Plane Y = 110mm

Fig. 46 - 3D transonic flow. Shear stress component  $u'w'$  in longitudinal planes



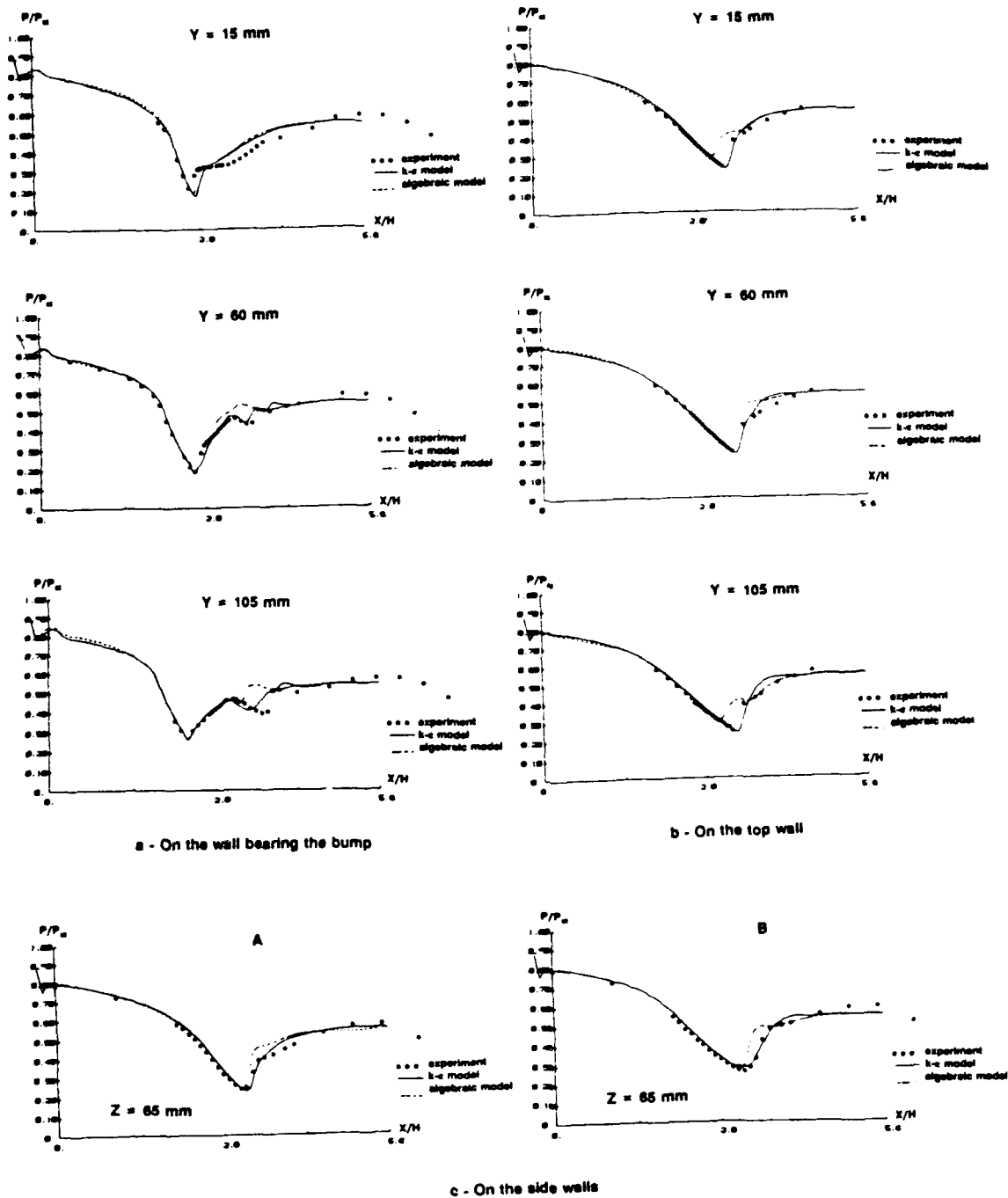


Fig. 47 - 3D transonic flow. Wall pressure distributions



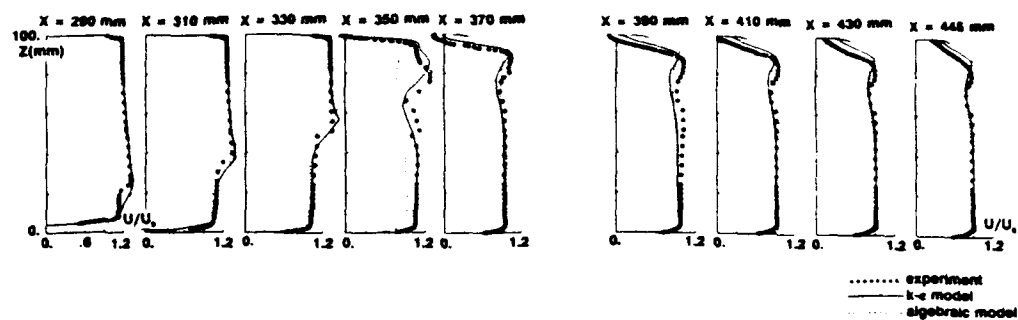


Fig. 48 - 3D transonic flow. Mean velocity profiles

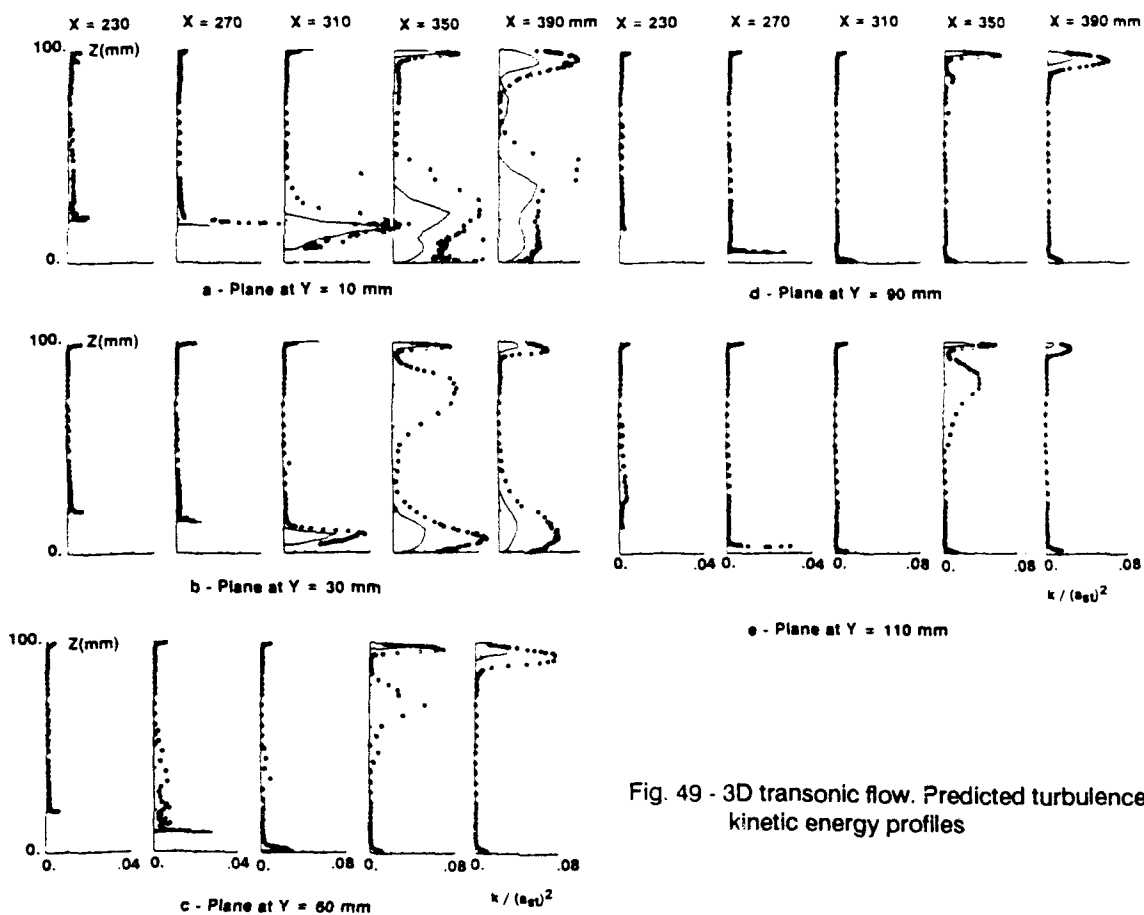


Fig. 49 - 3D transonic flow. Predicted turbulence kinetic energy profiles



TURBULENCE MODELLING FOR  
SHOCK WAVE/BOUNDARY LAYER INTERACTIONS  
SPECIFIC ISSUES AND EXAMPLES OF APPLICATIONS

D. Vandromme

Lab. de Mécanique des Fluides Numérique

CORIA - U.R.A. - C.N.R.S. 230

I.N.S.A. de Rouen, France

## 1. INTRODUCTION

Since the pionnering theory of Boussinesq /1/ and the first application indicated by Prandtl /2/, turbulence modelling has been continuously improved in order to allow effective prediction of turbulent flows. Since these early contributions, various methodologies were worked out to account properly for "complex" effects on turbulence. Among others, these "complex" effects are caused by curvature, body forces (gravitation or magnetic fields), unsteadiness and variable density. In fact, in real flows situations, it is often difficult to separate these effects, and the prediction of a flow configuration of industrial interest must always combine the simultaneous treatment of several effects. Depending on the application domain, some effects can be considered as dominant which allows neglect of others completely. As an example, geophysical flows in oceans are dominated by stratification and rotation, while compressibility or solid boundary effects can be neglected. In contrast, flows around an aircraft fuselage in real flight conditions are strongly influenced by compressibility and wall effects and not at all by gravitation or rotation. Because of the requirements imposed by a wide variety of industrial and aeronautical problems, one of the biggest challenges, during the last few years in the field of turbulence modelling has been the correct accountability of the variable density effects. Variable density can have different origins, which can result for instance from: i) the mixture of gases with different density, ii) a temperature gradient within an homogeneous fluid, iii) compressibility in high speed flows, or iv) reactive flows (for instance flames, chemical or gasdynamic laser flows). Unfortunately, until now, only a small fraction of the modelling effort has been devoted to these flows.

From an experimental viewpoint, the first works concerned equilibrium boundary layer along adiabatic smooth walls /3/, /4/, /5/ or compressible wakes /6/. These works led Morkovin /5/ to postulate that the dynamical field behaves like an incompressible one. From a different approach, Laufer /7/ came to an identical conclusion. Thus for some years, compressible problems have been handled with incompressible models, but with allowance for variation of mean density. The limits of such extensions are now beginning to be better understood /29/, /30/. Bradshaw /8/ reviewed the various domains of validity for Morkovin's hypothesis and noticed that it applies to flows where the density fluctuations



are moderate. Obviously, this excludes hypersonic boundary layers ( $Me > 5$ ) and the flows with strong pressure gradients such as shock-turbulent boundary layer interactions. Bradshaw concluded also that this approximation is not well suited for the supersonic shear layers. One of the conclusions of the 1972 Langley Free Shear Layer Conference /9/ confirmed that all then existing turbulence models were not adapted to the prediction of this type of flow.

Concerning the modelling, a limited number of significant results have been obtained so far. Most of the works consist in an analysis of existing incompressible models leading to an extension towards compressible flows, assuming that the existence of a variable density within the equations was sufficient to represent correctly the compressibility effects. Nevertheless, in presence of severe pressure gradients, these models do not produce satisfactory results /10/, /11/. In order to evaluate the respective importances of variable density and strict compressibility, Brown and Roshko /12/ studied experimentally the behaviour of a low speed mixing layer with variable density (helium-nitrogen mixing). They concluded with a complete independence of the mixing layer spreading rate with respect to the density ratio, bringing back the problem to compressibility effects.

## 2. BACKGROUND ASSUMPTIONS

As a starting point for any flow calculation, there are the Navier-Stokes equations. But, due to the large Reynolds number value of turbulent compressible flows, it is not yet conceivable to use direct simulation or even large eddy simulation with subgrid scale modelling for practical flow calculations. The first compressible turbulence direct simulation was reported in 1981 with Feiereisen's thesis /15/. At that time, the cost of a single simulation for a  $64 \times 64 \times 64$  mesh cube with periodic boundary conditions and constant shear was about 20 hours of CPU time on the ILLIAC IV computer (which had performances comparable to the Cray 1S machines). Even though simulation techniques are improving rapidly, we are still far from being able to predict complex compressible flows with simultaneously shock waves, separation mechanisms and eventually mixing and strong heat transfers. In fact, since Feiereisen's work, compressible turbulence simulations have been mostly devoted to 2-d configurations /16/, /28/, /104/.

To cope with this difficulty, it is preferable to work with a modified form of the Navier-Stokes equations. Rather than trying to produce a set of possible realizations and averaging to have a solution for the mean flow, the instantaneous Navier-Stokes equations can be submitted to a statistical treatment first, and then a single solution will represent all the characteristics of the mean flow. Then, the solution does not carry any information on the turbulence fluctuations. The averaging process can be considered as a filter. Nevertheless, turbulence information is still available through new specific turbulent variables which are correlations between fluctuating variables.

### 2.1. Averaging the variables

But let us examine more deeply the implications of this statistical treatment by defining the probability density function (pdf) for  $f$  to be inside the interval  $[a, b]$ .

$$\text{Probability } (a \leq f \leq b) = \int_a^b P(f) df \quad (2-1)$$

That definition implies naturally that the probability becomes equal to unity if  $a$  and  $b$  tend respectively towards  $-\infty$  or  $+\infty$ :



$$\int_{-\infty}^{+\infty} P(f) df = 1 \quad (2-2)$$

Thus the first moment of this pdf gives the mean value of  $f$ :

$$\langle f \rangle = \int_{-\infty}^{+\infty} f P(f) df \quad (2-3)$$

In practice, the possible variations of  $\langle f \rangle$  in space and time will depend only of the behaviour of  $P(f)$ . In place of this statistical average, which is formally an ensemble average, it is possible to substitute a time average if the ergodicity is verified. This requires a clear definition of the time involved by the averaging operator. Indeed, all the practical turbulent flows are neither steady nor completely homogeneous. Therefore the averaging intervals will have to be bounded, both in space and time. These intervals must be sufficiently large, compared to the characteristic scales of the turbulence but also small with respect to the macroscopic changes of the flow. Let  $T$  be a bounded time, the time average can be defined as:

$$\langle f(t) \rangle = \frac{1}{T} \int_0^T f(t + \tau) d\tau \quad (2-4)$$

The definition (3) yields, for two random variables  $f$  and  $g$ , the following relationships:

$$\begin{aligned} \langle f + g \rangle &= \langle f \rangle + \langle g \rangle \\ \langle f \cdot g \rangle &= \langle f \rangle \cdot \langle g \rangle \neq \langle f \cdot g \rangle \\ \left\langle \frac{df}{d\xi} \right\rangle &= \frac{d}{d\xi} \langle f \rangle \quad \text{if } \xi \in [x_1, x_2, x_3, t] \end{aligned} \quad (2-5)$$

Boussinesq /1/ and Reynolds /17/ established incompressible flows equations by applying this time averaging to the continuity and momentum equations. To do so, quantities such as velocity, pressure or density are split into a mean and a fluctuating component. This method was extended to compressible flows by Shubauer and Tchen /18/, Hinze /19/ and several other authors. When compared to the instantaneous equations, the averaged equations contain new terms, which have no counterpart in the original equations. These new terms are made of correlations between velocity fluctuations or between velocity and density fluctuations. The velocity correlations are the Reynolds stresses and represent the forces due to the turbulent agitation. Evidence of these new terms can be obtained quickly by examining the continuity equation for a variable density flow:

$$\frac{\partial \rho}{\partial t} + \frac{\partial}{\partial x_\alpha} (\rho v_\alpha) = 0 \quad (2-6)$$

$\rho$  is the density and  $v_\alpha$  are the velocity components with respect to the  $\alpha$  direction. Splitting of these instantaneous variables into mean  $(\bar{\phantom{x}})$  and fluctuating parts  $(\phantom{x})'$  yields

$$\begin{aligned} \rho &= \bar{\rho} + \rho' \\ v_\alpha &= \bar{v}_\alpha + v'_\alpha \end{aligned} \quad (2-7)$$

and the first consequences of the definition (2-3) are



$$\begin{aligned}\overline{\rho'} &= 0 \\ \overline{v'_\alpha} &= 0\end{aligned}\quad (2-8)$$

Thus, after averaging, the continuity equation is:

$$\frac{\partial \rho}{\partial t} + \frac{\partial}{\partial x_\alpha}(\rho v_\alpha) + \frac{\partial}{\partial x_\alpha}(\overline{\rho' v'_\alpha}) = 0 \quad (2-9)$$

The averaging process has introduced into the mean continuity equation the new variable,  $\overline{\rho' v'_\alpha}$ . Therefore, the closure of the simplest set of mean equations will be linked at least, to the knowledge of these correlations. Other authors (Hesselberg /20/, Dedeant and Wehrle /21/, Van Mieghen and Dufour /22/, Blackadar /23/ and Favre /24/) have derived mean equations by weighting the averaging operator with the instantaneous density. Later, Favre /25/ extended that formalism to all the dependent variables, except the density and the pressure.

That type of averaging can also be formulated statistically like an ordinary time average, by introducing the joint p.d.f.  $P(\rho, \phi)$  for  $\phi$  and  $\rho$ ,  $\phi$  being any dependent variable besides density and pressure (see for instance Bilger /26/). Let us define a density weighted pdf for a variable  $\phi$ :

$$\widetilde{P}(\phi) = \frac{1}{\rho} \int_0^\infty \rho P(\rho, \phi) d\rho \quad (2-10)$$

Thus mass weighted averages, covariances and higher order moments can be defined simply from this density weighted pdf as:

$$\begin{aligned}\bar{\phi} &= \frac{\overline{\rho\phi}}{\rho} = \int \phi \widetilde{P}(\phi) d\phi \\ \bar{\phi}''^2 &= \frac{\overline{\rho\phi^2}}{\rho} = \int (\phi - \bar{\phi})^2 \widetilde{P}(\phi) d\phi \\ \bar{\phi}''^3 &= \frac{\overline{\rho\phi^3}}{\rho} = \int (\phi - \bar{\phi})^3 \widetilde{P}(\phi) d\phi\end{aligned}\quad (2-11)$$

and also  $\widetilde{f(\phi)} = \int f(\phi) \widetilde{P}(\phi) d\phi$

In fact we can consider these two possible types of averaging simultaneously:

- 1) the classical time averaging based on a centered operator:

$$\begin{aligned}\phi &= \bar{\phi} + \phi' \\ \bar{\phi} &= \frac{1}{T} \int_T \phi(t) dt; \quad \overline{\phi'} = 0\end{aligned}\quad (2-12)$$

- 2) the mass weighted averaging, which is also a time averaging, but uncentered by the presence of the density:

$$\begin{aligned}\phi &= \bar{\phi} + \phi'' \\ \bar{\phi} &= \frac{\overline{\rho\phi}}{\rho}; \quad \overline{\phi''} \neq 0\end{aligned}\quad (2-13)$$

From the definitions, it is easy to derive a set of relations linking the two formalisms /27/:



$$\begin{aligned}
 \bar{\phi} &= \phi + \frac{\overline{\rho' \phi'}}{\rho} \\
 \overline{\rho \phi'} &= 0 \\
 \overline{\phi''} &= -\frac{\overline{\rho' \phi''}}{\rho} = -\frac{\overline{\rho' \phi'}}{\bar{\rho}} \\
 \phi_1'' \phi_2'' &= \phi_1' \phi_2' - \frac{1}{\bar{\rho}^2} \overline{\rho' \phi_1' \rho' \phi_2'} + \frac{1}{\bar{\rho}} \overline{\rho' \phi_1' \phi_2'}
 \end{aligned} \tag{2-14}$$

An immediate advantage of the Favre averaging appears when writing the mean continuity equation:

$$\frac{\partial \bar{\rho}}{\partial t} + \frac{\partial \bar{\rho} \bar{v}_\alpha}{\partial x_\alpha} = 0 \tag{2-15}$$

Equation (2-15) has now a form strictly similar to its instantaneous version, since the density velocity correlations do not appear explicitly. Similarly, all the convective parts in the motion equations are free of these density correlations. Thus the mass-weighted averaging is helpful to simplify the formulation of the turbulent equations when density varies, but it does not solve the problem of closing the set of equations. Two significant drawbacks are to be pointed out here:

The first one concerns the interpretation of the results when comparing measurements with calculated values. The mass weighted velocity, for instance, is well adapted to comparison with hot wire measurements, but not to the velocity obtained from a LDV device for which the centered time averaged quantity is more appropriate. Analogous remark could be made for heat flux or concentration measurements.

The second remark will become more obvious later, when the equation for the conservation of the dissipation rate of the turbulent kinetic energy is written. That equation, which is recognized as a weakness of several turbulence models is already complex in incompressible flows. Excepting the case of the convection terms, its formulation in mass weighted variables is still more complex, so that there is no hope to model it in a term-to-term manner and only a "global" modelling have been successfully used so far.

## 2.2. Open forms of the turbulent equations

Introduction of Favre decomposition and time averaging the equations yields forms which are open. The expression of the new unknowns is one aspect of the general problem of the closure. As natural convection will always be negligible in front of forced convection in the applications presented at the end of these notes, buoyancy terms are not included in the following equations.

### 2.2.1. Continuity or mass conservation

The instantaneous form of this equation is:

$$\frac{\partial \rho}{\partial t} + \frac{\partial}{\partial x_\alpha} (\rho v_\alpha) = 0 \tag{2-16}$$

The time average produces a closed equation similar (in form):

$$\frac{\partial \bar{\rho}}{\partial t} + \frac{\partial}{\partial x_\alpha} (\bar{\rho} \bar{v}_\alpha) = 0 \tag{2-17}$$



### 2.2.2. Momentum conservation

Instantaneous form for the  $v_\alpha$  component is:

$$\frac{\partial}{\partial t}(\rho v_\alpha) + \frac{\partial}{\partial x_\beta}(\rho v_\alpha v_\beta) = \frac{\partial}{\partial x_\beta}(\sigma_{\alpha\beta}) \quad (2-18)$$

with the viscous stress defined by (assuming that the Stokes Law is verified:  $(2\mu + 3\lambda = 0)$ :

$$\sigma_{\alpha\beta} = -p \delta_{\alpha\beta} + \mu S_{\alpha\beta} \quad (2-19)$$

$p$  is the pressure,  $\delta_{\alpha\beta}$  is the Kronecker symbol and  $\mu$  the molecular viscosity coefficient.  $S_{\alpha\beta}$  corresponds to the strain tensor for a compressible fluid:

$$S_{\alpha\beta} = \left( \frac{\partial v_\alpha}{\partial x_\beta} + \frac{\partial v_\beta}{\partial x_\alpha} \right) - \frac{2}{3} \delta_{\alpha\beta} \frac{\partial v_\gamma}{\partial x_\gamma} \quad (2-20)$$

For turbulent flows, equation (2-18) becomes:

$$\frac{\partial}{\partial t}(\bar{\rho} \tilde{v}_\alpha) + \frac{\partial}{\partial x_\beta}(\bar{\rho} \tilde{v}_\beta \tilde{v}_\alpha) = -\frac{\partial}{\partial x_\beta}(\overline{\rho v_\beta'' v_\alpha''}) - \frac{\partial p}{\partial x_\alpha} + \frac{\partial}{\partial x_\beta}(\mu \overline{S_{\beta\alpha}}) \quad (2-21)$$

The new term, which is due to the non linearity of the convective part is the Reynolds stress.

### 2.2.3. Energy conservation

In compressible flows, the pressure is related to the specific internal energy and to the density by an equation of state, which can be written as:

$$p = (\gamma - 1) \rho \epsilon \quad (2-22)$$

The total energy per mass unit is defined as:

$$E = \epsilon + \frac{v_\alpha v_\alpha}{2} \quad (2-23)$$

The conservation of this quantity follows the budget equation:

$$\frac{\partial}{\partial t}(\rho E) + \frac{\partial}{\partial x_\beta}(\rho v_\beta E) = \frac{\partial}{\partial x_\beta}(\sigma_{\alpha\beta} v_\alpha) - \frac{\partial}{\partial x_\beta}(Q_\beta) \quad (2-24)$$

The stress tensor  $\sigma_{\alpha\beta}$  is defined as previously. The heat flux is evaluated according to the Fourier's law as:

$$Q_\beta = -K \frac{\partial T}{\partial x_\beta} \quad (2-25)$$

After averaging, it comes:

$$\frac{\partial}{\partial t}(\rho \tilde{E}) + \frac{\partial}{\partial x_\beta}(\rho \tilde{v}_\beta \tilde{E}) = -\frac{\partial}{\partial x_\beta}(\overline{\rho v_\beta'' E''}) + \frac{\partial}{\partial x_\beta}(\overline{\sigma_{\alpha\beta} v_\alpha}) - \frac{\partial}{\partial x_\beta}(\overline{Q_\beta}) \quad (2-26)$$



The new term appearing in this equation characterizes the diffusion of the total energy by the turbulent motion. Similarly, averaging the equation of state (2-23) makes obvious the contribution of the turbulent kinetic energy in the total energy budget:

$$\tilde{E} = \bar{e} + \frac{\tilde{v}_\alpha \tilde{v}_\alpha}{2} + k \quad (2-27)$$

with  $k = \frac{\overline{v_\alpha v_\alpha}}{2}$

For flows in which strong heat transfer rather than strict compressibility effects are present (a typical example is a turbulent flame), it is more convenient to write the energy conservation through the enthalpy transport equation. For constant specific heat, the enthalpy is related to the temperature field as:

$$h = c_p T$$

The instantaneous budget equation is:

$$\frac{\partial}{\partial t}(\rho h) + \frac{\partial}{\partial x_j}(\rho v_j h) = \frac{\partial p}{\partial t} + v_j \frac{\partial p}{\partial x_j} + \Phi - \frac{\partial}{\partial x_j}(Q_j) \quad (2-28)$$

with  $Q_j$ , the heat flux in the  $x_j$  direction and  $\Phi$ , the dissipation function defined as:

$$\Phi = 0.5\mu \left( \frac{\partial v_\alpha}{\partial x_j} + \frac{\partial v_j}{\partial x_\alpha} \right)^2 - \frac{2}{3}\mu \frac{\partial v_\gamma}{\partial x_\gamma} \frac{\partial v_\delta}{\partial x_\delta} \quad (2-29)$$

After averaging, it comes:

$$\frac{\partial}{\partial t}(\rho \bar{h}) + \frac{\partial}{\partial x_j}(\rho \tilde{v}_j \bar{h}) = -\frac{\partial}{\partial x_j}(\overline{\rho v_j h''}) + \frac{\partial p}{\partial t} + \tilde{v}_j \frac{\partial p}{\partial x_j} + \overline{v_j} \frac{\partial p}{\partial x_j} + \bar{\Phi} - \frac{\partial}{\partial x_j}(\overline{Q_j}) \quad (2-30)$$

$\bar{\Phi}$  is defined now as a mean dissipation:

$$\bar{\Phi} = \mu \left[ \overline{S_{\alpha\beta}'' \left( \frac{\partial v_\beta''}{\partial x_\alpha} + \frac{\partial v_\alpha''}{\partial x_\beta} \right)} + \tilde{S}_{\alpha\beta} \left( \frac{\partial \tilde{v}_\beta}{\partial x_\alpha} + \frac{\partial \tilde{v}_\alpha}{\partial x_\beta} \right)^2 \right] \quad (2-31)$$

#### 2.2.4. Species or scalar conservation

For the case of mass fraction  $c_I$ , we have an instantaneous advection diffusion equation with non-zero source terms for chemically reacting flows:

$$\frac{\partial}{\partial t}(\rho c_I) + \frac{\partial}{\partial x_j}(\rho v_j c_I) = \frac{\partial}{\partial x_j}(J_{jI}) + S_I \quad (2-32)$$

which becomes in turbulent form:

$$\frac{\partial}{\partial t}(\rho \tilde{c}_I) + \frac{\partial}{\partial x_j}(\rho \tilde{v}_j \tilde{c}_I) = -\frac{\partial}{\partial x_j}(\overline{\rho v_j c_I''}) + \frac{\partial}{\partial x_j}(\overline{J_{jI}}) + \tilde{S}_I \quad (2-33)$$



This last equation can be used for any scalar provided that the interpretation of the diffusion term is correctly understood. In the specific case of the mass fraction, the term  $J_{\beta I}$  represents the diffusion flux of the species along the direction  $\beta$  under the action of molecular agitation.

### 2.2.5. Energy paths

To illustrate the implications of averaging compressible flow equations, as far as energy budget is concerned, figure 1 sketches the various paths taken by energy between mean motion, turbulent motion and fluid. Under the three headers corresponding respectively to the mean and turbulent kinetic energy and to the fluid internal energy, various algebraic terms are displayed with arrows to show the possible transfer mechanisms.

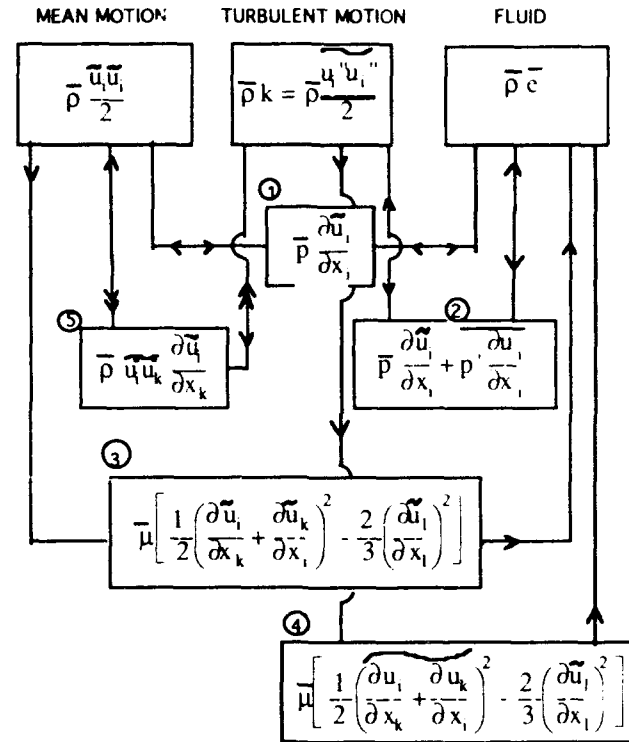


Figure 1: sketch of energy paths

Boxes 1 and 2 correspond to reversible work done under the action of pressure field. Boxes 3 and 4 are related to the irreversible transformation of mechanical energy into heat, because of the molecular viscosity. These terms correspond to the dissipation of mean and turbulent kinetic energy. Box 5 is the classical transformation of mean kinetic energy into turbulent one. The term appears with different signs in both equations. It is a sink term for the mean motion and a source (production) for the turbulent motion. The transfer is mostly done from large scale to smaller. But it can happen that inverse cascade (negative production) exists locally. This point requires a very careful attention in modelling when the sign of the turbulent energy production terms is forced to be positive (eddy viscosity models for instance).



### 3. ALGEBRAIC TURBULENCE MODELS

As shown in the previous chapter, the time-averaged equations of motion contain new unknown terms. In order to predict the mean velocity distribution or the mean temperature distribution, it is necessary to make an assumption or find a reasonable model for the Reynolds stresses and the turbulent flux terms. The more generally used concept has been, for many years, to establish an analogy between the viscous and the turbulent stresses. Then a linear relationship is assumed between the turbulent stress and the mean strain tensor (Boussinesq, /1/). The turbulent counterpart of the Newton's law is written as:

$$-\rho \overline{v'_\alpha v'_\beta} = \mu_t \left( \frac{\partial \overline{v}_\beta}{\partial x_\alpha} + \frac{\partial \overline{v}_\alpha}{\partial x_\beta} - \frac{2}{3} \delta_{\alpha\beta} \frac{\partial \overline{v}_\gamma}{\partial x_\gamma} \right) - \frac{2}{3} \delta_{\alpha\beta} \rho k \quad (3-1)$$

The second term of the R.H.S in equation (3-1) corresponds to the bulk dilatation existing in compressible flows. The last term, which is characteristic of the turbulent form, allows the trace of the Reynolds stress tensor to be different from zero. This last contribution plays the same role as the pressure in the kinetic theory of gases as a mean of the normal stresses.

All terms of the R.H.S of (3-1) are known, but  $\mu_t$ , the turbulent viscosity and  $k$ , the turbulent kinetic energy. Since the 60's, a large number of techniques have been, more or less successfully, worked out. Among them, it is possible to distinguish two general approaches. The first one relies on local equilibrium ideas to express directly the turbulent viscosity coefficient in terms of known quantities of the mean flow, such as the mean velocity gradient or some integral boundary layer parameter or even the wall distance. This approach is referred to as the class of algebraic turbulence models. A known short-cut of these methods is to neglect the energy term in (34) for the simple reason that the energy level cannot be accurately estimated. The second approach, which intends to be more general is to evaluate the viscosity coefficient from the rate of change of the Reynolds stress in the governing equations. The prediction methods which use these ideas are referred to as transport equation methods and will be discussed in the next chapter. In fact, they reduce to the algebraic methods when all the transport terms are small, i.e. assuming local equilibrium between generation and destruction of turbulent energy (see Cebeci and Smith, /31/).

From a simple dimensional analysis, the turbulent kinematic viscosity appears to be the product of a velocity and a length, for which a proper choice is not an easy task. In order to gain a generally applicable formula, Prandtl proposed his well-known mixing length theory, according to which the Reynolds stress is calculated (for boundary layer type flow) from:

$$\mu_t = \rho l^2 \left| \frac{\partial \bar{u}}{\partial y} \right| \quad (3-2)$$

The "mixing length"  $l$  is of course a quantity whose value has to be determined. For wall shear flows, Von Karman /33/ suggested the following relationship:

$$\mu_t = \rho \kappa^2 \frac{\left( \frac{\partial \bar{u}}{\partial y} \right)^3}{\frac{\partial^2 \bar{u}}{\partial y^2}} \quad (3-3)$$



$\kappa$  being the universal constant of the same name. Equations (3-2) and (3-3) give generally very good results in thin shear flows where production and dissipation mechanisms are approximately balanced (local equilibrium).

Besides these two original proposals, it is worth mentioning two other formulations for the eddy viscosity:

- The Taylor vorticity transfer theory /34/. In this proposal from 1915, it was assumed that lumps of fluid preserve their vorticity in turbulent flows instead of their momentum, as recommended by Prandtl theory:

$$\mu_t = 0.5 \rho l_z^2 \left| \frac{\partial u}{\partial y} \right| \quad (3-4)$$

Although based on different ideas, this formulation is analogous to Prandtl's.

- Assuming that the dimensions of the lumps of fluid, which move in a transverse direction during turbulent mixing are of the same order of magnitude as the width of the mixing zone, Reichardt /35/ proposed the following dependency:

$$\mu_t = \kappa_1 b (u_{max} - u_{min}) \quad (3-5)$$

where  $\kappa_1$  denotes a dimensionless number to be determined experimentally, and  $b$  is a characteristic transverse dimension of the shear layer.

It follows, from equation (3-5) that  $\mu_t$  remains constant over the whole width of the shear zone, whereas the previous proposals (equations (3-2), (3-3) and (3-4)) imply that it should vary even if the length scales are assumed constant. Furthermore, experimental results (Klebanoff, /32/) indicate that, in the wall region ( $0 \leq y/\delta \leq 0.15 - 0.20$ ), the eddy viscosity and mixing length vary linearly with the wall distance  $y$ . Both variables appear to have a maximum value somewhere between  $y/\delta = 0.20$  and  $y/\delta = 0.30$ . Consequently, a reasonable approximation for these two quantities in the inner region can be written as:

$$\mu_t = \kappa y u_{turb} \quad (3-6)$$

$$l = \kappa y \quad (3-7)$$

where  $\kappa$  is the universal constant of Von Karman, experimentally found to be in the range of 0.40 - 0.41. Variable  $u_{turb}$  is a characteristic scale of the velocity fluctuations. For  $y/\delta$  greater than approximately 0.20, the eddy viscosity begins to decrease slowly, but the mixing length remains more or less constant, so it can be approximated by:

$$l/\delta = const. \quad (3-8)$$

where the constant varies from 0.075 to 0.090, depending on the definition of boundary layer thickness  $\delta$ .

So far, examination of the eddy viscosity coefficient and the mixing length have allowed making distinctions of two different zones inside the boundary layer, the inner zone for  $y/\delta < 0.2$  and the outer region elsewhere. In fact, some caution must be taken for the global treatment of this outer region. As the free stream is approached, the turbulence becomes intermittent, i.e. for only a fraction  $\tau$  of the time is the flow turbulent. This is not a feature of the unique wall boundary layer. Indeed, the same phenomenon can be observed in free shear flows /12/.



The on-and-off character of the turbulence is a direct consequence of the intermittency. From the experimental results of Klebanoff /32/, it can be seen that, for values as small as  $y/\delta = 0.4$ , there are intervals of time during which the flow is truly turbulent, separated by laminar features. These features last longer with increasing distance from the wall. Obviously, outside the boundary layer ( $y/\delta \geq 1.0$ ), it is also possible to find some turbulent fluid packets, penetrating the free stream flow up to  $y/\delta \simeq 1.2$ . The intermittency factor, i.e. the ratio of the turbulent time with the total time, can be correctly approximated by the expression:

$$\Gamma = 0.5 \left( 1 - \operatorname{erf} \left( 5 \left( \frac{y}{\delta} - 0.78 \right) \right) \right) \quad (3-9)$$

### 3.1. THE CEBECI-SMITH-MOSINSKI MODEL

This model is an extension to compressible flows of the Cebeci-Smith model. Its basic philosophy is to make a coherent combination of the local approximations, which have been reviewed above, in order to build up a general model for the description of the whole boundary layer. The distribution of the mixing length  $l$  can be made with two separate functions. In the fully turbulent part of the inner region,  $l$  is proportional to  $y$ , the wall distance, and in the outer zone, the turbulent length scale is  $\delta$ , the boundary layer thickness. Therefore:

$$\begin{aligned} l_i &= \kappa y & 0 \leq y \leq y_c \\ l_o &= a_1 \delta & y_c < y \leq \delta \end{aligned} \quad (3-10)$$

where the  $y_c$  value is imposed by the required continuity of  $\mu_t$  across the two zones. According to the review paper of Escudier /36/, the parameters  $\kappa$  and  $a_1$  can vary slightly, but reasonable values are 0.40 and 0.075 respectively.

As a direct consequence of this composite definition, the eddy viscosity  $\mu_t$  also varies linearly with  $y$  in the inner region and is nearly constant (except for the intermittency) in the outer region. Its variation across the boundary layer can be conveniently described by the following formulas:

$$\begin{cases} (\mu_t)_i = \rho l^2 \left| \frac{\partial u}{\partial y} \right|; & 0 \leq y \leq y_c \\ (\mu_t)_o = \alpha \rho U_{max} \delta_i^* / (1 + 5.5(\frac{y}{\delta})^6); & y_c < y \leq \delta \end{cases} \quad (3-11)$$

Although it varies slightly with low momentum thickness Reynolds number, the parameter  $\alpha$  is generally taken as a constant equal to 0.0168. Equations (3-11) are designed for the fully turbulent part of the boundary layer, but not for the laminar sublayer and the buffer zone close to the wall. In order to make them applicable over the entire boundary layer, they must be modified by using empirical expressions, such as the one proposed by Van Driest /37/ in which the mixing length becomes:

$$l = \kappa y \left( 1 - \exp \left( -\frac{y}{A} \right) \right) \quad (3-12)$$

In equation (3-12), the vanishing character of the eddy viscosity at the wall is taken into account through the use of a damping length constant  $A$ , defined as:

$$A = 26 \frac{\nu}{\sqrt{\frac{\tau_w}{\rho}}} \quad (3-13)$$



This modified expression of the mixing length was obtained by using an analogy between the viscous sublayer and Stokes flow. According to Van Driest's definition of  $A$ , its use is restricted to flows with negligible pressure gradient and zero mass transfer. For compressible flows, this original formulation needs to be modified. The limitations of Van Driest formulation appear clearly in the case of strong pressure gradient, for instance. Indeed, for a flow with adverse pressure gradient,  $\tau_w$  may approach zero (flow separation), in which case the predicted inner eddy viscosity will be zero. The inner zone formulation was generalized by Cebeci /38/ and /39/ for flows with pressure gradient, mass and heat transfer. Starting from the Stokes flow analogy for the compressible equation, the shear wave propagation velocity is assumed to be the friction velocity obtained at a  $y^+$  value determined by the intersection of the linear and the logarithmic laws of the wall. This friction velocity is obtained from the local integration of the u-momentum equation between the wall and the intersecting point. This procedure leads to a rather complicated expression for the modified damping length constant  $A$  which is written as:

$$A = A^+ \frac{\nu}{N} \left( \frac{\tau_w}{\rho_w} \right)^{\frac{1}{2}} \left( \frac{\rho}{\rho_w} \right)^{-\frac{1}{2}} \quad (3-14)$$

in which  $A^+ = 26$  and  $N$  is defined as:

$$\frac{\mu}{\mu_e} \left( \frac{\rho_e}{\rho_w} \right)^2 \frac{p^+}{v_w^+} (1 - \exp(11.8 \frac{\mu_w}{\mu} v_w^+)) + \exp(11.8 \frac{\mu_w}{\mu} v_w^+) = N \quad (3-15)$$

with:

$$p^+ = \left( \frac{\nu_e u_e}{u_\tau^3} \right) \frac{\partial u_e}{\partial x} \quad v_w^+ = \frac{v_w}{u_\tau}$$

$$u_\tau = \frac{\tau_w}{\rho_w} \quad y_e^+ = \frac{y_e u_\tau}{\nu_w}$$

Many other attempts have been made to modify the Van Driest damping law to handle heat and mass transfers. For a rather complete inventory of these works, the reader is referred to the book of Cebeci and Smith /40/.

To complete the modelling of the whole boundary layer, the outer zone (in which the intermittency takes place) is calculated with constant mixing length inside the fully turbulent events. To account for the intermittency phenomenon, the result of Klebanoff /32/:

$$\Gamma = 0.5 (1 - \operatorname{erf}(5 (\frac{y}{\delta} - 0.78)))$$

introduces an analytical relationship with the wall distance  $y$ . A slightly simpler formulation which is used in the reference /41/ relates the intermittency factor to that wall distance with a power law:

$$\Gamma = \left( 1 + 5.5 \left( \frac{y}{\delta} \right)^6 \right)^{-1} \quad (3-16)$$

To summarize the so-called Cebeci-Smith-Mosinski model, the eddy viscosity is written as:

$$(\mu_t)_i = L^2 \rho \frac{\partial u}{\partial y} \quad 0 \leq y \leq y_c \quad (3-17)$$

$$(\mu_t)_i = \rho \alpha u_e \delta^* \Gamma^{-1} \quad y_c \leq y \leq \delta \quad (3-18)$$



in which  $L$  is defined by equations (45) and (47),  $\kappa = 0.41$ ,  $\alpha = 0.0168$  and the intermittency factor is evaluated with (49).

All these remarks are adequate under certain conditions for the description of momentum transport. To deal with significant heat transport, it is generally admitted to have a constant ratio between the eddy viscosity and the turbulent heat diffusivity coefficient. That leads to the definition of  $Pr_t$ , a turbulent Prandtl number. Unfortunately, experimental evidence shows that the turbulent Prandtl number varies across the boundary layer. Close to the wall, it is a strong function of the molecular Prandtl number (because viscous effects can be more important than turbulent ones), and away from the wall, it is independent of the molecular Prandtl number.

The eddy diffusivity formulation for heat transfer is the following:

$$(\mu_h)_i = \bar{\rho} \kappa \kappa_h y^2 (1 - \exp(-\frac{y}{A})) (1 - \exp(-\frac{y}{B})) |\frac{\partial u}{\partial y}| \quad (3-19)$$

$$(\mu_h)_o = \alpha_1 \bar{\rho} u_e \delta^* \Gamma$$

in which  $\kappa_h = 0.44$ ,  $\alpha_1 = 0.0168$  and:

$$B = B^+ \frac{\nu}{N} \left( \frac{\tau_w}{\rho_w} \right)^{-\frac{1}{2}} \left( \frac{\rho}{\rho_w} \right)^{\frac{1}{2}} \quad (3-20)$$

Then the turbulent Prandtl number, in the wall vicinity is evaluated as:

$$Pr_t = \frac{\kappa (1 - \exp(-\frac{y}{A}))}{\kappa_h (1 - \exp(-\frac{y}{B}))} \quad (3-21)$$

This first model has been tested on a wide variety of boundary layer flows including heat and mass transfer and also moderate pressure gradients for 2-dimensional as well as axisymmetric flows. For many years, that model has been recognized as the most robust for practical flow calculations.

Saxena and Mehta /86/ extended the domain of validity of this model with the introduction of wall functions. These authors were able to handle adiabatic boundary layer flows under adverse pressure gradient. The incompressible law of the wall is given by:

$$u^+ = \frac{1}{\kappa} \ln(y^+) + B \quad (3-22)$$

where  $\kappa = 0.41$  and  $B = 5.0$  and:

$$u^+ = \frac{u}{u_\tau}; \quad y^+ = \frac{y u_\tau}{\nu_w}; \quad \nu_w = \frac{\mu_w}{\rho_w}; \quad u_\tau = \left( \frac{\tau_w}{\rho_w} \right)^{\frac{1}{2}}$$

However, in the regions where adverse pressure gradients exist, the following law of the wall, due to Nakayama and Koyama /87/ has been employed:

$$u^+ = \frac{1}{k^*} \left[ 3(t - t_s) + \ln \left( \frac{t_s + 1}{t_s - 1} \frac{t - 1}{t + 1} \right) \right] \quad (3-23)$$



where:

$$\begin{cases} t = \sqrt{1 + \frac{2\tau^+}{3}} \\ t_s = \sqrt{1 + 0.047\alpha} \\ \tau^+ = 1 + \eta \\ \eta = \alpha y^+ \\ \alpha = \nu_w \sqrt{\rho_w} \frac{dp}{dx} \left(\frac{1}{\tau_w}\right)^{\frac{3}{2}} \\ k^* = \frac{0.4 + 0.6\alpha}{1 + \alpha} \end{cases} \quad (3-24)$$

Furthermore, at high Mach number ( $M_\infty > 4$ ), where the compressibility effects on turbulence becomes significant, the law of the wall is extended to compressible flow through the use of the Van Driest transformation /88/. Then the effective  $u^+$  becomes:

$$u^+ = \frac{1}{u_\tau} \int_0^u \sqrt{\frac{\rho}{\rho_w}} du \quad (3-25)$$

The wall values are evaluated by assuming that, in the very near wall region, the heat flux behaves as in Couette flow, namely:

$$q_y - u\tau_{xy} = q_w \quad (3-26)$$

which integrates, for adiabatic flow, as:

$$\begin{cases} T = T_w - \left(\frac{Pr}{2c_p}\right) u^2 & u < u_v \\ T = T_w - \left(\frac{Pr_t}{2c_p}\right) u^2 + \left[\frac{Pr_t - Pr}{2c_p}\right] u_v^2 & u \leq u_v \end{cases} \quad (3-27)$$

The laminar and turbulent Prandtl number,  $Pr$  and  $Pr_t$  are taken as 0.72 and 0.90 respectively. The matching between the two regions is assumed to occur at  $y^+ = 10$  (corresponding to  $y_v$  and  $u_v$ ).

Nevertheless, troubles arise when this model is used for turbulent flows where significant secondary effects are present, such as curvature or strong pressure gradients. A reason for this is, as stated previously, that all the modelling assumptions rely on the fact that the boundary layer is in strict equilibrium or close to that.

Alber /113/ proposed an improvement for separated flows. First, the damping law of Van Driest is modified to account for longitudinal pressure gradients in the following way:

$$l = \kappa y \left(1 - \exp\left(-\frac{y}{A + \mu_w} \sqrt{\rho \left(\tau_w + y \frac{\partial p}{\partial x}\right)}\right)\right) \quad (3-28)$$

Then in the evaluation of the momentum thickness for the outer viscosity, Alber suggested to start the integration from the zero velocity line rather than from the wall itself. For strongly separated flows, this could improve the flow prediction significantly.

### 3.2. THE BALDWIN-LOMAX MODEL



The major drawback of the Cebeci *et al.* model /41/ was experienced for shock wave turbulent boundary layer interactions. Indeed, the very strong adverse pressure gradients in the longitudinal direction provokes boundary layer separation, whereas pressure gradients in the transverse direction tend to invalidate the boundary layer character of the flow, and also the universal properties assumed for this type of flow in the modelling assumptions.

A practical problem with the use of the Cebeci *et al.* model /41/ is to find the exact position of the boundary layer edge when the flow separates or reattaches to the wall. The Baldwin-Lomax model /42/ (hereafter B-L) is an algebraic model patterned on the Cebeci-Smith-Mosinski proposal (hereafter C-S-M), with a modification to improve the prediction of separated flows. Before going into the detailed description of this model, it must be pointed out that it was developed primarily for 2-D and eventually 3-D flows. At the opposite of the C-S-M model which was designed for boundary layers, the B-L proposal was thought for Navier-Stokes calculations, where the two velocity components can be of equal importance. That feature explains why the B-L is slightly more general than the C-S-M for the evaluation of the turbulent scales.

Again, it is a two-layer eddy viscosity model in which  $\mu_t$  is given by:

$$\mu_t = \begin{cases} (\mu_t)_i & 0 \leq y \leq y_c \\ (\mu_t)_o & y_c \leq y \leq \delta \end{cases} \quad (3-29)$$

where  $y$  is the normal distance from the wall and  $y_c$  can be defined as the smallest value for which the two formulations are equal. For the inner region, the Prandtl mixing length formulation /2/ is used with a time scale linked to the local vorticity  $\omega$  rather than to a simple velocity gradient:

$$(\mu_t)_i = \rho l |\omega| \quad (3-30)$$

The mixing length itself uses the Van Driest concept of damping length /37/ to incorporate the wall viscosity effects:

$$l = \kappa y \left(1 - \exp\left(-\frac{y^+}{A^+}\right)\right) \quad (3-31)$$

The modulus of the local vorticity is evaluated from:

$$|\omega| = \sqrt{\left(\frac{\partial \bar{u}}{\partial y} - \frac{\partial \bar{v}}{\partial x}\right)^2 + \left(\frac{\partial \bar{v}}{\partial z} - \frac{\partial \bar{w}}{\partial y}\right)^2 + \left(\frac{\partial \bar{w}}{\partial x} - \frac{\partial \bar{u}}{\partial z}\right)^2} \quad (3-32)$$

and the wall units are expressed as:

$$y^+ = \frac{\rho_w u_\tau y}{\mu_w} = \frac{\sqrt{\rho_w \tau_w} y}{\mu_w} \quad (3-33)$$

There is no fundamental difference with the C-S-M model, up to that point except that using the vorticity variable makes the formulation more general. The major modification concerns the outer region:

$$(\mu_t)_o = \alpha C_{cp} \rho F_{wake} F_{Kleb}(y) \quad (3-34)$$



$\alpha$  is the same constant as in the previous model ( $\alpha = 0.0168$ ),  $C_{cp}$  is an additional constant and  $F_{wake}$  can be defined in two different manners, depending on the existence of a solid boundary or not. Thus:

$$F_{wake} = \begin{cases} y_{max} F_{max} \\ C_{wk} y_{max} u_{dif}^2 / F_{max} \end{cases} \quad (3-35)$$

$F_{wake}$  takes the smallest value between the two expressions in (3-35). The values of  $y_{max}$  and  $F_{max}$  are evaluated from an expression including a damping coefficient similar to the one used by Van Driest:

$$F(y) = y |\omega| (1 - \exp(-\frac{y^+}{A^+})) \quad (3-36)$$

The quantity  $F_{max}$  is the maximum value of  $F(y)$  which occurs in a profile, and  $y_{max}$  is the corresponding distance from the solid wall. As in the previous model, the outer region viscosity is weighted by an intermittency factor  $F_{kleb}$ , which is evaluated by the best fitting expression of the Klebanoff experimental data. The intermittency factor is:

$$F_{kleb}(y) = (1 + 5.5 (\frac{C_{kleb} y}{y_{max}})^6)^{-1} \quad (3-37)$$

The quantity  $u_{dif}$  represents a velocity scale equal to the difference between maximum and minimum total velocity in a given profile (i.e. at a fixed x station).

$$u_{dif} = \left( \sqrt{u^2 + v^2 + w^2} \right)_{max} - \left( \sqrt{u^2 + v^2 + w^2} \right)_{min} \quad (3-38)$$

Naturally, the second term in  $u_{dif}$  is zero for the case of attached flows. In wake flow configuration, both terms must be taken into account. For the case of separated boundary layer, it is advisable also to consider the direction of the velocity vector, at least in the separated region. In fact, the outer formulation, which is described with equations (3-34) and (3-35), can be used in wakes as well as in attached and in separated boundary layers. Practically, the product  $y_{max} F_{max}$  replaces  $\delta^* u_e$  in the C-S-M model and the combination  $y_{max} u_{dif}^2 / F_{max}$  replaces  $b u_{dif}$  in the Reichardt /35/ formulation. As a result, the distribution of vorticity is used to evaluate the length scales, so that determination of the boundary layer edge is not necessary. The use of that turbulence model requires the knowledge of various constants, for which the values are given in the following:

$$\begin{array}{llll} A^+ = 26 & C_{cp} = 1.6 & C_{kleb} = 0.3 & C_{wk} = 0.25 \\ \kappa = 0.4 & \alpha = 0.0168 & Pr = 0.72 & Pr_t = 0.9 \end{array}$$

So far, although being nearly as widely used as the C-S-M model, the B-L model has not been tested against flow configurations including strong heat and/or mass transfer. The heat transfer mechanisms are handled through the definition of a constant turbulent Prandtl number, and as discussed earlier, this remains a fairly reasonable assumption for air flows.

During its preliminary use, this model was slightly modified to produce a transition-like phenomenon. This was achieved by setting the turbulent viscosity equal to zero all across a given profile, unless, at least in one point, the calculated turbulent viscosity was larger than 14 times the molecular viscosity value. This technique was able to produce an



artificial transition-like process, although the physical mechanisms responsible for it in the reality, could not be accounted for in the time-averaged Navier-Stokes equations.

Another feature of this turbulence model is that its use has been restricted mostly to the thin layer approximation. Different from the boundary layer assumption which imposes drastic simplifications of the Navier-Stokes equations, the thin layer assumption neglects the diffusion processes parallel to the body surface but retains all three of the momentum equations (for 3-d flows) and makes no assumption about the pressure gradients normal to the solid wall. In the reference /42/, Baldwin and Lomax justify the use of the thin layer approximation, not only by the simplification brought to the coding, but also by stating that, due to the mesh stretching in the high shear zones, the diffusion terms parallel to the solid surface cannot be resolved properly.

Shang and Hankey /62/ suggested accounting for turbulence memory effects by displacing the eddy viscosity value along the main flow direction. This is equivalent to allowing a given response time of the turbulence to the mean field distortion. To perform this, the eddy viscosity is calculated as:

$$\mu_t = (\mu_t)_{up} + ((\mu_t)_{eq} - (\mu_t)_{up}) (1 - \exp(-\frac{\Delta x}{10\delta})) \quad (3-39)$$

where  $(\mu_t)_{up}$  is the calculated eddy viscosity at the initial location of the pressure disturbance,  $(\mu_t)_{eq}$  is the calculated equilibrium value. The streamwise distance between these two locations is denoted by  $\Delta x$  and  $\delta$  is the boundary layer thickness at the initial station. This modification has been implemented in a C-S-M model in which the intermittency function was removed.

### 3.3. THE MICHEL-QUEMARD-DURANT MODEL

This model, which is simpler than the previous ones has been proposed initially by Michel *et al.* in 1969 /112/. A unique law is used for inner and outer regions of equilibrium turbulent boundary layers. It writes as:

$$\mu_t = \bar{\rho} l^2 F^2 \left| \frac{\partial U}{\partial y} \right| \quad (3-40)$$

The mixing length behaves linearly with the wall distance in the wall region and becomes  $l = 0.085 \delta$  in the outer part. A common relationship is:

$$l = 0.085 \delta \tanh\left(\frac{\kappa y}{0.085\delta}\right) \quad (3-41)$$

As for the inner formulation of the previous model, the mixing length needs some damping to account for the dominant viscous effects in the very near wall region. To do so, the correcting function  $F$  is written as:

$$F = 1 - \exp\left(-\frac{l}{A + \kappa\mu} \sqrt{\bar{\rho}(\tau_l + \tau_t)}\right) \quad (3-42)$$

As  $\tau_r$  contains itself the turbulent viscosity, a classical Newton-Raphson method is needed to solve (3-40).



## 4. TRANSPORT EQUATION MODELS

The major criticism which can be addressed to all algebraic turbulence models, is that the turbulence is too tightly linked to the mean field. The turbulence is described only by mean flow properties rather than by the turbulence properties themselves. Therefore, it was suggested that the use of field equations to describe globally one or more characteristic turbulent scales would be a better approach. This technique allows the turbulence field have its own memory rather than being dependent only the local mean field values. The first attempt has been to use an equation for the turbulent kinetic energy  $k$ , in order to determine a characteristic velocity scale for the turbulent motion. Thus, the one-equation or kinetic energy model uses, in addition to the mean flow equations, a partial differential equation for the trace of the Reynolds stress tensor,  $k = \overline{u_i' u_i'}/2$ .

From a simple manipulation of the instantaneous Navier-Stokes equations, derivation of a transport equation for the Reynolds stress components yields:

$$\begin{aligned} \frac{\partial}{\partial t}(\rho \overline{v_\alpha' v_\beta'}) + \frac{\partial}{\partial x_\gamma} \left[ \rho \overline{v_\alpha' v_\beta' v_\gamma'} + \rho \overline{v_\alpha' v_\beta' v_\gamma'} + \delta_{\alpha\gamma} \overline{v_\beta' p'} + \delta_{\beta\gamma} \overline{v_\alpha' p'} - \mu (\overline{S_{\alpha\gamma} v_\beta'} + \overline{S_{\beta\gamma} v_\alpha'}) \right] \\ = -\bar{\rho} \left[ \overline{v_\alpha' v_\gamma'} \frac{\partial \overline{v_\beta'}}{\partial x_\gamma} + \overline{v_\beta' v_\gamma'} \frac{\partial \overline{v_\alpha'}}{\partial x_\gamma} \right] + \overline{p' \left( \frac{\partial v_\alpha'}{\partial x_\beta} + \frac{\partial v_\beta}{\partial x_\alpha} \right)} \\ - \mu \left[ \overline{S_{\alpha\gamma} \frac{\partial v_\beta'}{\partial x_\gamma}} + \overline{S_{\beta\gamma} \frac{\partial v_\alpha'}{\partial x_\gamma}} \right] - \overline{v_\alpha' \frac{\partial p}{\partial x_\beta}} - \overline{v_\beta' \frac{\partial p}{\partial x_\alpha}} \end{aligned} \quad (4-1)$$

By taking advantage of the contracted index convention ( $\alpha = \beta$  and summation) and dividing the resulting equation by 2, we obtain the exact form of the transport equation for the turbulent kinetic energy:

$$\begin{aligned} \frac{\partial}{\partial t}(\bar{\rho} k) + \frac{\partial}{\partial x_\gamma} \left( \bar{\rho} \overline{v_\gamma' k} + \rho \overline{v_\gamma' k} + \overline{v_\gamma' p'} - \mu \overline{v_\alpha' S_{\alpha\gamma}} \right) \\ = -\bar{\rho} \overline{v_\alpha' v_\gamma'} \frac{\partial \overline{v_\alpha'}}{\partial x_\gamma} + \overline{p' \frac{\partial v_\alpha'}{\partial x_\alpha}} - \overline{v_\alpha' \frac{\partial p}{\partial x_\alpha}} - \mu \overline{S_{\alpha\gamma} \frac{\partial v_\alpha'}{\partial x_\alpha}} \end{aligned} \quad (4-2)$$

The reader should note that, for variable density flows, the correlation between pressure fluctuations and the divergence of the velocity fluctuations is not strictly equal to zero as it is for incompressible flows. The same remark applies also to the mean pressure gradient contribution. A one-equation model for turbulent compressible flows was proposed by Rubesin /43/ and investigated by Viegas and Horstman /44/ for different cases of shock-boundary layer interactions.

The model, originated with Prandtl /45/ and Kolmogorov /46/ was based initially on local equilibrium assumptions for the turbulence. Under these conditions, the one-equation model is equivalent to a standard algebraic one. Glushko /47/ was the first to effectively solve the  $k$ -equation for incompressible boundary layers by using modelling assumptions to account for the different terms in the transport equation. Then it was studied later by Beckwith and Bushnell /48/ in more complicated boundary layer flows and finally was generalized by Rubesin /43/ to compressible flows using the mass-weighted decomposition /49/. A similar model has also been studied by Bradshaw *et al.* /53/ for boundary layers and by Lee and Harsha /54/ for free mixing problems. As with algebraic



turbulence models, Reynolds stresses are evaluated from a gradient flux approximation (see equation (3-1)). If  $\sqrt{k}$  is the turbulent characteristic velocity scale, the eddy viscosity must be written as:

$$\mu_t = \sqrt{k} l \quad (4-3)$$

in which  $l$  is a length scale which characterizes the size of the largest turbulent eddies. That length is to be determined in a more or less empirical fashion. Practically, the uncertainties concerning the evaluation of this parameter happened to be so large that the length scale itself was considered also as a field quantity. That leads to more complex turbulence models, in which at least two transport equations are needed to solve the turbulence field.

#### 4.1. A ONE-EQUATION MODEL FOR COMPRESSIBLE FLOWS

Independently from the determination of the length scale, it is necessary to establish a couple of modelling assumptions in order to solve the turbulent kinetic energy equation (4-2). Unknown terms correspond to various diffusion mechanisms, to the energy production, to the interaction between the pressure fluctuations and the instantaneous bulk dilatation, to the mean pressure gradient production and to the mechanical dissipation. The last term is linked directly to the evaluation of the second characteristic scale which will be discussed below. The modelling of the production term relies only on the basic gradient flux approximation to relate the Reynolds stresses to the mean quantities. But differently from the algebraic cases, the kinetic energy is not neglected in equation (3-1) and can appear explicitly. Therefore the production is written as:

$$-\rho \overline{v_\alpha'' v_\gamma''} \frac{\partial \overline{v_\alpha''}}{\partial x_\gamma} = \left[ \mu_t \left( \frac{\partial \overline{v_\alpha''}}{\partial x_\gamma} + \frac{\partial \overline{v_\gamma''}}{\partial x_\alpha} - \frac{2}{3} \delta_{\alpha\gamma} \frac{\partial \overline{v_s''}}{\partial x_s} \right) - \frac{2}{3} \delta_{\alpha\gamma} \rho k \right] \frac{\partial \overline{v_\alpha''}}{\partial x_\gamma} \quad (4-4)$$

The modelling of the diffusion terms is relatively easy after the following assumptions:

- for high values of the turbulent Reynolds number (which can be for instance, the ratio of the eddy viscosity to the molecular one), the viscous diffusion effects are negligible compared to the diffusion due to the velocity fluctuations. However, in the solid wall vicinity, this assumption does not hold and the molecular diffusion must be accounted for explicitly.
- the diffusion of turbulent kinetic energy by the pressure fluctuations is small and can be neglected (see for instance the incompressible experimental results of Irwin /50/).

The complete diffusion term can be written as:

$$\frac{\partial}{\partial x_\gamma} \left( \rho \overline{v_\gamma'' k} + \overline{v_\gamma'' p'} - \mu \overline{v_\beta'' S_{\beta\gamma}} \right) = \frac{\partial}{\partial x_\gamma} \left( -\mu_k \frac{\partial k}{\partial x_\gamma} \right) \quad (4-5)$$

in which  $\mu_k$  is the sum of the molecular diffusivity coefficient and its turbulent counterpart weighted by a turbulent Schmidt/Prandtl number. For wall bounded flows, the turbulent viscosity must depend upon the turbulent Reynolds number. This dependency is determined empirically to match experimental data. Rubesin /43/ proposed the following expression for the viscosity coefficient:

$$\mu_k = \mu + \frac{\mu_t}{Pr_k} \quad (4-6)$$



$$\mu_t = \alpha \mu (Re_t H) \left( \frac{Re_t}{R_0} \right) \quad (4-7)$$

with the turbulent Reynolds number defined as  $Re_t = \frac{\rho k l}{\mu}$  and

$$H(RR) = \begin{cases} RR & RR \leq 0.75 \\ RR - (RR - 0.75)^2 & 0.75 \leq RR \leq 1.25 \\ 1 & 1.25 \leq RR \end{cases} \quad (4-8)$$

$$\alpha = 0.2 \quad R_0 = 110. \quad (4-9)$$

The turbulent length scale is evaluated empirically, similarly to the Glushko proposal

$$L = \delta \begin{cases} y^* & y^* \leq 0.23 \\ (y^* + 0.37)/2.61 & 0.23 \leq y^* \leq 0.57 \\ (1.48 - y^*)/2.52 & 0.57 \leq y^* \leq 1.48 \end{cases} \quad (4-10)$$

where  $y^* = y/\delta$  and  $\delta$  is the boundary layer thickness defined arbitrarily as

$$\delta = C_\delta \delta^* \quad (4-11)$$

$C_\delta$  is a constant which relates, for each experiment, the boundary layer thickness  $\delta$  to the momentum thickness  $\delta^*$  ahead of the separation zone. Value of  $C_\delta$  for each flow tested at Ames is given below:

$$\begin{cases} \text{--transonic axisymmetric} & C_\delta = 4.54 \\ \text{--transonic 2-D} & C_\delta = 4.75 \\ \text{--supersonic compression} & C_\delta = 3.50 \\ \text{--oblique shock} & C_\delta = 4.00 \end{cases}$$

The scarcity of these values shows the weakness of the turbulence model, which appears to need a "tuning" for each flow configuration at the expense of a minimum of universality.

As stated previously, most of the applications having been done at NASA-Ames with this one-equation turbulence model /51/, /52/ did neglect the compressibility terms, in removing explicitly one of them from the equations and in setting to zero the constant  $\xi$ . Nevertheless, due to the scarcity of the various constants, which must be tuned to each flow application, it seems premature to neglect them at this point. Indeed we will see in a following paragraph, that with different models using also the turbulent kinetic energy equation, the existence of pressure gradient terms plays a non negligible influence on the prediction quality.

To summarize the formulation for the turbulent kinetic energy equation, the  $k$  transport is described with the following:

$$\begin{aligned} \frac{\partial}{\partial t}(\rho k) + \frac{\partial}{\partial x_\alpha}(\rho \tilde{v}_\alpha k) &= \mu_t \tilde{S}_{\alpha\beta} \frac{\partial \tilde{v}_\alpha}{\partial x_\beta} - \frac{2}{3} \rho k \frac{\partial \tilde{v}_\gamma}{\partial x_\gamma} \\ &+ \frac{\partial}{\partial x_\alpha} \left( \mu_k \frac{\partial k}{\partial x_\alpha} \right) - \tilde{v}_\alpha \frac{\partial p}{\partial x_\alpha} + \overline{p' \frac{\partial v_\alpha}{\partial x_\alpha}} - C_2 \frac{\mu k}{L^2} \end{aligned} \quad (4-12)$$

in which the compressibility terms are expressed according to /43/ and the constant  $C_2$  is equal to 3.93 and  $\xi$  equal to 8/11.



Independently of the use or neglect of the compressibility terms, a whole set of tests have been performed in the reference /55/ by Coakley and Viegas to parameterize the different constants used in the one equation turbulence model, e.g. the turbulent Prandtl numbers. Although they were able to gain an improvement in their flow predictions, they had to conclude however, that it was necessary to increase the transfer of information between the mean and the turbulent motions, in both directions. This notion is equivalent to an increase in the coupling between the Navier-Stokes and the turbulent transport equations. For this reason, two-equation models are more attractive, because they provide automatically a length scale which embodies more physics of the flow than the algebraic or the one-equation models do.

Another application of the one equation turbulence model has been proposed by Wolfshtein /114/ and modified by Chen and Patel /115/. The dissipation of turbulence is expressed as:

$$\epsilon = \frac{k^{3/2}}{l_t} \quad (4 - 13)$$

and the turbulent viscosity is:

$$\mu_t = C_\mu \sqrt{k} l_\mu \quad (4 - 14)$$

The turbulent length scales are written as:

$$\begin{aligned} l_\mu &= c_l y \left( 1 - \exp\left(-\frac{R_n}{A_\mu}\right) \right) \\ l_t &= c_l y \left( 1 - \exp\left(-\frac{R_n}{A_t}\right) \right) \end{aligned} \quad (4 - 15)$$

with the following parameters:

$$R_n = \frac{\sqrt{k}y}{\nu}; C_\mu = 0.09; c_l = 2.55; A_\mu = 70; A_t = 2c_l$$

## 4.2. THE TWO EQUATION TURBULENCE MODELS

Various choices are possible concerning the definition of the second characteristic turbulent scale. From dimensional analysis, it is clear that the determination of a viscosity coefficient requires a length and a velocity. This does not mean that a transport equation is strictly required for these two quantities. In fact, after the first choice has been made concerning a transport equation for the turbulent kinetic energy (as a velocity scale), the second transport equation can use any variable  $Z$  defined as:

$$Z = k^m L^n \quad (4 - 16)$$

in which each combination of the indexes  $m$  and  $n$  will define a different variable  $Z$ . The "game" in the two equation turbulence modelling consists in selecting the better combination. Launder and Spalding /56/ reviewed in 1972 the different variables having been tested at that time, and it seems that nothing new came out since that date, as far as the variable choice is concerned. Rather than exploring all possibilities, the emphasis will



be put in the following on two or three two equations models which have been effectively used for compressible flow calculations.

#### 4.2.1. THE $k - \epsilon$ MODEL FOR COMPRESSIBLE FLOWS

This model is certainly the most popular turbulence model of its class and the most widely used, at least for complex boundary layer flows. Its success is partly due to the physical meaning of the second transported variable which is the true dissipation of the turbulent kinetic energy. In the Reynolds stress transport equation, there is a dissipation term related to each of the stress components.

$$\epsilon_{\alpha\beta} = \nu S_{\alpha\gamma} \frac{\partial v_{\beta}''}{\partial x_{\gamma}} + \nu S_{\beta\gamma} \frac{\partial v_{\alpha}''}{\partial x_{\gamma}} \quad (4-17)$$

Contracting the indexes, summing and dividing by 2 yields the dissipation rate of the turbulent kinetic energy, as it appears in the exact transport equation. Assuming that the dissipative mechanisms, which are due to the molecular viscosity, exist only for the smallest scales of the turbulence and that these mechanisms are isotropic, the definition of the dissipation can be written as:

$$\epsilon = \frac{1}{2} \nu \left( \frac{\partial v_{\alpha}''}{\partial x_{\beta}} + \frac{\partial v_{\beta}''}{\partial x_{\alpha}} \right)^2 = \frac{2}{3} \nu \left( \frac{\partial v_{\alpha}''}{\partial x_{\alpha}} \right)^2 \quad (4-18)$$

The derivation of a transport equation for  $\epsilon$  is a tedious task. From a relatively long manipulation of the instantaneous Navier-Stokes equations, the result is an equation which covers more than a full page of paper (or two pages if the writing is not too tight, see for instance /85/ or /27/). This equation contains, in fact, a very large number of unknown correlations, which are not directly accessible to modelling. Although many attempts have been made earlier to evaluate and model in a term-to-term manner the different components of the equation, it is generally admitted now that its modelling can be made in a simpler manner with a global approach which establishes a functional similitude between turbulent kinetic energy and dissipation rate equations.

Before going on with the details of the dissipation rate equation, let us look again at the open form of the kinetic energy equation (4-2).

$$\begin{aligned} \frac{\partial}{\partial t}(\rho k) + \frac{\partial}{\partial x_{\gamma}} \left( \rho \tilde{v}_{\gamma} k + \rho \tilde{v}_{\gamma}'' k + \tilde{v}_{\gamma}'' p' - \mu \tilde{v}_{\alpha}'' S_{\alpha\gamma} \right) \\ = -\rho \tilde{v}_{\alpha}'' \tilde{v}_{\gamma}'' \frac{\partial \tilde{v}_{\alpha}}{\partial x_{\gamma}} + p' \frac{\partial \tilde{v}_{\alpha}''}{\partial x_{\alpha}} - \tilde{v}_{\alpha}'' \frac{\partial p}{\partial x_{\alpha}} - \mu S_{\alpha\gamma} \frac{\partial \tilde{v}_{\alpha}''}{\partial x_{\gamma}} \end{aligned}$$

The basic difference with the modelling in the one-equation model is the definition of the turbulent viscosity. Rather than being linked to an algebraic length scale, this viscosity can be determined with the dissipation rate through the relation:

$$\mu_t = C_{\mu} f_{\mu} \rho \frac{k^2}{\epsilon} \quad (4-19)$$

The constant  $C_{\mu}$  has the value 0.09 and the function  $f_{\mu}$ , which is turbulent Reynolds number dependent, allows damping the turbulent diffusion mechanisms in the wall vicinity



for the case of boundary layers. With the same approximations for the compressibility terms (mean pressure gradient and pressure velocity divergence correlation, see chapter 6), the modelled equation is written now as:

$$\frac{\partial}{\partial t}(\rho k) + \frac{\partial}{\partial x_\alpha}(\rho k \tilde{v}_\alpha - \mu_k \frac{\partial k}{\partial x_\alpha}) = P_k - \rho \epsilon^* - 2\mu \left( \frac{\partial \sqrt{k}}{\partial x_n} \right)^2 + \text{Compressibility} \quad (4-20)$$

in which  $P_k$ , the turbulent kinetic energy production stands for:

$$P_k = -\rho \tilde{v}_\alpha \tilde{v}_\gamma \frac{\partial \tilde{v}_\alpha}{\partial x_\gamma}$$

The third term on the R.H.S. is new. Its role is an aid for the numerical methods, which prefer to have classical Dirichlet boundary conditions such as  $\epsilon = 0$  at the wall. Indeed, the boundary value of the turbulent energy dissipation rate is different from zero. Jones and Launder /58/ showed that, because of the linear dependency of velocity fluctuations with the wall distance (in the very near wall region,  $y^+ \leq 1$ ), the total dissipation in this region behaves as a constant, depending on  $k$  profile:

$$\epsilon \rightarrow 2\nu \left( \frac{\partial \sqrt{k}}{\partial x_n} \right)^2 \neq 0 \quad \Longleftrightarrow \quad k \rightarrow C_\mu y^2$$

Such condition causes a numerical inconsistency when  $k \rightarrow 0$  in the ratio  $\epsilon^2/k$ . To avoid this, it is convenient to split the total dissipation into its isotropic and anisotropic parts. The isotropic part of the dissipation  $\epsilon^*$ , which cancels for  $y = 0$ , can then be expressed as:

$$\epsilon^* = \epsilon - 2\nu \left( \frac{\partial \sqrt{k}}{\partial x_n} \right)^2 \quad (4-21)$$

Therefore it is preferable to solve an equation for the isotropic dissipation. This equation should come formally from the instantaneous form. In fact, it has a form analogous to the  $k$ -equation provided that an explicit scale factor and suitable parameters allow distinguishing the different mechanisms from those in the turbulent kinetic energy equation. This equation is written as:

$$\begin{aligned} \frac{\partial}{\partial t}(\rho \epsilon^*) + \frac{\partial}{\partial x_\alpha}(\rho \epsilon^* \tilde{v}_\alpha - \mu_\epsilon \frac{\partial \epsilon^*}{\partial x_\alpha}) = & C_{\epsilon 1} \frac{\epsilon}{k} \rho P_k - C_{\epsilon 2} \rho f_2 \frac{\epsilon \epsilon^*}{k} \\ & + \frac{\mu \mu_t}{\rho} \left( \frac{\partial^2 \tilde{v}_n}{\partial x_n^2} \right)^2 + \text{Compressibility} \end{aligned} \quad (4-22)$$

The importance of the term preceding the compressibility terms is not as clearly justified as in the previous transport equation. The reasoning to support it, is related to the vortex stretching in the wall layer, but its form was determined in a rather empirical manner by Jones and Launder /58/. Practically, its effect is to locate correctly the position of the turbulent energy peak in the boundary layer profiles, when compared to the experimental data.

To complete the equations (4-18), (4-19) and (4-21), two turbulent Reynolds number dependent functions are needed for the correct treatment of the wall vicinity.

$$f_2 = 1 - 0.3 \exp(-Re_t); \quad f_\mu = \exp\left(\frac{-2.5}{1 + \frac{Re_t}{50}}\right) \quad (4-23)$$



and the turbulent Reynolds number is defined as:

$$Re_t = \frac{\rho k^2}{\mu \epsilon} \quad (4-24)$$

The diffusivity coefficients are expressed as:

$$\mu_k = \mu + \frac{\mu_t}{Pr_k} \quad (4-25)$$

$$\mu_\epsilon = \mu + \frac{\mu_t}{Pr_\epsilon} \quad (4-26)$$

where  $Pr_k$  and  $Pr_\epsilon$  are analogous to turbulent Schmidt/Prandtl numbers, of which the respective values are 1.0 and 1.3; the constants are  $C_{\epsilon 1} = 1.45$  and  $C_{\epsilon 2} = 1.94$ .

The topic of the influence of the compressibility terms, both in the equations for  $k$  and  $\epsilon$  is still an open question. These terms have always been neglected in the calculations performed at Ames. Nevertheless, the domain of applicability was always restricted to transonic or weakly supersonic flows. But it is quite easy to mention examples where these terms are really needed. Borghi and Escudier /59/ reported flame calculations in which the modelling of the pressure terms has to be included in the turbulence model. Furthermore, they observed that, any additive source contribution in the turbulent energy equation requires a counterpart in the dissipation equation. Usually that counterpart has a similar structure with a different characteristic time scale, but any attempt to solve the set of equations without it, is unsuccessful. The author /60/ obtained quite similar results for the calculation of the heterogeneous mixing layer of Brown and Roshko /12/. To account properly for the external pressure gradient and then, to match both the spreading rate of the mixing layer and the turbulent energy level, the pressure terms were needed in the two equations simultaneously. In reference /61/, Arina and Benocci experienced difficulties to calculate correctly compressible boundary layers in presence of strong pressure gradients. One of the reasons (but not all of them) is probably due to the total absence of explicit compressibility terms. A further motivation for these extra terms can be found in /27/, where an attempt to show the spreading rate of a supersonic shear layer for various free stream Mach number values. Without the compressibility terms, the calculation did not reproduce any influence from the free stream Mach number, whereas the presence of pressure terms (with slightly different modelling assumptions from those of Rubesin) allowed obtaining a correct dependence until  $M_\epsilon = 4$ .

When averaging the Navier-Stokes equations, not only the motion equations are affected, but also the energy equation. Consider the open form of the total energy equation:

$$\frac{\partial}{\partial t}(\bar{\rho} \tilde{E}) + \frac{\partial}{\partial x_\alpha}(\bar{\rho} \tilde{v}_\alpha \tilde{E}) + \frac{\partial}{\partial x_\alpha}(\bar{\rho} \tilde{v}_\alpha'' \tilde{E}'' - \overline{\sigma_{\alpha\beta} v_\beta} - \overline{Q_\alpha}) = 0 \quad (4-27)$$

Using the Newton's and Fourier's laws, it can be expressed as:

$$\begin{aligned} \frac{\partial}{\partial t}(\bar{\rho} \tilde{E}) + \frac{\partial}{\partial x_\alpha}(\bar{\rho} \tilde{v}_\alpha \tilde{E} + \bar{\rho} \tilde{v}_\alpha'' \tilde{E}'') &= \frac{\partial}{\partial x_\alpha} \left( K \frac{\partial \tilde{T}}{\partial x_\alpha} + \bar{p} \tilde{v}_\alpha \right. \\ &\quad \left. + \bar{p} \tilde{v}_\alpha'' + \overline{p' v_\alpha''} - \mu (\overline{S_{\alpha\beta} \tilde{v}_\beta} + \overline{S_{\alpha\beta}'' \tilde{v}_\beta} + \overline{S_{\alpha\beta} \tilde{v}_\beta''} + \overline{S_{\alpha\beta}'' \tilde{v}_\beta''}) \right) \end{aligned} \quad (4-28)$$



The equation of state relates the pressure to the temperature, and it follows for the fluctuations that:

$$\bar{p} \overline{v''_\alpha} + \overline{p'v''_\alpha} = (\gamma - 1) c_v \rho (\overline{\tilde{T}v''_\alpha} + \overline{T''v''_\alpha}) = (\gamma - 1) c_v \rho \overline{T''v''_\alpha} \quad (4-29)$$

The total energy can be expressed in terms of the internal and kinetic energies and this yields the introduction of the turbulent energy flux:

$$\bar{\rho} \overline{E''v''_\alpha} = c_v \rho \overline{T''v''_\alpha} + \bar{\rho} \overline{v''_\beta v''_\alpha v''_\beta} + \bar{\rho} \frac{\overline{v''_\alpha v''_\beta v''_\beta}}{2} \quad (4-30)$$

The use of gradient approximation for the temperature and the kinetic energy fluxes implies that:

$$-\bar{\rho} \overline{T''v''_\alpha} = \frac{\mu_t}{Pr_t} \frac{\partial \tilde{T}}{\partial x_\alpha} ; \quad -\bar{\rho} \overline{k v''_\alpha} = \frac{\mu_t}{Pr_k} \frac{\partial k}{\partial x_\alpha} \quad (4-31)$$

Finally, with the neglect of the fluctuations of the laminar viscosity, the energy equation can be written as:

$$\begin{aligned} \frac{\partial}{\partial t}(\bar{\rho} \tilde{E}) + \frac{\partial}{\partial x_\alpha} ((\bar{\rho} \tilde{E} + p + \frac{2}{3} \bar{\rho} k) \tilde{v}_\alpha - \tilde{v}_\beta (\mu + \mu_t) \tilde{S}_{\alpha\beta}) \\ + \frac{\partial}{\partial x_\alpha} (-\mu_k \frac{\partial k}{\partial x_\alpha} - (\gamma c_v \delta_{\alpha\beta} \frac{\mu_t}{Pr_t} + \delta_{\alpha\beta} K) \frac{\partial \tilde{T}}{\partial x_\beta}) \\ + \frac{\partial}{\partial x_\alpha} (\mu \tilde{S}_{\alpha\beta} \tilde{v}_\beta) = 0 \end{aligned} \quad (4-32)$$

in which  $\tilde{v}_\beta$  is part of the compressibility corrections still to be modelled (see chapter 6).

This points out that the modelled energy equation is significantly more complex than the instantaneous one.

Being the most popular two equation turbulence model, the  $k - \epsilon$  set of equations has also been extensively modified or adapted to various problems. Liakopoulos /65/ reported high speed boundary layer calculations with wall functions for the prescription of  $k$  and  $\epsilon$  boundary conditions. Chien /63/ proposed a modified version of the Jones-Launder model /58/ to describe more accurately the wall vicinity of an incompressible boundary layer. From a Taylor series expansion of the velocity fluctuations when  $y \rightarrow 0$ , Chien deduced a different form of the anisotropic dissipation at the wall:

$$D_w = 2\nu \frac{k}{y^2} \quad (4-33)$$

This quantity, that Chien qualifies "wall dissipation", is assumed to be one component of the dissipation term which must be present in the kinetic energy equation to handle properly the low-Reynolds number effects. Therefore the turbulent energy equation is expressed (in boundary layer form) as:

$$\frac{\partial}{\partial t}(\bar{\rho} k) + \frac{\partial}{\partial x_\alpha} (\bar{\rho} \tilde{v}_\alpha k) = \frac{\partial}{\partial y} \left( (\mu + \frac{\mu_t}{Pr_t k}) \frac{\partial k}{\partial y} \right) + \mu_t \left( \frac{\partial \tilde{u}}{\partial y} \right)^2 - \bar{\rho} \epsilon - \frac{2 \mu k}{y^2} \quad (4-34)$$



A damping effect is also included in the turbulent viscosity calculation to account for the presence of the solid wall:

$$\nu_t = C_\mu \frac{k^2}{\epsilon} \left( 1 - \exp\left(-\frac{C_3 u_\tau y}{\nu}\right) \right) \quad (4-35)$$

where  $\mu_t$  is the friction velocity and  $C_3$  is a constant to be optimized. The argument of the exponential is equivalent to a turbulent Reynolds number whose the length scale is the wall distance and the velocity scale is the friction velocity. As expected from previous remarks but with different reasoning, the  $\epsilon$ -equation must include a wall dissipation term, which is similar in form to eq. (91).

$$D_{w\epsilon} = \frac{2\nu\epsilon}{y^2} \exp\left(-\frac{C_4 u_\tau y}{\nu}\right) \quad (4-36)$$

where  $C_4$  is another constant. The  $\epsilon$ -dissipation term is also corrected with a turbulent Reynolds number function. To summarize, the dissipation equation for low Reynolds number form, is written as (in boundary layer form):

$$\begin{aligned} \frac{\partial}{\partial t}(\rho\epsilon) + \frac{\partial}{\partial x_\alpha}(\rho \tilde{v}_\alpha \epsilon) &= \frac{\partial}{\partial y} \left( (\mu + \mu_t) \frac{\partial \epsilon}{\partial y} \right) \\ &+ C_1 \frac{\epsilon}{k} \mu_t \left( \frac{\partial \tilde{u}}{\partial y} \right)^2 - \frac{\epsilon}{k} \left( C_2 \rho f_\epsilon \epsilon + \frac{2 \mu k \exp(-C_4 u_\tau y / \nu)}{y^2} \right) \end{aligned} \quad (4-37)$$

where the damping of the dissipation is

$$f_\epsilon = 1 - \frac{0.4}{1.8} \exp\left(-\frac{k^2}{6\nu\epsilon}\right) \quad (4-38)$$

In all the applications presented by Chien /63/, the following constants were used:

$$C_3 \in [0.01 - 0.0115]$$

$$C_4 \in 0.5$$

Although designed primarily for incompressible flows, this turbulence model has been readily extended to compressible flows by Coakley /57/ for the case of airfoil calculations and Viegas and Rubesin /66/. Sahu and Danberg /96/ included it also for their transonic calculations. Horstman /64/ used this model extensively for a wide variety of flow configurations from compressible flat plate boundary layers to 3-D shock boundary layer interactions.

El Tahry /85/ set up a complete  $k - \epsilon$  model for application to internal combustion engine flows. The basic methodology is the so-called "order of magnitude analysis". After an extensive comparison of the different terms present in the equations, the two turbulence equations are written as:

$$\begin{aligned} \underbrace{\frac{\partial}{\partial t}(\rho\epsilon)}_1 + \underbrace{\frac{\partial}{\partial x_\alpha}(\rho \tilde{v}_\alpha \epsilon)}_2 &= \underbrace{C_1 P_k \frac{\epsilon}{k}}_3 - \underbrace{C_2 \rho \frac{\epsilon^2}{k}}_4 + \underbrace{\frac{\mu_t}{\sigma_\epsilon} \frac{\partial \epsilon}{\partial x_\alpha}}_5 \\ &- \underbrace{\frac{1}{3} \tilde{\rho} \epsilon \frac{\partial \tilde{v}_\beta}{\partial x_\beta}}_6 + \underbrace{\frac{\epsilon}{\nu} \frac{\partial \mu}{\partial t}}_7 + \underbrace{\tilde{\rho} \tilde{v}_\beta \frac{\epsilon}{k} \frac{\partial \nu}{\partial x_\beta}}_8 - \underbrace{\frac{\mu_t}{\sigma_\epsilon \nu} \frac{\partial \nu}{\partial x_\beta} \frac{\partial \epsilon}{\partial x_\beta}}_9 - \underbrace{\frac{\mu_t}{\sigma_\epsilon \tilde{\rho}} \frac{\partial \tilde{\rho}}{\partial x_\beta} \frac{\partial \epsilon}{\partial x_\beta}}_{10} \end{aligned} \quad (4-39)$$



$$\begin{aligned}
& \underbrace{\frac{\partial}{\partial t}(\bar{\rho} k)}_{1'} + \underbrace{\frac{\partial}{\partial x_\alpha}(\bar{\rho} \tilde{v}_\alpha k)}_{2'} + \underbrace{\frac{\partial}{\partial t}(\bar{\rho}' k')}_{3'} + \underbrace{\tilde{v}_\alpha \frac{\partial}{\partial x_\alpha}(\bar{\rho}' k')}_{4'} - \underbrace{\bar{\rho}' v_\alpha \frac{\partial \tilde{v}_\alpha}{\partial t}}_{5'} + \underbrace{\bar{\rho}' v_\alpha \tilde{v}_\beta \frac{\partial \tilde{v}_\beta}{\partial x_\alpha}}_{6'} \\
& - \underbrace{\bar{\rho} \tilde{v}_\beta \tilde{v}_\alpha \frac{\partial \tilde{v}_\beta}{\partial x_\alpha}}_{7'} - \underbrace{\bar{\rho}' v_\beta v_\alpha \frac{\partial \tilde{v}_\beta}{\partial x_\alpha}}_{8'} - \underbrace{\bar{\rho}' k' \frac{\partial \tilde{v}_\beta}{\partial x_\beta}}_{9'} - \underbrace{\frac{\partial}{\partial x_\beta}(\tilde{v}_\beta \bar{\rho}')}_{10'} + \underbrace{\bar{\rho}' k' v_\beta}_{11'} + \underbrace{\bar{\rho} k' v_\beta}_{12'} \\
& + \underbrace{\bar{\rho}' \frac{\partial \tilde{v}_\beta}{\partial x_\beta}}_{13'} - \underbrace{\bar{\rho} \epsilon}_{14'} + \underbrace{\mu v_\alpha \frac{\partial^2 \tilde{v}_\beta}{\partial x_\alpha \partial x_\beta}}_{15'} + \underbrace{\frac{\partial \mu'}{\partial x_\beta} \frac{\partial k'}{\partial x_\beta}}_{16'} + \underbrace{\mu' \frac{\partial^2 k}{\partial x_\beta^2}}_{17'} - \underbrace{\frac{2}{3} \mu v_\alpha \frac{\partial^2 \tilde{v}_\beta}{\partial x_\alpha \partial x_\beta}}_{18'}
\end{aligned} \quad (4-40)$$

That rather complete model is supposed to describe flows with combustion. The discussion of the modelling of each of the terms is not reproduced here /85/ but relies heavily on standard approximations such as gradient flux laws, isotropic small scale motions and polytropic fluid behavior. Without combustion, most of the compressibility terms can be dropped (7, 8, 9, 10, 3', 4', 5', 6', 8', 9', 11', 13', 15', 16', 17' and 18').

The simplified form is then quite comparable to the model used by Watkins /89/:

$$\frac{\partial}{\partial t}(\bar{\rho} \epsilon) + \frac{\partial}{\partial x_\alpha}(\bar{\rho} \tilde{v}_\alpha \epsilon) = C_1 P_k \frac{\epsilon}{k} - C_2 \bar{\rho} \frac{\epsilon^2}{k} + \frac{\mu_t}{\sigma_\epsilon} \frac{\partial \epsilon}{\partial x_\alpha} + \bar{\rho} \epsilon \frac{\partial \tilde{v}_\beta}{\partial x_\beta} \quad (4-41)$$

$$\frac{\partial}{\partial t}(\bar{\rho} k) + \frac{\partial}{\partial x_\alpha}(\bar{\rho} \tilde{v}_\alpha k) = -\bar{\rho} \tilde{v}_\alpha \tilde{v}_\beta \frac{\partial \tilde{v}_\alpha}{\partial x_\beta} + \frac{\partial}{\partial x_\beta} \left( \frac{\mu_t}{\sigma_k} \frac{\partial k}{\partial x_\beta} \right) - \bar{\rho} \epsilon \quad (4-42)$$

The primary difference with Watkins work seems to be the value of the divergence term coefficient in the dissipation equation,  $-1/3$  for /85/ and  $1.0$  for /89/, although the analysis of Watkins results shows some non-realistic values for the computed turbulent length scale in engine cylinder applications.

Besides that, Reynolds /91/ and Morel and Mansour /92/ have considered the applicability of the  $k-\epsilon$  model to flows undergoing a rapid compression or expansion. From the analysis of the consequences of application of rapid distortion (spherical and/or unidirectional compression, see /92/) the  $\epsilon$ -equation is cast into the following form (by splitting out the production term and assigning different constants to the different parts):

$$\begin{aligned}
\bar{\rho} \frac{D\epsilon}{Dt} &= \frac{\epsilon}{k} \left[ 2 C_1 \mu_t S_{\alpha\beta}^2 - \frac{2}{3} C_1' \mu_t \tilde{D}^2 - \frac{2}{3} C_1'' \bar{\rho} k \tilde{D} \right] \\
&+ \bar{\rho} \tilde{D} - C_2 \bar{\rho} \frac{\epsilon^2}{k} + \text{diffusion}
\end{aligned} \quad (4-43)$$

in which the two new constants  $C_1'$  and  $C_1''$  depend on the mean flow strain tensor  $S_{\alpha\beta}$ , and  $\tilde{D}$  is the mean velocity divergence. As a result,  $C_1'$  and  $C_1''$  are not absolute constant, but vary through the flow field, depending of the local value of  $S_{\alpha\beta}$ , over the following moderate ranges:

$$C_1' \in [1.32, 1.44]$$

$$C_1'' \in [3.5, 4.5]$$

The resulting turbulence model has been applied to the prediction of a typical engine-like situation, i.e. axisymmetrical geometry with a piston producing a unidirectional compression. A similar  $\epsilon$ -equation is used by Gosman and Watkins /90/, Morel and Mansour



/92/ and in some extent by Ramos, Humphrey and Sirignano /95/, the values of the constant analogous to  $C'_1$  and  $C''_1$  are compared.

	/90/	/92/	/95/
$C'_1$	1.44	1.32	1.44
$C''_1$	1.44	4.50	2.95

In /95/, Ramos *et al.* use the same equation for the dissipation as Gosman and Watkins /90/, except for the term  $\rho\epsilon\bar{D}$ , which is dropped in /95/. This in effect gives them a different value of  $C'_1$ , which lies between the one of Gosman and Watkins and the one of Morel and Mansour. When looking at the numerical results, similar disagreement with the turbulent length scale appears, as it did previously when comparing with El Tahry results.

The differences issued from that type of comparison has been one of the motivations for the simulation of homogeneous compressed turbulence, done by Wu, Ferziger and Chapman /94/. In fact, the attention was specifically paid to the discrepancy in value and sign for the mean velocity divergence term coefficient, i.e.  $-2/3$  and  $+1.0$  for Watkins /89/ and Reynolds /91/ respectively. Tested with different strain rates, the results are not really different with low strain rate values, i.e. when the production of turbulence is about the same order of magnitude as the dissipation. This situation is a right illustration of an "equilibrium state". When the strain is so strong that the flow structure is out of equilibrium, none of the  $k - \epsilon$  models perform well. Furthermore, the Watkins model /89/ predicts growth of the length scale during compression, no matter how fast the compression is. The behavior of the length scale is reasonably well predicted by the Reynolds model /91/, but this model produces too much dissipation in the fast compression case (high strain rate value). Such failure of the two equation models lead Wu, Ferziger and Chapman to proposed an improvement by the introduction of a third equation, at the expense of a minimum complexity.

Their reasoning is as follows: in the two equation models, the turbulence energy determines the turbulence velocity scale, while the dissipation plays two roles; it is the rate of destruction of the turbulent kinetic energy, and it determines the turbulence length scale. The dissipation cannot do both jobs simultaneously in high strain rate flows in which the turbulent flow structure is out of equilibrium. To decouple the dissipation and length and time scales, it is proposed the addition of a model equation for a turbulence time scale  $\tau$ . The resulting three equation model has been applied only to homogeneous flows (isotropic decay, isotropic compression, axisymmetric expansion and one-dimensional compression).

#### 4.2.2. THE $k - \omega^2$ MODEL FOR COMPRESSIBLE FLOWS

The uncertainty with the  $k - \epsilon$  model is obviously the dissipation equation. In this paragraph, a different two equation model is presented with a more formal equation for the determination of the length scale.

The evaluation of the characteristic turbulent length scale is based on a different combination of indexes (m,n) in equation (4-16). Rather than solving for the dissipation rate of turbulent energy, the variable considered here is the specific dissipation, i.e. the amount of dissipation per kinetic energy unit. This model has been adapted from the



model of Saffman /69/, Wilcox and Alber /10/ and Wilcox and Traci /67/ by Wilcox and Rubesin /68/ to account accurately for compressibility effects. This model has been selected and used by Ames workers because it was specifically developed for boundary layer flows influenced by severe adverse pressure gradients as well as for equilibrium flows. Its constitutive relationship needs the definition of the turbulent viscosity:

$$\nu_t = \gamma^* \frac{k}{\omega} \quad (4-44)$$

The two turbulent parameters obey the following transport equations:

$$\frac{\partial}{\partial t}(\bar{\rho}k) + \frac{\partial}{\partial x_\alpha}(\bar{\rho} \widetilde{v_\alpha} k - (\mu + \sigma^* \mu_t) \frac{\partial k}{\partial x_\alpha}) = P_k - \beta^* \bar{\rho} \omega k \quad (4-45)$$

$$\frac{\partial}{\partial t}(\bar{\rho}\omega^2) + \frac{\partial}{\partial x_\alpha}(\bar{\rho} \widetilde{v_\alpha} \omega^2 - (\mu + \sigma \mu_t) \frac{\partial \omega^2}{\partial x_\alpha}) = \gamma \frac{\omega^2}{k} P_k - \left( \beta + 2\sigma \left( \frac{\partial L}{\partial x_\alpha} \right)^2 \right) \bar{\rho} \omega^3 \quad (4-46)$$

where the length scale is represented by:

$$L = \frac{\sqrt{k}}{\omega} \quad (4-48)$$

The modelling closure coefficients employed are as follows:

$$\beta = \frac{3}{20}; \quad \beta^* = \frac{9}{100}; \quad \sigma = \sigma^* = \frac{1}{2}$$

$$\gamma^* = \left( 1 - (1 - \lambda^2) \exp\left(-\frac{Re_t}{R\epsilon}\right) \right)$$

$$\gamma \gamma^* = \gamma_\infty \left( 1 - (1 - \lambda^2) \exp\left(-\frac{Re_t}{R_\omega}\right) \right)$$

$$\gamma_\infty = \frac{10}{9}; \quad \lambda = \frac{1}{11}; \quad Re_\epsilon = 1; \quad R_\omega = 2$$

and the turbulent Reynolds number is defined as

$$Re_t = \frac{\sqrt{k} \cdot L}{\nu} \quad (4-49)$$

It is important to note here the interpretation given to the turbulent parameters. The authors /68/ interpret  $k$  as a "mixing" energy of the order of  $9\bar{v}^2/4$  rather than the total kinetic energy present at a point of the boundary layer. Furthermore, they feel that  $\omega$ , the rate of dissipation of kinetic energy per unit of kinetic energy, is a more significant quantity than the rate of turbulence dissipation itself.

Asymptotic analysis in the wall vicinity allows prescribing the true value of  $\omega$  when  $y \rightarrow 0$ , even in the presence of a possibly rough or permeable wall. For a smooth impervious wall, the following boundary values are prescribed:

$$\begin{aligned} k &= 0 \\ \omega &= \frac{20\nu_w}{\beta y^2} \end{aligned} \quad (4-50)$$



This model also allows representing the Reynolds stresses that do not necessarily align with the mean rates of strain. The constitutive relationship is expressed as:

$$-\rho \widetilde{v''_{\alpha} v''_{\beta}} = -\frac{2}{3} \bar{\rho} \delta_{\alpha\beta} k + \mu_t \widetilde{S_{\alpha\beta}} + \frac{8}{9} \frac{k}{(\beta^* \omega^2 + 2d_{\gamma\delta} d_{\delta\gamma})} (d_{\alpha\gamma} r_{\gamma\beta} + d_{\beta\gamma} r_{\gamma\alpha}) \quad (4-51)$$

which contains an incompressible form of a strain tensor, together with the vorticity tensor:

$$r_{\alpha\beta} = \frac{1}{2} \left( \frac{\partial \widetilde{v_{\alpha}}}{\partial x_{\beta}} - \frac{\partial \widetilde{v_{\beta}}}{\partial x_{\alpha}} \right) \quad (4-52)$$

$$d_{\alpha\beta} = \frac{1}{2} \left( \frac{\partial \widetilde{v_{\alpha}}}{\partial x_{\beta}} + \frac{\partial \widetilde{v_{\beta}}}{\partial x_{\alpha}} \right) \quad (4-53)$$

In fact, the idea of misalignment between turbulent stress and strain was initially promoted by Saffman /70/ for incompressible flows. The relation which is used here is a rather drastic simplification of the original proposal, but the idea of misalignment is conserved. A definite advantage of this model is that it allows representing the anisotropy of the Reynolds stress components. The stress tensor can be developed as:

$$\begin{aligned} \tau_{xx} &= 2\mu_t \left( \frac{\partial \tilde{u}}{\partial x} \right) - \frac{2}{3} \left( \frac{\partial \tilde{v}_{\gamma}}{\partial x_{\gamma}} \right) - A_{\omega} \left( \left( \frac{\partial \tilde{u}}{\partial y} \right)^2 - \left( \frac{\partial \tilde{v}}{\partial x} \right)^2 \right) \\ \tau_{yy} &= 2\mu_t \left( \frac{\partial \tilde{v}}{\partial y} \right) - \frac{2}{3} \left( \frac{\partial \tilde{v}_{\gamma}}{\partial x_{\gamma}} \right) - A_{\omega} \left( \left( \frac{\partial \tilde{u}}{\partial y} \right)^2 - \left( \frac{\partial \tilde{v}}{\partial x} \right)^2 \right) \\ \tau_{xy} &= \mu_t \left( \frac{\partial \tilde{u}}{\partial y} + \frac{\partial \tilde{v}}{\partial x} \right) + \frac{1}{2} A_{\omega} \left( \frac{\partial \tilde{u}}{\partial x} - \frac{\partial \tilde{v}}{\partial y} \right) \left( \frac{\partial \tilde{v}}{\partial x} - \frac{\partial \tilde{u}}{\partial y} \right) \end{aligned} \quad (4-54)$$

with:

$$A_{\omega} = \frac{8}{9} \frac{\rho k}{\beta^* \omega^2 + 2 \left( \left( \frac{\partial \tilde{u}}{\partial x} \right)^2 + \left( \frac{\partial \tilde{v}}{\partial y} \right)^2 + \left( \frac{\partial \tilde{u}}{\partial y} + \frac{\partial \tilde{v}}{\partial x} \right)^2 \right)} \quad (4-55)$$

Different from the model proposed earlier by Wilcox and Alber /10/, this turbulence model does not contain any explicit compressibility terms. All applications of this model for transonic or weakly supersonic flows /57/, /55/, /44/, /66/, follow the original statement of Morkovin (and latter Bradshaw) by neglecting the compressibility.

#### 4.2.3. THE $q - \omega$ MODEL FOR COMPRESSIBLE FLOWS

Recently, Coakley /57/ worked out a different two-equation turbulence model based on different turbulence parameters which are similar to those of an early proposal of Kolmogorov /71/ mentioned in the reference /72/. The selected quantities are the characteristic turbulent velocity  $q$  which can be interpreted as the square root of the turbulent kinetic energy  $k$ , and the specific dissipation rate  $\omega$ . The first remark is that model could be classified as utilizing dependent variables namely the square root of the previous one\*\*. The turbulent viscosity is defined as:

$$\mu_t = C_{\mu} D \frac{\rho k}{\omega} \quad (4-56)$$

\* It differs however in other several details.



where  $D$  is a damping function based on the turbulent Reynolds number:

$$D = 1 - \exp(-\alpha R) \quad (4-57)$$

The transport equations for the turbulence parameters are:

$$\frac{\partial}{\partial t}(\bar{\rho} q) + \frac{\partial}{\partial x_\alpha}(\bar{\rho} \widetilde{v_\alpha} q) = \frac{1}{2}(C_\mu D \frac{\rho q}{\omega} P_k - \frac{2}{3} \bar{\rho} q \frac{\partial \widetilde{v_\gamma}}{\partial x_\gamma} - \bar{\rho} \omega q) + \text{diffusion} \quad (4-58)$$

$$\frac{\partial}{\partial t}(\bar{\rho} \omega) + \frac{\partial}{\partial x_\alpha}(\bar{\rho} \widetilde{v_\alpha} \omega) = C_1(C_\mu \bar{\rho} P_k - \frac{2}{3} \bar{\rho} \omega \frac{\partial \widetilde{v_\gamma}}{\partial x_\gamma}) - C_2 \bar{\rho} \omega^2 + \text{diffusion} \quad (4-59)$$

in which the various constants are:

$$C_\mu = 0.09; \quad C_1 = 0.405 D + 0.045; \quad C_2 = 0.92$$

$$Pr_t = 0.9; \quad Pr_q = 1.0; \quad Pr_\omega = 1.3; \quad \alpha = 0.0065$$

and the turbulent Reynolds number is defined now as.

$$R = \frac{q y}{\nu} \quad (4-60)$$

In the same paper, Coakley /57/ proposed different versions of this turbulence model by changing one or two constant values and by using a modified definition of the turbulent Reynolds number, but the basic reasoning remains unchanged.

The development of this model is discussed with the following arguments. The high Reynolds number part of the model is due to a direct transformation of the  $k - \epsilon$  model of Jones and Launder /73/ to the new variables. In this transformation, the kinetic energy was assumed constant in the diffusion terms. The low Reynolds number part of the model, through its damping functions, has been chosen to produce reasonably accurate distributions of skin friction, velocity and kinetic energy profiles in the calculation of low speed boundary layers and pipe flows. The use of  $q$  rather than  $k$  as turbulent variable avoids the need for the extra dissipation term in the  $k$  equation to balance the molecular diffusion in the wall vicinity. One of the modified version of Coakley's model is designed also to simulate the relaxational properties of the Reynolds stress tensor. Unfortunately, in the case of separated flows in which the velocity gradient undergoes a sign reversal, an unphysical discontinuity occurs in the expression of the turbulent stress, which must be artificially corrected.

#### 4.2.4. NON-EQUILIBRIUM TURBULENCE MODELS

Somewhere between the algebraic models and the transport equation models are a few algebraic models including memory effects. The first of them is due to Johnson and King /116/, /117/. With this algebraic formulation, the kinematic viscosity is provided with a two layers relationship:

$$\nu_t = \nu_{te} [1 - \exp(-\nu_{ti}/\nu_{te})] \quad (4-61)$$



which allows a smooth transition between the two zones. The two components are:

$$\begin{aligned}\nu_{ti} &= D^2 \kappa y (-\overline{u'' v''_{max}})^{1/2} \\ \nu_{te} &= C_a \Gamma^{-1}\end{aligned}\quad (4-62)$$

$D$  is the Van Driest damping function modified with  $A^+ = 15$ , and  $\kappa$  is the Von Karman constant ( $\kappa = 0.41$ ). For the outer formulation,  $C_a$  is an adjustable constant and  $\Gamma$  is the intermittency function of Klebanoff /32/.

Thus, the turbulent viscosity does not depend on the mean strain, but is determined by the maximum value of the turbulent shear stress. The  $C_a$  parameter is related to the location of the stress maximum, by satisfying to the following requirement:

$$\nu_{t,max} = \frac{(-\overline{u'' v''_{max}})^{1/2}}{(\partial \bar{u} / \partial y)_{max}} (-\overline{u'' v''_{max}})^{1/2} \approx L U \quad (4-63)$$

The maximum shear stress follows a simplified transport equation deduced from the turbulent kinetic energy equation as:

$$\bar{u} \frac{d(-\overline{u'' v''_{max}})}{dx} = a_1 \left[ (-\overline{u'' v''_{max}}) \left( \frac{\partial \bar{u}}{\partial y} \right)_{max} - \frac{(-\overline{u'' v''_{max}})^{3/2}}{L_{max}} - D_{max} \right] \quad (4-64)$$

This simple steady-state transport equation made of equilibrium between convection, diffusion, production and dissipation is based on the assumption that:

$$a_1 = \frac{(-\overline{u'' v''_{max}})}{k_{max}} \quad (4-65)$$

The associated closure assumptions are:

$$L_{max} \propto \frac{a_1^{3/2} k_{max}^{3/2}}{\epsilon_{max}} \begin{cases} L_{max} = 0.4 y_{max} & \frac{y_{max}}{\delta} \leq 0.225 \\ L_{max} = 0.09 \delta & \frac{y_{max}}{\delta} > 0.225 \end{cases} \quad (4-66)$$

The diffusion term is approximated by:

$$D_{max} = \frac{C_{dif} (-\overline{u'' v''_{max}})^{3/2}}{a_1 \delta (0.7 - (y/\delta)_{max})} \left| 1 - \left( \frac{\nu_{te}}{(\nu_{te})_{eq}} \right)^{1/2} \right| \quad (4-67)$$

with a new coefficient  $C_{dif}$  equal to 0.5.

For equilibrium turbulence, equation (4-64) resumes to:

$$\bar{u} \frac{d(-\overline{u'' v''_{max}})}{dx} = \frac{a_1}{L_{max}} (-\overline{u'' v''_{max}}) \left[ (-\overline{u'' v''_{max}})_{eq}^{1/2} - (-\overline{u'' v''_{max}})^{1/2} \right] - a_1 D_{max} \quad (4-68)$$

in which the equilibrium value of the turbulent shear stress relies on the classical turbulent viscosity

$$\begin{aligned}\nu_{ti} &= D^2 \kappa y (-\overline{u'' v''_{max}})_{eq}^{1/2} \\ \nu_{te} &= 0.0168 U_{ext} \delta_i^* \Gamma^{-1}\end{aligned}\quad (4-69)$$



## 5. SECOND ORDER CLOSURE

All the models which have been presented above are based on the use of the constitutive relationship between the turbulent stress and the mean strain tensor. Although this formalism seems suitable for flows in or close to equilibrium, there are still too many examples of flow configurations where none of these models is able to produce acceptable results. Therefore, research is going on to raise the closure level to one level higher in order to avoid the use of the gradient transport approximation. The route to achieve this, is to solve transport equations for the individual turbulent stresses and turbulent fluxes. The technique is known as the second order closure or sometimes as the Reynolds stress closure (RSE). This problem is being studied for compressible flows in different places in the world, but in the present notes, a general presentation of the topic is made.

Compared to direct simulations (DNS) or to large eddy simulation (LES-SGM) methods, the second order closure does not bring more information on the energy distribution in its frequency spectrum, i.e. a unique time scale is accessible. Nevertheless, a very important factor for turbulence modelling is the Reynolds stress anisotropy. This information is fundamental for the correct description of the different physical mechanisms governing the transport of the turbulence. Rather than representing the turbulence as a scalar quantity, it can be studied now as a tensor.

### 5.1. SECOND ORDER CLOSURE FOR COMPRESSIBLE FLOWS

The second order moment closures (or Reynolds stress models) are currently the most general one-point correlation models from the point of view of physical theory. These models require the solution of additional field equations for the complete set of Reynolds stresses  $\rho \overline{v_\alpha v_\beta}$ , the turbulent heat flux vector  $\rho \overline{v_\alpha T}$  and, frequently a scale equation which can be  $\epsilon$  or  $\omega^2$ , similar to that one used for the two-equation models. These models are obviously more complicated than the eddy viscosity based models. One of the most important physical properties contained in these models is however a stress relaxation property which cannot be correctly represented in the eddy viscosity models.

The modelling of the turbulent stresses and fluxes introduces a lot of new terms, so far not defined by experiments. It is not possible at this time to reach definitive conclusions on the validity of all these closures. For this reason, in the following, emphasis is put on the modelling of the Reynolds stresses whereas the remaining turbulent fluxes will be handled with a general anisotropic form of the gradient approximation.

This remark could seem very restrictive, but in fact the lack of experimental results makes the Reynolds stress modelling problem sufficiently complex to delay the equivalent treatment of others fluxes. Practically, the application domain will be restricted to compressible flows with moderate heat and mass transfers, although extension for combustion flows has been made already /97/.

Let us return now to the open transport equation for  $\rho \overline{v_\alpha v_\beta}$  (eq. (4-1)) in which all new unknown terms need to be modelled.

This equation can be modelled by extending the incompressible models of Launder, Reece and Rodi /74/ and Hanjalic and Launder /75/ to compressible conditions, i.e. using Favre decomposition, introducing the non-zero divergence terms that were eliminated in the original models and accounting for the non-zero mean mass-weighted fluctuating velocities /43/. In this course, we restrict the discussion to the important points of modelling.



- turbulent flux of Reynolds stress :  $= \overline{\rho v''_\alpha v''_\beta v''_\gamma}$

Starting from the exact transport equation for  $\overline{\rho v''_\alpha v''_\beta v''_\gamma}$ , it is possible, as shown by Hanjalic and Launder /76/, by neglecting diffusive and convective terms, to obtain the following form:

$$-\rho \overline{v''_\alpha v''_\beta v''_\gamma} = C_s \rho \frac{k}{\epsilon} (\overline{v''_\alpha v''_\beta} \frac{\partial}{\partial x_\beta} \overline{v''_\gamma} + \overline{v''_\beta v''_\gamma} \frac{\partial}{\partial x_\beta} \overline{v''_\alpha} + \overline{v''_\gamma v''_\alpha} \frac{\partial}{\partial x_\beta} \overline{v''_\beta}) \quad (5-1)$$

This form conserves the symmetric character of the third order tensor  $\overline{v''_\alpha v''_\beta v''_\gamma}$  but, for practical purposes, a simpler form, suggested by Daly and Harlow /77/ seems to produce results of similar quality.

$$-\rho \overline{v''_\alpha v''_\beta v''_\gamma} = C_s \rho \frac{k}{\epsilon} \overline{v''_\gamma v''_\beta} \frac{\partial}{\partial x_\beta} \overline{v''_\alpha} \quad (5-2)$$

- pressure diffusion:  $= \overline{v''_\alpha p'} \delta_{\beta\gamma} + \overline{v''_\beta p'} \delta_{\alpha\gamma}$

Most people neglect pressure-induced diffusion term, mainly due to the lack of experimental information. The measurements of Irwin /50/ in a wall jet suggest that this term cannot be very important. Furthermore, some authors argued that the pressure induced diffusion, if non negligible, would act to destroy the symmetry character of the triple correlation term and support the use of the compact form given by equation (5-2).

- viscous diffusion term:  $= -\frac{\partial}{\partial x_\gamma} (\overline{v''_\alpha \mu S_{\beta\gamma}} + \overline{v''_\beta \mu S_{\alpha\gamma}})$

Assuming that a) the correlation between viscosity fluctuations and other quantities is weak, b) the product of density correlations with velocity gradients is small. Then the development of the molecular diffusion term is written as:

$$\text{visc. diff.} = \frac{\partial}{\partial x_\gamma} \left( \mu \frac{\partial}{\partial x_\gamma} \overline{v''_\alpha v''_\beta} \right) + \frac{\partial}{\partial x_\gamma} \left( \overline{\mu v''_\alpha} \frac{\partial v''_\beta}{\partial x_\gamma} + \overline{\mu v''_\beta} \frac{\partial v''_\alpha}{\partial x_\gamma} \right) \quad (5-3)$$

If the flow is incompressible or solenoidal (weak compressibility, Dussauge /78/), the viscous diffusion can be written as:

$$\text{visc. diff.} = \frac{\partial}{\partial x_\gamma} \left( \mu \frac{\partial}{\partial x_\gamma} \overline{v''_\alpha v''_\beta} \right) \quad (5-4)$$

- \* pressure strain correlation:  $= p' \left( \frac{\partial v''_\alpha}{\partial x_\beta} + \frac{\partial v''_\beta}{\partial x_\alpha} \right)$

In strongly anisotropic flows, i.e. in situations where second order closures are needed, this term is a central piece for explaining the redistribution mechanism between Reynolds stresses. To model this term, the approach is an incompressible-like technique, which consists in integrating a Poisson equation for the fluctuating pressure. The result of this



integration, transposed to variable density flows is written as:

$$\begin{aligned} \overline{\rho' \left( \frac{\partial v_\alpha''}{\partial x_\beta} + \frac{\partial v_\beta''}{\partial x_\alpha} \right)} = & -\frac{C_2 + 8}{11} (\widetilde{P}_{\alpha\beta} - \frac{2}{3} \delta_{\alpha\beta} \widetilde{P}_k) - \frac{8C_2 - 2}{11} (\widetilde{D}_{\alpha\beta} - \frac{2}{3} \delta_{\alpha\beta} \widetilde{D}_k) \\ & - \frac{30C_2 - 2}{55} \rho k \widetilde{S}_{\alpha\beta} - C_1 f_1 \rho \frac{\epsilon}{k} (v_\alpha'' v_\beta'' - \frac{2}{3} \delta_{\alpha\beta} k) \\ & + \frac{k^{\frac{3}{2}}}{\epsilon x_n} \left( C_3 \rho \frac{\epsilon}{k} (v_\alpha'' v_\beta'' - \frac{2}{3} \delta_{\alpha\beta} k) + C_4 (\widetilde{P}_{\alpha\beta} - \widetilde{D}_{\alpha\beta}) \right. \\ & \left. + C_5 \rho k \left( \frac{\partial \widetilde{v}_\alpha}{\partial x_\beta} + \frac{\partial \widetilde{v}_\beta}{\partial x_\alpha} - \frac{2}{3} \delta_{\alpha\beta} \frac{\partial \widetilde{v}_\gamma}{\partial x_\gamma} \right) \right) \end{aligned} \quad (5-5)$$

where

$$\widetilde{P} = \widetilde{D} = -\rho v_\alpha'' v_\beta'' \frac{\partial \widetilde{v}_\alpha}{\partial x_\beta} = \widetilde{P}_k \quad (5-6)$$

and

$$\widetilde{P}_{\alpha\beta} = -\rho (v_\alpha'' v_\gamma'' \frac{\partial \widetilde{v}_\beta}{\partial x_\gamma} + v_\beta'' v_\gamma'' \frac{\partial \widetilde{v}_\alpha}{\partial x_\gamma}) \quad (5-7)$$

$$\widetilde{D}_{\alpha\beta} = -\rho (v_\alpha'' v_\gamma'' \frac{\partial \widetilde{v}_\gamma}{\partial x_\beta} + v_\beta'' v_\gamma'' \frac{\partial \widetilde{v}_\gamma}{\partial x_\alpha}) \quad (5-8)$$

The first two lines of equation (5-5) represent the redistribution mechanism in the flow field far from the wall (Launder, Reece and Rodi /74/) and the last two lines of this equation take into account the wall influence in this mechanism (Hanjalic and Launder /75/). The effect of this last contribution is twofold:

- \* it has an opposite effect to the classical return to isotropy term of Rotta /79/.
- \* it acts also as a rapid term to increase the anisotropy of the stress production terms.

It must be emphasized that the transposition of an original incompressible technique to a variable density situation is not free of uncertainties. For instance a corrective term appears in the development of the non linear contribution due to the use of Favre averaging (see ref. /80/). Also, the fourth rank tensor, corresponding to the high Reynolds number rapid term does not possess all the mathematical properties of its incompressible counterpart, e.g.

$$b_{\delta\alpha}^{\beta\gamma} \neq b_{\delta\alpha}^{\gamma\beta} \quad \text{or} \quad b_{\delta\alpha}^{\beta\alpha} \neq 0 \quad (5-9)$$

Finally, the whole term can be considered as a pure redistribution contribution only in the case of solenoidal turbulence field. Otherwise the bulk deformation is a source/sink term (Dussauge /78/, Vandromme /27/).

The real weakness of this approach is the use of an incompressible approach (Poisson equation) when the flow is compressible. It would be more justified to introduce a wave-like operator to evaluate the fluctuating pressure field, like Feiereisen /15/ tried from the results of his direct simulations. Unfortunately, the results, which have been obtained are nearly identical to those of the incompressible formulation.

$$* \text{ mean pressure gradient term: } = -\overline{v_\alpha''} \frac{\partial p}{\partial x_\beta} - \overline{v_\beta''} \frac{\partial p}{\partial x_\alpha}$$

According to Rubesin's proposal for the one-equation turbulence model, that term can be treated like compressibility terms for two-equation turbulence models, assuming a polytropic behaviour of the fluid (see chapter 6).



\* viscous dissipation

It has been shown, in incompressible case /81/, that the dissipation tensor is diagonally dominant and nearly spherical. The ratio of the deviatoric to the diagonal terms being related to the Reynolds stress anisotropy, the dissipation is described with a compound function which is scalar in the high turbulent Reynolds number zones and allows an anisotropic dissipation elsewhere (wall vicinity for instance).

$$\epsilon_{\alpha\beta} = \frac{\epsilon}{k} (\overline{v_\alpha v_\beta} f_s + (1 - f_s) \frac{2}{3} \delta_{\alpha\beta} k) \quad (5-10)$$

with  $f_s = 1/(1 + Re_t/10)$  and  $Re_t = k^2/\nu\epsilon$ . Nevertheless, some of the "slow" pressure strain terms may also represent anisotropic  $\epsilon_{ij}$ .

To summarize the assumptions made above, the modelled Reynolds stress equation can be written as:

$$\begin{aligned} \frac{\partial}{\partial t} (\rho \overline{v_\alpha v_\beta}) + \frac{\partial}{\partial x_\gamma} (\rho \overline{v_\gamma v_\alpha v_\beta} - C_3 \rho \frac{k}{\epsilon} \overline{v_\gamma v_\alpha} \frac{\partial}{\partial x_\beta} \overline{v_\alpha v_\beta} - \mu \frac{\partial}{\partial x_\gamma} \overline{v_\alpha v_\beta}) \\ = \overline{P_{\alpha\beta}} - \frac{C_2 + 8}{11} (\overline{P_{\alpha\beta}} - \frac{2}{3} \delta_{\alpha\beta} \overline{P_k}) - \frac{8C_2 - 2}{11} (\overline{D_{\alpha\beta}} - \frac{2}{3} \delta_{\alpha\beta} \overline{D}) \\ - \frac{30C_2 - 2}{55} \rho k \overline{S_{\alpha\beta}} - C_1 \rho \frac{\epsilon}{k} (\overline{v_\alpha v_\beta} - \frac{2}{3} \delta_{\alpha\beta} k) \\ - (\overline{v_\alpha} \frac{\partial p}{\partial x_\beta} + \overline{v_\beta} \frac{\partial p}{\partial x_\alpha}) - \rho \frac{\epsilon}{k} (\overline{v_\alpha v_\beta} f_s + (1 - f_s) \frac{2}{3} \delta_{\alpha\beta} k) \\ + \frac{k^{\frac{3}{2}}}{\epsilon x_n} \left( C_3 \rho \frac{\epsilon}{k} (\overline{v_\alpha v_\beta} - \frac{2}{3} \delta_{\alpha\beta} k) + C_4 (\overline{P_{\alpha\beta}} - \overline{D_{\alpha\beta}}) \right. \\ \left. + C_5 \rho k \left( \frac{\partial \overline{v_\alpha}}{\partial x_\beta} + \frac{\partial \overline{v_\beta}}{\partial x_\alpha} - \frac{2}{3} \delta_{\alpha\beta} \frac{\partial \overline{v_\gamma}}{\partial x_\gamma} \right) \right) \end{aligned} \quad (5-11)$$

The last unknown, which remains in the modelled Reynolds stress transport equation, is the turbulent dissipation rate  $\epsilon$ . The modelling of a transport equation for this quantity has been given already for the first two equation model, and only the discrepancies due to the different level of closure are of some interest here.

A basic difference compared to the eddy viscosity model is that the Reynolds stresses can be considered now as exact quantities. This yields a more accurate evaluation of  $\overline{P_k}$ , the production term. Furthermore, as the eddy viscosity does not exist any longer, the turbulent diffusion transport of the dissipation is modelled by a generalized gradient flux approximation from Launder /82/:

$$- \overline{v_\alpha} \epsilon = C_\epsilon \frac{k}{\epsilon} \overline{v_\alpha v_\beta} \frac{\partial \epsilon}{\partial x_\beta} \quad (5-12)$$

As far as compressibility terms are concerned for the dissipation equation, the exact derivation of the equation introduces variable density terms as shown in /80/ but the usual method is to ignore these terms and keep the  $\epsilon$ -equation similar to its incompressible counterpart. The modelling is done globally. If compressibility terms are introduced in the turbulent energy equation or here, in the Reynolds stress equations, experience shows that their counterpart is needed in the dissipation equation as well.



The modifications induced for the total energy equation are derived similarly: the turbulent fluxes are expressed with an anisotropic relationship and the triple correlations follow the same approximation as in the Reynolds stress equation. The modelled total energy equation writes now as:

$$\begin{aligned} & \frac{\partial}{\partial t}(\rho \tilde{E}) + \frac{\partial}{\partial x_\gamma} \left( (\rho \tilde{v}_\gamma \tilde{E} + p + \frac{2}{3} \mu \frac{\partial \tilde{v}_\gamma}{\partial x_\gamma}) \tilde{u}_\gamma + (\rho \tilde{v}_\alpha \tilde{v}_\gamma - \mu \frac{\partial \tilde{v}_\gamma}{\partial x_\alpha}) \tilde{u}_\alpha \right. \\ & - 0.5 C_s' \frac{k}{\epsilon} \tilde{v}_\gamma \tilde{v}_\delta \frac{\partial \tilde{v}_\alpha \tilde{v}_\alpha}{\partial x_\delta} - \mu \frac{\partial}{\partial x_\gamma} \left( \frac{\tilde{v}_\alpha \tilde{v}_\alpha}{2} + \frac{\tilde{v}_\alpha \tilde{v}_\alpha}{2} \right) \\ & \left. - (C_\epsilon C_v \gamma \rho \frac{k}{\epsilon} \tilde{v}_\alpha \tilde{v}_\gamma + \delta_{\beta\gamma} K) \frac{\partial \tilde{T}}{\partial x_\beta} - \mu \left( \frac{\partial \tilde{v}_\gamma}{\partial x_\beta} + \frac{\partial \tilde{v}_\beta}{\partial x_\gamma} - \frac{2}{3} \delta_{\gamma\beta} \frac{\partial \tilde{v}_\alpha}{\partial x_\alpha} \right) \tilde{u}_{\beta\gamma} \right) = 0 \end{aligned} \quad (5-13)$$

## 5.2. OTHER SECOND ORDER CLOSURE MODELS FOR COMPRESSIBLE FLOWS

In the above paragraph, a basic second order closure has been presented, which attempts to account for variable density effects. This is done, firstly by using Favre averaging and reintroducing all divergence terms everywhere they have been neglected for the case of constant density flows. But the sum of modelling approximations helps one to realize that, to-day there is still a long way before a complete closure including strong heat and mass transfers is obtained. For the basic closure, the effort has been made to emphasize modelling correctly the dynamical field, leaving room for later improvement of the heat transfer problems.

Other workers also progressed in this type of closure. Among them, Bonnet /83/ used a similar approach to the above, although he chose a different variable as a turbulent length scale. Rather than using a conventional length scale, he used the properties of the two-point correlation to define an integral length scale, for which he derived a transport equation. For wake calculations, no explicit compressibility terms were included. Conversely, he had to use such terms for studying the supersonic free shear layer spreading rate /14/.

Wilcox and Rubesin /68/ extended their two-equation model to second order closure. Independently from having a different scale equation, their modelling differs significantly from the basic version, even for incompressible flows, in the pressure strain correlation term. Rather than assuming a set of properties for a fourth rank tensor such as symmetry and incompressibility, they evaluated the constants belonging to this term, by forcing the Reynolds stress to follow the same distribution as the one indicated by the constitutive relationship with the two equation model. Furthermore, they neglect completely all compressibility terms. With this model, they obtain satisfactory results for the description of the compressible boundary layer with adverse and favorable pressure gradients. Thus, they concluded that second order closure models, with modelling coefficients that are independent of the pressure gradients, represent the experimental data better than a mixing length model with pressure gradient dependent modelling. This confirms the intrinsic general capability of this type of closure.

Janicka and Lumley /84/ used a different technique. Although they used a modified technique to derive their transport equations, they came out with a complete second order closure, applicable only for low Mach number flows. They applied that closure to the calculation of He-air and CO<sub>2</sub>-air jets. The significant result of interest in the present



course, is that they use variable density terms in the Reynolds stress equation having a similar counterpart in the scale equation, although it is not yet established that the density variations, in the flows studied are large enough to validate the use of these terms.

### Algebraic Reynolds stress models

A slightly different manner of departing from the simple isotropic eddy viscosity relationship is to use instead more generally applicable algebraic stress relations obtained from a drastic simplification of the transport equations for the individual stresses. This simplification is based on an idea of Rodi [104], who suggested relating the transport terms (i.e. convection + diffusion) of  $\bar{\rho} \widetilde{v''_\alpha v''_\beta}$  to the equivalent terms in the  $k$ -equation with a simple scale ratio:

$$\frac{D(\bar{\rho} \widetilde{v''_\alpha v''_\beta})}{Dt} - \text{Diff}(\widetilde{v''_\alpha v''_\beta}) = \frac{\widetilde{v''_\alpha v''_\beta}}{k} \left( \frac{D(\bar{\rho} k)}{Dt} - \text{Diff}(k) \right) \quad (5-14)$$

Introducing the source terms, the individual stresses can be solved from a set of implicit algebraic equations. As the source terms are modelled with similar closure assumptions as standard RSE models, ASM provide the same accuracy without the need to solve additive PDE's. The basic simplification is valid only when spatial and temporal changes of  $\frac{\widetilde{v''_\alpha v''_\beta}}{k}$  are small compared to the changes of  $\widetilde{v''_\alpha v''_\beta}$  itself.

Nevertheless, for non-equilibrium situations, the set of algebraic equations happens to be very difficult to solve in an efficient manner. To overcome this difficulty, various attempts have been made to treat the problem as a perturbation model with respect to a  $k - \epsilon$  model for instance [118], especially when expressing the turbulence production terms.



## 6. COMPRESSIBILITY EFFECTS

So far, the so-called compressibility terms have not yet been modelled, but although it is not quite established how important they are, most of the modelling effort is attached to their description. Beyond the correction to  $k-\epsilon$  model in a heuristic fashion /105/, /106/, consisting to add an explicit link of the eddy viscosity to some characteristic turbulent Mach number, special modelling effort can be given to the compressible terms in the transport equations. These terms are:

- density-velocity correlations
- pressure correlations
- compressible dissipation

The following represents the successive attempts to model properly these terms, from the pioneering work of Wilcox and Rubesin /10/, /43/, /68/ to the more recent developments which are currently in use.

### 6.1. DENSITY CORRELATIONS

The evaluation of the mean pressure gradient term is linked to the knowledge of the density-velocity correlations  $\rho' v_\alpha''$ . Two different techniques are available.

a) Let us assume first that the total temperature is constant in the whole flow or at least within the field of turbulent eddies:

$$T_{tot} = T + \frac{v_\alpha v_\alpha}{2C_p} = \text{const.} \quad (6-1)$$

Following the mass-weighted decomposition,  $T$  and  $u_\alpha$  can be replaced by mean and fluctuating quantities. Then equation (6-1) is written now after mass weighted time averaging as:

$$\tilde{T} + \frac{\widetilde{v_\alpha v_\alpha}}{2C_p} + \frac{\widetilde{v_\alpha'' v_\alpha''}}{2C_p} = T_{tot} \quad (6-2)$$

Subtracting from (6-1) its instantaneous form, yields:

$$T'' = -\frac{1}{C_p} \widetilde{v_\alpha} v_\alpha'' - \frac{1}{2C_p} (v_\alpha'' v_\alpha'' - \widetilde{v_\alpha'' v_\alpha''}) \quad (6-3)$$

Then it is reasonable to assume that the mean velocity, in at least one direction will be much larger than the fluctuating velocity in that direction, and to represent equation (6-3) with its leading terms only:

$$T'' = -\widetilde{v_\alpha} \frac{v_\alpha''}{C_p} \quad (6-4)$$

Rubesin /43/ assumes that the fluid behaves, at least locally, in a polytropic manner. Then:

$$\frac{p'}{p} = n \frac{\rho'}{\rho} = \frac{n}{n-1} \frac{\rho T''}{\rho \tilde{T}} = \frac{n}{n-1} \frac{\rho h''}{\rho \tilde{h}} \quad (6-5)$$

where  $n$  is the polytropic coefficient ( $n = 0$ , isobaric;  $n = 1$ , isothermal;  $n = C_p/C_v$ , isentropic; etc...). By combining the two equations above, it is possible to relate density to velocity fluctuations as:

$$\rho' = -\frac{\rho}{(n-1)C_p \tilde{T}} \widetilde{v_\alpha} v_\alpha'' \quad (6-6)$$



and therefore get the desired expression for the density velocity correlation:

$$\overline{v''_{\alpha}} = -\frac{\overline{\rho' v''_{\alpha}}}{\bar{\rho}} = \frac{1}{(n-1)C_p \tilde{T}} \tilde{v}_{\beta} \widetilde{v''_{\alpha} v''_{\beta}} \quad (6-7)$$

Then the gradient flux approximation can be used again and it comes:

$$\overline{v''_{\alpha}} = -\frac{\overline{\rho' v''_{\alpha}}}{\bar{\rho}} = \frac{1}{(n-1)C_p \tilde{T}} \tilde{v}_{\beta} \left( \frac{\mu_t}{\bar{\rho}} \widetilde{S_{\alpha\beta}} - \frac{2}{3} \delta_{\alpha\beta} k \right) \quad (6-8)$$

Now, it is possible to simplify further this expression by specifying that the flow has a principal velocity direction. Then the only appropriate value for the dummy index is  $i = 1$ , and consequently, equation (131) reduces to:

$$\overline{v''_{\alpha}} = \text{const.} \frac{\gamma - 1}{n - 1} \frac{\tilde{v}_1 k}{\tilde{a}^2} \quad (6-9)$$

Since the value of  $n$  is unknown, it becomes a modelling coefficient and its value can be included in the constant of equation (6-9). Note also, that  $n \rightarrow \infty$  for incompressible flows together with  $\overline{v''_{\alpha}} \rightarrow 0$  as required.  $k/a^2$  is a measure of the turbulence Mach number.  $n$  takes a value of about 1.2 as expected in non isentropic flows /43/. Wilcox and Alber /10/ proposed a form similar, except that  $n$  must be less than unity to have the same sign as in their work.

b) An alternative representation of  $\overline{v''_{\alpha}}$  that does not require the assumption of constant total temperature within the turbulence, is to use directly the polytropic law in the definition of the density velocity correlation. Then:

$$\overline{v''_{\alpha}} = -\frac{\overline{\rho' v''_{\alpha}}}{\bar{\rho}} = -\frac{1}{(n-1)\tilde{T}} \overline{T'' v''_{\alpha}} \quad (6-10)$$

and the problem is shifted to the evaluation of the turbulent heat flux. In absence of the use of either equation (6-7) or (6-10) to check against several sets of experimental data, it is not clear which is the best model. Most of the applications reported by Coakley *et al.* /51/ and Viegas and Coakley /52/ neglected the compressibility terms. Equation (6-10) has the advantage of being simpler and not requiring a constant total temperature assumption within an eddy. This latter hypothesis can be of importance, not only from a quantitative viewpoint but also in a phenomenological sense. Suppose a boundary layer flow with  $n > 1$ . Equation (6-7) will produce a constant positive sign to  $\overline{v''_{\alpha}}$ , whereas equation (6-10) can assign either positive or negative values, depending on whether the flow is over a cooled or a heated surface.

## 6.2. PRESSURE CORRELATIONS

The second compressibility term in the turbulent kinetic energy equation is due to the interaction between the fluctuating pressure and the divergence of the velocity fluctuations. The modelling of this term is possible following two different approaches due to Rubesin /43/ and Zeman /119/, /120/.

### 6.2.1. Rubesin's modelling of pressure divergence



From the polytropic behaviour assumption, this term is expressed as:

$$\overline{p' \frac{\partial v''_{\alpha}}{\partial x_{\alpha}}} = \frac{np}{\bar{\rho}} \overline{\rho' \frac{\partial v''_{\alpha}}{\partial x_{\alpha}}} \quad (6-11)$$

After manipulation of the continuity equation, and postulating that the turbulence intensity varies slowly along streamlines, Rubesin /43/ gets the following result:

$$\overline{\rho' \frac{\partial v''_{\alpha}}{\partial x_{\alpha}}} = \Gamma^2 \bar{\rho} \frac{\partial \widetilde{v_{\alpha}}}{\partial x_{\alpha}} \quad (6-12)$$

where  $\Gamma$  is the r.m.s. density fluctuation intensity:

$$\left\langle \frac{\rho'}{\rho} \right\rangle = \Gamma \quad (6-13)$$

The variation of turbulence intensity  $\Gamma$  from streamline to streamline, can be accounted for by setting  $\Gamma^2$  proportional to the local kinetic energy of the turbulence. Usually, the constant dominant flow direction implies that  $v_1 > v_2$ , even in separated flows, so that equation (6-6), when squared yields:

$$\Gamma^2 = \text{const.} \frac{\widetilde{v_1^2}}{a^2} \frac{k}{a^2} \quad (6-14)$$

and then introducing  $\xi$ , a new modelling coefficient, it comes:

$$\overline{p' \frac{\partial v''_{\alpha}}{\partial x_{\alpha}}} = \xi \bar{p} \frac{\widetilde{v_1^2}}{a^2} \frac{k}{a^2} \frac{\partial \widetilde{v_{\alpha}}}{\partial x_{\alpha}} \quad (6-15)$$

Various improvements have been brought to this modelling approach of the pressure correlation. Subtracting the mean continuity equation from the instantaneous form yields:

$$\bar{\rho} \frac{\partial v''_{\alpha}}{\partial x_{\alpha}} = -\frac{\partial \rho'}{\partial t} - v''_{\alpha} \frac{\partial \bar{\rho}}{\partial x_{\alpha}} - \rho' \frac{\partial \widetilde{v_{\alpha}}}{\partial x_{\alpha}} - \widetilde{v_{\alpha}} \frac{\partial \rho'}{\partial x_{\alpha}} - \frac{\partial \rho' v''_{\alpha}}{\partial x_{\alpha}} \quad (6-16)$$

For mass weighted variables, Taylor assumption writes as:

$$\frac{\partial \rho'}{\partial t} + \widetilde{v_{\alpha}} \frac{\partial \rho'}{\partial x_{\alpha}} - \frac{\rho' v''_{\alpha}}{\bar{\rho}} \frac{\partial \rho'}{\partial x_{\alpha}} = 0 \quad (6-17)$$

and (6-16) becomes:

$$\bar{\rho} \frac{\partial v''_{\alpha}}{\partial x_{\alpha}} = -\frac{\overline{\rho' v''_{\alpha}}}{\bar{\rho}} \frac{\partial \rho'}{\partial x_{\alpha}} - \rho' \frac{\partial \widetilde{v_{\alpha}}}{\partial x_{\alpha}} - v''_{\alpha} \frac{\partial \bar{\rho}}{\partial x_{\alpha}} - \frac{\partial \rho' v''_{\alpha}}{\partial x_{\alpha}} \quad (6-18)$$

Multiplying (6-18) with the pressure fluctuation and averaging produces the following form for the pressure divergence correlation:

$$\overline{p' \frac{\partial v''_{\alpha}}{\partial x_{\alpha}}} = -\frac{\overline{\rho' v''_{\alpha}}}{\bar{\rho}^2} \overline{p' \frac{\partial \rho'}{\partial x_{\alpha}}} - \frac{\overline{p' \rho'}}{\bar{\rho}} \frac{\partial \widetilde{v_{\alpha}}}{\partial x_{\alpha}} - \frac{\overline{p' v''_{\alpha}}}{\bar{\rho}} \frac{\partial \bar{\rho}}{\partial x_{\alpha}} - \frac{1}{\bar{\rho}} \overline{p' \frac{\partial \rho' v''_{\alpha}}{\partial x_{\alpha}}} \quad (6-19)$$



As pressure and density fluctuations are rather correlated (because of the equation of state), it can be expected that pressure fluctuations are weakly correlated to the density fluctuations derivatives since they belong to different spectrum ranges. That remark applies also for the last term on the RHS of equation (6-19). Using the polytropic assumption to relate the density and the velocity fluctuations

$$\rho' = -\frac{\rho v_\alpha''}{(n-1)C_p \tilde{T}} \tilde{v}_\alpha \quad (6-20)$$

it comes

$$\overline{p' \frac{\partial v_\alpha''}{\partial x_\alpha}} = -\frac{1}{\rho} \overline{p' v_\alpha''} \left[ \frac{\partial \bar{\rho}}{\partial x_\alpha} - \frac{\tilde{v}_\alpha \bar{\rho}}{(n-1)C_p \tilde{T}} \frac{\partial \tilde{v}_\alpha}{\partial x_\alpha} \right] \quad (6-21)$$

Using again the polytropic assumption

$$p' = n\rho' R\tilde{T} \implies \overline{p' v_\alpha''} = n\overline{\rho' v_\alpha''} R\tilde{T} \quad (6-22)$$

and the pressure-velocity correlation can be expressed in terms of the Reynolds stresses:

$$\overline{p' v_\alpha''} = -\frac{n(\gamma-1)}{\gamma(n-1)} \overline{\rho v_\beta v_\alpha'' v_\beta''} \quad (6-23)$$

To summarize, the compressibility terms can be modelled as:

$$\overline{p' \frac{\partial v_\alpha''}{\partial x_\alpha}} = \frac{n(\gamma-1)}{\gamma(n-1)} \overline{v_\beta v_\alpha'' v_\beta''} \left[ \frac{\partial \bar{\rho}}{\partial x_\alpha} - \frac{\tilde{v}_\alpha \bar{\rho}}{(n-1)\gamma C_p \tilde{T}} \frac{\partial \tilde{v}_\alpha}{\partial x_\alpha} \right] \quad (6-24)$$

$$-\overline{v_\alpha''} \frac{\partial \bar{p}}{\partial x_\alpha} = -\frac{\overline{v_\beta v_\alpha'' v_\beta''}}{(n-1)\gamma C_p \tilde{T}} \frac{1}{\bar{\rho}} \frac{\partial \bar{p}}{\partial x_\alpha} \quad (6-25)$$

Nevertheless, this modelling of the pressure correlations relies on relatively restrictive assumptions about the behaviour of the density fluctuations along a streamline and the absence of the total temperature fluctuations.

#### a) Total temperature fluctuations

To discard these restrictions, Rubesin performed a detailed analysis of experimental results. Consider again the total temperature expression:

$$H'' = h'' + \tilde{v}_\alpha v_\alpha'' + \left( \frac{v_\alpha'' v_\alpha''}{2} - k \right) = 0 \quad (6-26)$$

Neglecting the total temperature fluctuations and the higher order terms,

$$h'' = -\tilde{v}_\alpha v_\alpha'' \quad (6-27)$$

Rubesin noticed that in strong compressibility situations, those fluctuations could not be neglected. For instance, the experimental results cited in /106/ indicate that within



an hypersonic boundary layer, e.g. at  $M_e = 6.4$  over a cooled surface with  $T_w/T_{0e} = 0.46$ , the fluctuations can have magnitudes ranging from:

$$1.4\% < \frac{\langle H'' \rangle}{\tilde{H}} < 4.8\%$$

Equation (6-27), therefore, has to be modified to account for these fluctuations. To do so, Rubesin /109/ postulate a gradient law for the enthalpy fluctuations:

$$h'' = -\alpha v''_\alpha \frac{\partial \tilde{h}}{\partial x_\alpha} \quad (6-28)$$

By analogy with the turbulent heat flux law in a boundary layer flow, a reasonable expression is:

$$h'' = -c_e \bar{\rho} \frac{k}{\epsilon} v''_2 \frac{\partial \tilde{h}}{\partial x_2} \quad (6-29)$$

in which  $c_e = 0.35$  and subscript 2 stands for the normal direction in the boundary layer approximation.

From that, the polytropic assumption can be rewritten as:

$$\frac{\rho'}{\bar{\rho}} = \frac{1}{n-1} \frac{\rho h''}{\tilde{\rho} \tilde{h}} = -\frac{1}{n-1} c_e \frac{\rho}{\bar{\rho}} \frac{k}{\epsilon} \frac{1}{\tilde{h}} \frac{\partial \tilde{h}}{\partial x_\beta} v''_\beta \quad (6-30)$$

which can be used with the definition of  $\overline{v''_\alpha}$  to yield

$$\overline{v''_\alpha} = -\frac{\overline{\rho' v''_\alpha}}{\bar{\rho}} = \frac{1}{n-1} \frac{c_e}{\bar{\rho}} \frac{k}{\epsilon} \frac{1}{\tilde{h}} \frac{\partial \tilde{h}}{\partial x_\beta} \overline{\rho v''_\beta v''_\alpha} \quad (6-31)$$

Recall that enthalpy can be expressed in terms of the sound speed:

$$\tilde{h} = \frac{\tilde{a}^2}{(\gamma-1)} \quad (6-32)$$

so that equation (6-31) can be written as:

$$\overline{v''_\alpha} = \frac{(\gamma-1)}{(n-1)} c_e \frac{k}{\epsilon} \frac{\partial \tilde{h}}{\partial x_\beta} \left[ \frac{\overline{\rho v''_\beta v''_\alpha}}{\bar{\rho} \tilde{a}^2} \right] \quad (6-32)$$

As stated by Rubesin, the terms included in brackets can be considered as moments of turbulence Mach number, which vanish in incompressible flows, i.e.  $\tilde{a} \rightarrow \infty$ . Thus  $\overline{v''_\alpha}$  can be considered as a measure of the degree of compressibility of the turbulence. It is also interesting to notice that these compressibility effects are directly linked to the local heat transfer terms. If we restrict ourselves to the thin layer approximation, equation (6-32) can be written as:

$$\overline{v''_1} = \frac{(\gamma-1)}{(n-1)} c_e \frac{k}{\epsilon} \frac{\partial \tilde{h}}{\partial x_2} \left[ \frac{\overline{\rho v''_1 v''_2}}{\bar{\rho} \tilde{a}^2} \right] \quad (6-33)$$



This expression indicates that  $\overline{v_1''}$  can be either positive or negative, depending on the signs of Reynolds stress and static enthalpy gradients. In a jet flow, these two quantities will change sign simultaneously at the centerline, and therefore, the sign of  $\overline{v_1''}$  will remain constant across the flow. Differently, in a compressible boundary layer on a cooled surface,  $\tilde{h}$  has a maximum inside the boundary layer, whereas Reynolds stress do not. The induced change of sign of the density-velocity correlation will produce different influence on the  $k$  distribution in the boundary layer. This can represent the different behaviour of compressibility effects for attached boundary layers and free shear flows at similar Mach numbers.

### b) Density fluctuations

This improvement aims to avoid any assumption on the behaviour of density fluctuations. The continuity equation for fluctuating quantities can be written as:

$$\frac{\partial \rho'}{\partial t} + \frac{\partial}{\partial x_\alpha} (\rho' \tilde{v}_\alpha + \rho v_\alpha'') = 0 \quad (6-34)$$

which can be used for developing a transport equation for the density fluctuation variance:

$$\frac{\partial \overline{\rho'^2}}{\partial t} + \tilde{v}_\alpha \frac{\partial \overline{\rho'^2}}{\partial x_\alpha} + 2 \overline{\rho'^2} \frac{\partial \tilde{v}_\alpha}{\partial x_\alpha} + 2 \frac{\partial \tilde{\rho}}{\partial x_\alpha} \overline{\rho' v_\alpha''} + 2 \tilde{\rho} \rho' \frac{\partial v_\alpha''}{\partial x_\alpha} = 0 \quad (6-35)$$

Therefore, the pressure velocity divergence correlation can be expressed (using again the polytropic assumption

$$\overline{p' \frac{\partial v_\alpha''}{\partial x_\alpha}} = \frac{n \tilde{p}}{\tilde{\rho}} \overline{\rho' \frac{\partial v_\alpha''}{\partial x_\alpha}} \quad (6-36)$$

as:

$$\overline{p' \frac{\partial v_\alpha''}{\partial x_\alpha}} = n \tilde{p} \left\{ - \frac{\partial \tilde{v}_\alpha}{\partial x_\alpha} \frac{\overline{\rho'^2}}{\tilde{\rho}} - \frac{1}{\tilde{\rho}} \frac{\partial \tilde{\rho}}{\partial x_\alpha} \frac{\overline{\rho' v_\alpha''}}{\tilde{\rho}} - \frac{1}{2 \tilde{\rho}^2} \left[ \frac{\partial \overline{\rho'^2}}{\partial t} + \tilde{v}_\alpha \frac{\partial \overline{\rho'^2}}{\partial x_\alpha} \right] \right\} \quad (6-37)$$

Consider once more, the variance of the density fluctuations:  $\Gamma = \sqrt{\overline{\rho'^2}}/\tilde{\rho}$ . Using the mean continuity equation, (6-37) simplifies to give:

$$\overline{p' \frac{\partial v_\alpha''}{\partial x_\alpha}} = n \tilde{p} \left\{ \frac{1}{\tilde{\rho}} \frac{\partial \tilde{\rho}}{\partial x_\alpha} \overline{v_\alpha''} - \frac{1}{2} \left[ \frac{\partial \Gamma^2}{\partial t} + \tilde{v}_\alpha \frac{\partial \Gamma^2}{\partial x_\alpha} \right] \right\} \quad (6-38)$$

Combining equations (129) and (149) and neglecting higher order terms, the local value of the density variance can be expressed as:

$$\Gamma^2 = \left( \frac{c_e}{(n-1)\tilde{\rho}\tilde{h}} \frac{k}{\epsilon} \right)^2 \frac{1}{\tilde{\rho}} \left| \overline{\rho v_\alpha'' v_\beta''} \frac{\partial \tilde{h}}{\partial x_\alpha} \frac{\partial \tilde{h}}{\partial x_\beta} \right| \quad (6-39)$$

In the computation with a  $k - \epsilon$  model, each of the quantities in equation (6-39) are known and can be used to establish the  $\Gamma$  distribution. Doing so, the restriction to slow variations of density fluctuations has been discarded, and make possible the application to the crossing of shock waves for instance, provided that the local gradients are calculated



properly. Nevertheless, the shock wave crossing is still a problem which would require a more extensive testing.

### 6.2.2. Zeman's modelling of pressure divergence

#### a) density gradient

In a first approach, the zero pressure gradient compressible boundary layer was considered. With certain approximations, one can cast the equation for the pressure variance  $\overline{p'^2}$  in the following form:

$$\frac{1}{2} \left( \frac{\partial \overline{p'^2}}{\partial t} + \widetilde{v}_\alpha \frac{\partial \overline{p'^2}}{\partial x_\alpha} \right) = -\rho^2 \widetilde{a}^2 p \frac{\partial \overline{v_\alpha''}}{\partial x_\alpha} - \widetilde{a}^2 \frac{\partial \bar{\rho}}{\partial x_\beta} \overline{p v_\beta''} \quad (6-40)$$

Zeman expressed the pressure flux in terms of the turbulent mass flux (density/velocity correlation). That correlation, can be closed by a gradient approximation, i.e. a function of the mean density gradient. Then, Zeman assumes that, in the boundary layer approximation, the substantive derivative can be neglected and the transport equation reduces to the balance between the pressure dilatation and the density gradient term:

$$\overline{p' \frac{\partial v_\alpha''}{\partial x_\alpha}} = f_\rho(M_t) \tau_t \widetilde{v}_2^2 \left( \frac{\partial \bar{\rho}}{\partial x_2} \right)^2 \frac{a^2}{\bar{\rho}} \quad (6-41)$$

in which  $\tau_t$  is a turbulent time scale,  $f_\rho$  is a function of the turbulent Mach number  $M_t$ , which must satisfy the limit condition:

$$f_\rho \rightarrow M_t^2 \quad \text{as } M_t \rightarrow 0 \quad (6-42)$$

According to Zeman, the density-gradient contribution to the pressure dilatation is always positive and reflects the process of conversion of the potential energy to kinetic energy.

A correct choice of the appropriate form of the function  $f_\rho$  lead Zeman to the realization that inclusion of this contribution yielding results which agree with Van-Driest scaling.

#### b) Rapid compression contribution

By a rather straightforward manipulation of the flow equations for compressible homogeneous turbulence, Zeman and Blaisdell [113] proposed a model for the pressure dilatation correlation based on a term of exchange with the mean, on one side, and a mean velocity divergence on the other side.

$$\overline{p' \frac{\partial v_\alpha''}{\partial x_\alpha}} = (\bar{p}\gamma)^{-1} \left\{ \frac{(p^2 - p_e^2)}{\tau_f} + C_{div} \bar{p}^2 \nabla \cdot U \right\} \quad (6-43)$$

in which  $p_e^2$  is the equilibrium value of the pressure variance.

This model represents fairly well the physics involved in the DNS of Coleman and Mansour /121/ (spherical deformation), but unfortunately it is not able to reproduce the results of a rapid directional strain.

To overcome this difficulty, Durbin and Zeman /122/ used the Rapid Distorsion Theory to propose a compressible model sensitive to directional strain, based on the balance of the



transport equation for the  $\overline{p' \frac{\partial v''_\alpha}{\partial x_\alpha}}$  correlation. That model, which is bilinear with respect to the trace-free strain rate tensor and the turbulence anisotropy as well is written as:

$$\overline{p' \frac{\partial v''_\alpha}{\partial x_\alpha}} = -C_{d1} \bar{\rho} \frac{(\overline{p'^2})^{1/2}}{p M_t^2} k \tau \{ (S_{ij}^*)^2 + c_{d2} b_{ik} S_{kj}^* S_{ij}^* \} \quad (6-44)$$

where  $S_{ij}^* = \frac{1}{2}(U_{i,j} + U_{j,i} - \frac{2}{3} \delta_{ij})$  is the trace-free mean strain tensor and  $b_{ij}$  is the anisotropy tensor. In the present  $k-\epsilon$  model, because the anisotropy is not accessible for this level of closure, we used a simpler version

$$\overline{p' \frac{\partial v''_\alpha}{\partial x_\alpha}} = -c_{d1} \bar{\rho} k \tau (S_{ij}^*)^2. \quad (6-45)$$

This rapid contribution to  $\overline{p' \frac{\partial v''_\alpha}{\partial x_\alpha}}$  is expected to be very important in shock/turbulence interactions. It was identified as an important kinetic energy sink in the DNS of rapid directional compression of turbulence (as opposed to spherical compression where  $S_{ij}^* = 0$ ).

### 6.3. COMPRESSIBLE DISSIPATION

Although compressibility effects appear naturally in the pressure correlation terms, they can also be taken into account by other mechanisms like the dissipation.

Zeman /107/ and Sarkar *et al.* /108/ pointed out a compressible contribution in the dissipation terms. Recall the exact form of the dissipation for the Reynolds stress transport equation:

$$\rho \epsilon = \overline{\sigma''_{\alpha\gamma} \frac{\partial v''_\beta}{\partial x_\gamma}} + \overline{\sigma''_{\beta\gamma} \frac{\partial v''_\alpha}{\partial x_\gamma}} \quad (6-46)$$

which reduces for the turbulent kinetic energy equation to:

$$\rho \epsilon = \overline{\sigma''_{\alpha\beta} \frac{\partial v''_\alpha}{\partial x_\beta}} \quad (6-47)$$

in which  $\sigma''_{\alpha\beta}$  is the fluctuation of the stress component. Define the strain rate and vorticity tensors as:

$$s_{\alpha\beta} = \frac{1}{2} \left( \frac{\partial v_\alpha}{\partial x_\beta} + \frac{\partial v_\beta}{\partial x_\alpha} \right) \quad (6-48)$$

$$r_{\alpha\beta} = \frac{1}{2} \left( \frac{\partial v_\alpha}{\partial x_\beta} - \frac{\partial v_\beta}{\partial x_\alpha} \right) \quad (6-49)$$

For compressible flows, Newton's law gives the expression of viscous stresses:

$$\sigma_{\alpha\beta} = 2\mu s_{\alpha\beta} - \frac{2}{3} \delta_{\alpha\beta} \mu d \quad (6-50)$$

in which

$$d = \text{div} \vec{v} \quad (6-51)$$



Neglecting the viscosity fluctuations, the relation applies also to fluctuations. Preserving the symmetry properties of the stress and strain rate tensors, the dissipation can be written as:

$$\bar{\rho}\epsilon = \bar{\mu}(2\overline{s''_\alpha s''_\beta} - \frac{2}{3}\overline{d''^2}) \quad (6-52)$$

Now it is straightforward to show that:

$$\overline{s''_\alpha s''_\beta} = \overline{r''_\alpha r''_\beta} + \frac{\partial v''_\alpha}{\partial x_\beta} \frac{\partial v''_\beta}{\partial x_\alpha} \quad (6-53)$$

After some manipulation, it comes:

$$\frac{\partial v''_\alpha}{\partial x_\beta} \frac{\partial v''_\beta}{\partial x_\alpha} = \frac{\partial^2}{\partial x_\alpha \partial x_\beta} (\overline{v''_\alpha v''_\beta}) - 2 \frac{\partial}{\partial x_\beta} (\overline{\frac{\partial v''_\alpha}{\partial x_\alpha} v''_\beta}) + \overline{\frac{\partial v''_\alpha}{\partial x_\alpha} \frac{\partial v''_\beta}{\partial x_\beta}} \quad (6-54)$$

which simplifies for homogeneous turbulence to:

$$\frac{\partial v''_\alpha}{\partial x_\beta} \frac{\partial v''_\beta}{\partial x_\alpha} = \overline{d''^2} \quad (6-55)$$

The total dissipation becomes:

$$\bar{\rho}\epsilon = \bar{\mu} \left( 2\overline{r''_{\alpha\beta} r''_{\alpha\beta}} + \frac{4}{3}\overline{d''^2} \right) \quad (6-56)$$

Thus, the dissipation rate can be splitted in two components, the solenoidal dissipation  $\epsilon_s$  and the compressible dissipation (dilatation dissipation for Zeman)  $\epsilon_c$

$$\bar{\rho}\epsilon = \bar{\rho}\epsilon_s + \bar{\rho}\epsilon_c \quad (6-57)$$

with

$$\bar{\rho}\epsilon_s = \bar{\mu} 2\overline{r''_{\alpha\beta} r''_{\alpha\beta}} \quad (6-58)$$

$$\bar{\rho}\epsilon_c = \frac{4}{3}\bar{\mu}\overline{d''^2} \quad (6-59)$$

Sarkar *et al.* /108/ and Zeman /107/ suggest similar models for the compressible dissipation, based either on the observation of randomly distributed shocklet structures in the direct numerical simulations /111/, or on an asymptotic behaviour of the equations. For Zeman, the modelled dissipation has the form:

$$\epsilon = \epsilon_s(1 + c_d F(M_t, K)) \quad (6-60)$$

with  $M_t$  is a characteristic turbulent Mach number and  $K$  the kurtosis of the velocity fluctuations. For Sarkar *et al.*, the modelled dissipation is:

$$\epsilon = \epsilon_s(1 + \alpha_1 M_t^2) \quad (6-61)$$

in which  $\alpha_1$  is a constant equal to unity, and  $M_t$  is also the turbulent Mach number.



In a recent paper, Nichols /110/ proposed a  $k-\epsilon$  model for compressible flows. Besides the addition of the mean velocity divergence in the production term, Nichols worked out a transport equation for the turbulent kinetic energy in terms of unweighted averaged variables. This produces extra terms depending of density-velocity correlations. Among them, the most significant has been identified as a turbulent velocity-density dissipation:

$$2v_\alpha \overline{\rho' v'_\alpha} S_{\alpha\beta} \quad (6-62)$$

where  $S_{\alpha\beta}$  is the mean strain rate tensor:

$$S_{\alpha\beta} = \frac{1}{2} \left( \frac{\partial v_\alpha}{\partial x_\beta} + \frac{\partial v_\beta}{\partial x_\alpha} \right) \quad (6-63)$$

Using the differential form of the energy equation and neglecting the fluctuations of total temperature and pressure, density-velocity correlation is expressed as:

$$\frac{\overline{\rho' v'_\alpha}}{\rho v_\alpha} = (\gamma - 1) M^2 \frac{\overline{v'^2_\alpha}}{v^2_\alpha} \quad (6-64)$$

The modelled form of the turbulent velocity-density dissipation is:

$$2v_\alpha \overline{\rho' v'_\alpha} S_{\alpha\beta} = C_{p1} (\gamma - 1) M M_k^2 P \quad (6-65)$$

where  $M_k = \sqrt{k}/u$  is the turbulent Mach number and  $P$  is the production term (including including the mean velocity divergence). The constant  $C_{p1}$  was found to be 4.0 through numerical experimentation for jet spreading rate a function of Mach number. Equation (175) can be considered as a correction to the production term in the turbulent kinetic energy equation. The production term in the dissipation equation is calculated with the compressible Boussinesq approximation, but does not include the turbulent velocity-density dissipation term. It is assumed that the velocity-density correlation is associated with the large-scale structure of the flow while dissipation operates on the small-scale dissipative eddies.



## 7. MODEL IMPLEMENTATION

For many years, the development of numerical methods has been motivated by the need of solutions for the Navier-Stokes equations. Only recently, has interest increased in the solution of turbulence models and the development of accurate turbulence models has been recognized as a necessary route. Indeed, the interest in algebraic models has been due in part to their inherent simplicity, but also to the straightforward extension from laminar to turbulent cases by merely an alternate definition of the viscosity coefficient. Unfortunately, experience has shown that such a crude modelling assumption was not satisfactory as soon as the flow was slightly complex. The use of transport equation turbulence models introduces the turbulent kinetic energy, which needs to be accounted for in the total energy budget. For incompressible flows, this concept is not relevant, since the pressure is not a thermodynamic variable, but has only a mechanical role. In compressible flow the situation is quite different and the existence of  $k$  is felt everywhere in a Navier-Stokes solver, even inside the Euler part.

A second difficulty, which is associated with transport equations for turbulence models is the treatment of non conservative source terms. As most of numerical schemes for Navier-Stokes equations took advantage of their strong conservative character, problems related to the stability and the stiffness of source terms has often been discarded. We will examine in this paper, various techniques to handle these problems, especially in the framework of implicit schemes.

### 7.1. Energy coupling

The instantaneous form of the total energy definition is:

$$\rho E = \rho e + \frac{1}{2} \rho v_\alpha v_\alpha \quad (7-1)$$

In terms of Favre mean and fluctuating components, this equation becomes, after time averaging:

$$\tilde{E} = \tilde{e} + \frac{1}{2} \tilde{v}_\alpha \tilde{v}_\alpha + k \quad (7-2)$$

Therefore the solution of the temperature field from the total energy equation requires the knowledge of the turbulent kinetic energy. Neglecting that quantity [98] is equivalent to ignoring the energy which is extracted from the mean motion to constitute the turbulence energy. For incompressible flows, this is ignored and the turbulent motion is only superimposed to the mean. The coupling appears only through the mechanical role of the turbulent stresses, which are added to the viscous terms. For compressible flow calculations, all the energy exchanges between the various scale motions must be considered to satisfy the global energy budget. It is well understood that, in most of the inviscid part of a flow field, the turbulence level is very low and the energy budget is not affected. But in regions with high shear or strong pressure gradients, the turbulent kinetic energy can be of the order of the mean, and must not be neglected as done usually [44]/[51]/[99].

The complete formulation of the constitutive relationship for the Reynolds stress is written in terms of density weighted variables as:

$$-\rho \widetilde{v_\alpha v_\beta} = \mu_t \left[ \frac{\partial \tilde{v}_\alpha}{\partial x_\beta} + \frac{\partial \tilde{v}_\beta}{\partial x_\alpha} - \frac{2}{3} \delta_{\alpha\beta} \frac{\partial \tilde{v}_\gamma}{\partial x_\gamma} \right] - \frac{2}{3} \delta_{\alpha\beta} \bar{\rho} k \quad (7-3)$$



in which the turbulent kinetic energy term makes the contracted index form possible. This feature appears explicitly in the momentum and total energy equations where a turbulent normal stress is added to the mean pressure. A so-called effective pressure can be defined in the following way:

$$p^* = p + \frac{2}{3}\rho k \quad (7-4)$$

In fact, this turbulent contribution to the pressure field is only an approximation neglecting the anisotropic nature of the Reynolds stress tensor. It was only introduced to insure a non-zero trace of this tensor.

Such an approximation does not take place within the framework of a second order closure. In that case, the normal stresses appear explicitly in the momentum and total energy equations. Then, the relevant effective pressure is not isotropic any longer, but also depends on the turbulent energy distribution on its three normal components. For instance, in the  $\alpha$ -momentum equation, the effective pressure will be:

$$p_\alpha^* = p + \rho \tilde{v}_\alpha^2 \quad (7-5)$$

Unfortunately, the concept of an anisotropic pressure field is difficult to handle, especially with respect to the temperature field. Therefore, it is necessary to follow the same reasoning as for the static pressure definition from the kinetic theory of gases, and approximate the turbulent pressure by the mean of three components, i.e.  $\frac{2}{3}\rho k$ .

## 7.2. Diagonalization of jacobian matrices

To avoid the severe limitations of explicit methods, implicit schemes are preferred. A classical (but non unique) method for obtaining an implicit approximation is to take the time derivative of the original system /100/.

$$\frac{\partial}{\partial t} \left[ \frac{\partial U}{\partial t} + \frac{\partial F}{\partial x} + \frac{\partial G}{\partial y} = H \right] \quad (7-6)$$

with the vector elements:

$$U = \begin{bmatrix} \rho \\ \rho \tilde{u} \\ \rho \tilde{v} \\ \rho \tilde{E} \\ \rho k \\ \rho \epsilon \end{bmatrix} \quad F = \begin{bmatrix} \rho \tilde{u} \\ \rho \tilde{u}^2 + p + \frac{2}{3}\rho k \\ \rho \tilde{u} \tilde{v} \\ \rho \tilde{u} \tilde{E} + (p + \frac{2}{3}\rho k) \tilde{u} \\ \rho \tilde{u} k \\ \rho \tilde{u} \epsilon \end{bmatrix}$$

$$G = \begin{bmatrix} \rho \tilde{v} \\ \rho \tilde{u} \tilde{v} \\ \rho \tilde{v}^2 + p + \frac{2}{3}\rho k \\ \rho \tilde{v} \tilde{E} + (p + \frac{2}{3}\rho k) \tilde{v} \\ \rho \tilde{v} k \\ \rho \tilde{v} \epsilon \end{bmatrix} \quad H = \begin{bmatrix} 0 \\ 0 \\ 0 \\ 0 \\ H_k \\ H_\epsilon \end{bmatrix}$$

Define the jacobian matrices as:

$$A = \frac{\partial F}{\partial U}; \quad B = \frac{\partial G}{\partial U}; \quad C = \frac{\partial H}{\partial U}$$



the implicit approximation writes as:

$$(I + \Delta t \frac{\partial A_{\bullet}}{\partial x} + \Delta t \frac{\partial B_{\bullet}}{\partial y} - \Delta t C) \delta U^{n+1} = \Delta U^n \quad (7-7)$$

with the following increments:

$$\delta U^{n+1} = \Delta t \frac{\partial U^{n+1}}{\partial t}; \quad \Delta U^{n+1} = \Delta t \frac{\partial U^n}{\partial t}$$

Equation (7-7) can be solved either by approximate factorization or by classical relaxation methods such as line Gauss-Seidel or point Jacobi.

Equation (7-2) is used in the development of the diagonal form of the jacobian matrices  $A$  and  $B$ . Consider, for instance the x-direction, the jacobian  $A$  can be related to its diagonal form by the relation:

$$A = SX^{-1} \Lambda_A SX \quad (7-8)$$

Take one further assumption, the  $k - \epsilon$  two-equation turbulence model is used in conjunction with the Navier-Stokes equations. Then all matrices are dimensioned 6 by 6. The diagonal  $\Lambda_A$  is:

$$\Lambda_A = \begin{bmatrix} \tilde{u} & 0 & 0 & 0 & 0 & 0 \\ 0 & \tilde{u} + c^* & 0 & 0 & 0 & 0 \\ 0 & 0 & \tilde{u} & 0 & 0 & 0 \\ 0 & 0 & 0 & \tilde{u} - c^* & 0 & 0 \\ 0 & 0 & 0 & 0 & \tilde{u} & 0 \\ 0 & 0 & 0 & 0 & 0 & \tilde{u} \end{bmatrix} \quad (7-9)$$

The speed of sound  $c^*$  is a modified form which includes the turbulent pressure. The transformation matrices  $SX$  and  $SX^{-1}$  are written as:

$$SX = \begin{bmatrix} 1 - \frac{\alpha\beta}{c^{*2}} & \frac{\beta\tilde{u}}{c^{*2}} & \frac{\beta\tilde{v}}{c^{*2}} & -\frac{\beta}{c^{*2}} & -\frac{1}{c^{*2}}\left(\frac{2}{3} - \beta\right) & 0 \\ -\tilde{u}c^* + \alpha\beta & c^* - \beta\tilde{u} & -\beta\tilde{v} & \beta & \left(\frac{2}{3} - \beta\right) & 0 \\ -\frac{\tilde{v}}{\rho} & 0 & \frac{1}{\rho} & 0 & 0 & 0 \\ \tilde{u}c^* + \alpha\beta & -c^* - \beta\tilde{u} & -\beta\tilde{v} & \beta & \left(\frac{2}{3} - \beta\right) & 0 \\ -\frac{k}{\rho} & 0 & 0 & 0 & \frac{1}{\rho} & 0 \\ -\frac{\epsilon}{\rho} & 0 & 0 & 0 & 0 & \frac{1}{\rho} \end{bmatrix} \quad (7-10)$$

$$SX^{-1} = \begin{bmatrix} 1 & \frac{1}{2c^{*2}} & 0 & \frac{1}{2c^{*2}} & 0 & 0 \\ \tilde{u} & \frac{\tilde{u}}{2c^{*2}} + \frac{1}{2c^*} & 0 & \frac{\tilde{u}}{2c^{*2}} - \frac{1}{2c^*} & 0 & 0 \\ \tilde{v} & \frac{\tilde{v}}{2c^{*2}} & \rho & \frac{\tilde{v}}{2c^{*2}} & 0 & 0 \\ SXM41 & SXM42 & \rho\tilde{v} & SXM44 & -\frac{\rho}{\beta}\left(\frac{2}{3} - \beta\right) & 0 \\ k & \frac{k}{2c^{*2}} & 0 & \frac{k}{2c^{*2}} & \rho & 0 \\ \epsilon & \frac{\epsilon}{2c^{*2}} & 0 & \frac{\epsilon}{2c^{*2}} & 0 & \rho \end{bmatrix} \quad (7-11)$$



with

$$SXM41 = \alpha + \frac{k}{\beta} \left( \frac{2}{3} - \beta \right) \quad (7-12)$$

$$SXM42 = \frac{\alpha}{2c^{*2}} + \frac{\tilde{u}}{2c^*} + \frac{1}{2\beta} - \frac{k}{2\beta c^{*2}} \left( \frac{2}{3} - \beta \right) \quad (7-13)$$

$$SXM44 = \frac{\alpha}{2c^{*2}} - \frac{\tilde{u}}{2c^*} + \frac{1}{2\beta} - \frac{k}{2\beta c^{*2}} \left( \frac{2}{3} - \beta \right) \quad (7-14)$$

in which  $\alpha = (\tilde{u}^2 + \tilde{v}^2)/2$  and  $\beta = \gamma - 1$ . The jacobian  $A$  includes also the coupling through the turbulent energy  $k$ .

$$A = \begin{bmatrix} 0 & 1 & 0 & 0 & 0 & 0 \\ \alpha\beta - \tilde{u}^2 & (3 - \gamma)\tilde{u} & -\beta\tilde{v} & \beta & \frac{2}{3} - \beta & 0 \\ -\tilde{u}\tilde{v} & \tilde{v} & \tilde{u} & 0 & 0 & 0 \\ A41 & A42 & -3\tilde{u}\tilde{v} & \gamma\tilde{u} & \left( \frac{2}{3} - \beta \right) \tilde{u} & 0 \\ -\tilde{u}k & k & 0 & 0 & \tilde{u} & 0 \\ -\tilde{u}\epsilon & \epsilon & 0 & 0 & 0 & \tilde{u} \end{bmatrix} \quad (7-15)$$

$$A41 = 2\beta\alpha\tilde{u} - \gamma\tilde{E}\tilde{u} - \tilde{u}k \left( \frac{2}{3} - \beta \right) \quad (7-16)$$

$$A42 = \gamma\tilde{E} - \beta \frac{3\tilde{u}^2 + \tilde{v}^2}{2} + k \left( \frac{2}{3} - \beta \right) \quad (7-17)$$

A similar form is obtained with a second order closure turbulence model, but the matrix dimension is then 9 by 9. To illustrate that, only the  $A$  jacobian is shown here:

$$U = \begin{bmatrix} \rho \\ \rho\tilde{u} \\ \rho\tilde{v} \\ \rho\tilde{E} \\ \rho\tilde{u}\tilde{v} \\ \rho\epsilon \\ \rho\tilde{u}''^2 \\ \rho\tilde{v}''^2 \\ \rho\tilde{w}''^2 \end{bmatrix} \quad F = \begin{bmatrix} \rho\tilde{u} \\ \rho\tilde{u}^2 + p + \rho\tilde{u}''^2 \\ \rho\tilde{u}\tilde{v} + \rho\tilde{u}''\tilde{v}'' \\ \rho\tilde{u}\tilde{E} + (p + \rho\tilde{u}''^2)\tilde{u} + \rho\tilde{u}''\tilde{v}''\tilde{v} \\ \rho\tilde{u}\tilde{u}''\tilde{v}'' \\ \rho\tilde{u}\epsilon \\ \rho\tilde{u}\tilde{u}''^2 \\ \rho\tilde{u}\tilde{v}''^2 \\ \rho\tilde{u}\tilde{w}''^2 \end{bmatrix}$$

$$G = \begin{bmatrix} \rho\tilde{v} \\ \rho\tilde{u}\tilde{v} + \rho\tilde{u}''\tilde{v}'' \\ \rho\tilde{v}^2 + p + \rho\tilde{v}''^2 \\ \rho\tilde{v}\tilde{E} + (\tilde{p} + \rho\tilde{v}''^2)\tilde{v} + \rho\tilde{u}''\tilde{v}''\tilde{u} \\ \rho\tilde{v}\tilde{u}''\tilde{v}'' \\ \rho\tilde{v}\epsilon \\ \rho\tilde{v}\tilde{u}''^2 \\ \rho\tilde{v}\tilde{v}''^2 \\ \rho\tilde{v}\tilde{w}''^2 \end{bmatrix}$$



$$A = \begin{bmatrix} 0 & 1 & 0 & 0 & 0 & 0 & 0 & 0 & 0 \\ A21 & A22 & -\beta\tilde{v} & \beta & 0 & 0 & 1 - \frac{\beta}{2} & -\frac{\beta}{2} & -\frac{\beta}{2} \\ -\tilde{u}\tilde{v} & \tilde{v} & \tilde{u} & 0 & 0 & 0 & 0 & 0 & 0 \\ A41 & A42 & -\beta\tilde{u}\tilde{v} & \gamma\tilde{u} & \tilde{v} & 0 & \left(1 - \frac{\beta}{2}\right)\tilde{u} & -\beta\frac{\tilde{u}}{2} & -\beta\frac{\tilde{u}}{2} \\ -\widetilde{u''v''}\tilde{u} & \widetilde{u''v''} & 0 & 0 & \tilde{u} & 0 & 0 & 0 & 0 \\ -\widetilde{\epsilon\tilde{u}} & \widetilde{\epsilon} & 0 & 0 & 0 & \tilde{u} & 0 & 0 & 0 \\ -\widetilde{u''^2}\tilde{u} & \widetilde{u''^2} & 0 & 0 & 0 & 0 & \tilde{u} & 0 & 0 \\ -\widetilde{v''^2}\tilde{u} & \widetilde{v''^2} & 0 & 0 & 0 & 0 & 0 & \tilde{u} & 0 \\ -\widetilde{w''^2}\tilde{u} & \widetilde{w''^2} & 0 & 0 & 0 & 0 & 0 & 0 & \tilde{u} \end{bmatrix} \quad (7-18)$$

with the following terms:

$$\begin{aligned} A21 &= \alpha\beta - \tilde{u}^2 \\ A22 &= (2 - \beta)\tilde{u} \\ A41 &= 2\beta\alpha\tilde{u} - \gamma\tilde{E}\tilde{u} + \beta k - \tilde{v}\widetilde{u''v''} - \tilde{u}\widetilde{u''^2} \\ A42 &= \gamma\tilde{E} - \beta\frac{3\tilde{u}^2 + \tilde{v}^2}{2} - \beta k + \widetilde{u''^2} \end{aligned} \quad (7-19)$$

These matrices show clearly the coupling between the Navier-Stokes equations and the transport equations for the normal components of the Reynolds stress tensor, just because of the introduction of the turbulent kinetic energy in the global energy budget, whereas there is no apparent coupling with the shear stress and the dissipation rate equation. In fact, these equations are related to the previous through the source terms only.

### 7.3. Treatment of non-conservative equations

To treat implicitly the source terms, various techniques are available. Recall first the general implicit approximation:

$$(I + \Delta t \frac{\partial A_{\bullet}}{\partial x} + \Delta t \frac{\partial B_{\bullet}}{\partial y} - \Delta t.C) \delta U^{n+1} = \Delta U^n$$

The simplest way, which is somehow trivial, is to apply a first approximate factorization, without considering the formal content of the source terms. Then it comes:

$$(I + \Delta t \frac{\partial A_{\bullet}}{\partial x} + \Delta t \frac{\partial B_{\bullet}}{\partial y} - \Delta t.C) = (I + \Delta t \frac{\partial A_{\bullet}}{\partial x} + \Delta t \frac{\partial B_{\bullet}}{\partial y}) (I - \Delta t.C) + O(\Delta t^2) \quad (7-20)$$

The C matrix can be considered as diagonal whatever the formal content is, i.e.

$$C = \begin{bmatrix} 0 & 0 & 0 & 0 & 0 & 0 \\ 0 & 0 & 0 & 0 & 0 & 0 \\ 0 & 0 & 0 & 0 & 0 & 0 \\ 0 & 0 & 0 & 0 & 0 & 0 \\ 0 & 0 & 0 & 0 & \frac{H_k}{\bar{\rho}k} & 0 \\ 0 & 0 & 0 & 0 & 0 & \frac{H_\epsilon}{\bar{\rho}\epsilon} \end{bmatrix} \quad (7-21)$$



for the two equation model. With a second order closure, this matrix has the following form:

$$C = \begin{bmatrix} 0 & 0 & 0 & 0 & 0 & 0 & 0 & 0 & 0 \\ 0 & 0 & 0 & 0 & 0 & 0 & 0 & 0 & 0 \\ 0 & 0 & 0 & 0 & 0 & 0 & 0 & 0 & 0 \\ 0 & 0 & 0 & 0 & 0 & 0 & 0 & 0 & 0 \\ 0 & 0 & 0 & 0 & \frac{H_{u''v''}}{\bar{\rho} u'' v''} & 0 & 0 & 0 & 0 \\ 0 & 0 & 0 & 0 & 0 & \frac{H_\epsilon}{\bar{\rho} \epsilon} & 0 & 0 & 0 \\ 0 & 0 & 0 & 0 & 0 & 0 & \frac{H_{u''^2}}{\bar{\rho} u''^2} & 0 & 0 \\ 0 & 0 & 0 & 0 & 0 & 0 & 0 & \frac{H_{v''^2}}{\bar{\rho} v''^2} & 0 \\ 0 & 0 & 0 & 0 & 0 & 0 & 0 & 0 & \frac{H_{w''^2}}{\bar{\rho} w''^2} \end{bmatrix} \quad (7-22)$$

Before doing the work on the space operator, the inversion of the diagonal source term matrix is straightforward:

$$(I + \Delta t \frac{\partial A_\bullet}{\partial x} + \Delta t \frac{\partial B_\bullet}{\partial y}) \delta U^{n+1} = \Delta U^n \cdot (I + \Delta t |C|)^{-1} \quad (7-23)$$

Therefore, the explicit increment is modified first by the source term contribution, before being updated by the space derivative operator(s), either with an approximate factorization or a relaxation technique.

A slightly different method avoids the factorization for the source contribution. Then the source terms are grouped with the transverse advection operator /101/, /102/. In that case, the same eigenvalue is used, which is the the maximum value among all equations to be solved.

Unfortunately, the use of these blind forms, without accounting for the formal content of the source terms does not guarantee the stability. Therefore, it has been found necessary to develop more exact forms of the jacobian matrix. Although various developments are possible, we will develop here a typical form which has been worked out by Viegas and MacCormack /103/ for a  $k - \epsilon$  turbulence model.

Consider the set made only with the turbulence transport equations. The convective and diffusive parts are supposed already solved with the Reynolds averaged Navier-Stokes equations. Then we have only to work on:

$$\frac{\partial U}{\partial t} = H \quad (7-24)$$

where the two vectors  $U$  and  $H$  are now:

$$U = \begin{bmatrix} \bar{\rho} k \\ \bar{\rho} \epsilon \end{bmatrix} \quad H = \begin{bmatrix} H_k \\ H_\epsilon \end{bmatrix}$$

An implicit approximation of equation (7-25) is:

$$U^{n+1} = U^n + \Delta t \cdot H^{n+1}$$



in which  $H^{n+1}$  is evaluated at time  $(n+1)$ . This can be achieved by a first order serie expansion:

$$H^{n+1} = H^n + \frac{\partial H}{\partial U} \delta U; \quad \text{with } \delta U = U^{n+1} - U^n$$

Then the implicit approximation can be rewritten as:

$$(I - \Delta t \frac{\partial H}{\partial U}) \delta U = \Delta t H^n \quad (7-26)$$

The task is to evaluate properly the jacobian matrix. Let first discriminate between positive and negative source terms. An rather elementary stability analysis on equation (193) shows that stability cannot be obtained with an implicit approximation when the source term is positive. The same is true for an explicit approximation with negative source terms. Therefore we keep only in the implicit approximation the "good" terms, which are negative. Therefore:

$$\begin{aligned} H_k &= -\bar{\rho} \epsilon - \frac{2\mu k}{y^2} \\ H_\epsilon &= -C_{\epsilon 2} f_2 \frac{(\bar{\rho} \epsilon)^2}{\bar{\rho} k} \end{aligned} \quad (7-27)$$

Recall the definition of the turbulent viscosity (3-1),

$$\mu_t = C_\mu f_\mu \bar{\rho} \frac{k^2}{\epsilon}$$

Then the turbulent kinetic energy dissipation can be expressed as:

$$\bar{\rho} \epsilon = C_\mu f_\mu \frac{(\bar{\rho} k)^2}{\mu_t} \quad (7-28)$$

Then the source terms can be rewritten as:

$$\begin{aligned} H_k &= - \underbrace{\frac{C_\mu f_\mu}{\mu_t}}_* (\bar{\rho} k)^2 - \underbrace{\frac{2\mu}{\bar{\rho} y^2}}_* \bar{\rho} k \\ H_\epsilon &= - \underbrace{C_{\epsilon 2} f_2 \frac{(\bar{\rho} \epsilon)}{\bar{\rho} k}}_* \bar{\rho} \epsilon \end{aligned} \quad (7-29)$$

Quantities marked with a \* are considered as constant during the current time step, i.e. they lag in time by one time-step. The corresponding jacobian matrix can be written as:

$$\frac{\partial H}{\partial U} = \begin{bmatrix} \frac{\partial H_k}{\partial \bar{\rho} k} & \frac{\partial H_k}{\partial \bar{\rho} \epsilon} \\ \frac{\partial H_\epsilon}{\partial \bar{\rho} k} & \frac{\partial H_\epsilon}{\partial \bar{\rho} \epsilon} \end{bmatrix} \quad (7-30)$$



or

$$\frac{\partial H}{\partial U} = \begin{bmatrix} -\frac{2C_\mu f_\mu}{\mu_t} \bar{\rho} k - \frac{2\mu}{\bar{\rho} y^2} & 0 \\ C_{\epsilon 2} f_2 \frac{(\bar{\rho} \epsilon)^2}{(\bar{\rho} k)^2} & -2C_{\epsilon 2} f_2 \frac{\bar{\rho} \epsilon}{\bar{\rho} k} \end{bmatrix} \quad (7-31)$$

Then the implicit approximation can be written as:

$$\begin{bmatrix} 1 + \Delta t \left( \frac{2C_\mu f_\mu}{\mu_t} \bar{\rho} k - \frac{2\mu}{\bar{\rho} y^2} \right) & 0 \\ -C_{\epsilon 2} f_2 \frac{(\bar{\rho} \epsilon)^2}{(\bar{\rho} k)^2} & 1 + \Delta t \left( -2C_{\epsilon 2} f_2 \frac{\bar{\rho} \epsilon}{\bar{\rho} k} \right) \end{bmatrix} \begin{bmatrix} \delta(\bar{\rho} k) \\ \delta(\bar{\rho} \epsilon) \end{bmatrix} = \Delta t \begin{bmatrix} H_k^n \\ H_\epsilon^n \end{bmatrix} \quad (7-32)$$

As one of the off-diagonal terms is zero, equation (7-32) can be solved directly and we get:

$$\begin{aligned} \delta(\bar{\rho} k) &= \frac{\Delta t H_k^n}{1 + \Delta t \left( \frac{2C_\mu f_\mu}{\mu_t} \bar{\rho} k - \frac{2\mu}{\bar{\rho} y^2} \right)} \\ \delta(\bar{\rho} \epsilon) &= \frac{\Delta t H_\epsilon^n + \Delta t C_{\epsilon 2} f_2 \frac{(\bar{\rho} \epsilon)^2}{(\bar{\rho} k)^2} \delta(\bar{\rho} k)}{1 + \Delta t \left( 2C_{\epsilon 2} f_2 \frac{\bar{\rho} \epsilon}{\bar{\rho} k} \right)} = \frac{\Delta t H_\epsilon^n \left( 1 - \frac{\delta(\bar{\rho} k)}{\bar{\rho} k} \right)}{1 + \Delta t \left( 2C_{\epsilon 2} f_2 \frac{\bar{\rho} \epsilon}{\bar{\rho} k} \right)} \end{aligned} \quad (7-33)$$

This technique is closer to the physics but nevertheless suffers from being too strongly linked to the model itself. Any change in the form of the turbulence model requires a partial reformulation of the jacobian. Assume for instance, that we want to use a slightly different turbulence model, such as the following /85/, /91/, /92/:

$$\begin{aligned} H_k &= -\bar{\rho} \epsilon \\ H_\epsilon &= -C_{\epsilon 2} f_2 \bar{\rho} \frac{\epsilon^2}{k} + \frac{\epsilon}{k} XTRA \end{aligned} \quad (7-34)$$

in which  $XTRA$  represents an additive term we want to include for rotation or compressibility effects for instance. In equation (7-34), only the "good" terms have been retained, i.e. terms supposed to comply with implicit stability criteria. Consider the two possibilities for  $XTRA$ .

$XTRA < 0$ : Then this term is considered as "good" and must be included in the implicit procedure.

$$\begin{aligned} H_k &= -\bar{\rho} \epsilon = -\frac{C_\mu f_\mu}{\mu_t} (\bar{\rho} k)^2 \\ H_\epsilon &= -C_{\epsilon 2} f_2 \frac{(\bar{\rho} \epsilon)^2}{\bar{\rho} k} + \frac{\bar{\rho} \epsilon}{\bar{\rho} k} XTRA \end{aligned} \quad (7-34)$$

Then, approximation (7-32) writes now:

$$\begin{bmatrix} 1 + \Delta t \frac{2C_\mu f_\mu}{\mu_t} \bar{\rho} k & 0 \\ -\Delta t \frac{\bar{\rho} \epsilon}{(\bar{\rho} k)^2} (C_{\epsilon 2} f_2 \bar{\rho} \epsilon - XTRA) & 1 + \Delta t \left( 2C_{\epsilon 2} f_2 \frac{\bar{\rho} \epsilon}{\bar{\rho} k} - \frac{XTRA}{\bar{\rho} k} \right) \end{bmatrix} \begin{bmatrix} \delta(\bar{\rho} k) \\ \delta(\bar{\rho} \epsilon) \end{bmatrix} = \Delta t \begin{bmatrix} H_k^n \\ H_\epsilon^n \end{bmatrix} \quad (7-35)$$



and it comes:

$$\begin{aligned}\delta(\bar{\rho} k) &= \frac{\Delta t H_k^n}{1 + \Delta t 2 \frac{C_\mu f_\mu}{\mu_t} \bar{\rho} k} \\ \delta(\bar{\rho} \epsilon) &= \frac{\Delta t H_\epsilon^n + \Delta t \frac{\bar{\rho} \epsilon}{(\bar{\rho} k)^2} (C_{\epsilon 2} f_2 \bar{\rho} \epsilon - XTRA) \delta(\rho k)}{1 + \Delta t \left( \frac{2 C_{\epsilon 2} f_2 \bar{\rho} \epsilon}{\bar{\rho} k} - \frac{XTRA}{\bar{\rho} k} \right)}\end{aligned}\quad (7-36)$$

$XTRA > 0$ : Then this term is not appropriate to preserve finite values of transported quantities must be eliminate from the implicit side. Then the jacobian reduces to:

$$\frac{\partial H}{\partial U} = \begin{bmatrix} -\frac{2 C_\mu f_\mu}{\mu_t} \bar{\rho} k & 0 \\ C_{\epsilon 2} f_2 \frac{(\bar{\rho} \epsilon)^2}{(\bar{\rho} k)^2} & -2 C_{\epsilon 2} f_2 \frac{\bar{\rho} \epsilon}{\bar{\rho} k} \end{bmatrix} \quad (7-37)$$

and the implicit approximation writes:

$$\begin{bmatrix} 1 + \Delta t \frac{2 C_\mu f_\mu}{\mu_t} \bar{\rho} k & 0 \\ -\Delta t \frac{(\bar{\rho} \epsilon)^2}{(\bar{\rho} k)^2} C_{\epsilon 2} f_2 \bar{\rho} \epsilon & 1 + \Delta t 2 C_{\epsilon 2} f_2 \frac{\bar{\rho} \epsilon}{\bar{\rho} k} \end{bmatrix} \begin{bmatrix} \delta(\bar{\rho} k) \\ \delta(\bar{\rho} \epsilon) \end{bmatrix} = \Delta t \begin{bmatrix} H_k^n \\ H_\epsilon^n \end{bmatrix} \quad (7-38)$$

and the solution is:

$$\begin{aligned}\delta(\bar{\rho} k) &= \frac{\Delta t H_k^n}{1 + 2 \Delta t \frac{C_\mu f_\mu}{\mu_t} \bar{\rho} k} \\ \delta(\bar{\rho} \epsilon) &= \frac{\Delta t H_\epsilon^n \left( 1 - \frac{\delta(\bar{\rho} k)}{\bar{\rho} k} \right)}{1 + 2 \Delta t C_{\epsilon 2} f_2 \frac{\bar{\rho} \epsilon}{\bar{\rho} k}}\end{aligned}\quad (7-39)$$

Further refinement can be gained in the evaluation of the jacobian matrix, by considering a non diagonal form. A time serie expansion of term  $H$  writes as:

$$H^{n+1} = H^n + \Delta t C \frac{\partial U}{\partial t} + O(\Delta t^2) \quad (7-40)$$

The  $C$  matrix represents the exact jacobian of  $H$ . Using the fact that  $H$  itself contains space derivatives of the primitive variable  $U$ , equation (7-40) can be written as:

$$\begin{aligned}H^{n+1} &= H^n + H_1 \delta U + H_{2x} \frac{\partial(\delta U)}{\partial x} + H_{2y} \frac{\partial(\delta U)}{\partial y} \\ &\quad + H_{4x} \frac{\partial^2(\delta U)}{\partial x^2} + H_{4y} \frac{\partial^2(\delta U)}{\partial y^2}\end{aligned}\quad (7-41)$$

As a simplified example, let us consider the source terms of the turbulent energy equation (without the explicit compressibility effects), expanded for a two dimensional



plane flow problem. The sum of production and destruction mechanisms is written as:

$$H_k = 2\mu_t \left[ \left( \frac{\partial \tilde{u}}{\partial x} \right)^2 + \left( \frac{\partial \tilde{v}}{\partial y} \right)^2 - \frac{1}{3} \left( \frac{\partial \tilde{u}}{\partial x} + \frac{\partial \tilde{v}}{\partial y} \right)^2 \right] \\ + \mu_t \left( \frac{\partial \tilde{u}}{\partial y} + \frac{\partial \tilde{v}}{\partial x} \right)^2 - \frac{2}{3} \bar{\rho} k \left( \frac{\partial \tilde{u}}{\partial x} + \frac{\partial \tilde{v}}{\partial y} \right) - \rho \epsilon - \frac{1}{2} \frac{\mu}{k} \frac{\partial k^2}{\partial n} \quad (7-42)$$

in which  $n$  is a coordinate normal to the nearest solid wall. A first order expansion with respect to the non conservative variables yields:

$$H_k^{n+1} = H_k^n + 4\mu_t \left( \frac{\partial \tilde{u}}{\partial x} \frac{\partial(\delta \tilde{u})}{\partial x} + \frac{\partial \tilde{v}}{\partial y} \frac{\partial(\delta \tilde{v})}{\partial y} \right) - \frac{4}{3} \mu_t \left( \frac{\partial \tilde{u}}{\partial x} + \frac{\partial \tilde{v}}{\partial y} \right) \left( \frac{\partial(\delta \tilde{u})}{\partial x} + \frac{\partial(\delta \tilde{v})}{\partial y} \right) \\ + 2\mu_t \left( \frac{\partial \tilde{u}}{\partial y} + \frac{\partial \tilde{v}}{\partial x} \right) \left( \frac{\partial(\delta \tilde{u})}{\partial y} + \frac{\partial(\delta \tilde{v})}{\partial x} \right) - \frac{2}{3} \rho k \left( \frac{\partial(\delta \tilde{u})}{\partial x} + \frac{\partial(\delta \tilde{v})}{\partial y} \right) \\ - \frac{2}{3} \left( \frac{\partial \tilde{u}}{\partial x} + \frac{\partial \tilde{v}}{\partial y} \right) \delta(\bar{\rho} k) - \delta(\rho \epsilon) - \frac{1}{2} \frac{\mu}{\bar{\rho} k} \frac{\partial k^2}{\partial n} \delta \rho - \frac{\mu}{k} \frac{\partial k}{\partial n} \frac{\partial(\delta k)}{\partial n} \\ + \frac{1}{2} \frac{\mu}{\bar{\rho} k^2} \frac{\partial k^2}{\partial n} \delta(\bar{\rho} k) + O(\delta U^2) \quad (7-43)$$

To obtain a form close to equation (7-43) expressed in term of conservative variables, it is necessary to use the matrix  $N$  defined as:

$$\delta V = N \cdot \delta U \quad (7-44)$$

with

$$\delta U = \begin{bmatrix} \delta(\bar{\rho}) \\ \delta(\rho \tilde{u}) \\ \delta(\rho \tilde{v}) \\ \delta(\rho \tilde{E}) \\ \delta(\rho k) \\ \delta(\rho \epsilon) \end{bmatrix} \quad \delta V = \begin{bmatrix} \delta(\rho) \\ \delta(\tilde{u}) \\ \delta(\tilde{v}) \\ \delta(\tilde{e}) \\ \delta(k) \\ \delta(\epsilon) \end{bmatrix}$$

$$N = \begin{bmatrix} 1 & 0 & 0 & 0 & 0 & 0 \\ -\frac{\tilde{u}}{\bar{\rho}} & \frac{1}{\bar{\rho}} & 0 & 0 & 0 & 0 \\ -\frac{\tilde{v}}{\bar{\rho}} & 0 & \frac{1}{\bar{\rho}} & 0 & 0 & 0 \\ \frac{\alpha - \epsilon}{\bar{\rho}} & -\frac{\tilde{u}}{\bar{\rho}} & -\frac{\tilde{v}}{\bar{\rho}} & \frac{1}{\bar{\rho}} & -\frac{1}{\bar{\rho}} & 0 \\ -\frac{k}{\bar{\rho}} & 0 & 0 & 0 & \frac{1}{\bar{\rho}} & 0 \\ -\frac{\epsilon}{\bar{\rho}} & 0 & 0 & 0 & 0 & \frac{1}{\bar{\rho}} \end{bmatrix} \quad (7-45)$$

$\alpha$  is the kinetic energy of the mean motion:

$$\alpha = \frac{\tilde{u}^2 + \tilde{v}^2}{2} \quad (7-46)$$



Furthermore, equation (7-41) has to be written for the computational space with the general transformation:

$$\begin{aligned}
 \frac{\partial}{\partial x}(\delta U) &= +\frac{1}{d_{xy}} \left( \frac{\partial y}{\partial \eta} \frac{\partial(\delta U)}{\partial \xi} - \frac{\partial y}{\partial \xi} \frac{\partial(\delta U)}{\partial \eta} \right) \\
 \frac{\partial}{\partial y}(\delta U) &= -\frac{1}{d_{xy}} \left( \frac{\partial x}{\partial \eta} \frac{\partial(\delta U)}{\partial \xi} - \frac{\partial x}{\partial \xi} \frac{\partial(\delta U)}{\partial \eta} \right) \\
 \frac{\partial}{\partial n}(\delta U) &= \frac{\partial \eta}{\partial n} \frac{\partial(\delta U)}{\partial \eta} \\
 d_{xy} &= \frac{\partial x}{\partial \xi} \frac{\partial y}{\partial \eta} - \frac{\partial x}{\partial \eta} \frac{\partial y}{\partial \xi}
 \end{aligned} \tag{7-47}$$

Then the contribution of the turbulent kinetic energy to the vector equation (210) can be written as:

$$\begin{aligned}
 (H)_k^{n+1} &= (H)_k^n + (H_1)_k \delta U \\
 &+ (H_{2\xi})_k \frac{\partial(N \delta U)}{\partial \xi} + (H_{2\eta})_k \frac{\partial(N \delta U)}{\partial \eta}
 \end{aligned} \tag{7-48}$$

with the following matrix elements:

$$(H_1)_k = \begin{bmatrix} -\frac{1}{2} \frac{\mu}{\rho k} \left( \frac{\partial k}{\partial \eta} \right)^2 \\ 0 \\ 0 \\ 0 \\ -\frac{2}{3} \left( \frac{\partial \tilde{u}}{\partial x} + \frac{\partial \tilde{v}}{\partial y} \right) + \frac{1}{2} \frac{\mu}{\rho k^2} \left( \frac{\partial k}{\partial n} \right)^2 \\ -1 \end{bmatrix}^T \tag{7-49}$$

$$\begin{aligned}
 (H_{2\xi})_k &= \begin{bmatrix} 0 \\ HKU_\xi \frac{1}{d_{xy}} \\ HKV_\xi \frac{1}{d_{xy}} \\ 0 \\ 0 \\ 0 \end{bmatrix}^T & (H_{2\eta})_k &= \begin{bmatrix} 0 \\ HKU_\eta \frac{1}{d_{xy}} \\ HKV_\eta \frac{1}{d_{xy}} \\ 0 \\ -\frac{\mu}{k} \frac{\partial k}{\partial n} \frac{\partial \eta}{\partial \eta} \\ 0 \end{bmatrix}^T
 \end{aligned} \tag{7-50}$$

$$HKU_\xi = \left[ 4\mu_t \frac{\partial \tilde{u}}{\partial x} - \frac{4}{3} \mu_t \left( \frac{\partial \tilde{u}}{\partial x} + \frac{\partial \tilde{v}}{\partial y} \right) - \frac{2}{3} \bar{\rho} k \right] \frac{\partial y}{\partial \eta} - 2\mu_t \left( \frac{\partial \tilde{u}}{\partial y} + \frac{\partial \tilde{v}}{\partial x} \right) \frac{\partial x}{\partial \eta} \tag{7-51}$$

$$HKV_\xi = 2\mu_t \left( \frac{\partial \tilde{u}}{\partial y} + \frac{\partial \tilde{v}}{\partial x} \right) \frac{\partial y}{\partial \eta} - \left[ 4\mu_t \frac{\partial \tilde{v}}{\partial y} - \frac{4}{3} \mu_t \left( \frac{\partial \tilde{u}}{\partial x} + \frac{\partial \tilde{v}}{\partial y} \right) - \frac{2}{3} \bar{\rho} k \right] \frac{\partial x}{\partial \eta} \tag{7-52}$$

$$HKU_\eta = - \left[ 4\mu_t \frac{\partial \tilde{u}}{\partial x} - \frac{4}{3} \mu_t \left( \frac{\partial \tilde{u}}{\partial x} + \frac{\partial \tilde{v}}{\partial y} \right) - \frac{2}{3} \bar{\rho} k \right] \frac{\partial y}{\partial \xi} + 2\mu_t \left( \frac{\partial \tilde{u}}{\partial y} + \frac{\partial \tilde{v}}{\partial x} \right) \frac{\partial x}{\partial \xi} \tag{7-53}$$



$$HKV_\eta = -2\mu_t \left( \frac{\partial \tilde{u}}{\partial y} + \frac{\partial \tilde{v}}{\partial x} \right) \frac{\partial y}{\partial \xi} + \left[ 4\mu_t \frac{\partial \tilde{v}}{\partial y} - \frac{4}{3}\mu_t \left( \frac{\partial \tilde{u}}{\partial x} + \frac{\partial \tilde{v}}{\partial y} \right) - \frac{2}{3}\rho k \right] \frac{\partial x}{\partial \xi} \quad (7-54)$$

Similar derivation is made also for the  $\epsilon$  equation to form an equation having the form:

$$\begin{bmatrix} 0 \\ 0 \\ 0 \\ 0 \\ H_k \\ H_\epsilon \end{bmatrix}^{n+1} = \begin{bmatrix} 0 \\ 0 \\ 0 \\ 0 \\ H_k \\ H_\epsilon \end{bmatrix}^n + H_1 \delta U + H_{2\xi} \frac{\partial}{\partial \xi} (N \cdot \delta U) + H_{2\eta} \frac{\partial}{\partial \eta} (N \cdot \delta U) + H_{4\eta} \frac{\partial^2}{\partial \eta^2} (N \cdot \delta U) \quad (7-55)$$

Then the space derivatives acting on  $\delta U$  are expressed in terms of all points adjacent to the  $(ij)$  location, say  $(ij+1)$ ,  $(ij-1)$ ,  $(i-1,j)$ ,  $(i+1,j)$  with one sided and centered finite differences for first order and second order derivatives, respectively.



## 8. CONCLUSIONS

This course intends to give a general survey on the tools available to perform basic turbulence modelling for compressible flows. A special effort has been made to present in a logical manner the different model, from the simplest one to the more elaborate. In the author's opinion, the topic of the second order closure has been only touched through the problem of the Reynolds stress modelling. This hides a lot of problems, which are not solved yet, to extend this closure to a global problem with significant heat and mass transfer. The simplest model have been presented first, as a necessary step for anyone willing to go farther in the equations troubles...

It is recognized that simplest models are still capable of solving a large proportion of practical problems. Nevertheless, for variable density problems, it is important to distinguish three flow regimes: i) the low speed flows; ii) the weakly compressible flows; iii) the strongly compressible flows. From all remarks made above, it seems that the middle class does not need imperatively the explicit compressibility terms, but the results could be expected for transport equation model in the case of non equilibrium flows. In the first case, density variations can be significant for heterogeneous mixing and/or combustion. In such cases the explicit compressibility terms plays a significant role on the mean flow, and it appears that their use cannot be avoided. For the last case (strong compressibility), these terms are needed too, but the lack of turbulent experiments on such flows leave plenty of room for further research work.



## REFERENCES

1. J. BOUSSINESQ, 1897, "Théorie de l'écoulement tourbillonnant et tumultueux des liquides dans les lits rectilignes à grande section". Tome I-II. Gautier-Villars, Paris.
2. L. PRANDTL, 1925, "Über die ausgebildete Turbulenz". Z. Angew. Math. Mech., vol. 5, pp. 136-139.
3. E.R. VAN DRIEST, 1951, "Turbulent boundary layer in compressible fluids", J. Aero. Sciences, vol. 18, n. 3.
4. L.S.G. KOVASZNAY, 1953, "Turbulence in supersonic flow", J. Aero. Sciences, vol. 20.
5. M. MORKOVIN, 1962, "Effects of compressibility on turbulent flows", Mécanique de la Turbulence, C.N.R.S., A. Favre, editeur.
6. A. DEMITRIADES, 1970, "Turbulence measurements in supersonic two-dimensional wake", Phys. Fluids, vol. 13, n. 7.
7. J. LAUFER, 1969, "Thoughts on compressible turbulent boundary layers", Memorandum R.M. 5946-PR Rand Corp. or NASA-SP-216.
8. P. BRADSHAW, 1977, "Compressible turbulent shear layers", Annual Review of Fluid Mechanics, pp. 33-54.
9. M.V. MORKOVIN et al. 1972, "Report of Conference Evaluation Committee", Free Turbulent Shear Flows Conference Proceedings, Hampton, Virginia, NASA-SP-321.
10. D.C. WILCOX and I.E. ALBER, 1972, "A turbulence model for high speed flows", Proceedings of the 1972 Heat Transfer and Fluid Mechanics Institute, Stanford University Press, pp. 231-252.
11. P. BRADSHAW, 1974, "The effect of mean compression or dilatation on the turbulence structure of supersonic boundary layers", J.F.M., vol. 63-3
12. G.L. BROWN and A. ROSHKO, 1974, "On density effects and large structures in turbulent mixing layers", J.F.M. vol. 64-4, pp. 775-816.
13. Y.H. OH, 1974, "Analysis of two dimensional free turbulent mixing", A.I.A.A. Paper 74-594.
14. J.P. BONNET and B.E. LAUNDER, 1981, "Case 8501", 1980-81 AFOSR-HTTM Stanford Conference on Complex Turbulent Flows, ed. Kline, Cantwell and Lilley, Stanford University.
15. W.J. FEIEREISEN, J.H. FERZIGER and W.C. REYNOLDS, 1981, "Numerical simulation of a compressible homogeneous turbulent shear flow", Technical Report TF-13, Thermosciences Division, Stanford University
16. Ph. DELORME, 1984, "Numerical simulation of homogeneous isotropic twodimensional turbulence in compressible flow", La Recherche Aerospatiale, n° 1984-1.
17. O. REYNOLDS, 1894, "On the dynamical theory of incompressible viscous fluids and the determination of the criterion", Phil. Trans. Roy. Soc. London. A vol. 186, pp. 123-164.



18. G.B. SCHUBAUER and C.M. TCHEU, 1959, "Turbulent flows and heat transfer", C.C. Lin, ed., Princeton University Press.
19. J.O. HINZE, 1959, "Turbulence", Mac Graw Hill Co., New York.
20. HESSELBERG, 1925, "Die Gesetze der ausgeglichenen atmosphärischen Bewegungen", Beitz. Physik forien Atmosphere, vol. 12, pp. 141-160.
21. G. DEDEBANT and Ph. WEHRLE, 1938, "Sur les equations aux valeurs probables d'un fluide turbulent", C.R.A.S., tome 206, pp. 1790-1791.
22. VAN MIEGHEU, L. DUFOUR, 1948, "Thermodynamique de l'atmosphere", Mem Inst. Roy. Meteo. de Belgique, 30.
23. A.K. BLACKADAR, 1950, "The transformation of energy by the large scale eddy stress in the atmosphere", Meteor. Papers, vol. 1, n. 4, New York University.
24. A. FAVRE, 1958, "Equations statistiques des gaz turbulents", C.R.A.S. 246, p. 2576-2579, 2723-2725, 2839-2842, 3216-3219.
25. A. FAVRE, 1965, "Equations des gaz turbulents compressibles", J. de Mécanique, vol. 4, n. 3.
26. R.W. BILGER, 1975, "A note on Favre averaging in variable density flows", Combustion, Science and Technology, vol.11, pp. 215-217.
27. D. VANDROMME, 1983, "Contribution à la modélisation et la prédiction d'écoulements turbulents à masse volumique variable", Doctorat d'Etat, Université de Lille, France.
28. J. LEORAT, A. POUQUET and M. POYET, 1984, "Numerical relativity and gravitational collapse", in Numerical Simulation of Compressible Flows, ed. Bancel and Signore, Reidel Press.
29. A.L. KISTLER, 1959, "Fluctuations measurements in a supersonic turbulent boundary layer", Phys. Fluids, vol. 2, n. 290, pp. 69-72.
30. A.L. KISTLER and W.S. CHEN, 1963, "The fluctuating pressure field in a supersonic turbulent boundary layer", J.F.M., vol. 16, n. 41, p. 72.
31. T. CEBECI and A.M.O. SMITH, 1974, "Analysis of turbulent boundary layers", Applied Mathematics and Mechanics, Academic Press.
32. P.S. KLEBANOFF, 1954, "Characteristics of turbulence in a boundary layer with zero pressure gradient", N.A.C.A. Technical Note 3178.
33. Th. Von KARMAN, 1930, "Mechanische Ähnlichkeit und Turbulenz", N.A.C.A. Technical Memorandum 611.
34. G.I. TAYLOR, 1915, "The transport of vorticity and heat through fluids in turbulent motion", Phil. Trans., A 215, n. 1.
35. H. REICHARDT, 1942, "Gesetzmässigkeiten der freien Turbulenz", V.D.I., Forschungsheft 414, 1st ed., Berlin.
36. M.P. ESCUDIER, 1965, "The distribution of the mixing length in turbulent flows near walls", Rep. TWF/TN/1, Dept. Mech. Eng., Imperial College, London.



37. E.R. VAN DRIEST, 1956, "On turbulent flow near a wall", *Journal Aeronaut. Sciences*, vol. 23, p. 1007.
38. T. CEBECI, 1970, "Behaviour of turbulent flow near a porous wall with pressure gradient", *A.I.A.A. Journal*, n. 8, p. 2152.
39. T. CEBECI, 1971, "Calculation of compressible turbulent boundary layers with heat and mass transfer", *A.I.A.A. Journal*, n. 9, p. 1091.
40. T. CEBECI and A.M.O. SMITH, 1974, "Analysis of turbulent boundary layers", *Applied Mathematics and Mechanics*, Academic Press.
41. T. CEBECI, A.M.O. SMITH and S.G. MOSINSKI, 1970, "Calculations of compressible adiabatic turbulent boundary layer", *A.I.A.A. Journal*, n. 8, pp. 1974-1982.
42. B.S. BALDWIN and H. LOMAX, 1978, "Thin layer approximation and algebraic model for separated turbulent flows", *A.I.A.A. Paper*, 78-257.
43. M.W. RUBESIN, 1976, "A one-equation model of turbulence for use with the compressible Navier-Stokes equations", *NASA TM X-73.128*.
44. J.R. VIEGAS and C.C. HORSTMAN, 1978, "Comparison of multiequation turbulence models for several shock boundary layer interaction flows", *AIAA Journal*, vol. 13, n. 10, pp. 1368-1374.
45. L. PRANDTL, 1945, "Über ein neues Formelsystem für die ausgebildete Turbulenz", *Nachr. Akad. der Wissenschaft in Göttingen*, Göttingen, ed. Van der Loek.
46. A.N. KOLMOGOROV, 1942, "Equations of turbulent motion of an incompressible fluid", *Izv. Akad. Nauk. S.S.S.R., Ser. Phys.* 6, n. 1/2, pp. 55-58.
47. G.S. GLUSHKO, 1965, "Turbulent boundary layer on a flat plate in an incompressible fluid", *Bull. Acad. Sci. U.S.S.R., Mech. Ser.*, n° 4, pp. 13-23.
48. I.W. BECKWITH and D.M. BUSHNELL, 1968, "Detailed description and results of a method for computing mean and fluctuating quantities in turbulent boundary layers", *NASA TN-D. 4815*.
49. M.W. RUBESIN and W.C. ROSE, 1973, "The turbulent mean flow Reynolds stress and heat flux equations in mass averaged dependent variables", *NASA TM X-62. 248*.
50. H.P. IRWIN, 1974, "Measurements in blown boundary layers and their prediction by Reynolds stress modelling", *PhD Thesis, Mac Gill University*.
51. T.J. COAKLEY, J.R. VIEGAS and C.C. HORSTMAN, 1977, "Evaluation of turbulence models for three primary types of shock separated boundary layers", *AIAA Paper*, 77-692.
52. J.R. VIEGAS and T.J. COAKLEY, 1977, "Numerical investigation of turbulence models for shock separated boundary layers flows", *AIAA Paper*, 77-44.
53. P. BRADSHAW, D.H. FERRIS and N.P. ALTWELL, 1967, "Calculation of boundary layer development using the turbulent energy equation", *J.F.M.* vol. 28, part 3, pp. 593-616.
54. S.C. LEE and D.T. HARSHA, 1970, "Use of turbulent kinetic energy in free mixing studies", *AIAA Journal*, vol. 8, n° 6, pp. 1026-1032.



55. T.J. COAKLEY and J.R. VIEGAS, 1977, "Turbulence modelling of shock separated boundary layer flows", 1st Int. Symp. on Turbulent Shear Flows, Penn. State Univ., Univ. Park, Pennsylvania.
56. P. CHASSAING, 1979, "Mélange turbulent de gaz inertes dans un jet de tube libre", Doctorat d'Etat, Toulouse.
57. T.J. COAKLEY, 1983, "Turbulence modelling methods for the compressible Navier-Stokes equations", AIAA Paper, 83-1693.
58. W.P. JONES and B.E. LAUNDER, 1973, "The calculation of low Reynolds number phenomena with a two equation model of turbulence", Int. Jour. Heat Mass Transfer, vol. 16, pp. 1119-1130.
59. R. BORGHİ and D. ESCUDIER, 1984, "Assessment of a theoretical model of turbulent combustion by comparison with a single experiment", Combustion and Flame, vol. 56, pp. 149-164.
60. D. VANDROMME, 1980, "Turbulence modelling for variable density flows", PhD thesis, University of Brussel.
61. R. ARINA and C. BENOCCHI, 1985, "Turbulent boundary layers: examples of turbulence models", V.K.I. Lecture Serie, 1985-01, Belgium.
62. J.S. SHANG and W.L. HANKEY, 1975, "Numerical solution for supersonic turbulent flow over a compression ramp", A.I.A.A. Journal, vol. 13, n° 10.
63. K.Y. CHIEN, 1982, "Predictions of channel and boundary layers flows with a low-Reynolds number turbulence model", A.I.A.A. Journal, vol. 20, n° 1.
64. C.C. HORSTMAN, 1984, Private communication, NASA Ames Research Center.
65. A. LIAKOPOULOS, 1985, "Computation of high speed turbulent boundary layer flows using the  $k - \epsilon$  turbulence model", Int. J. Num. Meth. Fluids, vol. 5, pp. 81-97.
66. J.R. VIEGAS and M.W. RUBESIN, 1983, "Wall-function boundary conditions in the solution of the Navier-Stokes equations for complex compressible flows", A.I.A.A. Paper, 83-1694.
67. D.C. WILCOX and R.M. TRACI, 1976, "A complete model of turbulence", A.I.A.A. Paper, 76-351.
68. D.C. WILCOX and M.W. RUBESIN, 1980, "Progress in turbulence modelling for complex flow fields including the effects of compressibility" N.A.S.A. TP-1517.
69. P.G. SAFFMAN, 1970, "Turbulence model for boundary layer near walls", Proc. Roy. Soc., London, vol. A317, pp.417-433.
70. P.G. SAFFMAN, 1976, "Development of a complete model for the calculation of turbulent shear flows", 1976 Duke Turbulence Conf., Duke University, Durham.
71. A.N. KOLMOGOROV, 1942, "Equations of turbulent motion of an incompressible turbulent fluid", Izv. Akad. Nauk. SSSR Ser. Phys. VI, n° 1-2, p. 56.
72. B.E. LAUNDER and D.B. SPALDING, 1972, "Mathematical models of turbulence", Academic Press, London.



73. W.P. JONES and B.E. LAUNDER, 1972, "The prediction of laminarization with a two-equation model of turbulence", *Int. J. Heat Mass Transfer*, vol. 15, pp. 301-314.
74. B.E. LAUNDER, G.J. REECE and W. RODI, 1975, "Progress in the development of a Reynolds stress turbulence closure", *J.F.M.*, vol. 68, n° 3, pp. 527-566.
75. K. HANJALIC and B.E. LAUNDER, 1976, "Contribution towards a Reynolds stress closure for low Reynolds number turbulence", *J.F.M.*, vol. 74, n° 3, pp. 593-610.
76. K. HANJALIC and B.E. LAUNDER, 1972, "A Reynolds stress model of turbulence and its application to thin shear flows", *J.F.M.*, vol. 52, n° 4, pp. 609-638.
77. B.J. DALY and F.H. HARLOW, 1970, "Transport equations in turbulence", *Phys. Fluids*, vol. 13, n° 11.
78. J.P. DUSSAUGE, 1981 "Evolution de transferts turbulents dans une détente rapide en coulement supersonique", Doctorat d'Etat, Université d'Aix-Marseille.
79. J.C. ROTTA, 1951, "Statistische theorie nicht homogener Turbulenz", *Zeitschrift. Phys.*, vol. 129, pp. 547-572.
80. D.D. VANDROMME and H. HAMINH, 1984, "Solution of the compressible Navier-Stokes equations: applications to complex turbulent flows" V.K.I. LS 1984-4, Belgium.
81. J.L. LUMLEY, 1975, "Prediction methods for turbulent flows" V.K.I. LS 76.
82. B.E. LAUNDER, 1978, "Heat and mass transport", *Topics in Applied Physics: "Turbulence"*, Ed. P. Bradshaw, Springer Verlag.
83. J.P. BONNET, 1982, "Etude théorique et expérimentale de la turbulence dans un sillage supersonique", Doctorat d'Etat, Université de Poitiers.
84. J. JANICKA and J.L. LUMLEY, 1981, "Second order modelling in non constant density flows", Internal Report FDA-81-01, Cornell University.
85. S.H. EL TAHRY, 1983, " $k - \epsilon$  equation for compressible reciprocating engine flows", *J. ENERGY, A.I.A.A.*, vol. 7, n° 4.
86. S.K. SAXENA and R.C. METHA, 1986, "Shock/turbulent boundary layer interaction with wall function boundary conditions", *A.I.A.A. J.*, vol. 4, n° 7, pp. 1207-1209.
87. A. NAKAYAMA and H. KOYAMA, 1984, "A wall law for turbulent boundary layers in adverse pressure gradients", *A.I.A.A. J.*, vol. 22, pp. 1386-1389.
88. E.J. HOPKINS, E.R. KEENER, T.E. POLEK and H.A. DWYER, 1972, "Hypersonic turbulent skin friction and boundary layer profiles measured on nonadiabatic flat plates", *A.I.A.A. J.*, vol. 10, pp. 40-48.
89. A.P. WATKINS, 1977, "Flow and heat transfer in cylinder/piston assemblies", Ph.D. thesis, Imperial College, London.
90. A.D. GOSMAN and A.P. WATKINS, 1977, "A computer prediction method for turbulent flow and heat transfer in piston/cylinder assemblies", 1st Turb. Shear Flow, Pennsylvania State University, pp. 5.23-5.30.
91. W.C. REYNOLDS, 1980, "Modeling of fluid motions in engines: An introductory overview", *Symp. on Combustion Modeling in Reciprocating Engines*, Plenum Press, pp. 41-66.



92. T. MOREL and N.N. MANSOUR, 1982, "Modeling of turbulence in internal combustion engines", S.A.E. paper, n° 820040.
93. J.I. RAMOS and W.A. SIRIGNANO, 1980, "Axisymmetric flow model with and without swirl in a piston cylinder arrangement with idealized valve operation", S.A.E. paper, 800284.
94. C.T. WU, J.H. FERZIGER and D.R. CHAPMAN, 1985, "Simulation and modelling of homogeneous compressed turbulence", 5th Turb. Shear Flow, Cornell University, pp. 17.13-17.19.
95. J.I. RAMOS, A.C. HUMPHREY and W.A. SIRIGNANO, 1979, "Numerical prediction of axisymmetric laminar and turbulent flows in motored reciprocating internal combustion engines", S.A.E. paper, 790356.
96. J. SAHU and J.E. DANBERG, 1986, "Navier-Stokes computations of transonic flows with a two-equation turbulence model", AIAA J., vol. 24, n° 11, pp. 1744-1751.
97. P. BRUEL, 1988, "Etude numérique des écoulements turbulents dans un canal 2D avec injection pariétale d'un mélange réactif", Thèse de doctorat, Université de Poitiers.
98. H. VIVIAND, 1978, "Traitement des problèmes d'interaction fluide parfait - fluide visqueux en écoulement bidimensionnel compressible à partir des équations de Navier-Stokes", AGARD LS-94.
99. B.S. BALDWIN, R.W. MACCORMACK and G.S. DEIWERT, 1975, "Numerical techniques for the solution of the compressible Navier-Stokes equations and implementation of turbulence models", AGARD LS-73
- 100 R.W. MACCORMACK, 1981, "A numerical method for solving the equations of compressible viscous flow", AIAA paper 81-0110.
- 101 R.W. MACCORMACK, 1982, "Numerical solution of the equations of compressible viscous flow", **Transonic, shock and multidimensional flows** in Advances in Scientific Computing, Academic Press.
- 102 J.R. VIEGAS, M.W. RUBESIN, 1982, "Wall function boundary conditions in the solution of the Navier-Stokes equations for complex compressible flows", NASA T.P. 1517.
- 103 J.R. VIEGAS, R.W. MACCORMACK, 1988, Private communication.
- 104 W. RODI, 1976, "A new algebraic relation for the Reynolds stresses", ZAMM, 56, pp. 219-221.
- 105 S.M. DASH, D.E. WOLF, J.M. SEINER, 1975, "Analysis of turbulent underexpanded jets, part I: Parabolized Navier-Stokes model SCIPVIS", AIAA Journal, vol. 23, n° 4.
- 105 S.M. DASH, G. WEILERSTEIN, R. VAGLIO-LAURIN, 1975, "Compressibility effects in free turbulent shear flows", AFOSR-TR-75-1436.
- 106 F.K. OWEN, C.C. HORSTMAN, M.I. KUSSOY, 1975, "Mean and fluctuating flow measurements of a fully developed non-adiabatic hypersonic boundary layer", JFM, vol. 70, n° 11, pp. 2634-2649.



- 107 O. ZEMAN, 1990, "Dilatation dissipation: The concept and application in modelling compressible mixing layers", *Phys. Fluids*, vol. A2(2), pp. 178-188.
- 108 S. SARKAR, G. ERLEBACHER, M.Y. HUSSAINI, H.O. KREISS, 1989, "The analysis and modelling of dilatational terms in compressible turbulence", ICASE Report 89-79, NASA CR 181959.
- 109 M.W. RUBESIN, 1990, "Extra compressibility terms for Favre-averaged two-equation models of inhomogeneous turbulent flows", NASA CR 177556.
- 110 R.H. NICHOLS, 1990, "A two-equation model for compressible flows", AIAA paper 90-0494.
- 111 T. PASSOT, A. POUQUET, 1987, "Numerical simulation of three-dimensional supersonic flows", *JFM*, vol. 181, p. 441.
- 112 R. MICHEL, C. QUEMARD, R. DURANT, 1969, "Application d'un schéma longueur de mélange à l'étude de couches limites turbulentes d'équilibre", Note Technique ONERA n° 154.
- 113 I.E. ALBER, 1971, "Similar solutions for a family of separated turbulent boundary layers", AIAA Paper n° 71-203.
- 114 M. WOLFSHTEIN, 1969, "The velocity and temperature distribution in one dimensional flow with turbulence augmentation and pressure gradient", *Int. J. Heat Mass Transfer*, vol. 12, pp. 301-318.
- 115 H.C. CHEN, V.C. PATEL, 1987, "Practical near-wall turbulence models for complex flows including separation", AIAA paper 87-1300.
- 116 D.A. JOHNSON, L.S. KING, 1984, "A new turbulence closure model for boundary layer flows with strong adverse pressure gradients and separation", AIAA Paper n° 84-0175.
- 117 D.A. JOHNSON, L.S. KING, 1984, "A mathematically simple turbulence closure model for attached and separated boundary layers", AIAA Vol. 23, n° 11, pp. 1684-1692.
- 118 G. FRESKOS, 1992, private communication, CERFACS, Toulouse.
- 119 O. ZEMAN, 1991, "The role of pressure-dilatation correlation in rapidly compressed turbulence", CTR Annual Research Briefs, Stanford Univ., pp.105-117.
- 120 O. ZEMAN, G.N. COLEMAN, 1991, "Compressible turbulence subjected to shear and rapid compression", *Proceedings of the Eight Symposium on Turbulent Shear Flows*, Springer Verlag.
- 121 G. N. COLEMAN, N.N. MANSOUR, 1991, "Direct simulation of homogeneous compressible turbulence under isotropic mean compression", in *Proceedings of the Eight Symposium on Turbulent Shear Flows*, Technical University, Munich.
- 122 P. DURBIN, O. ZEMAN, 1992, "Rapid distortion theory for homogeneous compressed turbulence with application to modeling", to appear in *J. Fluid Mech.*



# HYPERSONIC SHOCK WAVE BOUNDARY LAYER INTERACTIONS OVER SIMPLIFIED DEFLECTED CONTROL SURFACE CONFIGURATIONS

G. SIMEONIDES

ESA / ESTEC (YPA)  
Aerothermodynamics section  
Postbus 299  
2200 AG Noordwijk  
The Netherlands

## ABSTRACT

The problem of hypersonic shock wave boundary layer interactions over simplified geometric configurations that simulate the vicinity of deflected control surfaces on lifting reentry vehicles is addressed. The discussion evolves primarily around surface pressure and heat transfer data over flat plate/two-dimensional and swept compression ramp configurations, and the axisymmetric hyperboloid / flare configuration, emphasizing the prediction of peak heating in regions of interaction, the promotion of laminar-turbulent transition, and the performance and validation of CFD codes. Following a brief overview of the fundamental physical phenomena associated with shock wave boundary layer interactions, as these have been identified and summarized in the extensive literature available on the subject, the paper is split into three main parts. The first part concentrates on the analysis of global pressure and heat transfer distributions and their comparison with simple boundary layer theory, emphasizing peak heating at the downstream end of the interaction region. The second part addresses the formation of streamwise striations in reattaching flow regions, and the associated spanwise heat transfer variations which may exceed  $\pm 50\%$  of the mean local heating level. Last but not least, the performance and limitations of state-of-the-art Navier-Stokes computations in computing hypersonic separated flows are illustrated by means of a series of CFD code validation test cases assembled in recent years.

## LIST OF SYMBOLS

AOA	angle of attack
C	Chapman-Rubesin linear viscosity law constant
$c_f$	skin friction coefficient ( $\frac{\tau_w}{\frac{1}{2}\rho_\infty u_\infty^2}$ )
$c_H$	heat transfer coefficient ( $\frac{q_s}{\rho_\infty u_\infty (H_0 - H_w)}$ )
$c_p$	specific heat at constant pressure
d	leading edge thickness
h	heat transfer coefficient ( $\frac{q_s}{(T_r - T_w)}$ )
H	enthalpy
$K_p$	pressure coefficient ( $\frac{p - p_\infty}{\frac{1}{2}\rho_\infty u_\infty^2} = \frac{p - p_\infty}{0.5\gamma p_\infty M_\infty^2}$ )
L	distance of hinge line from leading edge
$L_{pk}$	effective growth length of reattaching boundary layer to location of peak heating
M	Mach number

p	pressure
q	dynamic pressure ( $0.5\rho u^2$ )
$\dot{q}_s$	heat transfer rate into model surface
Re	Reynolds number
$Re_{unit}$	unit Reynolds number (per meter)
St	Stanton number ( $\frac{q_s}{\rho_\infty u_\infty (H_r - H_w)}$ )
T	temperature
u	velocity
x	distance from leading edge
$\alpha$	streamwise ramp deflection angle
$\alpha_s$	deflection angle of dividing streamline
$\beta$	ramp deflection angle normal to hinge line
$\gamma$	ratio of specific heats
$\delta_s$	shear layer thickness at reattachment
$\theta$	shock angle
$\rho$	density
$\tau_w$	wall shear stress
$\bar{\chi}$	hypersonic viscous interaction parameter ( $\frac{M^2}{\sqrt{Re}}\sqrt{C}$ )
$\psi$	sweep angle

## Subscripts

0	reservoir (total)
$\infty$	freestream
e	edge of boundary layer
p	pressure plateau
pk	peak heating
r	recovery (adiabatic, non-radiating wall)
reat	reattachment
ref	reference boundary layer
sep	separation
u.i.	upstream influence point
w	wall

## Superscript

*	at Eckert's reference temperature
---	-----------------------------------

## 1 INTRODUCTION

Shock wave boundary layer interactions have been the subject of extensive research. Over the past 50 years, since the phenomenon was first observed by Ferri [1], a large number of configurations have been investigated at a wide variety of flow conditions which are summarized in a number of review papers [2-14]. Emphasis, however, has been placed on applications in the field of missile aerodynamics and, consequently, on high Reynolds number flows with



fully developed turbulent oncoming boundary layers at relatively low Mach numbers, although some of the literature refers explicitly to hypersonic flows.

The recent boost in space transportation, as characterized by the appearance of a number of ambitious concepts for hypersonic vehicles worldwide (lifting reentry vehicles as well as single- or two-stage-to-orbit airbreathers), has been accompanied by an increased interest in fundamental research in ascent / reentry aerothermodynamics, much related to the development of a better understanding of the relevant flow processes and their modelling, as well as to the development and validation of Computational Fluid Dynamics (CFD) codes which are playing an increasingly important role in the design process. Noting that the design of control surfaces has been identified as one of the most critical areas in the design of hypersonic aircraft [15,16], a significant part of this research effort (experimental and theoretical) has been devoted to the subject of control effectiveness and heating.

Focusing on the lifting reentry of a spaceplane and, particularly, on its initial stages, the associated aerodynamics are characterized by high Mach numbers in excess of 10 or 15 and rather low Reynolds numbers, so that fully laminar boundary layers are expected to develop over many of the wetted surfaces of the reentry vehicle. This is the case with Hermes-type spaceplanes, where the small size further encourages laminar flow over large parts of the vehicle. With reference to Fig. 1, attention is drawn to control surfaces such as the body flap, the elevons and the rudders on the wing tip fins. During reentry, the vehicle is to fly at an incidence angle of  $30^\circ$  or  $40^\circ$ , in which case the body flap will face a relatively low Mach number (of the order of 3) flow with a laminar, transitional or turbulent oncoming boundary layer, depending on the altitude. The highly swept (because of the angle of attack of the vehicle) wing tip rudders, however, will face a high Mach number, low Reynolds number flow with a fully laminar boundary layer developing on the fins ahead of the hinge line. In both cases, deflection of the control surface is bound to cause an interaction between the oncoming boundary layer and the resulting shock wave, which may yield significant flow separation, particularly in cases where the oncoming boundary layer is laminar and, hence, less resistant to adverse pressure gradients. Consequently, significant losses in control effectiveness (bearing in mind the finite chord of the control surface) and excessive heating of the structure may be anticipated. Such interactions will be clearly influenced by three-dimensional effects associated with the finite span and/or sweep of the deflected control surfaces, as well as any three-dimensionality of the oncoming flow.

For the purposes of fundamental research, both ex-

perimental and computational, simplified geometric configurations are sought to simulate a deflected control surface. Such configurations are illustrated in Fig. 2: a flat plate followed by a swept or unswept compression ramp, an axisymmetric hyperboloid / flare configuration, and a delta wing followed by a deflected flap. It is noted that shock wave boundary layer interactions of a similar type may also be encountered in the nose-canopy region of the spaceplane, which has been approximated by double ellipsoid configurations.

The relevant flow conditions cover a wide range. Along a typical lifting reentry trajectory, at Mach numbers of less than, say, 15, the flowfield is adequately characterized by the Mach and Reynolds numbers. In this range the flow comprises a perfect gas which may be treated as a continuum; the oncoming boundary layer may be laminar or turbulent; and the interaction process may promote laminar-turbulent transition. For higher altitudes and/or velocities, the flowfield is significantly complicated by high enthalpies and the consequent thermo-chemical effects, as well as by rarefied gas effects.

The discussion hereafter is based on experimental, analytical and numerical results. The geometric characteristics of the interaction are addressed, but emphasis is placed on the pressure and heat transfer distributions in the vicinity of the shock wave boundary interaction. The continuum perfect gas regime is almost exclusively considered, due to the limited amount of data exhibiting significant real gas effects in regions of shock boundary layer interaction. For simplicity, the flat plate / two-dimensional ramp configuration is extensively used in the discussion, but more realistic three-dimensional and generic configurations are considered too.

In what follows, section 2 provides a qualitative description of the fundamental phenomena in the interaction region and the relevant flow and geometric parameters, and addresses incipient separation. Section 3 concentrates on global aspects of the effects of the interaction upon surface pressure and heat transfer distributions, and section 4 focuses on the localized striation heating phenomena observed in reattaching flow regions. The contribution of computational fluid dynamics to the shock boundary layer interaction problem is addressed in section 5, emphasizing validation issues. In conclusion, a synthesis of the current understanding of the control surface problem is given aimed primarily to the effects of shock boundary layer interactions upon control effectiveness and heating.

## 2 OVERVIEW OF THE FUNDAMENTAL ASPECTS OF THE PROBLEM

### 2.1 Qualitative description of the phenomena

With reference to the flat plate / two-dimensional



ramp configuration of Fig. 3, the physics of the interaction may be easily understood. First, if there was no boundary layer growing on the flat plate ahead of the deflected ramp, and the freestream velocity was higher than the local speed of sound, an "inviscid" oblique shock would form at the hinge line which would provide (discontinuously) the appropriate deflection to the oncoming supersonic or hypersonic flow. In practice, however, there is a boundary layer developing along the flat plate which involves a subsonic part close to the wall. Through this subsonic layer, information is transmitted upstream so that the oncoming flow is aware of the deflected ramp and the associated pressure rise upstream of the hinge line.

For moderate ramp deflection angles, the subsonic part of the boundary layer faces a continuous pressure rise (starting at the so-called upstream influence point), which causes the divergence of streamlines and the thickening of the subsonic sublayer. This, in turn, causes the deflection of the external super- or hypersonic stream, giving rise to the formation of a system of compression waves (with varying strength and inclination through the supersonic part of the boundary layer) which, eventually, coalesce into a single shock wave of the same strength as the inviscid shock. Such weak interactions are contained within a small region near the hinge line of the order of 2-3 times the boundary layer thickness [2].

With increasing ramp deflection angle, the oncoming boundary layer faces an increasing adverse pressure gradient, until it can no longer withstand it and separates. In well separated cases, the upstream influence of the deflected ramp is markedly augmented and the shock structure becomes significantly distinct from the inviscid case. The recirculating bubble that forms is bounded by a separation and a reattachment shock (or compression fan) which merge into a single shock that, eventually, is equivalent to the corresponding inviscid shock. The location of the separation point and the angle of the separated shear layer (and associated shock system) are fixed so that the pressure rise through separation corresponds to the pressure rise required for incipient separation of the oncoming boundary layer at the local conditions at the separation point, and is independent of the detailed character of the flow downstream and of the particular agent that causes the pressure rise and the interaction as a whole. This behaviour has been termed, after [17] "free interaction". The length of the separated shear layer is determined so as to be sufficiently reenergized for overcoming the residual pressure rise through reattachment.

The coalescence of the separation and reattachment compressions and/or shocks is similar to the inviscid double wedge problem [18]. At hypersonic Mach numbers, the two-shock compression near the body

surface is more efficient than the single inviscid shock compression, yielding at the intersection of the separation and reattachment shocks an expansion fan back towards the ramp surface and a slipline, across which an important entropy jump may occur. At hypersonic Mach numbers, the shock system lies very close to the model surface and may be contained, to a large extent, within the boundary layer, particularly when the latter is a thick turbulent one. Downstream of reattachment, the boundary layer thickness reaches a local minimum in the so-called neck region, beyond which it begins to grow towards a self-similar form. For strong interactions with extensive separated regions, the thinning of the boundary layer in the neck region may be so important that the effective origin of the reattaching boundary layer may be safely assumed to be in the close vicinity of reattachment. The latter statement is supported by experimental evidence and will be relevant in the development of peak heating prediction tools below.

The problem of the interaction between separation and reattachment shocks has been investigated by inviscid computations over double wedge configurations in [19], where the first wedge is aimed to represent the dividing streamline of the separated shear layer and the second wedge the deflected control surface. Two cases are depicted in Fig. 4 for an overall flow deflection of  $40^\circ$ . The configuration with a  $30^\circ$  angle first wedge at an oncoming Mach number of 4.54 represents a tailored situation where the near-wall compression through the two-shock system is exactly matched by the single shock compression of the outer flow. As a result, there is no pressure differential across the slipline emanating from the coalescence of the two shocks into a single shock and no further wave systems are featured downstream. The slipline, in this case, is parallel to the second wedge.

On the contrary, with a  $20^\circ$  angle first wedge at Mach 8, the near-wall two-shock compression yields a higher pressure rise than the single shock compression of the outer flow. Consequently, an expansion fan emanates from the shock coalescence point towards the second wedge, where it reflects also as an expansion. When the reflected expansion reaches the slipline, it is partially transmitted through as an expansion and partially reflected back towards the second wedge as a compression, which is reflected from the wedge also as a compression, and so on. This system of expansion and compression waves, downstream of the coalescence of the main shocks, causes the slipline to be curved, initially turning away from the second wedge and eventually, after some oscillations, parallel to it.

The pressure and Mach number distributions corresponding to this latter case are also shown in Fig. 4, along the inner flow region near the wall, as well as along the outer flow region just outside the zone



of the two-shock compression and slipline. The influence of the curvature of the slipline and the associated compression/expansion waves downstream of the primary two-shock (in the inner flow region) or single-shock (in the outer flow region) compressions is clearly illustrated.

It should be noted that, at lower Mach numbers, situations may arise where the near-wall two-shock compression gives a lower pressure rise than the outer flow single shock compression, whereby a compression wave forms at the coalescence of the two near-wall shocks towards the deflected wedge to further compress the near-wall flowfield.

Finally, the complexity that may arise in regions of shock wave boundary layer interaction over relatively simple configurations and the associated systems of compressions and expansions is illustrated in the combined oil flow / schlieren photograph of Fig. 5 [20]. In particular, the highly three-dimensional character of the separation with its large extent on the leeward side, the interaction between the bow shock and the flare shock on the windward side, and the interaction between the expansion and the flare shock towards the base of the configuration are noted.

## 2.2 Relevant parameters and trends

The relevant parameters for shock wave boundary layer interactions have been identified [2-14] as the Mach and Reynolds number of the undisturbed oncoming flow, the strength of the interaction (i.e. the magnitude of the overall pressure rise) and the nature of the disturbance that causes it, some measure of the thickness and status (laminar or turbulent) of the undisturbed boundary layer, and the wall-to-total temperature ratio. In cases where the shock generator has a finite length scale, this is imposed as an additional parameter. For dimensionless and infinite interactions (after the classification of [8]), the boundary layer thickness at the onset of the interaction is the only length scale appropriate for scaling the geometric characteristics of the interaction.

In general, for a laminar or moderate Reynolds number turbulent flow, low Mach number, high Reynolds number and high wall-to-total temperature ratio imply a greater upstream influence of the shock wave boundary layer interaction, and less resistance to separation (or larger extent of the separated region) for a given ramp deflection angle. It is reported, however, that with high Reynolds turbulent oncoming flows the effect of increasing Reynolds number is reversed resulting in a decrease of the extent of separation [5,11].

Clearly, laminar boundary layers are more prone to separation and, hence, give rise to more extensive separation in regions of shock wave boundary layer interaction than turbulent boundary layers. In other words, smaller interaction strengths are necessary to

separate a laminar boundary layer and, once separated, the pressure rise at separation of a laminar boundary layer is lower than that at separation of a turbulent boundary layer (section 3). In cases of transitional interactions, of course, the extent of the interaction decreases with Reynolds number as the interaction passes from an extensive laminar one to turbulent.

Intuitively, three-dimensionality must have a relieving effect on the interaction. This is, indeed, the case found in [21], where swept ramp configurations were investigated with the ramp deflection angle normal to the hinge line maintained constant; the effect of sweeping back the hinge line was, then, to reduce the strength of the interaction and, as a result, its streamwise extent (section 3, Figs. 11 and 16). In the investigations of [22,23], however, three-dimensional effects were studied with constant interaction strength configurations (with a constant overall pressure rise). Here, three-dimensionality had no relieving effect on the strength of the interaction, and sweeping back was found to have an adverse influence in the extent of the interaction [22] (Fig. 9) or no influence at all [23]. Noting the remarks of [9] that the relevant Mach number is given by the component normal to the foot of the inviscid shock and, after [21], more appropriately by the component normal to the upstream influence line, it is difficult to assess the effect of sweeping back in [22,23] in the absence of data indicating the sweep of this upstream influence line. It is plausible, however, that in the case of [22] the upstream influence line was increasingly swept back, so that the relevant Mach number normal to it was reduced with increasing sweep, thus causing an increase in the extent of the interaction. Conversely, the upstream influence line in [23] could be less affected by the sweep of the shock generator, in which case no influence should be expected in the extent of the interaction since its overall strength was maintained constant as well as all relevant parameters at its onset.

## 2.3 Incipient separation

A number of incipient separation criteria have been proposed for shock wave boundary layer interactions. However, there remains a debate as to the definition of incipient separation, and widely different experimental results have been obtained with different incipient separation observation techniques [11,24,25]. Specifically, it is pointed out in [11] that a small separation region may be almost always present near the hinge line of a deflected ramp, even with very weak interaction strengths. Consequently, a number of attempts have been made in the literature to more precisely define incipient separation which have, effectively, led to various distinctions and classifications. A first distinction is made between true and effective incipient separation, whereby the former corresponds to the hardly detectable, very small separation near



the hinge line that was referred to above. Effective separation, on the other hand, is the one of interest in practical applications, and this may be classified as small scale or large scale. Only the latter gives rise to a significant liftoff of the boundary layer and the formation of a pressure plateau within the separated region (section 3.1), hence, being easily detectable and of significance to engineering applications.

Free interaction theory [11,17] yields for the pressure distribution within the free interaction region over a two-dimensional adiabatic wall compression ramp,

$$K_p = \frac{p - p_{u,i}}{q_{u,i}} = F\left(\frac{x - x_{u,i}}{L}\right) \frac{(2c_{f,u,i})^{1/2}}{(M_e^2 - 1)^{1/4}} \quad (1)$$

where  $F\left(\frac{x - x_{u,i}}{L}\right)$  is a universal function independent of the Mach and Reynolds numbers. Experiments have shown that the function  $F$  at the separation point takes values of 0.81 to 1 for laminar and 4.22 for turbulent boundary layers. At the pressure plateau, that forms over well separated regions (section 3.1),  $F$  takes values between 1.47 and 1.8 for laminar and 6 for turbulent boundary layers [5,11,26,27]. It is pointed out in [11] that an overall pressure rise corresponding to the pressure rise to the separation point in a well separated case (given by eq. (1)) suffices to cause true incipient separation. For effective incipient separation, however, an overall pressure corresponding to the plateau pressure rise of well separated cases is necessary. The latter criterion, in turn, is thought to correspond to small scale effective incipient separation and is largely conservative particularly at high Mach numbers and cold wall conditions [26]. An alternative criterion has, therefore, been proposed in [14,26] for laminar large scale incipient separation at hypersonic flow conditions,

$$M_e \alpha_i = 80 \bar{\chi}_e^{1/2} \quad (2)$$

where  $\alpha_i$  is measured in degrees and  $\bar{\chi}$  is the hypersonic viscous interaction parameter. This result, together with a similar correlation for turbulent incipient separation, is depicted in Fig. 6.

Substituting in eq. (1) the perfect gas ( $\gamma = 1.4$ ) relation for the pressure coefficient,

$$K_p = \frac{5 M_e^2 \sin^2 \theta - 1}{3 M_e^2} = F\left(\frac{x - x_{u,i}}{L}\right) \frac{(2c_{f,u,i})^{1/2}}{(M_e^2 - 1)^{1/4}} \quad (3)$$

it is found that, with a normal shock and  $\sin \theta = 1$  (e.g. on the suction side of a transonic airfoil), small scale incipient separation is attained with an oncoming Mach number of just over 1 for a laminar boundary layer and a Mach number of approximately 1.25 for a turbulent boundary layer (assuming a Reynolds number of  $10^6$ ). These results are consistent with the experimental observations of [9,28]. At higher Mach numbers, the incipient separation shock angle,  $\theta_i$ , is decreasing with increasing Mach number, although

the overall pressure rise required for incipient separation (and, hence, the required component of the Mach number normal to the shock plane) is increasing.

This two-dimensional approach has been extended to three-dimensional interactions, making use of the Mach number component in the plane of the parent body normal to the footprint of the shock [8,9,28]. For a flat plate / sharp unswept fin (glancing shock) interaction, the aforementioned criterion yields for incipient separation of a turbulent boundary layer a Mach number normal to the plane of the shock of 1.2-1.3, which is consistent with the small scale incipient separation experimental data of [28,29]. If the shock is not normal to the parent body (in either two- or three-dimensional interactions, i.e. in swept or unswept compression ramp configurations as opposed to 2D normal or glancing shock interactions), the criterion based on eq. (3) indicates that small scale incipient separation will occur at a higher Mach number normal to the shock foot and, hence, will demand a higher pressure rise and a higher Mach number normal to the shock plane. In other words, a ramp interaction is more resistant to separation than a normal or glancing shock interaction as this has been experimentally demonstrated in [28,29]. Similar observations are also discussed in the extensive Russian literature available on shock wave boundary layer interactions [30].

It is finally noted that the bulk of incipient separation criteria available in the literature, including the ones discussed above, refer to boundary layers growing on flat plates (i.e. the parent body is a flat plate), and care must be taken when extrapolating this type of results to actual flight configurations [31].

### 3 GLOBAL SURFACE DISTRIBUTIONS IN REGIONS OF SHOCK WAVE BOUNDARY LAYER INTERACTION

#### 3.1 General

Typical distributions of surface pressure, skin friction and heat transfer over a flat plate / two-dimensional compression ramp shock boundary layer interaction at hypersonic Mach numbers are shown in Fig. 7 for a fully laminar interaction [32] (Mach 14.1,  $Re_L = 105,000$ ), and in Fig. 8 for a fully turbulent interaction [33] (Mach 8.6,  $Re_L = 22.5 \times 10^6$ ), for unseparated, incipient separated and well separated flow situations.

In both laminar and turbulent well separated cases, maximum pressure gradients correspond to the separation and reattachment points. Clearly, the laminar boundary layer is more prone to separation and the pressure rise to the plateau (that forms in well separated cases over the separated region) is lower than in the turbulent case. At the downstream end of the reattachment compression, in the laminar well



separated case of Fig. 7, a significant pressure overshoot is observed before the pressure field relaxes to the inviscid pressure level. This is due to the near-wall two-shock (separation and reattachment shock) compression that was discussed in section 2.1 to yield a higher pressure rise than the single inviscid shock compression at hypersonic Mach numbers. Although a pronounced pressure overshoot is not seen in the turbulent data of Fig. 8, this has been also observed in hypersonic turbulent interactions with significant separation [34,35]. Besides the importance of the pressure distribution upon control effectiveness (section 3.2), the presence of a significant pressure overshoot downstream of reattachment may become critical because of its implications on the heating of the deflected control surface (section 3.3). Lastly, similar to the pressure overshoot, the formation of a distinct pressure plateau over the separated region requires a significant separation; in cases of small scale separation, a continuous pressure rise or a kink is observed

With reference to Fig. 7, the skin friction coefficient is seen to decrease within the laminar interaction region, and in the separated cases takes negative values before it rises sharply on the deflected ramp through reattachment towards a maximum in the boundary layer neck region. Within the separated zone, the magnitude of the negative skin friction coefficient remains close to zero upstream of the hinge line but attains high (negative) values downstream of the hinge. A similar behaviour is observed in fully turbulent interactions.

Concerning the heat transfer distributions in Figs. 7 and 8 for the laminar and turbulent separated cases, they differ within the separated region insofar as the laminar distributions exhibit a drop in the heat transfer coefficient, whereas the turbulent distributions show a rise to a plateau level or kink (depending on the extent of the separation). Downstream, the heat transfer rises through reattachment to a peak level in the boundary layer neck region. The high heating level is clearly associated with the high local pressure and the thinning of the boundary layer caused by the interaction. In cases of transitional interactions, where laminar-turbulent transition is promoted by the reattachment process (section 3.3), a further rise of the ramp heating from the laminar to the turbulent level is bound to occur.

### 3.2 Surface pressure distributions

The pressure distributions measured over the adiabatic wall interaction region with flat plate / swept or unswept compression ramp configurations at Mach 2.95 ( $Re_L = 18.7 \times 10^6$ ) in [22] are illustrated in Fig. 9. The overall interaction strength in these experiments was maintained constant and the oncoming boundary layer was turbulent. It is seen that sweeping the deflected ramp beyond  $10^\circ$  is causing an increase in the upstream influence of the interaction

which is in contradiction with the findings of [23], as discussed in section 2.2.

Furthermore, contrasting Fig. 9 with Fig. 8, it is clear that a much lower ramp deflection angle and overall pressure rise is necessary to cause significant separation of a turbulent oncoming boundary layer at low Mach number than at high Mach number. It is also noted that with increasing Mach number and/or ramp deflection angle in well separated cases, an increasingly lower proportion of the increasing overall pressure rise is taken through separation and an increasingly higher proportion is left for the reattachment compression in accordance with the free interaction concept.

Typical pressure distributions over flat plate / two-dimensional ramp configurations measured at Mach 14 with  $Re_L = 1.8 \times 10^6$  [21] are shown in Fig. 10. Upstream of the onset of the interaction, the pressure field is determined by the angle of attack of the configuration, the bluntness of the nose and/or leading edge and viscous interaction due to the growth of the boundary layer. In the case of Fig. 10, the angle of attack was zero. The undisturbed flat plate pressure distribution is, therefore, well predicted by the superposition of the viscous interaction and (moderate) leading edge bluntness effects (typical leading edge thickness was  $55 \mu m \pm 5 \mu m$ ). For a weak viscous interaction over a cold wall, representative of the experiments in Fig. 10, the contribution to the flat plate pressure field is given after [36] for a Prandtl number of 0.725 by,

$$\frac{p_{e,v}}{p_\infty} = 1 + 0.578 \frac{\gamma(\gamma-1)}{4} \left[ 1 + 3.35 \frac{T_w}{T_0} \right] \bar{\chi}_\infty \quad (4)$$

Following the discussion in [37], the hypersonic viscous interaction parameter,  $\bar{\chi}$  is more appropriately defined at a reference temperature (e.g. Eckert's reference temperature [38]). The leading edge bluntness effect may be approximated by blast wave theory which, after [39], yields,

$$\frac{p_{e,b}}{p_\infty} = 0.56 + 0.121 M_\infty^2 \left[ \frac{c_{D,N}}{(x/d)} \right]^{2/3} \quad (5)$$

for  $\gamma=1.4$ . The leading edge drag coefficient,  $c_{D,N}$  depends on the shape of the leading edge; for a cylindrical leading edge it takes a value of  $4/3$ , and for a square leading edge a value of  $1.8$  [37].

The plateau pressure level, attained within the extensive separation region, is predicted on the basis of free interaction theory from the flow properties at the onset of the interaction. At high Mach numbers and cold wall conditions, the following expression has been proposed in [5] instead of eq. (1):

$$\frac{p_p - p_{u,i}}{p_{u,i}} = \bar{\chi}_{u,i}^{3/8} \quad (6)$$



On the deflected ramp, far downstream from the interaction, the inviscid ramp pressure level is attained as given by oblique shock relations [40] on the assumption of a single shock compression. Following the discussion in section 2.1, however, on the interaction between the separation and reattachment compressions (and, possibly, also with the nose/leading edge shock), a pressure overshoot is observed in this high Mach case at the end of the reattachment compression. For the particular cases of Fig. 10, which are characterized by relatively distinct and sharp separation and reattachment shocks, the assumption of a quasi-inviscid, two-shock near-wall compression provides a good approximation to the measured pressure peaks\*.

Similar comparisons of pressure distributions collected in the VKI Longshot tunnel at Mach 14 [21] but over flat plate / swept compression ramp (as well as 2D ramp) configurations are shown in Fig. 11. The data are plotted against distance from the ramp hinge line at selected spanwise locations where the distance between the model leading edge and the ramp hinge line is approximately 200 mm. The results show, in accordance with the discussion in section 2.2, that the extent of the interaction is reduced with increasing three-dimensionality which is equivalent to a decreasing overall pressure rise or effective streamwise flow deflection angle (note that in these experiments the ramp angle normal to the hinge line was maintained constant at  $15^\circ$  as the sweep angle was increased from  $0^\circ$  to  $30^\circ$  to  $60^\circ$ ). It is also noted that the upstream influence line in this set of experiments remained nearly parallel to the model leading edge, independent of the sweep of the hinge line, which simplified the prediction of the plateau pressure in the sense that the streamwise component of the Mach number was the relevant parameter in all cases.

Concerning the influence of shock wave boundary layer interaction on the pressure distribution and its implications upon control effectiveness, the primary effect is that of a stretching of the ramp induced pressure rise relative to the inviscid case (Fig. 12a). Since control effectiveness is a function of the integrated pressure field times distance from the center of gravity, the effects of the interaction are not evident. If the control surface and the interaction are a sufficiently large distance from the center of gravity, then the effect of the interaction is well approximated by the difference between the dotted areas and the hatched areas of the schematic in Fig. 12a. If the dotted area is larger, then the interaction yields a loss in control effectiveness; if it is smaller, then the interaction is beneficial to control effectiveness. Also,

in the case where the coalescence of the separation and reattachment shocks yields a pressure overshoot (at high Mach numbers) there is a further gain due to the interaction in control effectiveness, relative to the case where the two-shock compression is "tailored" yielding the same overall pressure rise as the outer flow inviscid shock.

Of course, the above assumes that the deflected control surface is sufficiently long to allow for a full pressure recovery, and that the oncoming boundary layer is thin so that distinct separation and reattachment compressions form. Also, the interaction of the control surface compression with any forebody shocks is neglected. A schematic illustration of the effects of a thick oncoming boundary layer and of the aforementioned shock/shock interaction that may occur at the coalescence of the control surface compression and a forebody shock is given in Fig. 12b after [31] as a plot of the actual pressure recovery along the deflected ramp normalized by the near-wall inviscid pressure recovery (in the absence of the expansion fan caused by the coalescence of the forebody and ramp shock systems). The effect of the interaction between the separation and reattachment shocks is neglected in this case. Clearly, thick boundary layers cause a longer extent of the interaction by virtue of viscous interaction, even in the absence of extensive separation, and possibly a loss in pressure recovery due to the modification of the effective body shape. The expansion fan caused by the interaction of the forebody and control surface shocks (at high freestream Mach numbers) is detrimental by effectively decreasing the pressure recovery to or below the level of the pressure rise through a single inviscid shock at freestream conditions. Control effectiveness issues will be further addressed in section 5.1 with the aid of computational data.

Lastly, the effect of leading edge bluntness on the pressure distribution over flat plate / two-dimensional ramp configurations is illustrated in Fig. 13 after [41] (Mach 10,  $Re_L = 2.1 \times 10^6$ ). The pressure increase upstream of the interaction resulting from increasing leading edge bluntness is noted, and also the reduction in upstream influence of the interaction due to the entropy layer. The flat plate pressure distribution upstream of the interaction is well predicted by the weak viscous interaction eq. (4) for the sharp leading edge case, and by the blast wave eq. (5) for the two blunt leading edges, noting that viscous interaction effects are negligible in the two blunt leading edge cases. The plateau pressure is well predicted by eq. (6) for the sharp leading edge case, but no predictions were made for the blunt leading edge cases because the effect of the entropy layer upon the boundary layer edge conditions was not estimated. Concerning the pressure recovery on the deflected ramp, a severe loss is detected relative to the inviscid single shock compression (from freestream con-

\* It is noted that in cases with thick oncoming boundary layers, the interaction may be characterized by a continuous near-isentropic compression rather than a distinct two-shock system.



ditions) and relative to the pressure overshoot found with the sharp leading edge. Clearly, the significant entropy layer in the blunt leading edge cases of [41] has a strong relieving effect upon the strength of the interaction (largely due to the resulting transverse Mach number gradient), which is associated with a loss in control effectiveness and reduced heating levels as will be seen in section 3.3.

### 3.3 Surface heat transfer distributions

The heat transfer distributions corresponding to the Mach 14 flat plate / two-dimensional ramp pressure data of Fig. 10 are shown in Fig. 14 for ramp deflection angles of 0°, 15° and 25° [21]. The theoretical predictions are based on the application of the reference temperature concept [38] to the incompressible zero pressure gradient boundary layer solution. The generalized result for any boundary layer edge conditions, following the development in [21,42], is

$$c_H (Re_{\infty,x})^n = \frac{A}{s} \left[ \frac{u_e p_e}{u_{\infty} p_{\infty}} \right]^{1-n} \left[ \frac{T_{\infty}}{T^*} \right]^{1-2n} \times (C^*)^n \left[ \frac{T_r - T_w}{T_0 - T_w} \right] \quad (7)$$

where  $n = 0.5$ ,  $A = 0.332$  and  $s = Pr^{2/3}$  for a laminar boundary layer, and  $n = 0.2$ ,  $A = 0.0296$  and  $s = 1$  for a turbulent boundary layer at high Mach numbers. It is also noted in [36] that in hypersonic cold wall cases, pressure gradient has a secondary effect on the heat transfer distribution, and so eq. (7) may be applied to non-zero pressure gradient attached flow situations provided that the local pressure field (induced either by viscous interaction and leading edge bluntness upstream of the interaction or by the ramp compression downstream of the interaction) is accounted for in the pressure ratio term.

With reference to Fig. 14, the success of the reference temperature method in predicting the heat transfer distribution over the attached flow regions upstream and downstream of the interaction is noted. Furthermore, a substantial improvement of the prediction quality over the deflected ramp is observed when the actual ramp pressure distribution of Fig. 10 is accounted for rather than being approximated by the inviscid ramp pressure. It is also noted that, whereas for the flat plate predictions the origin of the laminar boundary layer is taken at the leading edge of the model, the ramp predictions assume a virtual origin of the reattaching boundary layer at the reattachment point. This is done to account for the severe thinning of the boundary layer caused by the strong interaction and the turning/compression of the flow.

Moreover, the comparisons in Fig. 14 indicate that, although the boundary layer upstream of the interaction is laminar, turbulent heating levels are attained on the deflected ramp downstream of reattachment. This observation is fully consistent with schlieren

photographs and high frequency surface temperature-time data, both of which indicate [21] that laminar-turbulent transition is very effectively promoted by the interaction and, particularly, the reattachment process. Similar results on the promotion of transition have been found by many other investigators such as [41,43,44]. It is also noted that the effective transition of the boundary layer through reattachment further justifies the location of the virtual origin of the turbulent reattaching boundary layer in the close vicinity of the reattachment point.

In order to achieve a fully laminar interaction at Mach 14, experiments were performed in [21] at the minimum operational unit Reynolds number of the tunnel ( $Re_{unit} = 6.5 \times 10^6/m$ ) and with the hinge line of the deflected ramp shifted upstream to 70 mm from the leading edge (as opposed to 200 mm in the case of Figs. 10 and 14). It is seen from the heat transfer distributions of Fig. 15 that reducing the unit Reynolds number alone was not sufficient for a fully laminar interaction. However, the centerline heat transfer distribution with the forward two-dimensional ramp configuration shows a laminar reattachment with transition occurring a significant distance downstream on the ramp. This behaviour is also consistent with schlieren observations and fast response surface temperature signals [21].

With respect to the theoretical reference temperature predictions of Fig. 15, again the virtual origin of the reattaching boundary layer has been taken at reattachment to account for its thinning through the strong interaction. It is noted that if the origin had been assumed at the leading edge of the flat plate, the laminar peak heating at the end of the forward ramp reattachment compression would have been underpredicted by approximately a factor of 3.

The heat transfer data over the two-dimensional ramp configurations of Fig. 14 are compared to swept ramp data in Fig. 16 ( $Re_L = 2.5 \times 10^6$ ), in a similar manner as the pressure distributions in Fig. 11. Not only the relieving (in terms of streamwise extent) effect of three-dimensionality is illustrated in consistency with Fig. 11, but it is also noted that with increasing sweep (and, therefore, decreasing interaction strength) the effectiveness of the interaction in promoting laminar-turbulent transition is reduced. In particular, the 60° swept ramp data remain below the turbulent ramp heating level but, nevertheless, higher than the laminar predictions, thus indicating a long ineffective transition process that is not completed within the measurement domain.

Similar experiments with flat plate/swept and unswept compression ramp configurations have been performed at Mach 6 and the results are reported in [21,43]. In all cases with a nominally sharp leading edge, laminar-turbulent transition was promoted by the



interaction and, particularly, by the reattachment compression, as illustrated in Figs. 17 and 18. Similarly to the Mach 14 experiments, the reference temperature method was very successful in the prediction of the heat transfer distribution in the attached flow regions both upstream and downstream of the interaction.

In these studies, the effects of moderate leading edge bluntness were also examined. With reference to Fig. 19, it is noted that moderate leading edge bluntness has a retarding effect on the laminar-turbulent transition process in the reattachment region, but yields a greater upstream influence and larger extent of the interaction. The latter effect is, at least partially, related to the more laminar character of the flow with the blunter leading edges, but the modest entropy layer of the oncoming flow may also play a role.

The effects of more significant leading edge bluntness have been examined in [41]. The heat transfer distributions corresponding to the pressure data of Fig. 13 are illustrated in Fig. 20. Here, contrary to the data of Fig. 19, increasing leading edge bluntness is found to yield a reduction in the upstream influence of the interaction, which is related to the reduction in the strength of the interaction with increasing leading edge bluntness and to the modification of the effective Mach and Reynolds numbers of the undisturbed flow caused by the formation of a significant entropy layer. The reference temperature method is predicting well the laminar flat plate heat transfer distributions upstream of the onset of the interaction, when the pressure field induced by viscous interaction and, especially, by the leading edge bluntness is accounted for. Furthermore, comparison of the measurements to the reference temperature predictions on the deflected ramp, accounting for the measured pressure distributions of Fig. 13, indicates that the reattaching boundary layer is turbulent in the case of the sharp leading edge, but it remains laminar in the two blunt leading edge cases.

It is also noted that locating the virtual origin of the (turbulent) reattaching boundary layer at reattachment yields a good prediction for the ramp heat transfer distribution in the attached flow region downstream of reattachment in the sharp leading edge case of Fig. 20. This is consistent with the thinning of the boundary layer through the strong interaction (see sharp pressure rise in Fig. 13), and also with the rapid occurrence of laminar-turbulent transition in the close vicinity of reattachment. In the two blunt leading edge cases, however, it is seen that locating the virtual origin of the (laminar) reattaching boundary layer at reattachment yields an overprediction of the ramp heating just downstream of reattachment, although the comparison improves further downstream. A main reason for this discrepancy is believed to be the low strength of the interaction

(see respective pressure distributions in Fig. 13) and the consequent overestimation of the thinning of the reattaching boundary layer by the location of its virtual origin at reattachment. The relevance of the location of the virtual origin of the reattaching boundary layer to the correct prediction of peak heating will be further discussed in section 3.4.

It follows from the preceding discussion that the most relevant effect of shock wave boundary layer interactions in terms of heat transfer is the high heating levels attained on the deflected control surface. Evidently, the high heat transfer is related to the pressure rise and the thinning of the boundary layer on the control surface and, in some cases, to the promotion of laminar-turbulent transition by the adverse pressure gradient and flow concavity that characterize the reattachment region. The reference temperature method has been demonstrated to predict well the heat transfer distribution over attached flow regions, provided that the nature of the boundary layer is known, as well as the flow conditions at its edge and the location of its virtual origin. Application of the method may be extended beyond the two-dimensional zero pressure gradient case if an effective flow direction is identified and the local pressure distribution is accounted for. More comparisons between experimental data and reference temperature predictions are provided in [43].

It should be further noted that even in the absence of a strong shock wave boundary layer interaction and any extensive separated regions, the flow over the deflected control surface would still undergo a pressure rise and the boundary layer would be thinned to some extent and also encounter the destabilizing pressure gradient and flow concavity. Consequently, it should be borne in mind that significant peak heating levels may be attained on deflected controls in attached flow situations as well.

### 3.4 Peak heating correlations

Due to the importance of peak heating on deflected control surfaces and, generally, in regions of shock wave boundary layer interaction to the sizing of Thermal Protection Systems, the development of simple means for the prediction of interaction-induced heating rates is highly desirable. A large number of semi-empirical correlations has been developed to date, most of which are based on the pressure interaction concept [45] which stems from the generalized reference temperature result of eq. (7). The general form of such correlations is,

$$\frac{\dot{q}_{pk}}{\dot{q}_{ref}} \propto \left( \frac{p_{pk}}{p_{ref}} \right)^{(1-n)} \quad \text{or} \quad \left( \frac{p_3}{p_1} \right)^{(1-n)} \quad (8)$$

where the subscript  $ref$  denotes the undisturbed value on the parent body in the absence of an interaction (for example, over a flat plate). In some cases, the measured peak pressure ratio,  $p_{pk}/p_{ref}$ , has been replaced for simplicity by the inviscid pressure ratio,



$p_3/p_1$ , across a single oblique shock (for deflected control surfaces).

Typical pressure interaction peak heating correlations are presented in [42]. For laminar flow, the form

$$\frac{\dot{q}_{pk}}{\dot{q}_{ref}} = 1.1 \left( \frac{p_{pk}}{p_{ref}} \right)^{0.7} \quad (9)$$

is proposed, and for fully turbulent interactions (after [33,46],

$$\frac{\dot{q}_{pk}}{\dot{q}_{ref}} = \left( \frac{p_{pk}}{p_{ref}} \right)^{0.8} \quad (10)$$

A summary of various correlations of this type is presented in [47]. A major finding of this study, however, has been that different investigators have empirically determined widely different values of the exponent  $(1-n)$  in eq. (8), particularly so for fully laminar interactions. In fact, for fully laminar interactions, appropriate values of the exponent  $(1-n)$  are reported in [47] to cover the range 0.7-1.3; but for turbulent interactions, the range is reduced to values between 0.7 and 0.85. It was, therefore, reasonable to assume that the aforementioned discrepancies in fully laminar interactions were largely due to the fact that some of the experimental data considered were transitional (noting the discussion in section 3.3 on the promotion of laminar-turbulent transition by the interaction).

Consequently, a similar (pressure interaction) peak heating correlation was developed in [48] to cover transitional as well as fully laminar interactions. The result is illustrated in Fig. 21a with an exponent  $(1-n)$  of 1.13 and a constant of proportionality of 0.13 for fully laminar interactions, and a significant dependence on Reynolds number for transitional interactions. However, when the transitional data of [43] were plotted in the form of Fig. 21a, a rather poor comparison was found (Fig. 21b).

These observations led to a reevaluation of the pressure interaction concept and a revision of peak heating correlations in [21,43], based on the reference temperature result of eq. (7) (as were the previous pressure interaction correlations given by eq. (8)). In addition, however, to the correct knowledge of the pressure level and the nature of the boundary layer, account was taken for the observation made in section 3.3 that the heat transfer distribution over the deflected ramp is well predicted by the reference temperature theory only if the virtual origin of the reattaching boundary layer is chosen in the close vicinity of reattachment so as to account for the thinning of the boundary layer that occurs through the interaction. It is noted that this is a valid assumption for strong interaction cases exhibiting severe thinning of the boundary layer and/or the occurrence of laminar-turbulent transition in the close vicinity of reattachment. Clearly, in weaker interactions, this approach assumes an excessive thinning of

the reattaching boundary layer and, therefore, yields too high peak heating predictions, as has been illustrated by the data of Fig. 20, and by the comparison of weak interaction experimental data from [49] over a  $7.5^\circ$  ramp at Mach 6 with Navier-Stokes computations and reference temperature predictions in [21].

In fact, application of eq. (7) to a reference boundary layer (typically taken as one over a flat plate at zero incidence with freestream edge conditions, or the one developing on the parent body without flap deflection), with the origin of the boundary layer at the leading edge of the parent body, gives a reference value for the heat transfer rate (or coefficient) at the location of peak heating on the respective deflected control surface that would occur in the absence of a deflection and, thus, of an interaction. An estimate for the heat transfer coefficient at the location of peak heating, corresponding to the peak pressure and with the origin of the reattaching boundary layer also taken at the leading edge of the parent body, may be similarly obtained from eq. (7). But if the thinning of the reattaching boundary layer, caused by the reattachment compression, is to be accounted for, then its virtual origin must be taken in the vicinity of reattachment rather than at the leading edge of the configuration. The boundary layer growth length at the location of peak heating, used in the Reynolds number term of eq. (7), should then be  $L_{pk}$  rather than  $x_{pk}$ .

Taking the ratio of the two results yields a theoretically based correlation for peak heating [21,43]:

$$\frac{\dot{q}_{pk}}{\dot{q}_{ref}} = B [Re_{x_{pk}}^*]^a \left[ \frac{p_{pk} u_{pk}}{p_{ref} u_{ref}} \right]^{1-n} \left[ \frac{x_{pk}}{L_{pk}} \right]^n \quad (11)$$

with

$a=0$ ,  $B=1$  and  $n=0.5$  for fully laminar interactions with a laminar reference level,  
 $a=0$ ,  $B=1$  and  $n=0.2$  for fully turbulent interactions with a turbulent reference level, and  
 $a=0.3$ ,  $B=0.072$  and  $n=0.2$  for turbulent peak heating with a laminar reference level.

The length scale  $L_{pk}$ , that is the effective growth length of the reattaching boundary layer at the location of peak heating, has been found in [21,43] to be well approximated by the method proposed in [50], for strong / transitional interaction cases where the virtual origin of the reattaching boundary layer may be safely taken at the reattachment point. With reference to Fig. 22, the relation proposed in [50] is:

$$L_{pk} = \frac{\delta_s}{\sin(\alpha - \alpha_s)} \quad (12)$$

where the thickness of the shear layer at the reattachment point may be computed by the compressible Blasius result and the deflection angle of the separated shear layer from free interaction theory. The



velocity ratio  $u_{pk}/u_{ref}$  may often be neglected inducing an error typically of the order of 10%, and the pressure ratio  $p_{pk}/p_{ref}$  may be approximated by the inviscid pressure ratio through a single inviscid shock or a two-shock system (separation shock plus reattachment shock) or as the pressure ratio through an isentropic compression. The use of a Reynolds number, defined at Eckert's reference temperature [38], to correlate turbulent ramp data to a laminar flat plate reference heating level is also noted. Details of the development of this correlation law may be found in [21,43].

It is interesting to note that, for fully laminar or fully turbulent interactions (that is when the reference and ramp boundary layers are both laminar or both turbulent), and neglecting the velocity ratio term, eq. (11) reduces to:

$$\frac{\dot{q}_{pk}}{\dot{q}_{ref}} = \left[ \frac{p_{pk}}{p_{ref}} \right]^{1-n} \left[ \frac{x_{pk}}{L_{pk}} \right]^n \quad (13)$$

which is equivalent to the numerous pressure interaction semi-empirical peak heating correlations of the form of eq. (9) summarized in [47], but includes an additional term representing the relative growth lengths of the reference and reattaching boundary layers. Recalling the findings of [47] that eq. (8) has been very successful for fully turbulent interactions with an exponent  $(1-n)$  of close to 0.8 (that is the theoretical reference temperature value of eqs. (11) and (13)), but a complete failure for fully laminar interactions where exponents  $(1-n)$  in the range 0.7-1.3 have been determined as opposed to the theoretical value in eqs. (11) and (13) of 0.5, and noting in eq. (7) that the laminar heat transfer coefficient is much more sensitive to Reynolds number (exponent 0.5) than the turbulent heat transfer coefficient (exponent 0.2), it is believed that neglecting the thinning of the reattaching boundary layer caused by the interaction process has been partially responsible for the failure of eq. (8) in correlating fully laminar interaction data. In other words, the large differences in the empirically determined exponent  $(1-n)$  that are found among different investigators are not only due to the transitional nature of some of the experiments considered, but also due to the attempt to include the case-dependent relative boundary layer growth length term in the exponent of the also case-dependent pressure ratio term.

Accounting for the relative growth lengths of the reference and reattaching boundary layers in the form of eq. (11) or eq. (13) has been found in [21,43] to provide the grounds for a universal peak heating correlation in regions of both two- and three-dimensional shock wave boundary layer interactions. The result is illustrated in Fig. 23, where more than 200 data points from 23 references have been assembled [21,43], covering a Mach number range of 5-20 and five orders of magnitude variation in Reynolds

number, which implies a range of shock wave boundary layer interactions from fully laminar cases in the strong viscous interaction regime to transitional to fully turbulent cases. The geometries considered include two- and three-dimensional flat plate/ramp configurations, flat plates with swept or unswept impinging shocks, regions of glancing shock interaction (flat plates with vertical fins) and a double ellipsoid configuration. A laminar boundary layer developing over a flat plate at freestream conditions has been chosen as the reference case in this correlation.

## 4 LOCALIZED HEAT TRANSFER VARIATIONS : STRIATION HEATING

### 4.1 General

A number of shock wave boundary layer interaction investigations have revealed the formation of streamwise striations in the region of reattachment over various two dimensional, axisymmetric or three-dimensional configurations. Noting that until recently the bulk of such experiments has involved discrete gauge surface measurements, usually concentrated along the model centerline, the first indications of streamwise striations in supersonic and hypersonic flow came from surface oil flow and sublimation visualizations [51-54]. The phenomenon has been attributed to the development of Görtler vortices, similar to those encountered in subsonic flows [55], that is triggered and supported by the flow concavity associated with the turning of the separated shear layer parallel to, say, the deflected control surface. The relevance of striation phenomena to the design of hypersonic vehicles beyond the fundamental interest in instabilities and disturbance amplification, is twofold: first, they are linked to the occurrence of laminar-turbulent transition; and, secondly, they are associated with important spanwise heat transfer variations exhibiting highly localized peaks in heat transfer.

Noting that peak heating in the reattachment region may become critical to the design of hypersonic vehicles, leading to temperatures near or above the structural integrity limits of available materials, it is imperative that the mechanisms and effects of striations on reattachment heating levels are well understood. A significant effort in this field has, therefore, been undertaken recently with the aid of thermographic techniques, aiming primarily to the quantification of striation heating [21,41,43,56-61]. It should be noted, however, that striations have so far been extensively observed over a variety of configurations only in experimental setups and never in flight (e.g. during the reentry of either the Space Shuttle Orbiter or the Bor and Buran spaceplanes).

### 4.2 Qualitative description

A typical oil flow surface visualization and a typical sublimation photograph taken over flat plate / two-



dimensional compression ramp configurations, from [41] and [43] respectively, are shown in Fig. 24. The formation of streamwise striations in the flow reattachment region is illustrated in both photographs. The qualitative data of Fig. 24, within their limited spatial resolution, indicate that the mean spacing of the rather regular striations is constant throughout the model span. This was, in fact, proposed by [51,52], where a large number of data taken over backward facing step configurations were correlated to yield a nearly constant value (between 2 and 3) for the mean wavelength of the striations normalized by the undisturbed boundary layer thickness, independent of Mach and Reynolds numbers and the interaction strength.

Similar observations have been made by means of thermosensitive paints in [59] and infrared thermography in [60], and examples are shown in Fig. 25, also illustrating the aforementioned regular, short wavelength striations, as well as the associated significant spanwise heat transfer variations. The observations as to the regularity of the striations and their dependence upon the undisturbed boundary layer thickness are also supported by linear stability analyses [62,63] as well as by preliminary large eddy simulation results [64], examining the amplification of small, random initial perturbations.

However, contradictory, to some extent, observations have been made in the experimental investigations of [21,43]. A series of high resolution infrared images acquired in [43] over flat plate / two-dimensional ramp geometries at Mach 6 is given in Fig. 26. First, attention is drawn to Figs. 26a and b, corresponding to nominally identical experiments at a low Reynolds number and a weak overall pressure rise (ramp deflection angle of only  $10^\circ$ ); the only difference between the two tests is the detailed thickness distribution of the nominally sharp model leading edge ( $26\mu\text{m} \pm 10\mu\text{m}$  in the case of Fig. 26a and  $40\mu\text{m} \pm 20\mu\text{m}$  in the case of Fig. 26b). Clearly, not only the striation patterns are irregular in these figures (in terms of both spacing and intensity), but they are also found to be strongly dependent on the detailed shape of the model leading edge. For these low Reynolds number, weak interaction cases a qualitative correlation between the footprint of the striations and the leading edge thickness distribution has been found [43,57] (section 4.3). Additionally, comparison between Figs. 26b and c illustrates that striation patterns are not influenced by finite span effects.

As the interaction strength was increased in [43] (by increasing the ramp deflection angle) and / or the Reynolds number was increased (by shifting the hinge line backwards or increasing the unit Reynolds number), and for a given model leading edge, increasingly more regular striation patterns appeared to form in

the reattachment region which, however, persisted for increasingly shorter distances along the ramp surface and eventually disappeared within the resolution of the infrared technique (Figs. 26b-f).

To further investigate the observed dependence of the striation phenomena on the detailed leading edge thickness distribution, at least in the cases of weak interactions at low Reynolds number, experiments were also performed in [21,43] with a thicker and more uniform leading edge ( $98\mu\text{m} \pm 5\mu\text{m}$ ) with and without a regular distribution of perturbations attached to it (in the form of 0.2 mm thick, 25 mm long sandpaper strips distributed along the leading edge at wavelengths of 10 mm and 20 mm). The resulting infrared and sublimation results are illustrated in Fig. 27. The addition of discrete perturbations was found to enhance the intensity of the striations, while showing a close correlation between the initial disturbance distribution and the form of the striations. Similar observations were, in fact, made in [51], where high quality pointed nose axisymmetric configurations were found to be free of striations in the reattachment region, whereas discrete, regularly spaced leading edge perturbations were introduced to enhance spanwise variations and ease their measurement (section 4.3).

A possible interpretation of the contradictory observations as to the importance of leading edge irregularities and, moreover, as to their persisting signature in the formation of striations may be now proposed. First, hypersonic boundary layers are known to be extremely stable and, hence, the occurrence of instabilities requires either the presence of fairly strong amplification mechanisms, such as high Reynolds number and flow concavity/adverse pressure gradient, in accordance with linear stability theory, or the presence of significant initial perturbations (significant in the sense that they may not be considered small within the framework of linear stability analyses). The preceding observations are thought to be indicative of these competing instability agents, whereby in the strong interaction, high Reynolds number cases the amplification mechanisms are dominant, and in the weak interaction, low Reynolds number cases strong initial perturbations prevail.

Now, if the formation of streamwise striations (very likely the footprint of Görtler-type vortices) is viewed as an instability, it is reasonable to anticipate a close link between their presence and the occurrence of laminar-turbulent transition. In fact, this is in accordance with the discussion in [65], whereas embedded streamwise vortices have been observed in the transition process of both low and high speed flows, and not only over concave surfaces but also over flat and even convex surfaces [51,63,65]. This could, then, explain the effective promotion of laminar-turbulent transition by shock wave boundary layer interactions



and, in particular, by the reattachment process, in otherwise highly stable flowfields (i.e. where zero pressure gradient natural transition or even forced transition by means of tripping is most difficult; cite, for example, the severe tripping that was required in [21] to trip the oncoming Mach 14 laminar boundary layer relative to its highly effective transition over a  $15^\circ$  ramp, Fig. 14).

Furthermore, there remains a debate as to whether Görtler-type vortices may be sustained in fully turbulent flow. It may be argued that steady embedded vortical structures may not be sustained in a highly unsteady turbulent flowfield [66], but instead they break down as fully turbulent flow is attained [65,66]. Nevertheless, numerous investigators have reported the observation of striations in fully turbulent reattaching boundary layers, but to the author's view these reports (at least in hypersonic cases) have not been accompanied by a convincing demonstration of the assumed fully turbulent nature of the flow.

To sum up, there is evidence that the formation of steady streamwise striations is directly linked to the occurrence of laminar-turbulent transition, and these are damped out (or break down) as fully turbulent flow is attained on the deflected ramp (see also section 4.3). Understanding that, for a given experimental setup (including all initial disturbance sources), increasing Reynolds number and interaction strength is bound to accelerate the transition process (once it is triggered), the above argument is fully consistent with the observation that the streamwise extent of striations decreases with increasing Reynolds number and interaction strength. In addition, it has been argued that Görtler vortices should be sustained only within the region of concave flow curvature. The results of [21,43] summarized in Figs. 26 and 27 and the subsequent discussion in section 4.3 show that striations may, in some cases, extend far downstream from the concave flow reattachment region and disappear only when fully turbulent flow is attained.

Finally, it should be noted that similar striation effects have been observed over swept wings at low speed [67], where the formation of striations is associated with the development of co-rotating cross-flow vortices rather than contra-rotating Görtler vortices. The qualitative (surface visualization findings of [67] demonstrate that crossflow vortices accelerate laminar-turbulent transition, that they break down when turbulent flow is attained, and that their effectiveness in promoting transition depends on the magnitude and distribution of initial disturbances (roughness) in the leading edge region.

### 4.3 Quantitative description

Spanwise pitot pressure distributions have been measured in [51,52] within the boundary/shear layer along

a flat plate/backward facing step geometry that exhibits flow separation and the formation of streamwise striations in the region downstream of the step. The results are illustrated in Fig. 28, as the streamwise evolution of the spanwise pitot pressure distribution measured at selected distances from the model surface (always within the boundary / shear layer). The presence of small, irregular perturbations upstream of the interaction is noted, which are seen to amplify through the reattachment region. Downstream of the reattachment region, the disturbances are damped and practically disappear by the trailing edge of the configuration. The occurrence of laminar-turbulent transition over effectively the same region where spanwise pitot pressure variations are detected is noted.

Spanwise heat transfer measurements in the reattachment region of the aforementioned backward facing step configuration were also conducted in [51,52]. Following preliminary experiments, which established the relevance of the model leading edge in the formation of streamwise striations in the reattachment region, experiments were performed with a distribution of elements of adhesive tape along the model leading edge aimed to enhance the footprint of the striations. The results are illustrated in Fig. 29, where spanwise heat transfer variations of the order of  $\pm 50\%$  are found. Although these significant heating variations exhibit a regular spatial distribution, the close correspondence between heat transfer peaks and the edges of the regularly spaced adhesive tape elements is noted.

More recently, the subject of striation heating has been extensively investigated over flat plate / two-dimensional configurations at Mach 6 and, to a lesser extent, Mach 14 in [21,43,57]. A typical streamwise evolution of the spanwise heat transfer distribution over a  $10^\circ$  deflected ramp (corresponding to the thermogram of Fig. 26b) is shown in Fig. 30. The hinge line in this case is located at  $x=4$  cm downstream of the model leading edge. Clearly, initial disturbances are amplified through the reattachment region, reaching a maximum spanwise heat transfer variation, and subsequently decay towards a uniform heat transfer distribution over the entire model span. It is noted that the particular distribution, which corresponds to a weak, low Reynolds number interaction, shows no characteristic spanwise wavelength within the spatial resolution of the measurement, and the heat transfer variations are rather irregular.

The importance of the initial leading edge disturbances and the persistence of their signature through the disturbance amplification process in the reattachment flow region in low strength, low Reynolds number interactions is illustrated in Fig. 31. Selected spanwise heat transfer variations are shown over a  $10^\circ$  ramp for three model leading edges. In the for-



mer two cases, a qualitative correlation is found between leading edge thickness variations and spanwise heat transfer variations, whereas in the third case a close correspondence is observed between spanwise peaks in heat transfer and the edges of the additional leading edge disturbances (similar to the data of Fig. 29 [52]). Again, very high peaks in heat transfer are attained locally of up to 80% higher than the spanwise mean heating level.

For stronger interactions and/or higher Reynolds numbers, it was observed in section 4.2 that striations tend to be more regular (at least in spacing if not in amplitude), whereas their streamwise extent is reduced (for a given geometry and initial disturbance distribution). The streamwise evolution of the spanwise heat transfer variations over the configuration of Fig. 26e is depicted in Fig. 32 [43] showing more regular variations than those of Fig. 30 and the absence of any qualitative correlation with the 40  $\mu\text{m}$  leading edge thickness variations shown in Fig. 31. The hinge line of the 15° ramp is, in this case, located at 9 cm downstream of the model leading edge. Similarly, more regular striation patterns are observed in the spanwise heat transfer distributions of Fig. 33 [41,59], particularly for the blunt leading edge, and in the distributions of Fig. 34 [57] corresponding to a weak interaction, low Reynolds number case with also weak initial leading edge disturbances.

The streamwise extent and amplitude of striations and the associated spanwise heat transfer variations are better illustrated by plotting the bands between the minimum and maximum streamwise heat transfer distributions measured over the model span (excluding, of course, regions close to the model side edges). For a given model leading edge (i.e. for a given set of initial disturbances), typical results are shown in Fig. 35 in the form of streamwise heat transfer bands as a function of ramp deflection angle, hinge line location and unit Reynolds number. It becomes evident from Fig. 35 that significant spanwise heat transfer variations commence in the close vicinity of reattachment (corresponding closely to the region of maximum streamwise pressure and heat transfer gradients). It is also clear that the streamwise extent of striations is decreasing with increasing ramp angle and/or Reynolds number to the hinge line.

From the designer's point of view, however, the most relevant aspect of striation phenomena is their influence on peak heating over the deflected control surface. In this respect, the data of Fig. 35 show that the mean streamwise heat transfer distribution tends towards the predicted reference temperature turbulent heating level on the deflected ramp and that, as this level is approached, spanwise heat transfer variations reduce to effectively zero. It is also noted that the turbulent ramp heating level is hardly ex-

ceeded anywhere on the deflected ramp (within the uncertainty of the prediction). It may, therefore, be conjectured that the local turbulent ramp heating level approximates well the upper limit of local spanwise heat transfer peaks, and that the preceding discussion on the prediction of peak heating (sections 3.3 and 3.4) remains valid also in the presence of strong streamwise striations. Consequently, the proposed peak heating correlation may safely provide estimates for the maximum (turbulent) heat transfer that is to be anticipated on a deflected control surface, on the condition that the local boundary layer edge conditions are known as well as the local minimum boundary layer thickness in the peak heating "neck" region.

These findings that striation heating does not exceed significantly the local turbulent heat transfer are also supported by the spanwise heat transfer data of [21] at Mach 14, of [41,59] at Mach 10, and of [60] at Mach 7 and 8. Also, the fact that spanwise heat transfer variations reduce to effectively zero as the mean heat transfer level attains the local turbulent heating level supports the proposition that steady streamwise striations may no longer be sustained when fully turbulent flow is attained over the model span.

Finally, the influence of the model leading edge (initial disturbances) on the band between minimum and maximum streamwise heat transfer distributions is illustrated in Fig. 36 for a weak 10°, low Reynolds number case, where the model leading edge thickness and irregularities were found to be the most important. Despite the strong dependence of the detailed striation patterns, their amplitude and streamwise extent upon the detailed leading edge thickness distribution, and the persistence, in some cases, of significant spanwise heat transfer variations to the trailing edge of the ramp (indicative of a rather inefficient laminar-turbulent transition in cases with both weak initial disturbances and weak amplification mechanisms), the local ramp turbulent heating level is again hardly exceeded.

## 5 COMPUTATIONAL FLUID DYNAMICS: RESULTS AND VALIDATION

### 5.1 General

The rapid progress achieved in recent years in the field of Computational Fluid Dynamics (CFD), combined with the strict requirements imposed in the design of new hypersonic vehicles, the lack of full simulation capabilities in hypersonic ground test facilities and the difficulties involved in flight testing, has promoted the adoption of a new design philosophy that heavily relies upon CFD for the direct analysis of the flowfield at both flight and ground test conditions, as well as for the development of techniques for the extrapolation of ground test results to flight. This type of evolution, however, towards the effective



integration of ground testing, flight and computational results [68] (Fig. 37) not only imposes stringent requirements on the characterization and quality of measurements, but also calls for an in-depth qualification and validation of computational tools against realistic and well documented test cases, before they may be safely incorporated into the design cycle.

The specific problem of deflected control surfaces and, more generally, of shock wave boundary layer interaction (even over simplified geometric configurations) is particularly complicated as it involves strong viscous effects and often extensive separated flow regions. On the computational side, the situation may become critical with full Navier-Stokes solvers, where computer time and memory storage requirements can easily approach or exceed the capacity of computers currently available, particularly when three-dimensional configurations with transitional or turbulent flowfields and thermochemical effects are considered. An important problem with computations, which has only recently received the attention it deserves, is the need to demonstrate convergence and grid independence of the solutions [69], noting also that, with separated flows, criteria that have been well established for simpler attached flow situations may no longer be relied upon.

On the experimental side, it has become evident that experiments oriented towards CFD code validation are burdened with increased requirements insofar as the quality and the type of the measurements, and the definition of the flowfield, the geometry and the boundary conditions are concerned [70,71]. The problem here is that a large portion of the experimental shock wave boundary layer interaction studies dates back to an era where technological means were limited and a semi-empirical engineering philosophy prevailed. Consequently, very few experiments are sufficiently well documented for code validation purposes, the data are very limited relative to the detail provided by CFD and, at hypersonic Mach numbers in particular, flowfield measurements are scarce.

Nevertheless, the assembly of code validation oriented databases has received significant attention in recent years, and a respectable amount of data has been systematically collected [72-74] with the aid of code validation workshops. Shock wave boundary layer interaction test cases, exhibiting significant separated regions, in two and three dimensions and with laminar, transitional or turbulent boundary/shear layers form a major part of these novel databases. The bulk of the data, however, includes surface measurements only and is for the moment restricted to perfect gas cases, although some effort towards the examination of real gas effects has recently commenced. A selection of the aforementioned shock boundary layer interaction test cases will be discussed in the subsequent sections, aim-

ing primarily to illustrate the difficulties related to CFD validation and some of the remaining uncertainties and limitations, but also to briefly exemplify the potential of CFD in contributing towards the detailed understanding of complex flow phenomena and, eventually, towards bridging the gap between the partial ground simulation and flight.

Before proceeding to the detailed examination of various test cases, a general remark may be easily made on the geometric characteristics of high speed interacting flowfields with the aid of CFD results on simple flat plate / two-dimensional ramp interactions. Iso-Mach contours are shown in Fig. 38 for the Mach 14, 15° ramp case (corresponding to the rear ramp surface heat transfer data of Fig. 15) as obtained from an Euler computation and laminar and turbulent\* Navier-Stokes computations performed by W. Haase [21,75]. In the inviscid case, a single oblique shock forms at the hinge line of the deflected ramp at a very shallow angle due to the high Mach number of the oncoming flow.

In the case of the laminar computation, a significant streamwise scale of the interaction is observed including an extensive separation, despite the relatively thin oncoming boundary layer and the shallow angle of the separated shear layer and associated separation shock. In the turbulent computation, no separation is seen to occur in the vicinity of the hinge line for this modest ramp deflection angle, but still the interaction is found to have a significant streamwise extent due to the much increased thickness of the oncoming turbulent boundary layer. The result is that, in both laminar and turbulent cases, the normal extent of this high speed interaction is very limited. In the streamwise direction, however, it extends over a significant distance on the deflected ramp, independent of whether the approaching boundary layer is laminar exhibiting a large separated region, or turbulent remaining attached throughout the interaction. Noting that the typical length of control surfaces on lifting hypersonic vehicles is of the order of 10%-20% of the forebody length, it is evident that such shallow zones of shock wave boundary layer interaction at high Reynolds numbers (and, hence, in the weak viscous interaction regime) will strongly affect the flowfield over the deflected control surface and its effectiveness and heating, even when the oncoming boundary layer is turbulent (having been tripped near the nose of the forebody) and does not separate.

## 5.2 Planar two - dimensional fully laminar interactions

This section will concentrate on shock wave laminar boundary layer interactions over flat plate / two-dimensional ramp configurations at hypersonic Mach

\* The turbulent computations have used the Cebeci-Smith algebraic turbulence model, which is satisfactory for attached flow computations.



numbers. Amongst the early experiments with this configuration were performed at Mach 6 in [76] with an adiabatic or cooled wall. Some of the test cases of [76] were computed in the early 1970's by the Navier-Stokes solver of [77] with reasonable success. These computations revealed, however, one of the major problems still remaining with the computation of high speed separated flows, namely the underprediction of the streamwise extent of the interaction and of the separated region.

More recently, the adiabatic wall, Mach 6 data of [49] over a  $7.5^\circ$  ramp configuration have been computed by two Navier-Stokes solvers in [78]. The Reynolds number based on the distance from the leading edge to the hinge line was 400,000. The comparison between the measured and computed (over different meshes) surface pressure distributions is shown in Fig. 39 to reveal the strong dependence of the computed extent of the interaction upon the grid resolution. Clearly, significant mesh refinement has been necessary to arrive to grid-independent solutions. Indicatively, 50 mesh points in the streamwise direction within the separated region, and 20-30 mesh points in the wall normal direction within the boundary layer at the separation point have been necessary to adequately resolve the geometrical characteristics of the interaction. In addition to mesh refinement, particular attention had to be devoted to the monitoring of convergence, where it was noted that the location of the separation point required much more iterations and reduction of the residuals to converge than standard L2-norm criteria, developed for attached flows, would suggest. The movement of the separation point with iteration number and grid refinement is illustrated in Fig. 40. It should also be noted that preliminary attempts to compute a similar test case but with a cold wall [49] has met with substantial difficulties in correctly predicting the modest extent of the interaction, which are believed to be related to the inadequate resolution of the very thin oncoming boundary layer under the combined high Reynolds number and cold wall conditions of this test case [21].

Another early set of fully laminar, two-dimensional test cases at a Mach number of 14 and a Reynolds number (based on the distance from the leading edge to the hinge line) of about 100,000 has been that of [32] depicted in Fig. 7, which is also included in the database of [73]. The well separated  $24^\circ$  ramp case has been computed by a number of Navier-Stokes solvers [79-83], whereas the unseparated case with a  $15^\circ$  deflected ramp has been computed by the parabolized Navier-Stokes code of [84]. The Navier-Stokes computations, with their limited success, have again demonstrated the importance of sufficiently resolving the near-wall region to correctly predicting the extent of the interaction, but also the wall skin friction and heat transfer distributions. In fact, it will be illustrated below that some computations involve

such coarse grids that, not only do they not capture the extent of the interaction correctly, but also fail to resolve adequately the velocity and, more often, the temperature profile and, hence, yield poor skin friction and heat transfer predictions even in attached flow regions.

Of particular interest among the computations for the well separated case of [32] is the work of [79]. Following a grid dependence study with two-dimensional computations, a grid-independent solution was obtained which, however, strongly overpredicted the streamwise extent of the interaction (Fig. 41). Then, consultation with the experimentalists led to the conjecture that the experiment in question could be influenced by finite span effects due to the combination of a large separated region with a relatively small aspect ratio (ratio of model span to distance between the leading edge and the hinge line). Consequently, three-dimensional computations were performed which are seen in Fig. 41 to capture well the measured extent of the interaction and the overall pressure distribution. The lesson to be learned here is that two-dimensionality must be demonstrated in experiments with flat plate / two-dimensional ramp configurations, in the sense that the measured center-line distributions are not influenced by modification of the side boundary conditions (change in model span, addition of side fences, etc.). Also, it should be noted that the question of side boundary conditions arises in three-dimensional computations (similar to the computation of the flow over three-dimensional geometries, such as the swept ramp), where the most significant finite span effect is believed to be that of outflow through the sides of the model. In such cases, the recommended approach is to extend the computational domain beyond the side of the geometry a sufficient distance so as to allow for the application of freestream flow conditions at the extended side boundary.

In the aftermath of the first Antibes workshop [72a], where it was realized that the compression ramp test cases exhibited laminar-turbulent transition in the reattachment region (section 5.3), in accordance with the preceding discussion in section 3 and 4, new test cases were defined for the second workshop [72b] to ensure fully laminar flow over the interaction region. Very low Reynolds number experiments at Mach 10 [85] were chosen for this purpose with ramp deflection angles of  $15^\circ$  and  $20^\circ$ . During the workshop it was realized that the flow at such conditions falls in the strong viscous interaction regime and is dominated by the growth of the thick boundary layer rather than the ramp-induced interaction. In fact, it was found that the  $15^\circ$  ramp case was virtually unseparated, whereas the  $20^\circ$  ramp case very close to the effective incipient separation limit after the criterion of Fig. 6 and the computational results that were presented in [72b]. Consequently, the emphasis



in [85] was placed on a 25° ramp case, exhibiting significant separation, and the first comparisons with computations are shown in [85]. It is noted that, despite the low Reynolds number (30,000 based on the distance between the leading edge and the hinge line \*), this case is of particular interest because of the availability of quantitative electron beam fluorescence data in the flowfield (Fig. 42).

A further laminar test case at Mach 11.7 from the database of [73] was considered in the workshop of [72b]. The experimental data [86] are of interest as they include skin friction measurements in addition to wall pressure and heat transfer distributions. A review of the comparison between the various computations in [72b] and the experimental data of [86] is provided in [21]. In general, the computations have performed reasonably well for this moderate Reynolds number (240,000 to the hinge line) well separated case, provided that attention was given to the mesh resolution.

The laminar interaction Mach 14 data of [21], corresponding to the forward 15° ramp heat transfer distribution of Fig. 15 and a Reynolds number to the ramp hinge line of 450,000 have been computed in [75,78]. A comparison of the various computations with different mesh resolutions and the experimental heat transfer data is shown in Fig. 43, together with a comparison between the computed isodensity contours and the experimental schlieren photograph in Fig. 44. A grid independent solution has been attained which is in good agreement with the experimental data until the onset of transition downstream of the boundary layer neck region on the ramp (at approximately 0.12 m from the leading edge) that characterized the experiment. Indicatively, about 40 streamwise mesh points within the separated region and about 50 points in the wall-normal direction within the boundary layer at separation were required to adequately resolve the extent of the interaction in this case. The minimum wall-normal mesh size in the finest (352×160) Dornier mesh was  $5 \times 10^{-6}$  m. It is also interesting to note that the coarse mesh VKI computation on the 84×30 mesh with only 13 wall-normal mesh points in the boundary layer at separation also fails to resolve the thermal boundary layer and, consequently, yields an underprediction of the heat transfer in the attached flow regions both upstream and downstream of the interaction.

Overall, concerning laminar perfect gas shock wave boundary layer interactions over flat plate / two-dimensional ramp configurations, the general consensus is that they may be accurately predicted by Navier-Stokes solvers, provided that sufficient atten-

tion is given to obtaining grid independent solutions in cases exhibiting significant separation. This goal has been demonstrated to be attained with reasonable effort at low or moderate Reynolds numbers, but certain difficulties remain with well separated cases as the Reynolds number increases and, with it, the grid refinement requirements (see, for example, high Reynolds number laminar computations in section 5.3) which often lead to numerical stability problems. Evidently, the development of convergence criteria and grid resolution criteria applicable to super- or hypersonic separated flows is highly desirable. As a final remark, the computation of blunt flat plate / ramp geometries, such as the ones tested in [41], imposes the additional need for the adequate resolution of the bow shock, the small subsonic region around the leading edge and the resulting entropy layer. Consequently, the efficient treatment of such configurations may require the use of multiblock solvers.

### 5.3 Planar two - dimensional transitional interactions

The discussion in the previous sections illustrated that the reattachment region on the deflected ramp, that is associated with the presence of strong disturbance amplification mechanisms (namely, adverse pressure gradient and flow concavity), may provide the grounds for the promotion of laminar-turbulent transition. In fact, both the Mach 10 and Mach 14 two-dimensional ramp test cases considered in the first Antibes workshop [72a] were found to be transitional with transition taking place very efficiently in the close vicinity of reattachment\*.

Comparisons between the measured and computed heat transfer distributions for these two test cases are shown in Figs. 45 and 46, respectively, after [87]. Dramatic differences are found among the various computational results, all of which compare poorly with the experimental data. In fact, there are two issues of primary importance to be considered. First, the question of grid dependence which at the time of [72a] was not seriously addressed in any of the computations, and is primarily responsible for the large differences between the predictions of the location of the separation point. Secondly, the experiments exhibited laminar-turbulent transition in the close vicinity of reattachment, which may have an influence on the extent of the interaction and certainly has a significant effect on the heat transfer distribution downstream of reattachment/transition. The latter explains the significant discrepancies be-

\* It is noted that the Reynolds number to the hinge line corresponding to the experiments of [85] is 30,000 as opposed to a value of 18,000 specified in [72b].

\* The Mach 10 test case of [72a] corresponds to the sharp leading edge data of [41] illustrated in Figs. 13 and 20, with a Reynolds number to the hinge line of  $2.1 \times 10^6$ . The Mach 14 test case corresponds to the rear 15° ramp data of [21] illustrated in Fig. 15, with a Reynolds number to the hinge line of  $1.3 \times 10^6$ .



tween computational and experimental results on the ramp heat transfer distribution. Unfortunately, similar scatter of the computational results on the Mach 10 sharp leading edge test case of [41] was found in the second Antibes workshop [72b].

However, the computations of W. Haase presented in [72b] for the latter Mach 10 transitional test case [88] and in [75,78] for the Mach 14 transitional test case provide some insight to the computational treatment of transition. Noting that transition in these cases takes place very rapidly in the close vicinity of reattachment, it has been demonstrated that such transitional interactions may be computationally well approximated by running first a fully laminar computation and, subsequently, "switching on" a simple turbulence model (e.g. the Cebeci-Smith model) in the attached flow region downstream of reattachment. Following the discussion in [78], such an approach is expected to give the most adverse effects of the interaction. In particular, a grid-independent, fully laminar computation is bound to yield the largest possible extent of the interaction, and the associated effect on control effectiveness. The laminar computation will also yield the minimum boundary layer thickness in the boundary layer neck region at the downstream end of the reattachment compression. Finally, this minimum boundary layer thickness, combined with a turbulent computation (starting from the laminar solution at reattachment) will, in turn, yield an upper limit for the heat transfer on the ramp. These conjectures are illustrated by the comparison of experimental and computed heat transfer distributions in Figs. 47 and 48.

Before concluding this section, attention is drawn to the fully laminar computations of [78] corresponding to the Mach 14 transitional test case of [21] with a Reynolds number to the hinge line of  $1.3 \times 10^6$ . Contrary to the lower Reynolds number ( $Re_L = 450,000$ ) forward ramp case, also computed in [78] (Figs. 43 and 44), where a grid independent solution was demonstrated, this was not possible at the higher Reynolds number within the level of grid refinement performed in [78]. The grid dependence results of Fig. 49, thus, illustrate the aforementioned difficulties associated with the establishment of grid independent solutions at elevated Reynolds numbers and cold wall conditions.

#### 5.4 Planar two - dimensional fully turbulent interactions

The preceding discussion provided indications that the implementation of simple turbulence models in Navier-Stokes computations may yield reasonable estimates of the turbulent heat transfer distribution over attached flow regions, including high Mach number cases of transitional separated shock boundary layer interaction, provided that transition is fixed to the close vicinity of reattachment and turbulent flow

is limited to the attached flow region over the deflected ramp. In the case of fully turbulent interactions, however, exhibiting significant separation, the performance of computations may be impaired not only by the convergence and grid refinement issues addressed above, but also by the insufficiencies of available turbulence models [89] in separated flow situations. Turbulent shock wave boundary layer interactions and the development of appropriate turbulence models are treated in three other lectures in this course [90-92]. The discussion here will, therefore, be limited to a brief reference to available flat plate / two-dimensional ramp data (with a turbulent interacting boundary layer) and related computations.

Experimentally, the assessment of [74] has shown that very few turbulent, super- or hypersonic flat plate / two-dimensional ramp experiments are suited for code and turbulence model validation purposes. At hypersonic Mach numbers [34,93 and 33,46,73] they involve mean wall pressure, heat transfer and some skin friction measurements, but no flowfield mean or fluctuating quantities that would be desirable for the proper validation of turbulence models. A more recent Mach 5,  $35^\circ$  ramp turbulent test case has been defined in [72a], where the experimental surface pressure and heat transfer data were provided by [94]. Finally, two sets of Mach 3 experiments from the American and Russian literature are provided in [74], which also include pitot pressure and hot wire surveys of the flowfield.

Computationally, the limited performance of simple algebraic turbulence models is illustrated in Fig. 50 by the comparison of two computations from [72a] with the heat transfer data of [94], taken from the synthesis of [87]. Noting that, in the computations, turbulent flow is assumed from the model leading edge, whereas the experiment shows transition to occur between 0.10 and 0.15 m downstream of the leading edge (still upstream of the interaction), the discrepancies found between computational and experimental results upstream of the interaction are largely due to the poor choice of the effective virtual origin of the flat plate turbulent boundary layer. The features of the separated region and, subsequently, the heat transfer distribution on the deflected ramp are, however, very poorly predicted by the algebraic models, indicating the need for more sophisticated turbulence modelling in separated flow regions.

Still, recent investigations with two-equation turbulence models [95,96], including compressibility corrections, have also revealed significant difficulties in the prediction of interacting flowfields exhibiting separation, although reasonable predictions for attached turbulent flows were obtained.

Finally, application in [97] of the Baldwin-Lomax,



k- $\omega$  and Reynolds stress models to the Mach 3, 24° ramp test case of [74] has provided evidence that the performance of higher order Reynolds stress models in the prediction of turbulent separated flows is notably superior to that of two-equation models. This is illustrated by the comparison between predicted and measured pressure distributions in Fig. 51, whereby the extent of the separated region is generally underpredicted, except in the case of the Reynolds stress model where it is somewhat overpredicted. Noting, however, the comments of [74] that finite span effects have been significant in this high deflection angle experiment, the latter discrepancy is, at least partially, due to three-dimensional effects that are neglected in the computations.

### 5.5 Three-dimensional swept ramp interactions

Flat plate / swept compression ramp configurations have thus far received little attention, and the two sets of experimental results already used for code validation are the Mach 10 transitional data of [94] (that were used as a test case in [72a,b]) and the Mach 3 turbulent data of [98] that are included in the database of [74]. A limited amount of swept ramp data at Mach 6 and 14, exhibiting laminar-turbulent transition in the vicinity of reattachment are also provided in [21]. The swept ramp case is computationally complicated by its three-dimensional character (and the associated increase in the computational effort), and by the need to properly define appropriate side boundary conditions. The lateral extension of the domain beyond the model side edges and the imposition of freestream conditions at its edge is recommended on the basis of the arguments outlined in section 5.2.

An illustration of the limited performance of three-dimensional separated flow computations is given in Fig. 52, by the comparison of measured [94] and computed [99] streamwise heat transfer distributions at various spanwise stations. There are three main points to note. First, the 150×50×40 mesh employed in [99] is inadequate to resolve the attached laminar boundary layer upstream of the interaction and, hence, the computed heat transfer distribution in this region is lower than the experimental data and the laminar reference temperature predictions. A grid refinement performed in [99] for a flat plate computation has demonstrated this point. Secondly, the ramp heat transfer distribution is significantly underpredicted by the laminar computations, due to the transitional nature of the experiment and the attainment of turbulent flow downstream of reattachment. In addition, the computations underpredict the laminar ramp reference temperature predictions, indicating the aforementioned boundary layer resolution problem. As for the overprediction of the extent of the separated region, this is mainly due to the use of a laminar computation relative to a transitional experiment, although the poor mesh resolution and

poor prediction of the oncoming flowfield may also be responsible.

The turbulent Mach 3 cases have been computed in [98,100] and the problem is addressed in detail in the lecture of [92] in the present course. Although the experience with two-dimensional test cases has demonstrated that transitional interactions (with transition fixed to the reattachment region) may be satisfactorily predicted with simple turbulence models that perform well in attached turbulent flow regions, the current computational limitations in terms of computer power and mesh resolution, combined with the turbulence modelling limitations for interacting, separated turbulent flowfields, suggest that fully laminar three-dimensional interaction data may be more appropriate as a first step in the validation of three-dimensional Navier-Stokes solvers. An effort to obtain such well defined test cases is currently made in relation to the forthcoming qualification workshops planned for the end of 1994 and 1995 [101]. In this context, the flat plate / swept compression ramp configuration is no longer considered due to the inadequate definition of side boundary conditions by the experimentalists. Instead the delta wing / deflected flap configuration is found to be a more appropriate three-dimensional geometry.

### 5.6 Interactions over axisymmetric body/flare configurations

Following the extensive investigations of shock wave boundary layer interactions with a flat plate as the parent body, recent trends have favoured axisymmetric configurations to eliminate the uncertainty of side boundary conditions in quasi-two-dimensional experiments. At the same time, there has been an evolution of European hypersonic research priorities from very fundamental studies to applications-oriented ones involving generic vehicle configurations. Although there has been a number of axisymmetric body / flare investigations including skewed flares (cite, for example, [74]), the discussion here will be restricted to the hyperboloid / flare configuration that has been chosen as a test case for the forthcoming qualification workshops [101].

The definition of the hyperboloid / flare geometry, together with some first computations aimed to aid the "design" of the experiments, is provided in [102]. The contour of the hyperboloid represents the windward centerline of the Hermes spaceplane at 30° angle of attack (similar to the axisymmetric representation of the windward side of a double ellipse, illustrated in Fig. 53), thus allowing to examine the effects of realistic parameters, such as surface curvature of the parent body and nose bluntness. The nose bluntness, however, of the hyperboloid / flare configuration, effectively corresponding to the mid-plane radius of curvature of the stagnation region of the spaceplane at 30° angle of attack, is smaller than



the effective nose bluntness of the Hermes configuration because of the actual nose shape of the spaceplane. The simulated flap (flare) is conical and at an angle of  $43.6^\circ$  to the axis of the hyperboloid, which corresponds to a deflection of just over  $20^\circ$  relative to the inclination of the contour at the hinge line.

Experiments with this configuration are currently underway in both "cold" and high enthalpy hypersonic wind tunnels around Europe. On the basis of the experience acquired thus far with shock boundary layer interaction testing, experiments with sufficiently low Reynolds number are included to warrant fully laminar interactions.

Preliminary computational results at perfect gas conditions ( $M_\infty = 8.7$ ,  $Re_L \approx 42,000$ ) are shown in Fig. 54 in the form of pressure coefficient and Mach number contours [102], to illustrate the complexity of the flowfield in the shock boundary layer and shock / shock interaction region. Of particular interest is the strong forebody shock which, in this case, interacts first with the separation shock and shortly downstream with the reattachment shock. The second shock/shock interaction is stronger and yields a significant expansion towards the deflected flap which is reflected upon impingement on the surface. Also of interest is the continuous expansion along the forebody and its impact on the characteristics of the shock wave boundary layer interaction in the vicinity of the hinge line. The pressure and heat transfer distributions corresponding to the case of Fig. 54 are shown in Fig. 55, as computed independently by four different codes [103-105]. The aforementioned forebody expansion, the pressure plateau over the separated flow region, and the pressure and heat transfer rise on the flare are noted, as well as the reasonable agreement between the four computations (all performed on a rather fine mesh of  $228 \times 120$  points).

At different flow conditions, of course, situations may arise in which the separation and reattachment shocks coalesce inside the forebody shock layer and, subsequently, the resulting flare shock interacts with the forebody shock a significant distance downstream. An example is shown in Fig. 56 [106], where pressure contours are presented for the region near the hinge line of the hyperboloid / flare, at flow conditions corresponding to 77 km altitude of the reentry trajectory of the Hermes spaceplane. At such high enthalpy conditions, the thermochemical behaviour of air becomes important as illustrated by the different shock locations obtained in Fig. 56 with different thermochemical models (frozen, chemical nonequilibrium and thermochemical equilibrium air).

A better illustration of thermochemical effects at high enthalpy conditions is given in Fig. 57 by the corresponding surface pressure and heat transfer distributions computed in [106]. First, differences in temper-

ature in the forebody shock layer, due to the thermochemical behaviour of the air (frozen, chemical nonequilibrium or thermochemical equilibrium), cause important differences in the Mach number of the flow in the shock layer approaching the flare. Important differences are, therefore, found in the surface pressure recovery on the flare, whereby the frozen (perfect) gas computation yields a lower pressure rise than the equilibrium gas computation. More specifically, this is due to a lower temperature of the equilibrium gas (caused by dissociation in the forebody shock layer) and, consequently, a higher Mach number in the forebody shock layer. For similar reasons, the extent of the separated region is reduced in the case of thermochemical equilibrium. Secondly, important differences are detected in the heat transfer distribution, but here the wall thermochemical boundary condition also plays a role, in addition to the thermochemical behaviour of the outer inviscid flow.

To conclude this section, it is recalled that new high enthalpy facilities have been constructed to support the assessment of the effects of the thermochemical behaviour of air at high enthalpy reentry conditions, as these were illustrated above by the computational results of [106]. This type of ground simulation, however, is faced with a variety of difficulties. First, the complete ground simulation of flight conditions is not possible, and a compromise between Mach and Reynolds number simulation, on one hand, and total enthalpy/velocity and thermochemical characteristic lengthscale simulation, on the other, is necessary. A further complication arises from the possible thermochemical non-equilibrium in the freestream of ground test facilities (caused by the rapid nozzle expansion), which must also be accounted for in the interpretation of results. All in all, it is clear that, at high enthalpy conditions, the interpretation of wind tunnel data and their extrapolation-to-flight becomes a very complex task, which must rely heavily on well qualified and validated computations.

In addition, computations are beginning to prove useful and, in some cases, may become mandatory for the design of successful experiments. For example, the preliminary thermochemical non-equilibrium computations of [107] and their comparison with corresponding perfect gas computations from [105] have provided evidence that, with the current size of high enthalpy tunnels and their operating pressure limitations, significant difficulties may arise with the simulation of thermochemical effects over wide angle axisymmetric configurations, such as the hyperboloid / flare. Specifically, the small scale of the model (imposed by tunnel size constraints on the base diameter), combined with the relatively small nose bluntness of the hyperboloid, may support chemical freezing in the shock layer and, thus, inhibit the revelation of thermochemical effects in the experiment.



In this respect, the blunter double ellipsoid configuration (section 5.7) may be more appropriate for the experimental assessment of such effects on shock wave boundary layer interactions, at least as long as significant scale and operating pressure limitations remain in high enthalpy ground testing.

### 5.7 Interactions in the canopy region of spaceplanes: the double ellipsoid configuration

The double ellipse (two-dimensional) and double ellipsoid (three-dimensional) configurations have been widely investigated and included as major test cases in both Antibes workshops [72] and in the forthcoming ESTEC workshops [101], their relevance lying in the determination of nose/canopy heating. Under specific flow conditions and attitude (zero or low angle of attack), the flow phenomena in the region of the nose/canopy junction resemble closely the situation in the vicinity of deflected control surfaces. This configuration may, therefore, provide further insight to the shock wave boundary layer interaction problem, with the additional complications of important nose bluntness, surface curvature (of both the "parent body" - nose, and the "deflected control" - canopy), and three-dimensionality (in the case of the double ellipsoid). A major interest of this geometry lies in the revelation of thermochemical effects upon the interaction, which are strongly present in high enthalpy flowfields due to the significant nose bluntness.

Still, emphasis has so far been placed on 30° angle of attack cases (aimed to the study of canopy heating during reentry; results are summarized in [108]), in which configuration the canopy compression on the leeward side is rather weak due to the combined angle of attack and viscous effects (Fig. 58 [109,110]). A more representative configuration, in terms of the shock wave boundary layer interaction in the canopy region, is the one at zero angle of attack because it exhibits a stronger canopy shock and an interaction between the bow shock and the canopy shock near the body surface (Fig. 59 [111]). Noting, however, the limited amount of double ellipsoid data at zero angle of attack and that the bulk of the viscous computations to date have assumed equilibrium chemistry, with little effort placed towards systematic comparisons between perfect (frozen) gas, equilibrium and non-equilibrium chemistry results to assess thermochemical effects on shock wave boundary layer interactions, further progress in this area is anticipated within the framework of the European winged reentry vehicle program and the forthcoming qualification workshops [101].

## 6 SUMMARY AND CONCLUSIONS

Shock wave boundary layer interactions are of particular importance to the design of the control system of lifting ascent/reentry/cruise hypersonic vehicles, because of their effects on control effectiveness

as well as heating. Although, locally in the vicinity of deflected control surfaces on hypersonic vehicles, the effective Mach number of the interacting flowfield is often supersonic rather than hypersonic (due to forebody incidence, bluntness, etc.), supersonic flow investigations are not sufficient to resolve design problems as they do not readily contribute to some of the design issues that are specific to hypersonic flight. Such issues include the additional heating constraints to the design of control surfaces, and the effects of the forebody entropy layer and the interaction between the forebody and control shocks on both control effectiveness and heating.

In terms of control effectiveness, the problem reduces to the determination of the geometric characteristics of the interacting flowfield and of the pressure rise over the effective body shape in the vicinity of the control surface. Whether the interaction is sufficiently strong to promote flow separation or not, the presence of viscous effects causes a modification of the effective body shape which, in turn, may have a profound influence on the pressure recovery over the deflected control surface. In addition, the presence of an entropy layer approaching the deflected control surface, and the interaction between shocks near the deflected control (e.g. between forebody, separation and reattachment shocks) will further influence the pressure distribution and, thus, control effectiveness. The length of the deflected control surface is also important in determining whether a full pressure recovery is achieved.

For simplified cases, like the flat plate / flat ramp configurations discussed above, with thin boundary layers, the pressure distribution may be determined by combining inviscid oblique shock theory with the free interaction theory, provided that the geometric characteristics of the interaction are known. Thin boundary layers, in such cases, imply rather sharp pressure rises through separation and reattachment and, thus, the overall pressure recovery may be well approximated by the inviscid pressure rise through a single separation shock and a single reattachment shock. The interaction between the two, and the resulting expansion or compression at their intersection may be obtained through the inviscid double wedge theory.

In more realistic cases, however, involving nonuniform oncoming flows (entropy layer), and thick boundary layers, the pressure recovery over the deflected control surface will stretch over a significant distance relative to the actual length of the control surface (in contrast to the aforementioned single separation shock / single reattachment shock model). The resolution of such cases, when also adding the uncertainties in determining the geometric characteristics of the interaction, will likely require the performance of specific Navier-Stokes computations or full simula-



tion experiments. And noting that the uncertainties in the determination of interaction geometric characteristics are partly related to the transitional nature of many interactions, which computer or wind tunnel simulations fail to model for the moment, a designer may eventually be forced to incorporate worst case estimates in the design cycle (as, for example, the maximum fully laminar extent of the interaction).

In terms of heating of the deflected control surface, the detailed heat transfer distribution is not required by the designer. Instead, an estimate of the peak heating level on the deflected control is needed for sizing the thermal protection system of the control surface. The precise location of peak heating on the surface is less relevant. Noting that peak heating occurs at the end of the reattachment compression in an attached flow region, the problem mainly reduces to understanding the thickness and nature of the reattaching boundary layer at the location of peak heating, and the effective flow conditions at its edge.

For the simplified configurations considered herein, and conditions corresponding to cold wall wind tunnel testing, the reference temperature concept has been successfully applied to the prediction of the ramp heat transfer distribution and to the development of a peak heating correlation. For strong interactions, and for cases where laminar-turbulent transition was very efficiently promoted in the reattachment region, it has been found that the boundary layer thickness at the location of peak heating may be well approximated by simple geometric arguments, assuming a zero thickness at reattachment (i.e. assuming the virtual origin of the reattaching boundary layer to be located at reattachment). For weaker interactions, or interactions involving a thick oncoming boundary layer, this approach is bound to yield too small a boundary layer thickness and, thus, too high a peak heating estimate.

For more realistic cases, exhibiting strong pressure gradients in the vicinity of peak heating (mainly due to strong shock/shock interactions), and with hot wall configurations (representative of flight rather than wind tunnel conditions), the applicability of the zero pressure gradient reference temperature theory becomes questionable, and more sophisticated tools may be required for the prediction of peak heating. Such pressure gradient effects, and the influence of realistic geometric shapes (involving bluntness/entropy layers and surface curvature) upon the validity of the proposed pressure interaction peak heating correlation remain to be checked.

The formation of streamwise striations in reattaching flow regions has been found to depend on a balance between the presence and strength of initial disturbances (freestream turbulence, noise, geometric irregularities,...) and amplification mechanisms

(strength of the interaction i.e. adverse pressure gradient and flow concavity, Reynolds number,...). For the class of flow and geometric conditions examined herein, streamwise striations have been detected in cases where the oncoming forebody flow was stable and fully laminar, and have supported the occurrence of laminar-turbulent transition on the deflected control. Upon attainment of fully turbulent flow, striations have dissipated and the spanwise heating variations damped to effectively zero amplitude.

Concerning striation heating, all available data indicate that the macroscopic effects of striations may be treated as an integral part of laminar-turbulent transition. Despite the large spanwise heat transfer variations detected in a number of cases, the local turbulent heating level has consistently provided a good approximation to the upper limit of heat transfer peaks on the deflected control surface. Consequently, a maximum turbulent estimate for peak heating, corresponding to the minimum boundary layer thickness and maximum pressure on the control surface, such as the one given by the proposed correlation, remains valid even in the presence of strong striations. It is also noted that, similar to control effectiveness, the lack of adequate transition/striation models, may again force the designer to rely upon worst case estimates like the aforementioned turbulent peak heating level.

Tripping the oncoming boundary layer has been proposed as an effective way to minimize shock wave boundary layer interaction effects on control effectiveness and heating. The idea is that a turbulent oncoming boundary layer will most likely remain attached for typical control deflection angles, and this will not be to the detriment of control heating if the interaction with a laminar boundary layer is, anyway, expected to promote laminar-turbulent transition. It should be borne in mind, however, that a turbulent oncoming boundary layer will be thicker than a laminar one and, although there may be no separation, the extent of the turbulent interaction may be similar to the laminar case and not beneficial in terms of control effectiveness. Still in such a way, the minimum boundary layer thickness on the deflected control surface may be larger than in the transitional case (with transition occurring at reattachment) and, therefore, beneficial in terms of heating.

Clearly, the complexity of shock wave boundary layer interaction phenomena, particularly over realistic configurations, combined with the difficulties and measurement insufficiencies in wind tunnel testing make CFD a very important potential contributor to the design of control surfaces. But, despite the significant progress achieved in the field of Navier-Stokes simulation of hypersonic separated flows with important viscous-inviscid interactions, a number of difficulties (resolution, accuracy, computational efficiency,



...) and uncertainties in the quality of the results remain. Emphasis will, therefore, continue to be placed on CFD code validation with the help of workshop activities.

Although there is not much to be done with transition modelling (except for Large Eddy simulations), more realistic (and less conservative) worst case estimates may be obtained from reliable computations, particularly when complex configurations are considered. Assuming that transitional interactions (with transition occurring in the reattachment region) represent the most adverse case for both control effectiveness and heating (which is not evident with complex geometries), a computational strategy may be proposed. First, a converged, grid-independent fully laminar computation may be performed to provide the maximum possible extent of the interaction (and separation). Such a computation is also bound to yield the minimum possible thickness for the reattaching boundary layer. Continuing, thereafter, by "switching-on" a standard turbulence model in the attached flow region downstream of reattachment will provide a maximum possible turbulent heat transfer peak on the control surface corresponding to the minimum local boundary layer thickness. This approach has been shown to perform well with simple flat plate/ two-dimensional ramp geometries, but remains to be checked with more complex configurations, such as the hyperboloid / flare.

Finally, it is rather early to comment on real gas effects upon shock wave boundary layer interactions. Nevertheless, preliminary computational results have demonstrated an indirect effect through the influence of thermochemistry on the blunt forebody flow conditions approaching the region of interaction. Clearly, the situation may be significantly complicated if important thermochemical activity occurs within the interaction, but no explicit results are yet available in this area.

#### ACKNOWLEDGEMENTS

The greatest part of the author's work presented herein has been carried out at the von Karman Institute for Fluid Dynamics, partially supported by Dassault Aviation under the auspices of the Hermes R&D and RfQ programs. The author is indebted to John F. Wendt, Jean-Philippe Vermeulen, Werner Haase and Richard Schwane. The direct or indirect contributions of the numerous participants of the Hermes R&D and RfQ programs, and of the contributors to the European Hypersonic Database and the related Antibes workshops are also appreciated.

#### REFERENCES

1. Ferri, A., "Experimental results with airfoils tested in the high speed wind tunnel at Guidonia", NACA TM 946, 1940.
2. Green, J.E., "Interaction between shock waves and boundary layers", *Progress in Aerospace Sciences*, 11, 1970, pp. 235-340.
3. Korkegi, R.H., "Survey of viscous interactions associated with high Mach number flight", *AIAA J.*, 9, No. 5, May 1971, pp. 771-784.
4. Cinoux, J.J., "Interaction entre ondes de chocs et couches limites", in "Chocs et Ondes de Chocs", ed. A.L. Jaumotte, 2, Masson, 1973.
5. Hankey, W.L. Holden, M.S., "Two dimensional shock wave boundary layer interactions in high speed flows", *AGARDograph* 203, June 1975.
6. Adamson, T.C. and Messiter, A.F., "Analysis of two-dimensional interactions between shock waves and boundary layers", *Annual Review of Fluid Mechanics*, 12, 1980, pp. 103-138.
7. Peake, D.J. and Tobak, M., "Three-dimensional interactions and vortical flows with emphasis on high speeds", *AGARDograph* 252, July 1980.
8. Settles, G.S. and Dolling, D.S., "Swept shock wave boundary layer interactions", in "Tactical Missile Aerodynamics", eds. M.J. Hemsch and J.N. Nielsen, *Progress in Astronautics and Aeronautics*, 104, AIAA, 1986.
9. Settles, G.S. and Dolling, D.S., "Swept shock boundary layer interactions - tutorial and update", *AIAA Paper* 90-0375.
10. Holden, M.S., "A review of aerothermal problems associated with hypersonic flight", *AIAA Paper* 86-0267, January 1986.
11. Delery, J. and Marvin, J.G., "Shock wave boundary layer interactions", *AGARDograph* 280, 1986.
12. Delery, J., "Shock/shock and shock wave boundary layer interactions in hypersonic flows", in "Aerothermodynamics of Hypersonic Vehicles", *AGARD - FDP - VKI Special Course*, May 1988. *AGARD Report* 761, June 1989.
13. Stollery, J.L., "Glancing shock boundary layer interactions", in "Three-Dimensional Supersonic and Hypersonic Flows Including Separation", *AGARD Report* 764, January 1990.
14. Stollery, J.L., "Intake and nozzle flows (some problems caused by shock wave boundary layer interaction)", in *Proc. 3rd Joint Europe/U.S. Short Course on Hypersonics*, RWTH Aachen, October 1990.
15. Perrier, P. and Caupenne, Ph., "Concepts généraux aérodynamiques - aérothermique d' Hermes", in "Aerodynamics of Hypersonic Lifting Vehicles", *AGARD CP* 428, November 1987.
16. Neumann, R.D., "Missions and requirements", in "Aerothermodynamics of Hypersonic Vehicles", *AGARD-FDP-VKI Special Course*, May 1988. *AGARD Report* 761, June 1989.
17. Chapman, D.R., Kuehn, D.M. and Larson, H.K., "Investigation of separated flow in supersonic and subsonic streams with emphasis on the effect of transition", *NACA TN* 3869, 1957.
18. Sullivan, P.A., "Hypersonic flow over slender double wedges", *AIAA J.*, 1, No. 8, August 1963, pp. 1927.



19. Vierendeels, J., "Validation of a 3D Navier-Stokes solver for hypersonic flows with strong viscous-inviscid interactions", ESTEC (YPA) EWP 1713, December 1992.
20. Lusse, P.A., "Visualization study of a blunt cylinder / flare model in high supersonic flow", Delft U. of Technology Report, Dept. Aerospace Engineering, July 1992.
21. Simeonides, G., "Hypersonic shock wave boundary layer interactions over compression corners", Ph.D. Thesis, von Karman Institute / University of Bristol, April 1992.
22. Settles, G.S., Perkins, J.J. and Bogdonoff, S.M., "Investigation of three-dimensional shock boundary layer interactions at swept compression corners", AIAA J., 18, No. 7, July 1980, pp. 779-785.
23. Holden, M.S., "Experimental studies of quasi-two-dimensional and three-dimensional viscous interaction regions induced by skewed shock and swept shock boundary layer interactions", AIAA Paper 84-1677, 1984.
24. Hamed, A., "Flow separation in shock wave boundary layer interactions at hypersonic speeds", NASA CR 4274, February 1990.
25. Appels, C., "Incipient separation of a compressible turbulent boundary layer", von Karman Institute TN 99, April 1974.
26. Needham, D.A., "Laminar separation in hypersonic flow", Ph.D. Thesis, U. London, August 1965.
27. Katzer, E., "On the lengthscales of laminar shock boundary layer interaction", J. Fluid Mechanics, 206, 1989, pp. 477-496.
28. Korkegi, R.H., "A lower bound for three - dimensional turbulent separation in supersonic flow", AIAA J., 23, No. 3, March 1985, pp. 475-476.
29. Korkegi, R.H., "Comparison of shock-induced two- and three-dimensional incipient turbulent separation", AIAA J., 13, No. 4, April 1975, pp. 534-535.
30. Zheltovodov, A.A., Maksimov, A.I. and Shilein, E.K., "Development of turbulent separated flows in the vicinity of swept shock waves", in "The Interactions of Complex 3D Flows", ed. A.M. Kharitonov, Inst. of Theoretical and Applied Mechanics, USSR Academy of Sciences, Novosibirsk, 1987, pp. 67-91 (English translation, edited by G.S. Settles).
31. Neumann, R.D., "Developing configuration requirements for hypersonic flight", in Proc. 3rd Joint Europe/U.S. Short Course on Hypersonics, RWTH Aachen, October 1990.
32. Holden, M.S. and Moselle, J.R., "Theoretical and experimental studies of the shock wave boundary layer interaction on compression surfaces in hypersonic flow", ARL 70-0002, January 1970.
33. Holden, M.S., "Shock wave turbulent boundary layer interaction in hypersonic flow", AIAA Paper 72-74.
34. Elfstrom, G.M., "Turbulent hypersonic flow at a wedge compression corner", J. Fluid Mechanics, 53, Part 1, May 1972, pp. 113-127.
35. Appels, C., "Turbulent boundary layer separation at Mach 12", von Karman Institute TN 90, September 1973.
36. Hayes, W.D. and Probstein, R.F., "Hypersonic flow theory", Academic Press, 1959.
37. Anderson, J.D., "Hypersonic and high temperature gas dynamics", McGraw-Hill, 1989.
38. Eckert, E.R.G., "Engineering relations of friction and heat transfer to surfaces in high velocity flow", J. Aero. Sci., 22, 8, August 1955, pp. 585-587.
39. Lukaciewicz, J., "Hypersonic flow- blast wave analogy", AEDC TR-61-4, 1961.
40. Anonymous, "Equations, tables and charts for compressible flow", NACA TR 1135, 1953.
41. Coët, M.C., Chanetz, B. and Delery, J., "Shock wave boundary layer interaction with entropy layer effect in hypersonic flow", Colloque sur les Ecoulements Hypersoniques, Garchy, France, October 1992, ONERA TP 1992-181.
42. Neumann, R.D. and Hayes, J.R., "Introduction to aerodynamic heating analysis of supersonic missiles", in "Tactical Missile Aerodynamics", eds. M.J. Hensch and J.N. Nielsen, Progress in Astronautics and Aeronautics, 104, AIAA, 1986.
43. Vermeulen, J.P. and Simeonides, G., "Parametric studies of shock wave boundary layer interactions in two- dimensional compression corners at Mach 6, with emphasis on the formation of streamwise striations in the reattachment region", von Karman Institute TN 181, September 1992.
44. Matthews, R.K., "Boundary layer transition", in "Methodology of hypersonic testing", VKI/AEDC Special Course, February 1993.
45. Neumann, R.D., "Special topics in hypersonic flow", in "Aerodynamic Problems of Hypersonic Vehicles", AGARD LS 42, 1, July 1972.
46. Holden, M.S., "Shock wave turbulent boundary layer interaction in hypersonic flow", AIAA Paper 77-45.
47. Hung, F.T., "Interference heating due to shock wave impingement on laminar boundary layers", AIAA Paper 73-678.
48. Hung, F.T. and Barnett, D.O., "Shock wave boundary layer interference heating analysis", AIAA Paper 73-237.
49. Gautier, B. and Ginoux, J.J., "Improved computer program for calculation of viscous-inviscid interactions", von Karman Institute TN 82, March 1973.
50. Bushnell, D.M. and Weinstein, L.M., "Correlation of peak heating for reattachment of separated flows", J. Spacecraft and Rockets, 5, No. 9, September 1968, pp. 1111-1112.
51. Ginoux, J.J., "On some properties of reattaching laminar and transitional high speed flows", von Karman Institute TN 53, September 1969.
52. Ginoux, J.J., "Streamwise vortices in laminar flow", AGARDograph 97, Part I, May 1965.
53. Kipp, H.W. and Helms, V.T., "Some observa-



- tions on the occurrence of striation heating", AIAA Paper 85-0324.
54. Aihara, Y., Morishita, E. and Okunuki, T., "Experimental study on drag reduction of hypersonic transport configuration", in ICAS '90, Proc. 17th ICAS Congress, Stockholm, September 1990.
  55. Schlichting, H., "Boundary layer theory", McGraw-Hill, 4th ed., 1960.
  56. Simeonides, G., Vermeulen, J.P., Boerrigter, H.L. and Wendt, J.F., "Quantitative heat transfer measurements in hypersonic wind tunnels by means of infrared thermography", in Record of 14th ICIASF, NSWC, Rockville, October 1991, to appear in IEEE Transactions on Aerospace and Electronic Systems, July 1993.
  57. Simeonides, G., Vermeulen, J.P. and Zemsch, S., "Amplification of disturbances and the promotion of laminar-turbulent transition through regions of hypersonic shock wave boundary layer interactions", in "Aerothermochemistry of Spacecrafts and Associated Hypersonic Flows", IUTAM Symposium, Marseille, September 1992.
  58. Balageas, D., Boscher, D., Féom, A. and Gardette, G., "Heat transfer measurements in ONEKA supersonic and hypersonic wind tunnels using passive and active infrared thermography", in "Aerothermodynamics for Space Vehicles", ESA SP 318, May 1991, pp. 235-240.
  59. Chanetz, B., Coët, M.C. and Delery, J., "Etude expérimentale des variations transversales de flux de chaleur dans un recollement sur un dièdre en écoulement hypersonique", ONERA RT 15/4362, February 1991.
  - 60a. De Luca, L., Cardone, G., Carlomagno, G.M., Alziary de Roquefort, T. and Aymer de la Chevalerie, D., "Infrared measurements of aerodynamic heating in hypersonic wind tunnel", in "Aerothermodynamics for Space Vehicles", ESA SP 318, May 1991, pp. 229-234; and
  - 60b. Aymer de la Chevalerie, D., Private communication within Hermes RfQ program, CEAT Poitiers, May 1993.
  61. Henckels, A., Herzog, P. and Maurer, F., "Experimental study of hypersonic shock wave boundary layer interactions by means of infrared technique", in "Aerothermodynamics for Space Vehicles", ESA SP 318, May 1991, pp. 159-164.
  62. Inger, G.R., "Three-dimensional disturbances in reattaching separated flows", in "Flow separation", AGARD CP 168, November 1975.
  63. Arnal, D., "Laminar - turbulent transition problems in supersonic and hypersonic flows", in "Aerothermodynamics of Hypersonic Vehicles", AGARD - FDP - VKI Special Course, May 1988. AGARD Report 761, June 1989.
  64. David, E., Comte, P. and Lesieur, M., Private communication within Hermes RfQ program, Institut de Mécanique de Grenoble, April 1993.
  65. Floryan, J.M., "On the Görtler instability of boundary layers", Progress in Aerospace Sciences, 28, No. 3, 1991.
  66. Pauley, W.R. and Eaton, J.K., "The fluid dynamics and heat transfer effects of streamwise vortices embedded in a turbulent boundary layer", Stanford U. Report MD 51, August 1988.
  67. Saric, W.S., "Physical description of boundary layer transition: experimental evidence", in "Progress in Transition Modelling", AGARD - FDP / VKI Special Course, March 1993. AGARD Report 793.
  68. Smith, V.K., "Hypersonic overview", in "Methodology of hypersonic testing", VKI / AEDC Special Course, February 1993.
  69. Mehta, U.B., "Computational requirements for hypersonic flight performance estimates", J. Spacecraft and Rockets, 27, No. 2, 1990, pp. 103-112.
  70. Martin, J.G., "Future requirements of wind tunnels for computational fluid dynamics code verification", AIAA Paper 86-0752.
  71. Bogdonoff, S.M., "Comments on experiments for computational validation for fluid dynamic predictions", in "Hypersonic Flows for Reentry Problems", eds. J.A. Desideri, R. Glowinski and J. Periaux, Vol.1, Springer-Verlag, 1991.
  - 72a. Desideri, J.A., Glowinski, R. and Periaux, J., "Hypersonic flows for reentry problems", Vols. 1,2, Springer-Verlag, 1991.
  - 72b. Abgrall, R., Desideri, J.A., Glowinski, R., Mallet, M. and Periaux, J., "Hypersonic flows for reentry problems", Vol. 3, Springer-Verlag, 1992; and
  - 72c. Abgrall, R., Desideri, J.A., et al., "European Hypersonic Database (EHDB)", computerized database, INRIA, Sophia Antipolis, January 1993 (publicly unavailable at time of print).
  73. Holden, M.S. and Moselle, J.R., "A database of aerothermal measurements in hypersonic flow for CFD validation", AIAA Paper 92-4023 (data available on floppy).
  74. Settles, G.S. and Dodson, L.J., "Hypersonic shock boundary layer interaction database", AIAA 91-1763. NASA CR 177577 (data available on floppy).
  75. Simeonides, G. and Haase, W., "Experimental and computational investigations of hypersonic flows about compression ramps", von Karman Institute Preprint 1993-07/AR.
  76. Lewis, J.E., "Experimental investigation of supersonic laminar two-dimensional boundary layer separation in a compression corner with and without cooling", Ph.D. Thesis, California Institute of Technology, November 1966.
  77. Carter, J.E., "Numerical solutions of the Navier-Stokes equations for the supersonic laminar flow over a two-dimensional compression corner", NASA TR R 385, July 1972.
  78. Simeonides, G., Haase, W. and Manna, M., "Experimental, analytical and computational methods applied to hypersonic compression ramp flows", in "Theoretical and Experimental Methods in Hypersonic Flows", AGARD - FDP Symposium, Torino,



May 1992. AGARD CP 514.

79. Rudy, D.H., Thomas, J.L., Kumar, A., Gnoffo, P.A. and Chakravarthy, S.R., "A validation study of four Navier-Stokes codes for high speed flows", AIAA Paper 89-1838.
80. Hung, C.M. and Mac Cormack, R.W., "Numerical solutions of supersonic and hypersonic laminar compression corner flows", AIAA J., 14, No. 4, April 1976, pp. 475-481.
81. Power, G.D. and Barber, T.J., "Analysis of complex hypersonic flows with strong viscous/inviscid interaction", AIAA J., 26, No. 7, July 1988, pp. 832-840.
82. Rizzetta, D. and Mach, K., "Comparative numerical study of hypersonic compression ramp flows", AIAA Paper 89-1877.
83. Haase, W., "Viscous hypersonic flows over compression ramps", in "Numerical Methods in Fluid Mechanics", Proc. 8th GAMM Conference, Notes on Numerical Fluid Mechanics, 29, ed. P. Wesseling, Vieweg, 1990.
84. Lawrence, S.L., "Parabolized Navier-Stokes methods for hypersonic flows", in "Computational Fluid Dynamics", von Karman Institute LS 1991-01, February 1991.
85. Chanetz, B., Coët, M.C., Nicout, D. and Pot, T., "Shock wave boundary layer interaction in hypersonic two-dimensional laminar flow", Colloque sur les Ecoulements Hypersoniques, Garchy, France, October 1992, ONERA TP 1992-182.
86. Holden, M.S., "A study of flow separation in regions of shock wave boundary layer interaction in hypersonic flow", AIAA Paper 78-1169.
87. Wendt, J.F., Mallet, M. and Oskam, B., "A synthesis of results on the calculation of flow over a 2D ramp and a 3D obstacle", in "Hypersonic Flows for Reentry Problems", eds. J.A. Desideri, R. Glowinski and J. Periaux, 2, Springer-Verlag, 1991.
88. Haase, W., "Problem III: 2D ramp flows", in "Hypersonic Flows for Reentry Problems", eds. R. Abgrall, J.A. Desideri, R. Glowinski, M. Mallet and J. Periaux, 3, Springer-Verlag, 1992.
89. Marvin, J.G., "Turbulence modelling for hypersonic flows", in Proc. 3rd Europe/U.S. Short Course in Hypersonics, RWTH Aachen, October 1990.
90. Delery, J., "Contribution of Laser Doppler Velocimetry to the physical description of typical shock wave turbulent boundary layer interactions with emphasis on turbulence modelling", in "Shock Wave Boundary Layer Interactions in Supersonic and Hypersonic Flows", AGARD - FDP / VKI Special Course, May 1993. AGARD Report 792.
91. Vandromme, D., "Turbulence modelling for shock wave boundary layer interactions (specific issues and examples of applications)", in "Shock Wave Boundary Layer Interactions in Supersonic and Hypersonic Flows", AGARD - FDP / VKI Special Course, May 1993. AGARD Report 792.
92. Knight, D., "Numerical simulation of swept shock wave turbulent boundary layer interactions", in "Shock Wave Boundary Layer Interactions in Supersonic and Hypersonic Flows", AGARD - FDP / VKI Special Course, May 1993. AGARD Report 792.
93. Coleman, G.T. and Stollery, J.L., "Heat transfer in hypersonic turbulent separated flow", J. Fluid Mechanics, 56, Part 4, 1972, pp. 741-752.
94. Delery, J. and Coët, M.C., "Experiments on shock wave boundary layer interaction produced by two-dimensional ramps and three-dimensional obstacles", in "Hypersonic Flows for Reentry Problems", eds. J.A. Desideri, R. Glowinski and J. Periaux, 2, Springer-Verlag, 1991.
95. Horstman, C.C., "Hypersonic shock wave turbulent boundary layer interaction flows - experiment and computation", AIAA Paper 91-1760.
96. Coakley, T.J. and Huang, P.G., "Turbulence modelling for high speed flows", AIAA Paper 92-436.
97. Haidinger, F. and Friedrich, R., "Numerical simulation of strong shock turbulent boundary layer interactions using a Reynolds stress model", submitted to Zeitschrift für Flugwissenschaften und Weltraumforschung (ZFW), 1993.
98. Settles, G.S., Horstman, C.C. and McKenzie, T.M., "Experimental and computational study of a swept compression corner interaction flowfield", AIAA J., 24, No. 5, May 1986, pp. 744-752.
99. Jouet, C. and Borrel, M., "Navier-Stokes computation over a 3D ramp", in "Hypersonic Flows for Reentry Problems", eds. R. Abgrall, J.A. Desideri, R. Glowinski, M. Mallet and J. Periaux, 3, Springer-Verlag, 1992.
100. Knight, D., Horstman, C.C., Ruderich, R., Mao, M.F. and Bogdonoff, S.M., "Supersonic turbulent flow past a 3D swept compression corner at Mach 3", AIAA Paper 87-551.
101. Muylaert, J., "Test case evaluation for the ESTEC qualification workshop", ESA / ESTEC Doc. YPA/1358/JM, February 1993.
102. Schwane, R. and Muylaert, J., "Design of the validation experiment: hyperboloid / flare", ESA / ESTEC Doc. YPA/1256/RS, June 1992.
103. Schwane, R. and Wong, H., Private communication, ESA/ESTEC, Aerothermodynamics Section (YPA), April 1993.
104. Brenner, G., Private communication, DLR Göttingen, November 1992.
105. Netterfield, M.P., Private communication, Fluid Gravity Engineering, December 1992.
106. Brenner, G., Gerhold, T., Hannemann, K. and Rues, D., "Numerical simulation of shock/shock and shock wave boundary layer interactions in hypersonic flows", submitted to Computers Fluids, Pergamon Press, 1993.
107. Walpot, L.M.G., Adam, P.A. and Muylaert, J., "Numerical simulation of Electre and hyperboloid / flare in high enthalpy facility F4 and extrapolation to flight", ESA / ESTEC Doc. YPA/1704/LW, January 1993.



108. Hollanders, H., Kumar, A., Monnoyer, F., Olivier, H. and Desideri, J.A., "Synthesis of problem VI: double ellipse / ellipsoid and sphere", in "Hypersonic Flows for Reentry Problems", eds. R. Abgrall, J.A. Desideri, R. Glowinski, M. Mallet and J. Periaux, 3, Springer-Verlag, 1992.

109. Dortmann, K., "Hypersonic flowfield computations around a double ellipsoid and a blunt nose delta wing", in "Hypersonic Flows for Reentry Problems", eds. R. Abgrall, J.A. Desideri, R. Glowinski, M. Mallet and J. Periaux, 3, Springer-Verlag, 1992;

110. Rieger, H., Stock, H. and Wagner, B., "Computational aerothermodynamic methods for industrial applications to reentry and hypersonic cruise problems", in "Aerothermodynamics for Space Vehicles", ESA SP 318, May 1991, pp. 421-437.

111. Leyland, P. and Vos, J.B., "Real gas calculations for viscous hypersonic flows on 2D unstructured meshes", in "Aerothermodynamics for Space Vehicles", ESA SP 318, May 1991, pp. 439-446.

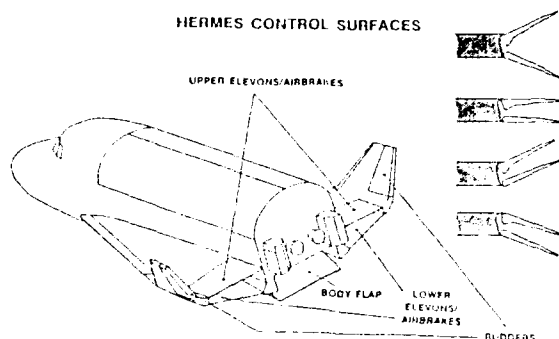


Fig. 1 - The Hermes spaceplane  
Areas of shock boundary layer interaction

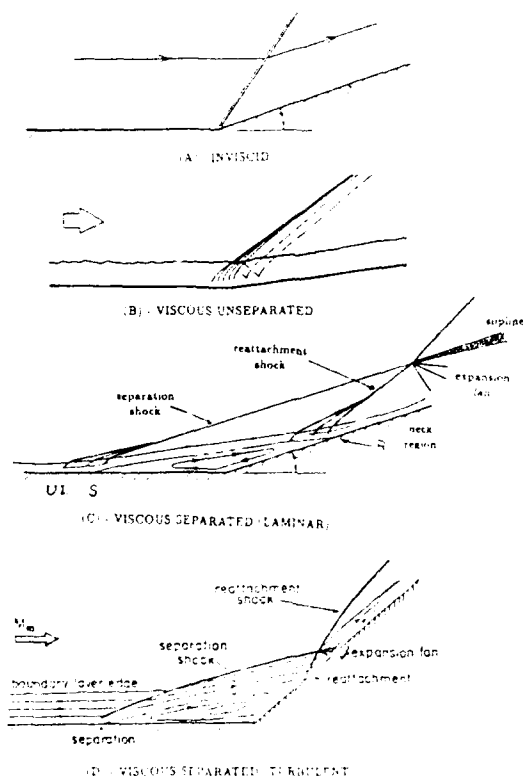
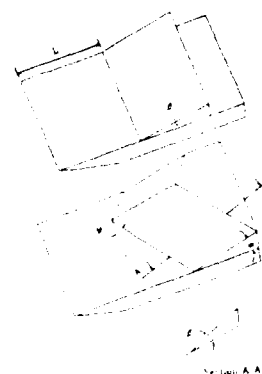


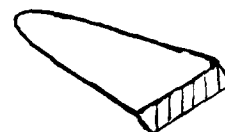
Fig. 3 - Schematic of the flowfield over a flat plate/two-dimensional compression ramp

2D ramp

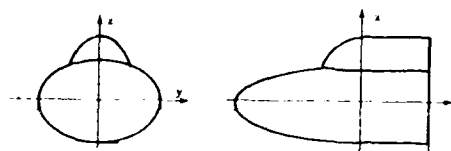
3D ramp



Delta wing/flap



Hyperboloid/flare



Double ellipse/ellipsoid

Fig. 2 - Simplified configurations exhibiting shock wave boundary layer interactions



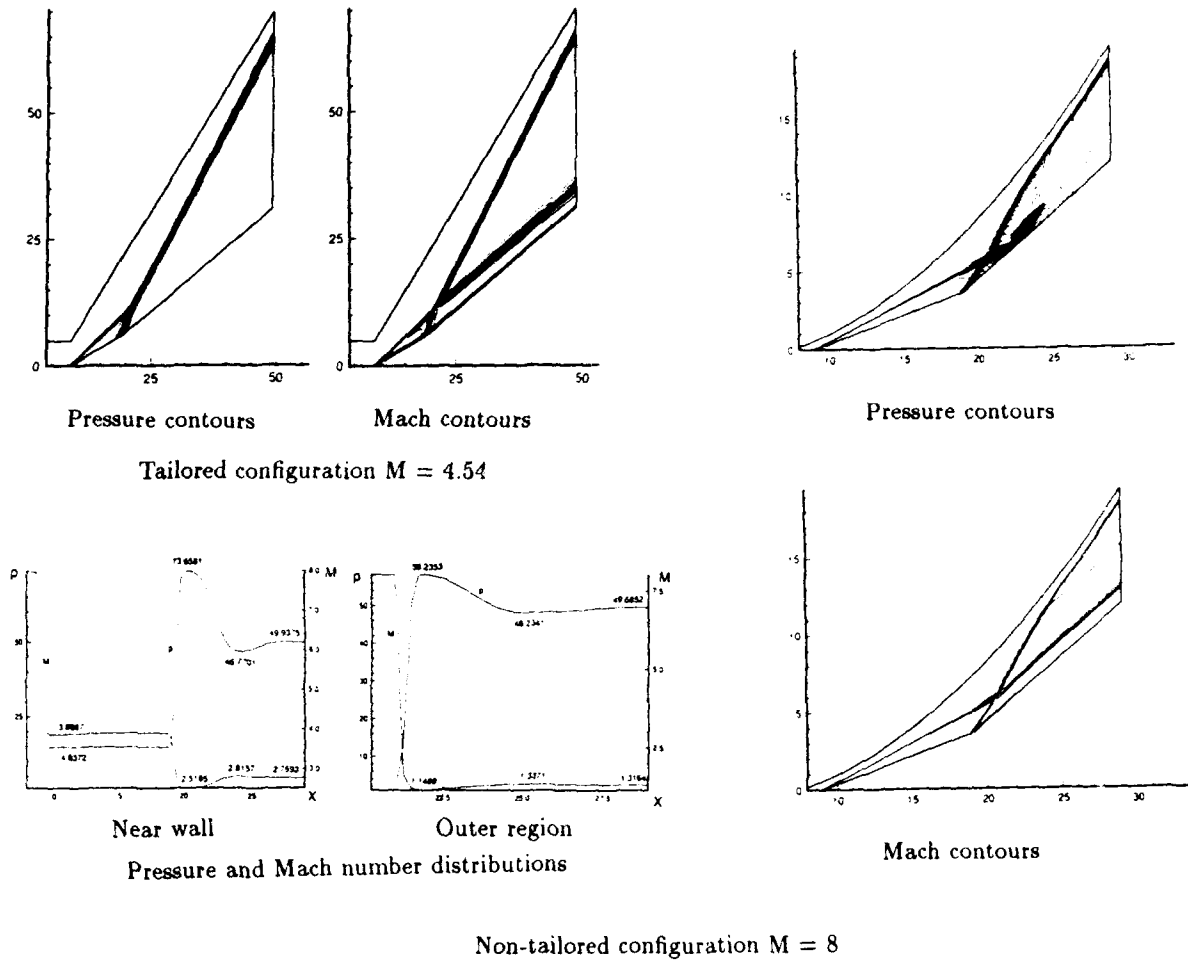


Fig. 4 - Inviscid shock/shock interaction over a double wedge configuration [19]

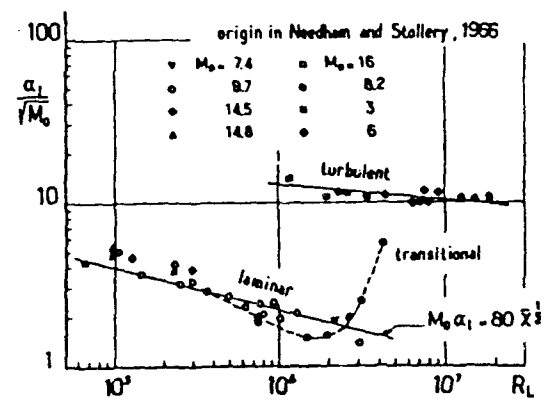
Fig. 5 - Combined oil flow and schlieren visualization  
 $M = 4$ ,  $AOA = 15$  degrees [20]

Fig. 6 - Incipient separation criteria for laminar and turbulent interactions over 2D compression corners [14,26]



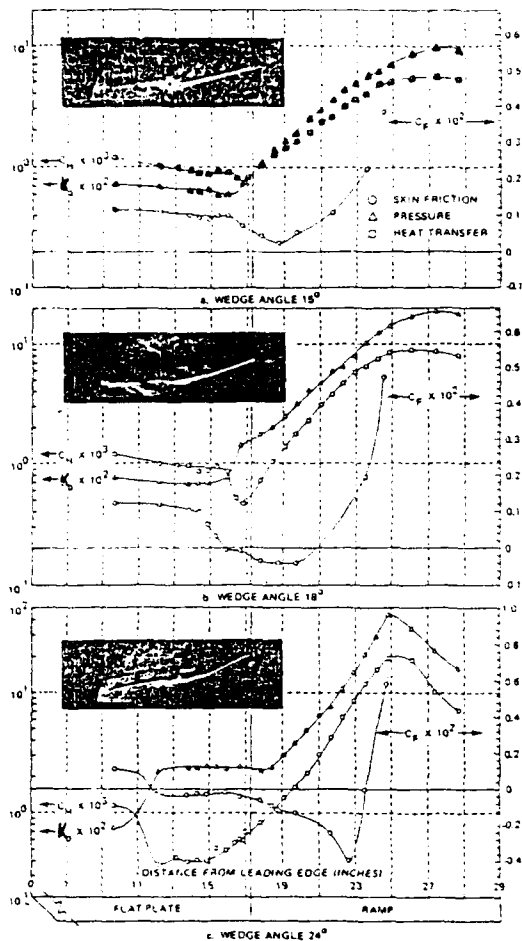


Fig. 7 - Pressure skin friction and heat transfer distributions over laminar 2D compression ramp interactions at Mach 14.1 with  $Re_L = 105,000$  and  $T_w/T_0 = 0.1$  [32]

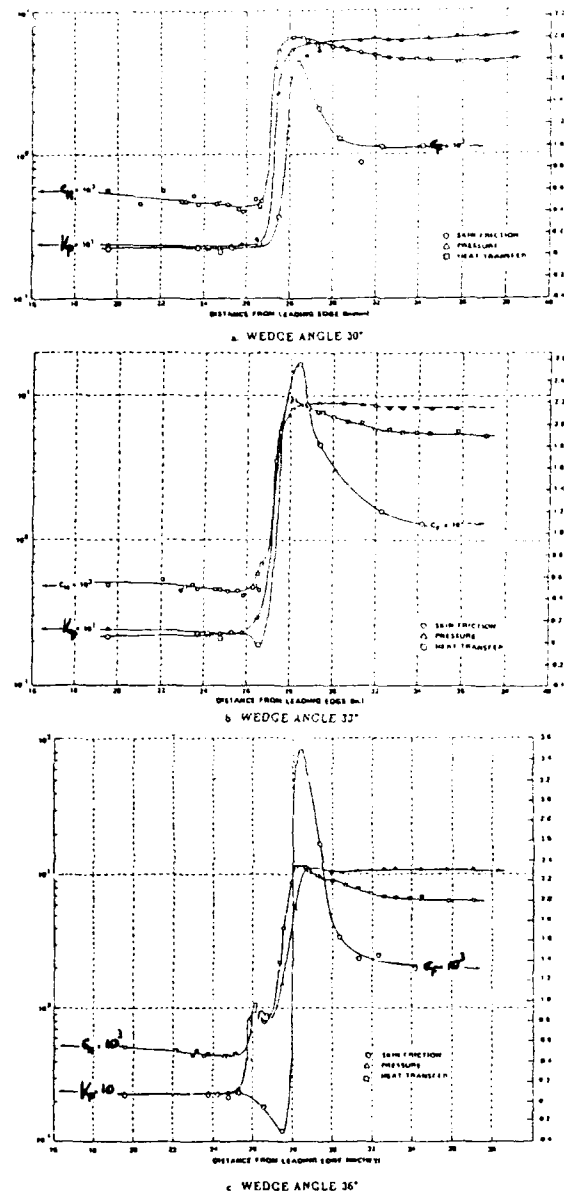
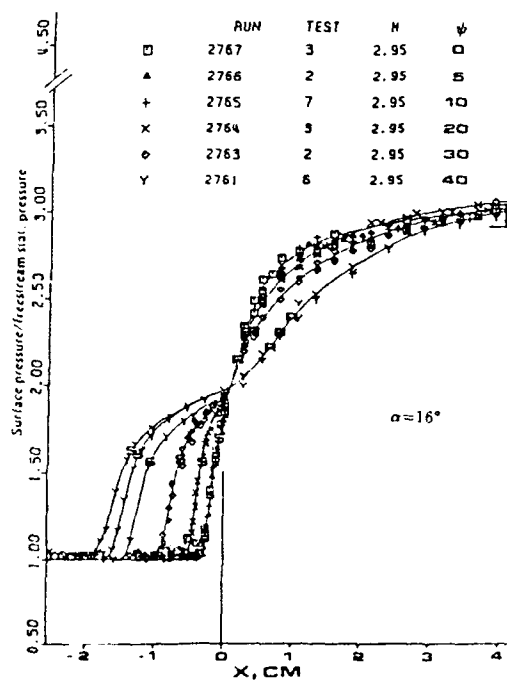


Fig. 8 - Pressure, skin friction and heat transfer distributions over turbulent 2D compression ramp interactions at Mach 8.6 with  $Re_L = 22.5 \times 10^6$  and  $T_w/T_0 = 0.3$  [33]

Fig. 9 - Pressure distributions over turbulent swept and unswept compression ramp interactions at Mach 2.95 with  $Re_L = 18.7 \times 10^6$  and adiabatic wall [22]



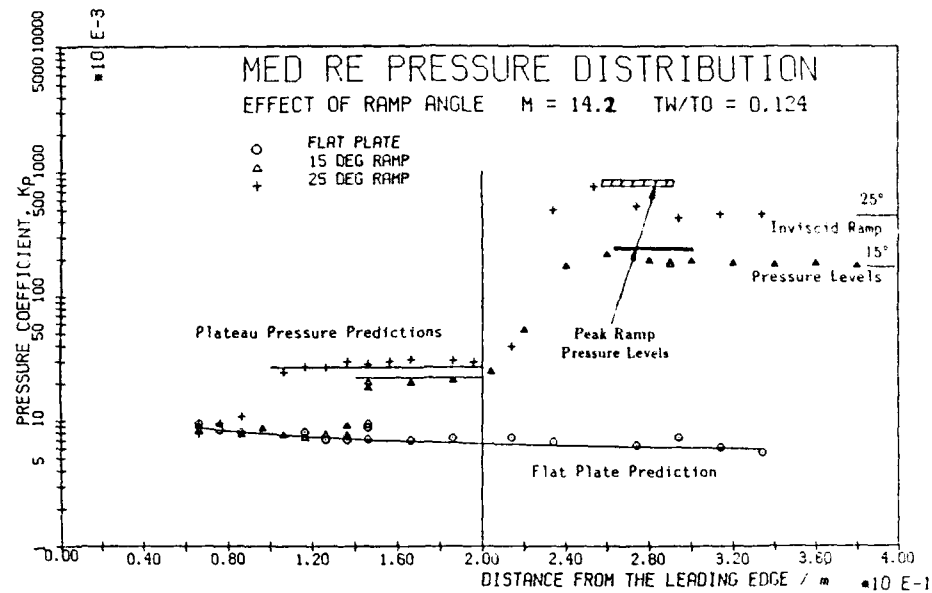


Fig. 10 - Pressure distributions over flat plate and flat plate / 2D ramp configurations at Mach 14.2 with  $Re_L = 1.8 \times 10^6$  and  $T_w/T_0 = 0.12$  [21]

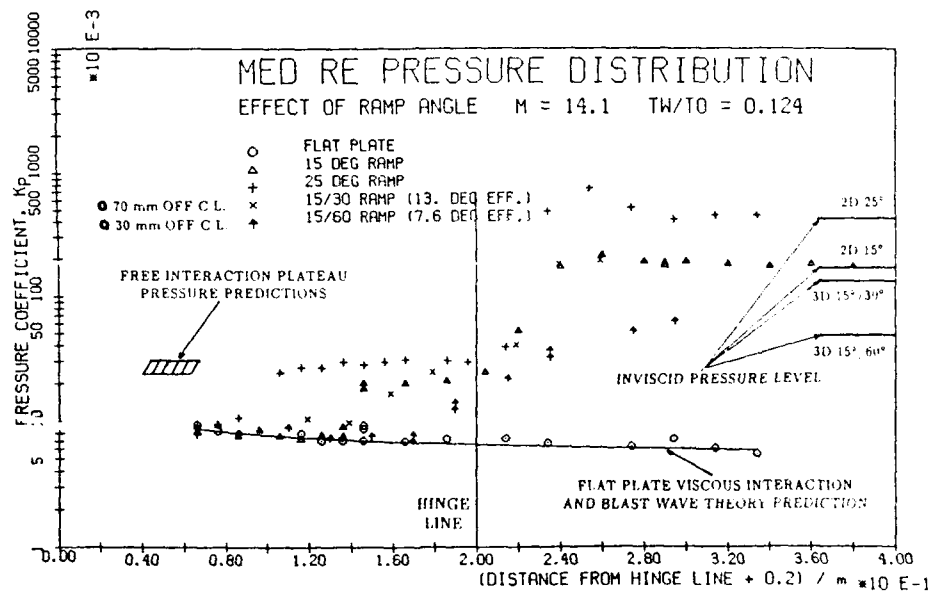


Fig. 11 - Pressure distributions over flat plate and flat plate / 2D and swept ramp configurations at Mach 14.2 with  $Re_L = 1.8 \times 10^6$  and  $T_w/T_0 = 0.12$  ( $\beta = 15^\circ$ ) [21]

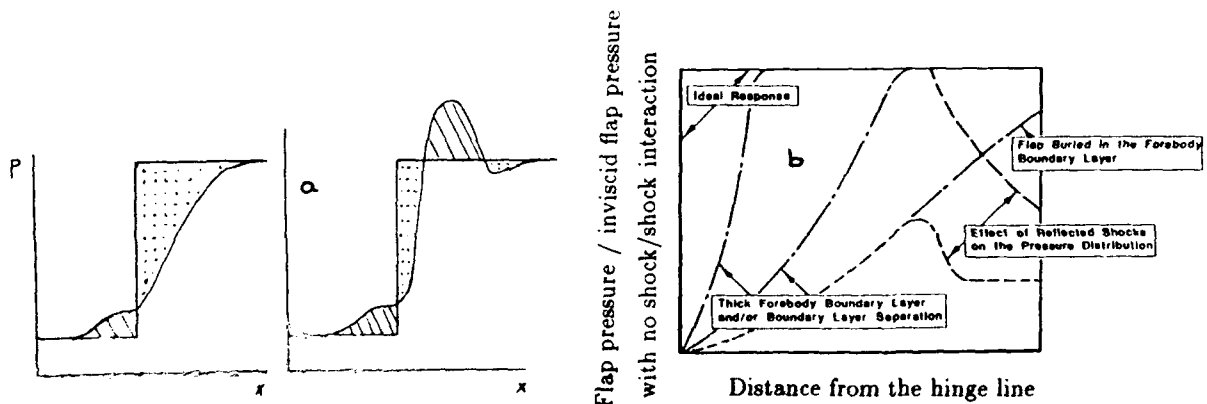


Fig. 12 - Schematic representation of viscous effects on pressure distribution and control effectiveness



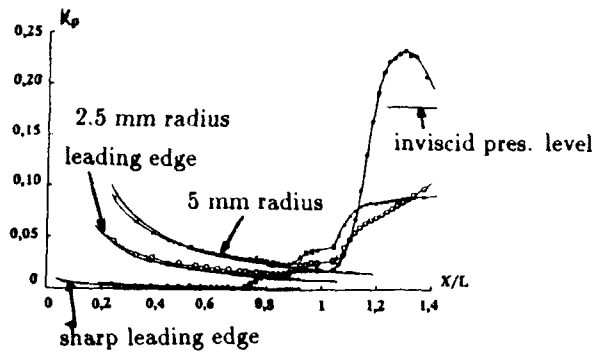


Fig. 13 - Effect of entropy layer (leading edge bluntness) on the pressure distribution over a flat plate / 2D 15° ramp configuration at Mach 10 with  $Re_L = 2.1 \times 10^6$  and  $T_w/T_0=0.26$  [41]

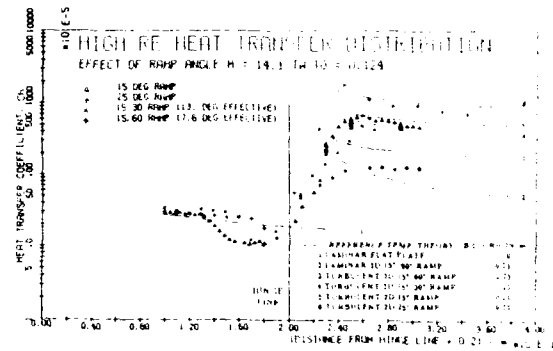


Fig. 16 - Heat transfer distributions over swept and unswept compression ramp configurations at Mach 14.3 with  $Re_L = 2.5 \times 10^6$  and  $T_w/T_0=0.12$  [21]

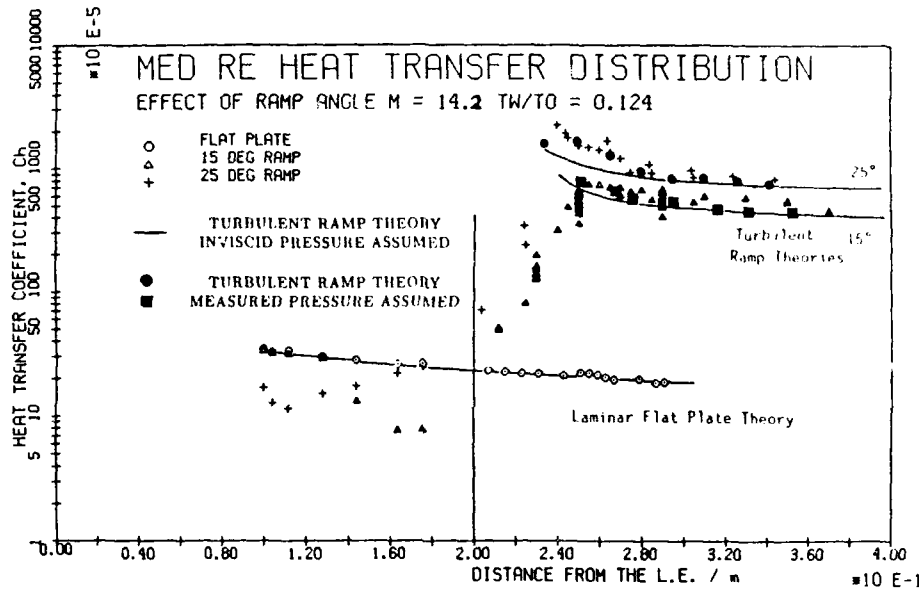


Fig. 14 - Heat transfer distributions over flat plate and flat plate / 2D ramp configurations at Mach 14.2 with  $Re_L = 1.8 \times 10^6$  and  $T_w/T_0=0.12$  [21]

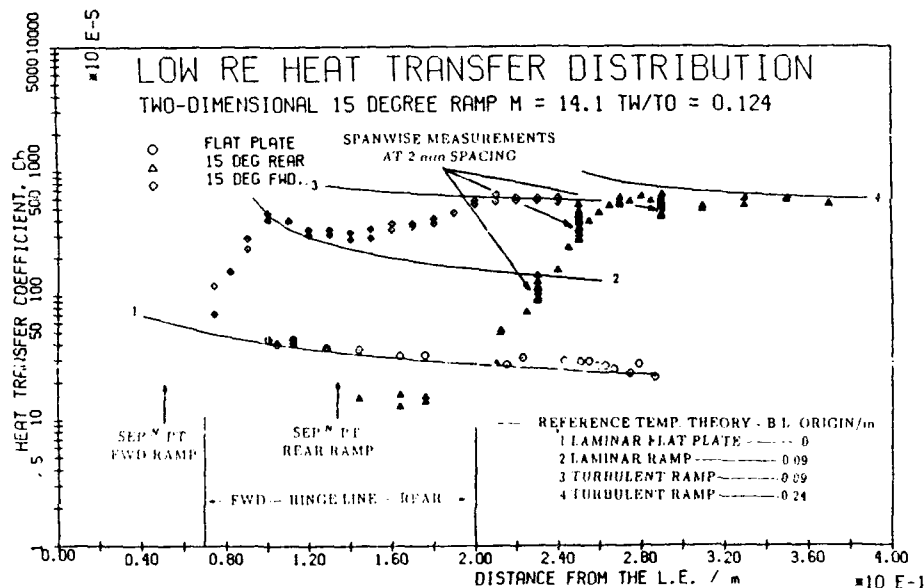


Fig. 15 - Heat transfer distributions over flat plate and flat plate / 2D ramp configurations at Mach 14.1 with  $Re_L = 1.3 \times 10^6$  and  $T_w/T_0=0.12$  [21]



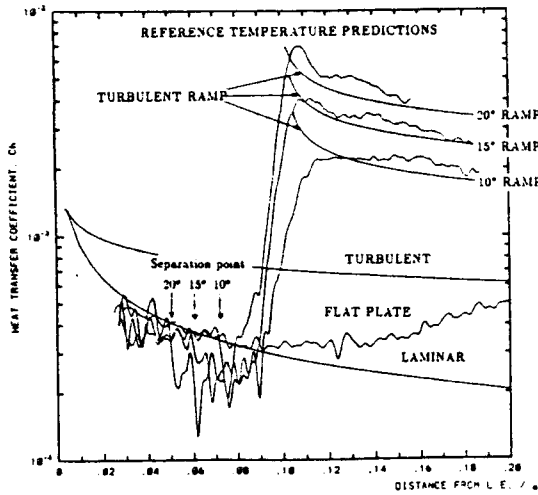


Fig. 17 - Heat transfer distributions over flat plate and flat plate / 2D ramp configurations at Mach 6 with  $Re_L=720,000$  and  $T_w/T_0=0.6$  [21,43]

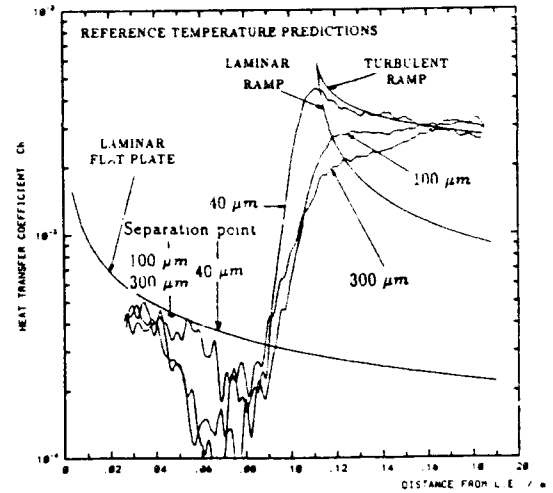


Fig. 19 - Heat transfer distributions over a flat plate / 2D 15° ramp configuration - effect of leading edge bluntness. Mach 6,  $Re_L=720,000$ ,  $T_w/T_0=0.6$  [43]

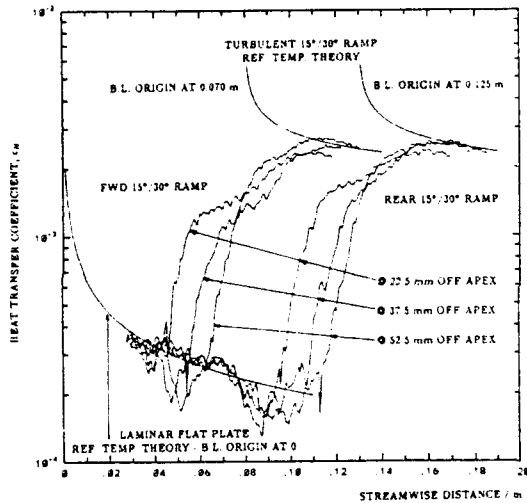


Fig. 18 - Heat transfer distributions over 15° ramps swept by 30° at Mach 6 [21]

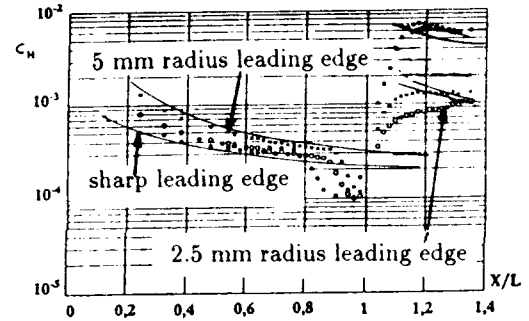


Fig. 20 - Effect of entropy layer (leading edge bluntness) on the heat transfer distribution over a flat plate / 2D 15° ramp configuration at Mach 10 with  $Re_L=2.1 \times 10^6$  and  $T_w/T_0=0.26$  [41]

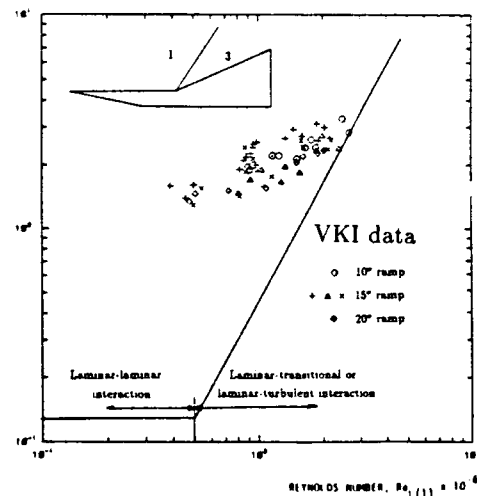
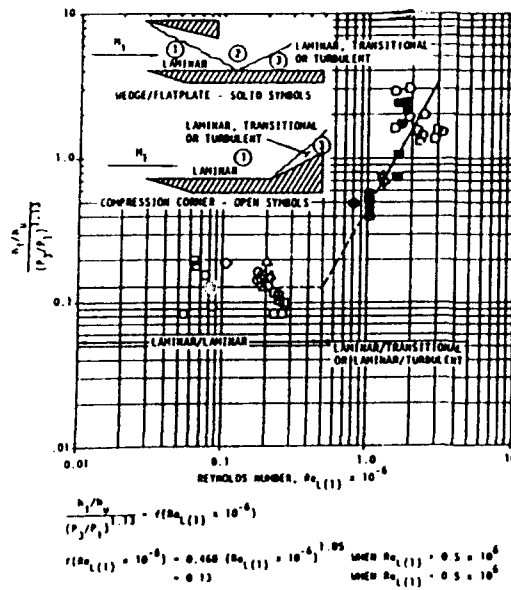
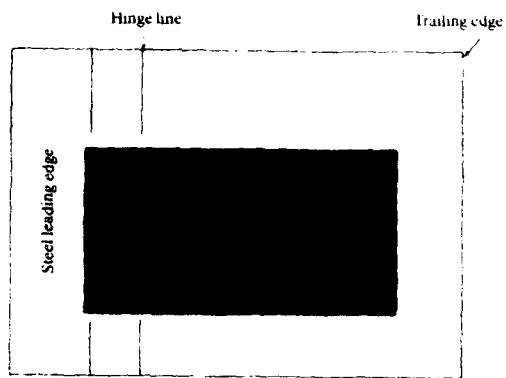


Fig. 21 - Hung-Barnett peak heating correlation [48] and comparison to recent Mach 6 data [43]

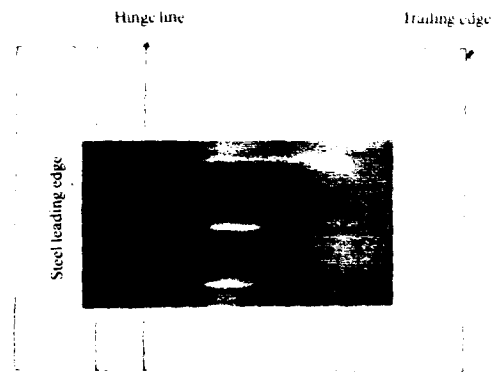




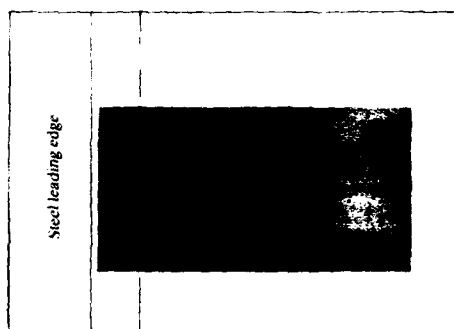




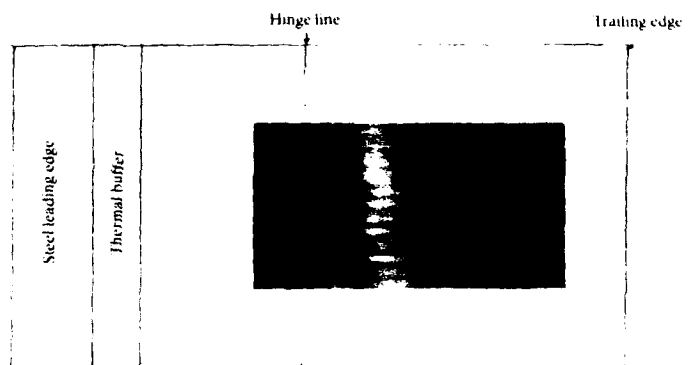
(a) 10° forward ramp;  $Re_L = 320,000$   
 $26\mu\text{m} \pm 10\mu\text{m}$  leading edge



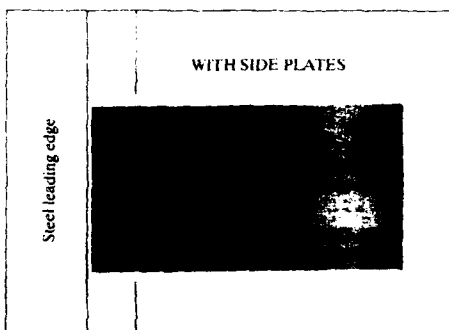
(d) 15° forward ramp;  $Re_L = 320,000$   
 $40\mu\text{m} \pm 20\mu\text{m}$  leading edge



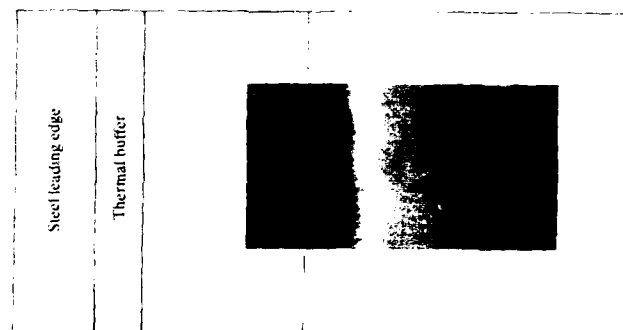
(b) 10° forward ramp;  $Re_L = 320,000$   
 $40\mu\text{m} \pm 20\mu\text{m}$  leading edge



(e) 15° rear ramp;  $Re_L = 720,000$   
 $40\mu\text{m} \pm 20\mu\text{m}$  leading edge



(c) 10° forward ramp;  $Re_L = 320,000$   
 $40\mu\text{m} \pm 20\mu\text{m}$  leading edge  
 same as (b) but with side plates



(f) 15° rear ramp;  $Re_L = 1.8 \times 10^6$   
 $40\mu\text{m} \pm 20\mu\text{m}$  leading edge



Fig. 26 - Infrared thermograms over flat plate / 2D ramp configurations at Mach 6 with  $T_w/T_0=0.6$  [21,43]



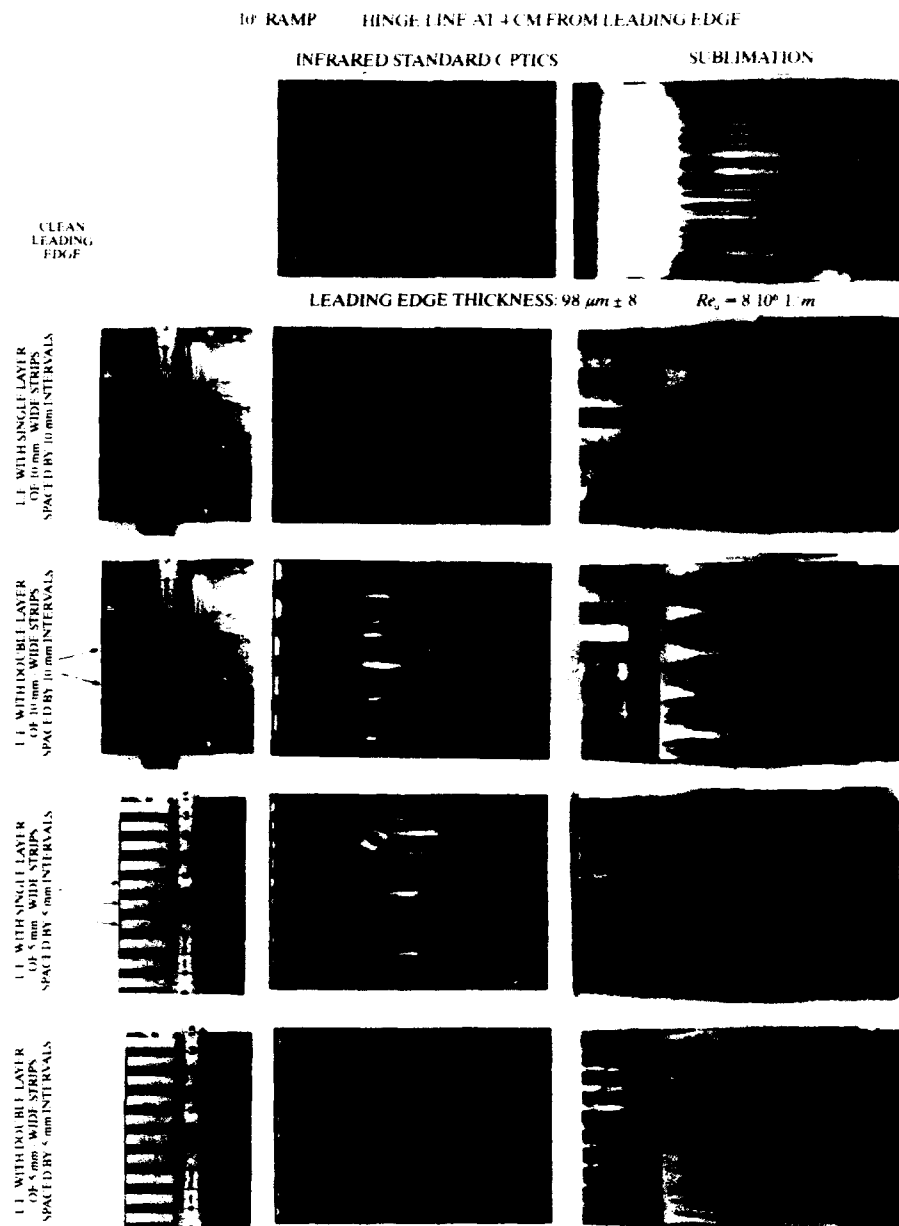


Fig. 27 - Infrared and sublimation observation of effect of leading edge perturbations on the formation of striations over a flat plate / 10° ramp configuration at Mach 6 with  $Re_L = 320,000$  and  $T_w/T_0 = 0.6$  [21,43]

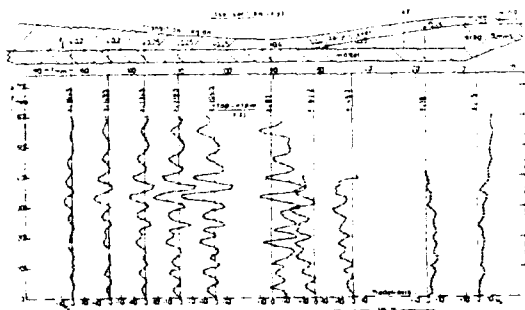


Fig. 28 - Streamwise evolution of spanwise pitot pressure distributions in the boundary / shear layer over a flat plate / 2D backward facing step configuration [52]

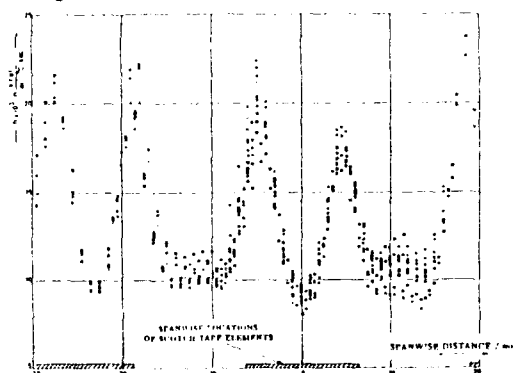


Fig. 29 - Spanwise heat transfer distribution in the reattachment region on the flat plate / 2D backward facing step configuration - with discrete perturbations at leading edge [51,52]



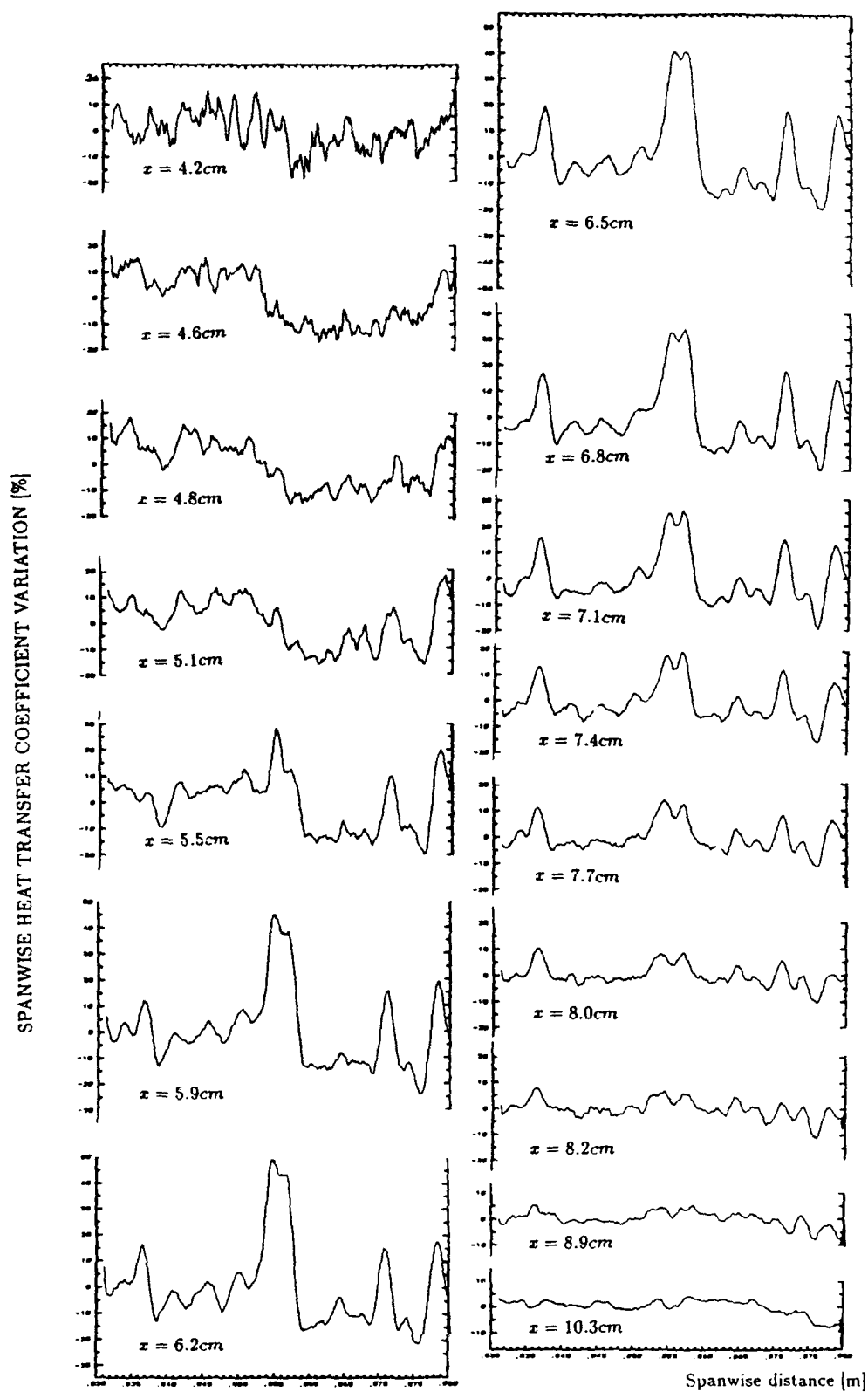


Fig. 30 - Streamwise evolution of spanwise heat transfer distribution over a 10° ramp configuration at Mach 6,  $Re_L = 320,000$  from thermogram of Fig. 26b (40  $\mu\text{m}$  leading edge) [21,43]



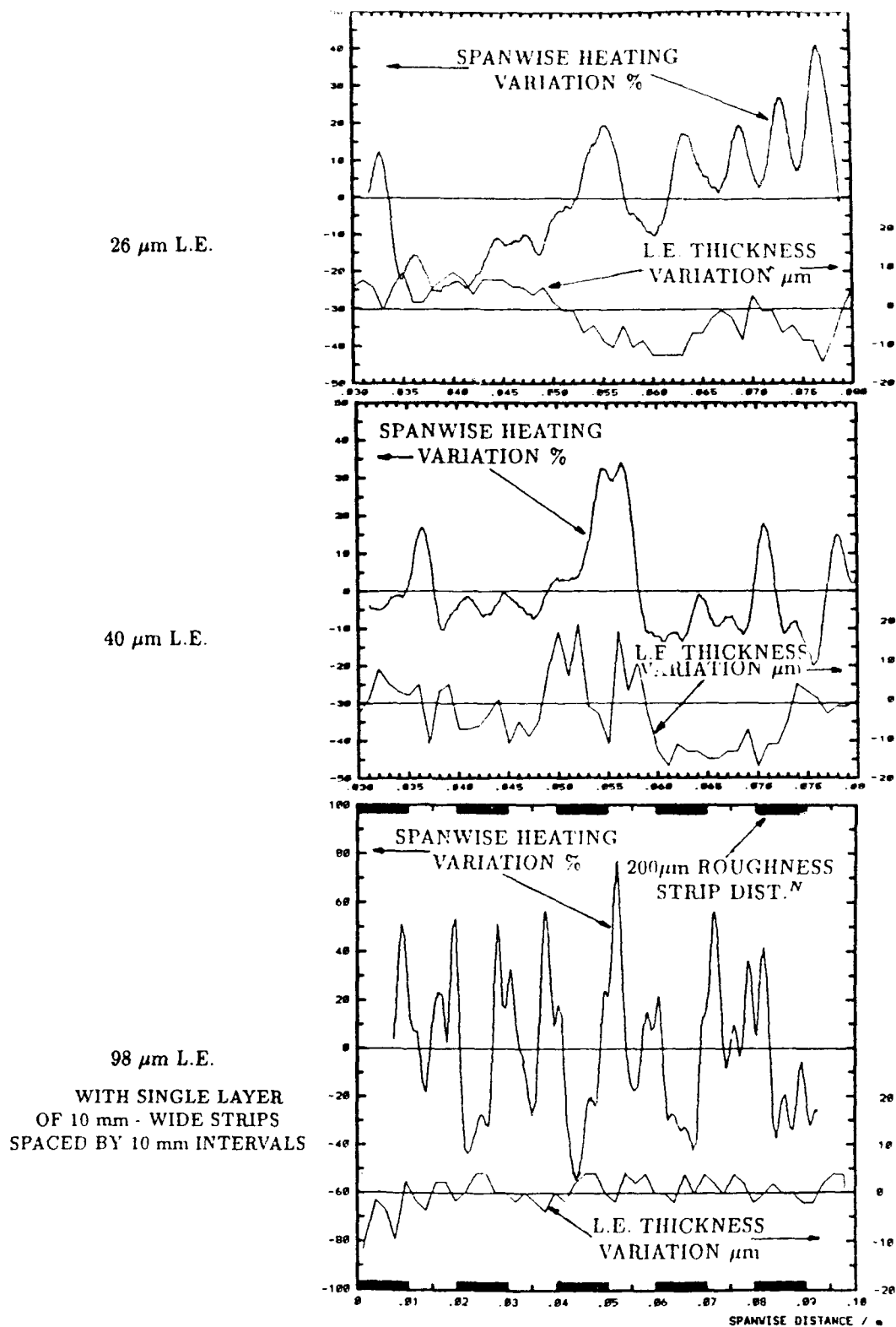


Fig. 31 - Effect of model leading edge thickness and/or disturbance distribution on spanwise heat transfer distribution on  $10^\circ$  deflected ramp at Mach 6,  $Re_L = 320,000$  [21,43]



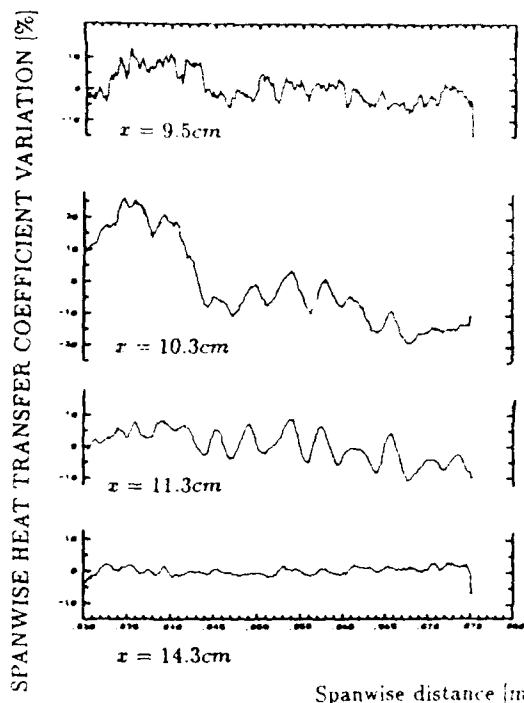


Fig. 32 - Streamwise evolution of spanwise heat transfer distribution over a  $15^\circ$  ramp configuration at Mach 6,  $Re_L = 720,000$  from thermogram of Fig. 26e ( $40 \mu\text{m}$  leading edge) [21,43]

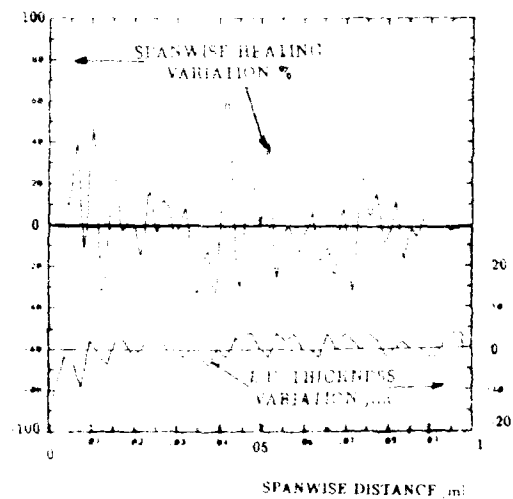


Fig. 34 - Spanwise heat transfer distribution over  $10^\circ$  ramp at Mach 6,  $Re_L = 320,000$  from a thermogram of Fig. 27 ( $98 \mu\text{m}$  clean leading edge) [57]

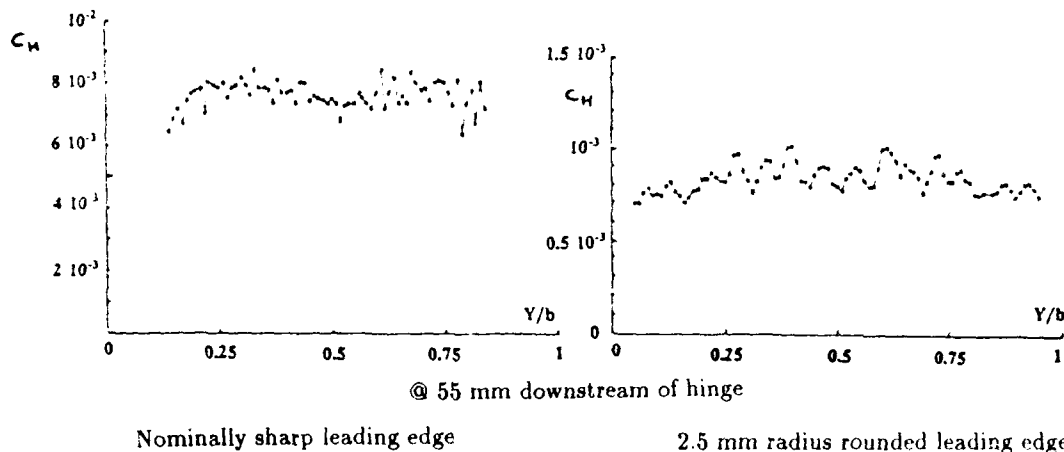
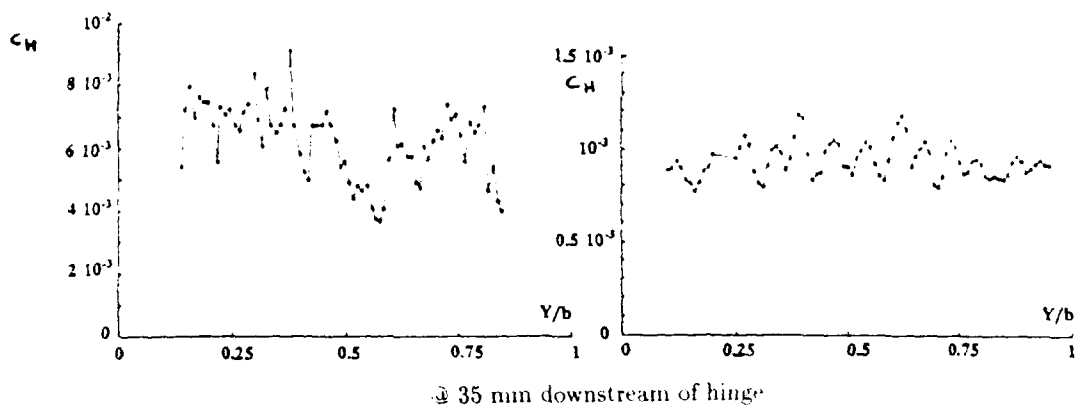


Fig. 33 - Spanwise heat transfer distributions on  $15^\circ$  ramp at Mach 10,  $Re_L = 2.1 \times 10^6$  [41,59]



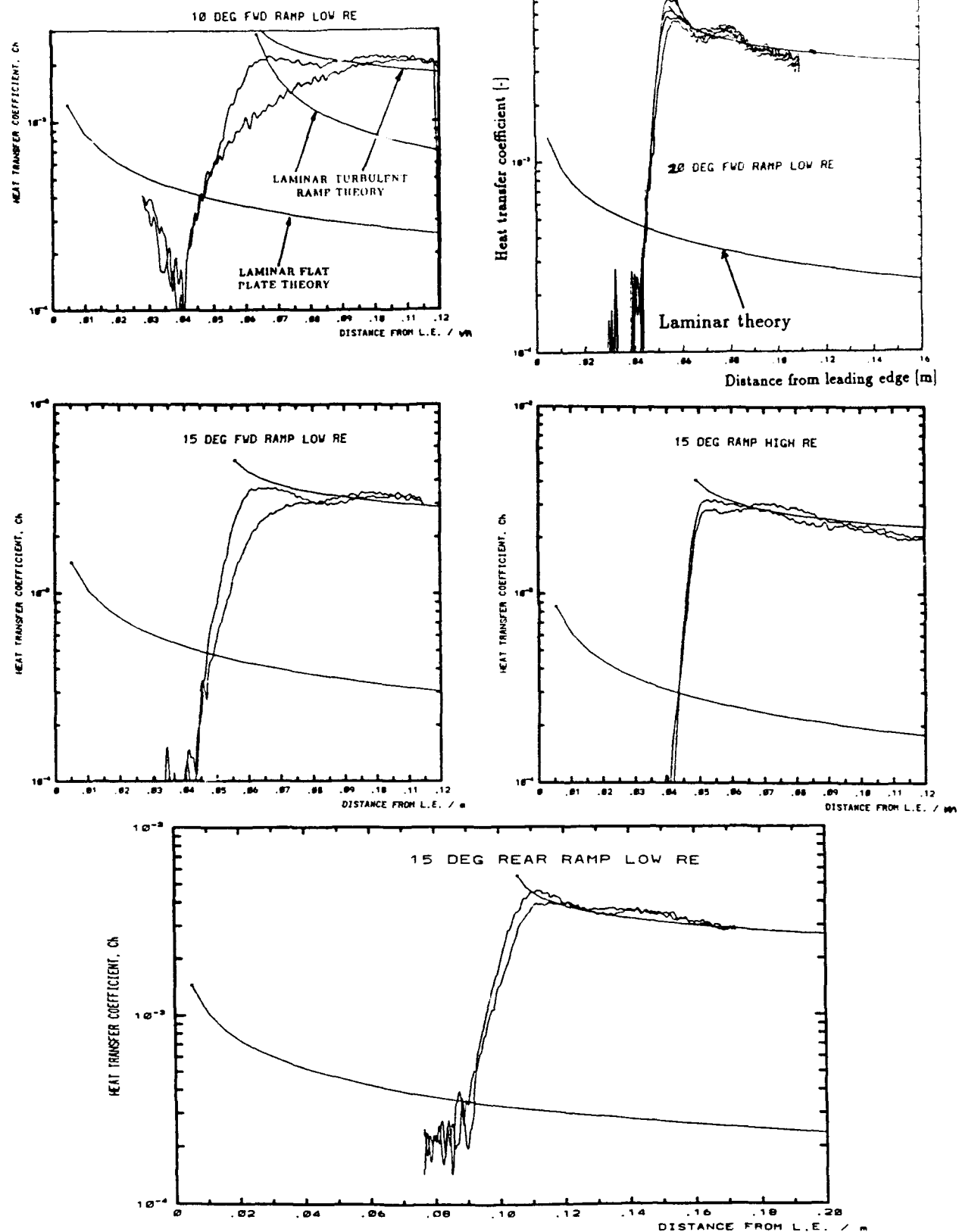


Fig. 35 - Minimum and maximum streamwise heat transfer distributions along flat plate / 2D ramp configurations at Mach 6 - effect of unit Reynolds number, ramp deflection and location (40  $\mu$ m leading edge) [21,43]



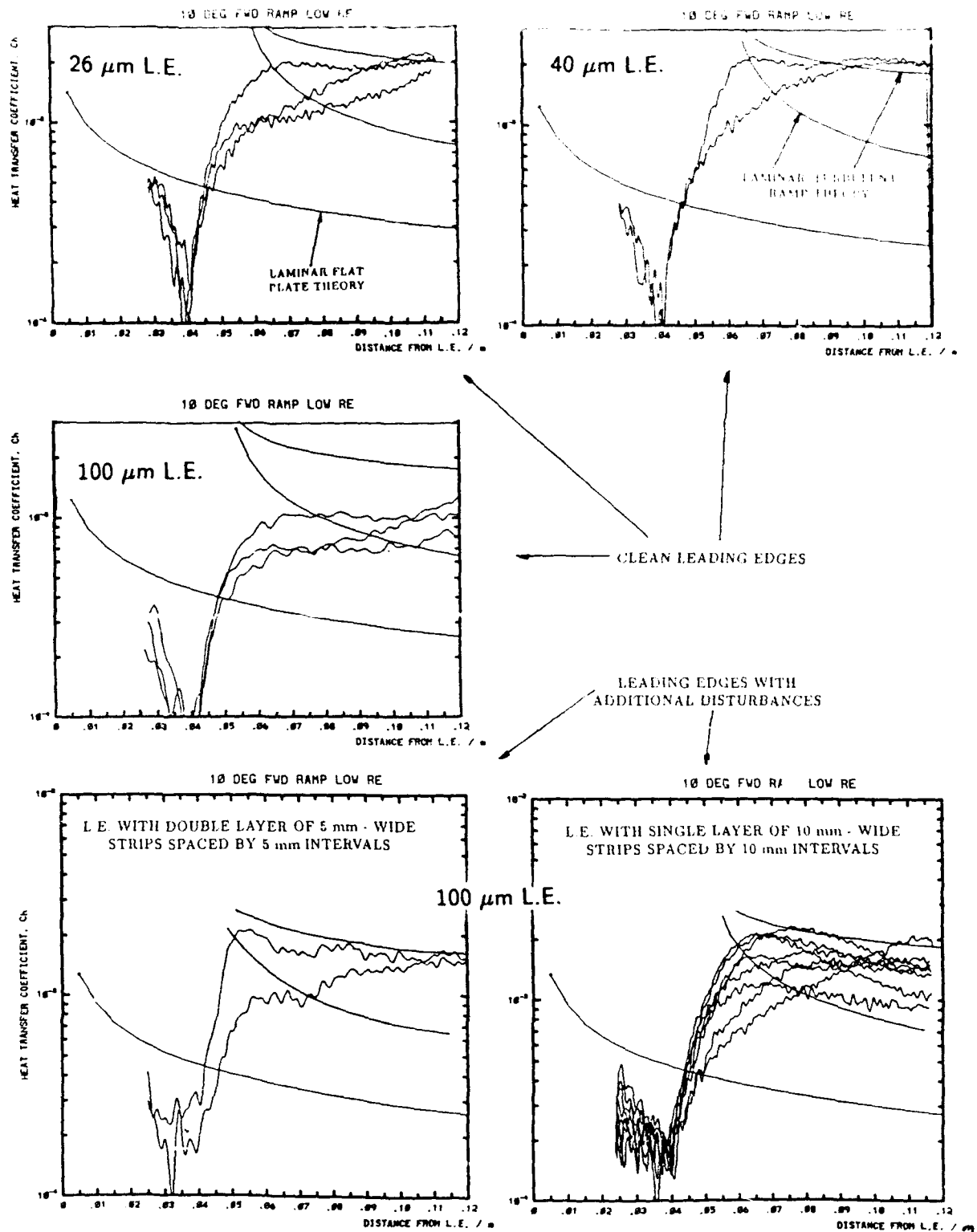


Fig. 36 - Minimum and maximum streamwise heat transfer distributions along flat plate / 2D 10° ramp configurations at Mach 6 with  $Re_L = 320,000$  - effect of leading edge thickness and irregularities / perturbations [21,43]



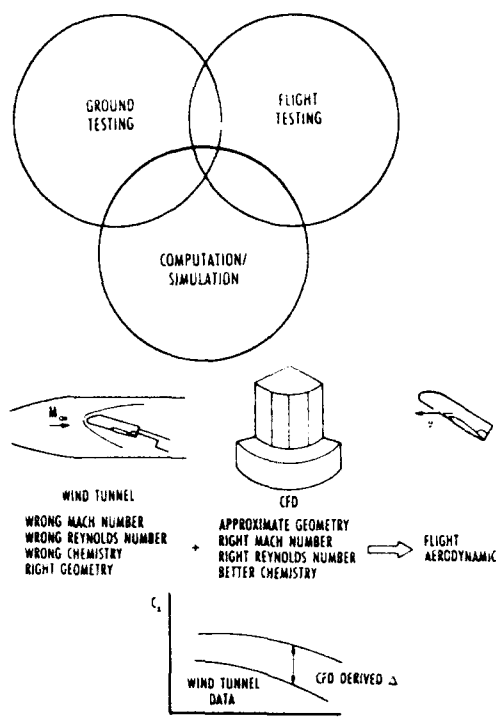


Fig. 37 - Integration of ground testing, computations and flight [68]

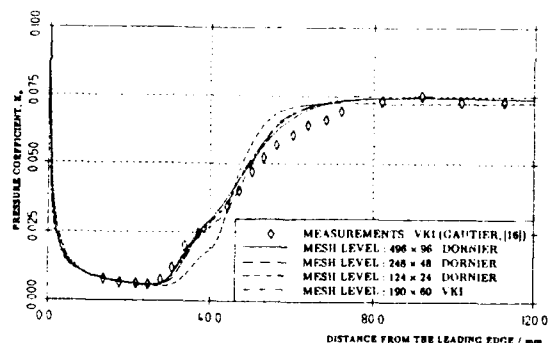


Fig. 39 - Comparison of measured and computed pressure distributions over a flat plate / 7.5° ramp configuration at Mach 6 with  $Re_L = 400,000$  and adiabatic wall temperature [78]

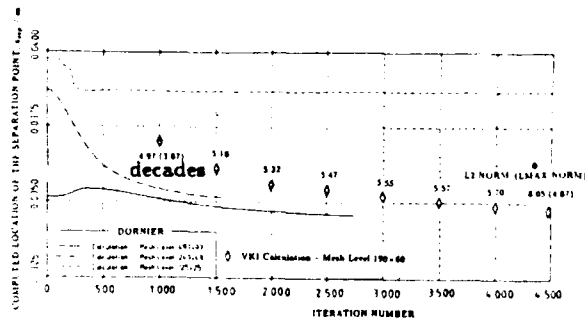


Fig. 40 - Evolution of the computed location of the separation point with number of iterations and grid refinement for the Mach 6, 7.5° ramp test case of Fig. 39 [78]

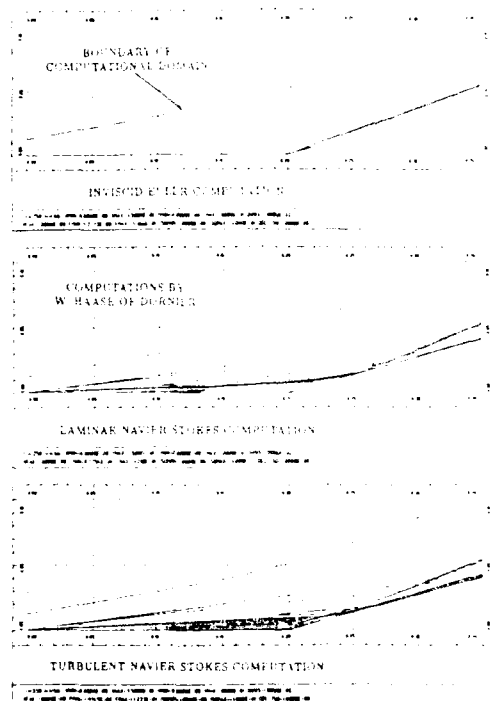


Fig. 38 - Computed Mach number contours over 15° compression ramp geometry at Mach 14.1 - inviscid, laminar and turbulent results,  $Re_L = 1.3 \times 10^6$  [75]

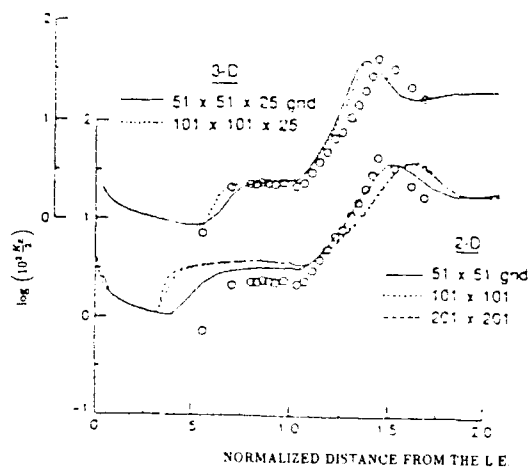


Fig. 41 - Comparison of measured and computed pressure distributions over a flat plate / 24° ramp configuration at Mach 14.1 with  $Re_L = 105,000$  and  $T_w/T_0 = 0.1$  [79]



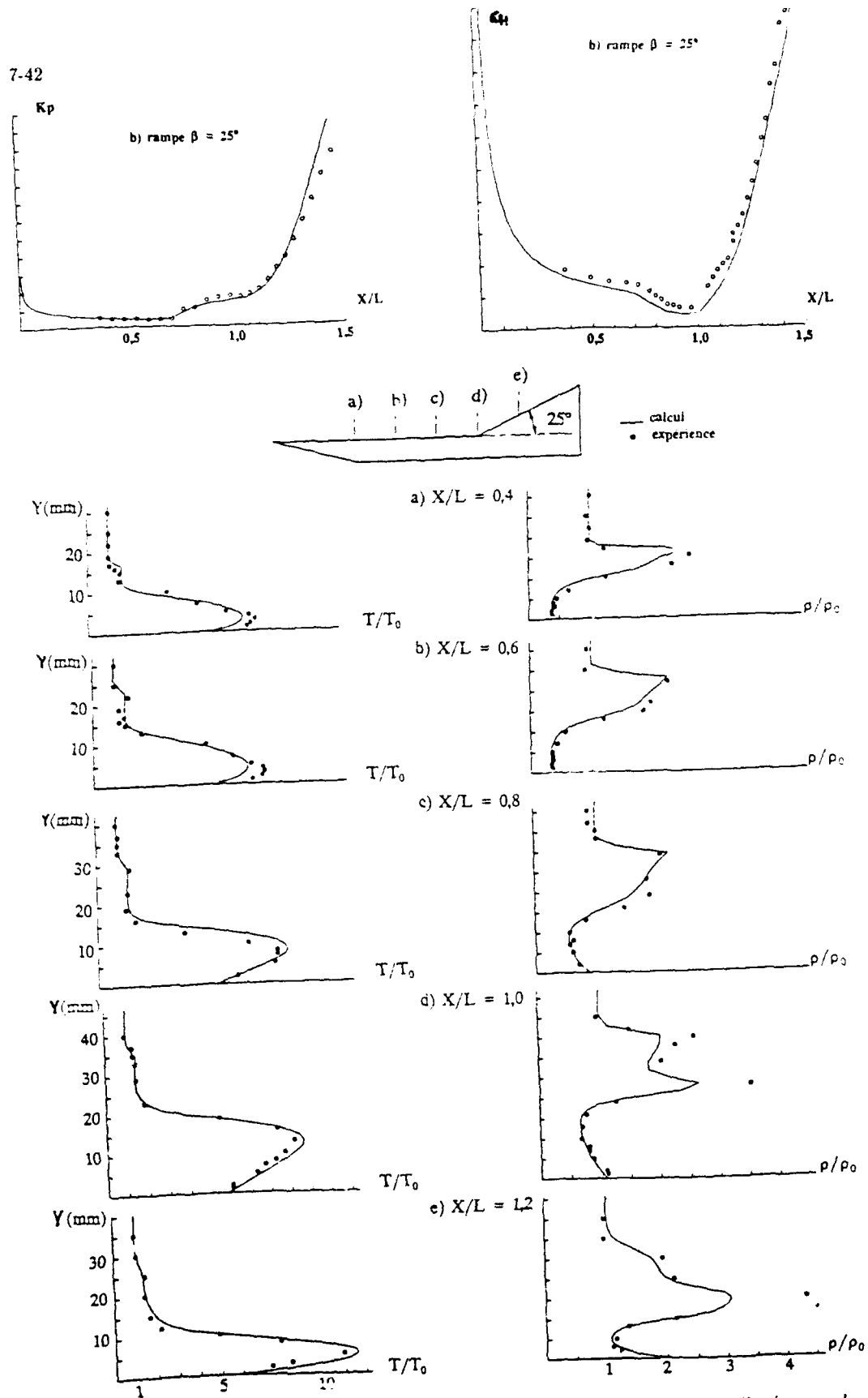


Fig. 42 - Comparison of measured and computed pressure and heat transfer distributions, and temperature and density profiles over a flat plate /  $25^\circ$  ramp configuration at Mach 10 with  $Re_L = 30,000$  [85]



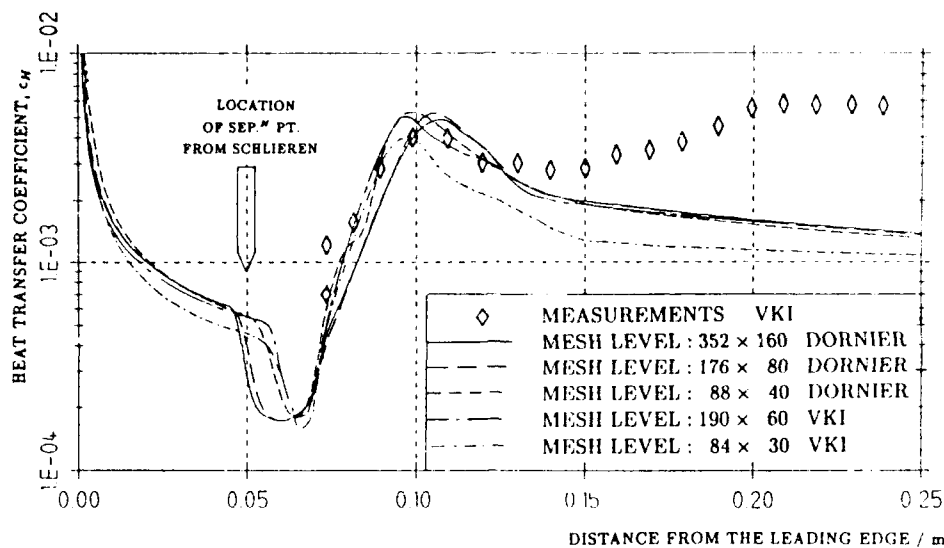


Fig. 43 - Comparison of measured and computed (laminar) heat transfer distributions over a flat plate / 15° ramp configuration at Mach 14.1 with  $Re_L = 450,000$  and  $T_w/T_0 = 0.12$  [75,78]

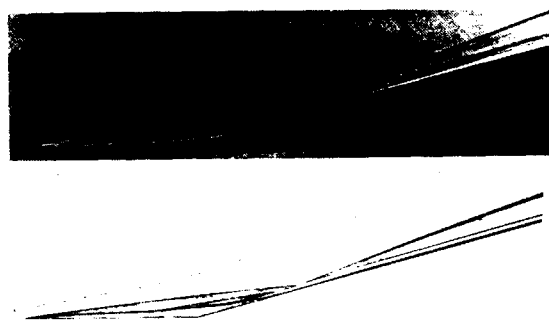


Fig. 44 - Comparison of computed (laminar) density contours with the schlieren photograph for the Mach 14 forward 15° ramp test case of Fig. 43 [75]

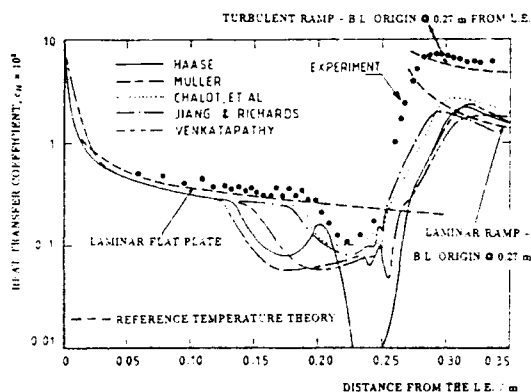


Fig. 45 - Comparison of measured and computed (laminar) heat transfer distributions over a flat plate / 15° ramp configuration at Mach 10 with  $Re_L = 2.1 \times 10^6$  and  $T_w/T_0 = 0.26$  [87]

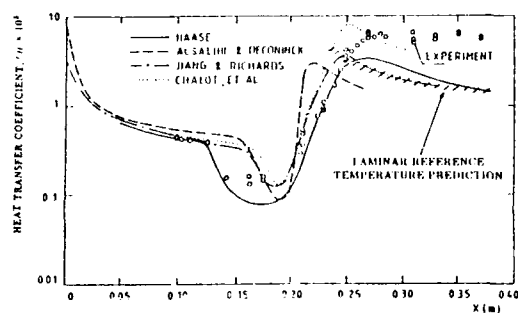


Fig. 46 - Comparison of measured and computed (laminar) heat transfer distributions over a flat plate / 15° ramp configuration at Mach 14.1 with  $Re_L = 1.3 \times 10^6$  and  $T_w/T_0 = 0.12$  [87]



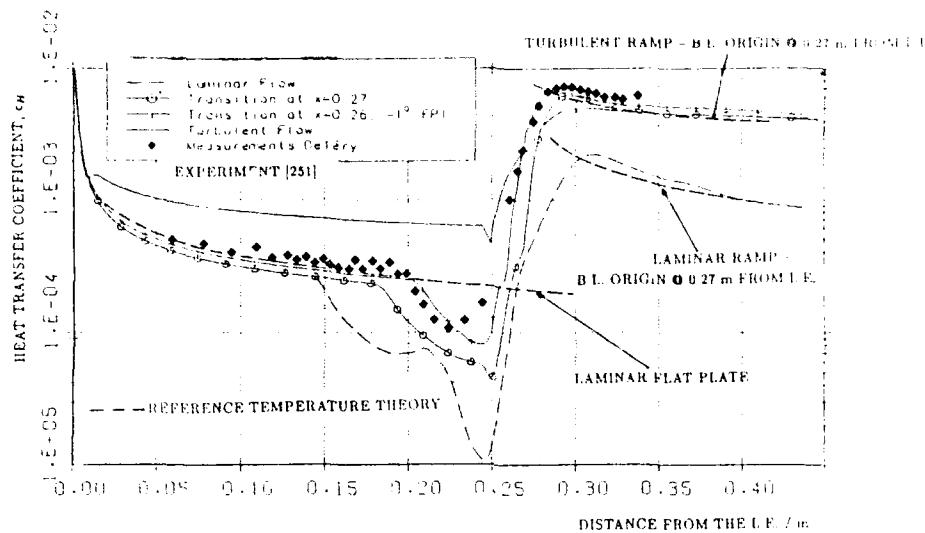


Fig. 47 - Comparison of measured and computed heat transfer distributions over the flat plate / rear 15° ramp configuration at Mach 10 with  $Re_L = 2.1 \times 10^6$  and  $T_w/T_0 = 0.26$  - laminar, turbulent and transitional computations with turbulence model "switched-on" at reattachment [88]

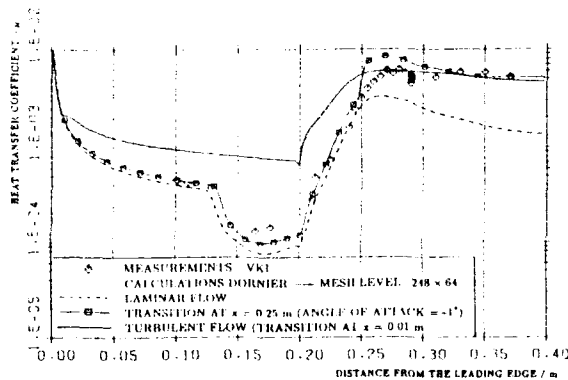


Fig. 48 - Comparison of measured and computed heat transfer distributions over the flat plate / rear 15° ramp configuration at Mach 14.1 with  $Re_L = 1.3 \times 10^6$  and  $T_w/T_0 = 0.12$  - laminar, turbulent and transitional computations with turbulence model "switched-on" at reattachment [75,78]

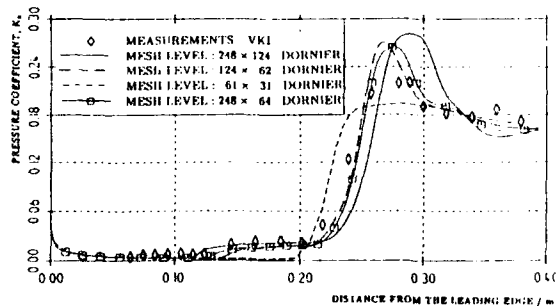


Fig. 49 - Comparison of measured and computed (laminar) pressure distributions over the flat plate / rear 15° ramp configuration at Mach 14.1 with  $Re_L = 1.3 \times 10^6$  and  $T_w/T_0 = 0.12$  - grid dependence study [78]

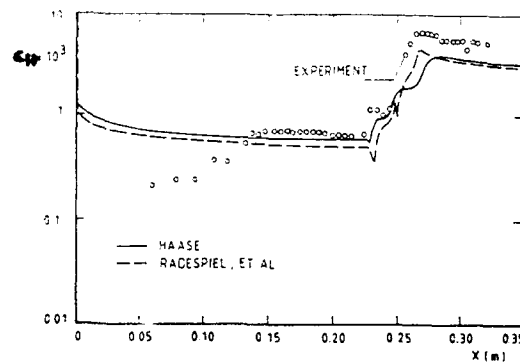
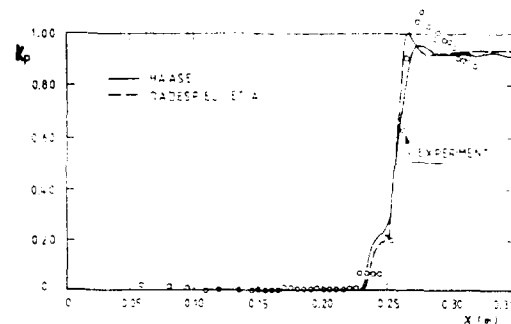


Fig. 50 - Comparison of measured and computed (turbulent) pressure and heat transfer distributions over a flat plate / 35° ramp configuration at Mach 5 - algebraic turbulence models [87]



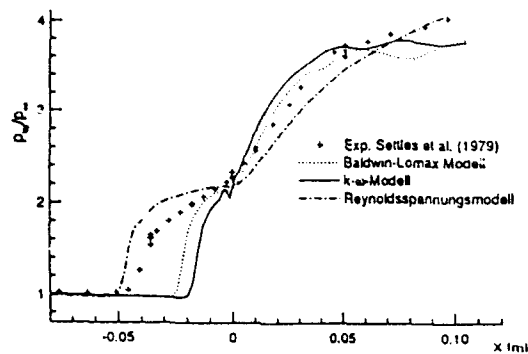


Fig. 51 - Comparison of measured and computed (turbulent) pressure distributions over an adiabatic wall flat plate / 24° ramp configuration at Mach 3 - influence of turbulence models [97]

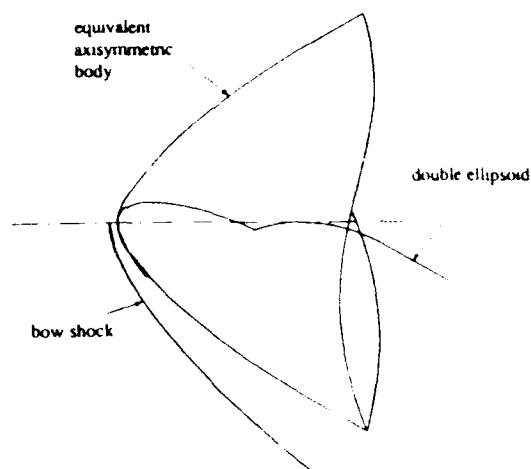


Fig. 53 - Schematic representation of the definition of the axisymmetric equivalent of a configuration at angle of attack

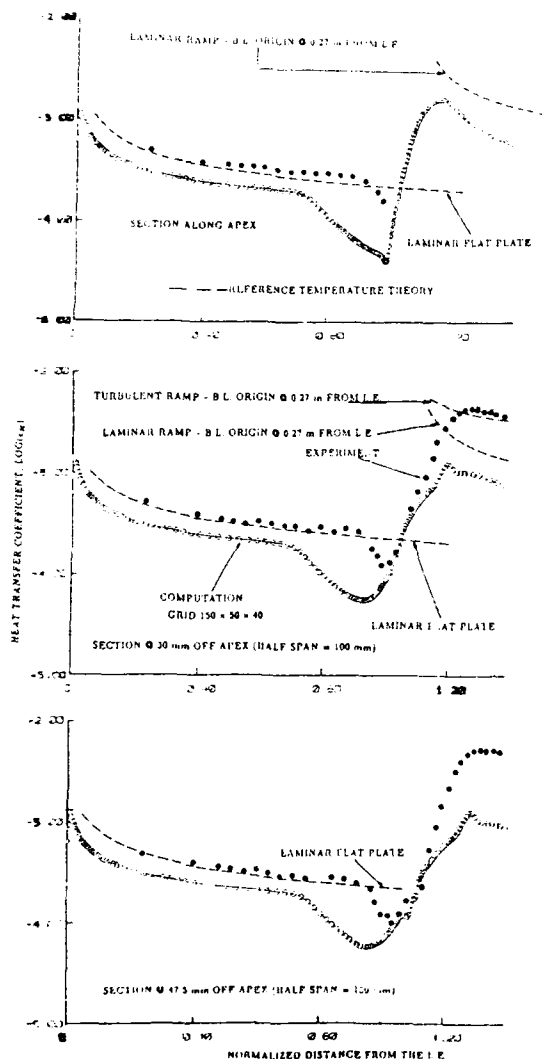


Fig. 52 - Comparison of measured and computed (laminar) heat transfer distributions over a flat plate / 30° swept, 15° ramp configuration at Mach 10, with  $Re_{apex} = 2.1 \times 10^6$  and  $T_w/T_0 = 0.26$  [94,99]

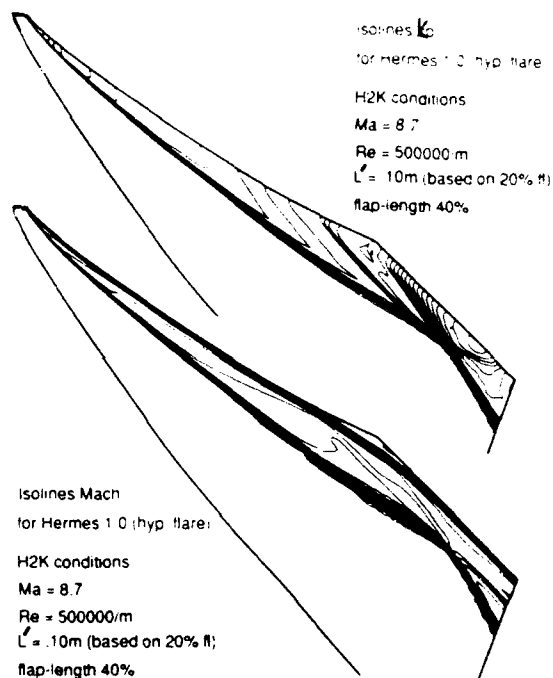


Fig. 54 - Pressure and Mach contours around the hyperboloid / flare configuration at Mach 8.7 [102]



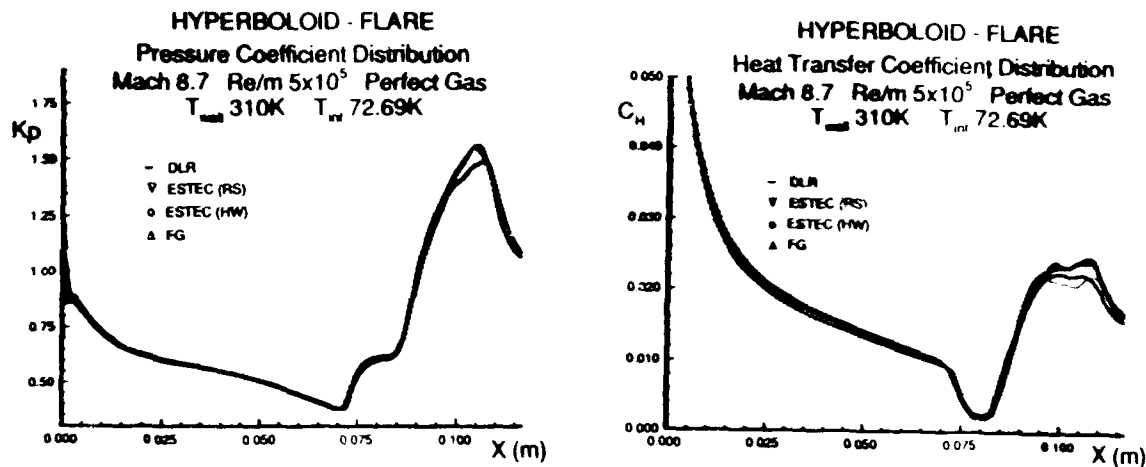


Fig. 55 - Comparison between predictions of the pressure and heat transfer distributions over the hyperboloid / flare configuration at Mach 8.7 [103-105]

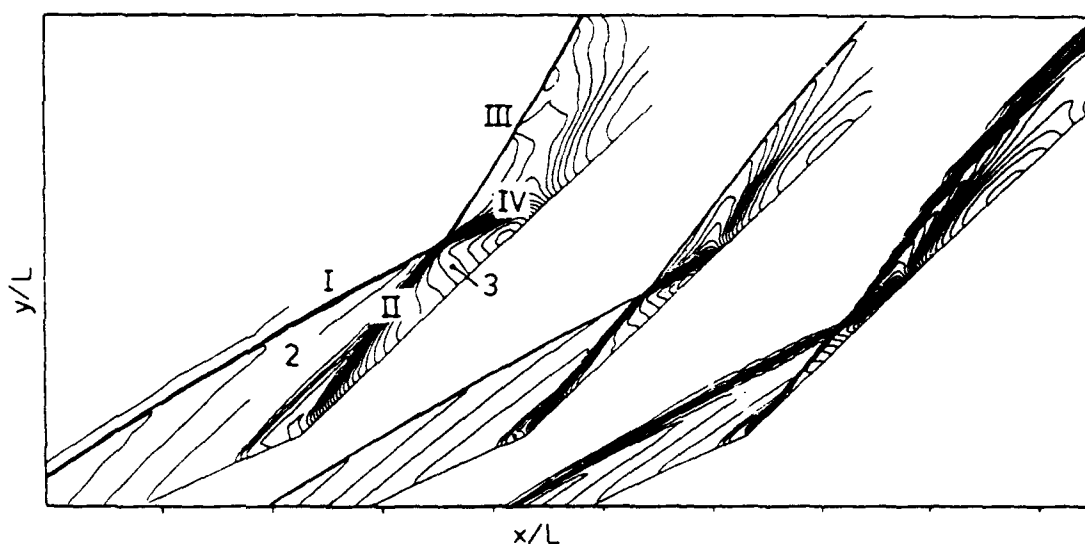


Fig. 56 - Pressure contours near the hinge line of the hyperboloid / flare configuration at Mach 25,  $Re_L = 120,000$ ,  $T_w = 800$  K,  $T_\infty = 192$  K (flight conditions, 77 km altitude); left: frozen air perfect gas model; center: chemical nonequilibrium air model; right: thermochemical equilibrium air model [106]

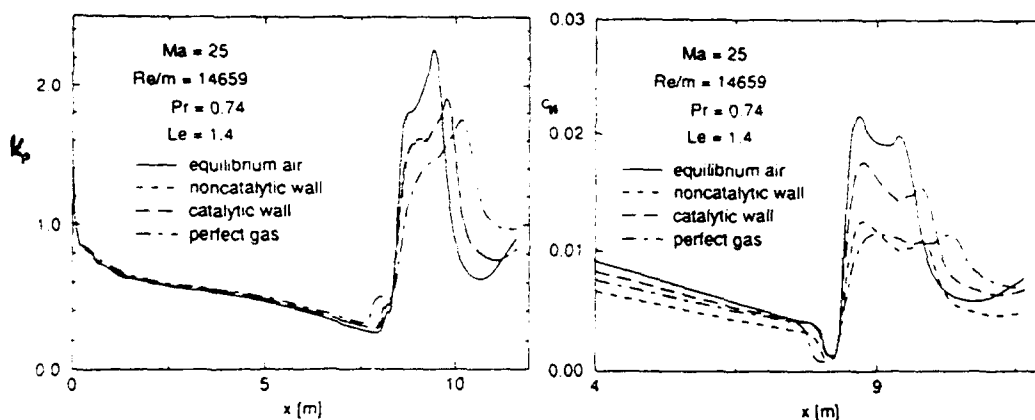


Fig. 57 - Effects of thermochemical air model on the pressure and heat transfer distributions over the hyperboloid / flare configuration at 77 km altitude flight conditions [106]





Fig. 58 - Temperature contours over double ellipsoid configuration at  $30^\circ$  angle of attack, Mach 25 - equilibrium gas computation [110]

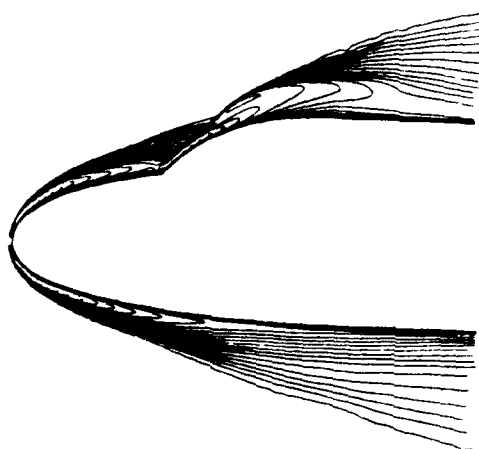


Fig. 59 - Temperature contours over double ellipsoid configuration at zero angle of attack, Mach 6.6 - equilibrium gas computation [111]



# REPORT DOCUMENTATION PAGE

<b>1. Recipient's Reference</b>	<b>2. Originator's Reference</b>	<b>3. Further Reference</b>	<b>4. Security Classification of Document</b>										
	AGARD-R-792	ISBN 92-835-0718-5	UNCLASSIFIED UNLIMITED										
<b>5. Originator</b>	Advisory Group for Aerospace Research and Development North Atlantic Treaty Organization 7 Rue Ancelle, 92200 Neuilly sur Seine, France												
<b>6. Title</b>	SPECIAL COURSE ON SHOCK-WAVE BOUNDARY-LAYER INTERACTIONS IN SUPERSONIC AND HYPERSONIC FLOWS												
<b>7. Presented at</b>	an AGARD-FDP-VKI Special Course at the VKI, Rhode-Saint-Genese, Belgium, 24th—28th May 1993.												
<b>8. Author(s)/Editor(s)</b>	Various		<b>9. Date</b> August 1993										
<b>10. Author's/Editor's Address</b>	Various		<b>11. Pages</b> 296										
<b>12. Distribution Statement</b>	There are no restrictions on the distribution of this document. Information about the availability of this and other AGARD unclassified publications is given on the back cover.												
<b>13. Keywords/Descriptors</b>	<table border="0"> <tr> <td>Supersonic flow</td> <td>Computerized simulation</td> </tr> <tr> <td>Hypersonic flow</td> <td>Numerical analysis</td> </tr> <tr> <td>Shock waves</td> <td>Laminar flow</td> </tr> <tr> <td>Boundary layer flow</td> <td>Turbulent flow</td> </tr> <tr> <td>Swept wings</td> <td>Flow distribution</td> </tr> </table>			Supersonic flow	Computerized simulation	Hypersonic flow	Numerical analysis	Shock waves	Laminar flow	Boundary layer flow	Turbulent flow	Swept wings	Flow distribution
Supersonic flow	Computerized simulation												
Hypersonic flow	Numerical analysis												
Shock waves	Laminar flow												
Boundary layer flow	Turbulent flow												
Swept wings	Flow distribution												
<b>14. Abstract</b>	<p>Lecture notes for the AGARD Fluid Dynamics Panel (FDP) Special Course on "Shock-Wave Boundary-Layer Interactions in Supersonic and Hypersonic Flows" are contained in this report. The objective of this course was to report on results from recent international research programmes with the aim of providing a consolidated review of these activities and a sound basis for developing more reliable methodologies for future vehicle design.</p> <p>The course also provided a focussed review of recent progress for swept interactions in both laminar and turbulent flows, including discussions on the following topics:</p> <ul style="list-style-type: none"> <li>— flowfield structure</li> <li>— scaling and similarity laws</li> <li>— effect of shock strength on flow features</li> <li>— effect of shock generator geometry for a given shock strength</li> <li>— experimental techniques for investigating swept interactions, particularly optical techniques</li> <li>— contributions of numerical simulations to the understanding of swept interactions.</li> </ul> <p>An indepth coverage of the effects of turbulence and turbulence modelling on the flowfields and other related phenomena resulting from swept-shock-wave/boundary-layer interactions is also provided in these notes.</p> <p>The material assembled in this report was prepared under the combined sponsorship of the AGARD Fluid Dynamics Panel and the von Kármán Institute (VKI) for Fluid Dynamics.</p>												



<p>AGARD Report 792 Advisory Group for Aerospace Research and Development, NATO SPECIAL COURSE ON SHOCK-WAVE/BOUNDARY-LAYER INTERACTIONS IN SUPERSONIC AND HYPERSONIC FLOWS Published August 1993 296 pages</p> <p>Lecture notes for the AGARD Fluid Dynamics Panel (FDP) Special Course on "Shock-Wave/Boundary-Layer Interactions in Supersonic and Hypersonic Flows" are contained in this report. The objective of this course was to report on results from recent international research programmes with the aim of providing a consolidated review of these activities and a sound basis for developing more reliable methodologies for future vehicle design.</p> <p>P.T.O.</p>	<p>AGARD-R-792</p> <p>Supersonic flow Hypersonic flow Shock waves Boundary layer flow Swept wings Computerized simulation Numerical analysis Laminar flow Turbulent flow Flow distribution</p>	<p>AGARD Report 792 Advisory Group for Aerospace Research and Development, NATO SPECIAL COURSE ON SHOCK-WAVE/BOUNDARY-LAYER INTERACTIONS IN SUPERSONIC AND HYPERSONIC FLOWS Published August 1993 296 pages</p> <p>Lecture notes for the AGARD Fluid Dynamics Panel (FDP) Special Course on "Shock-Wave/Boundary-Layer Interactions in Supersonic and Hypersonic Flows" are contained in this report. The objective of this course was to report on results from recent international research programmes with the aim of providing a consolidated review of these activities and a sound basis for developing more reliable methodologies for future vehicle design.</p> <p>P.T.O.</p>	<p>AGARD-R-792</p> <p>Supersonic flow Hypersonic flow Shock waves Boundary layer flow Swept wings Computerized simulation Numerical analysis Laminar flow Turbulent flow Flow distribution</p>
<p>AGARD Report 792 Advisory Group for Aerospace Research and Development, NATO SPECIAL COURSE ON SHOCK-WAVE/BOUNDARY-LAYER INTERACTIONS IN SUPERSONIC AND HYPERSONIC FLOWS Published August 1993 296 pages</p> <p>Lecture notes for the AGARD Fluid Dynamics Panel (FDP) Special Course on "Shock-Wave/Boundary-Layer Interactions in Supersonic and Hypersonic Flows" are contained in this report. The objective of this course was to report on results from recent international research programmes with the aim of providing a consolidated review of these activities and a sound basis for developing more reliable methodologies for future vehicle design.</p> <p>P.T.O.</p>	<p>AGARD-R-792</p> <p>Supersonic flow Hypersonic flow Shock waves Boundary layer flow Swept wings Computerized simulation Numerical analysis Laminar flow Turbulent flow Flow distribution</p>	<p>AGARD Report 792 Advisory Group for Aerospace Research and Development, NATO SPECIAL COURSE ON SHOCK-WAVE/BOUNDARY-LAYER INTERACTIONS IN SUPERSONIC AND HYPERSONIC FLOWS Published August 1993 296 pages</p> <p>Lecture notes for the AGARD Fluid Dynamics Panel (FDP) Special Course on "Shock-Wave/Boundary-Layer Interactions in Supersonic and Hypersonic Flows" are contained in this report. The objective of this course was to report on results from recent international research programmes with the aim of providing a consolidated review of these activities and a sound basis for developing more reliable methodologies for future vehicle design.</p> <p>P.T.O.</p>	<p>AGARD-R-792</p> <p>Supersonic flow Hypersonic flow Shock waves Boundary layer flow Swept wings Computerized simulation Numerical analysis Laminar flow Turbulent flow Flow distribution</p>



<p>The course also provided a focussed review of recent progress for swept interactions in both laminar and turbulent flows, including discussions on the following topics:</p> <ul style="list-style-type: none"> <li>— flowfield structure</li> <li>— scaling and similarity laws</li> <li>— effect of shock strength on flow features</li> <li>— effect of shock generator geometry for a given shock strength</li> <li>— experimental techniques for investigating swept interactions, particularly optical techniques</li> <li>— contributions of numerical simulations to the understanding of swept interactions.</li> </ul> <p>An in-depth coverage of the effects of turbulence and turbulence modelling on the flowfields and other related phenomena resulting from swept-shock-wave boundary-layer interactions is also provided in these notes.</p> <p>The material assembled in this report was prepared under the combined sponsorship of the AGARD Fluid Dynamics Panel and the von Karman Institute (VKI) for Fluid Dynamics. It was presented as an AGARD FDP/VKI Special Course at the VKI, Rhode-Saint-Genèse, Belgium, 24th—28th May 1993.</p> <p>ISBN 92-835-0718-5</p>	<p>The course also provided a focussed review of recent progress for swept interactions in both laminar and turbulent flows, including discussions on the following topics:</p> <ul style="list-style-type: none"> <li>— flowfield structure</li> <li>— scaling and similarity laws</li> <li>— effect of shock strength on flow features</li> <li>— effect of shock generator geometry for a given shock strength</li> <li>— experimental techniques for investigating swept interactions, particularly optical techniques</li> <li>— contributions of numerical simulations to the understanding of swept interactions.</li> </ul> <p>An in-depth coverage of the effects of turbulence and turbulence modelling on the flowfields and other related phenomena resulting from swept-shock-wave boundary-layer interactions is also provided in these notes.</p> <p>The material assembled in this report was prepared under the combined sponsorship of the AGARD Fluid Dynamics Panel and the von Karman Institute (VKI) for Fluid Dynamics. It was presented as an AGARD FDP/VKI Special Course at the VKI, Rhode-Saint-Genèse, Belgium, 24th—28th May 1993.</p> <p>ISBN 92-835-0718-5</p>
<p>The course also provided a focussed review of recent progress for swept interactions in both laminar and turbulent flows, including discussions on the following topics:</p> <ul style="list-style-type: none"> <li>— flowfield structure</li> <li>— scaling and similarity laws</li> <li>— effect of shock strength on flow features</li> <li>— effect of shock generator geometry for a given shock strength</li> <li>— experimental techniques for investigating swept interactions, particularly optical techniques</li> <li>— contributions of numerical simulations to the understanding of swept interactions.</li> </ul> <p>An in-depth coverage of the effects of turbulence and turbulence modelling on the flowfields and other related phenomena resulting from swept-shock-wave boundary-layer interactions is also provided in these notes.</p> <p>The material assembled in this report was prepared under the combined sponsorship of the AGARD Fluid Dynamics Panel and the von Karman Institute (VKI) for Fluid Dynamics. It was presented as an AGARD FDP/VKI Special Course at the VKI, Rhode-Saint-Genèse, Belgium, 24th—28th May 1993.</p> <p>ISBN 92-835-0718-5</p>	<p>The course also provided a focussed review of recent progress for swept interactions in both laminar and turbulent flows, including discussions on the following topics:</p> <ul style="list-style-type: none"> <li>— flowfield structure</li> <li>— scaling and similarity laws</li> <li>— effect of shock strength on flow features</li> <li>— effect of shock generator geometry for a given shock strength</li> <li>— experimental techniques for investigating swept interactions, particularly optical techniques</li> <li>— contributions of numerical simulations to the understanding of swept interactions.</li> </ul> <p>An in-depth coverage of the effects of turbulence and turbulence modelling on the flowfields and other related phenomena resulting from swept-shock-wave boundary-layer interactions is also provided in these notes.</p> <p>The material assembled in this report was prepared under the combined sponsorship of the AGARD Fluid Dynamics Panel and the von Karman Institute (VKI) for Fluid Dynamics. It was presented as an AGARD FDP/VKI Special Course at the VKI, Rhode-Saint-Genèse, Belgium, 24th—28th May 1993.</p> <p>ISBN 92-835-0718-5</p>



# DISCLAIMER NOTICE



THIS DOCUMENT IS BEST QUALITY AVAILABLE. THE COPY FURNISHED TO DTIC CONTAINED A SIGNIFICANT NUMBER OF COLOR PAGES WHICH DO NOT REPRODUCE LEGIBLY ON BLACK AND WHITE MICROFICHE.



AGARD

NATO  OTAN

7 RUE ANCELLE · 92200 NEUILLY-SUR-SEINE  
FRANCE

Télécopie (1)47.38.57.99 · Télax 610 176

DIFFUSION DES PUBLICATIONS  
AGARD NON CLASSIFIEES

Aucun stock de publications n'a existé à AGARD. A partir de 1993, AGARD détiendra un stock limité des publications associées aux cycles de conférences et cours spéciaux ainsi que les AGARDographies et les rapports des groupes de travail, organisés et publiés à partir de 1993 inclus. Les demandes de renseignements doivent être adressées à AGARD par lettre ou par fax à l'adresse indiquée ci-dessus. *Veillez ne pas téléphoner.* La diffusion initiale de toutes les publications de l'AGARD est effectuée auprès des pays membres de l'OTAN par l'intermédiaire des centres de distribution nationaux indiqués ci-dessous. Des exemplaires supplémentaires peuvent parfois être obtenus auprès de ces centres (à l'exception des Etats-Unis). Si vous souhaitez recevoir toutes les publications de l'AGARD, ou simplement celles qui concernent certains Panels, vous pouvez demander à être inclus sur la liste d'envoi de l'un de ces centres. Les publications de l'AGARD sont en vente auprès des agences indiquées ci-dessous, sous forme de photocopie ou de microfiche.

CENTRES DE DIFFUSION NATIONAUX

**ALLEMAGNE**

Fachinformationszentrum,  
Karlsruhe  
D-7514 Eggenstein-Leopoldshafen 2

**BELGIQUE**

Coordonnateur AGARD-VSL  
Etat-Major de la Force Aérienne  
Quartier Reine Elisabeth  
Rue d'Evere, 1140 Bruxelles

**CANADA**

Directeur du Service des Renseignements Scientifiques  
Ministère de la Défense Nationale  
Ottawa, Ontario K1A 0K2

**DANEMARK**

Danish Defence Research Establishment  
Ryvangs Allé 1  
P.O. Box 2715  
DK-2100 Copenhagen Ø

**ESPAGNE**

INTA (AGARD Publications)  
Pintor Rosales 34  
28008 Madrid

**ETATS-UNIS**

National Aeronautics and Space Administration  
Langley Research Center  
M/S 180  
Hampton, Virginia 23665

**FRANCE**

O.N.E.R.A. (Direction)  
29, Avenue de la Division Leclerc  
92322 Châtillon Cedex

**GRECE**

Hellenic Air Force  
Air War College  
Scientific and Technical Library  
Dekelia Air Force Base  
Dekelia, Athens TGA 1010

**ISLANDE**

Director of Aviation  
c/o Flugrad  
Reykjavik

**ITALIE**

Aeronautica Militare  
Ufficio del Delegato Nazionale all'AGARD  
Aeroporto Pratica di Mare  
00040 Pomezia (Roma)

**LUXEMBOURG**

Voir Belgique

**NORVEGE**

Norwegian Defence Research Establishment  
Attn: Biblioteket  
P.O. Box 25  
N-2007 Kjeller

**PAYS-BAS**

Netherlands Delegation to AGARD  
National Aerospace Laboratory NLR  
P.O. Box 90502  
1006 BM Amsterdam

**PORTUGAL**

Força Aérea Portuguesa  
Centro de Documentação e Informação  
Alfragide  
2700 Amadora

**ROYAUME UNI**

Defence Research Information Centre  
Kentigern House  
65 Brown Street  
Glasgow G2 8EX

**TURQUIE**

Milli Savunma Başkanlığı (MSB)  
ARGE Daire Başkanlığı (ARGE)  
Ankara

Le centre de distribution national des Etats-Unis (NASA/Langley) ne détient PAS de stocks des publications de l'AGARD. D'éventuelles demandes de photocopies doivent être formulées directement auprès du NASA Center for Aerospace Information (CASI) à l'adresse suivante:

AGENCES DE VENTE

NASA Center for  
Aerospace Information (CASI)  
800 Elkridge Landing Road  
Linthicum Heights, MD 21090-2934  
United States

ESA/Information Retrieval Service  
European Space Agency  
10, rue Mario Nikis  
75015 Paris  
France

The British Library  
Document Supply Division  
Boston Spa, Wetherby  
West Yorkshire LS23 7BQ  
Royaume Uni

Les demandes de microfiches ou de photocopies de documents AGARD (y compris les demandes faites auprès du CASI) doivent comporter la dénomination AGARD, ainsi que le numéro de série d'AGARD (par exemple AGARD-AG-315). Des informations analogues, telles que le titre et la date de publication sont souhaitables. Veuillez noter qu'il y a lieu de spécifier AGARD-R-nnn et AGARD-AR-nnn lors de la commande des rapports AGARD et des rapports consultatifs AGARD respectivement. Des références bibliographiques complètes ainsi que des résumés des publications AGARD figurent dans les journaux suivants:

Scientific and Technical Aerospace Reports (STAR)  
publié par la NASA Scientific and Technical  
Information Program  
NASA Headquarters (JTT)  
Washington D.C. 20546  
Etats-Unis

Government Reports Announcements and Index (GRA&I)  
publié par le National Technical Information Service  
Springfield  
Virginia 22161  
Etats-Unis  
(accessible également en mode interactif dans la base de  
données bibliographiques en ligne du NTIS, et sur CD-ROM)

  
Imprimé par Specialised Printing Services Limited  
40 Chigwell Lane, Loughborough, Essex IG10 3TZ